



ISSN 1580-3155

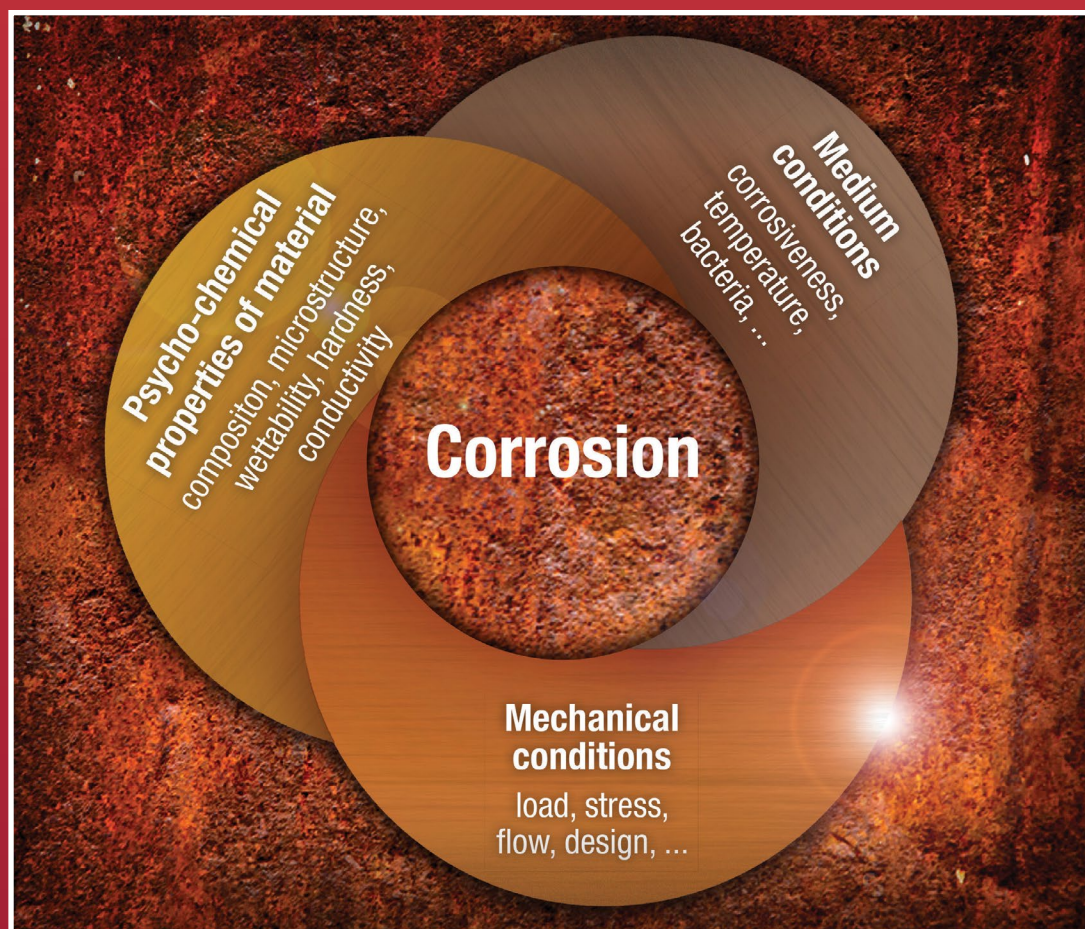
Pages 510–750 ■ Year 2019, Vol. 66, No. 3

Slovensko kemijsko društvo  
Slovenian Chemical Society



# ActaChimicaSlo ActaChimicaSlo SlovenicaActaC 3

66/2019



---

## EDITOR-IN-CHIEF

KSENIJA KOGEJ

Slovenian Chemical Society, Hajdrihova 19, SI-1000 Ljubljana, Slovenija,

E-mail: ACSi@fkt.uni-lj.si, Telephone: (+386)-1-479-8538

## ASSOCIATE EDITORS

Janez Cerkovnik, University of Ljubljana, Slovenia

Krištof Kranjc, University of Ljubljana, Slovenia

Ksenija Kogej, University of Ljubljana, Slovenia

Franc Perdih, University of Ljubljana, Slovenia

Aleš Podgornik, University of Ljubljana, Slovenia

Helena Prosen, University of Ljubljana, Slovenia

Damjana Rozman, University of Ljubljana, Slovenia

Melita Tramšek, Jožef Stefan Institute, Slovenia

Irena Vovk, National Institute of Chemistry, Slovenia

## ADMINISTRATIVE ASSISTANT

Marjana Gantar Albreht, National Institute of Chemistry, Slovenia

---

## EDITORIAL BOARD

Wolfgang Buchberger, Johannes Kepler University, Austria

Alojz Demšar, University of Ljubljana, Slovenia

Stanislav Gobec, University of Ljubljana, Slovenia

Marko Goličnik, University of Ljubljana, Slovenia

Günter Grampp, Graz University of Technology, Austria

Wojciech Grochala, University of Warsaw, Poland

Danijel Kikelj, Faculty of Pharmacy, Slovenia

Janez Košmrlj, University of Ljubljana, Slovenia

Blaž Likozar, National Institute of Chemistry, Slovenia

Mahesh K. Lakshman, The City College and

The City University of New York, USA

Janez Mavri, National Institute of Chemistry, Slovenia

Friedrich Sreenc, University of Minnesota, USA

Walter Steiner, Graz University of Technology, Austria

Jurij Svete, University of Ljubljana, Slovenia

Ivan Švancara, University of Pardubice, Czech Republic

Jiri Pinkas, Masaryk University Brno, Czech Republic

Gašper Tavčar, Jožef Stefan Institute, Slovenia

Christine Wandrey, EPFL Lausanne, Switzerland

Ennio Zangrando, University of Trieste, Italy

---

## ADVISORY EDITORIAL BOARD

### Chairman

Branko Stanovnik, Slovenia

### Members

Josef Barthel, Germany

Udo A. Th. Brinkman, The Netherlands

Attilio Cesaro, Italy

Dušan Hadži, Slovenia

Vida Hudnik, Slovenia

Venčeslav Kaučič, Slovenia

Željko Knez, Slovenia

Radovan Komel, Slovenia

Janez Levec, Slovenia

Stane Pejovnik, Slovenia

Anton Perdih, Slovenia

Slavko Pečar, Slovenia

Andrej Petrič, Slovenia

Boris Pihlar, Slovenia

Milan Randić, Des Moines, USA

Jože Škerjanc, Slovenia

Miha Tišler, Slovenia

Đurđa Vasić-Rački, Croatia

Marjan Veber, Slovenia

Gorazd Vesnaver, Slovenia

Jure Zupan, Slovenia

Boris Žemva, Slovenia

Majda Žigon, Slovenia

*Acta Chimica Slovenica* is indexed in: Academic Search Complete, Central & Eastern European Academic Source, Chemical Abstracts Plus, Chemical Engineering Collection (India), Chemistry Citation Index Expanded, Current Contents (Physical, Chemical and Earth Sciences), Digitalna knjižnica Slovenije (dLib.si), DOAJ, ISI Alerting Services, PubMed, Science Citation Index Expanded, SciFinder (CAS), Scopus and Web of Science. Impact factor for 2017 is IF = 1.104.



Articles in this journal are published under the  
Creative Commons Attribution 4.0 International License

### Izdaja – Published by:

SLOVENSKO KEMIJSKO DRUŠTVO – SLOVENIAN CHEMICAL SOCIETY

Naslov redakcije in uprave – Address of the Editorial Board and Administration

Hajdrihova 19, SI-1000 Ljubljana, Slovenija

Tel.: (+386)-1-476-0252; Fax: (+386)-1-476-0300; E-mail: chem.soc@ki.si

### Izdajanje sofinancirajo – Financially supported by:

Slovenian Research Agency, Ljubljana, Slovenia

National Institute of Chemistry, Ljubljana, Slovenia

Jožef Stefan Institute, Ljubljana, Slovenia

Faculty of Chemistry and Chemical Technology at University of Ljubljana, Slovenia

Faculty of Chemistry and Chemical Engineering at University of Maribor, Slovenia

Faculty of Pharmacy at University of Ljubljana, Slovenia

University of Nova Gorica, Nova Gorica, Slovenia

Slovensko kemijsko društvo  
Slovenian Chemical Society



*Acta Chimica Slovenica* izhaja štirikrat letno v elektronski obliki na spletni strani <http://acta.chem-soc.si>. V primeru posvečenih številkih izhaja revija tudi v tiskani obliki v omejenem številu izvodov.

*Acta Chimica Slovenica* appears quarterly in electronic form on the web site <http://acta.chem-soc.si>. In case of dedicated issues, a limited number of printed copies are issued as well.

Transakcijski račun: 02053-0013322846 Bank Account No.: SI56020530013322846-Nova Ljubljanska banka d. d., Trg republike 2, SI-1520 Ljubljana, Slovenia, SWIFT Code: LJBA SI 2X

Oblikovanje ovitka – Design cover: KULT, oblikovalski studio, Simon KAJTNA, s. p. Grafična priprava za tisk: Majanafin, d. o. o.

## Graphical Contents



Acta Chimica Slo  
Acta Chimica Slo  
Slovenica Acta C

Year 2019, Vol. 66, No. 3

## REVIEW

511–533 General chemistry

### Contemporary Modes of Corrosion Protection and Functionalization of Materials

Ingrid Milošev

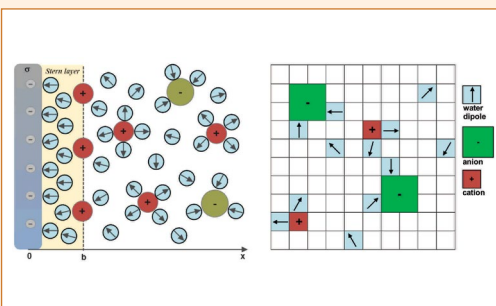


## FEATURE ARTICLE

534–541 Feature article

### Differential Capacitance of Electric Double Layer – Influence of Asymmetric Size of Ions, Thickness of Stern Layer and Orientational Ordering of Water Dipoles

Aleš Iglič, Ekaterina Gongadze and Veronika Kralj-Iglič

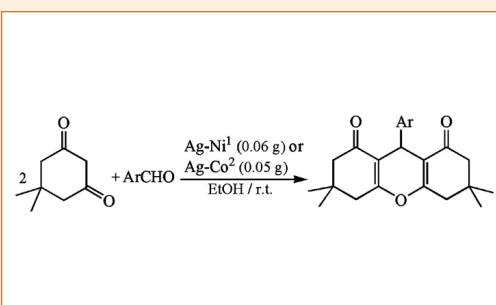


## SCIENTIFIC PAPER

542–551 Organic chemistry

### Synthesis and Study of Catalytic, Anti-Bacterial, Anti-Oxidant, and DNA Cleavage Properties of Ag–Co and Ag–Ni Magnetic Nanoparticles

Keveh Pravanak Boroujeni, Mansooreh Shahrokh, Jamshid Karvani, Niloofar Moradi, Ahmad Farokhnia and Mohsen Mobini



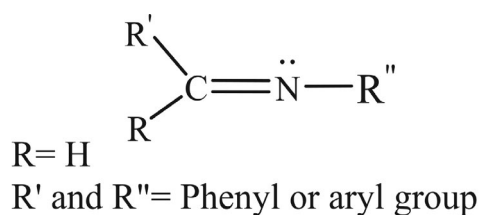


552–559

Organic chemistry

## Synthesis and Characterization of Novel Five-Membered Heterocycles and Their Activity against Candida Yeasts

Hiba Maher Tawfeeq, Rasim Farraj Muslim, Obaid Hasan Abid and Mustafa Nadhim Owaid

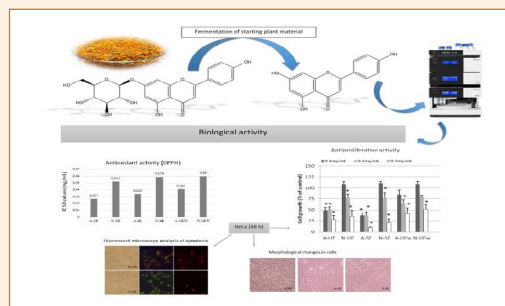


560–569

Biomedical applications

## Autofermentation of Chamomile Ligulate Flowers Promote Antitumor Effects *in vitro*

Marijana Jukić, Aleksandra Cvetanović, Katarina Mišković Špoljarić, Saša Savić, Jaroslava Švarc-Gajić, Zoran Zeković and Ljubica Glavaš-Obrovac

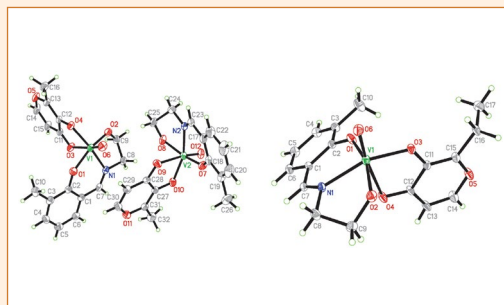


570–575

Inorganic chemistry

## Synthesis, Characterization and Crystal Structures of Oxidovanadium(V) Complexes with Schiff Base and Pyrone Ligands and Their Antimicrobial Activity

Guo-Xu He, Ling-Wei Xue, Qin-Long Peng, Pan-Pan Wang and Hui-Jie Zhang

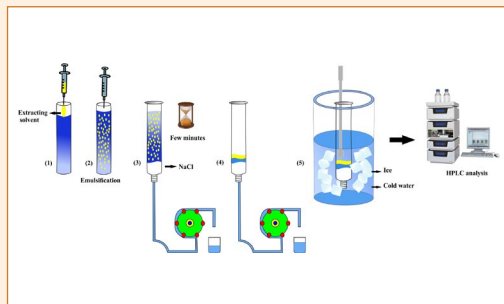


576–583

Analytical chemistry

## Screening of Parabens in Natural Water by Salting-out Based Centrifugeless Dispersive Liquid-liquid Microextraction Combined with HPLC-UV

Hadi Farahani

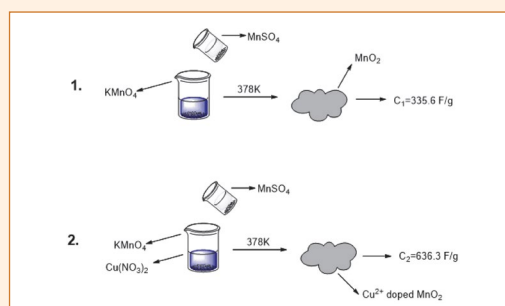


584–591

Materials science

## Synthesis of Copper-Doped MnO<sub>2</sub> Electrode Materials by One-Step Hydrothermal Method for High Performance

Dongxia An, Yu Zhang, Hong Zhang, Gang Ma, Cuimiao Zhang and Zhiguang Ma



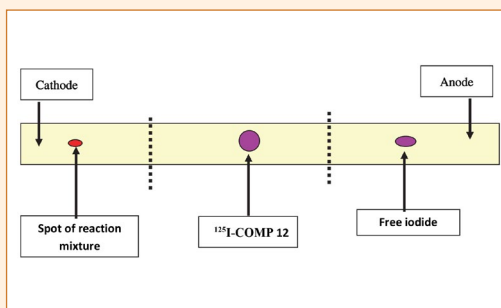


592–602

Organic chemistry

## Synthesis, Labeling and Biological Evolution of New Thiopyrano[2,3-*b*]Pyridine Derivatives as Potential Anticancer Agents

Mamdouh Abdel-Monem Sofan, Wafaa Salama Hamama, Ibrahim Ibrahim EL-Hawary, Ismail Taha Ibrahim and Hanafi Hassan Zoorob

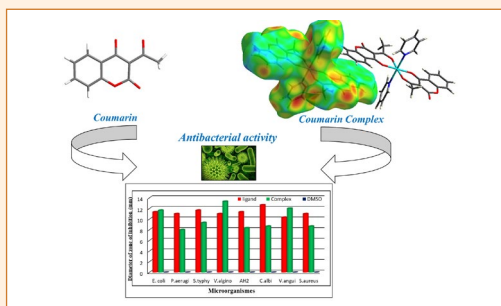


603–613

Inorganic chemistry

## Crystal Structure, Hirshfeld Surface Analysis and Biological Activities of *trans*-Dipyridinebis (3-Acetyl-2-Oxo-2*H*-Chromen-4-Olato)Cobalt(II)

Linda Bejaoui, Jan Rohlíček, Vaclav Eigner, Amel Ismail, Monia El Bour and Rached Ben Hassen

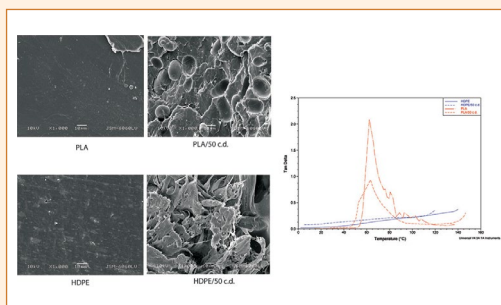


614–621

Materials science

## The Influence of Cardboard Dust on Structural, Morphological and Mechanical Properties of Biocomposite PLA and HDPE Filaments for 3D Printing

Diana Gregor-Svetec, Urška Stankovič Elesini, Raša Urbas, Mirjam Leskovšek and Urška Vrabič Brodnjak

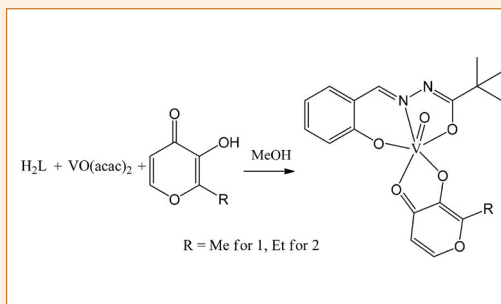


622–628

Inorganic chemistry

## Synthesis, Crystal Structures and Antimicrobial Activity of Oxidovanadium(V) Complexes with Hydrazone and Pyrone Ligands

Ling-Wei Xue, Yong-Jun Han and Xiao-Qiang Luo

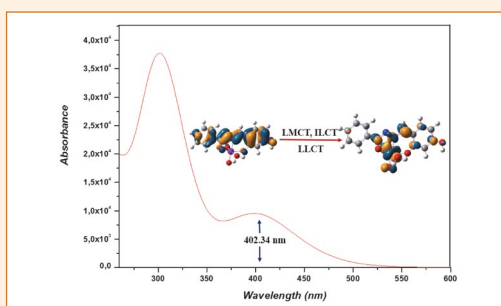


629–637

Physical chemistry

## DFT/TDDFT Investigation on the Electronic Structure and Spectroscopic Properties of Cis-Dioxomolybdenum (VI) Complexes

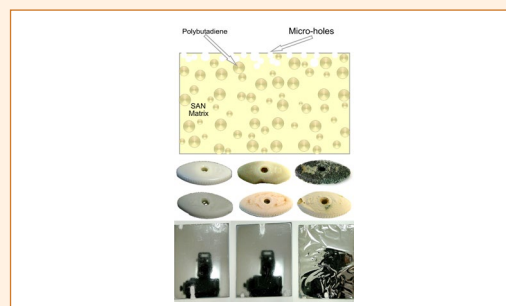
Imane Seghir, Nadia Nebbache, Yazid Meftah, Salah Eddine Hachani and Samira Maou



638–647 Materials science

## Effect of Swelling of Chemical Reagents and the Sulfuric-Chromic Acid Bath on Surface Texturizing of Poly(Acrylonitrile-Butadiene-Styrene)

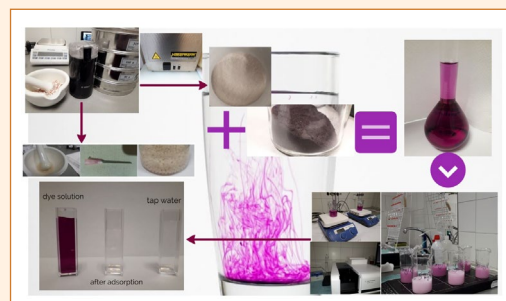
Lorena Magallón Cacho, José de Jesús Pérez Bueno, Yunny Meas Vong and Guy Stremsdoerfer



648–658 Chemical, biochemical and environmental engineering

## Adsorptive Removal of Remazol Brilliant Violet-5R Dye from Aqueous Solutions using Calcined Eggshell as Biosorbent

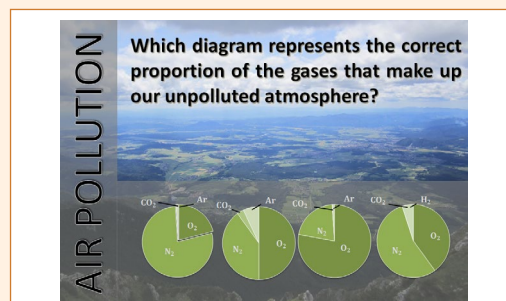
Eszter Rápó, Katalin Posta, Maria Suciú, Robert Szép and Szende Tonk



659–667 Chemical education

## Assessment of the 14- and 15-Year-Old Students' Understanding of the Atmospheric Phenomena

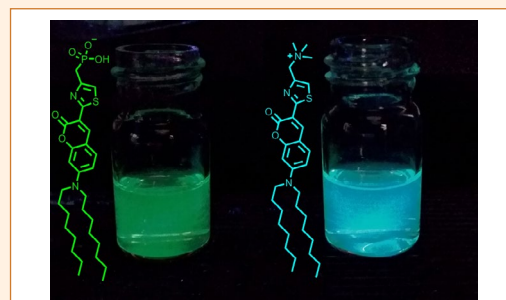
Janja Majer, Miha Slapničar and Iztok Devetak



668–674 Organic chemistry

## Fluorescent Membrane Probes Based on a Coumarin-Thiazole Scaffold

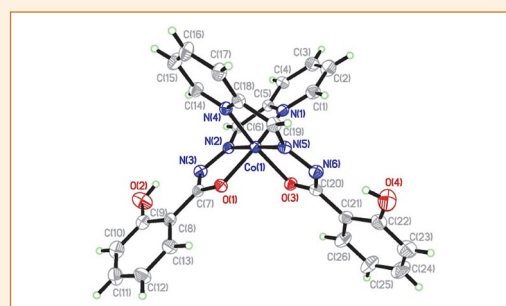
Stane Pajk, Maja Garvas and Janez Štrancar



675–680 Inorganic chemistry

## Synthesis, Characterization and Crystal Structures of Cobalt(II), Zinc(II) and Cadmium(II) Complexes Derived from 2-Hydroxy-N'-(pyridin-2-ylmethylene)benzohydrazide with Antimicrobial Activity

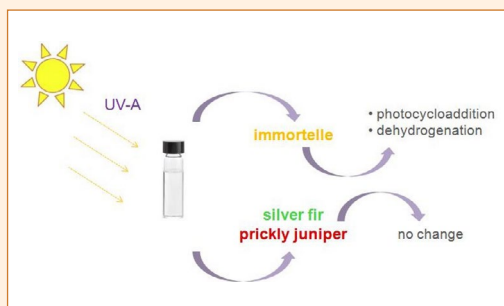
Li-Hang Wang, Xiao-Yang Qiu and Shu-Juan Liu



681–685 Applied chemistry

## Alteration in the Chemical Composition of Immortelle, Silver Fir and Prickly Juniper Essential Oils Induced by Light

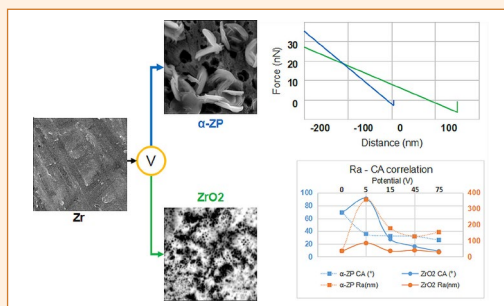
Ilijana Odak, Irena Škorić, Daria Grbavac, Ana Ratković and Ivana Šagud



686–693 Materials science

## Micro and Nanostructure Surface and Interface Characterization of Anodized Zr in Two Different Electrolytes

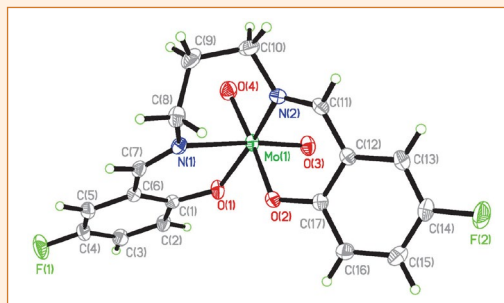
Andrei Bogdan Stoian, Maria Vardaki and Ioana Demetrescu



694–700 Inorganic chemistry

## Synthesis, Crystal Structures and Catalytic Property of Dioxomolybdenum(VI) and Nickel(II) Complexes Derived from bis-Schiff Bases

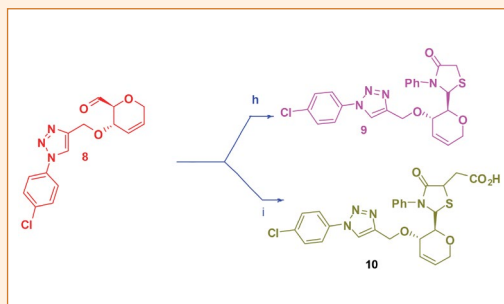
Ling-Wei Xue, Qin-Long Peng, Pan-Pan Wang, Hui-Jie Zhang



700–710 Organic chemistry

## Microwave-Assisted Synthesis and Anticancer Activity of Triazolyl Thiazolidine Derivatives of Pyrene

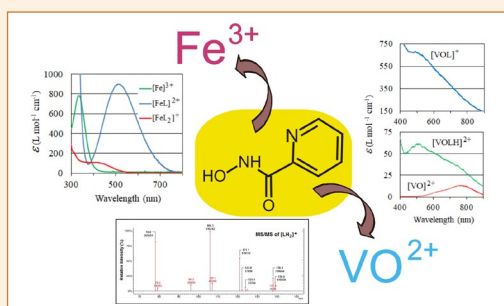
Avula Srinivas, Pulluri Karthik, Malladi Sunitha and Koduri Vasumathi Reddy



711–718 Inorganic chemistry

## Spectroscopic Determination of Metal-Ligand Coordination by Biologically Active 2-Picolinehydroxamic Acid with Iron(III) and Oxidovanadium(IV) in Aqueous Solutions

Magdalena Woźniczka, Mirosława Świątek, Joanna Gądek-Sobczyńska, Beata Pasternak and Aleksander Kufelnicki



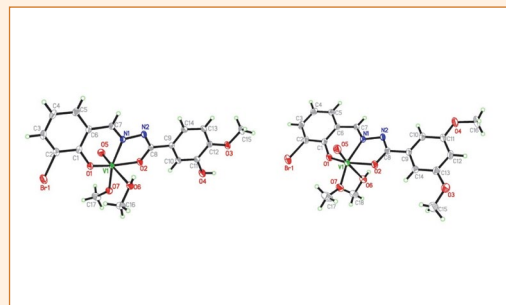


719–725

Organic chemistry

## Vanadium(V) Complexes with Bromo-Substituted Hydrazones: Synthesis, Characterization, X-ray Crystal Structures and Antimicrobial Activity

Cui-Lin Zhang, Xiao-Yang Qiu and Shu-Juan Liu

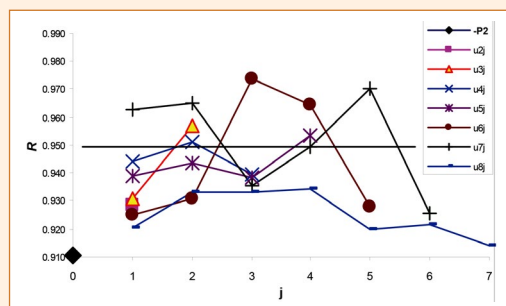


726–731

General chemistry

## Usefulness of Combinations of Vertex-Degree Weighted Path Indices and Elements of a Universal Matrix

Anton Perdih

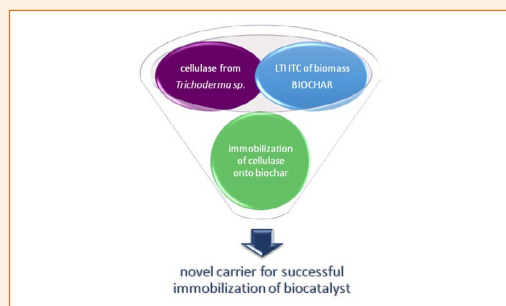


732–739

Chemical, biochemical and environmental engineering

## Enzyme Immobilization Onto Biochar Produced by the Hydrothermal Carbonization of Biomass

Mateja Primožič, Gordana Hojnik Podrepšek, Irena Pavlovič, Mojca Škerget, Željko Knez, and Maja Leitgeb



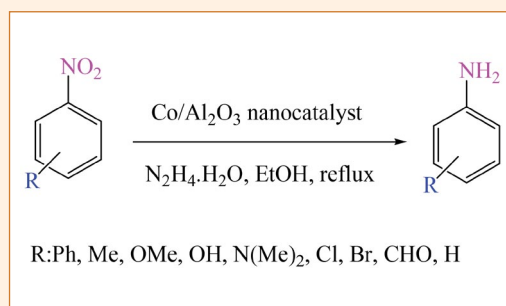
## SHORT COMMUNICATION

740–744

Organic chemistry

## Chemoselective Reduction of Nitroarenes with Hydrazine over a Highly Active Alumina-Supported Cobalt Nanocatalyst

Jalal Albadi, Heshmat Allah Samimi and Mehdi Jalali

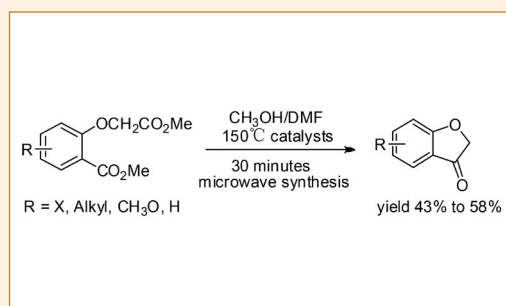


745–750

Organic chemistry

## Microwave-Assisted Synthesis of Benzofuran-3(2H)-ones

Xiaojing Hu, Huimin Lai, Fangfei Zhao, Shuyu Hu, Qianqian Sun and Lizhen Fang



## Review

# Contemporary Modes of Corrosion Protection and Functionalization of Materials

Ingrid Milošev\*

Jožef Stefan Institute, Department of Physical and Organic Chemistry, Jamova c. 39, SI-1000, Ljubljana, Slovenia

\* Corresponding author: E-mail: [ingrid.milosev@ijs.si](mailto:ingrid.milosev@ijs.si), URL: <http://www.ijs.si/ijsw/K3-en/Milosev>,  
<https://orcid.org/0000-0002-7633-9954>, Google Scholar Ingrid Milosev  
Tel: +386-1-477-34-52; Fax: +386-1-251-93-85

Received: 04-02-2019

Paper presented as key-note lecture at the 24<sup>th</sup> Annual Meeting of the Slovenian Chemical Society, Portorož, 19. – 21. 9. 2018

## Abstract

Corrosion protection is an important global issue. Corrosion affects all metal materials in industry, infrastructure, civil engineering, transport, biomedicine, etc. causing their deterioration and degradation. Corrosion protection is a necessity which enables the safe and well-functioning of metal structures and devices. In addition to long-term efficiency, corrosion protection should be environmentally and economically acceptable. Growing population with needs on modern and high-tech technologies is boosting consumption of base and rare earth metals. All these issues are putting high demands on area of corrosion protection with the main goal to prolong the life-time of metal materials, reduce the need for steeply increasing production and thus preserve resources. In this review contemporary modes of corrosion protection of metal materials with the emphasis on copper and aluminium base alloys as one of most important base metals are presented. These include corrosion inhibitors, conversion, sol-gel and hydrophobic coatings. Examples are our research studies over the last decade are presented.

**Keywords:** Corrosion; corrosion protection; inhibitors; conversion coatings; sol-gel coatings; hydrophobic coatings

## 1. Introduction

### 1. 1. Corrosion and Related Costs

Corrosion is a degradation of a material (usually a metal) due to its reaction with environment. It is a naturally occurring phenomenon of a material that results from a chemical or electrochemical reaction with its environment.<sup>1</sup> Majority of corrosion processes are electrochemical in nature as the electron transfer is involved. The occurrence of corrosion is dependent on number of factors including inherent material properties like composition and microstructure and environmental conditions such as corrosiveness of medium, temperature, stress, load, etc. (Fig. 1).

Corrosion takes place on the metal surface where heterogeneous sites exist (anodic and cathodic sites). These sites are present at the same metal specimen due to heterogeneity of the surface related to metal impurities, microstructure, grain orientation, local composition, etc. At anodic sites reaction of metal dissolution takes place, while at cathodic sites the reduction of oxygen or protons

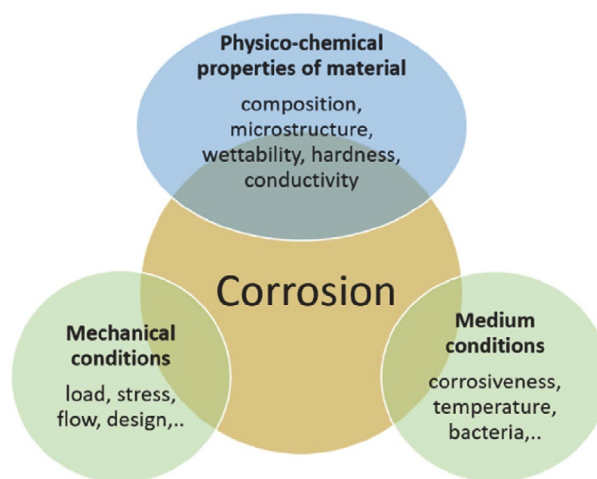


Figure 1. Factors influencing corrosion process of metal materials.

in electrolyte occurs. Two basic modes of corrosion processes can be distinguished: uniform corrosion which pro-

ceeds uniformly at the whole surface, and localized corrosion which is limited to certain sites at the surfaces; these are usually sites insufficiently protected by the protective layer. Localized corrosion processes are for example pitting, crevice and intergranular corrosion and dealloying (Fig. 2).

Almost all metals and alloys are prior exposure subjected to some type of corrosion protection aiming to prolong the life-time under operating conditions.<sup>1,2</sup> Environmental conditions to which metals and alloys are exposed to are versatile and comprise urban and industrial atmospheres, marine and soil environments, elevated temperature, load or pressure, etc. Materials are consequently often subjected to very harsh conditions containing corrosive species like chloride or sulphide ions. Corrosion protection is therefore a required procedure which enables the industrial sector, infrastructure, transportation, etc. and our daily life to operate under optimal conditions and to maintain a high level of functional performance. Last but not least, well protected surfaces assure a safe performance of a structure or device. Let us not forget that serious accidents can happen due to loss of structure integrity of devices, vehicles, or infrastructures like bridges or cable cars.<sup>3</sup>

including automobiles, railways, airplanes, etc. (ca. 24%), energy including coal mining, fossil fuel power, oil and gas industry, etc. (ca. 20%), infrastructure including roads, bridges, etc. (ca. 7%) and water including water supply and drainage (ca. 1%).<sup>5</sup> When taking into consideration direct costs in five major anti-corrosion measures the largest share accounts for coatings (ca. 66%), corrosion-resistant materials (ca. 19%), surface treatments (ca. 13%), electrochemical protection (ca. 0.6%), corrosion inhibitors (ca. 0.5%) and rust preventing oils and greases (ca. 0.2%).<sup>5</sup>

## 1. 2. Copper and Aluminium Alloys as Important Technological Materials

Copper and aluminium together with iron, zinc and lead belong to so called base metals which are utilized in everyday life. Precious metals are gold, silver and platinum, while rare earth metals like neodymium, dysprosium, samarium, etc. are becoming increasingly important due to high-tech industries. Global demand for base metals such as iron, copper and aluminium, is rising steeply in 21<sup>st</sup> century.<sup>6,7,8,9,10</sup> This trend is the result of increasing global population, economic growth in large and highly

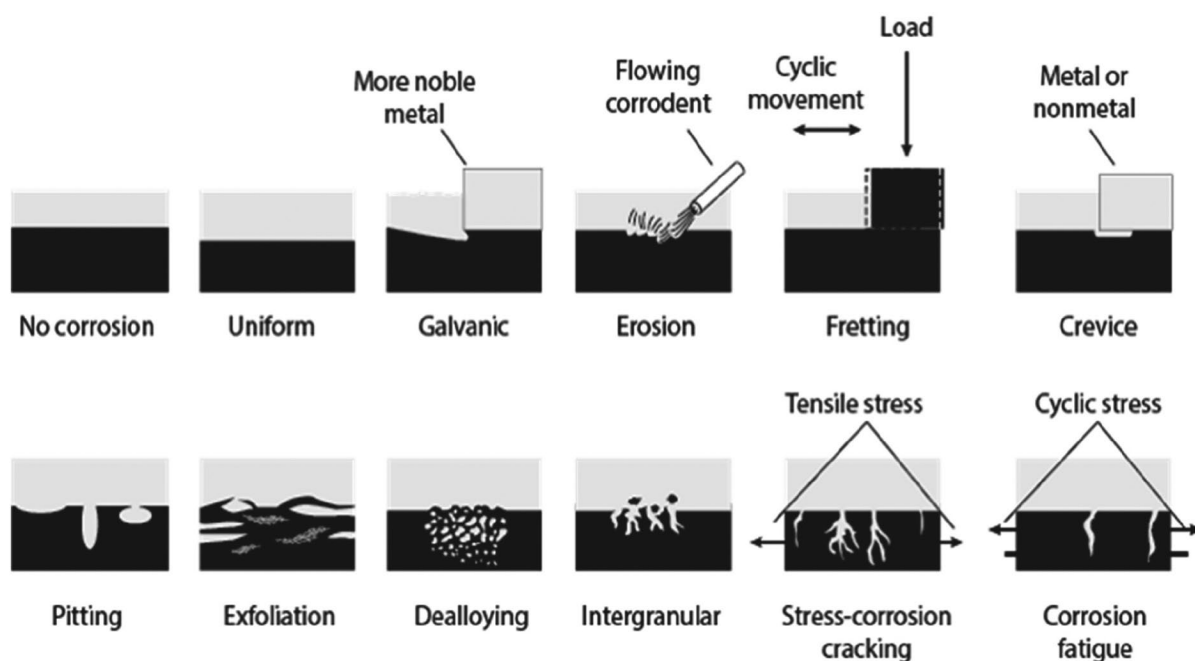


Figure 2. Different modes of corrosion processes

Annual costs due to corrosion amount to over 300 billion USD in USA and over 310 billion USD in China, representing about 3.3% of the gross domestic product.<sup>1,4,5</sup> When taking into consideration direct corrosion costs in five major economic sectors the highest costs are associated with *manufacturing and public services* including chemical industry, electronics, agriculture production and cultural heritage (ca. 48%), following by *transportation*

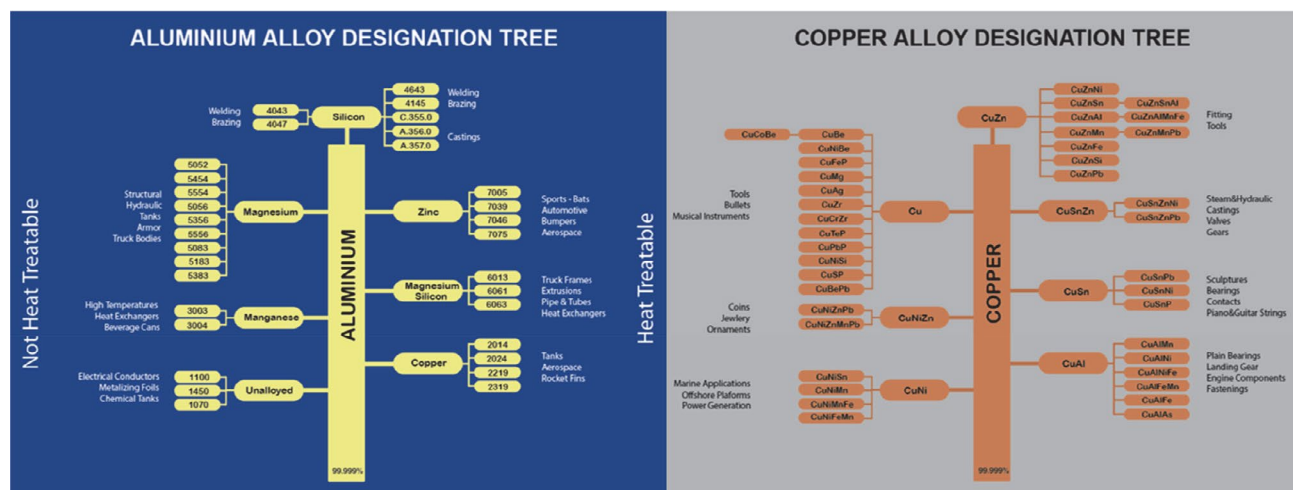
populated countries, and the transition to a more sustainable society due to increase of copper- and aluminium-intensive low-carbon energy and electrification of transport technologies.<sup>9,10</sup> Annual production of aluminium was estimated to approximately 63.2 million tonnes in 2017 with a 5.8% increase compared to year before.<sup>8</sup> Annual mine production of copper was estimated to approximately 21 million tonnes in 2018.<sup>11</sup> A 50% increase is expected



in 10 years, even up to 350% by 2050.<sup>9,10</sup> Considering these data it is reasonable to conclude that an efficient corrosion protection of base metal resources is a necessity.

This paper will focus on Cu- and Al alloys. Although copper plays an important role in modern society, it was used already by the ancient Egyptians. Today, copper tubes comprise ca. 90% of European and North American hot and cold water supplies.<sup>12</sup> Copper exhibits good mechanical properties such as hardness, strength and ductility; it has the best electrical conductivity and good thermal conductivity. These properties are the basis for applications of copper alloys in heat transfer, e.g. for heat exchangers, radiators, power distribution systems, etc. Copper is chemically relatively inert and when exposed to the atmosphere, protective layers of oxides and poorly soluble salts are formed on the surface. Copper alloys are suitable for marine environments, as well as for outdoor housing constructions, sculptures and statues, etc. Copper can be readily joined, e.g. by brazing and soldering. It is also suitable for recycling. Copper alloys can be divided in several families (Fig. 3) based on their composition: brasses and manganese bronze (Cu-Zn, Cu-Zn-Mg), bronze (Cu-Sn, Cu-Al, Cu-Si) copper-nickels (Cu-Ni), nickel-silver alloys (Cu-Ni-Zn), gunmetals (Cu-Sn-Zn-Pb) and copper-beryllium alloys (Cu-Be). According to temper, copper alloys are classified as annealed (A), manufactured (M), cold-worked (H), heat-treated (T), quench-hardened (Q), etc.<sup>13</sup> Areas of applications of various aluminium alloys are denoted in Fig.

relatively good corrosion resistance, as well as their appearance and low cost (current price of Al ca. 1,900 USD/tonne and for Cu ca. 6,300 USD/tonne<sup>14</sup>). These materials are used in a variety of applications, especially in aircraft, architecture, automotive and marine industries.<sup>16</sup> Alloying aluminium results in improved mechanical properties but also in a heterogeneous microstructure containing numerous intermetallic particles (IMPs). Due to strong galvanic coupling between IMPs and the aluminium matrix, exposure of aluminium alloys to aqueous solutions containing chlorides leads to localised corrosion.<sup>17</sup> Eight types of wrought aluminium alloys are designed depending on the major alloying element (Fig. 3): 1xxx (unalloyed), 2xxx with copper, 3xxx with manganese, 4xxx with silicon, 5xxx with magnesium, 6xxx with magnesium and silicon, 7xxx with zinc as major alloying element, and 8xxx with other major elements. Alloys are divided into heat-treatable (2xxx, 6xxx and 7xxx) and non-heat treatable (1xxx, 3xxx, 4xxx and 5xxx). Aluminium alloys are designated with four digits (xxxx): the first digit indicates the principal alloying element, the second digit, if different from 0, indicates a modification of the specific alloy, and the third and fourth digits are arbitrary numbers given to identify a specific alloy in the series. Basic temper designations include letters F (as fabricated), O (annealed), H (strain hardened), W (solution heat-treated) and T (thermally treated).<sup>17</sup> Areas of applications of various aluminium alloys are denoted in Fig. 3. Aluminium alloys are suitable material for recycling.



cludes (i) modification of electrolyte metal is exposed to by inhibitors, (ii) use of various surface treatments or coatings, or (iii) change of the potential by achieving cathodic protection (sacrificial anodes or impressed current) or anodic protection (maintaining of stable passive film).<sup>1,2</sup> In this review, former two approaches will be treated, i.e. corrosion inhibitors and coatings.

Copper and copper alloys are extremely resistant to corrosion, but subjected to superficial discolouring tarnish which can be avoided by applying thin clear protective coatings to their surfaces. There are hundreds of useful clear coating products on the market, formulated from numerous polymers, solvents, and additives.<sup>18</sup> Although the palette of colours of copper alloys is broad, in some applications may be desirable to change the colour, most commonly using brown or statuary finishes for bronze and green or patina finishes for copper.<sup>18</sup> Contemporary pre-treatments specifically for aluminium alloys are chemical conversion coatings – chromate- or chromium(I-II)-based, zirconium- and titanium-based, and anodization.<sup>19,20,21,22</sup> Finishing procedure is usually phosphating or electrophoretic paint (electro-coating).<sup>23</sup>

In past, the most important conversion coatings used for corrosion protection of ferrous and non-ferrous metal substrates are chromate conversion coatings (CCCs) and phosphate coatings. These treatments were invented approximately 100 years ago<sup>24</sup> and they have been used in large-scale commercial applications over the last 60–70 years.<sup>25</sup> Chromate conversion coatings (CCCs) were first developed in 1915 by Bauer and Vogel<sup>24</sup> by treating aluminium for 2 h at 90 °C in a solution of potassium carbonate, sodium bicarbonate and potassium dichromate. The method was modified and then patented in 1923 (modified Bauer Vogel, MBV process) including immersion in  $\text{Na}_2\text{CO}_3$  and  $\text{Na}_2\text{Cr}_2\text{O}_7$  for 5–10 min. Over the years, the process has been further modified but all CCC baths use chromate compounds. CCCs are highly corrosion protective. They consist of a backbone of chromium oxide/hydroxide with Cr in the 3+ oxidation state and also contain compounds with Cr in the 6+ oxidation state.<sup>26,27</sup> The Cr(VI) provides the characteristic of self-healing, which is the ability to reform a protective coating after it has been breached by a mechanical or chemical process. It proceeds by the reduction of remaining Cr(VI) in the coating to an insoluble  $\text{Cr}^{3+}$  compound. The phosphating process, on the other hand, was patented in 1943 with the introduction of Jernstadt salt (disodium phosphate containing titanium), which developed into zinc phosphate coatings. Phosphate coatings are hard, continuous, insoluble and electrically non-conducting and are used in numerous applications in the automotive, agriculture and appliance industries.<sup>28</sup>

Chromate compounds are toxic and carcinogenic and thus unacceptable for contact by humans and contamination of the environment. The use of hexavalent chromium is restricted in the European Union and the USA.<sup>29,30</sup> In European Union is restricted by the Restriction of Hazard-

ous Substances (RoHS) Directive 2002/95/EC (EU RoHS 1), which took effect in 2006 and was replaced by the Directive EU RoHS 2 in 2011.<sup>29</sup> Both directives restrict the use of certain hazardous substances in electrical and electronic equipment (hexavalent chromium is limited to a maximum concentration value of 0.1 % by weight). The use of hexavalent chromium is further restricted by the European Chemical Agency (ECHA)<sup>31</sup> and the related REACH<sup>31</sup> (Registration, Evaluation, Authorization and Restriction of Chemicals) regulation. Hexavalent chromium belongs to the SVHC (Substances of Very High Concern) list which cannot be placed on the market or used after a given date (“sunset date”), unless the authorization is granted for their specific use, or the use is exempted from authorization. Most recent sunset date for chromium(VI) compounds was January 2019.<sup>31</sup> Applications for authorisation have been prepared by some industrial consortia, e.g. aerospace, for the use of some chromates, i.e. chromium trioxide.

Problems related to phosphate coatings are associated impact of phosphate discharge on groundwater sources due to eutrophication in fresh water lakes and reservoirs caused by phosphorus. Environmental regulations therefore restrict the use of phosphorus.<sup>32</sup> Operating temperature of phosphating baths is typically about 50 °C, which requires energy input. Furthermore, production of phosphate coatings is related to the formation of a sludge containing metal ions, which necessitates frequent desludging to maintain optimum bath operation.

As a result of these issues, both chromium and phosphate conversion coatings are being increasingly replaced and alternatives are being continuously sought. In this review, various modes of corrosion protection of copper- and aluminium-alloys—inhibitors, conversion coatings, sol-gel coatings, hydrophobic coatings—are presented aiming to retrospect our own investigations in this exciting field of research which is becoming increasingly important for the society as a whole. Different modes of preparation of protective layers or coatings on metal surface are schematically presented in Fig. 4.

NaCl solution is taken as a model corrosive electrolyte (usually concentrations of 0.1 M, 0.5 M or 3.5 wt.% are used). Inhibitors can be either added directly to NaCl followed by electrochemical measurements in the same solution, or inhibitor layers can be pre-formed by immersion of metal sample in ethanol solution of inhibitor (or other solvent where inhibitor is soluble) followed by measurements in NaCl. The same principle is valid for conversion coatings – either rare earth salt is added directly to NaCl and then immersed for a certain period of time a conversion to occur, or conversion layer can be pre-formed in solution of rare earth salt, usually with hydrogen peroxide added to stimulate the conversion, followed by measurements in NaCl. Sol-gel and hydrophobic coatings are always pre-deposited prior measurements in NaCl using dipping, spinning or spraying. These coatings act as barrier protection. When inhibitor is added to sol-gel or hydro-

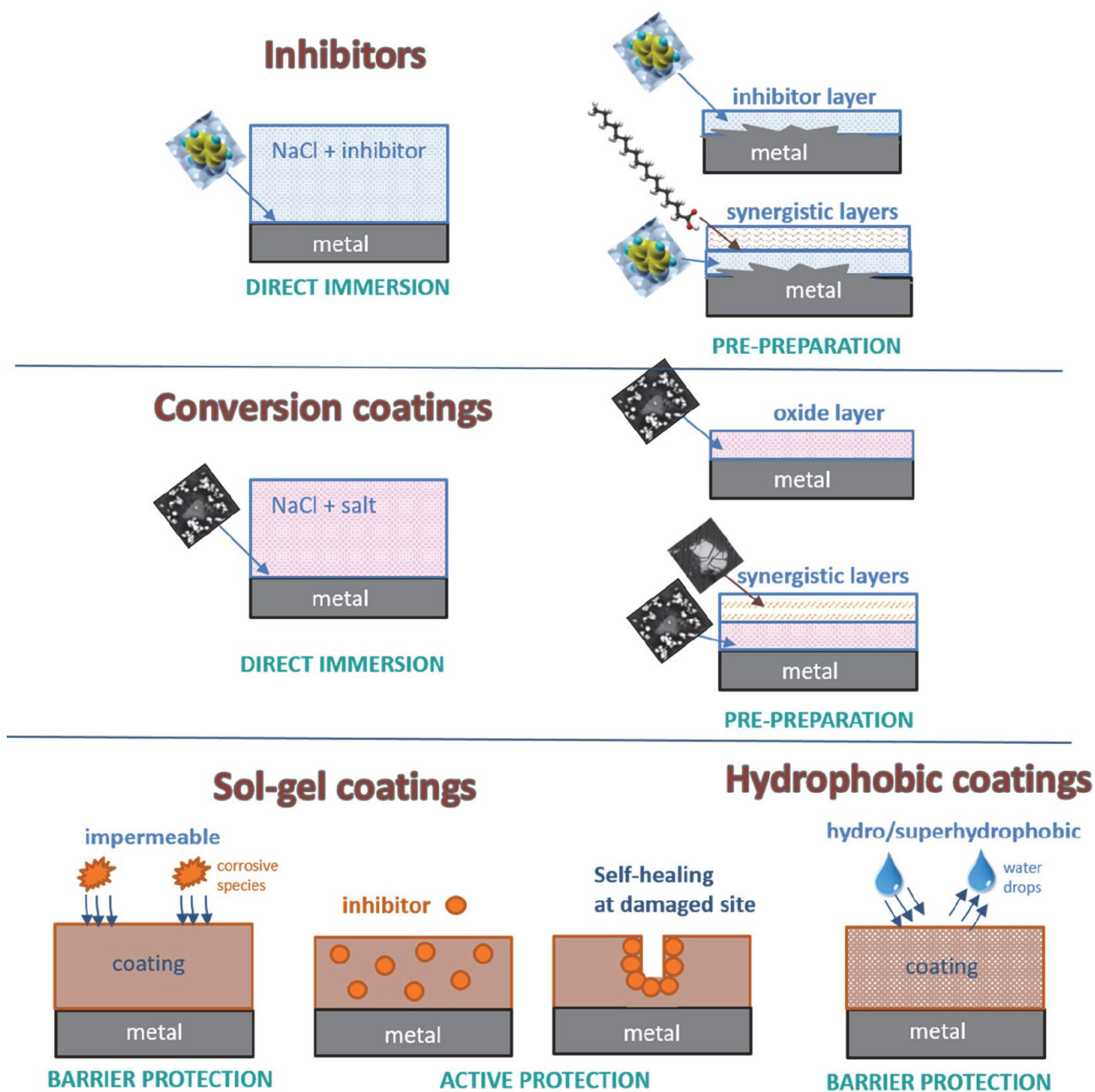


Figure 4. Modifications of metal surfaces using various strategies.

phobic coating to gain the active protection, artificially made scribe is made to simulate the corrosion damage and then self-healing of damaged site is followed by electrochemical or non-electrochemical methods.

## 2. Corrosion Inhibitors

The inhibition of corrosion using corrosion inhibitors has been for decades one of the most important method of corrosion protection. Inhibitors are inorganic or organic compounds which when added in small concentra-

tions form a surface layer that protects the underlying metal surface from dissolution and, consequently, decreases the corrosion rate. The choice of inhibitors is based on its inhibition efficiency but also on price and environmental harmlessness.

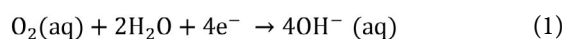
Inhibitors can be basically divided to (i) environmental conditioners (scavengers) and (ii) interface inhibitors.<sup>1</sup> (i) Scavengers decrease corrosivity of the medium by removing aggressive species, e.g. addition of hydrazine reduces the oxygen content and consequently the rate of cathodic reaction. (ii) Interface inhibitors can be divided to liquid- and vapour-phase inhibitors.



Liquid-based inhibitors can be classified as anodic, cathodic and mixed depending on whether they mainly affect anodic, cathodic or both reactions, respectively.<sup>1</sup> The mechanism of inhibition is usually based on adsorption of inhibitors on the metal surface and formation of a protective layer. Anodic inhibitors are thus commonly referred as passivating inhibitors such as chromate, nitrite, molybdate, etc. resulting in the formation of sparingly soluble oxide, hydroxides or salts. These inhibitors are most efficient and widely used. Due to chromate toxicity, however, seek for alternatives is of a priority. Cathodic inhibitors can be classified as (i) so called cathodic poisons and (ii) cathodic precipitators. (i) Cathodic poisons form adsorbed (sulphides, selenides) metallic layers (As, Bi, Sb), or protective layers (silicates, phosphates, borates) and decrease the rate of cathodic reaction by limiting the diffusion of oxygen to metal surface. (ii) Precipitators precipitate at selective sites at the surface to form insoluble compounds (Ca, Zn, or Mg carbonates). Mixed inhibitors affect both anodic and cathodic reaction and can act through physisorption, chemisorption and film formation.<sup>1</sup>

Vapour-phase inhibitors are substances which slowly release chemical compounds within a sealed airspace that actively prevents surface corrosion, e.g. to protect stored tools or parts inside bags, boxes or cupboards.<sup>1</sup>

Electrochemical reactions on copper immersed in NaCl corrosion medium comprise the cathodic reaction of reduction of oxygen, reaction (1) and anodic reaction of copper electrodisolution, reactions (2)–(6).<sup>33,34</sup> The mechanism of copper electrodisolution in chloride media has been widely investigated.<sup>35</sup> It proceeds through direct dissolution of metal and formation of  $\text{CuCl}_2^-$  complex (reaction 2):<sup>35,36</sup>



or through intermediate formation of CuCl (reactions 3–4):

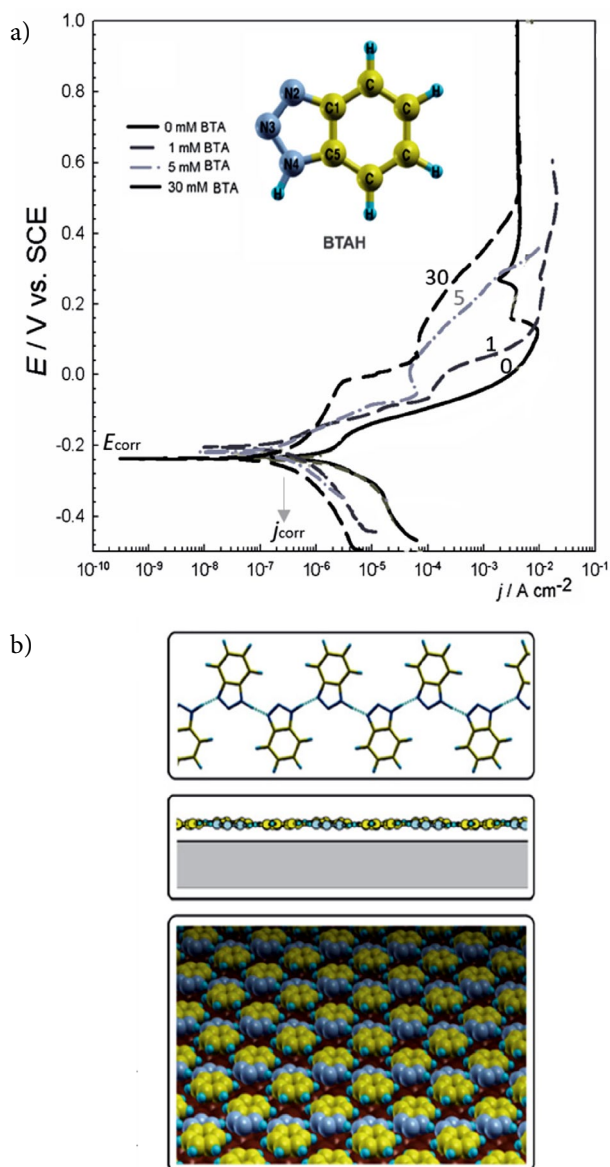
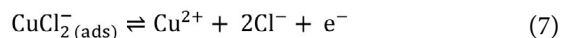


or through reaction between cuprous and chloride ions (reactions 5–6):



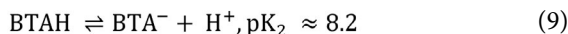
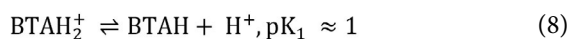
At potentials close to corrosion potential ( $E_{\text{corr}}$ ) the anodic reaction is under mixed charge transfer and mass transport control (rate of movement of cuprous chloride complex away from the surface to bulk electrolyte) (Fig. 5).<sup>37,38,39</sup> At approximately 0.1 V the peak in current is at a

minimum, indicating that the CuCl covers the surface. The CuCl layer is not protective and reacts further, forming the  $\text{CuCl}_2^-$  complex which is soluble in aqueous media and can either diffuse into the solution or can be further oxidized. This process takes place at potentials more positive than 0.1 V:<sup>37</sup>



**Figure 5.** (a) Polarization curves recorded for copper in 0.5 M NaCl with and without benzotriazole (BTA) added in concentration of 1, 5 and 30 mM. Scan rate was 1 mV/s. (Reprinted from the publication by T. Kosec, I. Milošev, B. Pihlar, *Appl. Surf. Sci.*, **2007**, 253, 8863–8873 with permission from Elsevier.<sup>37</sup>) Skeletal structure of BTA is given in inset. (b) The structure of BTA is planar and therefore favourable for physisorption on metal surface as shown by tentative structure; planar physisorbed BTAH polymers are packed so as to form compact and thin film. (Reprinted from the publication by M. Finšgar, A. Lesar, A. Kokalj, I. Milošev, *Electrochim. Acta*, **2008**, 53, 8287–8297 with permission from Elsevier.<sup>39</sup>)

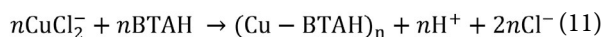
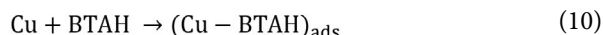
Among the most important inhibitors for copper are triazole and imidazole-based inhibitors. Benzotriazole (BTAH) has been known since 1947 to be a very effective inhibitor of corrosion for copper and copper alloys.<sup>40</sup> BTAH is a heterocyclic organic compound with a molar mass of 119.124 g/mol; at room temperature is a whitish powder which is sufficiently soluble in water solutions. It is only slightly toxic so it does not constitute a major environmental hazard.<sup>40</sup> The form of the molecule in aqueous solution depends on the pH and can be either neutral (BTAH), negatively charged ( $\text{BTA}^-$ ) or protonated ( $\text{BTAH}_2^+$ ), 41, .<sup>40</sup>



In slightly acidic environments benzotriazole is present mainly in the undissociated form as BTAH, whilst at alkaline pH the molecule is predominantly present in the  $\text{BTA}^-$  form.<sup>39</sup> BTAH is protonated at the N3-nitrogen atom in an acidic environment (Fig. 5). Protonation decreases  $\pi$  orbital energy which leads to lower resonance energy and, in consequence, the interaction between benzotriazole and metal becomes weaker.<sup>40</sup> Therefore, BTAH is less effective in an acidic environment. The instability of Cu oxides in acidic environments could further reduce the effectiveness of the copper surface protection. Moreover, the build-up of a polymerized network of Cu-BTA chains is

most strongly favored at an oxidized Cu surface, i.e. in solutions where copper oxide is stable.<sup>39</sup>

In NaCl solution containing BTAH above 0.05 mM, a barrier film is formed which causes the reduction of current density in both cathodic and, especially, anodic region, while the corrosion potential does not change significantly (Fig. 5). Therefore, BTAH acts primarily as anodic inhibitor that retards exodus of Cu ions, reaction (5), and, secondarily, as a cathodic inhibitor preventing oxygen reduction, reaction (1). The formation of barrier layer can be expressed as:<sup>40</sup>



Barrier layer is a mixture of cuprous species and Cu(I)-BTA complex forming a polymerized network.<sup>38</sup> The thickness of the barrier layer formed in inhibitor-containing solution is much smaller than of that formed in chloride solution, i.e. 2.4 nm compared to 8.5 nm, respectively.<sup>38</sup> The film formed at near neutral pH, where the stability of cuprous species is high, is very stable and dense. Density functional molecular electronic structure revealed that BTAH has the ability to for planar H-bonded poly-

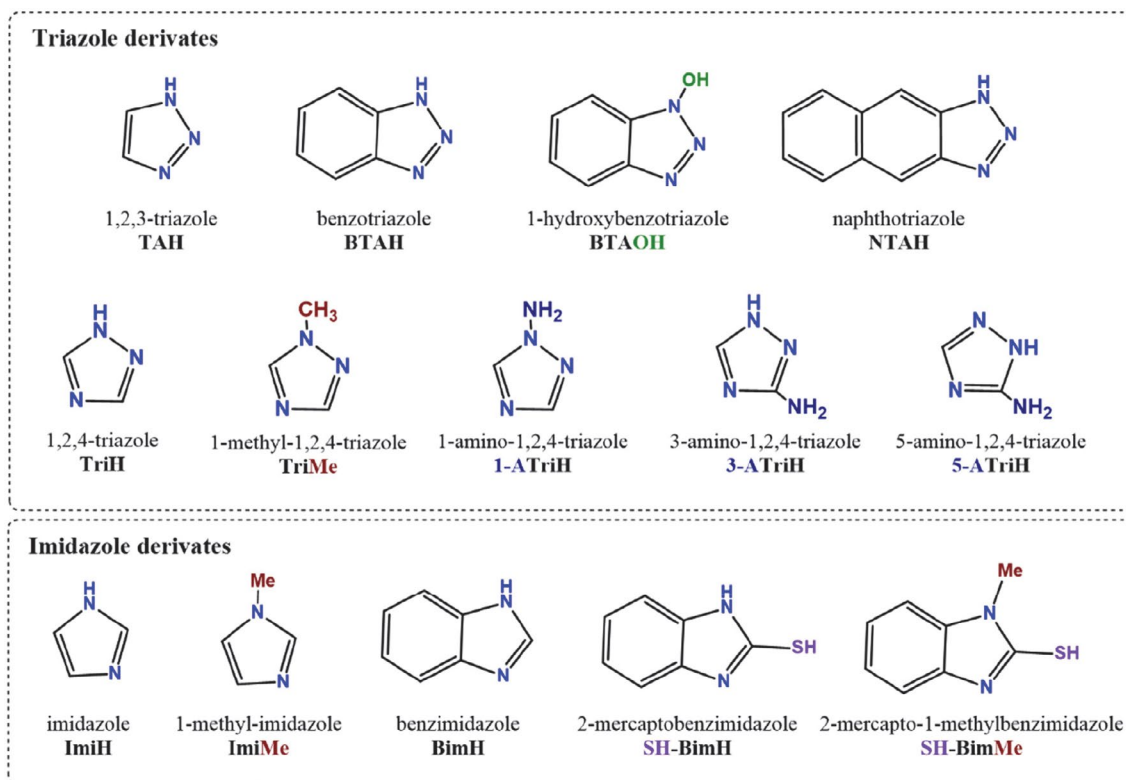
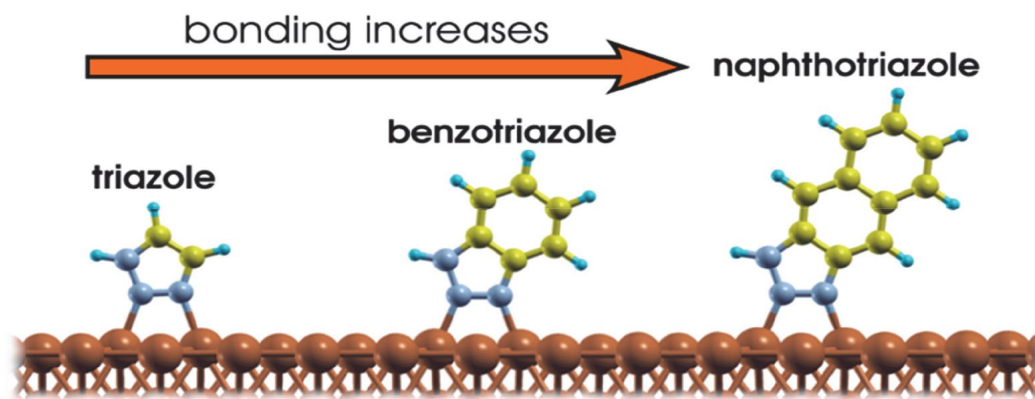


Figure 6. Skeletal formulae of triazole and imidazole derivatives used as corrosion inhibitors.



**Figure 7.** Optimized physisorption/chemisorption structures of triazole (TAH), benzotriazole (BTAH) and naphthotriazole (NTAH) on Cu surface. The bonding increases with molecular size from TAH to NTAH as calculated by density functional theory (DFT) calculations. (Reprinted from the publication by A. Kokalj, N. Kovačević, S. Peljhan, M. Finšgar, A. Lesar, I. Milošev, *ChemPhysChem*, **2011**, 12, 3547–3555 with permission from John Wiley and Sons.<sup>47</sup>)

mers of favourable geometry form physisorption.<sup>42</sup> These can be packed on the surface and form a thin and compact layer (Fig. 5b).<sup>39</sup> The interplay between molecular structure, adsorption (chemisorption and physisorption) and intramolecular bonding (e.g. H-bonding) is crucial for the formation of efficient inhibitors.<sup>42</sup>

Benzotriazole is efficient inhibitor for copper in chloride containing solution but also for brasses (Cu-xZn alloys).<sup>37,38</sup> Derivatives of BTAH are also considered as inhibitors for copper corrosion (Fig. 6). 1-hydroxybenzotriazole (BTAOH) exhibits poorer inhibition efficiency compared to BTAH which was ascribed to its non-planar structure and inability to form thin polymer films.<sup>43,44</sup> Amino derivatives of 1,2,4-triazole (TriH<sup>1</sup>) were also considered: 3-amino-1,2,4-triazole (3-ATriH), 5-amino-1,2,4-triazole (5-ATriH) and 1-amino-1,2,4-triazole (1-ATriH) (Fig. 6). 3-ATriH was shown to be the most effective inhibitor, the effectiveness decreasing in the order 3-ATriH > 5-ATriH > 1-ATriH > TriH.<sup>45</sup> Compared to BTAH, however, shows A-TriH less efficient inhibition.<sup>46</sup> Triazole derivatives with NH<sub>2</sub> group bonded to either of the C atoms have stronger inhibition properties than those of 1,2,4-triazole or of that with the amino group bonded to ring N atom.<sup>45</sup> Further, the molecular electronic and adsorption properties of 1,2,3-triazole (TAH), benzotriazole (BTAH) and naphthotriazole (NTAH) molecules were compared.<sup>47</sup> The molecule–surface bond strength increases with increasing the molecular size, thus following the TriH < BTAH < NTAH sequence (Fig. 7).<sup>47</sup> The molecules chemisorbed in an upright geometry; molecular electronegativity and chemical hardness decrease monotonously as the molecular size increases. BTAH and NTAH can physisorb positioning the molecular plane almost parallel to the surface. However, although NTAH seems to be more efficient inhibitor than BTAH, high price limits its usage.<sup>47</sup>

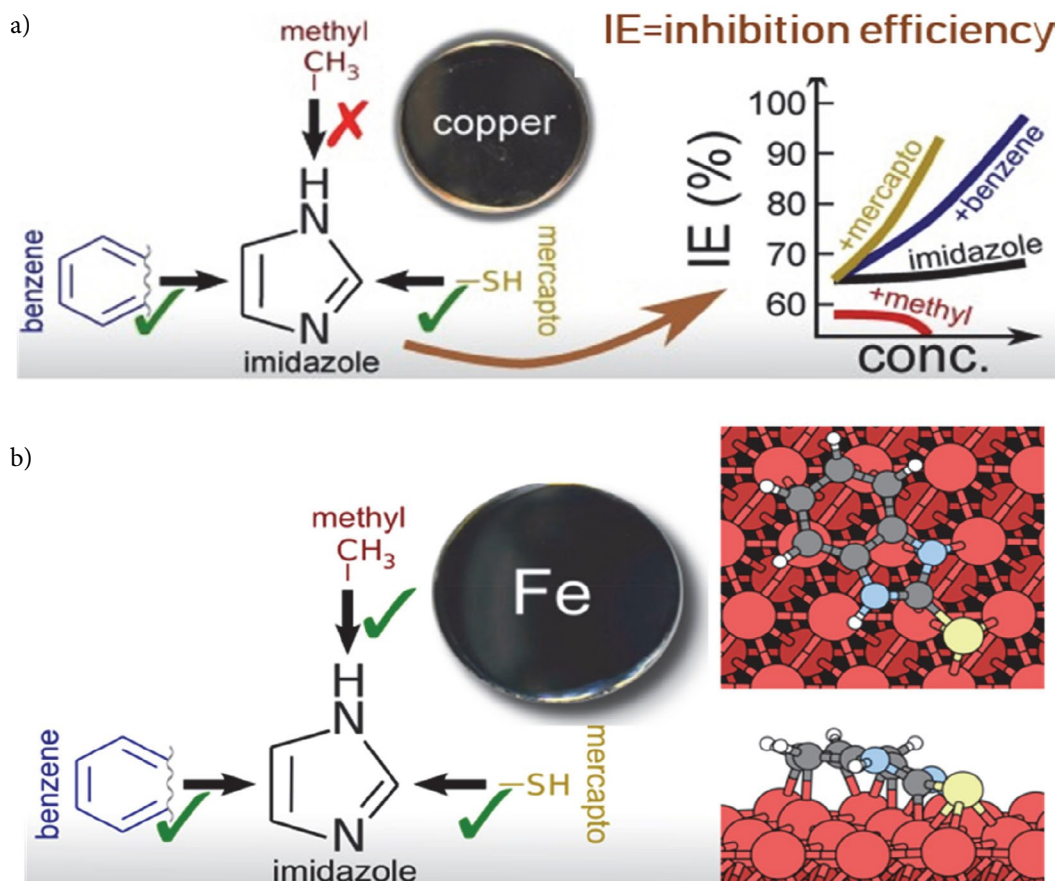
In addition to triazoles, imidazole and its derivatives were investigated (Fig. 6). Imidazole (ImiH) is less effective

inhibitor than most of its derivatives, which was partly ascribed to its high solubility.<sup>48,49</sup> The benzene, methyl and mercapto derivatives of imidazoles were investigated: benzimidazole (BimH), 1-methyl-imidazole (ImiMe), 2-mercapto-1-methyl-imidazole (SH-ImiMe) and 2-mercapto-benzimidazole (SH-BimH) (Fig. 8a).<sup>48,49</sup> The inhibition efficiency of these compounds, deduced from electrochemical measurements, differs markedly. At inhibitor concentration of 1 mM the following trend was established: SH-BimH > SH-ImiMe > BimH > ImiH > ImiMe (Fig. 8a). These inhibitors act as mixed inhibitors with a stronger effect on the anodic reaction, i.e. dissolution of copper, reaction (5). The mercapto group and benzene group are shown to have a beneficial effect on corrosion inhibition, whereas the effect of the methyl group is, interestingly, different: at lower concentrations (0.1 and 1 mM) the effect is only slightly disadvantageous, but at higher concentrations the disadvantageous effect is amplified and ImiMe even accelerates the corrosion at 10 mM.<sup>48,50</sup> After one month's immersion in solution containing ImiH and ImiMe cupric compounds were detected; cupric complexes are soluble and ImiH and ImiMe are consequently poor inhibitors.

Another factors which has to be taken into account when considering efficiency of an inhibitor is the effect of inhibitor-substrate interactions: DFT calculations revealed that ImiMe, SH-ImiMe, BimH and SH-BimH inhibitors bind stronger to iron than to copper surfaces, but this has no direct relevance to corrosion inhibition.<sup>51</sup> As iron is chemically more reactive to copper, in general it binds adsorbates stronger than copper. In contrast to copper, where mercapto containing derivatives of imidazoles were beneficial for all concentrations tested, their inhibition of iron corrosion was advantageous compared to other derivatives only at low concentration (Fig. 8b).<sup>51</sup> Furthermore, methyl-derivative of imidazole had a positive impact on inhibition of iron corrosion at all concentrations. Therefore, relative adsorption bonding strength of inhibitors com-

1 1,2,4-triazole was denoted ATA in original publication.<sup>45</sup>





**Figure 8.** The inhibition efficiency as a function of imidazole derivative and substrate for (a) copper and (b) iron. (b) Optimized molecular adsorption modes of SH-BimMe on iron surface. (a) Reprinted from the publication by I. Milošev, N. Kovačević, A. Kokalj, *Corros. Sci.*, **2015**, 98, 107–118 with permission from Elsevier.<sup>48</sup>

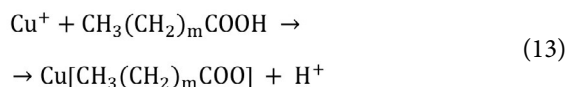
pared to that of corrosive species such as chloride is relevant.<sup>52</sup> This finding confirms that the inhibition effect of given inhibitor is strongly dependent on the substrate and that efficiency of the inhibitor cannot be predicted *per se* without considering the substrate as well.<sup>52</sup>

Other organic compounds were also considered as corrosion inhibitors, specifically in context of using environmentally friendly compounds. We considered amino acids and naturally driven compounds, such as phytic acid which is in chemical structure inositol hexaphosphate (IP6).<sup>53</sup> When copper surface is optimally pre-treated, i.e. roughened in sulphuric acid, and then immersed in 0.01 mM phytic acid the inhibition efficiency of 77% was achieved in NaCl solution. Among 11 amino acids tested, cysteine achieved the highest inhibitor efficiency reaching 52% at a concentration of 10 mM.<sup>54</sup> Thiol (mercapto) group was shown to be responsible for superior inhibition efficiency compared to other amino acids among which some acted even as corrosion activators.

## 2. 1. Synergistic Action of Inhibitors

One of the recent trends in corrosion protection is the synergistic use of inhibitors. The combination of differ-

ent inhibitors can either increase the effect of each inhibitor individually, or bring additional functional property, for examples hydrophobicity.<sup>55,56,57,58,59,60,61</sup> Illustrative example is the combination of classical inhibitors for copper and copper-based alloys—2-mercapto benzimidazole (SH-BimH<sup>2</sup>) and benzotriazole (BTAH)—and carboxylic acids.<sup>57,58,59,60,61</sup> Immersion of metal in a solution containing carboxylic acid, especially those with long alkyl chain, results in the formation of carboxylate layer at the surface which contributes to hydrophobicity of the surface.



The combination of octadecanoic (stearic) acid (SA) and SH-BimH will be described as an example. Inhibitor layers were prepared by self-assembly in ethanol solution of inhibitors, either as individual (SA and SH-BimH), binary (SH-BimH/SA) and mixed (SH-BimH+SA). Corrosion properties were evaluated in simulated urban rain (0.2 g/L Na<sub>2</sub>SO<sub>4</sub>, 0.2 g/L NaHCO<sub>3</sub> and 0.2 g/L NaNO<sub>3</sub>,

2

2-mercaptobenzimidazole was denoted 2-MBI in original publication.<sup>57,58,59,60,61</sup>

pH=5). This medium was chosen due to application of copper-based alloys, such as bronze and brass, for outdoor infrastructures and monuments. Under simulated urban rain conditions, the combination of SH-BimH and SA achieved much better inhibition efficiency compared to individual inhibitors (Fig. 9).<sup>57</sup> The morphology of the individual layers is quite different. After immersion in SA, the surface was covered by a flower-like features leaving an open substrate surface. In contrast, immersion in SH-BimH resulted in the formation of a compact nano-grain layer covered with longitudinal features. When SA and SH-BimH were combined, an uneven surfaces with large cuffs, which is interpreted as accounting for the hydrophobicity of the layer with contact angles exceeding 110°.

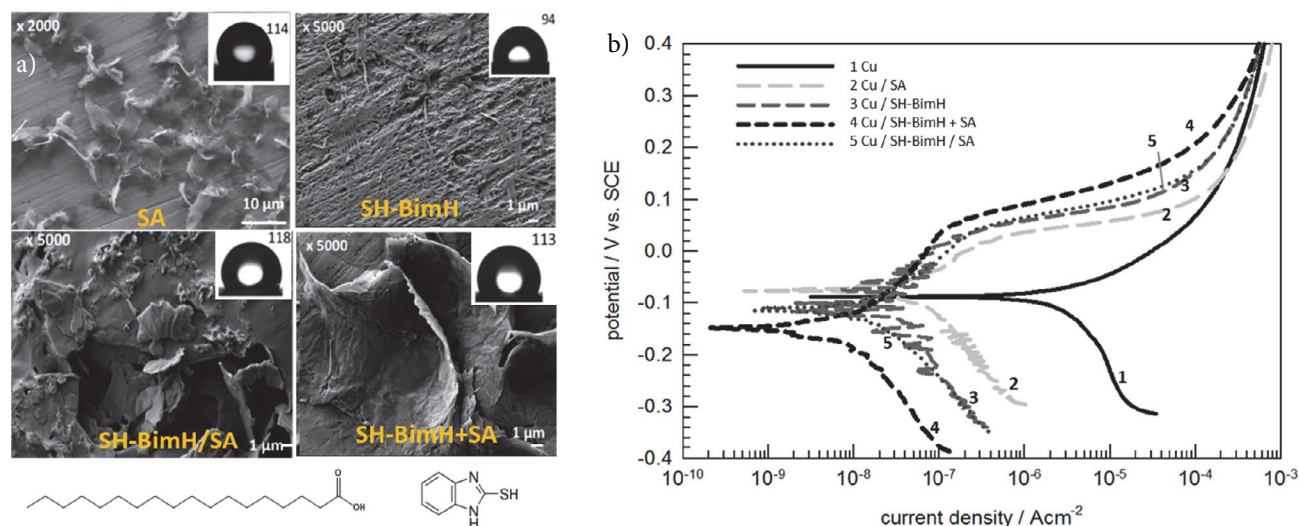
Electrochemical potentiodynamic measurements in simulated urban rain revealed differences in the mechanism of corrosion inhibition (Fig. 9b).<sup>57</sup> Both inhibitors act as mixed inhibitors, i.e. affect both cathodic and anodic current density, but SH-BimH shifts the corrosion potential more in the cathodic direction. Both combinations of SH-BimH and SA, i.e. formed one layer above another, or mixed within one layer, exhibited three orders magnitude smaller current density compared to that of individual inhibitors. Therefore, the layers formed by the combination of stearic acid and organic inhibitors achieve improved corrosion protection ability and offer hydrophobicity as an additional functional property. Further reading offer details on the use of carboxylic acid of different chain length as inhibitors of copper corrosion, and SH-BimH and BTAH combined with stearic acid as corrosion inhibitors for Cu-10Zn, Cu-40Zn and Zn.<sup>59,60</sup> Synergistic increase of corrosion resistance when combining SH-BimH or BTAH with stearic acid was attributed to the carboxylate formation process of SA, reaction (13), which acts as a barrier,

whereas BTAH and SH-BimH adsorb on the Cu surface according to their well-known corrosion inhibition mechanism.<sup>37,38,39,47,49,50</sup> These two processes occur simultaneously.

### 3. Conversion Coatings (Based on Rare Earth Salts)

Conversion coatings can be defined as coatings formed by conversion from soluble salt to a slightly soluble or insoluble oxide and/or hydroxide which precipitates either throughout the metal surface, or at intermetallic particles which are electrochemically more noble in respect to surrounding matrix and where oxygen reduction takes place.<sup>62</sup> Today two main types of conversion coatings are being explored on aluminium alloys: rare earth coatings<sup>63</sup> or zirconium and/or titanium coatings.<sup>21</sup> Inhibitory action of these conversion coatings is based on the retardation of cathode reaction (i.e. oxygen evolution) on corroding surfaces.

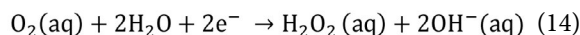
Rare earth compounds are environmentally friendly, exhibit low toxicity and are available in natural sources at a reasonable price. Hinton et al. were the first to observe that rare earth salts, especially cerium, inhibit redox reaction on aluminium alloys.<sup>62</sup> Precipitation of rare earth hydroxide deposits is pH-driven process which starts at cathodic sites on the aluminium alloy surface that are electrochemically less negative (more noble) relative to aluminium matrix.<sup>62,63</sup> Depending on the cation,  $\text{Ce}(\text{OH})_3$ ,  $\text{La}(\text{OH})_3$ ,  $\text{Nd}(\text{OH})_3$ , etc. are formed once the critical pH for their deposition is reached. For Ce, critical value is above pH 9.5.<sup>64</sup> Among rare earth compounds mainly cerium and lanthanum have been investigated and show the highest potential for further applications, although compounds of



**Figure 9.** (a) SEM images of copper surface in ethanol solution of different organic compounds: immersed for 20 minutes in 0.05 M octadecanoic (stearic) acid (SA), immersed for 1 h in 0.01 M 2-mercaptobenzimidazole (SH-BimH), 1 h in 0.01 M 2-MBI followed by 20 minutes in 0.05 M SA (SH-BimH/SA), and 1 h in mixture of 0.01 M SH-BimH and 0.05 M SA. (b) Polarization curves recorded for bare copper and modified by inhibitors after 1 h immersion in simulated urban rain.  $dE/dt=1$  mV/s. Skeletal formulae of SA and 2-MBI are presented. (Reprinted from the publication by G. Žerjav, I. Milošev, *Corros. Sci.*, **2015**, 98, 180–191 with permission from Elsevier.<sup>57</sup>)

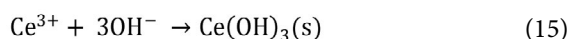
other rare earth elements like neodymium and praseodymium have also been addressed.<sup>63</sup> Different types of salts have been used, i.e. chloride, nitrites, acetate, sulphate and dibutyl-phosphate. Conversion of rare earth salts to hydroxides can be accelerated by the addition of hydrogen peroxide whose role is three-fold – a complexing agent, an oxidant and a crystallisation inhibitor.<sup>65</sup>

Cathodic curve in potentiodynamic polarization curve is related to reduction of dissolved oxygen which can proceed through  $4e^-$  reaction, reaction (1), or  $2e^-$  reaction, reaction (14).<sup>65</sup>



In reaction (1)  $O_2$  is completely reduced to hydroxyl ( $OH^-$ ), while in reaction (14)  $O_2$  is reduced to  $OH^-$  and  $H_2O_2$ . Alkalization caused by reactions (1) and (14) reaches pH above 9.5 required for precipitation of  $Ce(OH)_3$ .<sup>64</sup> Polarization curve recorded for AA7075-T6 in NaCl solution are presented in Fig. 10.  $E_{corr}$  is  $-0.70$  V, and  $j_{corr}$   $1.9 \mu A cm^{-2}$ . AA7075-T6 is highly susceptible to corrosion in chloride environment. The rapid increase in anodic current density with increasing potential is associated with the pitting corrosion related to dissolution of IMPs.<sup>21,27</sup> The addition of Ce(III) salts to NaCl solution improved corrosion properties of AA7075-T6, resulting in reduced  $j_{corr}$ , a shift in  $E_{corr}$  and the appearance of a passive region (Fig. 10a).<sup>66</sup> In the presence of  $CeCl_3$  and  $Ce(Ac)_3$   $E_{corr}$  was shifted more negative by more than 200 mV. The cathodic current density was significantly reduced. This behaviour is typical for efficient cathodic inhibitors, as described by Hinton *et al.*<sup>62</sup> The absence of pitting was ascribed to displacement of  $E_{corr}$  away from  $E_{pit}$  in the negative direction. The span of  $\Delta E = |E_{corr} - E_{pit}|$  is taken as the measure of initiation of pit nucleation.<sup>62</sup> The effect of  $Ce(NO_3)_3$  was, however, different, i.e., it changed the value of  $E_{corr}$  to more positive and slowed down the dissolution, due to the stimulation of oxide formation.<sup>66</sup>

The range of cerium distribution over the surface of AA7075-T6 immersed for 24 h in NaCl with added 3 mM  $CeCl_3$  or  $Ce(Ac)_3$  was investigated SEM/EDS mapping (Fig. 10b).<sup>67</sup> After immersion in NaCl, corrosion is located on IMPs as these electrochemically differ from surrounding alloy matrix and are sites where localized corrosion begins.<sup>67</sup> The deposition of cerium oxide proceeds at IMPs containing copper as these sites present the sites of oxygen reduction where alkalization required for precipitation of cerium oxide is the highest.<sup>68</sup> The formation of Ce(III) oxide can be presented as:



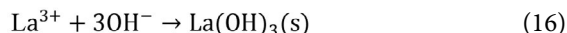
The precipitated area is rich in Ce and O conforming the formation of cerium oxide (Fig. 10b). The XPS analysis, which can differentiate between different oxidation states of an element, confirmed that the oxides formed

usually contain a mixture of Ce(III) and Ce(IV).<sup>68</sup> In the sample immersed in  $Ce(Ac)_3$ , Ce is identified in much higher concentrations than in the sample immersed in  $CeCl_3$  (Fig. 10b). Cerium is detected in bright agglomerates at the matrix surface, as well as in a large gray IMPs.

The presented results show that the efficiency of rare earth conversion coating is dependent on type of anion. Following example will prove that it is dependent also on the type of cation. In the presence of  $CeCl_3$  the cathodic current density was one order of magnitude smaller (Fig. 11a) with a strong cathodic shift of  $E_{corr}$ .<sup>69</sup> When  $LaCl_3$  was added, however, cathodic current density was smaller to lesser extent than for  $CeCl_3$  and  $E_{corr}$  shifted more negative by only 10 mV. Thus, the effect of adding  $LaCl_3$  was less than that of adding  $CeCl_3$ .

Similar as for inhibitors, we explored the possibility to improve the efficiency of conversion coatings by acting synergistically, i.e. combining different rare earth salts.<sup>69,70,71</sup> In the presence of mixtures of  $CeCl_3$  and  $LaCl_3$  in NaCl solution the cathodic curves were shifted in a more negative direction by approximately 200 mV, resulting in an  $E_{corr}$  of  $-0.84$  V (Fig. 11a).<sup>69</sup> The values of  $j_{corr}$  were smaller than in the presence of  $CeCl_3$  or  $LaCl_3$  alone. Thus, when added together to the solution, the two inhibitors act synergistically, since better results were achieved than when used individually. At a constant inhibitor concentration of 0.01 M the effect of mixing different inhibitors is slightly beneficial for  $CeCl_3$  but especially so for  $LaCl_3$ , which show improved inhibition effectiveness when mixed with  $CeCl_3$ . As lanthanum compounds are in general less effective than cerium compounds, mixing with cerium is a method for improving its protectiveness in near neutral chloride medium.

Compositional SEM images<sup>3</sup> revealed that rare earth deposits are formed primarily over IMPs (Fig. 11b).<sup>69</sup> Deposits formed in  $CeCl_3$  containing solution are round are thick containing Ce oxide, reaction (15). Deposits formed in  $LaCl_3$  solution are smaller, thinner and contain La oxide which is formed according to reaction:



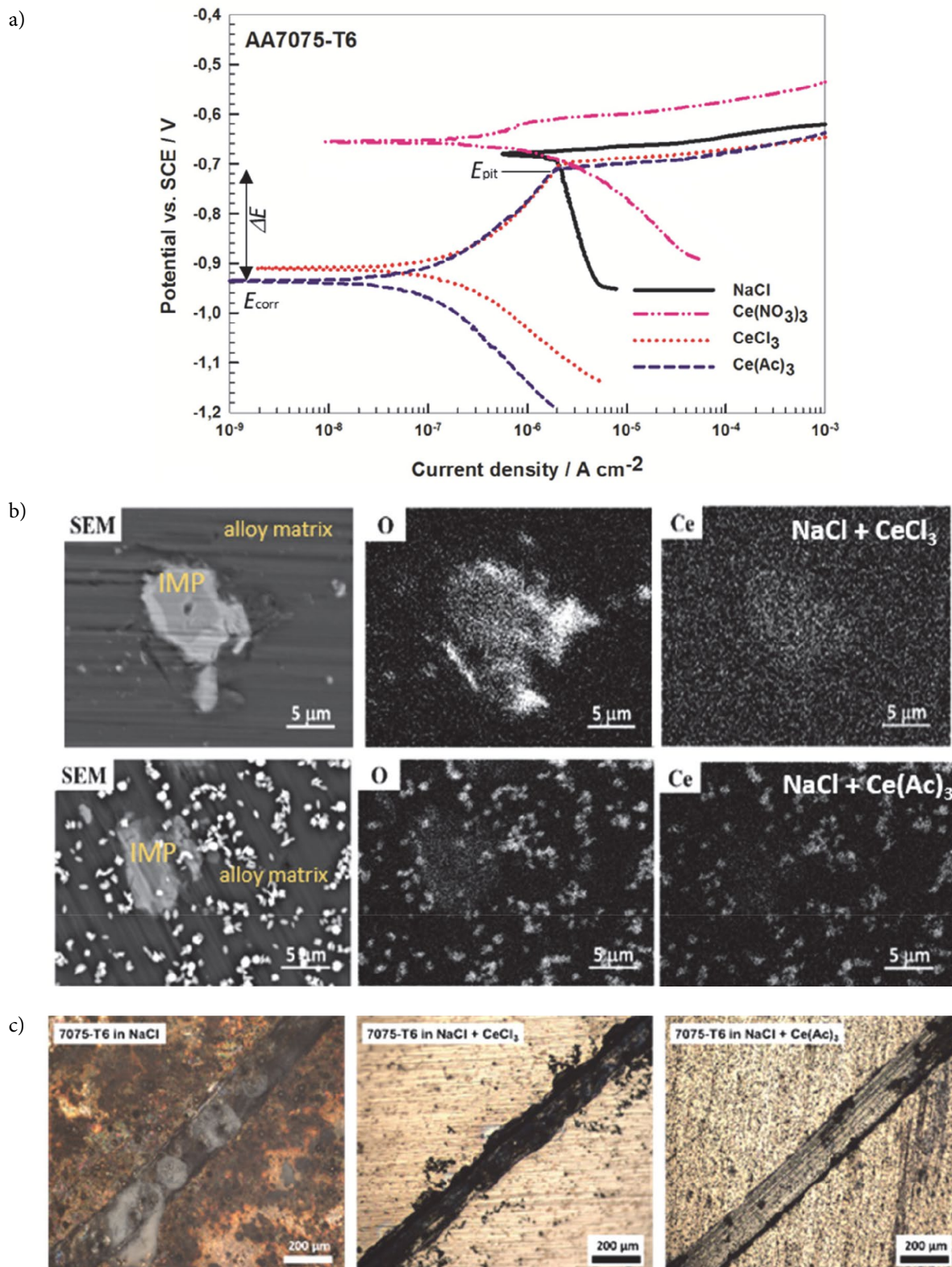
The morphology of deposits formed in the mixture of  $CeCl_3$  and  $LaCl_3$  salts is the combination of individual Ce and La contributions: deposits were brighter than when using  $LaCl_3$  only, and less bright when using  $CeCl_3$  only (Fig. 11b). EDS spectra confirmed the formation of a mixed Ce- and La oxide and/or hydroxide.<sup>69,70</sup>

### 3. 1. Conversion Coatings with Active Function

Important property of chromate coatings is the ability to repassivate when damaged.<sup>24,25,26,27</sup> In search for chro-

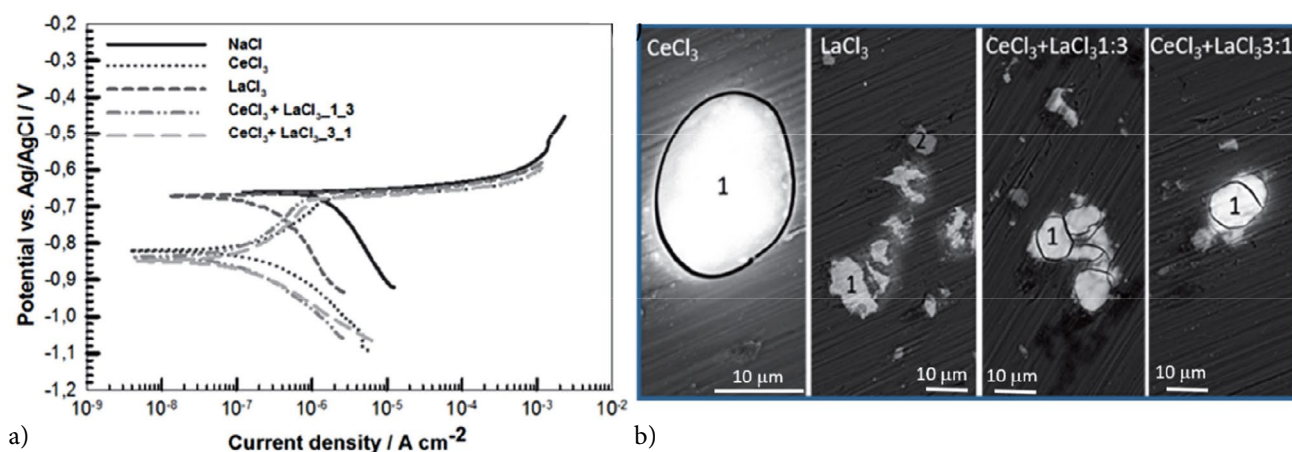
3 In compositional SEM mode the heavier elements appear brighter than lighter elements.





**Figure 10.** (a) Polarization curves recorded for aluminium alloy AA7075-T6 in 0.1 M NaCl solution with and without added 3 mM cerium(III) nitrate, chloride and acetate salts. Corrosion potential ( $E_{\text{corr}}$ ), pitting potential ( $E_{\text{pit}}$ ) and the span of passivity region ( $\Delta E$ ) are denoted.  $dE/dt=1$  mV/s. (Reprinted from the publication by P. Rodič, I. Milošev, *J. Electrochem. Soc.*, **2016**, 163, C85–C93 with permission from The Electrochemical Society.<sup>66</sup>) (b) SEM images of AA7075-T6 immersed for 24 h in 0.1 M NaCl + 3 mM  $\text{CeCl}_3$  and 3 mM  $\text{Ce}(\text{Ac})_3$  for 24 h and EDS mapping for O and Ce elements. (c) Confocal microscope images of artificially made scratch on AA7075-T6 after 72 h immersion in 0.1 M NaCl and 0.1 M NaCl with added 3 mM  $\text{CeCl}_3$  and 3 mM  $\text{Ce}(\text{Ac})_3$ . (Reprinted from the publication by I. Milošev, P. Rodič, *Corrosion*, **2016**, 72, 1021–1034 with permission from NACE.<sup>67</sup>)

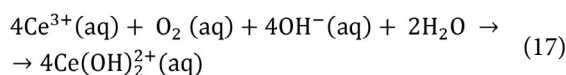




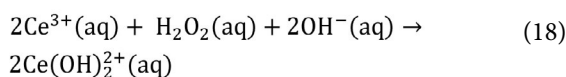
**Figure 11.** a) Polarization curves recorded for aluminium alloy AA7075-T6 in 0.1 M NaCl solution with and without added 0.01 M cerium(III) chloride, lanthanum(III) chloride and their mixtures in ratio 1:3 and 3:1.  $dE/dt=1$  mV/s. (b) SEM images recorded in compositional mode of AA7075-T6 immersed for 12 h in 0.1 M NaCl with added  $\text{CeCl}_3$ ,  $\text{LaCl}_3$  and their mixtures. (Reprinted from the publication by B. Volarič, I. Milošev, *Corr. Eng. Sci. Technol.*, 2017, 52, 201–211 with permission from Taylor & Francis.<sup>69</sup>)

mate replacement alternatives it is therefore necessary to inspect also this ability. Self-healing, active protection and self-repassivation are terms used to denote the ability of the coating to recover after damage.<sup>72</sup> Cerium based coating exhibit this ability due to the existence of two oxidation states, Ce(III) and Ce(IV), which are in dynamic equilibrium.<sup>62</sup> In order to investigate the self-healing, the surface has to be artificially damaged, and the repassivation over damaged is then followed. Optical microscope images of the scratched surface after 48 h immersion in 0.1 M NaCl with and without addition of 3 mM  $\text{CeCl}_3$  and 3 mM  $\text{Ce}(\text{Ac})_3$  are presented in Fig. 10c.<sup>67</sup> Scratched surface could not repassivate in NaCl solution and the scratch was filled with voluminous whitish corrosion product. When  $\text{CeCl}_3$  was added to NaCl solution, the surface within the scratch remained black but without corrosion product. Surrounding surface was protected, unlike in NaCl, preserving a metallic appearance. When  $\text{Ce}(\text{Ac})_3$  was present in the solution, the scratch was covered with the same layer as the surrounding surface, proving the repassivation within the defect.<sup>67</sup> The ability to repassivate and self-heal the surface defects during immersion in chloride solution is based on the dynamic equilibrium between Ce(III) and Ce(IV) species which eventually results in the formation of almost insoluble hydroxide and oxide within defects.<sup>62,63,65</sup>

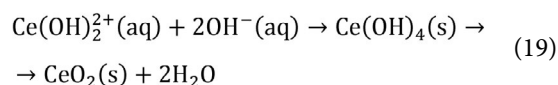
The mechanism of oxidation of Ce(III) to Ce(IV) can proceed via two alternative paths.  $\text{O}_2$  can act as oxidant and Ce(III) as a reductant:<sup>63,65</sup>



or may be reduced at cathodic sites, generating  $\text{H}_2\text{O}_2$  which can then oxidize Ce(III) to Ce(IV):



The soluble Ce(IV) species then precipitate as insoluble  $\text{CeO}_2$  due to the local rise in pH caused by the production of  $\text{OH}^{-}$  ions:<sup>63,65</sup>

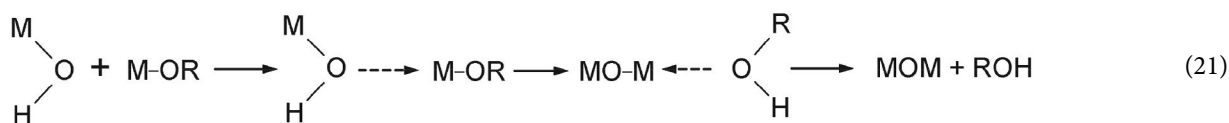
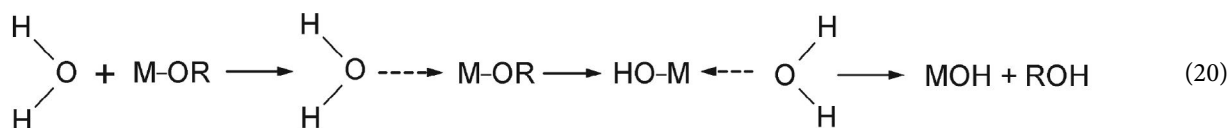


It was shown that the solubility of precipitated layer can be further reduced by the addition of sulphate ions resulting in the formation of  $\text{Ce}(\text{OH})_a(\text{SO}_4)_b$  product.<sup>73</sup>

## 4. Sol-Gel Coatings

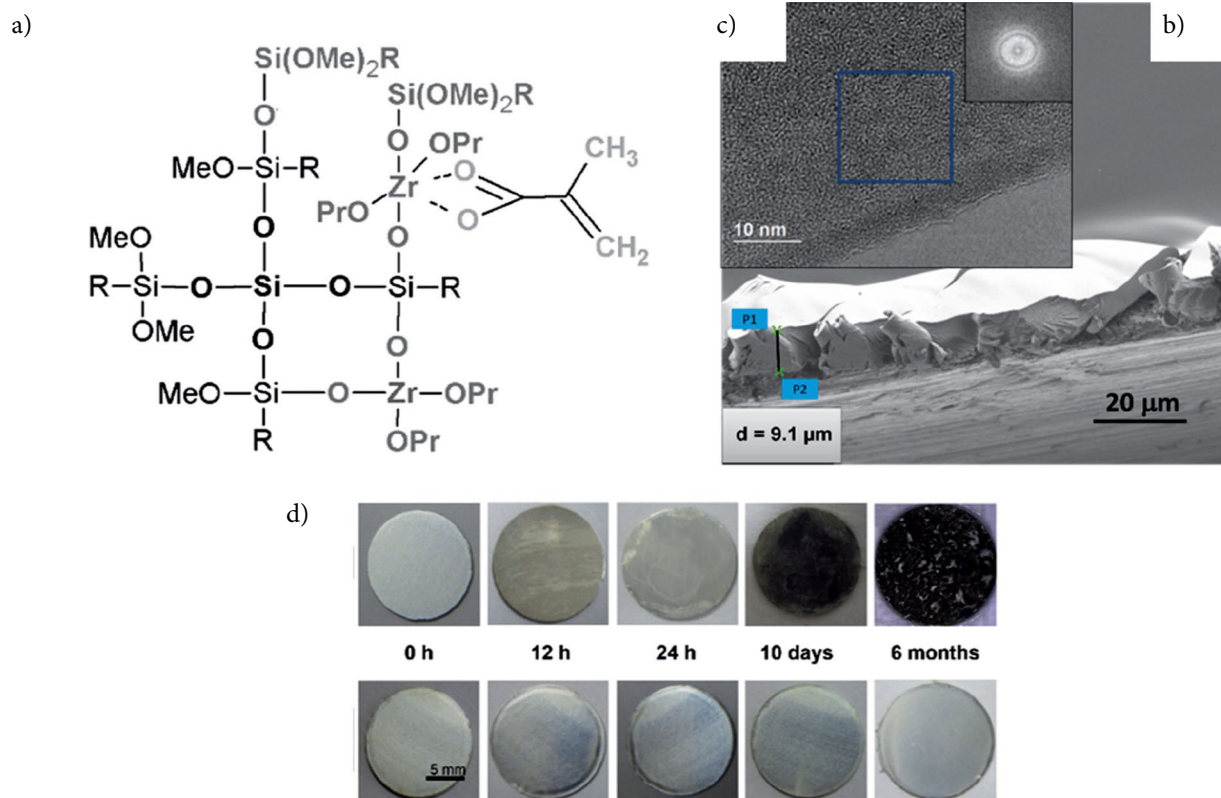
### 4.1. Barrier Sol-Gel Coatings

In the last two decades sol-gel coatings have been extensively studied for corrosion protection applications.<sup>74</sup> According to the definition, sol-gel is every process which starts from the precursor's solution and goes through the stage of *sol* and *gel*.<sup>75</sup> *Sol* is a stable suspension of colloidal particles within a liquid, and *gel* is a rigid and interconnected network. Precursors can be inorganic and organic, nowadays usually hybrid sol-gels are explored which consist of both inorganic and organic precursors. Inorganic precursors are metal alkoxides  $\text{M}(\text{OR})_4$  and organic precursors are organic alkoxides  $(\text{R}-\text{O})_{4-n}\text{MR}_n'$ , where M represents a network-forming element (Si, Ti, Zr, Al), R is an alkyl group ( $\text{C}_x\text{H}_{2x+1}$ ), and  $\text{R}_n'$  is carbon chain containing functional group, e.g. epoxy, amino, etc. Precursors can be transformed to a *gel* by chemical transformation, i.e. hydrolysis of metal alkoxide, where  $(-\text{OR})$  groups are replaced by  $(-\text{OH})$  groups, in the presence of water and catalyst (acid or basic), and polycondensation of hydroxyl groups leading to a gel network. The conversion of the precursors into hybrid sol-gel coatings proceeds through the formation of  $\text{M}-\text{O}-\text{M}$  bonds.



Sol-gel can be applied to metal surface using various techniques, such as dipping, spinning, spraying. Once deposited onto a metal surface, sol-gel coating is subjected to thermal treatment (or curing) for final condensation and densification. Due to complex chemical transformations it is necessary to use versatile methodology for sol and coating characterization.<sup>76</sup> Chemical transformations within the sol were studied using *in situ* Fourier transform infrared spectroscopy (FTIR), <sup>1</sup>H and <sup>29</sup>Si liquid

state NMR (nuclear magnetic resonance) spectroscopy, dynamic light scattering (DLS), UV-vis-NIR spectroscopy and thermogravimetric analysis (TGA). Chemical composition and morphology of the coatings were characterized using attenuated total reflectance FTIR (ATR FTIR), X-ray diffraction (XRD), glow discharge optical emission spectroscopy (GDOES), X-ray photoelectron spectroscopy (XPS), time-of-flight secondary ion mass spectrometry (ToF-SIMS), transmission electron microscopy (TEM)



**Figure 12.** (a) Schematic presentation of the hybrid TMZ network formed by a sol-gel process using TEOS (tetraethyl orthosilicate), MAPTMS (3-methacryloxypropyl trimethoxysilane), ZTP (zirconium(IV) propoxide) and MMA (methacrylic acid). (Reprinted from the publication by P. Rodič, J. Iskra, I. Milošev, *J. Non-Cryst. Solids*, **2014**, 396–397, 25–35 with permission from Elsevier.<sup>78</sup>) (b) SEM image of cross-section of TMZ coating showing homogeneous and dense structure. Coating thickness is cca. 9 μm thick. (Reprinted from the publication by P. Rodič, A. Mertelj, M. Borovšak, A. Benčan, D. Mihailović, B. Malič, I. Milošev, *Surf. Coat. Technol.*, **2016**, 286, 388–396 with permission from Elsevier.<sup>79</sup>) (c) (TEM) micrograph of amorphous TMZ coating with the corresponding fast Fourier transform (FFT) in the marked region. (Reprinted from the publication by P. Rodič, A. Mertelj, M. Borovšak, A. Benčan, D. Mihailović, B. Malič, I. Milošev, *Surf. Coat. Technol.*, **2016**, 286, 388–396 with permission from Elsevier.<sup>79</sup>) (d) Images of samples immersed in dilute Harrison's solution (3.5 g/L (NH<sub>4</sub>)<sub>2</sub>SO<sub>4</sub> + 0.5 g/L NaCl, pH=5) for different periods of time: bare aluminium alloy A7075-T6 and coated with TMZ coating. (Reprinted from the publication by P. Rodič, I. Milošev, *J. Electrochem. Soc.*, **2014**, 161, C412–C420 with permission from The Electrochemical Society.<sup>80</sup>)

and scanning electron microscopy with chemical analysis (SEM/EDS).

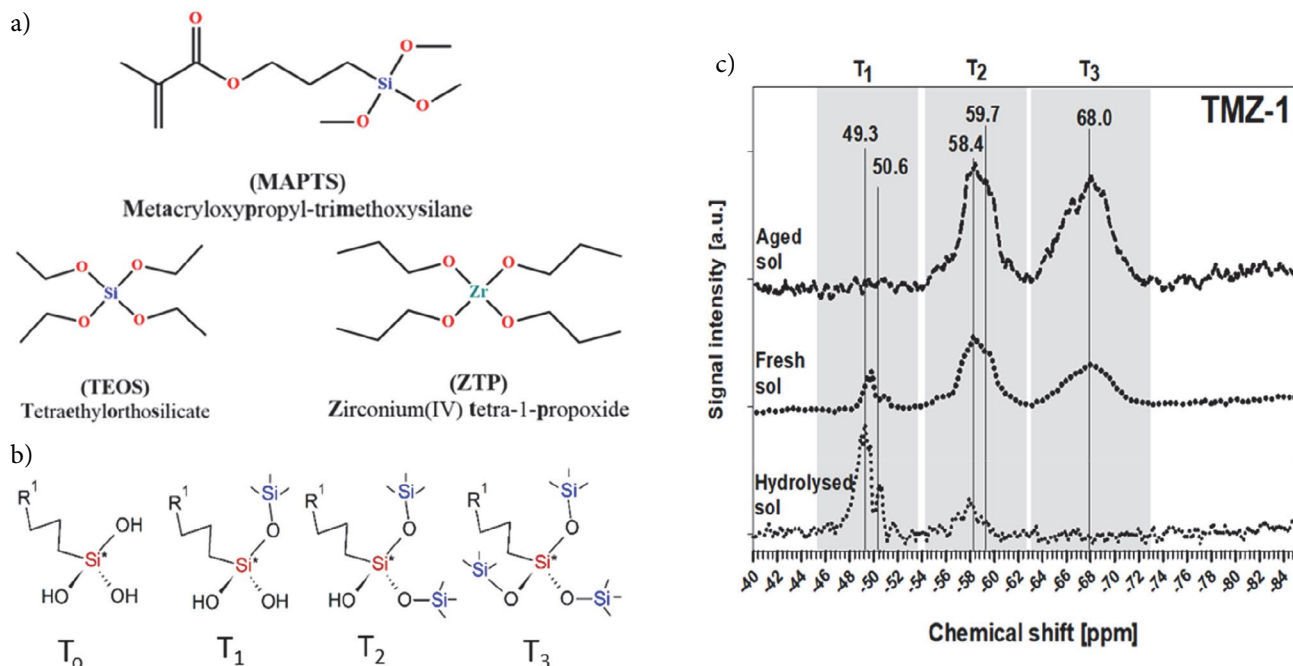
In our laboratory several hybrid sol-gel coatings were developed and will be briefly presented herein. TMZ coating is formed in a two-step process: (i) tetraethyl orthosilicate (TEOS) and 3-methacryloxypropyl trimethoxysilane (MAPTMS) were mixed and hydrolysed to obtained organosiloxane sol, and (ii) zirconium(IV) propoxide (ZTP) chelated with methacrylic acid (MAA) to obtain inorganic siloxane (skeletal formulae given below). After combining two sols, Zr initiates a condensation reaction that results in a network.<sup>77</sup> After ageing of the sol the coating was deposited on AA7075-T6 aluminium alloy substrate and cured at 100 °C. During that period, the condensation reactions were completed with the formation of Si–O–Si and Si–O–Zr bonds (Fig. 12a).<sup>77,78</sup> This transparent coating was up to 10 µm thick, homogeneous and dense (Fig. 12b).<sup>79</sup> No cracks or pores were formed. Based on XRD and TEM analyses we concluded that the coating is amorphous (Fig. 12c).<sup>79</sup> Inclusion of zirconium in sol-gel network does not lead to the formation of nanoparticles but is rather randomly distributed within amorphous inorganic-organic polymerized silicon oxide matrix.

The corrosion resistance of synthesized hybrid TMZ coatings deposited onto AA7075-T6 substrate was investigated in dilute Harrison's solution (3.5 g/L (NH<sub>4</sub>)<sub>2</sub>SO<sub>4</sub>, 0.5 g/L NaCl, pH 5.2) which simulates aircraft conditions.<sup>80</sup> The choice of solution stems from the use of this type of aluminium alloy in aerospace applications. Images of bare

AA7075-T6 sample and sample coated with TMZ coating are presented in Fig 12d<sup>80</sup> after immersion up to 6 months in dilute Harrison's solution. Corrosion of uncoated sample was visible after 12 h, followed by progressive corrosion to the end of the test. In contrast, TMZ coating remained virtually unchanged by the end of the test.

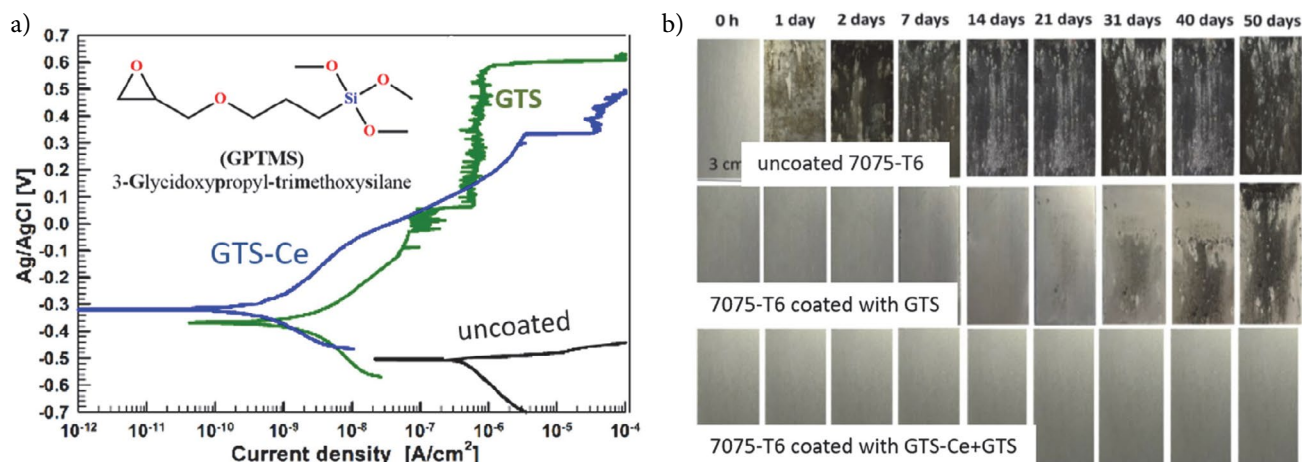
Ageing and curing are beneficial due to improved condensation and polymerization of the network.<sup>81</sup> This was proved by evaluation of content of different silanol species at different synthesis steps by <sup>29</sup>Si NMR spectroscopy (Fig. 13).<sup>81</sup> Skeletal formulae of TEOS, MAPTMS and ZTP are given in Fig. 13a. Hydrolysed sol containing only MAPTMS and TEOS contain mainly T<sub>1</sub> species indicating the initial stage of condensation (Fig. 13b). The addition of ZTP chelated with MAA to hydrolysed siloxane sol was essential to induce the condensation reactions and formation of larger silicon domains resulting in a higher degree of polycondensation, i.e. higher content of T<sub>2</sub> and T<sub>3</sub> species. The latter increased further with ageing of the sol (Fig. 13c). The establishment of Si–O–Si, and especially Si–O–Zr, bonds is crucial to achieve excellent corrosion protection: a lower number of free silanol groups (fewer T<sub>1</sub> silicon species) and formation of more condensed T<sub>2</sub> and T<sub>3</sub> silicon species improved coating properties.<sup>81,83</sup>

TMZ coatings are acrylate-based (MAPTMS and MMA). Another type of coatings developed in our laboratory are GTS epoxy-based coating prepared from TEOS and 3-glycidoxypropyl-trimethoxysilane (GPTMS) as precursors (Fig. 14a).<sup>82</sup> Silica SiO<sub>2</sub> (Ludox) particles were



**Figure 13.** (a) Skeletal formulae of MAPTMS, TEOS and ZTP precursors for TZM coatings. (b) Different siloxane species with: three silanol groups (T<sub>0</sub>), two silanol groups (T<sub>1</sub>), one silanol group (T<sub>2</sub>) and no silanol groups (T<sub>3</sub>). (c) <sup>29</sup>Si NMR spectra for hydrolysed, fresh and aged TMZ-1 sol showing increasing content of T<sub>2</sub> and T<sub>3</sub> species with ageing of the sol. (Reprinted from the publication by P. Rodič, I. Milošev, M. Lekka, F. Andreatta, L. Fedrizzi, *Prog. Org. Coat.*, **2018**, 124, 286–295 with permission from Elsevier.<sup>81</sup>)





**Figure 14.** (a) Potentiodynamic polarization curves recorded in 0.1 M NaCl, after 1 h stabilization for bare AA7075-T6 aluminium alloy and coated with GTS and GTS-Ce coatings.  $dE/dt = 1$  mV/s. (Reprinted from the publication by U. Tiringir, I. Milošev, A. Durán, Y. Castro, *J. Sol-Gel Sci. Technol.*, **2018**, 85, 546–557 with permission from Springer Nature.<sup>82</sup>) Skeletal formula of GPTMS is given in inset. (b) Images of uncoated aluminium alloy 7075-T6 and coated with GTS and GTS-Ce+GTS coatings during an immersion test in 0.1 M NaCl. Images were taken at different times of immersion up to 50 days. (Reprinted from the publication by U. Tiringir, A. Durán, Y. Castro, I. Milošev, *J. Electrochem. Soc.*, **2018**, 165, C1–C13 with permission from The Electrochemical Society.<sup>87</sup>)

added to achieve a barrier properties of coating. Organic polymerization with opening of the epoxy ring was initiated by the acidification and strong exothermic reaction.<sup>82</sup> The polymerisation continued during the synthesis, in the liquid state, resulting in a more cross-linked and dense Si–O–Si network. The degree of inorganic and organic polycondensation were 93.3 % and 80.3 % indicating high degree of condensation, especially of inorganic network. Further improvements were achieved by addition of cerium ions, as will be shown below.<sup>83</sup> Potentiodynamic polarization curves recorded in 0.1 M NaCl are presented for uncoated AA7075-T6 substrate and coated with GTS coating subjected to ramp heating up to 120 °C (Fig. 14a).<sup>82</sup> Uncoated substrate exhibits poor corrosion resistance in chloride solution as evidenced by a strong increase in current density at potentials above  $E_{\text{corr}}$ . This increase is related to pitting and intergranular localized corrosion of the alloy.<sup>1,84</sup>

Polarization curves for substrate coated with GTS coating show reduced current density for several orders of magnitude and a shift of  $E_{\text{corr}}$  to more positive values. The coating acts as an efficient barrier for preventing dissolution of substrate. This was proved also by immersion long-term testing in NaCl solution (Fig. 14b). Whilst uncoated AA7075-T6 substrate showed heavy corrosion already after 1 day, GTS-coated substrates did not show signs of corrosion up to 21 days.

## 4. 2. Sol-Gel Coatings with Active Function

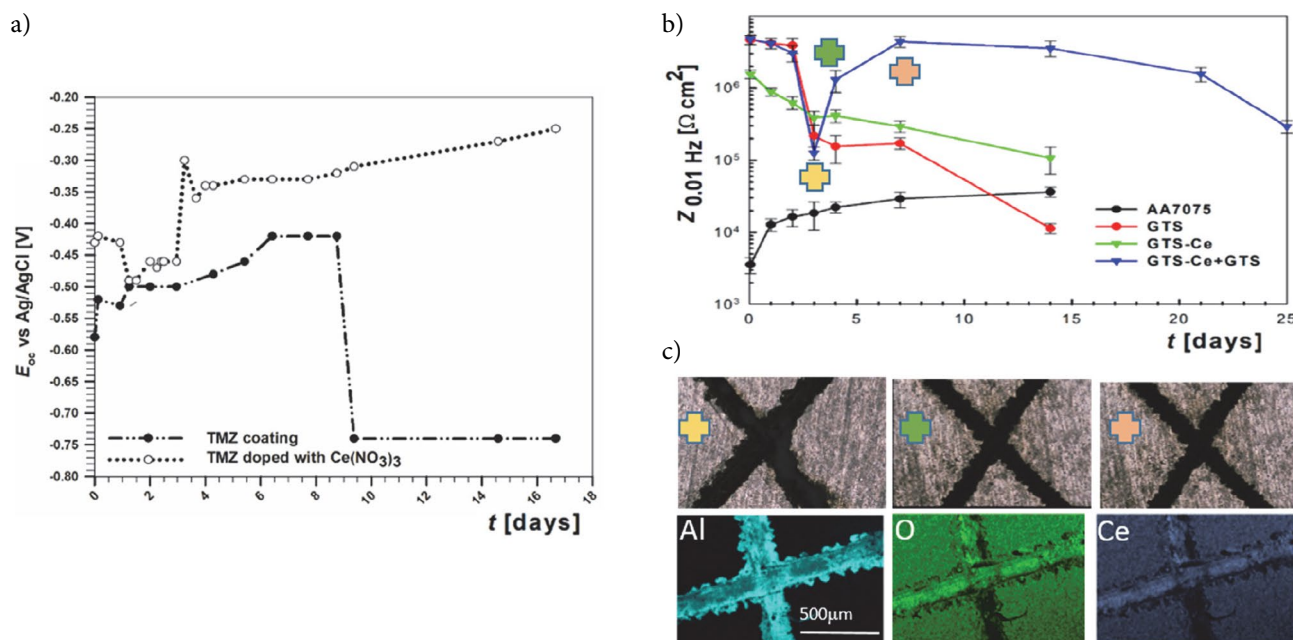
Hybrid sol-gel coatings used in corrosion protection act as barrier, i.e. prevent the penetration of electrolyte to underlying substrate due to their thickness up to ten micrometres, homogeneity and density. In real applications,

barrier protection is often not sufficient to resist corrosion attack. Once damaged, coating will become permeable to aggressive medium eventually leading to corrosion of substrate. Once corrosion process begins, it cannot be stopped. One of the solutions is to incorporate inhibitors into sol-gel matrix which would then contribute the active recovery necessary to prolong the protection.<sup>85</sup>

Cerium salts are known inhibitors, as presented in previous section. Incorporation of cerium in the sol-gel coatings is associated with a more porous network enabling the release and migration of incorporated cerium ions within the coatings.<sup>82</sup> It is noteworthy, however, that an optimal content of cerium should be incorporated since too large concentration may destruct the structural integrity of the coating.<sup>86,87</sup> At the same time, it has to be assured that doping of the coating with cerium does not reduce the barrier properties of the coating, as cerium ions are bigger in size (1.978 Å) compared to silicon atoms (1.068 Å). Larger Ce addition can cause lattice deformation and formation of nanopores and consequently change dramatically the characteristics of the coating.<sup>86</sup>

Self-healing of the coating can be followed electrochemically by measuring the open circuit potential ( $E_{\text{oc}}$ )<sup>86</sup> or impedance at low frequency range.<sup>87</sup> Upon immersion of TMZ coating,  $E_{\text{oc}}$  was cca. –0.58 V and then shifted in more positive direction reaching –0.42 V after approximately 9 days (Fig. 15a).<sup>86</sup> However, at longer immersion times the values shifted to more negative values, due to the progressive degradation of TMZ coatings. On the other hand, for the TMZ-Ce coating,  $E_{\text{oc}}$  remained stable progressing in the positive direction. This behavior may be the consequence of cerium ions in the coating which increase barrier effect but may also contribute to the self-healing effect.





**Figure 15.** Electrochemical methods used to follow the self-healing of the sol-gel coating containing cerium inhibitor to assure active protection: (a) The dependence of open circuit potential ( $E_{oc}$ ) on immersion time in 0.1 M NaCl for TMZ-3 and TMZ-3-Ce coatings. (Reprinted from the publication by P. Rodič, J. Katič, D. Korte, p.M. Desimone, M. Franko, S.M. Cer, M. Metikoš-Huković, I. Milošev, *Metals*, **2018**, 8, met8040248 with permission from MDPI.<sup>86</sup>) (b) Values of  $Z_{0.01\text{ Hz}}$  (impedance at 0.01 Hz) determined from EIS spectra for scratched uncoated AA7075-T6 and coated with GTS, GTS-Ce and GTS-Ce+GTS coating as a function of immersion time in 0.1 M NaCl. Crossed-shapes denote the time periods at which optical images in (c) were taken: yellow (3 days), green (4 days) and orange (7 days). (Reprinted from the publication by U. Tiring, A. Durán, Y. Castro, I. Milošev, *J. Electrochem. Soc.*, **2018**, 165, C1–C13 with permission from The Electrochemical Society.<sup>87</sup>) (c) Optical images taken at different immersion periods and EDS mapping spectra for scratched GTS-Ce+GTS coated AA7075-T6 after 72 h immersion. (Reprinted from the publication by U. Tiring, A. Durán, Y. Castro, I. Milošev, *J. Electrochem. Soc.*, **2018**, 165, C1–C13 with permission from The Electrochemical Society.<sup>87</sup>)

Cerium ions were added also to GTS coatings.<sup>82,83,87</sup> GTS-Ce coatings exhibited enhanced corrosion properties, as shown by reduced current density in polarization curves (Fig. 14a)<sup>82</sup> and excellent protection during long-term immersion up to 50 days in NaCl solution (Fig. 14b).<sup>87</sup> It is noteworthy that the addition of cerium increases the lifespan of hybrid sol-gel coating and has a role in self-healing if it is locked within the first layer of the multilayer coating, denoted as GTS-Ce+GTS (Fig. 15b).<sup>87</sup> Active role of cerium in the inhibition process was proved by long-term EIS measurements and immersion test on non-scribed and scribed coatings. Scribe was intentionally made by a diamond tip to simulate corrosion damage. As a decisive parameter, impedance at low frequency ( $Z_{0.01\text{ Hz}}$ ) was taken as it reflects the corrosion process at the substrate/coating interface (Fig. 15b).<sup>87</sup> Upon immersion of scribed samples, impedance was decreasing with immersion time indicating that progressive penetration of electrolyte took place leading to corrosion of the substrate. Self-healing of the GTS-Ce+GTS coating starts after 4 days of immersion in 0.1 M NaCl. After an initial decrease, the impedance at low frequency increased by more than one order of magnitude proving the self-healing process. Optical microscopy images of the scribed after 1, 3 and 4 days show that the damage re-passivate (Fig. 15c).<sup>87</sup> EDS mapping of the scribed

area proved the deposition of cerium within the scribe. Therefore, cerium ions are able to migrate within the coating and deposit in the form of insoluble hydroxide. As shown in previous section, cerium hydroxide reduces the kinetics of the cathodic reaction and overall corrosion process. XPS analysis showed that although gradually transformed into Ce(IV) hydroxide, reactions (17) – (19), both oxidation states, Ce(III) and Ce(IV), were identified, even after 14 days of immersion, indicating that the self-healing process was still operative. The self-healing ability may be achieved by the migration of  $Ce(OH)_2^{2+}$  to local damaged regions where these ions precipitate as  $Ce(OH)_4$  and  $CeO_2$ , which are highly insoluble. The self-healing cycle can be repeated as long as  $Ce^{3+}$  are present in the coating.<sup>63</sup> At a longer immersion time (21 days), the magnitude of impedance decreased, indicating diminished self-healing ability. However, the overall coating stability was still much higher than that of the coating without cerium (GTS), or single GTS-Ce coating (Fig. 14b).<sup>87</sup>

The addition of cerium to sol-gel has multifold effect. In addition to self-healing ability another important role is the effect on network formation. Cerium stimulates the polycondensation reaction at lower temperatures, in the inorganic and organic parts of hybrid sols.<sup>81,82,83,86</sup> The role of cerium is ascribed to the fact that it can act as a

Lewis acid and thus can facilitate the reaction of hydrolysis of the inorganic part and the polymerization of the organic phase of the network.<sup>83</sup>

Active protection or functionalization of the surface is beneficial not only against corrosion damage but also in other applications. Biomedical alloys like titanium alloys, cobalt chromium alloys and stainless steel are required to exhibit high corrosion resistance and biocompatibility, fatigue strength and high specific strength-to-weight ratios.<sup>88</sup> Advantageous abilities of biomedical alloys are the ability to osseointegrate and to resist bacteria attack. Whilst osseointegration assures stable long-term interface between bone and implant, resistance to adherence and colonization of bacteria on implant surface reduces the risk of infection.

Several types of sol-gel coatings were developed as functional coatings for biomedical alloys.<sup>89,90,91</sup> Titanium dioxide ( $\text{TiO}_2$ ) has received considerable attention in the field of materials science and has been extensively studied and prepared also by sol-gel methodologies. In majority of routes the obtained coatings were annealed up to 500 °C to obtain desired phase composition. Synthesis under acidic conditions using  $\text{TiCl}_4$ , HCl and  $\text{H}_2\text{O}_2$  resulted in the formation of  $\text{TiO}_2$  with predominantly rutile microstructure according to the XRD data.<sup>90</sup> This route is based on the green chemistry principles and the curing is performed at low temperature, up to 100 °C. The sol-gel  $\text{TiO}_2$  coatings were highly protective with resistance values in the  $\text{M}\Omega \text{ cm}^2$  range, as confirmed by polarization and electrochemical impedance measurements.<sup>90</sup> Furthermore, this type of sol-gel is suitable for further functionalization in terms of antibacterial ability. Silver is known for its inherent antibacterial activity against different microorganisms.<sup>92</sup> Silver(I) nitrate was added to  $\text{TiO}_2$  sol which resulted in the incorporation of silver nanoparticles in the coating structure.<sup>90</sup> Once  $\text{TiO}_2$ -Ag coating was exposed to bacteria, the adhesion of *P. aeruginosa* was reduced and bacteria shape destroyed.

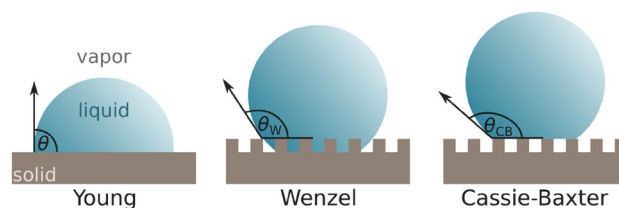
Instead using Ag nanoparticles to  $\text{TiO}_2$  sol-gel matrix, we can add  $\text{TiO}_2$  particles to inorganic-epoxy-based matrix. Illuminated  $\text{TiO}_2$  has the ability of photo-killing of bacteria by photocatalytic action which proceeds in three stages: disordering of outer membrane of bacteria cell by reactive species ( $\cdot\text{OH}$ ,  $\text{H}_2\text{O}_2$ ,  $\cdot\text{O}_2^-$ ), disordering of the inner membrane (cytoplasmic) and killing the cell, and decomposition of the dead cell.<sup>92</sup> Epoxy-based precursor GPTMS was used in combination with zirconium-based inorganic precursor ZTP and acetic acid as catalyst (coating denoted as ZG).<sup>89</sup> The final sol contains  $\text{Zr-O-Zr}$ ,  $\text{Si-O-Si}$  and  $\text{Zr-O-Si}$  bonds and incorporates acetate in its structure in a bidentate chelate coordination. After deposition of the sol in the form of a coating on titanium substrate and curing at 150 °C the opening of the epoxy ring at GPTMS leads to complete polymerization of the organic network and formation of a dense and homogeneous coating suitable for biomedical application.<sup>89</sup> After addition of

$\text{TiO}_2$  nanoparticles to sol and their incorporation in the coating, the antibacterial activity was gained. Survival of bacteria *St. aureus* on Ti coated by ZG coating with addition of  $\text{TiO}_2$  nanoparticles decreased 5-fold compared to untreated Ti.<sup>93</sup>

Osseointegration is another property important in biomedical applications. Biomimetic materials such as hydroxyapatite coatings, with a structure close to the bone matrix, have been introduced and widely investigated. Fluorohydroxyapatite (FHA) and fluoroapatite (FA) were deposited aiming to substitute of  $\text{F}^-$  for  $\text{OH}^-$  in order to lower the solubility of apatite, since high solubility could weaken the bond between implant and newly grown bone.<sup>91</sup> Total substitution with FA would not be a good solution since it is too stable and appears to be non-osteconductive. The initial triethyl phosphite precursor was hydrolyzed to phosphate after the addition of ammonium fluoride and calcium nitrate. Depending on the amount of ammonium fluoride added, FA or FHA sol gels resulted.<sup>91</sup> The consistency of FA was denser than that of FHA, much richer in small particles and contained larger fluoride content. The coatings exhibit the hydrophilic behavior that is recommended for osteoblast differentiation in tissue engineering and, consequently, for osseointegration.

## 5. Hydrophobic and Superhydrophobic Coatings

Wettability of the surface may affect different properties of the metal or coated metal.<sup>94</sup> The contact angle ( $\theta$ ) is the angle, conventionally measured through the liquid, where a liquid-vapor interface meets a solid surface (Fig. 16).



**Figure 16.** Schematic presentation of different wetting models: Young model on flat surface, and Wenzel and Cassie-Baxter models on rough surfaces.  $\theta$  is contact angle of liquid drop.

Contact angle quantifies the wettability of a solid surface by a liquid via the Young equation:

$$\cos \theta = \frac{\gamma_{sv} - \gamma_{sl}}{\gamma_{lv}} \quad (22)$$

where  $\gamma$  is surface tension ( $\gamma_{sv}$  is solid-vapour,  $\gamma_{sl}$  is solid-liquid and  $\gamma_{lv}$  is liquid-vapour). Young's equation is valid for ideal flat surfaces. On rough surfaces, the Wenzel regime is usually recognized as homogeneous wetting, since the liquid completely penetrates into the grooves

$$\cos \theta_w = r \cos \theta \quad (23)$$

where  $\theta_w$  is Wenzel's contact angle and  $r$  is roughness parameter. While under some circumstances, especially the increase of the surface roughness, vapour pockets may be trapped underneath the liquid yielding a composite interface. This heterogeneous wetting is usually described by the Cassie-Baxter:

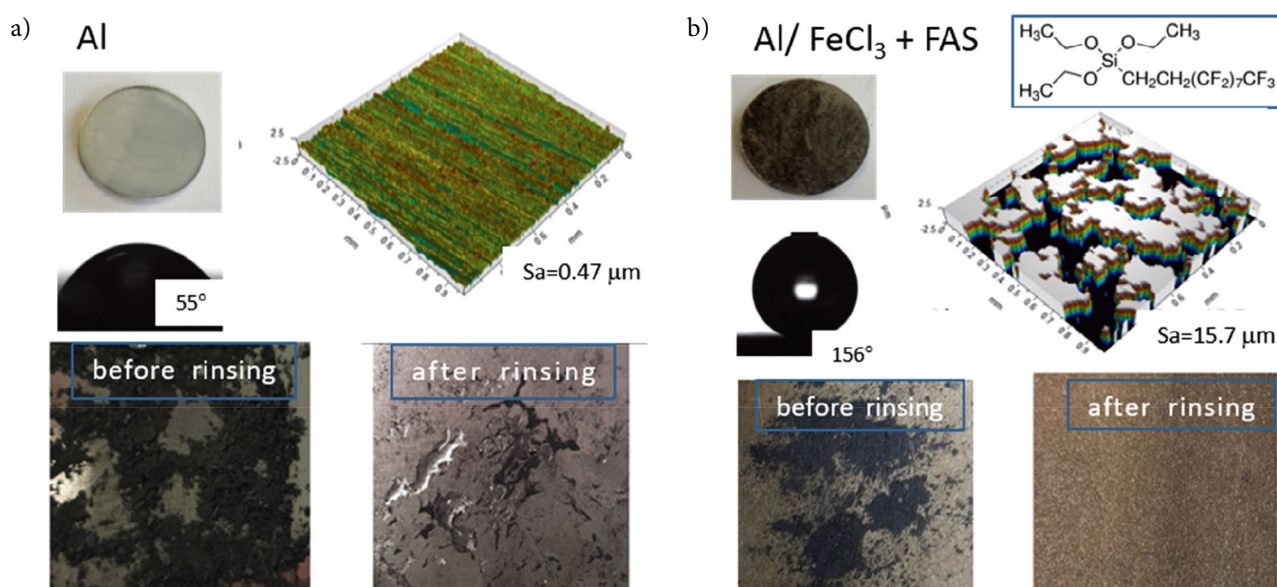
$$\cos \theta_{CB} = f_1 \cos \theta_1 + f_2 \cos \theta_2 \quad (24)$$

where  $\theta_{CB}$  is Cassie-Baxter contact angle,  $f_1$  is the fraction of surface area with contact angle  $\theta_1$  ( $f_1 + f_2 = 1$ ). It can be assumed that liquid is in contact with the solid only at the roughness tips. Due to the presence of air in pockets between rough protrusion, majority of solid surface is not wetted.

In general, superhydrophilic surface has contact angle of liquid drop  $\theta < 10^\circ$ , hydrophilic surface has  $10^\circ < \theta < 90^\circ$ , and hydrophobic  $90^\circ < \theta < 150^\circ$ . Superhydrophobic surfaces, i.e. those which have a tendency to repel water drops, are characterized by a high apparent contact angle, ( $\theta > 150^\circ$ ), low contact angle hysteresis ( $< 10^\circ$ ), and low sliding angle ( $\alpha < 5^\circ$ ).<sup>94</sup> The interest in superhydrophobic surfaces has been rising considerably as reflected by numerous review papers published in the last decade, see for example.<sup>95,96</sup> Superhydrophobic materials are useful in various industrial and every-day applications, for example as water repellent surfaces, anti-icing, self-cleaning, anti-fogging, anti-fouling, etc. Superhydrophobicity of the surface is achieved by an appropriate combination of surface roughness, texture, and low surface energy.<sup>97</sup>

To produce a superhydrophobic surface usually a two-step process is used. The first step is a mechanical modification, i.e. extensive roughening of the surface under alkaline or acid etching aiming to produce protrusions at the surface which would allow the formation of CB regime. The second step is the chemical modification, i.e. coverage of the rough surface by compound of a low surface energy. These compounds usually include long chain alkyl-, silane- or fluorinated compounds. As these chemicals are slightly soluble in water, the immersion is usually carried out in their ethanol solution.

An example is given for production of superhydrophobic aluminium. After grinding on SiC papers the surface of aluminium has an average roughness of  $0.47 \mu\text{m}$  (Fig. 17a).<sup>98</sup> This surface is hydrophilic, with  $\theta = 55^\circ$ . In order to increase the roughness, the surface was etched in solution of iron(III) chloride. This process increased the roughness to  $15.7 \mu\text{m}$  (Fig. 17b). After immersion in ethanol solution of fluoroalkyl silane (FAS) perfluorodecyl triethoxysilane the surface became superhydrophobic with  $\theta = 156^\circ$  (Fig. 17b). Fluorosilane is adsorbed on metal surface *via* siloxane Si–O–Si bonds which are formed between hydroxyl group at the metal surface and Si–O bonds of silane compound.<sup>99</sup> Perfluoro chain of FAS bonds *via* silyl Si–C bonds and accounts for hydrophobic character of the formed layer. Such hydrophobic surface acts as a corrosion barrier as it prevents the ingress of aggressive chloride anions to reach the aluminium substrate thereby promoting its dissolution. Furthermore, superhydrophobic surface exhibits the self-cleaning ability. Due to large water contact angle and small sliding angle the dirt particle



**Figure 17.** (a) Images of ground aluminium sample, water drop on its surface (contact angle  $55^\circ$ ), 3-D topographical profile (mean surface roughness  $S_a$   $0.47 \mu\text{m}$ ) and images of sample covered with carbon particles simulating dirt before and after cleaning with water jet. (b) Images of ground aluminium sample, etched using  $\text{FeCl}_3$  and immersed in ethanol solution of FAS (perfluorodecyl triethoxysilane), water drop on its surface (contact angle  $156^\circ$ ), 3-D topographical profile (mean surface roughness  $S_a$   $15.7 \mu\text{m}$ ) and images of sample covered with carbon particles simulating dirt before and after cleaning with water jet. Skeletal formula of FAS is given in (b).<sup>98</sup>

can roll-off the surface. This is known as lotus effect. Image in Fig. 17 show the unmodified and FAS-modified Al surface covered with carbon particles simulating dirt. After rinsing with water, the particles remained at the surface of unmodified Al together with water drop. Because the surface is hydrophilic, the water drop did not roll-off. In contrast, on superhydrophobic surface the same procedure produced a cleaned surface.

## 4. Concluding Remarks

Growing consumption of materials worldwide is putting requirements on materials for increased functionality and versatile physico-chemical properties such as corrosion resistance, thermal barrier, antifouling and antimicrobial properties and mechanical properties such as wear resistance hardness and strength, etc. Let us not forget environmental impact – production of materials should be in line with strict environmental standards. Price of surface treatment is also an important issue governing its marketability. When considering corrosion resistance, it would be desirable for a material to show not only barrier protection but also to respond to triggers from environment, i.e. to recover when damaged. Furthermore, the protective coating should promote subsequent adhesion of topcoat. Corrosion protection is usually a combination of several layers: pre-treatment, followed by primer and toplayer. Therefore, versatility in modes and treatments is desirable. These high requirements and strict environmental and economic rules are setting high demands on industrial producers and, consequently, boosting research studies in industrial and academic sectors aiming for new materials and integrative solutions.

## 5. Acknowledgements

I would like to thank my colleagues at the Department of Physical and Organic Chemistry doc. dr. Anton Kokalj, dr. Antonija Lesar, prof. dr. Jernej Iskra and prof. dr. Stojan Stavber for fruitful collaboration. Valuable research work of Ph.D. students and coworkers in last 15 years is acknowledged: dr. Tadeja Kosec, dr. Matjaž Finšgar, dr. Sebastijan Peljhan, dr. Nataša Kovačević, dr. Jasminka Pavlinac, Dunja Gustinčič, M.Chem., dr. Gregor Žerjav, dr. Peter Rodič, dr. Nicoleta Cotoian, dr. Daniela Covaciu Romoňi, dr. Urša Tiringner, dr. Barbara Volarič, Gavriilo Šekularac, M.Chem., Barbara Kapun, B.Sc., and dr. Matic Poberžnik. I would like to acknowledge Katja Milošev, M.Arch., for drawing Figures 2 and 3, Dolores Zimerl, M.Chem., for drawing Figure 6 and dr. Matic Poberžnik for drawing Figure 16. The financial support of our research work by the Slovenian Research Agency is greatly appreciated (research core funding No. P2-0393).

## List of symbols:

$E$  – electrode potential [V]  
 $E_{oc}$  – open circuit potential [V]  
 $E_{corr}$  – corrosion potential [V]  
 $E_{pit}$  – pitting potential [V]  
 $\Delta E = |E_{corr} - E_{pit}|$  – pseudo-passive range [V]  
 $j$  – current density [ $A\ cm^{-2}$ ]  
 $j_{corr}$  – corrosion current density [ $A\ cm^{-2}$ ]  
 $\theta$  – contact angle [°]  
 $\alpha$  – sliding angle [°]  
 $\gamma$  – surface tension [ $N\ m^{-1}$ ]

## List of abbreviations:

A – annealed (temper designation for Cu alloys)  
 ATR FTIR – attenuated total reflectance Fourier transform infrared spectroscopy  
 1-ATriH – 1-amino-1,2,4-triazole  
 3-ATriH – 3-amino-1,2,4-triazole  
 5-ATriH – 5-amino-1,2,4-triazole  
 BimH – benzimidazole  
 BTAH – benzotriazole  
 BTAOH – 1-hydroxybenzotriazole  
 CCC – chromate conversion coating  
 DFT – Density Functional Theory  
 DLS – dynamic light scattering  
 ECHA – European Chemical Agency  
 EDS – energy dispersive X-ray spectrometry  
 F – as fabricated (temper designation for Al alloys)  
 FA – fluoroapatite  
 FAS – fluoroalkyl silane  
 FHA – fluorohydroxypatite  
 GDOES – glow discharge optical emission spectroscopy  
 GPTMS – 3-glycidoxypentyl-trimethoxysilane  
 GTS – coating based on GPTMS, TEOS and  $SiO_2$   
 GTS-Ce – coating based on GPTMS, TEOS,  $SiO_2$  and  $Ce(NO_3)_3$   
 H – strain hardened (temper designation for Al alloys)  
 H – cold-worked (temper designation for Cu alloys)  
 ImiH – imidazole  
 ImiMe – 1-methyl-imidazole  
 IMP – intermetallic particles  
 M – manufactured (temper designation for Cu alloys)  
 MAA – methacrylic acid  
 MAPTMS – 3-methacryloxypropyl trimethoxysilane  
 MBV – modified Bauer Vogel process  
 NMR – nuclear magnetic resonance  
 NTAH – naphthotriazole  
 O – annealed (temper designation for Al alloys)  
 Q – quench-hardened (temper designation for Cu alloys)  
 REACH – Registration, Evaluation, Authorization and Restriction of Chemicals  
 ROHS – Restriction of Hazardous Substances  
 SEM – scanning electron microscopy  
 SH-BimH – 2-mercaptobenzimidazole



SH-BimMe – 2-mercapto-1-methylbenzimidazole  
 SVCH – Substances of Very High Concern  
 T – thermally treated (temper designation for Al alloys)  
 T – heat-treated (temper designation for Cu alloys)  
 TAH – 1,2,3-triazole  
 TEM – transmission electron microscopy  
 TEOS – tetraethyl orthosilicate  
 TGA – thermogravimetric analysis  
 TMZ – coating based on TEOS, MAPTMS and ZTP  
 ToF-SIMS – time-of-flight secondary ions mass spectrometry  
 TriH – 1,2,4-triazole  
 TriMe – 1-methyl-1,2,4-triazole  
 UV-vis-NIR – ultraviolet-visible near infrared  
 W – solution heat-treated (temper designation for Al alloys)  
 XPS – X-ray photoelectron spectroscopy  
 XRD – X-ray diffraction  
 ZG – coating based on Zirconium(IV) propoxide and GPTMS  
 ZTP – zirconium(IV) propoxide

### Author biography

Prof. Ingrid Milošev received her BSc degree at the Faculty of Technology University of Zagreb and PhD degree at the Faculty of Natural Sciences University of Ljubljana. She has been employed at the Jožef Stefan Institute (JSI) since 1987. Since 2001 she holds additional position as a research fellow at the Valdoltra Orthopaedic Hospital. She was a post-doctoral fellow at the Heinrich-Heine University of Düsseldorf, Germany. Since 2005 she has been the head of the Department of Physical and Organic Chemistry at the JSI and since 2013 full professor at the Jožef Stefan International Postgraduate School (JSIPS). From 2007 to 2019 she was the member of the Scientific Council of the JSI, she is currently the member of the Scientific Council of the JSIPS. She has been involved as a project leader or a co-worker in numerous national and European projects such as M-Era.Net, MSC ITN, COST, Interreg, etc.

Dr. Milošev's scientific interests include corrosion processes and corrosion protection of technological and biomedical materials aiming to prolong their life-time and functional abilities. Methodologies of corrosion protection are versatile from sol-gel and conversion coatings, inorganic coatings, self-assembled layers to corrosion inhibitors.

She has published over 170 scientific papers in peer-reviewed journals, presented over 130 contributions at international and national symposia, delivered 14 invited lectures, including the prestigious Gordon conference in USA in 2016, and wrote 6 chapters in scientific books published by international publishing houses. Her publications were cited more than 4500 times (hirsch index 38). Dr. Milošev supervised 8 and co-supervised 3 doctoral

(PhD) theses. She was the guest-editor in *Acta Chimica Slovenica* (2014), *Croatia Chimica Acta* (2017) and *Corrosion* (2017) journals. In last few years she has been awarded *outstanding reviewer* status in several eminent journals. Since 2016 she has been the associate editor of the journal *npj Materials Degradation* within the Nature Journal Group.

In 2011 Dr. Milošev was awarded the Slovenian national award - *Zois Certificate of Recognition for significant achievements*, and in 2016 *Pregl award* of the National Institute of Chemistry for exceptional achievements.

## 6. References

1. Uhlig's Corrosion Handbook, edited by R. Winston Revie, Second edition, Electrochemical Society Series, Wiley-Interscience, **2006**.
2. D. Pletcher, F.C. Walsh, Industrial Electrochemistry, Chapman and Hall, **1990**.
3. <https://corrosion-doctors.org/Forms/Accidents.htm>
4. G. Schmitt, M. Schütze, G.F. Hays, W. Burns, E.-H. Han, A. Pourbaix, G. Jacobson: White paper Global Need for Knowledge Dissemination, Research, and Development in Materials Deterioration and Corrosion Control, The World Corrosion Organization, 2009 [http://corrosion.org/Corrosion+Resources/Publications/\\_/whitepaper.pdf](http://corrosion.org/Corrosion+Resources/Publications/_/whitepaper.pdf)
5. B. Hou, X. Li, X. Ma, C. Du, D. Zhang, M. Zhen, W. Xu, D. Lu, F. Ma, *npj Materials Degradation* **2017**, 1, 4: DOI:10.1038/s41529-017-0005.
6. O. Vidal, B. Goffé, N. Arndt, *Nature Geosci.* **2013**, 6, 894–896. DOI:10.1038/s41529-017-0005-2
7. <http://www.mining.com/global-energy-transition-powersurge-demand-metals/>
8. <https://www.aluminium-messe.com/en/ALUMINIUM-2020/Demand-for-aluminium-is-growing-worldwide/758/>
9. B.W. Schipper, H.-C. Lin, M.A. Meloni, K. Wansleben, R. Heijungs, E. van der Voet, *Resources, Conservation & Recycling*, **2018**, 132, 28–36. DOI:10.1016/j.resconrec.2018.01.004
10. A. Elshkaki, T.E. Graedel, L. Ciacchi, B.K. Reck, *Global Environ. Change* **2016**, 29, 305–315. DOI:10.1016/j.gloenvcha.2016.06.006
11. <https://www.statista.com/statistics/254839/copper-production-by-country/>
12. <https://copperalliance.eu/about-copper/copper-and-its-alloys/properties/>
13. ASTM B 601-02, Standard Classification for Temper Designation for Copper and Copper Alloys—Wrought and Cast.
14. <https://ycharts.com>
15. <http://www.fabricatingandmetalworking.com>
16. G. Šekularac, I. Milošev, *Corros. Sci.* **2018**, 144, 54–73. DOI:10.1016/j.corsci.2018.08.038
17. J. R. Davis. *Corrosion of Aluminum and Aluminum Alloys*, p. 327, ASM International, (1999).
18. [https://www.copper.org/resources/properties/protection/clear\\_finishes.html](https://www.copper.org/resources/properties/protection/clear_finishes.html)

19. O. Gharbi, S. Thomas, C. Smith, N. Biribilis, *npj Mater. Degrad.* **2018**, 2, article no. 12, 1–8.  
DOI:10.1038/s41529-018-0034-5
20. Z. Gao, D. Zhang, X. Li, S. Jiang, Q. Zhang, *Colloids Surf. A* **2018**, 546, 221–236. DOI:10.1016/j.colsurfa.2018.03.018
21. I. Milošev, G.S. Frankel, *J. Electrochem. Soc.* **2018**, 165, C1–C18. DOI:10.1149/2.0371803jes
22. S.T. Abrahami, J.M.M. de Kok, H. Terryn, J.M.C. Mol, *Front. Chem. Sci. Eng.* **2017**, 11, 465–482.  
DOI:10.1007/s11705-017-1641-3
23. <https://www.european-aluminium.eu/>
24. O. Bauer, O. Vogel, German Patent Specification, U.S. Patent no. 423758.
25. M.W. Kendig, R.G. Buchheit, *Corrosion* **2003**, 59, 379–400.  
DOI:10.5006/1.3277570
26. J. K. Hawkins, H. S. Isaacs, S. M. Heald, J. Tranquada, G.E. Thompson, G.C. Wood, *Corros. Sci.* **1987**, 27, 391–399.  
DOI:10.1016/0010-938X(87)90081-3
27. J. Zhao, G.S. Frankel, R.L. McCreery, *J. Electrochem. Soc.* **1998**, 145, 2258–2264. DOI:10.1149/1.1838630
28. S. Adhikari, K.A. Unocic, Y. Zhai, G.S. Frankel, J. Zimmerman, *Electrochim. Acta* **2011**, 56, 1912–1924.  
DOI:10.1016/j.electacta.2010.07.037
29. <https://www.rohsguide.com/>
30. <https://www.osha.gov/>
31. <https://echa.europa.eu/>
32. [http://europa.eu/rapid/press-release\\_IP-10-1465\\_en.htm](http://europa.eu/rapid/press-release_IP-10-1465_en.htm)
33. D.J. Gardiner, A.C. Gorvin, C. Gutteridge, A.R. Jackson, E.S. Raper, *Corros. Sci.* **1985**, 25, 1019–1027.  
DOI:10.1016/0010-938X(85)90069-1
34. C. Deslouis, B. Tribollet, G. Mengoli, M. Musiani, *J. Appl. Electrochem.* **1988**, 18, 374–383. DOI:10.1007/BF01093751
35. G. Kear, B. D. Barker, F. C. Walsh, *Corros. Sci.* **2004**, 46, 109–135. DOI:10.1016/S0010-938X(02)00257-3
36. I. Milošev, M. Metikoš-Huković, *J. Electrochem. Soc.* **1991**, 138, 61–67.
37. T. Kosec, I. Milošev, B. Pihlar, *Appl. Surf. Sci.* **2007**, 253, 8863–8873. DOI:10.1016/j.apsusc.2007.04.083
38. T. Kosec, D. Kek Merl, I. Milošev, *Corros. Sci.* **2008**, 50, 1987–1997. DOI:10.1016/j.corsci.2008.04.016
39. M. Finšgar, A. Lesar, A. Kokalj, I. Milošev, *Electrochim. Acta* **2008**, 53, 8287–8297. DOI:10.1016/j.electacta.2008.06.061
40. M. Finšgar, I. Milošev, *Corros. Sci.* **2010**, 52, 2737–2749.  
DOI:10.1016/j.corsci.2010.05.002
41. D. Tromans, R.-H. Sun, *J. Electrochem. Soc.* **138** (1991) 3235–3244. DOI:10.1149/1.2085397
42. A. Kokalj, S. Peljhan, M. Finšgar, I. Milošev, *J. Am. Chem. Soc.* **2010**, 132, 16657–16668. DOI:10.1021/ja107704y
43. M. Finšgar, J. Kovač, I. Milošev, *J. Electrochem. Soc.* **2010**, 157, C52–C60. DOI:10.1016/j.corsci.2010.04.001
44. M. Finšgar, I. Milošev, *Mater. Corr.* **2011**, 62, 956–966.  
DOI:10.1002/maco.201005645
45. A. Lesar, I. Milošev, *Chem. Phys. Lett.* **2009**, 483, 198–203.  
DOI:10.1016/j.cplett.2009.10.082
46. M. Finšgar, I. Milošev, B. Pihlar, *Acta Chim. Slov.* **2007**, 54, 591–597.
47. A. Kokalj, N. Kovačević, S. Peljhan, M. Finšgar, A. Lesar, I. Milošev, *ChemPhysChem* **2011**, 12, 3547–3555.  
DOI:10.1002/cphc.201100537
48. I. Milošev, N. Kovačević, A. Kokalj, *Corros. Sci.* **2015**, 98, 107–118. DOI:10.1016/j.corsci.2015.05.006
49. N. Kovačević, I. Milošev, A. Kokalj, *Corros. Sci.* **2015**, 98, 457–470. DOI:10.1016/j.corsci.2015.05.041
50. N. Kovačević, I. Milošev, A. Kokalj, *Corros. Sci.* **2017**, 124, 25–34. DOI:10.1016/j.corsci.2017.04.021
51. I. Milošev, N. Kovačević, A. Kokalj, *Acta Chim. Slov.* **2016**, 63, 544–559. DOI:10.17344/acsi.2016.2326
52. A. Kokalj, Molecular Modeling of Corrosion Inhibitors, In: Reference Module in Chemistry, Molecular Sciences and Chemical Engineering, Elsevier, vol. 61, **2018**, pp. 332–345.  
DOI:10.1016/B978-0-12-409547-2.13444-4
53. D. Peca, B. Pihlar, Milošev, *Acta Chim. Slov.* **2014**, 61, 457–467.
54. I. Milošev, J. Pavlinac, M. Hodošček, A. Lesar, *J. Serb. Chem. Soc.* **2013**, 78, 2069–2086. DOI:10.2298/JSC131126146M
55. I. Milošev, T. Kosec, M. Bele, *J. Appl. Electrochem.* **2010**, 40, 1317–1323. DOI:10.1007/s10800-010-0078-x
56. T. Kosec, A. Legat, I. Milošev, *Prog. Org. Coat.* **2010**, 69, 199–206. DOI:10.1016/j.porgcoat.2010.04.010
57. G. Žerjav, I. Milošev, *Corros. Sci.* **2015**, 98, 180–191.  
DOI:10.1016/j.corsci.2015.05.023
58. G. Žerjav, I. Milošev, *Int. J. Electrochem. Soc.* **2014**, 9, 2696–2715.
59. G. Žerjav, I. Milošev, *Mater. Corr.* **2015**, 66, 1402–1413.  
DOI:10.1002/maco.201508383
60. G. Žerjav, I. Milošev, *Mater. Corr.* **2016**, 67, 92–103.  
DOI:10.1002/maco.201508384
61. G. Žerjav, A. Lanzutti, F. Andreatta, L. Fedrizzi, I. Milošev, *Mater. Corr.* **2017**, 68, 30–41. DOI:10.1002/maco.201608954
62. B.R.W. Hinton, D.R. Arnott, N.E. Ryan, *Met. Forum* **1985**, 7, 211–217.
63. T. G. Harvey, *Corr. Eng. Sci. Technol.* **2013**, 48, 248–269.  
DOI:10.1179/1743278213Y.0000000089
64. K.A. Yasakau, M.L. Zheludkevich, S.V. Lamaka, M.G.S. Ferreira, *J. Phys. Chem. B* **2006**, 110, 5515–5528.  
DOI:10.1021/jp0560664
65. F.H. Scholes, C. Soste, A.E. Hughes, S.G. Hardin, P.R. Curtis, *Appl. Surf. Sci.* **2006**, 253, 1770–1780.  
DOI:10.1016/j.apsusc.2006.03.010
66. P. Rodič, I. Milošev, *J. Electrochem. Soc.* **2016**, 163, C85–C93.  
DOI:10.1149/2.0431603jes
67. I. Milošev, P. Rodič, *Corrosion* **2016**, 72, 1021–1034.
68. I. Santana, A. Pepe, E. Jimenez-Pique, S. Pellice, I. Milošev, S. Ceré, *Surf. Coat. Technol.* **2015**, 265, 106–115.  
DOI:10.1016/j.surfcoat.2015.01.050
69. B. Volarič, I. Milošev, *Corr. Eng. Sci. Technol.* **2017**, 52, 201–211. DOI:10.1080/1478422X.2016.1245957
70. I. Milošev, B. Volarič, *Corrosion* **2017**, 73, 822–843.  
DOI:10.5006/2353
71. B. Volarič, A. Manzare, S. Virtanen, I. Milošev, to be submitted.
72. Y. Gonzales-Garcia, S.J. Garcia, J.M.C. Mol, Chapter 9, In:

- Active Protective Coatings, edited by A.E. Hughes, J.M.C. Mol, M.L. Zheludkevich, R.G. Buchheit, Springer Series in Materials Science, vol. 233, **2016**, pp. 203–240.
73. P. Rodič, I. Milošev, *Corros. Sci.* **2019**, *149*, 108–122. DOI:10.1016/j.corsci.2018.10.021
  74. R.B. Figueira, C.J.R. Silva, E.V. Pereira, *J. Coat. Technol. Res.* **2015**, *12*, 1–35. DOI:10.1007/s11998-014-9595-6
  75. A.C. Pierre, Introduction to Sol-Gel Processing, Springer US, **1998**. DOI:10.1007/978-1-4615-5659-6
  76. I. Milošev, Ž. Jovanović, J.B. Bajat, R. Jančić-Heinemann, V.B. Mišković-Stanković, *J. Electrochem. Soc.* **2012**, *159*, C303–C311. DOI:10.1149/2.042207jes
  77. P. Rodič, J. Iskra, I. Milošev, *J. Sol-Gel Sci. Technol.* **2014**, *70*, 90–103. DOI:10.1007/s10971-014-3278-8
  78. P. Rodič, J. Iskra, I. Milošev, *J. Non-Cryst. Solids* **2014**, 396–397, 25–35. DOI:10.1016/j.jnoncrysol.2014.04.013
  79. P. Rodič, A. Mertelj, M. Borovšak, A. Benčan, D. Mihailović, B. Malič, I. Milošev, *Surf. Coat. Technol.* **2016**, *286*, 388–396. DOI:10.1016/j.surfcoat.2015.12.036
  80. P. Rodič, I. Milošev, *J. Electrochem. Soc.* **2014**, *161*, C412–C420. DOI:10.1149/2.1091409jes
  81. P. Rodič, I. Milošev, M. Lekka, F. Andreatta, L. Fedrizzi, *Prog. Org. Coat.* **2018**, *124*, 286–295. DOI:10.1016/j.porgcoat.2018.02.025
  82. U. Tiringier, I. Milošev, A. Durán, Y. Castro, *J. Sol-Gel Sci. Technol.* **2018**, *85*, 546–557. DOI:10.1007/s10971-017-4577-7
  83. U. Tiringier, B. Mušič, D. Zimerl, G. Šekularac, S. Stavber, I. Milošev, *J. Non-Cryst. Solids* **2019**, *510*, 93–100. DOI:10.1016/j.jnoncrysol.2018.12.021
  84. U. Tiringier, J. Kovač, I. Milošev, *Corros. Sci.* **2017**, *119*, 46–59. DOI:10.1016/j.corsci.2017.02.018
  85. H.R. Fischer, S.J. Garcia, Chapter 7, In: Active Protective Coatings, edited by A.E. Hughes, J.M.C. Mol, M.L. Zheludkevich, R.G. Buchheit, Springer Series in Materials Science, vol. 233, **2016**, pp. 139–156.
  86. P. Rodič, J. Katič, D. Korte, P.M. Desimone, M. Franko, S.M. Ceré, M. Metikoš-Huković, I. Milošev, *Metals* **2018**, *8*, met8040248. DOI:10.3390/met8040248
  87. U. Tiringier, A. Durán, Y. Castro, I. Milošev, *J. Electrochem. Soc.* **2018**, *165*, C1–C13.
  88. I. Milošev, *Pure & Appl. Chem.* **2011**, *83*, 309–324. DOI:10.1351/PAC-CON-10-07-09
  89. I. Milošev, B. Kapun, P. Rodič, J. Iskra, *J. Sol-Gel Sci. Technol.* **2015**, *74*, 447–459. DOI:10.1007/s10971-015-3620-9
  90. N. Cotoian, M. Rak, M. Bele, A. Cör, L.M. Muresan, I. Milošev, *Surf. Coat. Technol.* **2016**, *307*, 790–799. DOI:10.1016/j.surfcoat.2016.09.082
  91. D. Covaciu Romoñi, J. Iskra, M. Bele, I. Demetrescu, I. Milošev, *J. Alloys Compd.* **2016**, *665*, 355–364. DOI:10.1016/j.jallcom.2016.01.072
  92. I. Milošev, In: Biomedical and Pharmaceutical Applications of Electrochemistry, edited by S. Djokić, Modern Aspects of Electrochemistry, vol. 60, Springer, **2016**, pp. 1–88.
  93. B. Kapun, J. Iskra, P. Rodič, M. Bele, N. Veronovski, F. Šulek, M. Rak, A. Cör, I. Milošev, In: Book of Abstracts, edited by Z. Kravanja, D. Brodnik-Vončina, M. Bogataj, Slovenski kemijski dnevi 2012, Portorož, 12.–14. 9. 2012. p. 49. DOI:10.1007/s15200-012-0649-5
  94. N.J. Shirtcliffe, G. McHale, S. Atherton, and M.I. Newton, *Adv. Colloid Interface Sci.*, **2010**, *161*, 124–138. DOI:10.1016/j.cis.2009.11.001
  95. S. Das, S. Kumar, S.K. Samal, S. Mohanty, and S.K. Nayak, *Ind. Eng. Chem. Res.* **2018**, *57*, 2727–2745.
  96. J. Jeevahan, M. Chandrasekaran, G. Britto Joseph, R.B. Durairaj, and G. Mageshwaran, *J. Coat. Res. Technol.*, **2018**, *15*, 231–250. DOI:10.1021/acs.iecr.7b04887
  - DOI:10.1007/s11998-017-0011-x
  97. I. Milošev, T. Bakarič, S. Zanna, A. Seyeux, P. Rodič, M. Poberžnik, F. Chiter, P. Cornette, D. Costa, A. Kokalj, P. Marcus, *J. Electrochem. Soc.* **2019**, *166*, C1–C16. DOI:10.1149/2.0181911jes
  98. S. Iskra, P. Rodič, I. Milošev, J. Pust, golden award at the 50th Meeting of young researchers of Slovenia **2016**, Zavod za tehnično kulturo Slovenije.
  99. P. Rodič, I. Milošev, *Surf. Coat. Technol.* **2019**, *368*, 175–185. DOI:10.1016/j.surfcoat.2019.03.082

## Povzetek

Zaščita pred korozijo je pomembno globalno vprašanje. Korozija vpliva na vse kovinske materiale v industriji, infrastrukturi, gradbeništvu, prometu, biomedicini, itn., kar povzroča njihov propad. Zato je zaščita pred korozijo nujnost, ki omogoča varno in dobro delovanje kovinskih konstrukcij in naprav. Poleg dolgoročne učinkovitosti mora biti zaščita pred korozijo okoljsko in ekonomsko sprejemljiva. Rastoča populacija s potrebami po modernih in visokotehnoloških tehnologijah povečuje porabo osnovnih in redkih kovin. Vsa ta dejstva postavljajo na področje korozijske zaščite visoke zahteve, katerih glavni cilj je podaljšati življenjsko dobo kovinskih materialov, zmanjšati potrebo po strmo naraščajoči proizvodnji in s tem ohraniti naravne vire. V tem preglednem članku so predstavljeni sodobni načini korozijske zaščite materialov, zlasti bakrovih in aluminijevih zlitin kot enih najpomembnejših osnovnih kovin. Ti načini zaščite vključujejo inhibitorje korozije, konverzijske, sol-gel in hidrofbne prevleke. Podani so primeri naših raziskav v zadnjem desetletju.



Except when otherwise noted, articles in this journal are published under the terms and conditions of the Creative Commons Attribution 4.0 International License

# Differential Capacitance of Electric Double Layer – Influence of Asymmetric Size of Ions, Thickness of Stern Layer and Orientational Ordering of Water Dipoles

Aleš Iglič,<sup>1,2,\*</sup> Ekaterina Gongadze<sup>1</sup> and Veronika Kralj-Iglič<sup>3</sup>

<sup>1</sup> Laboratory of Physics, Faculty of Electrical Engineering, University of Ljubljana, Tržaška cesta 25, SI-1000 Ljubljana, Slovenia

<sup>2</sup> Laboratory of Clinical Biophysics, Faculty of Medicine, University of Ljubljana, Zaloška 9, SI-1000 Ljubljana, Slovenia

<sup>3</sup> Laboratory of Clinical Biophysics, Faculty of Health Sciences, University of Ljubljana, Zdravstvena pot 5, SI-1000 Ljubljana, Slovenia

\* Corresponding author: E-mail: ales.iglic@fe.uni-lj.si

Received: 08-02-2019

## Abstract

The mean-field theoretical model of the electric double layer which takes into account the asymmetric finite size of anions and cations and the orientational ordering of water dipoles in the Stern and the diffuse layers is described together with a short description of the main concepts and a brief review of the literature in the theory of the electric double layer. As an example of the application of the described mean-field lattice model of the electric double layer, the influence of different sizes of anions and cations, the influence of the thickness of the Stern layer and the influence of the orientational ordering of water molecules on the asymmetric, bimodal camel-like dependence of differential capacitance on the surface potential is theoretically considered.

The presented theoretical model of the electric double layer is flexible enough to be in the future extended to more complicated multicomponent systems with molecules of different sizes and the orientational ordering of molecules.

**Keywords:** Asymmetric size of ions; relative permittivity; water ordering; Stern layer; differential capacitance

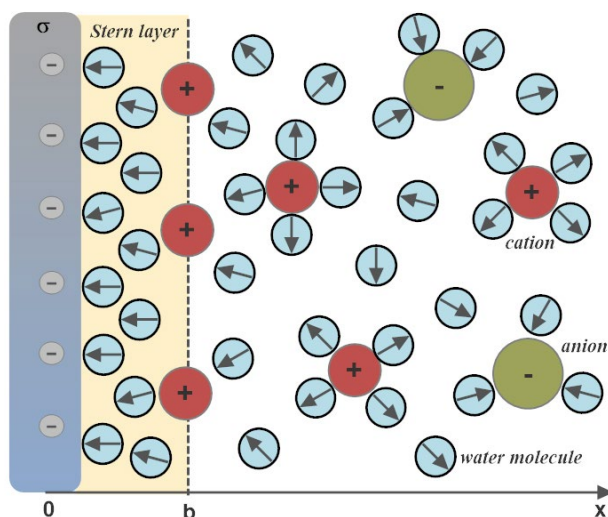
## 1. Introduction

Strong interactions between the charged surface and ions in electrolyte solution result in the formation of the electric double layer (EDL) in the close vicinity of the charged surface.<sup>1</sup> In EDL, the ions with the electric charge of the opposite sign than the charged surface (counterions) are accumulated, while the ions with a charge of the same sign as the surface (coions) are depleted from the space close to the charged surface (Fig. 1). Due to a high magnitude of electric field strength in EDL, the water dipoles near the charged surface are strongly oriented<sup>2,3</sup> (Fig. 1). Due to a non-homogeneous distribution of ions and water molecules and the orientation of water molecules in EDL, the electric field strength is screened at larger distances from the charged surface.<sup>1</sup>

EDL has been theoretically first described by Helmholtz<sup>4</sup> who neglected the effects of entropy and proposed that a single layer of counterions is formed at the charged surface. Later, Gouy and Chapman described the spatial distribution of point-like coions and counterions by Boltzmann distributions<sup>5,6</sup> corresponding to the minimum of the system free energy.<sup>7</sup> The finite size of coions and counterions has been first described by Stern<sup>8</sup> by introducing the distance of the closest approach (Fig. 1) and has later been developed further by Bikerman, Eigen, Wicke, Freise<sup>9–12</sup> and many other authors.<sup>13–24,25–28</sup>

The orientational ordering of the water dipoles in the electric field near the charged surface (Fig. 1) has been shown to strongly influence the electric field in the Stern and the diffuse layers, among others reflected also in a strong local decrease in relative permittivity.<sup>30–43</sup> The de-





**Figure 1.** A schematic figure of electrolyte solution near a negatively charged planar surface ( $\sigma < 0$ ), consisting of the Stern layer ( $0 \leq x \leq b$ ) and the diffuse layer ( $b \leq x \leq \infty$ ), where  $b$  denotes the thickness of the Stern layer, approximately equal to the distance of the closest approach of hydrated counterions. Sodium cations are weakly hydrated and have a tendency to disrupt the aqueous bulk structure without strongly ordering the water molecules.<sup>29</sup> Chemisorbed or adsorbed ions are taken into account in the value of the surface charge density  $\sigma$ .

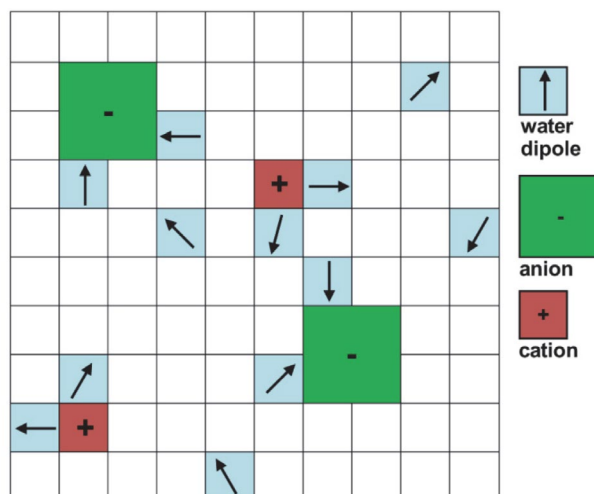
crease in the relative permittivity near the charged surface is influenced also by the excluded volume effect due to the competition between counterions and water molecules.<sup>2,35</sup>

Based on the ideas of some previous studies,<sup>9,12,44,45</sup> the mean-field model of EDL which takes into account the asymmetry of the anion and cation finite sizes and the orientational ordering of water molecules was introduced recently.<sup>46</sup> This model, named here as the modified Góngadze-Iglič (GI) model,<sup>2,46,47</sup> is shortly described in the following section.

## 2. Modified GI Model

The water molecules in the modified GI lattice model<sup>2,46</sup> were described within the modified Kirkwood approach<sup>45</sup> as point-like dipoles at the centers of finite sized spheres with permittivity equal to the square of the optical refractive index of water  $n$ .<sup>34</sup>

Within the modified GI model, the expressions for the spatial dependencies of the number densities of monovalent cations ( $n_+(x)$ ), anions ( $n_-(x)$ ) and water ( $n_w(x)$ ) in the electrolyte solution can be derived by using the method of lattice statistics with Boltzmann correction factors.<sup>2,46</sup> The method of lattice statistics with Boltzmann correction factors has been shown to be equivalent to the method of minimization of the free energy of the system.<sup>40,48</sup> The number of densities ( $n_+(x)$ , ( $n_-(x)$ ) and ( $n_w(x)$ ) are thus proportional to the probabilities that a single lat-



**Figure 2.** Lattice model of electrolyte solution.<sup>46</sup> The single positive ion and the single negative ion, each of them together with the surrounding water molecules, occupy  $\alpha_+$  and  $\alpha_-$  lattice sites, respectively. In the schematic figure  $\alpha_+ = 4$  and  $\alpha_- = 6$ , while a single water molecule occupies just one lattice site. In the model, it is assumed that the water molecules and the ions in the hydration layer which contribute to  $\alpha_+$  and  $\alpha_-$  give rise to electronic polarization only, described by the term  $n^2$  in Eq. (6). It is therefore assumed that the water dipoles which composed the hydration layer around positive or negative ions do not contribute to the orientational ordering/polarization in the electrolyte solution.

tice site in the bulk solution is occupied by one of the three particles (i.e., cations, anions or water molecules):<sup>2,46</sup>

$$n_+(x) = n_0 e^{-e_0 \phi \beta} \frac{n_s}{\mathcal{D}_A(\phi, E)} \quad (1)$$

$$n_-(x) = n_0 e^{e_0 \phi \beta} \frac{n_s}{\mathcal{D}_A(\phi, E)} \quad (2)$$

$$n_w(x) = \frac{n_{0w} n_s}{\mathcal{D}_A(\phi, E)} \frac{\sinh(\gamma p_0 E \beta)}{\gamma p_0 E \beta} \quad (3)$$

$$\mathcal{D}_A(\phi) = \alpha_+ n_0 e^{-e_0 \phi \beta} + \alpha_- n_0 e^{+e_0 \phi \beta} + \frac{n_{0w}}{\gamma p_0 E \beta} \sinh(\gamma p_0 E \beta), \quad (4)$$

where it is assumed that all lattice sites are occupied, i.e.  $n_s = \alpha_+ n_+(x) + \alpha_- n_-(x) + n_w(x)$ .

Here, the parameters  $\alpha_+$  and  $\alpha_-$  are the number of lattice sites occupied by a single positive and negative hydrated ion, respectively<sup>46</sup> (Fig. 2). A single water molecule occupies just one lattice site, therefore the reduced number density of lattice sites  $n_s/N_A = 55 \text{ mol/l}$  is equal to the concentration of pure water. The symbol  $n_{0w}$  stands for the bulk number density of water molecules,  $n_0$  is the bulk number density of anions and cations,  $\beta = 1/kT$ ,  $kT$  is thermal energy,  $e_0$  is unit charge,  $\phi$  is electric potential,  $p_0$  is magnitude of the external water dipole moment,<sup>46,48</sup>  $E$  is magnitude of electric field strength,  $x$  is distance from the

negatively charged planar surface (Fig. 1),  $\gamma$  is given by<sup>34,46</sup>:  $\gamma = (2 + n^2)/2$  and  $n$  is optical refractive index of water. In bulk,  $n_s = \alpha_+ n_0 + \alpha_- n_0 + n_{0w}$ .

In the model, a single ion together with water molecules in its first hydration layer do not contribute to orientational polarization in the solution because the orientations of the water dipoles around the ions are predominantly determined by the ion.<sup>2</sup> This assumption is in accordance with the model of Giese et al.,<sup>49</sup> where the authors proposed that each ion *together* with the strongly interacting surrounding water molecules does *not* contribute to the orientational polarization in the electrolyte solution and is considered to be a sphere consisting of a homogeneous dielectric medium with permittivity equal to 2. In our model,<sup>46</sup> it is assumed that the relative permittivity of water due to electronic polarizability is equal to the square of refractive index ( $n^2 \cong 1.8$ , where  $n = 1.33$ ) (see Eqs. (7) and (8)), which is the value very close to 2.

The Poisson's equation for the region  $x \geq b$  (see Fig. 1) can be written as:<sup>30,46</sup>

$$\frac{d}{dx} \left[ \epsilon_0 \epsilon_r(x) \frac{d\phi}{dx} \right] = 2e_0 n_s n_0 \frac{\sinh(e_0 \phi \beta)}{\mathcal{D}_A(\phi, E)}, \quad (5)$$

where  $\epsilon_r(x)$  is the spatial dependence of the relative permittivity:

$$\epsilon_r(x) = n^2 + n_{0w} n_s \frac{p_0}{\epsilon_0} \left( \frac{2 + n^2}{3} \right) \left( \frac{\mathcal{F}(\gamma p_0 E \beta)}{\mathcal{D}_A(\phi, E) E} \right) \quad (6)$$

and  $\epsilon_0$  is the permittivity of free space. The function  $\mathcal{F}(u)$  is defined as  $\mathcal{F}(u) = \mathcal{L}(u)/(\sinh u/u)$ , where  $\mathcal{L}(u)$  is the Langevin function. Eq. (6) predicts the linear decreasing of the relative permittivity in the bulk solution with an increasing salt concentration and gives the value of  $\epsilon_{r,b} \cong 78.5$  for zero bulk salt concentration.<sup>46,2</sup>

The described modified GI model includes the Helmholtz/Stern layer filled with water dipoles<sup>30,50,51</sup> (see Fig. 1). The thickness of the Helmholtz/Stern layer is defined by the distance of closest approach (Fig. 1), which is not the same for cations and anions (see for example<sup>50–54</sup>). In the Stern layer (Fig. 1), there are no free ions close to the charged surface, i.e.,  $n_+(x) = n_-(x) = 0$ . Therefore, in the Stern layer, the general expression for the relative permittivity  $\epsilon_r(x)$  (Eq. (6)) transforms into:<sup>50,51</sup>

$$\epsilon_s = n^2 + n_s \frac{p_0}{\epsilon_0} \left( \frac{2 + n^2}{3} \right) \frac{\mathcal{L}(\gamma p_0 E \beta)}{E}. \quad (7)$$

Note that the ions which are adsorbed and/or chemisorbed to the charged surface are taken into account in the model by the appropriately modified value of the surface charge density at  $x = 0$  (Fig. 1). Combining the boundary condition  $d\phi/dx(x=0) = -\sigma/\epsilon_0 \epsilon_s$  (see Fig. 1) and Eq. (7) results in the non-linear equation for the magnitude of electric field,  $E$ , in the Stern layer:<sup>30,50,51</sup>

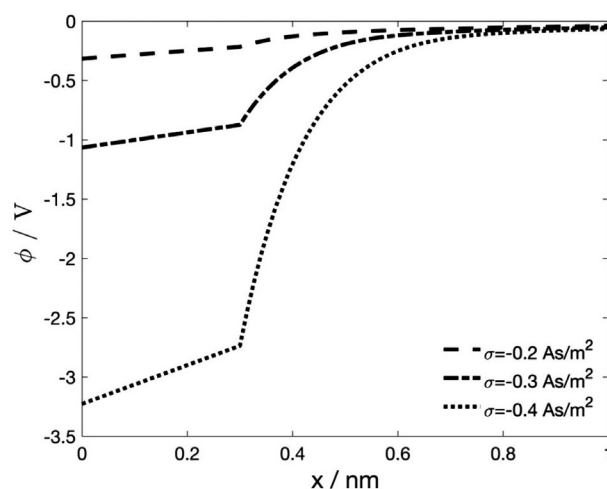
$$\epsilon_0 E \left( n^2 + n_s \frac{p_0}{\epsilon_0} \left( \frac{2 + n^2}{3} \right) \frac{\mathcal{L}(\gamma p_0 E \beta)}{E} \right) = |\sigma|. \quad (8)$$

Inserting the calculated value of  $E$  in Eq. (7) gives the value of the relative permittivity in the Stern layer ( $\epsilon_s$ ) for a given surface charge density  $\sigma$ . In this way, it was shown that relative permittivity in the Stern layer ( $\epsilon_s$ ) strongly decreases with the increasing magnitude of  $\sigma$  due to the saturation of the orientational ordering of water dipoles in a strong electric field at large values of  $\sigma$ .<sup>2,34,50</sup> (see also Fig. 4).

In the next section of the present paper, we examine the influence of asymmetric size of ions, the thickness of the Stern layer and the orientation of water dipoles in the Stern and the diffuse layers on the differential capacitance of the electric double layer calculated within the modified GI model.

### 3. Results and Discussion

Fig. 3 shows the calculated dependence of electric potential in the Stern and the diffuse double layers at the distance from the charged plane (Fig. 1). It can be that within the Stern layer, depleted of charged particles, the electric potential depends linearly on the distance from the charged surface at  $x = 0$  (see also Fig. 1). Accordingly, the electric field strength in this region with zero volume charge distribution is constant and can be determined from Eq. (8). As a consequence, the relative permittivity is also constant in the Stern layer in the whole layer. However, as shown in Fig. 4, relative permittivity in the Stern layer ( $\epsilon_s$ ) (Fig. 4B) and electric field strength (Fig. 4A) strongly depend on the surface charge density  $\sigma$ . Therefore, the



**Figure 3.** Electric potential as a function of the distance from the charged surface for different values of surface charge density  $\sigma$ , calculated within the modified GI model for  $\alpha_+ = 5$  and  $\alpha_- = 2$  (for definition of  $\alpha_+$  and  $\alpha_-$  see Fig. 2), the thickness of the Stern layer  $b = 0.3$  nm (see Fig. 1 for definition) and the bulk concentration of ions  $n_0/N_A = 0.15$  mol/l. The values of other model parameters are:  $n = 1.33$ ,  $p_0 = 3.1$  D<sup>46</sup>,  $n_s/N_A = 55$  mol/l<sup>2,30</sup> and  $T = 298$  K.

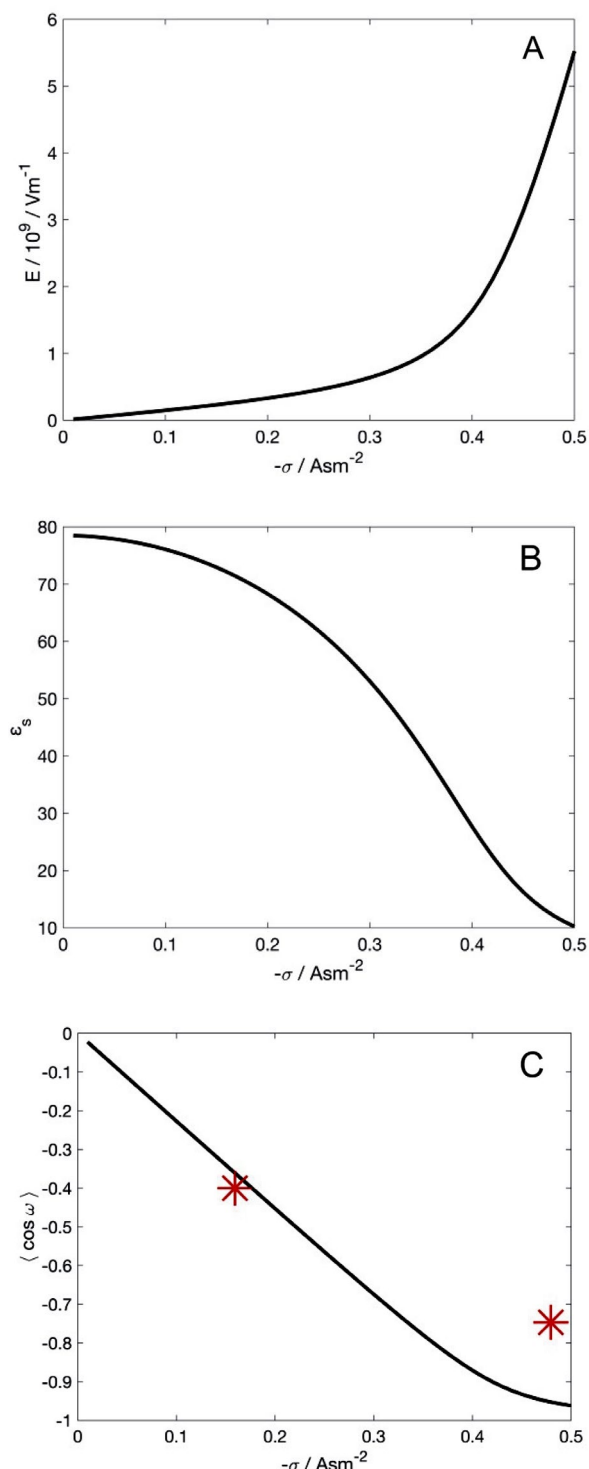
assumption of constant relative permittivity in the Stern layer, as assumed in many theoretical models of the electric double layer (see for example<sup>55</sup> and references therein), is not realistic.

The strong dependence of relative permittivity in the Stern layer (Fig. 4B) is a consequence of the orientational ordering of water dipoles in this layer (Fig. 4C), which can certainly not be neglected as suggested in some oversimplified macroscopic phenomenological theoretical models<sup>55</sup>, based on the 19<sup>th</sup> century Maxwell's mixture formula.<sup>56</sup>

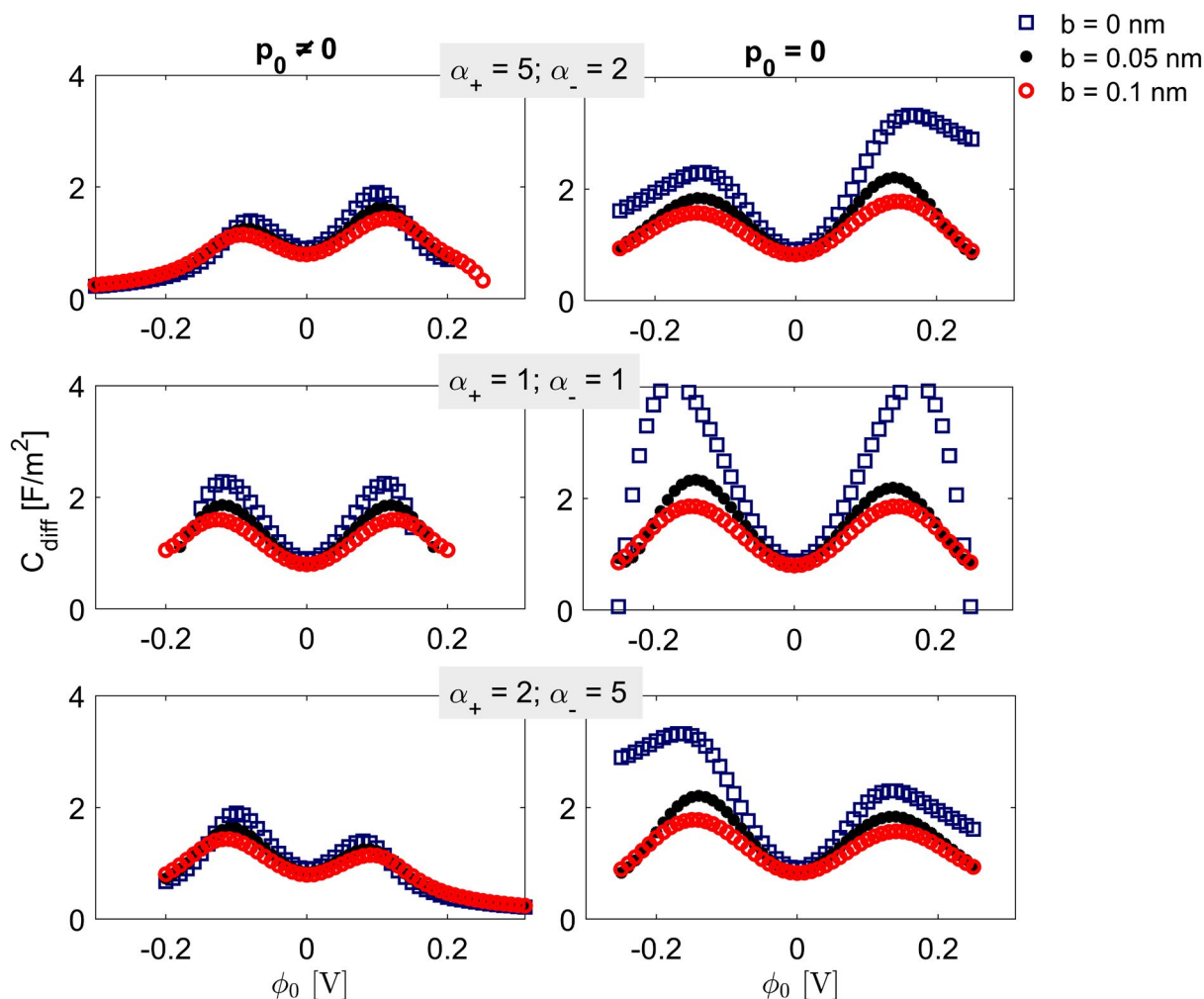
The predicted decrease in relative permittivity in the Stern and the diffuse layers is clearly to a large extent a consequence of the orientational ordering of water dipoles close to the saturation regime (Fig. 4C) as proved theoretically in<sup>31,34,37,40,46,57,58</sup> and on the other hand totally neglected in phenomenological approaches.<sup>55</sup> Neglecting the statistical mechanics approach and the orientational ordering of water molecules in electrolyte solution close to the charged surface cannot contribute to a better understanding of the physics of the electric double layer.

It was further proposed recently by Lopez-Garcia et al.<sup>55</sup> that close to the charged surface nearly all water molecules belong to water shells around the ions, while free water molecules practically do not exist in this region. The results of Monte Carlo (MC) simulations<sup>59</sup> strongly oppose this assumption<sup>55</sup> and clearly show the increased ordering of water dipoles in the direction towards the charged surface (including Stern region)<sup>59</sup> as predicted also within the GI model (see Fig. 4C). MS simulations predict strong orientational ordering in the vicinity of the charged surface even for high salt concentrations, also in agreement with our theoretical predictions (Fig. 4C). Strikingly, MC simulations show practically no difference in the average orientation and space distribution of water dipoles close to the charged surface in the case without NaCl and with NaCl (at concentration 0.5 mol/l NaCl) in water solution.<sup>59</sup> In general, for low enough magnitudes of the surface charge density, where the mean-field approach is valid, the profile of the average orientation of water dipoles in the Stern and the diffuse layers is only weakly influenced by salt concentration.<sup>59</sup>

It is argued in<sup>55</sup> that in the modified GI model,<sup>46</sup> described also in this paper, the space occupied by the ions behaves just as a vacuum. This is certainly not true since the modified GI model<sup>46</sup> assumes that the permittivity of hydrated ions is equal to the square of the refractive index of water (see also<sup>2,3,28,45,46,48</sup>). This means that in the modified GI model, the electronic polarizability of hydrated ions is equal to the electronic polarizability of water.<sup>30,34,46,48</sup> In addition, the authors of<sup>55</sup> also completely overlooked that the modified GI model<sup>46</sup> is not based on the limiting Onsager model, but instead on the generalized Kirkwood-Onsager-Fröhlich's theory<sup>2,3,45</sup> which is valid also in the saturation regime of the water dipole orientation and polarization.



**Figure 4.** The magnitude of the electric field strength  $E$  (panel A), relative permittivity (panel B) and the average orientation of water dipoles (panel C) in the Stern layer calculated as a function of the surface charge density  $\sigma$ . The average orientation of water molecules is described by the average  $\cos(\omega)$  (panel C), where  $\omega$  is the angle between the gradient of the electric potential and the vector of the water dipole moment.<sup>35,48</sup> The two asterisks denote the values of the average  $\cos(\omega)$  determined by Monte-Carlo simulations.<sup>59</sup> The values of the model parameters are:  $p_0 = 3.1$  D,  $\alpha_+ = 5$  and  $\alpha_- = 2$ ,  $b = 0$ , the bulk concentration of ions,  $n_0/N_A = 0.5$  mol/l,  $n = 1.33$ ,  $n_s/N_A = 55$  mol/l and  $T = 298$  K.



**Figure 5.** Calculated differential capacitance as a function of the surface potential  $\phi_0$  for different combinations of the values of parameters  $\alpha_+$  and  $\alpha_-$  and different values of the thickness of the Stern layer  $b$  calculated for  $p_0 = 3.1$  D (left panels) and  $p_0 = 0$  (right panels) within the modified GI model. The values of the other model parameters are: bulk concentration of ions  $n_0/N_A = 0.15$  mol/L,  $n = 1.33$ ,  $n_0/N_A = 55$  mol/L and  $T = 298$  K.

Fig. 5 shows differential capacitance  $C_{diff} = d\sigma/d\phi_0$  as a function of surface potential  $\phi_0 = \phi(x=0)$  calculated within the modified GI model for different values of parameters  $\alpha_+$  and  $\alpha_-$ , different values of the thickness of the Stern layer ( $b$ ) and two values of the magnitude of the external water dipole moment ( $p_0$ ). It can be seen in Fig. 5 that the consideration of non-zero  $p_0$  and the orientation ordering of water dipoles in the electric double layer decreases the calculated differential capacitance of EDL.

In general, the differential capacitance first increases with increasing absolute value the surface potential  $\phi_0$  and after first reaching its maximum, it starts to strongly decrease, attaining the so-called bimodal camel-like dependence of differential capacitance on  $\phi_0$ , similarly as observed in experiments,<sup>60,61</sup> in Monte-Carlo<sup>62</sup> and also in molecular dynamic simulations.<sup>63</sup>

Neglecting the finite size of ions (the Gouy-Chapman approach) would lead to monotonously increasing the differential capacitance with the increasing absolute

value of  $\phi_0$ .<sup>64</sup> As shown in Fig. 5, asymmetry in the finite size of positive and negative ions (i.e.  $\alpha_+ \neq \alpha_-$ ) leads to asymmetric bimodal camel-like dependence of differential capacitance on the surface potential as observed also in experiments.<sup>60,61,65</sup>

It can be further seen in Fig. 5 that the increased thickness of the Stern layer ( $b$ ) (see Fig. 1) decreases the differential capacitance. The increased thickness of the Stern layer ( $b$ ) also moves the surface potential to higher absolute values.<sup>30,50</sup> Considering different values of the thickness of the Stern layer for positive and negative  $\phi_0$ , i.e. different distance of closest approach for hydrated negative and positive counterions,<sup>51</sup> would additionally change the relative height of both maxima of the differential capacitance asymmetric camel-like curve.<sup>51</sup> Namely, in the case of negatively charged surface, the distance of closest approach  $b$  is defined by positively charged counterions, while in the case of positively charged surface, the parameter  $b$  describes the distance of closest approach for



negatively charged counterions.<sup>51</sup> It was thus shown<sup>51</sup> that the differential capacitance curve becomes asymmetric also when only different values of the thickness of the Stern layer ( $b$ ) are used for negative and positive surface potential  $\phi_0$  and the potential (charge) dependent relative permittivity in the Stern layer is taken into account,<sup>2,28,34</sup> while the finite asymmetric size of ions in the diffuse layer is neglected.

To conclude, different values of the thickness of the Stern layer ( $b$ ) for negative and positive surface potential  $\phi_0$  mean that the distance of closest approach is not the same for negatively and positively charged counterions. In Fig. 5, we should therefore take into account that the thickness of the Stern layer ( $b$ ) is not the same for negative and positive values of the surface potential  $\phi_0$ , i.e. in Fig. 5, the value of  $b$  for positive  $\phi_0$  is not the same as the value of  $b$  for negative  $\phi_0$ .

## 4. Conclusions

In this paper we describe the modified GI model<sup>12,46,47,66</sup> of the electric double layer, which takes into account within the mean-field theoretical approach the finite and asymmetric size of anions and cations and the orientational ordering of water dipoles in the Stern and the diffuse layers. The modified GI model<sup>46</sup> can be derived either by the minimization of the free energy of the system<sup>7,40,48,66</sup> or by applying the method of lattice statistics with Boltzmann correction factors<sup>46,66,67</sup> which has been shown to be equivalent to the method of the minimization of the free energy of the system.<sup>48,66,67</sup> The model predicts a decrease in the relative permittivity in electrolyte solution near the charged surface, including a decrease in the relative permittivity in the Stern layer (Fig. 4B). The decrease in the relative permittivity is a consequence of saturation in an average orientational ordering of water dipoles (Fig. 4C) at high electric field strengths (Fig. 4A). In accordance with experimental observation, an asymmetric bimodal camel-like dependence of differential capacitance on the surface potential was predicted, where the relative height of both maxima of the curve depends on the asymmetric size of the anions and cations, the orientational ordering of water dipoles in the Stern and the diffuse layers and the values of the thickness of the Stern layer ( $b$ ) for negative and positive surface potential  $\phi_0$ .

To conclude, it was recently pointed out by Zhang and Huang<sup>47</sup> that the modified GI model<sup>46</sup> captures all the major phenomena of the asymmetric ion-size effect and is also flexible enough to be extended in the future to more complicated multicomponent systems as it is just a simple binary electrolyte water solution. In comparison to the most of the other mean-field EDL models, the GI model<sup>46,2,30</sup> contains also the statistical mechanical description of the water dipole orientational ordering in EDL, a phenomenon which is not included in the other theoretical

mean-field models of asymmetric ion-size effect in EDL<sup>47</sup>, but is essential to realistically describe the physical properties of EDL, as indicated also in this paper.

## 5. Acknowledgements

### Funding

This work was partly supported by the Slovenian Research Agency (ARRS), grants numbers P2-0232, P3-0388, J5-7098, J3-9262, J1-9162, J2-8166 and J2-8169.

### Author biographies

Prof. ddr. **Aleš Iglič** received his B.Sc. and Ph.D. degrees in physics, M.Sc. degree in biophysics and his second Ph.D. degree in electrical engineering, all from the University of Ljubljana, in 1994 and 1995, respectively. He is currently a professor and head of the Laboratory of Physics at the Faculty of Electrical Engineering at the University of Ljubljana. His research interests are in physics of electric double layer, electrostatics and statistical physics of biological membranes, synthesis of inorganic nanomaterials and interactions of inorganic nanomaterials with biological cells and liposomes. Since 2009, he has been the editor of the Elsevier book series *Advances in Biomembranes and Lipid Self-Assembly*. He is the coordinator of the interdisciplinary doctoral study *Nanosciences* at the University of Ljubljana. He has been a supervisor or co-supervisor to more than 25 Ph.D. and postdoctoral students.

Dr. **Ekaterina Gongadze** received her B.Sc. degree from the Faculty of Industrial Engineering at the Technical University of Sofia in 2006 and her M.Sc. and Dr. Ing. degree from the Faculty of Computer Science and Electrical Engineering at the University of Rostock in 2008 and 2012, respectively. She is currently working as a senior research associate at the Faculty of Engineering at the University of Bristol, United Kingdom, and as a research associate in Laboratory of Physics, Faculty of Electrical Engineering at the University of Ljubljana. Her research interests are in numerical modeling and simulation.

Prof. dr. **Veronika Kralj-Iglič** received her B.Sc. and Ph.D. degrees in physics and M.Sc. degree in biophysics from the Department of Physics at the University of Ljubljana. She is a professor of biophysics at the same university. Her research interests are in biophysics and medicine of extracellular vesicles, electrostatics, biomechanics and statistical physics of biological membranes and biomechanics of the hip. She is head of the Laboratory of Clinical Biophysics at the Faculty of Health Sciences of the University of Ljubljana. She is the coordinator of the interdisciplinary doctoral study *Bioengineering in Health Sciences* at the University of Ljubljana. She has been a supervisor or co-supervisor to 22 Ph.D. doctoral students.

## 6. References

1. S. McLaughlin, *Ann. Rev. Biophys. Chem.* **1989**, *18*, 113–136. DOI:10.1146/annurev.bb.18.060189.000553
2. E. Gongadze, L. Mesarec, V. Kralj-Iglič, A. Iglič, *Mini-Rev. Med. Chem.* **2018**, *18*, 1559–1566. DOI:10.2174/1389557518666180626111927
3. F. Booth, *J. Chem. Phys.* **1951**, *19*, 391–394. DOI:10.1063/1.1748233
4. H. Helmholtz, *Ann. Phys.* **1879**, *243*, 337–382. DOI:10.1002/andp.18792430702
5. M. G. Gouy, *J. Phys. Radium* **1910**, *9*, 457–468. DOI:10.1051/jphys:1910090045700
6. D. L. Chapman, *Philos. Mag.* **1913**, *6*, 475–481. DOI:10.1080/14786440408634187
7. V. Kralj-Iglič, A. Iglič, *J. Phys. II (France)* **1996**, *6*, 477–491.
8. O. Stern, *Z. Elektrochemie* **1924**, *30*, 508–516.
9. J. J. Bikerman, *Phil. Mag.* **1942**, *33*, 384–397. DOI:10.1080/1478644208520813
10. E. Wicke, M. Eigen, *Z. Elektrochem.* **1952**, *38*, 551–561.
11. V. Freise, *Z. Elektrochem.* **1952**, *56*, 822–827.
12. M. Eigen, E. Wicke, *J. Phys. Chem.* **1954**, *58*, 702–714. DOI:10.1021/j150519a007
13. S. Lamperski, C. W. Outhwaite, *Langmuir* **2002**, *18*, 3423–3424. DOI:10.1021/la0111852v
14. L. Bhuiyan, C. Outhwaite, *J. Coll. Int. Sci.* **2009**, *331*, 543–547. DOI:10.1016/j.jcis.2008.11.059
15. S. Kenkel, J. MacDdonald, *J. Chem. Phys.* **1984**, *81*, 3215–3222. DOI:10.1063/1.448028
16. P. Nielaba, F. Forstmann, *Chem. Phys. Lett.* **1985**, *117*, 46–48. DOI:10.1016/0009-2614(85)80402-4
17. C. Caccamo, G. Pizzimenti, L. Blum, *J. Chem. Phys.* **1986**, *84*, 3327–3335. DOI:10.1063/1.450267
18. R. Kjellander, S. Marčelja, *Chem. Phys. Lett.* **1986**, *127*, 402–407. DOI:10.1016/0009-2614(86)80304-9
19. M. Plischke, D. Henderson, *J. Chem. Phys.* **1988**, *88*, 2712–2718. DOI:10.1063/1.454001
20. L. Mier-y-Teran, S. Suh, H. White, H. Davis, *J. Chem. Phys.* **1990**, *92*, 5087–5098. DOI:10.1063/1.458542
21. P. Strating, F. Wiegel, *J. Phys. A Math. Gen.* **1993**, *26*, 3383–3391. DOI:10.1088/0305-4470/26/14/007
22. I. Borukhov, *J. Polym. Sci. Part B: Polym. Phys.* **2004**, *42*, 3598–3615. DOI:10.1002/polb.20204
23. G. Torrie, J. Valleau, *J. Chem. Phys.* **1980**, *73*, 5807–5816. DOI:10.1063/1.440065
24. G. M. Torrie, J. P. Valleau, *J. Phys. Chem.* **1982**, *86*, 3251–3257. DOI:10.1021/j100213a035
25. C. Lian, K. Liu, K. L. Van Aken, Y. Gogotsi, D. J. Wesolowski, H. L. Liu, D. E. Jiang, J. Z. Wu, *ACS Energy Lett.* **2016**, *1*, 21–26. DOI:10.1021/acsenergylett.6b00010
26. J. W. Lee, R. H. Nilson, J. A. Templeton, S. K. Griffiths, A. Kung, B. M. Wong, *J. Chem. Theory Comput.* **2012**, *8*, 2012–2022. DOI:10.1021/ct3001156
27. A. A. Kornyshev, *J. Phys. Chem. B* **2007**, *111*, 5545–5557. DOI:10.1021/jp067857o
28. S. Mohajernia, A. Mazare, E. Gongadze, V. Kralj-Iglič, A. Iglič, P. Schmuki, *Electrochim. Acta* **2017**, *245*, 25–31. DOI:10.1016/j.electacta.2017.05.115
29. J. Mähler, I. Persson, *Inorg. Chem.* **2012**, *51*, 425–438. DOI:10.1021/ic2018693
30. A. V. Dubtsov, S. V. Pasechnik, D. V. Shmeliova, A. Sh. Saidgatiev, E. Gongadze, A. Iglič, S. Kralj, *Soft Matter* **2018**, *14*(47), 9619–9630. DOI:10.1039/C8SM01529E
31. C. Outhwaite, *Mol. Phys.* **1976**, *31*, 1345–1357. DOI:10.1080/00268977600101061
32. A. Abrashkin, D. Andelman, H. Orland, *Phys. Rev. Lett.* **2007**, *99*, 077801. DOI:10.1103/PhysRevLett.99.077801
33. M. Bazant, M. Kilic, B. Storey, A. Ajdari, *Adv. Coll. Int. Sci.* **2009**, *152*, 48–88. DOI:10.1016/j.cis.2009.10.001
34. E. Gongadze, A. Iglič, *Bioelectrochemistry* **2012**, *87*, 199–203. DOI:10.1016/j.bioelechem.2011.12.001
35. E. Gongadze, A. Velikonja, S. Perutkova, P. Kramar, A. Maček-Lebar, V. Kralj-Iglič, A. Iglič, *Electrochim. Acta* **2014**, *126*, 42–60. DOI:10.1016/j.electacta.2013.07.147
36. M. A. Quiroga, K. H. Xue, T. K. Nguyen, M. Tulodziecki, H. Huang, A. A. Franco, *J. Electrochem. Soc.* **2014**, *161*, E3302–E3310. DOI:10.1149/2.029408jes
37. C. Outhwaite, *Mol. Phys.* **1983**, *48*, 599–614. DOI:10.1080/00268978300100431
38. E. Gongadze, T. Slivnik, V. Kralj-Iglič, A. Iglič, *Electrochim. Acta* **2013**, *109*, 656–662. DOI:10.1016/j.electacta.2013.07.126
39. T. Nagy, D. Henderson, D. Boda, *J. Phys. Chem. B* **2011**, *115*, 11409–11419. DOI:10.1021/jp2063244
40. A. Iglič, E. Gongadze, K. Bohinc, *Bioelectrochemistry* **2010**, *79*, 223–227. DOI:10.1016/j.bioelechem.2010.05.003
41. E. Gongadze, U. van Rienen, V. Kralj-Iglič, A. Iglič, *Gen. Physiol. Biophys.* **2011**, *30*, 130–137. DOI:10.4149/gpb\_2011\_02\_130
42. R. Misra, S. Das, S. Mitra, *J. Chem. Phys.* **2013**, *138*, 114703. DOI:10.1063/1.4794784
43. J. Sin, S. J. Im, K. I. Kim, *Electrochim. Acta* **2015**, *153*, 531–539. DOI:10.1016/j.electacta.2014.11.119
44. R. Schlögl, *Z. Physik. Chem.* **1954**, *202*, 379–389.
45. H. Fröhlich, *Theory of Dielectrics*, Clarendon Press, Oxford, UK, **1964**.
46. E. Gongadze, A. Iglič, *Electrochim. Acta* **2015**, *178*, 541–545. DOI:10.1016/j.electacta.2015.07.179
47. Y. Zhang, J. Huang, *J. Phys. Chem. C*, **2018**, *122*, 28652–28664. DOI:10.1021/acs.jpcc.8b08298
48. M. Drab, E. Gongadze, L. Mesarec, S. Kralj, V. Kralj-Iglič, A. Iglič, *Elektrotehniški Vestnik (Journal of Electrical Engineering and Computer Science)* **2017**, *84*, 221–234.
49. K. Giese, U. Kaatz, R. Pottel, *J. Phys. Chem.* **1970**, *74*, 3718–3725. DOI:10.1021/j100715a005
50. A. Velikonja, E. Gongadze, V. Kralj-Iglič, A. Iglič, *Int. J. Electrochem.* **2014**, *9*, 5885–5894.
51. A. Velikonja, V. Kralj-Iglič, A. Iglič, *Int. J. Electrochem.* **2015**, *10*, 1–7.
52. M. Lorenzetti, E. Gongadze, M. Kulkarni, I. Junkar, A. Iglič, *Nanoscale Res. Lett.* **2016**, *11*, 378. DOI:10.1186/s11671-016-1594-3

53. C. Outhwaite, L. Bhuiyan, *J. Chem. Phys.* **1986**, 84, 3461–3471. DOI:10.1063/1.450231
54. J. Yu, G. Aguilar-Pineda, A. Antillon, S. Dong, M. Lozada-Cassou, *J. Coll. Int. Sci.* **2006**, 295, 124–134. DOI:10.1016/j.jcis.2005.08.016
55. J. J. Lopez-Garcia, J. Hornoa, C. Grosse, *J. Coll. Int. Sci.* **2017**, 496, 531–539. DOI:10.1016/j.jcis.2017.02.043
56. J. C. Maxwell, *A Treatise on Electricity and Magnetism*, vol. 1, Clarendon, Oxford, **1892**.
57. I. Szalai, S. Nagy, S. Dietrich, *J. Chem. Phys.* **2009**, 131, 154905. DOI:10.1063/1.3248242
58. I. Szalai, S. Dietrich, *J. Phys.: Condens. Matter* **2008**, 20, 204122. DOI:10.1088/0953-8984/20/20/204122
59. A. Marcovitz, A. Naftaly, Y. Levy, *J. Chem. Phys.* **2015**, 142, 085102. DOI:10.1063/1.4913370
60. V. Lockett, R. Sedev, J. Ralston, M. Horne, T. Rodopoulos, *J. Phys. Chem. C* **2008**, 1124, 7486–7495. DOI:10.1021/jp7100732
61. V. Lockett, M. Horne, R. Sedev, T. Rodopoulos, J. Ralston, *Phys. Chem. Chem. Phys.* **2010**, 12, 12499–12512. DOI:10.1039/c0cp00170h
62. M. V. Fedorov, N. Georgi, A. A. Kornyshev, *Electrochem. Commun.* **2010**, 12, 296–299. DOI:10.1016/j.elecom.2009.12.019
63. M. V. Fedorov, A. A. Kornyshev, *Electrochim. Acta* **2008**, 53, 6835–6840. DOI:10.1016/j.electacta.2008.02.065
64. D. F. Evans, H. Wennerström, *The Colloidal Domain: where physics, chemistry, biology, and technology meet*, 2nd ed., Wiley-VCH, New York, **1999**.
65. D. Grahame, *J. Am. Chem. Soc.* **1954**, 76, 4819–4823. DOI:10.1021/ja01648a014
66. A. Iglič, D. Drobne, V. Kralj-Iglič, *Nanostructures in Biological Systems: Theory and Applications*. Pan Stanford, New York; Boca Raton: CRC Press, **2015**. DOI:10.1201/b18607
67. S. A. Safran, *Statistical Thermodynamics of Surfaces, Interfaces, and Membranes*, Addison-Wesley, Reading, Menlo Park, New York, **1994**.

## Povzetek

V članku opišemo model električne dvojne plasti, ki v okviru približka povprečnega polja upošteva asimetrično končno velikost anionov in kationov ter orientacijsko urejanje vodnih molekul v Sternovi in difuzni plasti elektrolitske raztopine v stiku z ravno naelektreno površino. Pri tem podamo tudi kratek opis nekaterih osnovnih konceptov ter pregled literature na področju teorije električne dvojne plasti. Kot primer uporabe opisanega teoretičnega modela električne dvojne plasti prikažemo vpliv velikosti anionov in kationov, debeline Sternove plasti ter orientacijskega urejanja vodnih molekul na asimetrično bimodalno diferencialno kapacitivnost električne dvojne plasti.



Except when otherwise noted, articles in this journal are published under the terms and conditions of the Creative Commons Attribution 4.0 International License

*Scientific paper*

# Synthesis and Study of Catalytic, Anti-Bacterial, Anti-Oxidant, and DNA Cleavage Properties of Ag-Co and Ag-Ni Magnetic Nanoparticles

Keveh Pravanak Boroujeni,<sup>1,\*</sup> Mansooreh Shahrokh,<sup>1</sup> Jamshid Karvani,<sup>1</sup>  
Niloofar Moradi,<sup>1</sup> Ahmad Farokhnia<sup>1</sup> and Mohsen Mobini<sup>2</sup>

<sup>1</sup> Department of Chemistry, Shahrekord University, Shahrekord (115), Iran

<sup>2</sup> Department of Genetics, Shahrekord University, Shahrekord (115), Iran

\* Corresponding author: E-mail: parvanak-ka@sci.sku.ac.ir  
Tel.: +0098-38-32324401; fax: 0098-38-32324419

Received: 03-06-2018

*Dedicated to the memory of Mrs Zohreh Hoseini*

## Abstract

Magnetic Ag-Co and Ag-Ni alloy nanoparticles were prepared through a chemical reduction method using their corresponding  $[\text{Co}(\text{NH}_3)_6]\text{Cl}_3$  and  $[\text{Ni}(\text{C}_2\text{O}_4)_2]\text{K}_2$  complexes, and  $\text{AgNO}_3$ . In this reaction, hydrazine monohydrate was used as reducing agent. The obtained nanoparticles were characterized by Fourier transform infrared spectroscopy (FT-IR), scanning electron microscopy (SEM), energy dispersive spectroscopy (EDS), X-ray diffraction (XRD), and vibrating sample magnetometer (VSM). Ag-Co and Ag-Ni nanoalloys exhibited excellent catalytic performance in the preparation of 1,8-dioxooctahydroxanthenes from the reaction of 5,5-dimethyl-1,3-cyclohexanedione (dimedone) with aromatic aldehydes. Catalysts were separated by an external permanent magnet and reused. Both, Ag-Co and Ag-Ni nanoalloys possess antibacterial and antioxidant properties and have no significant effect on DNA cleavage.

**Keywords:** Nanoalloys; magnetism and magnetic properties; 1,8-dioxooctahydroxanthenes; anti-bacterial activity; anti-oxidant activity; DNA cleavage properties

## 1. Introduction

Binary or multi-metal alloys have attracted growing research interest in recent years in both industrial and laboratory chemical processes due to their unique and novel optical, electrical, and catalytic properties.<sup>1–4</sup> Alloying two or more metals can improve the mechanical, chemical, electrical, and thermal conductivity properties of pure metals.<sup>5</sup> Among metallic alloys, nanoalloys are gaining increasing importance and have several advantages over their corresponding bulk forms. For example, the Ag-Ni alloy is immiscible in bulk form, and have no tendency to form any solid solution.<sup>6</sup> Further, the bulk form of Ag-Co has large miscibility gaps,<sup>7</sup> whereas both Ag-Ni and Ag-Co nanoalloys show good solid solubility properties.<sup>8,9</sup>

Among multiple nanoalloys, silver nanoalloys have many specific properties that make them very attractive

and valuable in biomedical areas, catalysis, and magnetic imaging purposes.<sup>10</sup> For instance, Ag-Ni nanoalloys have strong anti-oxidation properties<sup>11</sup> and have been used in the electrocatalytic reduction of benzyl chloride.<sup>12</sup> Also, Ag-Co nanoalloys have the ability to catalyze the oxygen reduction reactions<sup>13</sup> and have been used in catalytic oxidation of formaldehyde.<sup>14</sup>

Xanthene derivatives containing reactive pyran ring system are particularly attractive because of their biological and therapeutic properties such as anti-inflammatory,<sup>15</sup> anti-depressant,<sup>16</sup> and anticancer activities.<sup>17</sup> Xanthene-dye-labelled phosphatidylethanolamines have been used as probes for fluorescence-ratio measurements of interfacial pH in cellular systems.<sup>18</sup> Also, xanthenes have been shown to be efficient laser dyes with high photostability.<sup>19</sup> 1,8-Dioxooctahydroxanthenes are one of the most important derivatives of xanthenes. A convenient method for the synthesis of 1,8-dioxooctahydroxanthenes is reac-



tion between an aldehyde (1 equiv) and dimesone (2 equiv) in the presence of a catalyst such as *p*-dodecylbenzenesulfonic acid,<sup>20</sup> Amberlyst-15,<sup>21</sup>  $\text{SmCl}_3$ ,<sup>22</sup> carboxy functionalized ionic liquid,<sup>23</sup>  $\text{SiCl}_4$ ,<sup>24</sup> ceric ammonium nitrate (CAN),<sup>25</sup>  $[\text{Et}_3\text{NH}][\text{HSO}_4]$ ,<sup>26</sup> CAN-supported HY-zeolite,<sup>27</sup> piperidine/HCl,<sup>28</sup> Mg–Al hydrotalcite,<sup>29</sup> thiourea dioxide,<sup>30</sup> hydroxylamine-*O*-sulfonic acid,<sup>31</sup> carbon nanotube- $\text{BuSO}_3\text{H}$ ,<sup>32</sup> cellulose/ $\text{Al}_2\text{O}_3$ -[MeIm]Cl- $\text{XAlCl}_3$ ,<sup>33</sup> sulfated zirconia,<sup>34</sup> and L-pyrrolidine-2-carboxylic acid sulfate (LPCAS).<sup>35</sup> Most of these catalysts, however, have numerous disadvantages such as waste production, corrosion problems, no catalyst recovery, low yields, high reaction temperature, long reaction times, tedious work-up, and the formation of the uncyclized product 2,2'-aryl-methylenbis(3-hydroxy-2-cyclohexene-1-one) derivatives. Thus, it is an exciting challenge to find new catalysts with high activity and selectivity.

One of the most important strategies for magnetic nanoalloys synthesis is a reduction method, and one of the most useful agents for this reaction is hydrazine monohydrate.<sup>36</sup> During the reduction process, if primary elements have different reduction properties they will form a core shell structure, otherwise this reaction will lead to a bimetallic nanoalloy generation.<sup>37</sup> Along this line and in continuation of our ongoing research on the synthesis and applications of nanocatalysts and nanoalloys,<sup>38,39</sup> we were prompted to explore the efficacy of Ag–Co and Ag–Ni magnetic nanoalloys as heterogeneous catalysts for the synthesis of 1,8-dioxooctahydroxanthenes. Also, the biological activities of these nanoalloys were studied.

## 2. Experimental

### 2.1. Materials and Methods

Commercially available reagent grade chemicals were used as received. Two bacterial strains were used: *E. coli* (ATCC 35218) and *S. aureus* (ATCC 6538). XRD patterns were recorded by a Phillips, X-ray diffractometer using graphite monochromatized Cu K $\alpha$  radiation. Scanning electron microscopy (SEM) images were taken with a MIRA3 FEG-SEM, and energy-dispersive spectroscopy (EDS) analysis was studied by LEO 1455 VP microscope. Room temperature magnetic properties were investigated by Lakeshore device in an applied magnetic field sweeping between  $\pm 10000$  Oe. Reaction monitoring and purity determination of the products were accomplished by GLC or TLC on silica-gel polygram SILG/UV254 plates. Gas chromatography was recorded on Shimadzu GC 14–A. IR spectra were obtained by a Shimadzu model 8300 FT-IR spectrophotometer.  $^1\text{H}$  NMR spectra were recorded on 400 MHz spectrometer in  $\text{CDCl}_3$ . Melting points were determined on a Fisher–Jones melting-point apparatus.

### 2.2. Synthesis of Ag–M (M = Ni, Co) Nanoalloys

$[\text{Ni}(\text{C}_2\text{O}_4)_2]\text{K}_2$  and  $[\text{Co}(\text{NH}_3)_6]\text{Cl}_3$  complexes were synthesized using as described in the literature, respectively.<sup>40,41</sup> In a typical procedure, 0.5 g (1.60 mmol) of  $[\text{Ni}(\text{C}_2\text{O}_4)_2]\text{K}_2$  complex was dissolved in 25 mL of a mixture of water–ethanol (50:50). Then, a solution of  $\text{AgNO}_3$  (25 mL, 0.064 M) was gradually added to the above solution. After that, 5 mL of hydrazine (excess) and 5 mL of NaOH (4 M) were added to above mixture at 70–80 °C and the resulting mixture was stirred at this temperature. As the reduction reaction proceeded, the solution turned to black after 1 h. The Ag–Ni nanoalloys were carefully decanted and washed repeatedly with doubly distilled water. Then, the product was dried at room temperature for 24 h.

The Ag–Co nanoalloys were synthesized in similar method with 0.5 g (1.87 mmol) of  $[\text{Co}(\text{NH}_3)_6]\text{Cl}_3$  complex and 25 mL of  $\text{AgNO}_3$  (0.075 M).

### 2.3. Typical Procedure for the Preparation of 1,8-Dioxooctahydroxanthene Using Ag–Ni and Ag–Co Nanoalloys

To a solution of 3-nitrobenzaldehyde (1 mmol, 0.15 g), dimesone (2 mmol, 0.28 g) and ethanol (3 mL) in a round-bottom flask, Ag–Ni (0.06 g) or Ag–Co nanoalloys (0.05 g) was added. The reaction mixture was magnetically stirred at room temperature. Progress of the reaction was monitored by TLC and GC. After completion of the reaction, the catalyst was removed by an external magnet and washed with ethanol ( $2 \times 10$  mL). Then, the filtrate was concentrated on a rotary evaporator under reduced pressure and the crude product recrystallized from ethanol to afford the pure product 3,4,6,7-tetrahydro-3,3,6,6-tetramethyl-9-(3-nitrophenyl)-2H-xanthene-1,8(5H,9H)-dione.  $^1\text{H}$  NMR (400 MHz,  $\text{CDCl}_3$ )  $\delta$  = 1.02 (6H, s, 2CH<sub>3</sub>), 1.14 (6H, s, 2CH<sub>3</sub>), 2.17–2.29 (4H, m, 2CH<sub>2</sub>), 2.53 (4H, s, 2CH<sub>2</sub>), 4.86 (1H, s, CH), 7.41–8.04 (4H, m, Ar-H).

### 2.4. Antibacterial Performance of Ag–Ni and Ag–Co Nanoalloys

Disk diffusion test is performed by applying a bacterial inoculum to the surface of Muller-Hinton agar plates (100 mm diameter) using sterile swabs. First, *E. coli* and *S. aureus* cells were separately cultured from pure bacterial to nutrient broth media, and incubated at 37 °C until reaching to 0.5 McFarland standards. After incubation of plates at 37 °C for 24 h and growth of the bacterial, distinct equal wells have been created in the agar plates for antibacterial diffusion assay. Afterwards, dispersed solutions of Ag–Ni or Ag–Co nanoalloys (0.64, 0.32, 0.16 or 0.08 mg/mL) were individually poured into the wells. Plates were incubated for 18–24 h at 37 °C to determine the zone sizes of bacterial growth inhibition in millimeter

scale. Sterile distilled water and standard antibiotic discs were used as negative and positive controls, respectively.

## 2. 5. Free Radical Scavenging Activity of Ag–Ni and Ag–Co Nanoalloys

At first, a methanol solution of DPPH (0.1 mM) was prepared. Then, Tris–HCl buffer (450  $\mu$ L, pH = 7.4) and methanolic DPPH solution (1 mL) were added to 50  $\mu$ L of Ag–Ni and Ag–Co nanoalloys with distinct concentrations (2.5, 5, 10 or 20  $\mu$ g/mL). The mixtures were kept at room temperature for 30 min in dark. Afterwards, the absorbance of mixtures was measured at 517 nm. The methanol was used as a blank solution. The same experiment was performed with BHT as a positive control. The DPPH free radical scavenging activity was subsequently calculated as: % DPPH radical scavenging = Control OD- sample OD/ Control OD  $\times$  100.

## 2. 6. DNA Cleavage Assays

Agarose gel electrophoresis was used to identify the cleavage of pET-28 plasmid DNA by Ag–Ni and Ag–Co nanoalloys. Each 40  $\mu$ L of Ag–Ni or Ag–Co nanoalloys with distinct concentrations (0.25, 0.5, 1 or 2 mg/mL) were added to plasmid DNA solution (5  $\mu$ L, 0.25  $\mu$ g/mL) in sterile 1.5 mL micro tubes and incubated at 37  $^{\circ}$ C for 24 h. Then, the obtained mixture (10  $\mu$ L) was combined with 1  $\mu$ L of gel loading solution (Sigma, G2526-5ML) and loaded into the 1% agarose gel (W/V) wells. The agarose gel was prepared with TBE 1X buffer (Tris–HCl (0.07 M, pH = 7.4), EDTA (4 mL, 0.5 M, pH = 8.0), and boric acid (5.5 g) in water (1 L). After electrophoresis (40 mA and 80 volt for 45 min), the agarose gel was observed in the gel duct device under UV rays (UVItec Limited BTS-20M).

# 3. Results and Discussion

## 3. 1. Characterization of Magnetic Ag–Co and Ag–Ni Nanoalloys

Vibration spectra (FT–IR) of Ag–Co and Ag–Ni nanoalloys are shown in Figure 1. During the chemical reactions, complete destruction of primary complexes occurs and all spherical ligand vibration disappears. Therefore, FT–IR spectra have no absorption bands in the medium IR region, just the weak absorption bands due to the water in the alloy nanoalloys are observed in the infrared spectrum.

The XRD pattern of Ag–Co and Ag–Ni nanoalloys were studied (Figure 2). Figure 2a shows that Ag–Co nanoalloys were formed of cobalt and silver phase (Figure 2a) and in this respect, cobalt reflects two structures fcc and hcp. The difference between XRD pattern of fcc and hcp cobalt is in the  $2\theta$  region 51 related to the structure of

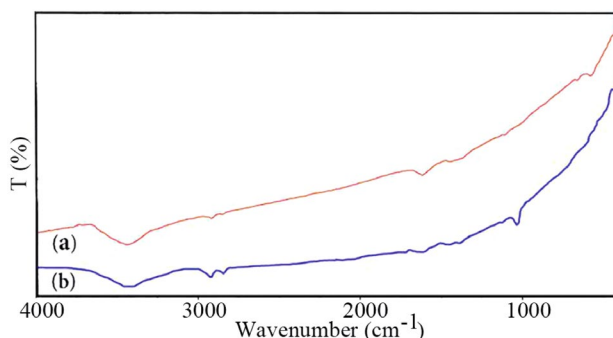


Figure 1. FT–IR spectra of (a) Ag–Co and (b) Ag–Ni nanoalloys.

fcc and hcp related to the structure of hcp (with card numbers 01-1259 and 01-1254, respectively). As shown in Figure 2a distinct diffraction peaks for structure fcc of metallic silver (with a card number 87-0717) were clearly observed at  $2\theta$  values of 38.5978, 44.7753, 64.8870 and 77.7717, corresponding to the reflections of the (111), (200), (220) and (311) crystal planes, respectively. Also, the diffraction peaks for Ag–Ni nanoalloys (Figure 2b) show that these nanoalloys are in the fcc phase. As shown in Figure 2b, this compound can be considered as Ag–Ni bimetallic nanoalloy. The results show that diffraction peaks were in good agreement with the standard values given nickel (with card no. 87-0712) and silver (with card no. 87-0717). In Figure 2b distinct diffraction peaks of metallic Ag are clearly observed at  $2\theta$  values of 38.3378, 44.7020, 64.6517 and 77.5765, corresponding to the reflections of the (111), (200), (220) and (311) crystal planes, respectively. In most studies of the grain size of nanocrystalline materials, X-ray line-broadening analysis is used. The crystal size of Ag–Ni and Ag–Co nanoalloys were calculated to be about 24.45 and 35.64 nm, respectively, by applying a full width at half maximum (FWHM) of the diffraction peaks and using the Debye–Scherrer equation.

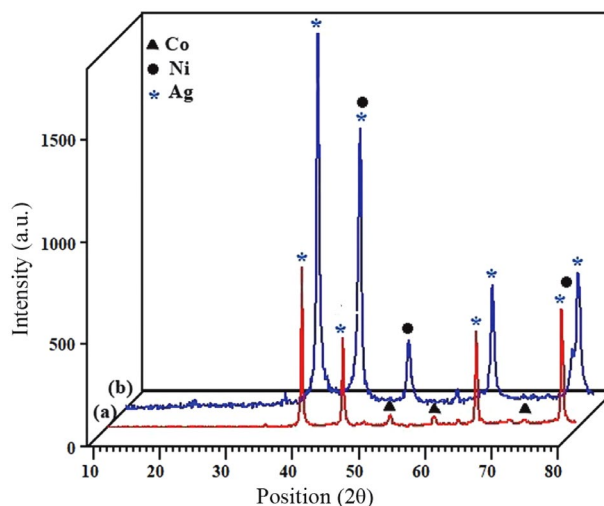


Figure 2. XRD patterns for (a) Ag–Co and (b) Ag–Ni nanoalloys.

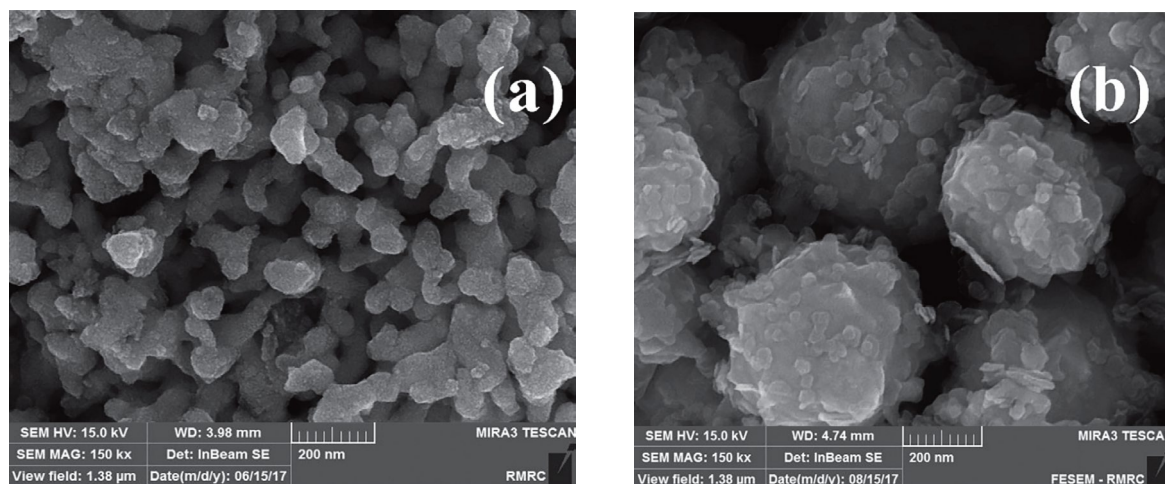


Figure 3. FE-SEM images of (a) Ag-Co and (b) Ag-Ni nanoalloys.

FE-SEM provides valuable information regarding the structural arrangement, density and geometric features of materials in the solid state. Figure 3 shows FE-SEM

photographs of Ag-Co and Ag-Ni nanoalloys prepared. The FE-SEM images of Ag-Co samples (Figure 3a) show agglomerated spherical particles. The particle size distri-

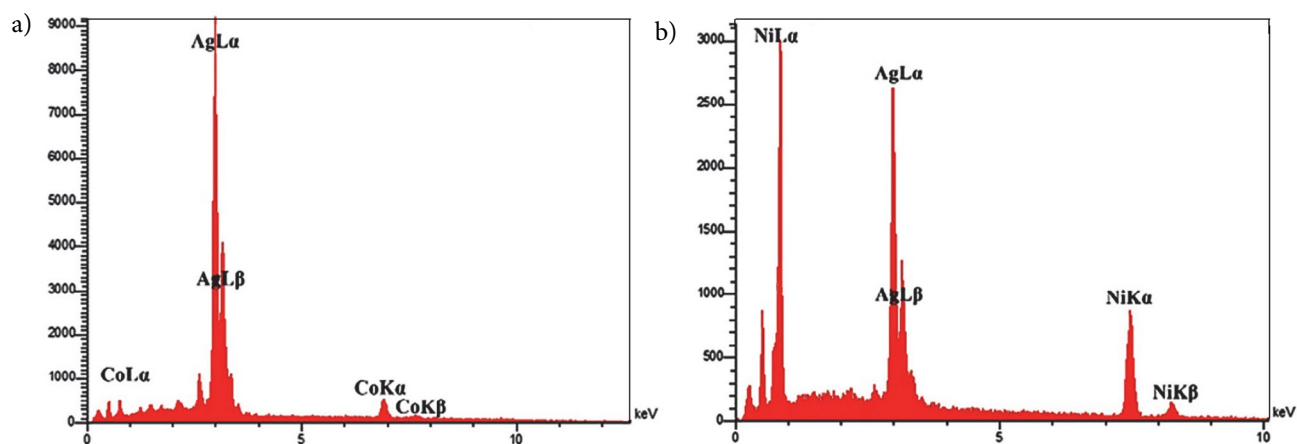


Figure 4. EDX spectra of (a) Ag-Co and (b) Ag-Ni nanoalloys.

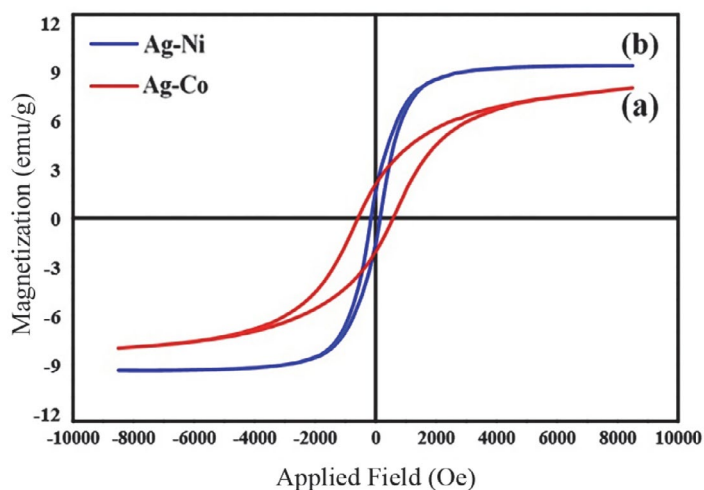


Figure 5. The magnetization curves and  $M_s$  of (a) Ag-Co and (b) Ag-Ni nanoalloys.

bution graphs for Ag–Co samples obtained from FE–SEM analysis, according to which the average diameter of a maximum number of particles is in the range of 40–50 nm. Also, the FE–SEM images show that the Ag–Ni nanoalloys have cabbage form (Figure 3b). The sizes of the nanoalloys in the lowest and maximum sizes were 26.61 and 38.23 nm, respectively.

Besides FE–SEM micrographs, the different dispersion of the phases formed using the metals can be also argued by considering energy–dispersive X–ray (EDX) data. The EDX spectra acquired at a low magnification of the powders are shown in Figure 4. EDX analysis of Ag–Co and Ag–Ni nanoalloys revealed that they are all pure bi-metallic nanoalloys.

The magnetic data taken from VSM measurement of Ag–Co and Ag–Ni nanoalloys have shown in Figure 5. The hysteresis loops revealed that the resultant Ag–Co and Ag–Ni nanoalloys are ferromagnetic materials. The saturation magnetization (Ms) of Ag–Co and Ag–Ni samples (6 and 8 emu/g, at 300 K, respectively) have declined compared to Co and Ni pure nanoparticles (14 and 43 emu/g,

at 300 K, respectively).<sup>42,43</sup> The reason for the decrease in Ms of Ag–Co and Ag–Ni samples is due to the presence of dissolved Co and Ni in the Ag matrix.

### 3. 2. Catalytic Applications of Ag–Co and Ag–Ni Nanoalloys

After synthesis and characterization of Ag–Co and Ag–Ni nanoalloys, we decided to investigate the efficiency of Ag–Co and Ag–Ni nanoalloys as catalysts in the synthesis of 1,8-dioxooctahydroxanthene derivatives. To optimize the amount of the catalyst, solvent and the reaction temperature, the reaction of 3-nitrobenzaldehyde (1 mmol) with dimedone (2 mmol) was studied in the various solvents and also under solvent-free conditions at different temperatures in the presence of different amounts of Ag–Co and Ag–Ni nanoalloys. The results showed that the reaction using 0.06 g of Ag–Ni nanoalloys or 0.05 g of Ag–Co nanoalloys proceeded in highest yield in ethanol at room temperature. Using lower amounts of Ag–Co and Ag–Ni nanoalloys resulted in lower yields, while higher amounts of

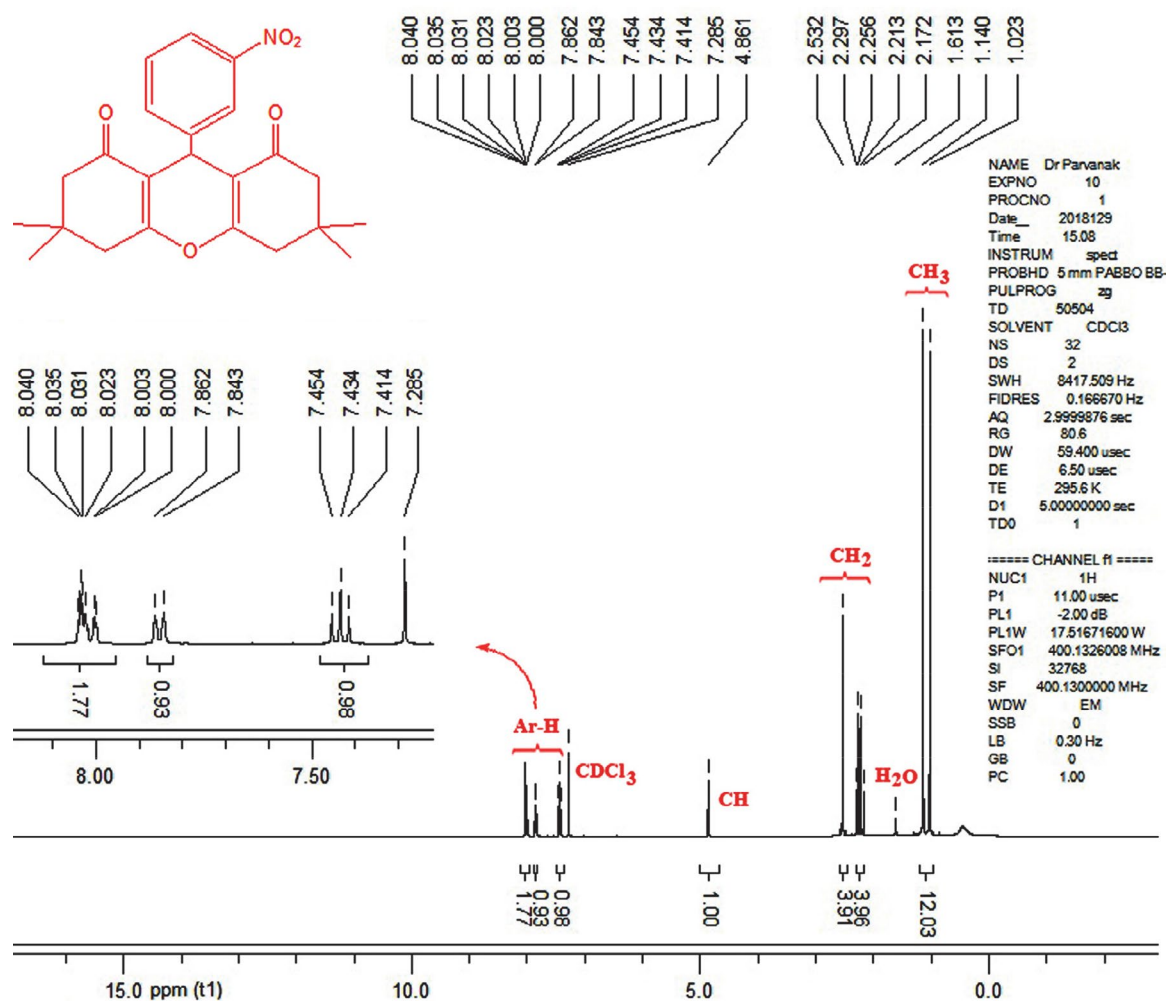


Figure 6. <sup>1</sup>H NMR spectrum of the 3,4,6,7-tetrahydro-3,3,6,6-tetramethyl-9-(3-nitrophenyl)-2H-xanthene-1,8(5H,9H)-dione.



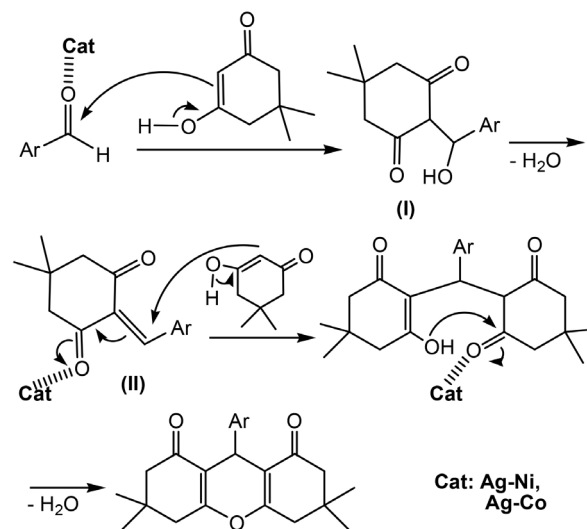
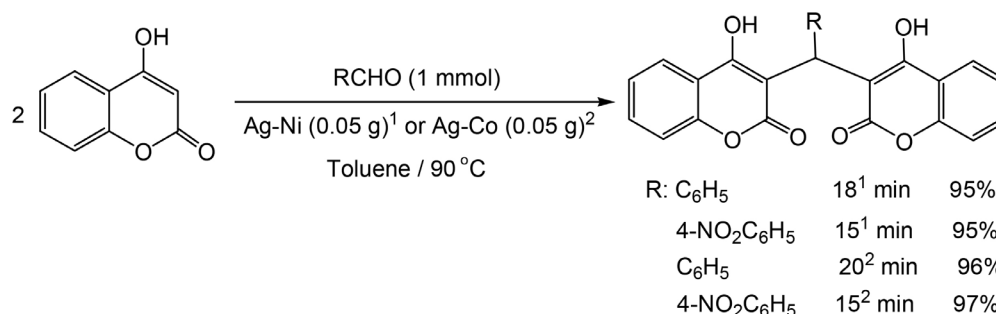
**Table 1:** Synthesis of 1,8-dioxooctahydroxanthenes.

Entry	Aldehyde	Time (min)	Yield (%) <sup>a,b</sup>	mp (°C) (lit.) <sup>ref.</sup>
1	Benzaldehyde	18 <sup>1</sup> ,17 <sup>2</sup>	96 <sup>1</sup> ,95 <sup>2</sup>	200–203 (202–204) <sup>20</sup>
2	4-Methylbenzaldehyde	20 <sup>1</sup> ,19 <sup>2</sup>	95 <sup>1</sup> ,94 <sup>2</sup>	214–216 (217–218) <sup>20</sup>
3	4-Methoxybenzaldehyde	25 <sup>1</sup> ,25 <sup>2</sup>	94 <sup>1</sup> ,95 <sup>2</sup>	240–243 (242–244) <sup>20</sup>
4	4-Chlorobenzaldehyde	17 <sup>1</sup> ,18 <sup>2</sup>	97 <sup>1</sup> ,96 <sup>2</sup>	226–228 (228–230) <sup>20</sup>
5	2,4-Dichlorobenzaldehyde	16 <sup>1</sup> ,17 <sup>2</sup>	97 <sup>1</sup> ,98 <sup>2</sup>	254–255 (253–254) <sup>20</sup>
6	4-Hydroxybenzaldehyde	20 <sup>1</sup> ,19 <sup>2</sup>	95 <sup>1</sup> ,95 <sup>2</sup>	244–248 (246–248) <sup>20</sup>
7	4-Bromobenzaldehyde	19 <sup>1</sup> ,20 <sup>2</sup>	96 <sup>1</sup> ,97 <sup>2</sup>	243–245 (240–242) <sup>30</sup>
8	4-Cyanobenzaldehyde	17 <sup>1</sup> ,17 <sup>2</sup>	97 <sup>1</sup> ,96 <sup>2</sup>	217–221 (218–220) <sup>30</sup>
9	4-Nitrobenzaldehyde	15 <sup>1</sup> ,16 <sup>2</sup>	97 <sup>1</sup> ,97 <sup>2</sup>	222–224 (226–228) <sup>20</sup>
10	3-Nitrobenzaldehyde	16 <sup>1</sup> ,17 <sup>2</sup>	96 <sup>1</sup> ,98 <sup>2</sup>	169–172 (168–170) <sup>20</sup>
11	1-Naphthaldehyde	21 <sup>1</sup> ,22 <sup>2</sup>	95 <sup>1</sup> ,94 <sup>2</sup>	225–226 (227–231) <sup>33</sup>
12	Cinnamaldehyde	27 <sup>1</sup> ,24 <sup>2</sup>	91 <sup>1</sup> ,94 <sup>2</sup>	174–176 (178–180) <sup>26</sup>
13	2-Thienyl carbaldehyde	21 <sup>1</sup> ,23 <sup>2</sup>	96 <sup>1</sup> ,24 <sup>2</sup>	163–165 (164–166) <sup>23</sup>
14	2-Furanyl carbaldehyde	20 <sup>1</sup> ,22 <sup>2</sup>	96 <sup>1</sup> ,95 <sup>2</sup>	65–67 (62–63) <sup>29</sup>

<sup>a</sup> Yields refer to the isolated pure products, <sup>b</sup> All the products were identified by comparing the analytical data (the spectral properties and melting points) with those reported in the literature.<sup>20–35</sup>

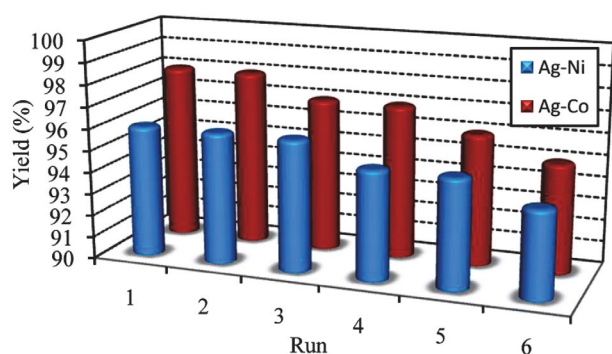
the catalysts did not affect the reaction yields and in the absence of the catalyst, nearly no product could be detected. With these results in hand, we extended our studies using different substituted benzaldehydes with both electron-withdrawing and electron-donating groups (Table 1, entries 1–10). Also, 1-naphthaldehyde and cinnamaldehyde were treated with dimedone to give the corresponding products in excellent yields (entry 11,12). Acid-sensitive aldehydes such as 2-thienyl and 2-furanyl carbaldehydes (entries 13,14) were converted to their corresponding 1,8-dioxooctahydroxanthenes without formation of any polymeric by-products. <sup>1</sup>H NMR spectrum of the 3,4,6,7-tetrahydro-3,3,6,6-tetramethyl-9-(3-nitrophenyl)-2H-xanthene-1,8(5H,9H)-dione is shown in Figure 6.

The proposed mechanism for the preparation of 1,8-dioxooctahydroxanthenes is given below in Scheme 1. The aromatic aldehyde is first activated by Ag–Co or Ag–Ni nanoalloys, which is then attacked by dimedone to yield intermediate I. Then, dehydration of intermediate I

**Scheme 1.** The proposed mechanism for the synthesis of 1,8-dioxooctahydroxanthenes.**Scheme 2.** Synthesis of biscoumarins in the presence of Ag–Co and Ag–Ni nanoalloys.

in the presence of nanoalloys gives the other intermediate II. Addition of a second molecule of dimedone on activated intermediate II, followed by intramolecular cyclodehydration affords the 1,8-dioxooctahydroxanthene. Based on this mechanism, it is clear that the electron withdrawing groups substituted on aromatic aldehyde in intermediate II increase the rate of nucleophilic addition of dimedone. Thus, arylaldehydes bearing the electron withdrawing groups react with dimedone faster than those containing electron releasing groups (Table 1, entries 8–10).

Following these results, we further investigated the potential of Ag–Co and Ag–Ni nanoalloys for the two component condensation of aldehydes and 4-hydroxycoumarin. As shown in Scheme 2, biscoumarins were obtained in high to excellent yields in short times.



**Figure 7.** Recyclability of Ag–Co (0.05 g) and Ag–Ni (0.06 g) nanoalloys in the reaction of 3-nitrobenzaldehyde (1 mmol) with dimedone (2 mmol) in ethanol at room temperature after 17 and 16 min, respectively.

The reusability of the catalysts was studied. After each reaction, the catalysts were removed by an external magnet and reused for subsequent reactions with slight loss of activity (Figure 7).

By comparison of the catalytic performance of Ag–Ni and Ag–Co nanoalloys with other reported catalysts, it will be clear that these catalysts led to desired products in lower reaction times, with higher yields, at room temperature.

### 3. 3. Biological Activity of Ag–Co and Ag–Ni Nanoalloys

Most bacteria won't hurt humans-less than 1 percent of different types cause an infection in the human body and make people sick. Examples of bacteria that cause bacterial infections include Streptococcus, Staphylococcus, and Escherichia coli. Antibiotics are the common treatment for bacterial infections. However, numerous studies have provided strong evidence that the widespread use of antibiotics has led to the emergence of multidrug-resistant bacterial strains.<sup>44</sup> Despite different types of available antibiotics, few have proved effective against bacterial resistant strains. To overcome the above shortcoming of antibiotics, substantial efforts have been made by researchers constantly to introduce novel viable alternatives, for example some different types of nanoparticle-based materials with antibacterial activity. Of the range of nanoparticle options available, silver nanoparticles have received intensive interest.<sup>45</sup> The good performance of these nanoparticles arises from the fact that nanoparticle would be less prone to promoting resistance in bacteria than antibiotics because the mode of

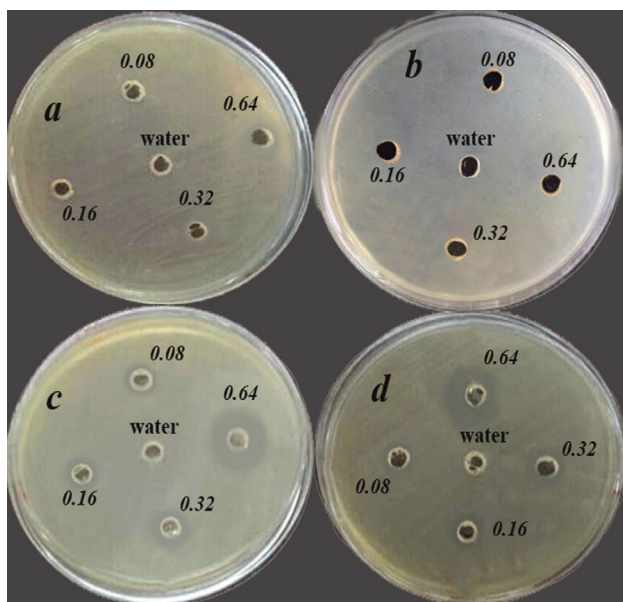
**Table 2:** Comparison of the efficiencies of a number of different reported catalysts with that of Ag–Co and Ag–Ni nanoalloys in the reaction of benzaldehyde with dimedone.

Entry	Reaction conditions	Time (min)	Yield (%) <sup>a</sup>
1	<i>p</i> -Dodecylbenzenesulfonic acid, H <sub>2</sub> O, reflux	360	89 <sup>20</sup>
2	Amberlyst-15, CH <sub>3</sub> CN, reflux	300	92 <sup>21</sup>
3	SmCl <sub>3</sub> , solvent-free, 120 °C	540	98 <sup>22</sup>
4	Ionic liquid, ultrasound irradiation, r.t.	50	87 <sup>23</sup>
5	SiCl <sub>4</sub> , dichloroethane, 60–70 °C	180	90 <sup>24</sup>
6	CAN, 2-propanol, ultrasound irradiation, 50 °C	35	98 <sup>25</sup>
7	[Et <sub>3</sub> NH][HSO <sub>4</sub> ], solvent-free, 100 °C	20	94 <sup>26</sup>
8	CAN supported HY-zeolite, solvent-free, 80 °C	90	88 <sup>27</sup>
9	Piperidine/HCl, ethanol/water, r.t.	10	69 <sup>28</sup>
10	Mg–Al hydrotalcite, H <sub>2</sub> O, reflux	180	85 <sup>29</sup>
11	Thiourea dioxide, H <sub>2</sub> O, 50–60 °C	45	96 <sup>30</sup>
12	Hydroxylamine-O-sulfonic acid, solvent-free, 90 °C	35	92 <sup>31</sup>
13	Carbon nanotube-BuSO <sub>3</sub> H, EtOH, r.t.	30	95 <sup>32</sup>
14	Cellulose/Al <sub>2</sub> O <sub>3</sub> -[MeIm]Cl-XAlCl <sub>3</sub> , EtOH, r.t.	25	91 <sup>33</sup>
15	Sulfated zirconia, EtOH, 70 °C	480	95 <sup>34</sup>
16	LPCAS, solvent free, 100 °C	5	95 <sup>35</sup>
17	Ag–Co nanoalloys, EtOH, r.t	17	95
18	Ag–Ni nanoalloys, EtOH, r.t	18	96

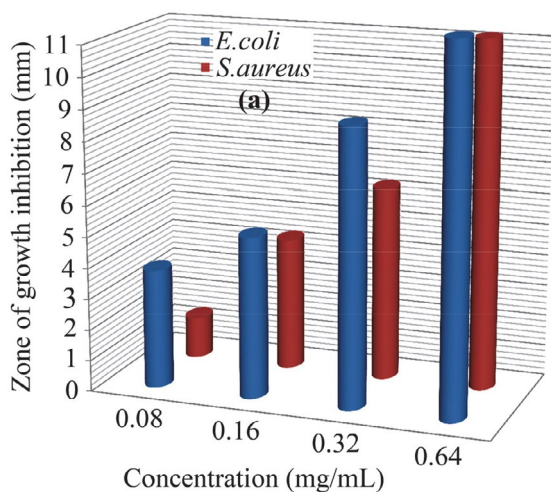
<sup>a</sup>Isolated yield.

action of nanoparticles is direct contact with the bacterial cell wall, without the need to penetrate the cell.

Following the obtained results of the catalytic activity of Ag–Co and Ag–Ni nanoalloys, we try to investigate the anti-bacterial properties of these nanoalloys on viable typical microorganisms. One of the simplest tests for the evaluation of the resistance of bacteria to different materials is the disk-diffusion testing. This test is an easy, cheap and official method that is used in many clinical microbiology laboratories for antibacterial susceptibility testing. Figures 8 and 9 show the antibacterial effect of Ag–Co and Ag–Ni nanoalloys with distinct concentrations (0.64, 0.32, 0.16 or 0.08 mg/mL) on cultured microorganisms (*E.coli*



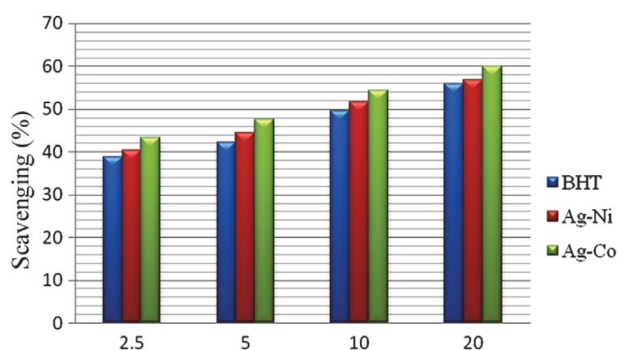
**Figure 8.** Evaluation of the antimicrobial activity of (a) Ag–Ni nanoalloys against *E.coli*; (b) Ag–Ni nanoalloys against *S.aureus*; (c) Ag–Co nanoalloys against *E.coli*; (d) Ag–Co nanoalloys against *S.aureus*.



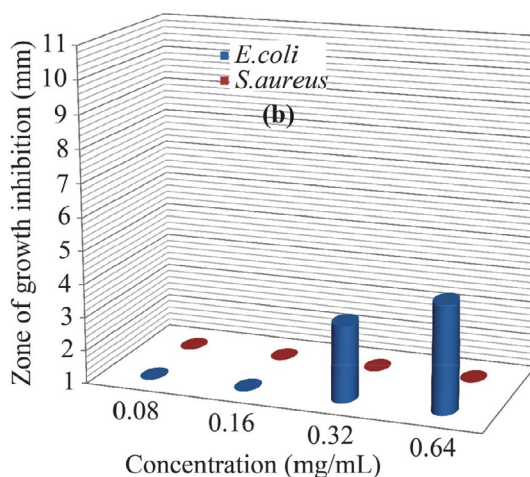
and *S.aureus* cells). The results show that Ag–Co and Ag–Ni nanoalloys exhibit antibacterial properties against *E.coli* cells. In this case, Ag–Co nanoalloys have a stronger degree of bacteria growth inhibition than Ag–Ni nanoalloys. Ag–Ni nanoalloys do not show antibacterial activity against *S.aureus* cells, while Ag–Co nanoalloys have an efficient antibacterial effect on these bacteria. In each case, it is observed that the zone of growth inhibition increased with increasing the concentration of nanoalloys.

Reactive oxygen species (ROS) and reactive nitrogen species (RNS) are the cellular oxidants and the free radicals which play a key role in human cancer development. Antioxidants have a defense function against carcinogens and oxidants. Recently, the estimate of antioxidant activity of nanoparticles has become one of the important basic studies in nano science.<sup>46,47</sup> To determine the antioxidant activity of nanoparticles, a common procedure is radical scavenging method which in 2,2-diphenyl-2-picrylhydrazyl hydrate (DPPH) is used as an electron acceptor.

Encouraged by the results obtained from the antibacterial activity of Ag–Co and Ag–Ni nanoalloys, we tried to evaluate antioxidant activity of these nanoalloys with distinct concentrations (2.5, 5, 10, and 20 µg/mL) us-



**Figure 10.** The DPPH radical scavenging activity of the Ag–Co and Ag–Ni nanoalloys and BHT.



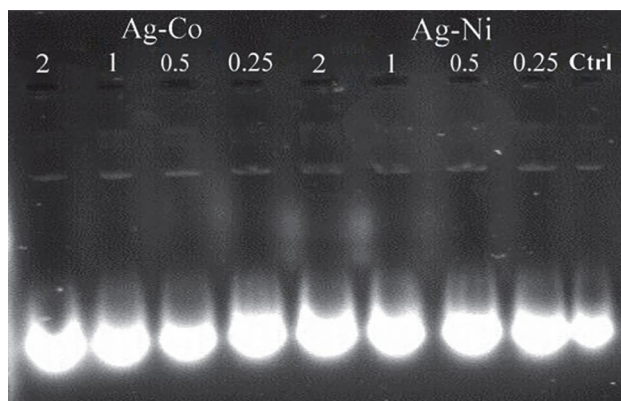
**Figure 9.** Antibacterial activity of (a) Ag–Co and (b) Ag–Ni nanoalloys.

**Table 3:** The IC<sub>50</sub> values of Ag–Co and Ag–Ni nanoalloys and BHT.

Sample	IC <sub>50</sub> (μg/mL)
Ag–Co nanoalloys	7.94 ± 1.48
Ag–Ni nanoalloys	11.28 ± 1.98
BHT	12.53 ± 2.43

ing butyl hydroxytoluene (BHT) as a positive control and DPPH. As the results in Figure 10 show, the following order of the antioxidant activity was observed: Ag–Co nanoalloys > Ag–Ni nanoalloys > BHT. Table 3 shows IC<sub>50</sub> (the concentration of sample required to scavenge 50 % of the DPPH free radicals) value of the Ag–Co and Ag–Ni nanoalloys and BHT.

Recently, studies on the possibility of the DNA cleavage by synthetic materials such as nanoparticles have stimulated great interest.<sup>48</sup> Damage in DNA by free radicals is a likely reason of mutations which, if they occur in genes, may cause some of the diseases such as birth defects, genetic diseases, and cancer.<sup>49</sup> Following our results on antibacterial and antioxidant activities of Ag–Co and Ag–Ni nanoalloys, we decided to investigate whether or not these nanoalloys have destructive effects on DNA molecules. Based on this, we examined the effect of the distinct concentrations (0.25, 0.5, 1, and 2 mg/mL) of Ag–Co and Ag–Ni nanoalloys on the DNA cleavage. Figure 11 shows the agarose gel electrophoresis. Plasmid DNA mixed with water was used as the negative control. After exposure of plasmid DNA to different concentration of the nanomaterial suspensions, we did not observe any destructive effects on DNA molecules.

**Figure 11.** Effect of the distinct concentrations of Ag–Co and Ag–Ni nanoalloys on the DNA cleavage.

## 4. Conclusion

In summary, Ag–Co and Ag–Ni nanoalloys were easily prepared from their basic ingredients and used as highly efficient heterogeneous catalytic systems for the synthesis of 1,8-dioxooctahydroxanthene derivatives from

the reaction of dimedone with aromatic aldehydes in ethanol as a green solvent at room temperature. The catalysts can be easily separated using an external magnet and their catalytic activity remains after several reaction cycles. The procedure offers several advantages including cleaner reaction profiles, simple experimental and work-up procedures, no competitive side reactions, high reaction rates, and excellent yields. To the best of our knowledge, these nanoalloys have not yet been evaluated in catalytic reactions in organic synthesis. Also, Ag–Co and Ag–Ni nanoalloys showed antibacterial and antioxidant properties and they had no destructive effects on DNA molecules.

## 5. Acknowledgement

We gratefully acknowledge the partial support of this study by the Shahrekord University of Technology Research Council, Iran.

## 6. References

1. R. Ferrando, J. Jellinek, R. L. Johnston, *Chem. Rev.* **2008**, *108*, 845–910. DOI:10.1021/cr040090g
2. A. Akdag, A. Tuncay Ozyilmaz, *Acta Chim. Slov.* **2017**, *64*, 312–318. DOI:10.17344/acsi.2016.3119
3. I. Škugor Rončević, N. Vladislavić, M. Buzuk, *Acta Chim. Slov.* **2018**, *65*, 698–708. DOI:10.17344/acsi.2018.4400
4. N. Bahrami Panah, I. Danaee, M. Payehghadr, A. Madahi, *Acta Chim. Slov.* **2018**, *65*, 312–318. DOI:10.17344/acsi.2017.3953
5. K. D. Gilroy, A. Ruditskiy, H. C. Peng, D. Qin, Y. Xia, *Chem. Rev.* **2016**, *116*, 10414–10472. DOI:10.1021/acs.chemrev.6b00211
6. C. Tang, L. Li, H. Gao, G. Li, X. Qiu, J. Liu, *J. Power Sources* **2009**, *188*, 397–403. DOI:10.1016/j.jpowsour.2008.12.011
7. T. Van Hoof, M. Hou, *Phys. Rev. B: Condens. Matter* **2005**, *72*, 115434–115446. DOI:10.1103/PhysRevB.72.115434
8. I. Karakaya, W. T. Thompson, *Bull. Alloy Phase Diagrams* **1988**, *9*, 237–243. DOI:10.1007/BF02881271
9. J. Xu, U. Herr, T. Klassen, R. S. Averback, *J. Appl. Phys.* **1996**, *79*, 3935–3945. DOI:10.1063/1.361820
10. J. P. Liu, E. Fullerton, O. Gutfleisch, D. J. Sellmyer (Eds.): *Nanoscale Magnetic Materials and Applications*, Springer, **2009**.
11. C. C. Lee, D. H. Chen, *Nanotechnol.* **2006**, *17*, 3094–3099. DOI:10.1088/0957-4484/17/13/002
12. H. H. Zhou, Y. L. Li, J. Q. Huang, C. X. Fang, S. H. Dan, Y. F. Kuang, *Trans. Nonferrous Met. Soc. China* **2015**, *25*, 4001–4007. DOI:10.1016/S1003-6326(15)64049-3
13. A. Holewinski, J. C. Idrobo, S. Linic, *Nat. Chem.* **2014**, *6*, 828–834. DOI:10.1038/nchem.2032
14. Z. Qu, D. Chen, Y. Sun, Y. Wang, *Appl. Catal., A* **2014**, *487*, 100–109. DOI:10.1016/j.apcata.2014.08.044
15. T. Librowski, R. Czarnecki, T. Czekaj, H. Marona, *Medicina (Kaunas)* **2005**, *41*, 54–58.



- DOI:10.1515/hc-2017-0215
16. H. Herken, A. Gurel, S. Selek, F. Armutcu, M. E. Ozen, M. Bulut, O. Kap, M. Yumru, H. A. Savas, O. Akyol, *Arch. Med. Res.* **2007**, 38, 247–252. DOI:10.1016/j.arcmed.2006.10.005
  17. M. S. L. Kumar, J. Singh, S. K. Manna, S. Maji, R. Konwar, G. Panda, *Bioorg. Med. Chem. Lett.* **2018**, 28, 778–782. DOI:10.1016/j.bmcl.2017.12.065
  18. C. G. Knight, T. Stephens, *Biochem. J.* **1989**, 258, 683–687. DOI:10.1042/bj2580683
  19. M. Ahmad, T. A. King, D. K. Ko, B. H. Cha, J. Lee, *J. Phys. D: Appl. Phys.* **2002**, 35, 1473–1476. DOI:10.1088/0022-3727/35/13/303
  20. T. S. Jin, J. S. Zhang, J. C. Xiao, A. Q. Wang, T. S. Li, *Synlett* **2004**, 2004, 866–870.
  21. B. Das, P. Thirupathi, I. Mahender, V. S. Reddy, Y. K. Rao, *J. Mol. Catal. A: Chem.* **2006**, 247, 233–239. DOI:10.1016/j.molcata.2005.11.048
  22. A. Ilangovan, S. Malayappasamy, S. Muralidharan, S. Maruthamuthu, *Chem. Cent. J.* **2011**, 5, 81–87. DOI:10.1186/1752-153X-5-81
  23. A. N. Dadhania, V. K. Patel, D. K. Raval, *C.R. Chim.* **2012**, 15, 378–383. DOI:10.1016/j.crci.2012.01.006
  24. H. A. Soliman, T. A. Salama, *Chin. Chem. Lett.* **2013**, 24, 404–406. DOI:10.1016/j.cclet.2013.03.021
  25. N. Mulakayala, G. P. Kumar, D. Rambabu, M. Aeluri, M. B. Rao, M. Pal, *Tetrahedron Lett.* **2012**, 53, 6923–6926. DOI:10.1016/j.tetlet.2012.10.024
  26. Z. Zhou, X. Deng, *J. Mol. Catal. A: Chem.* **2013**, 367, 99–102. DOI:10.1016/j.molcata.2012.11.002
  27. P. Sivaguru, A. Lalitha, *Chin. Chem. Lett.* **2014**, 25, 321–323. DOI:10.1016/j.cclet.2013.11.043
  28. A. M. Reeve, *J. Chem. Educ.* **2014**, 92, 582–585. DOI:10.1021/ed400457c
  29. R. Gupta, S. Ladage, L. Ravishankar, *Chem. J.* **2015**, 1, 1–4.
  30. P. S. Bhale, S. B. Dongare, Y. B. Mule, *Chem. Sci. Trans.* **2015**, 4, 246–250. DOI:10.7598/cst2015.969
  31. M. A. Zolfigol, M. Yarie, *Org. Chem. Res.* **2016**, 2, 1–8.
  32. K. Parvanak Boroujeni, Z. Heidari, R. Khalifeh, *Acta Chim. Slov.* **2016**, 63, 602–608. DOI:10.17344/acsi.2016.2291
  33. K. Parvanak Boroujeni, P. Tahani, *Inorg. Nano-Met. Chem.* **2017**, 47, 1150–1156. DOI:10.1080/24701556.2017.1284103
  34. S. S. Kahandal, A. S. Burange, S. R. Kale, P. Prinsen, R. Luque, R. V. Jayaram, *Catal. Commun.* **2017**, 97, 138–145. DOI:10.1016/j.catcom.2017.03.017
  35. V. W. Godse, S. S. Rindhe, L. Kótai, S. R. Bembalkar, R. D. Ingle, R. P. Pawar, *Eur. Chem. Bull.* **2017**, 6, 1–4. DOI:10.17628/ecb.2017.6.1-4
  36. S. A. Kahani, F. Mashhadian, *J. Alloys Compd.* **2016**, 660, 310–315. DOI:10.1016/j.jallcom.2015.11.070
  37. M. B. Gawande, A. Goswami, T. Asefa, H. Guo, A. V. Biradar, D. L. Peng, R. Zboril, R. S. Varma, *Chem. Soc. Rev.* **2015**, 44, 7540–7590. DOI:10.1039/C5CS00343A
  38. K. Parvanak Boroujeni, S. Hadizadeh, S. Hasani, A. Fadavi, M. Shahrokh, *Acta Chim. Slov.* **2017**, 64, 692–700. DOI:10.17344/acsi.2017.3437
  39. S. A. Kahani, M. Shahrokh, *RSC Adv.* **2015**, 5, 71601–71607. DOI:10.1039/C5RA09385F
  40. D. P. Graddon, *J. Inorg. Nucl. Chem.* **1956**, 3, 308–322. DOI:10.1016/0022-1902(56)80041-9
  41. D. R. Brown, R. R. Pavlis, *J. Chem. Educ.* **1985**, 62, 807–808. DOI:10.1021/ed062p807
  42. H. T. Yang, Y. K. Su, C. M. Shen, T. Z. Yang, H. J. Gao, *Surf. Interface Anal.* **2004**, 36, 155–160. DOI:10.1002/sia.1675
  43. J. H. Hwang, V. P. Dravid, M. H. Teng, J. J. Host, B. R. Elliott, D. L. Johnson, T. O. Mason, *J. Mater. Res.* **1997**, 12, 1076–1082. DOI:10.1557/JMR.1997.0150
  44. L. Wang, C. Hu, L. Shao, *Int. J. Nanomed.* **2017**, 12, 1227–1249. DOI:10.2147/IJN.S121956
  45. D. Singh, V. Rathod, S. Ningangouda, J. Herimath, P. Kulkarni, *J. Pharm. Res.* **2013**, 7, 448–453. DOI:10.1016/j.jopr.2013.06.003
  46. M. Carochi, I. C. Ferreira, *Food Chem. Toxicol.* **2013**, 51, 15–25. DOI:10.1016/j.fct.2012.09.021
  47. D. Das, B. C. Nath, P. Phukon, S. K. Dolui, *Colloids Surf., B* **2013**, 101, 430–433. DOI:10.1016/j.colsurfb.2012.07.002
  48. G. Bhabra, A. Sood, B. Fisher, L. Cartwright, M. Saunders, W. H. Evans, A. Surprenant, G. Lopez-Castejon, S. Mann, S. A. Davis, L. A. Hails, *Nat. Nanotechnol.* **2009**, 4, 876–883. DOI:10.1038/nnano.2009.313
  49. A. Agarwal, T. M. Said, *Hum. Reprod. Update* **2003**, 9, 331–345. DOI:10.1093/humupd/dmg027

## Povzetek

V prispevku je predstavljena priprava magnetnih nanodelcev zlitin Ag–Co in Ag–Ni s pomočjo kemijske redukcije z uporabo  $[\text{Co}(\text{NH}_3)_6]\text{Cl}_3$  in  $[\text{Ni}(\text{C}_2\text{O}_4)_2]\text{K}_2$  kompleksov ter  $\text{AgNO}_3$ . Kot redukcijsko sredstvo so avtorji uporabili hidrazin monohidrat. Dobljene nanodelce so karakterizirali s FT-IR spektroskopijo, SEM mikroskopijo, spektroskopijo energijske disperzije (EDS), rentgensko difrakcijo (XRD) in vibracijskim magnetometrom (VSM). Nano-zlitini Ag–Co in Ag–Ni sta pokazali odlično katalitično učinkovitost pri pripravi 1,8-diooksoctahidroksantenov v reakciji 5,5-dimetil-1,3-cikloheksandiona (dimedona) z aromatskimi aldehidi. Katalizator so po reakciji izolirali iz reakcije zmesi s pomočjo zunanega magnetnega polja in ga ponovno uporabili. Obe, tako Ag–Co kot Ag–Ni nano-zlitina, izkazujeta antibakterijske in antioksidativne lastnosti, hkrati pa ne vplivata na cepitev DNA.



Except when otherwise noted, articles in this journal are published under the terms and conditions of the Creative Commons Attribution 4.0 International License

# Synthesis and Characterization of Novel Five-Membered Heterocycles and Their Activity against *Candida* Yeasts

Hiba Maher Tawfeeq,<sup>1</sup> Rasim Farraj Muslim,<sup>2</sup> Obaid Hasan Abid<sup>3</sup>  
and Mustafa Nadhim Owaid<sup>2,4</sup>

<sup>1</sup> Department of Chemistry, College of Education for Pure Sciences, University Of Anbar, Anbar 31001, Iraq

<sup>2</sup> Department of Ecology, College of Applied Sciences, University Of Anbar, Anbar 31007, Iraq

<sup>3</sup> Department of Scientific Affairs and Graduate Studies, University of Fallujah, Anbar, Iraq

<sup>4</sup> Department of Heet Education, General Directorate of Education in Anbar, Ministry of Education, Anbar 31007, Iraq

\* Corresponding author: E-mail: dr.rasim92hmts@gmail.com

Received: 09-14-2018

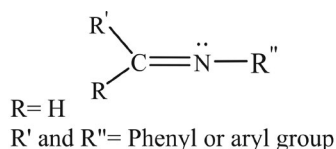
## Abstract

Some new tetrazole derivatives were prepared by the reaction between the prepared azomethine compounds **I**<sub>6</sub>–**I**<sub>10</sub> with sodium azide in anhydrous tetrahydrofuran (THF) with a few drops of distilled water and under reflux conditions. Azomethine compounds were prepared by thermal condensation reactions of aromatic aldehydes with primary aromatic amines. The prepared compounds (tetrazole derivatives) were screened for their antibacterial activity (by disc diffusion method). Compound **I**<sub>6</sub> is the most active derivative that has recorded a significantly ( $p < 0.01$ ) stronger influence to inhibit the growth of *Candida zeylanoides* with an average zone of inhibition of 26.0 mm. Derivatives **I**<sub>7</sub> and **I**<sub>9</sub> showed the lowest zone of inhibition of 8.0 mm against *Candida zeylanoides*. This study may be helpful in designing more potential anticandidal agents for therapeutic use in the future.

**Keywords:** *Candida* sp.; pharmaceutical; azomethine; sodium azide; biological activity.

## 1. Introduction

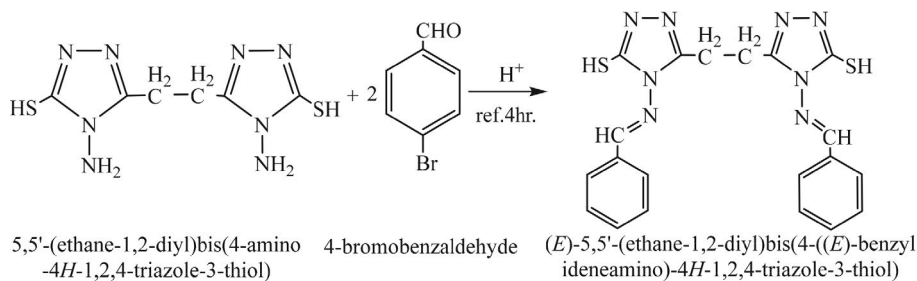
Azomethine compounds discovered by Hugo Schiff in 1864, can be prepared by different methods, one of the more important being the condensation reaction between primary amine with aldehyde.<sup>1</sup> Azomethine compounds contain the N=C group.<sup>2</sup> Some of the azomethine compounds are used as antibacterial agents.<sup>3,4</sup> The structure of azomethine compounds usually includes a phenyl or aryl group with the double bond between the carbon atom and the nitrogen atom.<sup>5,6</sup> (Scheme 1)



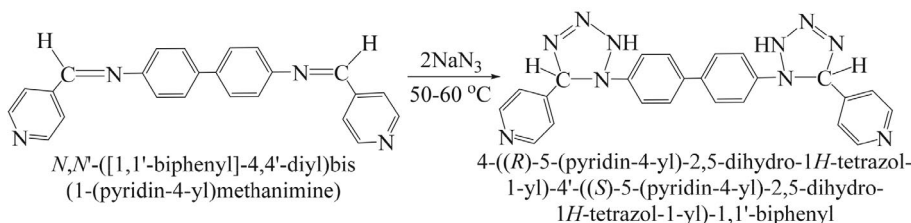
Scheme 1. Structure of azomethine compounds

The reaction of triazole diamine compound with 4-bromobenzaldehyde in the presence of glacial acetic acid gave the next product.<sup>7</sup> (Scheme 2)

Tetrazole derivatives are heterocyclic compounds containing four nitrogen atoms and one carbon atom within one ring.<sup>8</sup> Tetrazoles as a group of heterocyclic compounds appear in IR spectra as broad signals; having peculiar biological activities.<sup>9,10</sup> Tetrazole derivatives have a special structure and can display anti-bacterial properties, such as antiviral and anti-allergic.<sup>11–13</sup> There are several methods to prepare tetrazole derivatives, and each method depends on the constituents of the reaction.<sup>14</sup> Recently, there were many various types of compounds (including such containing a metal centre coordinated with suitable ligands) tested against *Candida albicans*, with a varying degree of success.<sup>15–17</sup> An example of one of tetrazole derivatives is the product from the reaction between azomethine compound (biphenyl bis



Scheme 2. Using glacial acetic acid to prepare the azomethine compound



Scheme 3. Use of sodium azide to prepare tetrazole derivatives

(1-(pyridin-4-yl) methanimine)) with sodium azide.<sup>18</sup> (Scheme 3)

Many of tetrazole derivatives can be prepared by the reaction between a different aldehyde and different amines.<sup>10</sup> (Scheme 4)

In this study, tetrazole derivatives derived from the reaction of the prepared azomethine compounds with sodium azide were evaluated for their biological activity against four types of *Candida* yeasts. The products were identified by their melting points, FT-IR and <sup>1</sup>H NMR spectra.

## 2. Experimental

### 2.1. Apparatuses

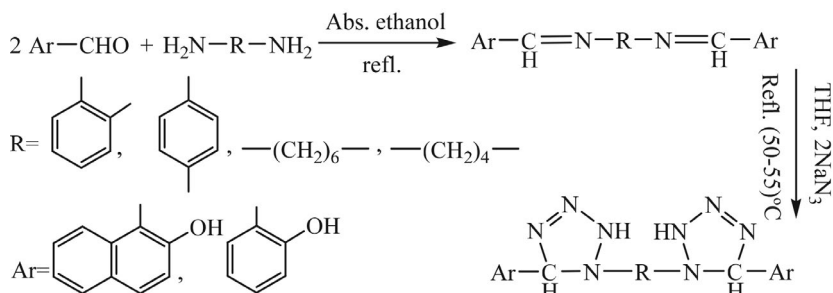
The measurement of melting point was conducted by the electrothermal melting point apparatus. IR spectra were recorded at room temperature in the range of 400–4000 cm<sup>-1</sup> by a Fourier transform infra-red Spectrophotometer Model Tensor 27 Bruker Co., Germany. The <sup>1</sup>H NMR spectra were recorded on Bruker Ac-300 MHz spectrometer.

### 2.2. Preparation of Azomethine Compounds I<sub>1</sub>–I<sub>5</sub>

Azomethine compounds were prepared according to the literature procedure,<sup>19,20</sup> as shown in Table 1. An equimolar mixture 0.02 mole of aldehydes and 0.02 mole of amines and trace of acidic catalyst in 25 mL absolute ethanol were reacted at reflux temperature for 4 hours, whereby a crystalline solid separated out. The products were filtered off and recrystallized from absolute ethanol.

### 2.3. Preparation of Tetrazole Derivatives I<sub>6</sub>–I<sub>10</sub>

A mixture of azomethine compounds (0.01 mol) and sodium azide (0.01 mol) was dissolved in 20 mL of THF and 2 mL distilled water and refluxed for 4 hour and left to stand for 24 hour at room temperature, then the solid product separated out.<sup>21</sup> The products were filtered off and recrystallized from absolute ethanol as shown in Table 2.



Scheme 4. Prepared tetrazole derivatives with double rings

**Table 1.** Names, structural formulae, symbol, yields, colors and melting points of azomethine compounds I<sub>1</sub>–I<sub>5</sub>

Nomenclature	Structural formula	Compound	Yield %	Color	m.p. °C
( <i>E</i> )-4,6-dimethyl- <i>N</i> -(4-nitrobenzylidene) pyrimidin-2-amine		I <sub>1</sub>	78%	Bright pale yellow	79–81
( <i>E</i> )-5-((2-(2,4-dinitro phenyl)hydrazono)methyl)-2-methoxyphenol		I <sub>2</sub>	80%	Dark red	250–252
( <i>E</i> )-1-(4-chlorobenzylidene)-2-(2,4-dinitro phenyl)hydrazine		I <sub>3</sub>	82%	Orange	236–238
( <i>E</i> )-1-(4-bromobenzylidene)-2-(2,4-dinitro phenyl)hydrazine		I <sub>4</sub>	84%	Orange	232–234
( <i>E</i> )-4-((2-(2,4-dinitro phenyl)hydrazono)methyl)phenol		I <sub>5</sub>	80%	Bright Dark red	240–242

**Table 2.** Names, structural formulae, symbol, yields, colors and melting points of tetrazole derivatives I<sub>6</sub>–I<sub>10</sub>

Nomenclature	Structural formula	Compound	Yield %	Color	m.p. °C
4,6-dimethyl-2-(5-( <i>p</i> -nitrophenyl)-4,5-dihydro-1 <i>H</i> -tetrazol-yl)pyrimidine		I <sub>6</sub>	76%	Bright tan	96–98
5-((2,4-dinitrophenyl)amino)-4,5-dihydro-1 <i>H</i> -tetrazol-yl-2-methoxy phenol		I <sub>7</sub>	83%	Red	276–279
5-( <i>p</i> -chlorophenyl)- <i>N</i> -(2,4-dinitrophenyl)-4,5-dihydro-1 <i>H</i> -tetrazol-1-amine		I <sub>8</sub>	78%	Orange	256–258
5-( <i>p</i> -bromophenyl)- <i>N</i> -(2,4-dinitrophenyl)-4,5-dihydro-1 <i>H</i> -tetrazol-1-amine		I <sub>9</sub>	78%	Orange	260–262
4-(1-((2,4-dinitrophenyl)amino)-4,5-dihydro-1 <i>H</i> -tetrazol-yl) phenol		I <sub>10</sub>	92%	Orange	272–274

## 2. 4. Activity against *Candida* Yeasts

This test was carried out *in vitro* to investigate the inhibitory effects of the prepared tetrazole derivatives using well diffusion method on Muller-Hinton agar. This experiment was done as mentioned by Owaid *et al.* with some modifications.<sup>22</sup> Four milligrams of the prepared tetrazole derivatives were applied separately in 6 mm-well. After 18 hour at 37 °C, the zone of inhibition was measured using the ruler in millimeters.

## 3. Results and Discussion

Tables 1 and 2 show structural formulae, names, yields, melting points and color of all prepared compounds I<sub>1</sub>–I<sub>10</sub>. The best yield achieved for the prepared azomethine compounds was for compounds I<sub>3</sub> 82% and I<sub>4</sub> 84%, while the lowest yield was for compound I<sub>1</sub> 78% and the best yield of the prepared tetrazole derivatives was for I<sub>10</sub> 92%, while the lowest yield was for I<sub>6</sub> 76%. The highest melting point for azomethine compounds was for com-



pound **I**<sub>2</sub>, the lowest melting point was for compound **I**<sub>1</sub>, while the highest melting point of the prepared tetrazole derivatives was for compound **I**<sub>7</sub>, the lowest melting point was for compound **I**<sub>6</sub>. The different colors and melting points of the products compared with the raw material are initial evidence of interaction.

### 3. 1. Azomethine Compounds **I**<sub>1</sub>–**I**<sub>5</sub>

Azomethine compounds were prepared from commercially available aldehydes with primary amines and identified by their melting points and FT-IR spectra. Table 3 shows the appearance of the stretching absorption bands of the characteristic groups of the resulting group (C=N) at 1609–1681 cm<sup>-1</sup> beside the characteristic bands of the residual groups in the structure, being indicative of the formation of the products.<sup>23,24</sup> 4, 9a- Tetrahydrobenzo [e] [1,3] oxazepin- 5(5aH

The reaction involves a nucleophile attack of the electron pair of the amino group (NH<sub>2</sub>) of aromatic amine on the carbonyl group (C=O) of aromatic aldehydes to form an *N*-substituted hemiaminal; in a suitable medium it can eliminate a water molecule to give the stable compound (azomethine).<sup>20</sup>

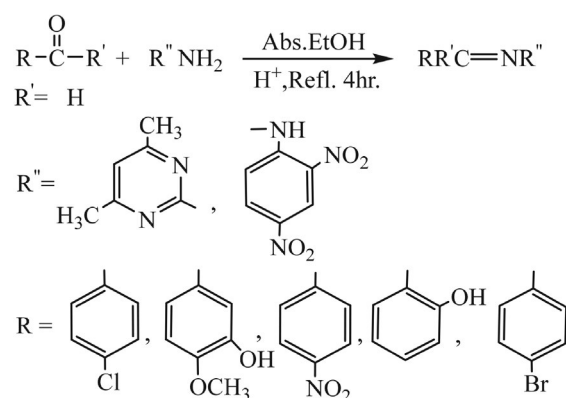
### 3. 2. Tetrazole Derivatives **I**<sub>6</sub>–**I**<sub>10</sub>

In this work, the preparation of tetrazole compounds was achieved by the reaction between prepared azomethine compounds (**I**<sub>1</sub>–**I**<sub>5</sub>) with sodium azide. The resulting products were identified using the melting points, FT-IR and <sup>1</sup>H NMR spectra. Table 4 shows characteristic stretching absorption bands at 1219–1286 cm<sup>-1</sup>, 1007–1083 cm<sup>-1</sup> and 1487–1509 cm<sup>-1</sup> indicative of C–N, N–N and N=N bonds of tetrazol rings beside the characteristic stretching absorption bands of the residual groups in their structure.<sup>27</sup>

Table 3. FT-IR of azomethine compounds **I**<sub>1</sub>–**I**<sub>5</sub>

Compound	C=N	C=C Aromatic	FT-IR, ν (cm <sup>-1</sup> )				Others
			C–H Aromatic	C–H Alkene	C–H Aliphatic Asymmetric	C–H Aliphatic Symmetric	
<b>I</b> <sub>1</sub>	1681	1601	3042	3105	2969	2849	NO <sub>2</sub> 1529, 1340, C=N pyrimidine 1634
<b>I</b> <sub>2</sub>	1609	1580	3042	3113	2972	2945	NO <sub>2</sub> 1500, 1328 O–H 3491, NH 3278
<b>I</b> <sub>3</sub>	1609	1581	3041	3089	–	–	NO <sub>2</sub> 1508, 1317 N–H 3283, C–Cl 823
<b>I</b> <sub>4</sub>	1611	1581	3042	3087	–	–	NO <sub>2</sub> 1505, 1324 N–H 3263
<b>I</b> <sub>5</sub>	1615	1592	3042	3112	–	–	NO <sub>2</sub> 1508, 1305 O–H 3422, N–H 3257

The general equation (Scheme 5) represents the main reaction through which the prepared azomethine compounds were obtained. The mechanism of azomethine compounds formation was thoroughly studied and established by many authors in the literature.<sup>25,26</sup>



Scheme 5. The main reaction of azomethine compounds

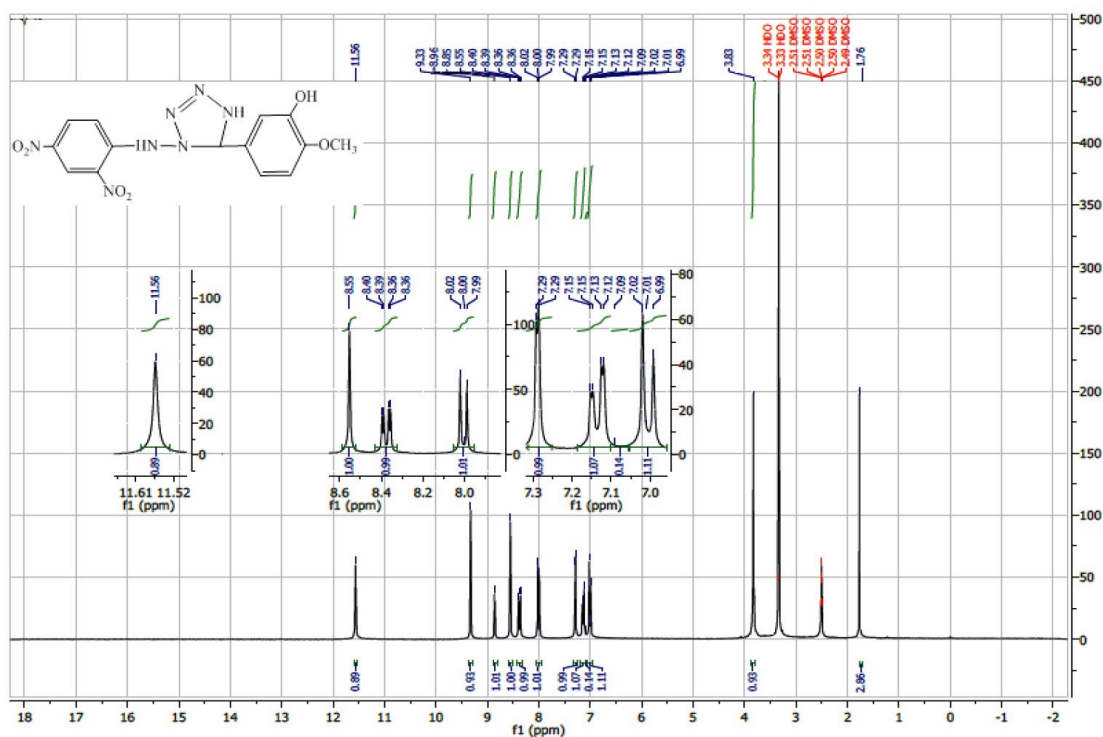
The <sup>1</sup>H NMR spectrum of compound **I**<sub>7</sub> (Fig. 1, in solvent DMSO-*d*<sub>6</sub>) showed the following signals: singlet at δ 1.76 indicating the presence of 3H as *o* methoxy group (OCH<sub>3</sub>), singlet at δ 3.83 indicating the presence of 1H as an NH group (NH outside of the tetrazole ring), singlet at δ 8.55 indicating the presence of 1H as another NH group (NH inside of the tetrazole ring), singlet at δ 9.33 indicating the presence of 1H as one CH group (N-CH), singlet at δ 11.56 indicating the presence of 1H as one hydroxy group (OH), multiplet at δ 8.96–6.99 indicating the presence of 6H of aromatic protons. <sup>1</sup>H NMR spectrum of compound **I**<sub>8</sub> (Fig. 2) shows the following signals: singlet at δ 3.33 indicating the presence of 1H as an NH group (NH outside of the tetrazole ring), singlet at δ 8.71 indicating the presence of 1H as another NH group (NH inside of the tetrazole ring), singlet at δ 11.71 indicating the presence of 1H as one CH group (N-CH), multiplet and doublet of doublet at δ 8.41–7.56 indicating the presence of 7H of aromatic protons.<sup>27</sup> Other chemical shifts for compounds **I**<sub>6</sub>, **I**<sub>9</sub> and **I**<sub>10</sub> are given in Table 5.

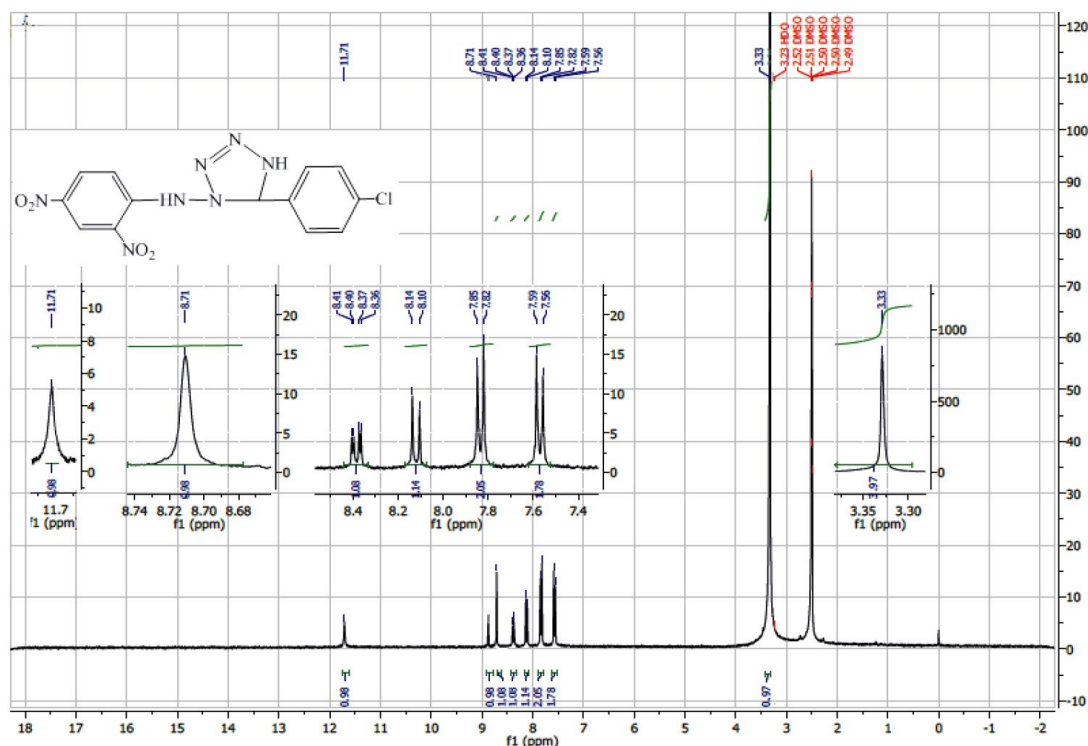
Table 4. FT-IR of tetrazole derivatives I<sub>6</sub>–I<sub>10</sub>

Compound	N–H	N–N	N=N	C–N	FT-IR $\nu$ (cm <sup>-1</sup> )		C–H Aliphatic		Others
					C=C Aromatic	C–H Aromatic	Asymmetric	Symmetric	
I <sub>6</sub>	3383	1007	1500	1286	1606	3044	2976	2849	NO <sub>2</sub> 1541, 1345
I <sub>7</sub>	3280	1020	1509	1273	1614	3113	2972	2880	O–H b 3497 NO <sub>2</sub> 1540, 1339
I <sub>8</sub>	3266	1083	1489	1219	1615	3088	–	–	NO <sub>2</sub> 1514, 1339 C–Cl 833 C–H 2951
I <sub>9</sub>	3299	1083	1487	1269	1585	3067	–	–	NO <sub>2</sub> 1512, 1330 C–H 2950 O–H b 3423
I <sub>10</sub>	3258	1074	1488	1276	1612	3113	–	–	NO <sub>2</sub> 1509, 1305 C–H 2977

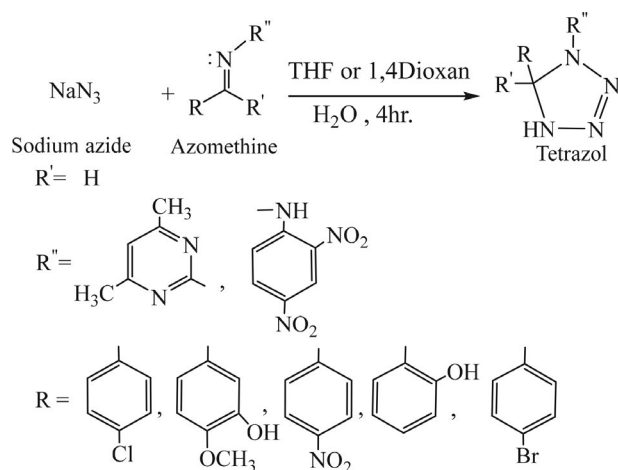
Table 5. The <sup>1</sup>H NMR spectral data of tetrazole derivatives I<sub>6</sub>–I<sub>10</sub> (in DMSO-*d*<sub>6</sub>).

Compound	Chemical Shifts $\delta$ (ppm)
I <sub>6</sub>	Singlet at 1.28 (6H, 2 $\text{CH}_3$ ), singlet at 8.68 (H, $\text{-NH}$ ), singlet at 10.19 (1H, N- $\text{CH}$ ), singlet at 9.77 (1H, $\text{-OH}$ ), singlet and doublet of doublet at 8.43–8.08 (5H, aromatic protons).
I <sub>7</sub>	Singlet at 1.76 (3H, O- $\text{CH}_3$ ), singlet at 3.83 (1H, $\text{NH out}$ ), singlet at 8.55 (1H, $\text{NH in}$ ), singlet at 9.33 (1H, N- $\text{CH}$ ), singlet at 11.56 (1H, $\text{-OH}$ ), multiplet at 8.96–6.99 (6H, aromatic protons).
I <sub>8</sub>	Singlet at 3.33 (1H, $\text{NH}$ outside of the tetrazole ring), singlet at 8.71 (1H, $\text{NH}$ inside of the tetrazole ring), singlet at 11.71 (1H, N- $\text{CH}$ ), multiplet and doublet of doublet at 8.41–7.56 (7H, aromatic protons).
I <sub>9</sub>	Singlet at 3.26 (1H, $\text{NH}$ outside of the tetrazole ring), singlet at 8.69 (1H, $\text{NH}$ inside of the tetrazole ring), singlet at 11.71 (1H, N- $\text{CH}$ ), multiplet at 8.41–7.79 (7H, aromatic protons).
I <sub>10</sub>	Singlet at 3.40 (1H, $\text{NH out}$ ), singlet at 8.88 (1H, $\text{NH in}$ ), singlet at 10.07 (H, N- $\text{CH}$ ), singlet at 11.57 (1H, $\text{-OH}$ ), multiplet and doublet of doublet at 8.59–6.85 fr (7H, aromatic protons).

Figure 1. <sup>1</sup>H NMR Spectrum of I<sub>7</sub>

Figure 2.  $^1\text{H}$  NMR Spectrum of  $\text{I}_8$ 

The reaction of the azomethine compounds with sodium azide is given in the equation in Scheme 6.



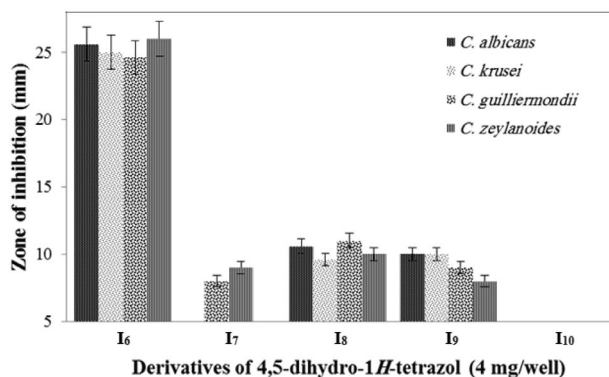
Scheme 6. The main reaction of the prepared tetrazole derivatives

From the reaction course and the suggested mechanism it may be concluded that the reaction takes place *via* concerted mechanism (Huisgen 1,3-dipolar cycloaddition).<sup>28</sup>

### 3. 3. Activity against *Candida* Yeasts

Zone of inhibition of some human pathogenic yeasts was determined by the well-diffusion method and used to

test the potential of the prepared tetrazole derivatives ( $\text{I}_6$ – $\text{I}_{10}$ ) as shown in Fig. 3 and 4. Compound  $\text{I}_6$  was found to be the best derivative that has significantly ( $p < 0.01$ ) recorded a stronger influence to inhibit the growth of *Candida zeylanoides* at an average of the zone of inhibition of 26.0 mm, followed by 24.6–25.6 mm for the rest of the species of *Candida*. Next,  $\text{I}_8$  derivative recorded zone of inhibition of 11.0 mm toward *Candida guilliermondii*. Furthermore,  $\text{I}_7$  and  $\text{I}_9$  showed the lowest zone of inhibition of only 8.0 mm against *Candida zeylanoides*. Additionally,  $\text{I}_6$  derivative recorded zone of inhibition of 11.3 mm against *Candida guilliermondii* and *Candida zeylanoides*, respectively. Compound  $\text{I}_{10}$  did not inhibit the growth of *Candida* species as shown in Fig. 3. Resistance mechanism depends on which specific paths are inhibited by the drugs

Figure 3. Zone of inhibition of *Candida* sp. using the prepared tetrazole derivatives

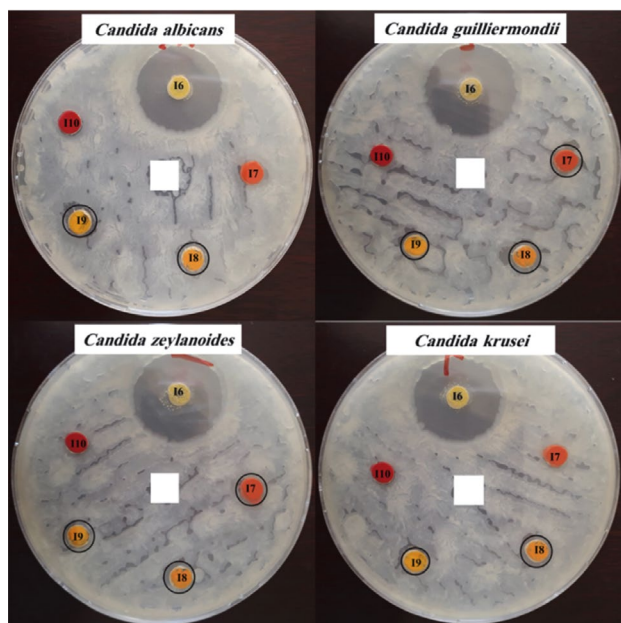


Figure 4. Activity against *Candida* yeasts of the prepared tetrazole derivatives  $I_6$ – $I_{10}$

and if the alternative paths are available to substitute for those paths that the compound has inhibited; in this way the microorganism can modify its pathways and be able to survive by developing resistance.<sup>29,30</sup> These results agree with some recent studies which described the synthesis of hybrid heterocycles proving to have *in vitro* antimicrobial, antibacterial and antifungal activities.

## 4. Conclusions

The results of FT-IR and  $^1\text{H}$  NMR showed that the five-membered ring compounds were the least obstructed during all preparation processes and that neither light nor humidity affect the prepared compounds, this proving that the prepared compounds have an excellent stability.  $I_6$  is the best derivative that has significantly ( $p < 0.01$ ) recorded a stronger influence to inhibit the growth of *Candida zeylanoides* at an average zone of inhibition of 26.0 mm. This study may be helpful in designing more potential anticandidal agents for therapeutic use in the future.

## 5. Acknowledgements

Special thanks to Anbar University's President Professor Dr. Khalid Battal Najim for his continuous support to publishing the research in certified international journals, thanks to Dr. Jalal Abdul Kareem for helping to measure the  $^1\text{H}$  NMR spectra. Also, grateful is for College of Education for Pure Sciences, University Of Anbar for helping to measurement the FT-IR spectra.

## 6. References

1. A. Adabiardakani, H. Mohammad, H. Kargar, *World Appl. Progr.* **2012**, 2, 472–476.
2. M. A. Ashraf, K. Mahmood, A. Wajid, M. J. Maah, I. Yusoff, *Int. Proc. Chem. Biol. Environ. Eng.* **2011**, 10, 1–7.
3. M. A. Ashraf, A. Wajid, K. Mahmood, M. J. Maah, I. Yusoff, *Orient. J. Chem.* **2011**, 27, 363–372.
4. A. Golcu, M. Tumer, H. Demirelli, R. A. Wheatley, *Inorg. Chim. Acta* **2005**, 358, 1785–1797. DOI:10.1016/j.ica.2004.11.026
5. K. Brodowska, E. Łodyga-Chruścińska, *Chemik* **2014**, 68, 129–134.
6. Z. Hussain, Z. Fadhil, H. Adil, M. Khalaf, B. Abdullah, E. Yousif, *Res. J. Pharm. Biol. Chem. Sci.* **2016**, 7, 1500–1510.
7. A. A. Younus, N. R. Jber, *J. Al-Nahrain Uni-Sci.* **2017**, 20, 1–6. DOI:10.22401/JNUS.20.2.01
8. R. Ranjith, *J. Chem. Pharm. Res.* **2016**, 8, 505–526.
9. B. Akhlaghinia, S. Rezazadeh, *J. Braz. Chem. Soc.* **2012**, 23, 2197–2203. DOI:10.1590/S0103-50532013005000005
10. H. A. Basheer, A. A. Ibrahim, M. S. Ahmed, *Swift J. Pure Appl. Chem.* **2016**, 2, 1–3.
11. T. Mavromoustakos, A. Kolocouris, M. Zervou, P. Roumelioti, J. Matsoukas, R. Weisemann, *J. Med. Chem.* **1999**, 42, 1714–1722. DOI:10.1021/jm980499w
12. N. Mekni, A. Baklouti, *J. Fluorine Chem.* **2008**, 129, 1073–1075. DOI:10.1016/j.jfluchem.2008.06.019
13. D. Varadaraji, S. S. Suban, V. R. Ramasamy, K. Kubendiran, J. S. K. Raguraman, S. K. Nalilu, H. N. Pati, *Org. Commun.* **2010**, 3, 45–56.
14. L. Myznikov, A. Hrabalek, G. Koldobskii, *Chem. Heterocycl. Comp.* **2007**, 43 1–9. DOI:10.1007/s10593-007-0001-5
15. J. Lazarević, A. Kolarević, G. Stojanović, A. Šmelcerović, P. Ciuffreda, E. Santaniello, *Acta Chim. Slov.* **2018**, 65, 801–810. DOI:10.17344/acsi.2018.4380
16. A. Srinivas, M. Sunitha, P. Karthik, K. V. Reddy, *Acta Chim. Slov.* **2017**, 64, 1030–1041. DOI:10.17344/acsi.2017.3805
17. Y. J. Han, L. Wang, Q. B. Li, L. W. Xue, *Acta Chim. Slov.* **2017**, 64, 179–185.
18. R. M. Al-Juburi, *J. Al-Nahrain Uni-Sci.* **2012**, 15, 60–67. DOI:10.22401/JNUS.15.4.07
19. O. H. Abid, R. F. Muslim, K. M. Mohammed, *J. Uni. Anbar Pure Sci.* **2016**, 10, 1–9.
20. R. F. Muslim, H. M. Tawfeeq, M. N. Owaid, O. H. Abid, *Acta Pharm. Sci.* **2018**, 56, 39–57. DOI:10.23893/1307-2080.APS.05610
21. B. P. A. M. R. B. Srinivas, *Der Pharma Chemica.* **2016**, 8, 84–93.
22. M. N. Owaid, J. Raman, H. Lakshmanan, S. S. S. Al-Saeedi, V. Sabaratnam, I. A. Abed, *Mater. Lett.* **2015**, 153, 186–190. DOI:10.1016/j.matlet.2015.04.023
23. R. M. A. K. M. O. Abid, *J. Uni. Anbar Pure Sci.* **2016**, 10, 8–18.
24. O. H. Abid, H. M. Tawfeeq, R. F. Muslim, *Acta Pharm. Sci.* **2017**, 55, 43–55.
25. J. Simek, Organic Chemistry, Pearson education, Inc., New York, 2013.



26. O. Abid, A. Ahmed, Spectrometric identification of organic compounds, John Wiley and Sons, Inc., New York, 2005.
28. R. Das, N. Majumdar, A. Lahiri, *Int. J. Radiat. Phys. Chem.* **2014**, *4*, 467–472.
29. F. C. Tenover, *Am. J. Med.* **2006**, *119*, S3–S10.  
DOI:10.1016/j.amjmed.2006.03.011
30. M. N. Owaid, R. F. Muslim, H. A. Hamad, *Jordan J. Biol. Sci.* **2018**, *11*, 401–405.

## Povzetek

Z reakcijo natrijevega azida s predhodno pripravljenimi azometinskimi spojinami **I**<sub>6</sub>–**I**<sub>10</sub> smo v brezvodnem tetrahidrofuranu (THF) ob dodatku nekaj kapljic destilirane vode pod pogoji refluksa pripravili nekaj novih derivatov tetrazola. Azometinske spojine smo sintetizirali s termično kondenzacijo aromatskih aldehydov s primarnimi aromatskimi amini. Pripravljenim spojinam (derivatom tetrazola) smo določili antibakterijske aktivnosti (z metodo difuzije v disku). Spojina **I**<sub>6</sub> se je izkazala za najbolj aktivni derivat z visoko ( $p < 0.01$ ) povečanim vplivom zaviranja rasti organizma *Candida zeylanoides* (s povprečno vrednostjo premera inhibicije 26.0 mm). Derivata **I**<sub>7</sub> in **I**<sub>9</sub> pa sta izkazala najslabše inhibitorno delovanje s premerom inhibicije le 8.00 mm proti istemu organizmu (*Candida zeylanoides*). Ta študija bi lahko pomagala pri načrtovanju novih bolj učinkovitih spojin proti kvasom iz rodu *Candida*, ki bi bile v prihodnosti celo uporabne v terapevtske namene.



Except when otherwise noted, articles in this journal are published under the terms and conditions of the Creative Commons Attribution 4.0 International License

Scientific paper

# Autofermentation of Chamomile Ligulate Flowers Promote Antitumor Effects *in vitro*

Marijana Jukić,<sup>1#</sup> Aleksandra Cvetanović,<sup>2#</sup> Katarina Mišković Špoljarić,<sup>1</sup>  
Saša Savić,<sup>3</sup> Jaroslava Švarc-Gajić,<sup>2</sup> Zoran Zeković<sup>2</sup> and Ljubica Glavaš-Obrovac<sup>1,\*</sup>

<sup>1</sup> Department of Medicinal Chemistry, Biochemistry and Clinical Chemistry, Faculty of Medicine,  
J. J. Strossmayer University of Osijek, J. Hottlera 4, HR-31000 Osijek, Croatia

<sup>2</sup> Department of Pharmaceutical Engineering and Biotechnology, Faculty of Technology, University of Novi Sad,  
Bulevar cara Lazara 1, 21 000 Novi Sad, Serbia

<sup>3</sup> Faculty of Technology, Bulevar Oslobođenja 124, 16000 Leskovac, Serbia

\* Corresponding author: E-mail: lgobrovac@mefos.hr;  
Tel.: +385-91-224-1446; Fax: +385-31-399-613.

Received: 10-11-2018

<sup>#</sup>These authors contributed equally to this work.

## Abstract

In the frame of this paper, the enzyme-assisted hydrolysis coupled with ultrasound and Soxhlet extraction was applied in order to get extracts of chamomile ligulate flowers (CLF). Obtained extracts were characterized in terms to their apigenin and apigenin glucoside composition, as well as antiproliferative potential against tumour cells. Antioxidant activity was determined by two different assays based on different mechanisms showing that autofermented extracts have higher reduction potential. Autofermented extracts prepared by ultrasound and Soxhlet extraction had a stronger impact on the treated carcinoma (HeLa and NCI-H358) and leukemia (K562) cells' growth reduction in comparison to the native extracts, 30–35% greater inhibition at the lowest concentration (0.01 mg/mL), in two observed time points (48 and 72 h). Leukemia cells are more sensitive to all tested extracts. The autofermented CLF extracts with highest antiproliferative efficacy induced morphological changes and apoptosis in the HeLa cells. Obtained results clearly showed that the combination of enzymatic hydrolysis with cavitation phenomenon results in extracts with higher apigenin content and increased biological potential.

**Keywords:** Chamomile flowers; extraction; apigenin; antiproliferative activity; apoptosis

## 1. Introduction

It is well known that some natural plant compounds exhibit positive impact on human health demonstrating additive or synergistic diseases-fighting activities.<sup>1</sup> Flavonoids, especially flavons, flavonols and flavanones, are often key bioactive compounds for antioxidant and anticancer effects.<sup>2,3</sup>

Apigenin (4',5,7-trihydroxyflavone) is a flavon with relatively low molecular weight. Different studies have shown that apigenin demonstrates broad spectrum of beneficial effects being considered as a molecule with promising pharmacological and biological characteristics. Studies have shown that apigenin is a potent antioxidant, antiviral,

antimicrobial and chemo preventive agent.<sup>4–7</sup> In the structure of this compound three hydroxyl groups together with double bonds at C2 and C3 are present. Such chemical structure provides that apigenin can acts as a phytoestrogen. Furthermore, high cytotoxic activity of apigenin<sup>8</sup> was proved in numerous studies. It is capable to induce apoptosis in different tumour cells like monocytic and lymphocytic leukemia cells, cervical, lung, breast, and colon carcinoma cells as well.<sup>6,9,10</sup> Conducted studies have provided data related to its chemoprotective effects. It was demonstrated that apigenin are able to block signal transduction pathways in different models of prostate cancer.<sup>11</sup> Further, treatment of prostate cancer with apigenin can stop the cell cycle in the G0-G1 phase.<sup>12,13</sup> It can inhibit

growth of cancer cells and induce apoptosis in them; however it does not influence the growth of normal cells.<sup>14</sup> Thus, it is considered as high-selective molecule. Low toxicity of apigenin was also proven. In fact, it shows lower toxicity in comparison to some other structurally similar molecules (quercetin, kaempferol, luteolin, and others).<sup>15</sup>

Apigenin is common constituent of different fruits, vegetables, medicinal plant, teas or other plants based beverages. However, one of the most common dietary sources of apigenin is herbal tea prepared from chamomile (*Matricaria chamomilla* L.). The chamomile inflorescences (so-called anthodia), consisting of white (ligulate) and yellow (tubulare) flowers, contain different chemical constituents. Apigenin is present only in chamomile ligulate flowers (CLF) where it can be accumulated in a different form: (1) form of free aglycone; (2) form of glycoside – apigenin-7-O- $\beta$ -glucoside (Ap-7-Glc); (3) form of different acetylated derivatives of Ap-7-Glc.<sup>16</sup> Earlier research has shown content of free apigenin is much lower than content of its bound forms.<sup>17</sup> However, from the biological point of view, high concentration of free apigenin in chamomile extracts is of great importance. An increase of its content in starting plant material and further in extracts is very notable task and different method for hydrolysis of apigenin glycosides into aglycone have been reported in the literature.

In this study, apigenin was liberated from its glycosides by enzymatic biotransformation, i.e. autofermentation. The conducted process was based on activation of  $\beta$ -glucosidase, an enzyme which is naturally present in chamomile and has the ability to hydrolyse apigenin glycosides to apigenin. Autofermented chamomile ligulate flowers (A-CLF) together with native ones (N-CLF) were used for the extracts preparation. In order to ensure the maximal content of desired compound in the final extract, novel extraction technique was applied. Namely, enzyme-assisted hydrolysis was combined with cavitation phenomenon in ultrasound extraction system. Simultaneously, extraction was done by reference technique (Soxhlet extraction), as well. Moreover, green and safe solvents were used to obtain extracts with improved apigenin content, which is in agreement with the efforts of modern science to produce safe and healthy products without the traces of organic/toxic solvents. Detailed chemical profiles of the obtained extracts were defined by UHPLC-MS-MS analysis. The bio-potentials of native (N-CLF) and autofermented (A-CLF) extracts were compared, including evaluation of apoptosis and morphological changes which had been influenced by extracts.

## 2. Exsperimental

### 2. 1. Sample Preparation

Dry plant material (CLF) was purchased from the Institute of Field and Vegetable Crops, Bački Petrovac, Ser-

bia. The autofermentation of CLF was performed in the manner previously described elsewhere.<sup>18</sup> Obtained autofermented (A-CLF) as well as native (N-CLF) flowers were used for extraction process.

### 2. 2. Ultrasound-assisted extraction (UE)

The UE was carried out in an ultrasonic bath (Branson, USA) at a frequency of 55 Hz. N-CLF and A-CLF were extracted by both ethanol and water. A mass of plant material used for the extraction was 5 g, while volume of the solvent was 250 mL. UE was performed within 40 minutes. Obtained extracts were filtered and dried at 40 °C. Extraction runs were performed in triplicates.

### 2. 3. Soxhlet extraction (SE)

Plant samples (N-CLF or A-CLF) were subjected to extraction in a Soxhlet extractor by using ethanol as a solvent. Extraction process was carried out for eight hours, i.e. until the solvent discoloration. After cooling, the solvent was removed from obtained extracts by evaporation and the extracts were dried at 40 °C. Thus obtained SE extracts were kept in a glass vessel and stored at 4 °C until analysis. Extraction runs were performed in triplicates.

### 2. 4. Determination of the total extraction yield, total phenols (TP) and flavonoids (TF) content

Determination of the total extraction yield was carried out according to the method previously described in Ph. Jug. IV.<sup>19</sup> Yield of each extract was expressed as mass of dry extract per 100 g of dry plant material (g/100 g DP).

Total phenols (TP) and flavonoids (TF) content was determined according to the methods previously described by Singleton and Rossi<sup>20</sup> and Markham,<sup>21</sup> respectively. In case of phenols content, the obtained results were expressed as a mass of chlorogenic acid equivalents (CAE) per g of dry extract (mg CAE/g). The content of total flavonoids in examined extracts was expressed as a mass of rutin equivalents (RE) per g of dry extract (mg RE/g). All measurements were done in triplicates.

### 2. 5. TLC-UV Determination of Apigenin and Apigenin-7-O-glucoside Content

TLC-UV measurement of apigenin and Ap-7-Glc content was done according to the procedure previously described elsewhere.<sup>22</sup> Mobile phase was made by mixing toluene, methyl ethyl ketone and methanol in the ratio of 55:30:15 (v/v/v), while stationary phase was silica gel GF<sub>254</sub> (thickness of the layer was 0.5 mm). Standard compounds (apigenin and Ap-7-Glc; analytical grade of purity  $\geq$  99%) were dissolved in ethanol and used for calibration curve

preparation. Calibration curve for apigenin was defined for the concentration range 0.02–0.1 mg/mL ( $C_{\text{Apigenin}} = \frac{A-0.03}{6.91}$ ,  $R^2 = 0.9981$ ). For Ap-7-Glc this concentration range was 0.01–0.09 mg/mL, and the curve had the following expression:  $C_{\text{Ap-7-Glc}} = \frac{A-0.03}{2.43}$ , ( $R^2 = 0.9978$ ).

## 2. 6. UHPLC-DAD-HESI-MS/MS Analysis

The analysis was performed by using Thermo Scientific liquid chromatography system (UHPLC) (Thermo Fisher Scientific, San Jose, California, USA). Xcalibur (version 2.2 SP1.48) and LCQ Fleet (version 2.7.0.1103 SP1) software were used for instrument control, data acquisition and data analysis. Separations were performed on a Hypersil gold C18 column (50 × 2.1 mm, 1.9 μm). The used mobile phase was consisted of (A) water + 0.2% formic acid and (B) acetonitrile. The volume of 5 μL of each extract was injected into the system. The column was thermostated at 25 °C and the analysis was performed according to the method previously described in the literature.<sup>18,23</sup> Detected compounds were identified according to corresponding spectral characteristics: mass spectra, accurate mass and characteristic fragmentation. Quantification of apigenin and Ap-7-Glc was made by using the external standard method.

## 2. 7. Antioxidant Activity

The ability of the extracts to act as antioxidants was determined by two different assays: DPPH and reducing power methods. DPPH test was done followed the method of Espín<sup>24</sup> while reducing powers ability was measured according to the Oyaizu<sup>25</sup> method. The obtained results were expressed as IC<sub>50</sub> (mg/mL) and EC<sub>50</sub> (mg/mL) values, respectively (Table 1).

## 2. 8. Cell Lines and Culturing

The experiments were carried out on cervix adenocarcinoma (HeLa), bronchoalveolar carcinoma (NCI-H358), chronic myeloid leukemia in blast crisis (K562), and normal Madin-Darby canine kidney fibroblast like cells (MDCK I; p = 33–35). HeLa and MDCK I cells were cultured in DMEM supplemented with 10% heat-inactivated FBS and 2 mM glutamine. NCI-H358 and K562, were grown in RPMI 1640 medium supplemented with 10% FBS, 2 mM glutamine, 10 mM sodium pyruvate and 2 mM HEPES. The cells were grown as monolayers or suspensions in tissue culture flasks (BD Falcon, Germany) in the humidified atmosphere under the conditions of 37 °C/5% of CO<sub>2</sub> gas in the CO<sub>2</sub> incubator (IGO 150 CELLlife,<sup>TM</sup> JOUAN, ThermoFisher Scientific, Waltham, MA, USA). The trypan blue dye exclusion method was used to assess cell viability.

## 2. 9. Cytotoxicity Evaluation

The effects of observed CLF and A-CLF extracts on the growth of normal and tumor cells were determined using the MTT assay. The adherent cells, MDCK I, HeLa, and NCI-H358, were seeded in 96 micro-well plates at concentration of 2 × 10<sup>4</sup> cells/mL. The cells were incubated during the night in the CO<sub>2</sub>. Afterwards, the cells were treated with extracts and incubated for 48 and 72 h. Immediately after, medium was replaced with MTT solution (5 mg/mL) and the resulting formazane crystals were dissolved in DMSO. In case of leukemia cells, the cells were seeded at the plates in the concentration of 1 × 10<sup>5</sup> cells/mL, and incubated for 72 h. After that, MTT solution (5 mg/mL) was added to the each well and incubation was performed for 4 h in CO<sub>2</sub> humidified atmosphere. In order to dissolve water-insoluble MTT-formazane crystals, 10% SDS with 0.01 M HCl was added to each well. The absorbance was read at 595 nm on ELISA microplate reader.

All experiments were performed at least three times in triplicates. The percentage of cell growth was calculated in the manner given in the literature.<sup>26</sup>

The results were expressed as GI<sub>50</sub> value, i.e. as a concentration of the extract which are able to reduce the cell growth by 50%.

## 2. 10. Detection of Apoptosis

The ApoAlert Annexin V-FITC staining kit was used to detect apoptosis at the single cell level. Experiments were performed according to manufacturer's instructions, with modification in propidium iodide concentration (reduced 1.5 x). Briefly, 1 × 10<sup>5</sup> cells/mL HeLa cells were seeded on 8-wells chamber slides with silicon borders and incubated in DMEM overnight. Growing medium was replaced with a fresh medium containing GI<sub>50</sub> concentration of A-UE (0.098 mg/mL) and A-SE extracts (0.079 mg/mL) for 24 and 48 hrs, respectively. The GI<sub>50</sub> concentration (0.008 mg/mL) for commercially available apigenin was determined on HeLa cell line by MTT test.

The cells were analysed by fluorescent microscope in a combination with appropriate filters ( $\lambda_{\text{exc}} = 450\text{--}490\text{ nm}$ ;  $\lambda_{\text{em}} = 520\text{ nm}$  (f3);  $\lambda_{\text{exc}} = 530\text{--}585\text{ nm}$ ;  $\lambda_{\text{em}} = 615\text{ nm}$  (f2)).

## 2. 11. Morphological Changes

The HeLa cells were seeded in 6-wells plate at a concentration 1 × 10<sup>5</sup> cells/mL and incubated overnight in CO<sub>2</sub> incubator. The cells were exposed to the GI<sub>50</sub> concentration of A-UE (0.098 mg/mL) and A-SE extracts (0.079 mg/mL) for 48 and 72 hrs and monitored by inverted microscope.

## 2. 12. Statistical Analysis

Statistical analysis was performed by Statistic 11.0 for Windows. Data are expressed as a mean value (X) and



standard deviation (SD) of three independent experiments done in triplicate. A nonparametric Mann-Whitney test was applied and statistical significance was set at the  $p < 0.05$  to compare treated cells to control (non-treated) cells

### 3. Results and Discussion

#### 3. 1. Content of Apigenin and Apigenin-7-O-glucoside (Ap-7-Glc) in the Obtained Extracts

Due to the considerable bioactivity of apigenin we performed the bioconversion of Ap-7-Glc in the plant material prior to extraction process to increase concentration of its free form. In order to define extraction method that would provide the highest yield of apigenin, both, native and autofermented chamomile ligulate flowers, were extracted by applying ultrasound-assisted and Soxhlet extractions. The ultrasound extraction represents a modern technique in which desorption of the analytes from the matrix is enhanced due to cavitation phenomenon. However, cavitation can also provoke the destruction of the target analytes. From this reason, scrutiny of the polyphenols' behaviour in different extraction systems is necessary. For this purpose, the Soxhlet extraction, as a reference technique, was used. Apart of the technique, used solvent has multiple influence on extraction efficiency, and choosing the optimal solvent or their mixture is one of the most important task in the extraction process of bioactive molecules.

Ethanol and water, as well as their mixture are classified as GRAS (generally recognized as safe) and suitable for the recovery of nutraceuticals. Even ethanol is not highly selective for phenols, its use is preferable in comparison to other organic solvents, especially for food and pharmaceutical products. For these reasons, ethanol was used for sonification of native (N-UE) and autofermented (A-UE) CLF. The same solvent was used for the Soxhlet extraction of nonfermented (N-SE) and autofermented (A-SE) samples. Additionally, water was used as a solvent for ultrasound extraction of native (N-UE<sub>W</sub>), as well as autofermented (A-UE<sub>W</sub>) CLF.

The first step in our research was to determine the success of the fermentation process. For that reason, N-CLF and A-CLF extracts were subjected to TLC-UV analysis. Appearance of obtained TLC chromatogram suggested that apigenin was present in all samples and the intensity of its spots was stronger in autofermented samples than in native ones. The Ap-7-Glc was also present in all extracts, but on contrary to the apigenin, the intensity of Ap-7-Glc spots in A-CLF samples was lower. Although literature data suggest that apigenin is poorly soluble in water,<sup>11</sup> apigenin was present in CLF water extracts. Presence of the apigenin in water extracts was previously reported

in the literature.<sup>11</sup> Taking into account that concentration of apigenin in hot water tea could be up to 1.2% it can be assumed, that specific experimental condition could isolate this flavon. Taking into account that physico-chemical properties of solvents are altered in the ultrasonic field and very often the solvating properties are enhanced, we suppose that the ultrasound modified solvating properties of water. Nevertheless, the concentration of both flavonoid forms was higher in ethanolic samples. As presented in Table 1, results of quantifications of Ap-7-Glc and apigenin show increased concentration of apigenin after fermentation process.

**Table 1.** Content of apigenin and apigenin-7-O-glucoside in obtained extracts.

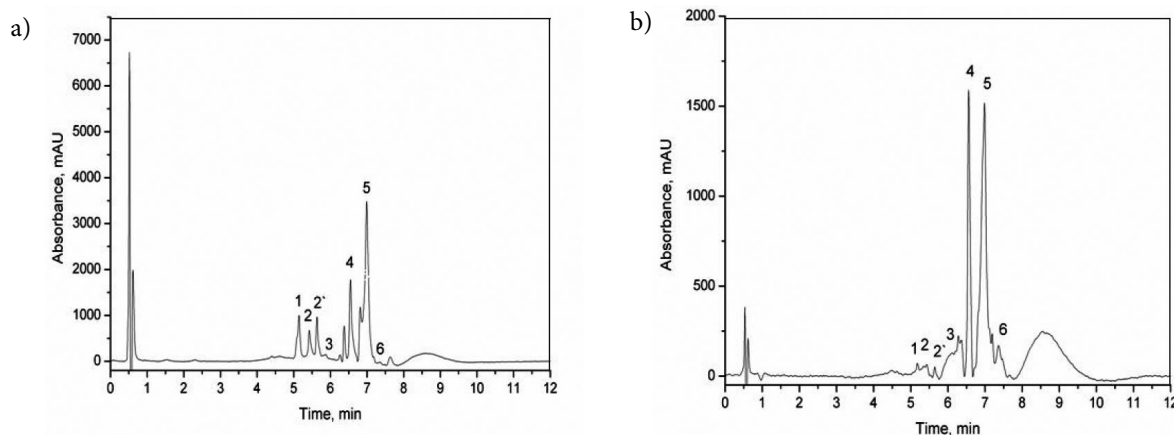
Extracts	Apigenin (mg/g)	Ap-7-Glc (mg/g)
A-UE <sup>1</sup>	2.51 ± 0.18	1.35 ± 0.05
N-UE <sup>2</sup>	0.39 ± 0.07	0.89 ± 0.13
A-SE <sup>3</sup>	2.42 ± 0.02	1.31 ± 0.09
N-SE <sup>4</sup>	0.02 ± 0.00	0.06 ± 0.02
A-UE <sub>W</sub> <sup>5</sup>	1.37 ± 0.07	0.91 ± 0.06
N-UE <sub>W</sub> <sup>6</sup>	0.18 ± 0.01	0.53 ± 0.02

Data represent mean value of three independent experiments done in triplicate.

<sup>1</sup>A-UE ethanol extract of autofermented flowers prepared by ultrasound extraction; <sup>2</sup>N-UE ethanol extract of native flowers prepared by ultrasound extraction; <sup>3</sup>A-SE ethanol extract of autofermented flowers prepared by Soxhlet extraction; <sup>4</sup>N-SE ethanol extract prepared from native flowers by Soxhlet extraction; <sup>5</sup>A-UE<sub>W</sub> aqueous extract prepared from autofermented flowers by ultrasound extraction; <sup>6</sup>N-UE<sub>W</sub> aqueous extract prepared from native flowers by ultrasound extraction

However, the biotransformation of Ap-7-Glc was not complete, possibly due to the presence of other apigenin derivatives. Namely, according to the literature data, chamomile may contain up to 12 different derivatives of Ap-7-Glc.<sup>16</sup> Thus it can be assumed that during the fermentation those derivatives, in first place mono- and diacetylated, were transformed into Ap-7-Glc. In this way, during the fermentation a particular amount of Ap-7-Glc was transformed into apigenin.

Based on the results presented in the Table 1, it is evident that the content of apigenin was much higher in A-CLF. This confirmed successful hydrolysis of apigenin glucosides in chamomile by the plants' own enzymes. Although, TLC was performed for fast screening of target substances, there was need for more relevant analysis like an UHPLC-MS-MS analysis which was performed with two selected samples (A-UE and N-UE). The content of target compounds in these samples was previously reported,<sup>18</sup> and its chromatograms are presented in the Fig. 1. Quantification of apigenin and Ap-7-Glc was made by using the external standard method. Obtained results were in accordance with those obtained by the TLC (Table 1).



**Figure 1.** HPLC chromatograms of native (A) and fermented (B) chamomile extract obtained by UE technique. Identified compounds are labelled as peaks 1–6: 1- apigenin-7-*O*-glucoside; 2, 2'- derivate of apigenin-7-*O*-glucoside; 3-apigenin; 4, 5- derivate of flavonoids; 6-chlorogenic acid

### 3. 2. Extraction Yield, Total Phenols (TP) and Flavonoids (TF) Content

In order to achieve the highest yields of biologically active compounds in obtained extracts the comparative analysis of solvents and extraction techniques for their isolation was done. The total extraction yields, TP and TF contents in different extracts are shown in the Table 2.

**Table 2.** Total extraction yield, total phenols and flavonoids contents in the obtained extracts

Extracts	Total extraction yield (%) w/w	Total phenols content (mg CAE/g)	Total flavonoids content (mg RE/g)
A-UE	31.00 ± 1.56	198.64 ± 0.93	39.10 ± 0.26
N-UE	27.80 ± 0.17	133.26 ± 1.24	31.27 ± 0.11
A-SE	28.93 ± 0.18	198.07 ± 1.10	38.98 ± 0.09
N-SE	27.62 ± 0.81	132.04 ± 1.04	32.35 ± 0.21
A-UE <sub>w</sub>	30.50 ± 0.57	135.09 ± 0.45	35.63 ± 1.59
N-UE <sub>w</sub>	31.70 ± 0.27	130.82 ± 0.96	29.80 ± 0.17

Data represent mean value of three independent experiments done in triplicate.

A-UE ethanol extract of autofermented flowers prepared by ultrasound extraction; N-UE ethanol extract of native flowers prepared by ultrasound extraction; A-SE ethanol extract of autofermented flowers prepared by Soxhlet extraction; N-SE ethanol extract prepared from native flowers by Soxhlet extraction; A-UE<sub>w</sub> aqueous extract prepared from autofermented flowers by ultrasound extraction; N-UE<sub>w</sub> aqueous extract prepared from native flowers by ultrasound extraction

Total extraction yield was between 27.62% (in case of N-SE) and 31.70% (in case of N-UE<sub>w</sub>). Ethanol extracts of autofermented samples had higher total extraction yield than native, while in the case of water extracts, autofermented samples had lower total extraction yield. In general, UE was proved to be more efficient for the recovery of chamomile compounds. Those results were in correlation with literature data.<sup>27</sup>

The yield of TP in explored samples was determined by using previously described Folin-Ciocalteu method and different yields of phenols were achieved for different solvents and techniques used (Table 2).

Autofermented samples were proved as much better sources of phenols independently on the extraction technique and solvent used (Table 2). Contents of the total phenolic compounds in A-UE (198.64 mg CAE/g) and A-SE (198.07 mg CAE/g) extracts were very similar, while total phenols content in autofermented sonicated water sample (A-UE<sub>w</sub>) was about 1.5 times lower than in the autofermented sonicated ethanol (A-UE) sample (135.09 mg CAE/g). In the case of native samples, the situation was the same, i.e. the total phenols content for the N-UE (133.26 mg CAE/g) was close to that of the N-SE (133.04 mg CAE/g). Phenolic content in water extracts was the lowest (130.82 mg CAE/g). By comparing water and ethanol extracts obtained by ultrasonic extraction, water extracts were characterized with lower phenols content. The significant difference in phenols content was observed in autofermented sample, whereas this difference in the case of native samples was not so pronounced.

As a part of chemical composition analysis, the TF content in the native and in the autofermented CLF extracts was determined, as well. Flavonoids are important biomolecules which are present in surprisingly high concentrations in the plants. In this study their content was between 29.80 mg RE/g (N-UE<sub>w</sub>) and 39.10 mg RE/mL (A-UE). As well as in the case of phenols, all autofermented samples exhibited higher contents of flavonoid compounds. Results, presented in the Table 2, indicate the highest flavonoids content in ethanolic A-UE extract followed by A-SE and A-UE<sub>w</sub> extracts. In case of native samples, flavonoids content decreased as follows: N-SE > N-UE > N-UE<sub>w</sub>.

According to obtained results, it can be concluded that ultrasonic extraction technique was more efficient in comparison to Soxhlet extraction. This is certainly a consequence of increased liberation of the solutes from sam-

ple matrix due to the cavitation phenomenon. Presented results show that regardless on the applied extraction technique or used solvent the autofermented samples have more phenolic bioactive compounds than the native ones.

### 3. 3. The Antioxidant Activity

Polyphenols are well recognized for their health-promoting properties. Different studies indicated their wide spectrum of biological activities.<sup>28,29</sup> Reducing properties of polyphenols as hydrogen or electron-donating agents predict their free-radical scavenging as well as antioxidant ability. The free-radical scavenging ability of obtained extracts (N-CLF and A-CLF) was tested using stable radical DPPH. Reducing power of tested extracts served as an indicator of their antioxidant ability. As shown in Table 3, all tested extracts showed an antioxidant potential in accordance with their total polyphenols content. Autofermented extracts exhibited better antioxidant capacity that could be linked to previously discussed polyphenols content. In this respect, the most potent extract was found to be the A-UE extract ( $IC_{50} = 0.0270$  mg/mL). On the other hand, the N-UE<sub>W</sub> showed the highest  $IC_{50}$  value (0.0601 mg/mL) indicating the lowest antioxidant ability. However, significant differences among the extracts in this respect were not observed. The  $IC_{50}$  values increased in the following sequence: A-UE (0.0270 mg/mL) > A-SE (0.0341 mg/mL) > A-UE<sub>W</sub> (0.0418 mg/mL) > N-UE (0.0528 mg/mL) > N-SE (0.0595 mg/mL) > N-UE<sub>W</sub> (0.0601 mg/mL).

The potential of the obtained extracts to fight against free radicals was also examined by determination of their reduction power. In the conducted analysis the electron-donating capacity of antioxidants was measured through the change of yellow colour of the test solutions to various shades of green and blue, depending on the reducing power of each sample.<sup>30</sup> The presence of reducing agent causes a reduction of the  $Fe^{3+}$ /ferricyanide complex

to the ferrous form. The reducing power of extracts is a function of their concentration. All investigated N-CLF and A-CLF extracts showed good reducing power but as it could be expected, the highest reduction potential was detected in A-UE extracts with  $EC_{50}$  value of 0.520 mg/mL, which represented the lowest value in all examined extracts.

The differences between  $EC_{50}$  values of A-UE (0.520 mg/mL) and A-SE (0.523 mg/mL) was insignificant, indicating similar reducing powers of those extracts. A-UE<sub>W</sub> extracts had slightly higher  $EC_{50}$  value (0.550 mg/mL). Scavenging ability of native samples decreased in the following order: N-UE<sub>W</sub> > N-UE > N-SE. Focusing on the solvent influence it was evident that in the case of autofermented UE samples ethanol was superior, while in the case of native UE samples water was better solvent for extracting components with good reducing capacity. Autofermented samples again proved to be a better source of antioxidants in comparison to extracts obtained from the native CLF. Accordingly, it could be assumed that autofermented samples contain higher concentrations of reductones, which could react with free radicals to stabilize and block radical chain reactions.

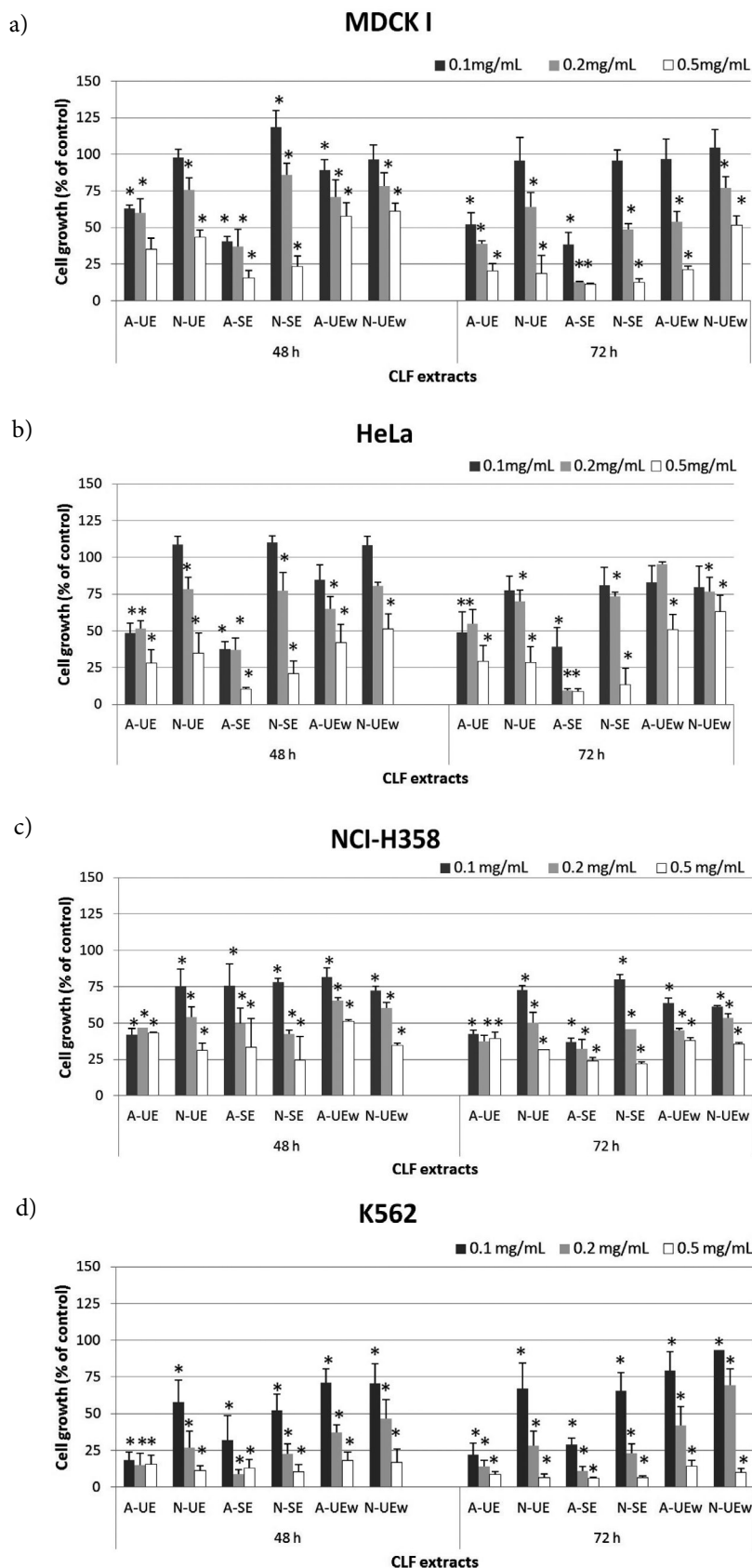
### 3. 4. The Antiproliferative Activity of the CLF Extracts

Chamomile flavonoids, the most important of which are apigenin conjugates, are recognized as natural compounds which exhibit broad biological activities.<sup>31</sup> Apigenin acts by scavenging of free radicals and has significant antitumor activity *in vitro* and *in vivo*.<sup>5,32</sup> Taking into account considerable biological potential of the apigenin<sup>11,18,27</sup> its free form was increased in this study by bioconversion of the Ap-7-Glc before extraction processes. Antiproliferative capacity of obtained extracts was evaluated on normal and tumour cells during 48 and 72 h, respectively. The statistically significant difference in the antiproliferative activity between autofermented and native extracts, and between treated and non-treated cells' growth were observed (Fig. 4). The observed effects were various and depended on the applied concentration and treated cells type as well. The obtained results show that all analysed extracts in two highest applied concentrations of 0.2 and 0.5 mg/mL reduced cells' viability, particularly after 72 h of exposure. More potent extracts proved to be the autofermented extracts with highest content of apigenin, A-UE and A-SE, which exhibited better antioxidant capacity and the highest reduction potential as well. Extracts A-UE and A-SE, applied in the concentration of 0.1 mg/mL during 48 and 72 h, inhibited cells' growth for near 60%. The most sensible were treated leukemia cells K562, whose growth was significantly reduced (up to 80%) after 48 h of exposure. Observed results correlate with published data based on the cytotoxic effect of apigenin on leukemia cells<sup>33,34</sup> described significant influence of apigenin on the growth of myeloid (HL-60 and K562) com-

**Table 3.** Antioxidative activity of chamomile extracts obtained by a different extraction technique

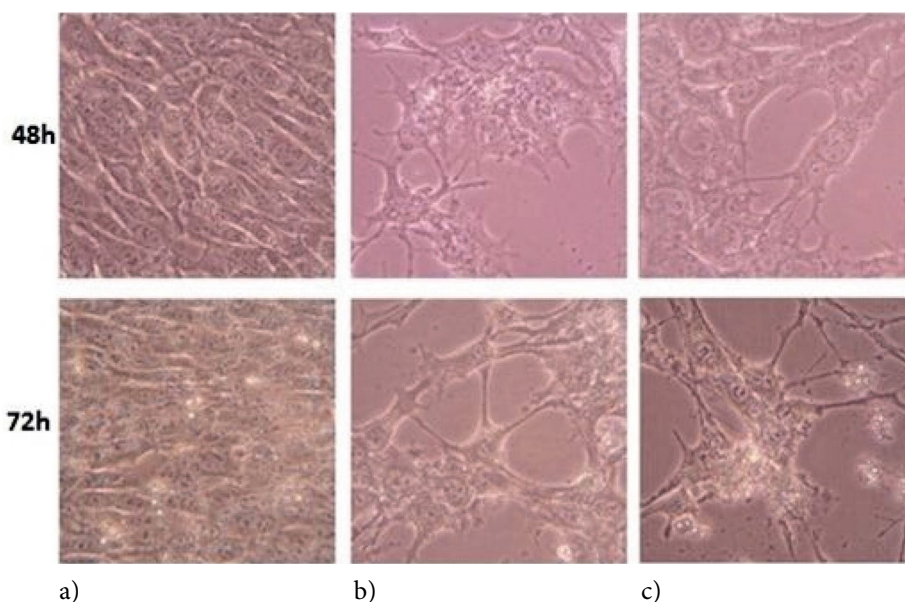
Extracts	A-UE	N-UE	A-SE	N-SE	A-UE <sub>W</sub>	N-UE <sub>W</sub>
DPPH						
$IC_{50}$ (mg/mL)	0.027	0.053	0.034	0.060	0.042	0.060
Reducing power $EC_{50}$ (mg/mL)	0.520	0.770	0.523	0.840	0.550	0.570

A-UE ethanol extract of autofermented flowers prepared by ultrasound extraction; N-UE ethanol extract of native flowers prepared by ultrasound extraction; A-SE ethanol extract of autofermented flowers prepared by Soxhlet extraction; N-SE ethanol extract prepared from native flowers by Soxhlet extraction; A-UE<sub>W</sub> aqueous extract prepared from autofermented flowers by ultrasound extraction; N-UE<sub>W</sub> aqueous extract prepared from native flowers by ultrasound extraction



**Figure 2.** Cytotoxic effect of autofermented and native extracts in different cell lines. MDCK I (a), HeLa (b), NCI-H358 (c) and K562 (d) cells were treated with 0.5, 0.2 and 0.1 mg/mL of extract respectively. Cytotoxicity was assessed after 48 and 72 h by the MTT survival assay. Data represent mean value of three independent experiments done in triplicate. \*Statistically significant change ( $p < 0.05$ ) compared to control (non-treated) cells.





**Figure 3.** Morphological changes in the HeLa cells. HeLa cells were treated with A-UE (0.098 mg/mL) and A-SE (0.079 mg/mL) for 48 and 72 h. Native photographs are taken by the inverted microscope Olympus 1X51 with Olympus SP-500 UZ camera. Follows: a) control cells; b) A-UE extract and c) A-SE extract. Magnification 400 x.

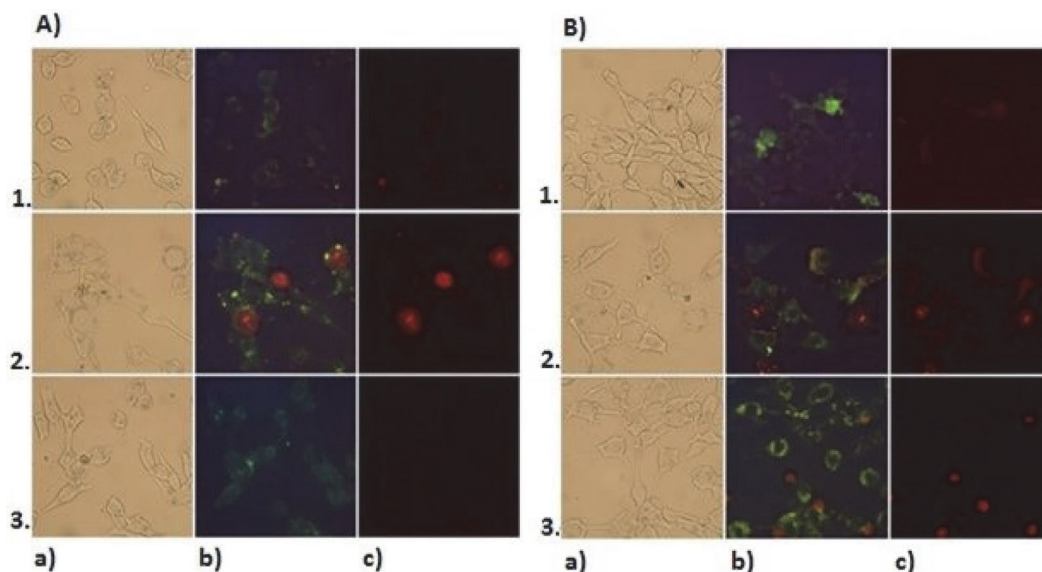
pared to the erythroid (TF1) leukemia cells. Lower tested concentrations (0.01, 0.001 and 0.0001 mg/mL) only slightly affected the growth of treated cells (data not shown). The inhibitory effect of all tested extracts on normal cells was lower in comparison with effect on tumour cells after 48h of exposure. That is in a good correlation with literature data where the selectivity in the antiproliferative activity of apigenin was described.<sup>6,8,12,35</sup>

Noticed morphological changes support observed cytotoxic results. A-UE and A-SE extracts applied at  $GI_{50}$

concentration evidently reduced the number of treated HeLa cells (Fig. 5) after 48 and 72 h of exposition.

### 3. 5. Proapoptotic Effects of the Autofermented CLF Extracts

Among six different samples, ethanolic extracts of A-CLF, A-UE and A-SE, had the highest antiproliferative activity, thus those extracts were further subjected for testing on proapoptotic potential. In the  $GI_{50}$  concentrations, A-UE



**Figure 4.** The fluorescent microscopy analysis of apoptosis caused by CLF extracts in the HeLa cells. HeLa cells were treated with A-UE (0.098 mg/mL) and A-SE (0.079 mg/mL) for 24 h (A) and 48 h (B). The cells were subsequently analyzed by the Carl Zeiss fluorescent microscope: a) visible light b) Annexin V-FITC (green fluorescence) and c) PI (red fluorescence); 1. apigenin standard (positive control) 2. A-UE extract and 3. A-SE extract. Magnification 400 x.

(0.098 mg/mL) and A-SE (0.079 mg/mL) extracts, applied on HeLa cells for 24 and 48 h, induced time depended apoptotic features. The exposure of phosphatidylserine (PS) on the external leaflet of the plasma membrane as an early marker of apoptosis,<sup>36</sup> is visible in the HeLa cells with preserved cell shape (Fig. 6). The blebbing of the cell membrane was seen after 48 h of treatment with the A-UE extract. The standard compound apigenin in the applied concentration evoked less proapoptotic effect in comparison with tested extracts. The obtained results suggest that although apigenin has been proven as the compound able to inhibit tumour cell growth through apoptosis induction<sup>37,38,39</sup> the treatment with autofermented CLF ethanolic extracts, which are mixtures of apigenin, its derivatives, and polyphenols as well, have improved proapoptotic efficacy.

## 4. Conclusions

Enzymatic hydrolysis assisted with plant's own enzyme (auto-fermentation) resulted in increased polyphenolic and flavonoid content in plant material. Moreover, the content of main flavone-apigenin was increased influencing higher antioxidant activity. Broad antiproliferative study of chamomile extracts proved high and dose-dependent potential of all examined samples. However, extracts made by autofermented chamomile had significantly stronger impact on the treated tumour cells' growth reduction in comparison to the native CLF extracts. Leukemia cells showed to be more sensitive to all tested CLF extracts. The CLF extracts with highest antiproliferative efficacy induced morphological changes and apoptosis in the HeLa cells. Based on these results regarding the antiproliferative capacity of tested extracts, further research may be carried out to investigate the biological mechanisms of action of observed extracts and apigenin. Additionally, green and safe solvents were used in this study which in combination with enzyme-assisted ultrasound extraction of chamomile offers new platform for design of nutraceuticals and/or pharmaceuticals from chamomile.

## 5. Acknowledgment

The present work was carried out within the project of the Serbian Ministry of Education, Science and Technological Development, (Project No. TR 31013). Research was also supported by J.J. Strossmayer University of Osijek internal fund VIF-2015-MEFOS-2. The authors are grateful to Dr Dušan Adamović, Institute of Field and Vegetable Crops, Bački Petrovac, Serbia, for his support in supplying plant material.

## Conflict of interest

The authors declare that there are no conflicts of interest.

## 6. Reference

1. R. H. Liu, *Am. J. Clin. Nutr.* **2003**, 78, 3–6.
2. M. Abotaleb, S. Mathews Samuel, E. Varghese, S. Varghese, P. Kubatka, A. Liskova, D. Büsselberg, *Cancers*, **2019**, 11, 1–39. DOI:10.3390/cancers11010028
3. D. Raffa, B. Maggio, M. V. Raimondi, F. Plescia, G. Daidone, *Eur J Med Chem.*, **2017**, 142:213–228. DOI:10.1016/j.ejmech.2017.07.034
4. D. Patel, S. Shukla, S. Gupta, *Int. J. Oncol.*, **2007**, 30, 233–245.
5. S. Shukla, S. Gupta, *Pharm. Res.*, **2010**, 27, 962–978. DOI:10.1007/s11095-010-0089-7
6. K. Banerjee, M. Mandal, *Redox Biology*, **2015**, 5, 153–162. DOI:10.1016/j.redox.2015.04.009
7. A. Kowalczyk, A. Bodalska, M. Miranowicz, K. Karłowicz-Bodalska, *Adv Clin Exp Med.*, **2017**, 26, 1143–1146. DOI:10.17219/acem/41978
8. J. Madunić, I. Vrhovac Madunić, G. Gajski, J. Popić, V. Garaj Vrhovac, *Cancer Lett.*, **2018**, 413, 11–22. DOI:10.1016/j.canlet.2017.10.041
9. T. D. Way, M. C. Kao, J. K. Lin, *J. Biol. Chem.*, **2004**, 279, 4479–4489. DOI:10.1074/jbc.M305529200
10. D. Kashyapa, A. Sharmab, H. Singh Tulic, K. Sakd, V. Kumar Garge, H. Singh Buttarf, W. N. Setzerg, G. Sethih, *Journal of Functional Foods*, **2018**, 48, 457–471.
11. S. Shukla, S. Gupta, Shukla S, Gupta S, Bioactive Foods in Promoting Health, Fruits and Vegetables: Apigenin and cancer chemoprevention, London, Elsevier Ltd, **2009**, pp. 663–689. DOI:10.1016/B978-0-12-374628-3.00041-4
12. S. Shukla, S. Gupta, *Cell Cycle*, **2007**, 6, 1102–1114. DOI:10.4161/cc.6.9.4146
13. X. Yan, M. Qi, P. Li, Y. Zhan, H. Shao, *Cell Biosci.*, **2017**, 7:50, 1–16. DOI:10.1186/s13578-017-0179-x
14. T. C. Hsia, J. S. Yang, G. W. Chen, T. H. Chiu, H. F. Lu, M. D. Yang, F. S. Yu, K. C. Liu, K. C. Lai, C. C. Lin, J. G. Chung, *Anticancer Res*, **2009**, 29, 309–318.
15. S. Gupta, F. Afaq, H. Mukhtar, *Biochem. Biophys. Res. Commun.*, **2001**, 287, 914–920. DOI:10.1006/bbrc.2001.5672
16. V. Švehlíková, R. N. Bennett, F. A. Mellon, P. W. Needs, S. Piacente, P. A. Kroon, Y. Bao, *Phytochem*, **2004**, 65, 2323–2332. DOI:10.1016/j.phytochem.2004.07.011
17. J. K. Srivastava, E. Shankar, S. Gupta, *Mol. Med. Rep.*, **2010**, 3, 895–901.
18. A. Cvetanović, J. Švarc-Gajić, Z. Zeković, S. Savić, J. Vulić, P. Mašković, G. Četković, *Planta*, **2015**, 242, 721–732. DOI:10.1007/s00425-015-2308-2
19. Federal Office of Public Health (Beograd): Pharmacopoeia Jugoslavica editio quarta, (Ph. Jug. IV), **1984**.
20. V. L. Singleton, J. A. J. Rossi, *Am. J. Enology Vitic.*, **1965**, 16, 144–158.
21. K. R. Markham, *Methods in Plant Biochemistry: Flavones, flavonoids, and their glycosides*, London: Academic Press Ltd., **1989**, pp. 197–235. DOI:10.1016/B978-0-12-461011-8.50012-3
22. A. Cvetanović, J. Švarc-Gajić, U. Gašić, Ž. Tešić, G. Zengin,

- Z. Zeković, S. Đurović, *J. Supercrit. Fluids.*, **2017**, *120*, 32–42. DOI:10.1016/j.supflu.2016.10.012
23. S. Kečkeš, U. Gašić, T. Čirković-Veličković, D. Milojković-Opsenica, M. Natić, Ž. Tešić, *Food Chem.*, **2013**, *138*, 32–40. DOI:10.1016/j.foodchem.2012.10.025
24. J. C. Espín, C. Soler-Rivas, H. J. Wichers, *J. Agric. Food Chem.*, **2000**, *48*, 648–656. DOI:10.1021/jf9908188
25. M. Oyaizu, *J. Hum. Nutr. Diet.*, **1986**, *44*, 307–315. DOI:10.5264/eiyogakuzashi.44.307
26. J. Kašnar-Šamprec, I. Ratkaj, K. Mišković, M. Pavlak, M. Baus-Lončar, S. Kraljević Pavelić, Lj. Glavaš-Obrovac, B. Žinić, *Invest. New Drugs*, **2012**, *30*, 981–990. DOI:10.1007/s10637-011-9657-x
27. P. C. Roy. Optimizing the Ultrasound Assisted Extraction of Phenolic Antioxidant Compounds from *Centella Asiatica* Leaves [Master's thesis], Kolkata (India): Jadavpur University, **2014**.
28. D. R. Pavlović, S. Branković, N. Kovačević, D. Kitić, S. Veljković, *Phytothe Res.*, **2011**, *25*, 749–754. DOI:10.1002/ptr.3460
29. P. H. Li, Y. W. Lin, W. C. Lu, J. M. Hu, D. W. Huang, *Int. J. Food Prop.*, **2015**, *19*, 1786–1797.
30. I.C.F.R. Ferreira, P. Baptista, M. Vilas-Boas, L. Barros, *Food Chem.*, **2007**, *100*, 1511–1516. DOI:10.1016/j.foodchem.2005.11.043
31. S. Shukla, S. Gupta, *See comment in PubMed Commons below-Free Radic. Biol. Med.*, **2008**, *44*, 1833–1845. DOI:10.1016/j.freeradbiomed.2008.02.007
32. Y. Liao, W. Shen, G. Kong, H. Lv, W. Tao, P. Bo, *PloS One*, **2014**, *9*, e92007. DOI:10.1371/journal.pone.0092007
33. R. R. Ruela-de-Sousa, G. M. Fuhler, N. Blom, C. V. Ferreira, H. Aoyama, M. P. Peppelenbosch, *Cell Death Dis*, **2010**, *1*, e19. DOI:10.1038/cddis.2009.18
34. J. M. Mohammad Salmani, Z. Xiao-Ping, J. A. Jacob, C. Bao-An, *Chin J Nat Med.*, **2017**, *15*, 321–329. DOI:10.1016/S1875-5364(17)30052-3
35. X. Cao, B. Liu, W. Cao, W. Zhang, F. Zhang, H. Zhao, R. Meng, L. Zhang, R. Niu, X. Hao, B. Zhang, *Chin. J. Cancer Res*, **2013**, *25*, 212–222.
36. S.H. Lee, X.W. Meng, K.S. Flatten, D.A. Loegering, S.H. Kaufmann, *Cell Death Differ.*, **2013**, *20*, 64–76. DOI:10.1038/cdd.2012.93
37. P. W. Zheng, L. C. Chiang, C. C. Lin, *Life Sci.*, **2005**, *76*, 1367–1379. DOI:10.1016/j.lfs.2004.08.023
38. F. Papachristou, E. Chatzaki, A. Petrou, I. Kougioumtzi, N. Katsikogiannis, A. Papalambros, G. Tripsianis, C. Simopoulos, A. K. Tsaroucha, *Chin. Med.*, **2013**, *8*, 1–9. DOI:10.1186/1749-8546-8-9
39. R. P. Souza, P. de S. Bonfim-Mendonça, F. Gimenes, B. A. Ratti, V. Kaplum, M. L. Bruschi, C. V. Nakamura, S. O. Silva, S. S. Maria-Engler, M. E. L. Consolaro, *Oxid Med Cell Longev.*, **2017**, *2017*, 1–18. DOI:10.1155/2017/1512745

## Povzetek

Članek obravnava apigenin v cvetovih kamilice in njegovo biološko aktivnost. Nefermentirane nativne cvetove kamilice (N-CLF) in avto fermentirane cvetovi (A-CLF) smo ekstrahirali z različnimi tehnikami ekstrakcije (ultrazvok-UE, Soxhlet-SE) in različnimi topili. Dobljene ekstrakte smo primerjali glede na kemijsko sestavo in bio-potencial. Biološka aktivnost (antiproliferativni učinek, apoptoza) ekstraktov kamilice je bila raziskana na celičnih linijah MDCK I, HeLa, NCI-H358 in K562. V primerjavi z nativnimi ekstrakti so bili avtofermentirani ekstrakti opredeljeni z višjo vsebnostjo apigenina, večjim izkoristkom ekstrakcije, kot tudi večjo vsebnostjo skupnih fenolov in flavonoidov. Vsi ovrednoteni ekstrakti so pokazali pomembno antiproliferativno aktivnost proti tumorskim celičnim linijam. Najbolj občutljive so bile celice K562, ki so se po 48 urah izpostavljenosti zmanjšale za 80 %. Morfološke spremembe in apoptozo smo odkrili v celicah HeLa, ki so bile izpostavljene ekstraktom A-UE (0,098 mg/ml) in A-SE (0,079 mg/ml).



Except when otherwise noted, articles in this journal are published under the terms and conditions of the Creative Commons Attribution 4.0 International License

# Synthesis, Characterization and Crystal Structures of Oxidovanadium(V) Complexes with Schiff Base and Pyrone Ligands and Their Antimicrobial Activity

Guo-Xu He, Ling-Wei Xue\*, Qin-Long Peng, Pan-Pan Wang and Hui-Jie Zhang

College of Chemistry and Chemical Engineering, Pingdingshan University, Pingdingshan Henan 467000, P.R. China

\* Corresponding author: E-mail: pdsuchemistry@163.com

Received: 11-23-2018

## Abstract

Two oxidovanadium(V) complexes, [VOLL<sup>a</sup>] (1) and [VOLL<sup>b</sup>] (2), where L is the dianionic form of the Schiff base ligand 2-(((2-hydroxyethyl)imino)methyl)-6-methylphenol (H<sub>2</sub>L), L<sup>a</sup> and L<sup>b</sup> are the deprotonated forms of 3-hydroxy-2-methyl-4H-pyran-4-one (HL<sup>a</sup>) and 2-ethyl-3-hydroxy-4H-pyran-4-one (HL<sup>b</sup>), respectively, have been prepared and characterized by elemental analyses, IR, UV-Vis, <sup>1</sup>H NMR and single-crystal X-ray crystallographic determination. The V atoms in the complexes are in octahedral coordination, with the Schiff base ligand mer-coordinated to the metal atoms through the phenolate O, imino N and hydroxyl O atoms, and with the pyrone ligands coordinated to the metal atoms through the two O atoms. The effect of the compounds on the antimicrobial activity against *Staphylococcus aureus*, *Escherichia coli*, and *Candida albicans* was studied.

**Keywords:** Schiff base; pyrone; vanadium complex; crystal structure; antimicrobial activity

## 1. Introduction

Schiff bases with typical imine group, C=N, are interesting ligands in coordination chemistry.<sup>1</sup> In recent years, metal complexes of Schiff bases have attracted remarkable attention due to their versatile biological activity, such as antifungal, antibacterial and antitumor.<sup>2</sup> Schiff base complexes derived from salicylaldehyde and its derivatives with primary amines, bearing the NNO, NNS, NOO or NSO donor sets, have particular biological activities.<sup>3</sup> Pyrone compounds are bidentate ligands in various metal complexes.<sup>4</sup> Most complexes with pyrone ligands have interesting biological properties.<sup>5</sup> In the present work, two oxidovanadium(V) complexes, [VOLL<sup>a</sup>] (1) and [VOLL<sup>b</sup>] (2), where L is the dianionic form of the Schiff base ligand 2-(((2-hydroxyethyl)imino)methyl)-6-methylphenol (H<sub>2</sub>L), L<sup>a</sup> and L<sup>b</sup> are the deprotonated form of 3-hydroxy-2-methyl-4H-pyran-4-one (HL<sup>a</sup>; maltol) and 2-ethyl-3-hydroxy-4H-pyran-4-one (HL<sup>b</sup>; ethyl maltol), respectively, are reported.

## 2. Experimental

### 2.1. Material and Methods

3-Methylsalicylaldehyde, 2-aminoethanol, 3-hydroxy-2-methyl-4H-pyran-4-one and 2-ethyl-3-hydroxy-

4H-pyran-4-one were purchased from Fluka. Other reagents and solvents were analytical grade and used without further purification. Elemental (C, H, and N) analyses were made on a Perkin-Elmer Model 240B automatic analyser. Infrared (IR) spectra were recorded on an IR-408 Shimadzu 568 spectrophotometer. UV-Vis spectra were recorded on a Lambda 35 spectrometer. <sup>1</sup>H NMR spectra were recorded on a Bruker 300 MHz instrument. X-ray diffraction was carried out on a Bruker SMART 1000 CCD area diffractometer.

### 2.2. Synthesis of Complex 1

3-Methylsalicylaldehyde (13.6 mg, 0.1 mmol) was dissolved in methanol (10 mL), to which was added dropwise a methanol solution (10 mL) containing 2-aminoethanol (6.1 mg, 0.1 mmol). The mixture was stirred at ambient temperature for 1 h. Then, 3-hydroxy-2-methyl-4H-pyran-4-one (12.6 mg, 0.1 mmol) and VO(acac)<sub>2</sub> (26.5 mg, 0.1 mmol) dissolved in methanol (10 mL) was added. The mixture was stirred for 1 h at ambient temperature to give a deep brown solution. Brown block-shaped single crystals suitable for X-ray diffraction were formed by slow evaporation of the solution in air for several days. The yield is 32% (based on V). IR data (KBr, cm<sup>-1</sup>): 1628 (C=O), 1597



(C=N), 958 (V=O). UV–Vis data in methanol [ $\lambda_{\max}$  (nm),  $\epsilon$  (L · mol<sup>-1</sup> · cm<sup>-1</sup>): 218, 14,352; 280, 7,765; 407, 2,230. Anal. Calcd. (%) for C<sub>16</sub>H<sub>16</sub>NO<sub>6</sub>V: C, 52.0; H, 4.4; N, 3.8. Found (%): C, 52.2; H, 4.3; N, 3.9. <sup>1</sup>H NMR (300 MHz, *d*<sup>6</sup>-DMSO)  $\delta$ , ppm: 8.94 (s, 1H, CH=N), 8.20 (d, 1H, ArH), 7.43 (d, 1H, ArH), 7.36 (d, 1H, ArH), 6.80 (t, 1H, ArH), 6.41 (d, 1H, ArH), 4.80 (d, 1H, CH<sub>2</sub>), 4.70 (t, 2H, CH<sub>2</sub>), 4.40 (t, 1H, CH<sub>2</sub>), 2.46 (s, 3H, CH<sub>3</sub>), 1.99 (s, 3H, CH<sub>3</sub>).

### 2. 3. Synthesis of Complex 2

Complex 2 was prepared by the same method as described for complex 1, with 3-hydroxy-2-methyl-4H-pyran-4-one replaced by 3-hydroxy-2-ethyl-4H-pyran-4-one (14.0 mg, 0.1 mmol). The yield is 37% (based on V). IR data (KBr, cm<sup>-1</sup>): 1626 (C=O), 1596 (C=N), 961 (V=O). UV–Vis data in methanol [ $\lambda_{\max}$  (nm),  $\epsilon$  (L · mol<sup>-1</sup> · cm<sup>-1</sup>): 220, 15,120; 280, 8,210; 409, 2,545. Anal. Calcd. (%) for C<sub>17</sub>H<sub>18</sub>NO<sub>6</sub>V: C, 53.3; H, 4.7; N, 3.7. Found (%): C, 53.2; H, 4.9; N, 3.5. <sup>1</sup>H NMR (300 MHz, *d*<sup>6</sup>-DMSO)  $\delta$ , ppm: 8.94 (s, 1H, CH=N), 8.23 (d, 1H, ArH), 7.43 (d, 1H, ArH), 7.36 (d, 1H, ArH), 6.80 (t, 1H, ArH), 6.41 (d, 1H, ArH), 4.80 (d, 1H, CH<sub>2</sub>), 4.72 (t, 2H, CH<sub>2</sub>), 4.35 (t, 1H, CH<sub>2</sub>), 2.85 (m, 2H, CH<sub>2</sub>), 1.98 (s, 3H, CH<sub>3</sub>), 1.23 (t, 3H, CH<sub>3</sub>).

### 2. 4. X-Ray Structure Determination

Data were collected from selected crystals mounted on glass fibres. The data for the two complexes were processed with SAINT<sup>6</sup> and corrected for absorption using SADABS.<sup>7</sup> Multi-scan absorption corrections were applied with  $\psi$ -scans.<sup>8</sup> The structures were solved by direct methods using the program SHELXS-97 and were refined by full-matrix least-squares techniques on *F*<sup>2</sup> using anisotropic displacement parameters.<sup>9</sup> The structures were refined by SHELXL-97 program.<sup>10</sup> All hydrogen atoms were placed at the calculated positions. Idealized H atoms were refined with isotropic displacement parameters set to 1.2 (1.5 for methyl groups) times the equivalent isotropic *U* values of the parent atoms. The crystallographic data for the complexes are listed in Table 1, selected bond lengths and bond angles for compounds 1 and 2 are given in Table 2.

### 2. 5. Antimicrobial Assay

Qualitative determination of antimicrobial activity was done using the disk diffusion method as described in the literature.<sup>11</sup> Suspensions in sterile peptone water from 24-h cultures of microorganisms were adjusted to 0.5 Mc-

Table 1. Crystallographic data and refinement parameters for complexes 1 and 2

Parameters	1	2
Habit, color	Block, brown	Block, brown
Molecular formula	C <sub>16</sub> H <sub>16</sub> NO <sub>6</sub> V	C <sub>17</sub> H <sub>18</sub> NO <sub>6</sub> V
Formula weight	369.24	383.26
Temperature, K	298(2)	298(2)
Crystal size, mm	0.31 × 0.27 × 0.26	0.32 × 0.30 × 0.30
Radiation ( $\lambda$ , Å)	MoK $\alpha$ (0.71073)	MoK $\alpha$ (0.71073)
Crystal system	Triclinic	Monoclinic
Space group	<i>P</i> 1	<i>P</i> 2 <sub>1</sub> / <i>c</i>
Unit cell dimensions:		
<i>a</i> , Å	7.654(2)	7.5888(7)
<i>b</i> , Å	14.692(3)	25.1559(13)
<i>c</i> , Å	14.692(3)	9.5310(9)
$\alpha$ , °	89.640(3)	90
$\beta$ , °	81.053(3)	107.309(1)
$\gamma$ , °	81.053(3)	90
<i>V</i> , Å <sup>3</sup>	1611.9(6)	1737.1(2)
<i>Z</i>	4	4
$\rho_{\text{calcd}}$ , g cm <sup>-3</sup>	1.521	1.465
<i>F</i> (000)	760	792
Absorption coefficient, mm <sup>-1</sup>	0.647	0.604
$\theta$ Range for data collection, deg	1.97–25.50	2.76–25.49
Index ranges, <i>h</i> , <i>k</i> , <i>l</i>	–9 ≤ <i>h</i> ≤ 9; –17 ≤ <i>k</i> ≤ 10; –17 ≤ <i>l</i> ≤ 14	–9 ≤ <i>h</i> ≤ 9; –30 ≤ <i>k</i> ≤ 30; –11 ≤ <i>l</i> ≤ 11
Reflections collected	3971	12701
Independent reflections	2606	3139
Data/parameters	2083/437	2625/228
Restraints	0	0
Final <i>R</i> indices ( <i>I</i> > 2 $\sigma$ ( <i>I</i> ))	<i>R</i> <sub>1</sub> = 0.0419, <i>wR</i> <sub>2</sub> = 0.1029	<i>R</i> <sub>1</sub> = 0.0660, <i>wR</i> <sub>2</sub> = 0.1321
<i>R</i> indices (all data)	<i>R</i> <sub>1</sub> = 0.0519, <i>wR</i> <sub>2</sub> = 0.1084	<i>R</i> <sub>1</sub> = 0.0802, <i>wR</i> <sub>2</sub> = 0.1371
Goodness-of-fit on <i>F</i> <sup>2</sup>	0.967	1.200

**Table 2.** Selected bond lengths (Å) and bond angles (°) for complexes 1 and 2

1			
V1–O1	1.890(3)	V1–O2	1.829(3)
V1–O3	2.292(3)	V1–O4	1.920(3)
V1–O6	1.606(3)	V1–N1	2.140(4)
V2–O7	1.880(3)	V2–O8	1.835(3)
V2–O9	2.279(3)	V2–O10	1.917(3)
V2–O12	1.597(3)	V2–N2	2.130(4)
O6–V1–O2	98.52(17)	O6–V1–O1	96.53(16)
O2–V1–O1	157.72(14)	O6–V1–O4	94.97(15)
O2–V1–O4	95.55(14)	O1–V1–O4	99.41(14)
O6–V1–N1	108.63(16)	O2–V1–N1	77.73(13)
O1–V1–N1	81.96(13)	O4–V1–N1	156.10(13)
O6–V1–O3	171.28(16)	O2–V1–O3	85.00(14)
O1–V1–O3	82.51(14)	O4–V1–O3	76.69(11)
N1–V1–O3	79.87(12)	O12–V2–O8	99.40(17)
O12–V2–O7	95.71(16)	O8–V2–O7	157.75(15)
O12–V2–O10	95.74(16)	O8–V2–O10	95.36(15)
O7–V2–O10	99.30(13)	O12–V2–N2	106.87(17)
O8–V2–N2	77.60(15)	O7–V2–N2	82.44(13)
O10–V2–N2	157.08(15)	O12–V2–O9	171.99(15)
O8–V2–O9	84.90(15)	O7–V2–O9	82.19(14)
O10–V2–O9	77.05(11)	N2–V2–O9	80.58(13)

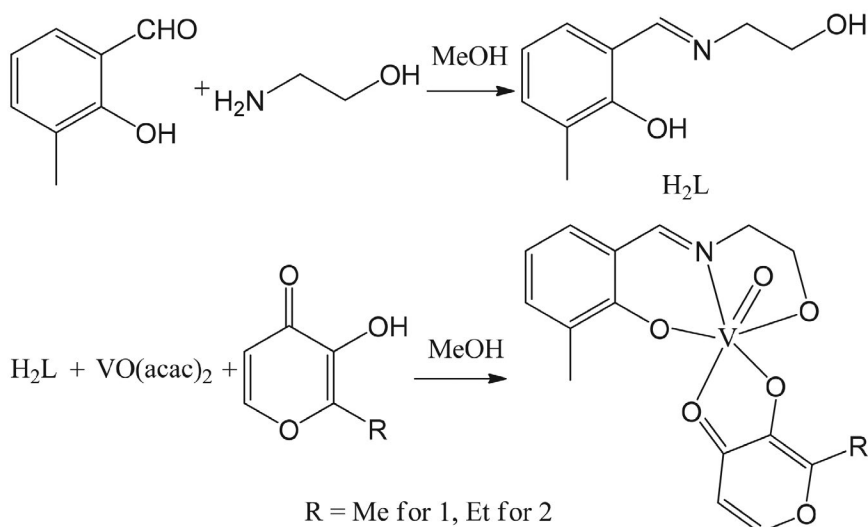
2			
V1–O1	1.867(3)	V1–O2	1.838(3)
V1–O3	1.909(3)	V1–O4	2.303(3)
V1–O6	1.591(3)	V1–N1	2.120(4)
O6–V1–O2	97.60(17)	O6–V1–O1	97.82(16)
O2–V1–O1	157.86(14)	O6–V1–O3	95.40(15)
O2–V1–O3	98.51(14)	O1–V1–O3	95.75(14)
O6–V1–N1	107.45(16)	O2–V1–N1	77.86(14)
O1–V1–N1	82.42(14)	O3–V1–N1	157.13(13)
O6–V1–O4	172.29(14)	O2–V1–O4	83.49(14)
O1–V1–O4	83.36(14)	O3–V1–O4	76.89(11)
N1–V1–O4	80.26(12)		

Farland. Muller–Hinton Petri dishes of 90 mm were inoculated using these suspensions. Paper disks (6 mm in diameter) containing 10 µL of the substance to be tested (at a concentration of 2048 µg/mL in DMSO) were placed in a circular pattern in each inoculated plate. Incubation of the plates was done at 37 °C for 18–24 h. Reading of the results was done by measuring the diameters of the inhibition zones generated by the test substance. Tetracycline was used as a reference substance. Determination of MIC was done using the serial dilutions in liquid broth method. The materials used were 96–well plates, suspensions of micro-organism (0.5 McFarland), Muller–Hinton broth (Merck) and stock solutions of each substance to be tested (2048 µg/mL in DMSO). The following concentrations of the substances to be tested were obtained in the 96–well plates: 1024, 512, 256, 128, 64, 32, 16, 8, 4 and 2 µg/mL. After incubation at 37 °C for 18–24 h, the MIC for each tested substance was determined by microscopic observation of microbial growth. It corresponds to the well with the lowest concentration of the tested substance where microbial growth was clearly inhibited.

### 3. Results and Discussion

#### 3.1. Chemistry

The Schiff base compound H<sub>2</sub>L was prepared by the condensation of equimolar quantities of 3-methylsalicylaldehyde with 2-aminoethanol in methanol. Complexes 1 and 2 were readily synthesized by reaction of the Schiff base compound H<sub>2</sub>L with VO(acac)<sub>2</sub> in methanol in the presence of 3-hydroxy-2-methyl-4*H*-pyran-4-one and 2-ethyl-3-hydroxy-4*H*-pyran-4-one, respectively (Scheme 1). All the compounds are very stable at room temperature in the solid state, and soluble in common organic solvents, such as methanol, ethanol, and acetonitrile. The results of

**Scheme 1.** The synthetic procedure of the complexes.

the elemental analyses are in accord with the composition suggested for the Schiff base and the complexes.

### 3. 2. IR and UV-Vis Spectra

For the IR spectrum of  $H_2L$  (Fig. S1), the typical band indicative of the azomethine group was observed at  $1622\text{ cm}^{-1}$ , while in the complexes (Figs. S2 and S3), it was observed at  $1597\text{ cm}^{-1}$  for 1 and  $1596\text{ cm}^{-1}$  for 2. The strong absorptions at  $1626\text{--}1628\text{ cm}^{-1}$  in the spectra of the complexes are assigned to the stretching vibration of the  $C=O$  bonds of the pyrone ligands. The weak absorption at  $3439\text{ cm}^{-1}$  for  $H_2L$  can be attributed to the vibration of  $O-H$  groups, while in the complexes, there are no such absorption. The absence of this absorption indicates the coordination of the hydroxyl groups in the deprotonated form. The bands indicative of the  $V=O$  groups of the complexes are observed at about  $960\text{ cm}^{-1}$ . UV-Vis spectra of  $H_2L$  and the complexes were measured in methanol. In the spectrum of the Schiff base (Fig. S4), the band centered at  $325\text{ nm}$  is attributed to the azomethine chromophore  $\pi\text{--}\pi^*$  transition. The band at higher energy ( $272\text{ nm}$ ) is associated with the benzene  $\pi\text{--}\pi^*$  transition. In the spectra of the complexes (Figs. S5 and S6), the bands at  $407\text{--}409\text{ nm}$  are attributed to the intramolecular charge transfer transitions from the  $p_\pi$  orbital on the phenolate O to the empty  $d$  orbitals of the V atoms.<sup>12</sup>

### 3. 3. Structure Description of the Complexes

The molecular structures of complexes 1 and 2 are shown in Figs. 1 and 2, respectively. There are two independent molecules in complex 1. The V atoms are mer-coordinated by one Schiff base ligand, one pyrone ligand, and one oxo O group. The Schiff base ligand coordinated to the V atom through the phenolate O, imino N, and deprotonated hydroxyl O atoms. The pyrone ligands are coordinated to the V atoms through the deprotonated hydroxyl O and carbonyl O atoms. The V atoms are in octahedral coordination, with the three donor atoms of the Schiff base ligand, and the hydroxyl O atom of the pyrone ligand defining the equatorial plane, and with the carbonyl O atom of the pyrone ligand, and the oxo O group occupying the axial positions. In the two complexes, the corresponding bond distances around the V atoms are comparable to each other, and also similar to the corresponding bonds observed in the similar vanadium complexes with Schiff bases or pyrones.<sup>13</sup> The *cis* and *trans* coordinate bond angles in the equatorial planes are range from  $77.73(13)$  to  $99.41(14)^\circ$  and from  $156.10(13)$  to  $157.72(14)^\circ$  for the V1 atom of complex 1, from  $77.60(15)$  to  $99.30(13)^\circ$  and from  $157.08(15)$  to  $157.75(15)^\circ$  for the V2 atom of complex 1, and from  $77.86(14)$  to  $98.51(14)^\circ$  and from  $157.13(13)$  to  $157.86(14)^\circ$  for the V atom of complex 2, respectively. In addition, the values for the axial *trans* O–V–O angles are  $171.28(16)^\circ$  and  $171.99(15)^\circ$ , respec-

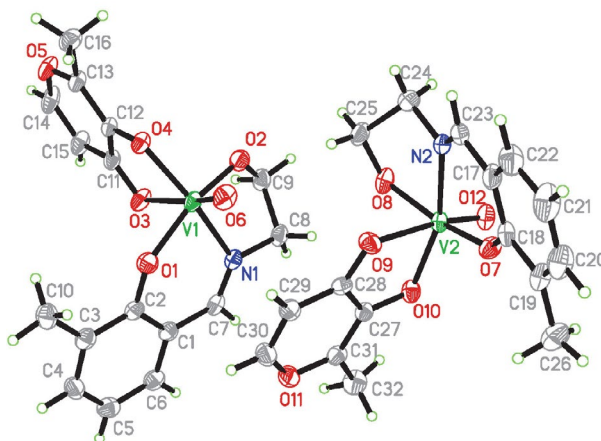


Fig. 1. Perspective view of complex 1 with 30% probability thermal ellipsoids.

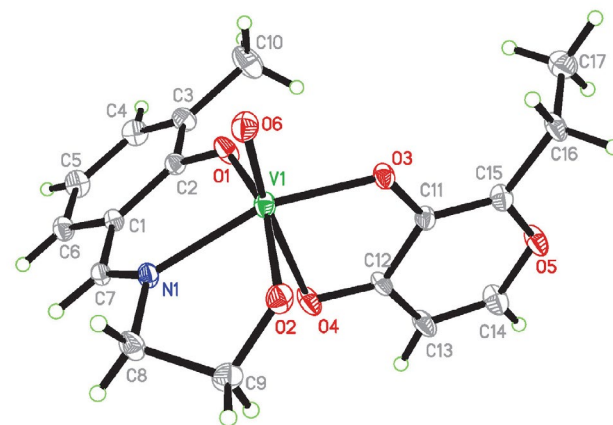


Fig. 2. Perspective view of complex 2 with 30% probability thermal ellipsoids.

tively, for the V1 and V2 atoms of complex 1, and  $172.29(14)^\circ$  for the V atom of complex 2. All the above bond values indicating the distortion of the octahedral coordination from ideal geometry.

### 3. 4. Antimicrobial Activity

The antimicrobial activity results are summarized in Table 3. A comparative study of minimum inhibitory concentration (MIC) values of the Schiff base and the complexes indicates that the complexes have better activity than the free Schiff base. Generally, this is caused by the greater lipophilic nature of the complexes than the ligand. Such increased activity of the metal chelates can be explained on the basis of chelating theory.<sup>14</sup> On chelating, the polarity of the metal atoms will be reduced to a greater extent due to the overlap of the ligand orbital and partial sharing of positive charge of the metal atoms with donor atoms. Further, it increases the delocalization of  $p$ -electrons over the whole chelate ring and enhances the lipophilicity of the complexes. This increased lipophilicity en-

Table 3. MIC values ( $\mu\text{g/mL}$ ) for the antimicrobial activities of the tested compounds

Compounds	<i>Staphylococcus aureus</i>	<i>Escherichia coli</i>	<i>Candida albicans</i>
H <sub>2</sub> L	128	64	> 512
1	4.0	1.0	32
2	4.0	1.0	32
Tetracycline	0.32	2.12	> 1024

hances the penetration of the complexes into lipid membrane and blocks the metal binding sites on enzymes of microorganisms.

From the results, it is obvious that the two complexes have higher antibacterial and antifungal activities against *Staphylococcus aureus*, *Escherichia coli*, and *Candida albicans* when compared to the free Schiff base. This phenomenon is in accordance with those reported in literature.<sup>15</sup> The two complexes have in general the same activities against all the bacteria and fungi strains. The complexes have strong activity against *Escherichia coli*, with MIC value of 1.0  $\mu\text{g/mL}$ , which is superior to Tetracycline. The complexes have strong activity against *Staphylococcus aureus*, yet, they are weaker than Tetracycline. It is interesting that both complexes have medium activity against *Candida albicans*, which is rarely seen in metal complexes.

#### 4. Material

CCDC 1880706 for 1, and 1880707 for 2 contain the supplementary crystallographic data for this paper. These data can be obtained free of charge at <http://www.ccdc.cam.ac.uk/const/retrieving.html> or from the Cambridge Crystallographic Data Centre, 12 Union Road, Cambridge CB2 1EZ, UK; fax: +44(0)1223-336033 or email: [deposit@ccdc.cam.ac.uk](mailto:deposit@ccdc.cam.ac.uk).

#### 5. Acknowledgments

This research was supported by the Top-class foundation of Pingdingshan University (no. PXY-BSQD-2018006 and PXY-PYJJ-2018002).

#### 6. References

- (a) X. W. Zhu, *Russ. J. Coord. Chem.* **2018**, 44, 421–424; DOI:10.1134/S1070328418070084  
(b) D. L. Peng, *Russ. J. Coord. Chem.* **2017**, 43, 189–195; DOI:10.1134/S1070328417030058  
(c) D.-L. Peng, *J. Struct. Chem.* **2018**, 59, 589–594; DOI:10.1134/S0022476618030125  
(d) X.-W. Zhu, *Acta Chim. Slov.* **2018**, 65, 939–945. DOI:10.17344/acsi.2018.4607
- (a) Z.-C. Liu, B.-D. Wang, Z.-Y. Yang, Y. Li, D.-D. Qin, T.-R. Li, *Eur. J. Med. Chem.* **2009**, 44, 4477–4484; DOI:10.1016/j.ejmech.2009.06.009  
(b) D.-D. Qin, Z.-Y. Yang, G.-F. Qi, T.-R. Li, *Transition Met. Chem.* **2009**, 34, 499–505; DOI:10.1007/s11243-009-9222-z  
(c) Y.-Y. Yu, H.-D. Xian, J.-F. Liu, G.-L. Zhao, *Molecules* **2009**, 14, 1747–1754. DOI:10.3390/molecules14051747
- (a) Y.-T. Li, J.-W. Dong, Y. Lu, Y.-T. Gu, C.-N. Shang, F.-Y. Liu, Y. Xin, C.-L. Jing, Z.-L. You, *Chinese J. Inorg. Chem.* **2018**, 34, 1192–1198;  
(b) Z. You, H. Yu, Z. Li, W. Zhai, Y. Jiang, A. Li, S. Guo, K. Li, C. Lv, C. Zhang, *Inorg. Chim. Acta* **2018**, 480, 120–126; DOI:10.1016/j.ica.2018.05.020  
(c) L. W. Xue, G. Q. Zhao, Y. J. Han, Y. X. Feng, *Russ. J. Coord. Chem.* **2011**, 37, 262–269; DOI:10.1134/S1070328411030110  
(d) Z. You, H. Yu, B. Zheng, C. Zhang, C. Lv, K. Li, L. Pan, *Inorg. Chim. Acta* **2018**, 469, 44–50; DOI:10.1016/j.ica.2017.09.011  
(e) L. W. Xue, Y. J. Han, G. Q. Zhao, Y. X. Feng, *Russ. J. Coord. Chem.* **2012**, 38, 24–28. DOI:10.1134/S1070328411120104
- (a) B. Song, K. Saatchi, G. H. Rawji, C. Orvig, *Inorg. Chim. Acta* **2002**, 339, 393–399; DOI:10.1016/S0020-1693(02)00961-1  
(b) W. Y. Hsieh, S. Liu, *Synth. React. Inorg. Met.-Org. Nano-Met. Chem.* **2005**, 35, 61–70; (c) W. Y. Hsieh, C. M. Zaleski, V. L. Pecoraro, P. E. Fanwick, S. A. Liu, *Inorg. Chim. Acta* **2006**, 359, 228–236; (d) V. Vrdoljak, B. Prugovečki, M. Cindrić, D. Matković-Čalogović, A. Brbot-Šaranović, *Acta Chim. Slov.* **2008**, 55, 828–833;  
(e) S. Guo, N. Sun, Y. Ding, A. Li, Y. Jiang, W. Zhai, Z. Li, D. Qu, Z. You, Z. *Anorg. Allg. Chem.* **2018**, 644, 1172–1176. DOI:10.1002/zaac.201800060
- (a) M. Rangel, A. Tamura, C. Fukushima, H. Sakurai, *J. Biol. Inorg. Chem.* **2001**, 6, 128–132; DOI:10.1007/s007750000180  
(b) C.-T. Yang, S. G. Sreerama, W.-Y. Hsieh, S. Liu, *Inorg. Chem.* **2008**, 47, 2719–2727; DOI:10.1021/ic7022506  
(c) D. Sanna, L. Biro, P. Buglyo, G. Micera, E. Garribba, *J. Inorg. Biochem.* **2012**, 115, 87–99; DOI:10.1016/j.jinorgbio.2012.04.020  
(d) E. A. Enyedy, O. Domotor, E. Varga, L. Kiss, R. Trondl, C. G. Hartinger, B. K. Keppler, *J. Inorg. Biochem.* **2012**, 117, 189–197. DOI:10.1016/j.jinorgbio.2012.08.005
- SMART and SAINT. Area Detector Control and Integration Software, Madison (WI, USA): Bruker Analytical X-ray Instruments Inc., 1997.
- G. M. Sheldrick, *SADABS, Program for Empirical Absorp-*

- tion Correction of Area Detector Data, Göttingen (Germany): Univ. of Göttingen, 1997.
8. A. C. T. North, D. C. Phillips, F. S. Mathews, *Acta Crystallogr. A* **1968**, *24*, 351–359. DOI:10.1107/S0567739468000707
  9. G. M. Sheldrick, *SHELXL-97, Program for the Refinement of Crystal Structures*, Göttingen (Germany): Univ. of Göttingen, 1997.
  10. G. M. Sheldrick, *Acta Crystallogr.* **2015**, *C71*, 3–8.
  11. (a) A. Barry, *Procedures and Theoretical Considerations for Testing Antimicrobial Agents in Agar Media*, In: *Antibiotics in Laboratory Medicine*, Lorian, V. (Ed.), Baltimore: Williams and Wilkins, 1991;  
(b) T. Rosu, M. Negoiu, S. Pasculescu, E. Pahontu, D. Poirier, A. Gulea, *Eur. J. Med. Chem.* **2010**, *45*, 774–781. DOI:10.1016/j.ejmech.2009.10.034
  12. G. Asgedom, A. Sreedhara, J. Kivikoski, E. Kolehmainen, C. P. Rao, *J. Chem. Soc. Dalton Trans.* **1996**, 93–97. DOI:10.1039/dt9960000093
  13. (a) D.-L. Peng, *Russ. J. Coord. Chem.* **2017**, *43*, 404–410; DOI:10.1134/S1070328417060045  
(b) N. Lotfi, I. Sheikhshoei, S. Y. Ebrahimipour, H. Krautsc-  
heid, *J. Mol. Struct.* **2017**, *1149*, 432–438; DOI:10.1016/j.molstruc.2017.08.010  
(c) H. Y. Qian, *Russ. J. Coord. Chem.* **2017**, *43*, 780–786; DOI:10.1134/S1070328417110070  
(d) S. K. Mal, M. Mitra, H. R. Yadav, C. S. Purohit, A. R. Choudhury, R. Ghosh, *Polyhedron* **2016**, *111*, 118–122; DOI:10.1016/j.poly.2016.03.033  
(e) I. Sheikhshoei, S. Y. Ebrahimipour, N. Lotfi, J. T. Mague, M. Khaleghi, *Inorg. Chim. Acta* **2016**, *442*, 151–157; DOI:10.1016/j.ica.2015.11.026  
(f) S. S. Qian, Y. Huo, Y. T. Ye, Z. You, H. L. Zhu, *Russ. J. Coord. Chem.* **2015**, *41*, 261–266. DOI:10.1134/S107032841504003X
  14. J. W. Searl, R. C. Smith, S. Wyard, *J. Proc. Phys. Soc.* **1961**, *78*, 1174–1181. DOI:10.1088/0370-1328/78/6/311
  15. (a) X. W. Zhu, *Russ. J. Coord. Chem.* **2018**, *44*, 335–339; DOI:10.3103/S1068367418040213  
(b) H. Y. Qian, *Russ. J. Coord. Chem.* **2018**, *44*, 32–38; DOI:10.1134/S1070328418010074  
(c) D.-L. Peng, N. Sun, *Acta Chim. Slov.* **2018**, *65*, 895–901. DOI:10.17344/acsi.2018.4543

## Povzetek

Sintetizirali smo dve kompleksni spojini oksidovanadija(V), [VOLL<sup>a</sup>] (1) in [VOLL<sup>b</sup>] (2), kjer je L dianionska oblika liganda Schiffove baze 2-(((2-hidroksietil imino) metil)-6-metilfenola (H<sub>2</sub>L), L<sup>a</sup> in L<sup>b</sup> sta deprotonirani obliki 3-hidroksi-2-metil-4H-piran-4-ona (HL<sup>a</sup>) in 2-etil-3-hidroksi-4H-piran-4-ona (HL<sup>b</sup>). Spojini smo karakterizirali z naslednjimi metodami: infrardečo spektroskopijo (IR), UV-Vis spektroskopijo, NMR spektroskopijo in rentgensko strukturno analizo monokristalov. Atomi vanadija v spojinah so okatedrično koordinirani z atomi kisika in dušika, ki pripadajo obema ligandoma. Preučevali smo tudi protimikrobno učinkovitost spojin napram *Staphylococcus aureus*, *Escherichia coli* in *Candida albicans*.



Except when otherwise noted, articles in this journal are published under the terms and conditions of the Creative Commons Attribution 4.0 International License



# Screening of Parabens in Natural Water by Salting-out Based Centrifugeless Dispersive Liquid-liquid Microextraction Combined with HPLC-UV

Hadi Farahani\*

Research Institute of Petroleum Industry (RIPI), P. O. Box 1485733111, Tehran, Iran

\* Corresponding author: E-mail: farahaniha@ripi.ir  
Tel.: + 98 21 48255261; Fax: + 98 21 44739713

Received: 21-01-2018

## Abstract

A simple, efficient and quick salting-out based centrifugeless dispersive liquid-liquid microextraction combined with high-performance liquid chromatography-ultraviolet detection (HPLC-UV) has been successfully developed for the determination of selected parabens in environmental water samples. Herein, following the dispersion of the extracting solvent (1-undecanol) whose melting point is near the room temperature into the sample solution, the cloudy mixture is passed through a test tube filled with sodium chloride, acting as separating agent based on salting-out phenomenon. By immersing the tube inside an ice bath, the fine droplets of the extraction solvent are solidified, easily collected and after returning to the liquid state, injected into HPLC-UV. The values of the detection limit were in the range of 2.5-5.0  $\mu\text{g L}^{-1}$  while the intra-day ( $n = 7$ ) and inter-day ( $n = 9$ , within three days) precision were below 3.7 and 4.7%, respectively. A satisfactory linearity ( $0.997 \geq r^2 \geq 0.996$ ) and quite a broad linear range (5.0-250  $\mu\text{g L}^{-1}$ ) were achieved. The relative errors as the accuracy were less than 6.4% in all experiments. The method was eventually employed for the preconcentration and determination of the analytes in various natural water samples and acceptable results were achieved.

**Keywords:** Centrifugeless dispersive liquid-liquid microextraction, high-performance liquid chromatography-ultra violet detection; natural water; parabens

## 1. Introduction

Parabens (PBs) are well-known synthetic chemicals that are widely applied as antimicrobial preservatives in food, cosmetics, personal care, and pharmaceutical products due to their low cost, water solubility, and high stability.<sup>1</sup> Despite the low toxicity, they pose a potential health risk to human and wildlife in the long term on account of their estrogenic activities.<sup>2</sup> The adverse effects comprise disruption to the endocrine system, female breast cancer, irritant contact dermatitis and the development of malignant melanomas.<sup>3,4</sup> There is a notable concern, although, regarding the ubiquitous use in terms of the possible environmental impacts of PBs.<sup>5,6</sup> The chemicals may enter the aquatic environment through numerous pathways including discharge of effluents from industries and wastewater treatment plants.<sup>7,8</sup> Therefore, by raising public attention over the environment, screening of the organic compounds has been considered a substantial issue.

High-performance liquid chromatography (HPLC),<sup>9,10</sup> gas chromatography (GC),<sup>11,12</sup> and capillary electrophore-

sis (CE)<sup>13,14</sup> have been most commonly reported for the determination of PBs in different matrices. Furthermore, the extraction methods which are frequently utilized prior to the instrumental analysis are liquid-liquid extraction (LLE)<sup>15</sup> and solid phase extraction (SPE)<sup>16,17</sup>. Conversely, the particular methods require either a large amount of sample and organic solvents while they are considered as labor-intensive, time-consuming and costly procedures.

To ameliorate the conventional methodologies, researchers across the world have been aiming towards the development of new approaches which are rapid, inexpensive and environmentally friendly.<sup>18</sup> The introduction of solid-phase microextraction (SPME) primarily introduced the interest in microextraction methods in the early 1990s.<sup>19</sup> SPME has obtained expanding popularity in analytical laboratories worldwide attributable to its simplicity, rapidity, sensitivity and high potential for automation.<sup>20</sup> Simultaneously, attention was given to the application of small volumes of organic solvents for extraction and preconcentration of analytes, named liquid-phase microex-

traction (LPME).<sup>21,22</sup> During the last years, LPME as an efficient, simple and quick sample preparation technique combined with widely available instruments, has been extensively applied for preconcentration and determination of interesting analytes.<sup>23,24</sup>

Introduction of dispersive liquid-liquid microextraction (DLLME) in 2006 has considerably contributed towards meeting the mentioned aims of sample pretreatment, owing to its distinctive merits of easy operation, low cost, good enrichment factor, and recovery along with notably short extraction time.<sup>25</sup> DLLME is based on a ternary component solvent system, in which extraction and disperser solvents are expeditiously injected inside the aqueous sample to make a cloudy solution. After centrifugation, the extraction solvent is sedimented at the bottom of the test tube and removed by a microsyringe for following instrumental analysis. Because of its convenience and quickness, DLLME has been broadly applied for the extraction and preconcentration of numerous types of analytes from various matrices.<sup>26,27</sup>

Recently, Rajabi et al. has published a novel salting-out based centrifugeless DLLME method for the determination of some analytes in several matrices.<sup>28,29</sup> Herein, an organic solvent whose melting point is near the room temperature is dispersed into the sample solution to facilitate the extraction process. Then, by passing the mixture through a test tube filled with a certain amount of sodium chloride, the phase separation is easily achieved. Subsequently and after immersing the tube inside an ice bath, the fine droplets of the extraction solvent are solidified on the top of mixture, collected and after returning to the liquid state, injected into an analytical instrument. This predominant and environmentally friendly method is an efficient and acceptable analytical procedure, for which excellent accuracy and precision are confirmed, being easy and sensitive enough for the enrichment and determination.

The objective of the present study is to assess the salting-out based centrifugeless DLLME technique applicability for the determination of methyl paraben (MP), ethyl paraben (EP), propyl paraben (PP), and butyl paraben (BP) in various natural water samples with quite complex matrices. The factors controlling the microextraction efficiency were investigated in detail and the optimum conditions were properly set. The developed method was in the end validated for the quantitative purposes and employed to real sample analysis in combination with high-performance liquid chromatography-ultraviolet detection (HPLC-UV).

## 2. Experimental

### 2.1. Reagents

Four studied compounds including MP, EP, PP, and BP were purchased in the highest available purities ( $\geq 99\%$ ) from Alfa Aesar (Lancashire, UK). Analytical re-

agent grade methanol, sodium chloride (NaCl), nitric acid ( $\text{HNO}_3$ ), sodium hydroxide (NaOH), hydrochloric acid (HCl, 37%), acetone, 1-dodecanol, 1-undecanol and *n*-tetradecane were acquired from Merck Company (Darmstadt, Germany). HPLC grade acetonitrile (Fisher Chemicals, Fair Lawn, NJ, USA) and ultra-pure water (Millipore, Bedford, MA, USA) were used in all experiments. Stock standard solutions of each analyte ( $100 \text{ mg L}^{-1}$ ) were prepared in methanol. Working solutions were freshly prepared by diluting the standard solutions with the ultra-pure water to required concentrations. All the solutions were stored at  $4^\circ\text{C}$  and protected from the light. All glassware and bottles (Schott Duran, Germany) were kept overnight in 20% (*v/v*) nitric acid solution and rinsed with the ultra-pure water before use.

### 2.2. Apparatus

A HPLC system (Shimadzu, Kyoto, Japan) including a pump, an automatic injector equipped with  $20 \mu\text{L}$  sample loop and a UV detector (set at  $254 \text{ nm}$ ) was applied for the analysis of the PBs. The analytical column chosen for the separation was a RP-C18 (LiChrospher, Merck Millipore, Darmstadt, Germany) with  $5 \mu\text{m}$  particle size and dimensions of  $250 \text{ mm} \times 4.6 \text{ mm i.d.}$ , at room temperature of  $20 \pm 0.5^\circ\text{C}$ . Isocratic elution consisted of acetonitrile and water (65:35, *v/v*) at a flow rate of  $0.8 \text{ mL min}^{-1}$  that was run through the column. The mobile phase was filtered using a  $0.2 \mu\text{m}$  membrane filter (Millipore, Bedford, MA, USA) and it was degassed continuously by an online degasser.

### 2.3. Real Samples

The performance of the proposed method was evaluated by analyzing the PBs in four different natural water samples including Caspian Sea (Noushahr Coast, the north part of Iran), Persian Gulf (Bandar Khamir Coast, the south part of Iran), Jajroud River (the east part of Tehran, Iran) and Amir Kabir Dam (the west part of Tehran, Iran). The samples were collected in 1 L amber glass bottles. The real water samples were filtered before the analysis using a  $0.45 \mu\text{m}$  nylon membrane filter (Whatman, Maidstone, UK) to eliminate possible solid particles. All the samples were stored in the refrigerator at  $4^\circ\text{C}$  until their analysis time.

### 2.4. The Microextraction Procedure

The microextraction procedure has been introduced in detail<sup>28</sup> and presented as a schematic diagram in Fig. 1. To begin with,  $10.0 \text{ mL}$  of the sample solution was poured to a  $15.0 \text{ mL}$  screw cap glass test tube while  $75 \mu\text{L}$  of 1-undecanol was added into the sample solution as the solidifiable extracting solvent. The mixture was quickly sucked into a  $10.0 \text{ mL}$  glass syringe and then injected into the tube by a syringe needle for 10 times. Due to the dispersion of fine droplets of the extracting solvent through the aqueous

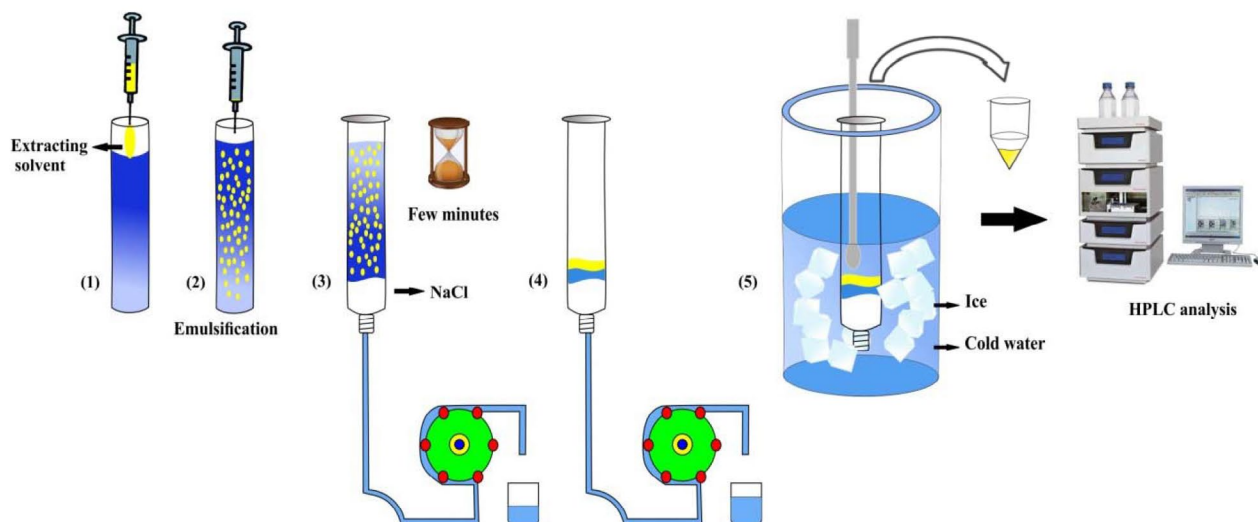


Figure 1. The schematic diagram of the salting-out based centrifugeless DLLME-HPLC.

bulk, the mixture became turbid during every cycle. In the next step, a filter was fixed at the bottom of a cleaned 10.0 mL glass syringe barrel while 5 g NaCl was poured into the barrel and compressed with the syringe plunger. The mixture was then passed through the barrel with a flow rate of  $2.0 \text{ mL min}^{-1}$ . The fine droplets of the extracting solvent rose through the mixture and formed a separate layer on the top of the sample solution which was collected as a result of the salting-out effect. By blocking the bottom of the barrel, the separate layer was immersed in an ice water bath for a few minutes. The extracting solvent was solidified, carefully collected using a spatula and transferred into a small vial, where it melted promptly. In the end, a  $20 \mu\text{L}$  of the extracting phase was injected into the HPLC-UV system for the following analysis.

### 3. Results and Discussion

A one-factor-at-a-time approach was employed to optimize the influencing parameters on the microextraction efficiency. A fixed concentration of the analytes ( $100.0 \mu\text{g L}^{-1}$ ) was used in the optimization process. All the quantifications were performed in the average of three replicate measurements. Blank samples were run to confirm the absence of any interference.

#### 3. 1. The Selection of Extraction Solvent

Generally, the selection of a proper organic solvent in LPME methods is of great importance for the effective analyte preconcentration.<sup>30,31</sup> There are some criteria for the solvent selection as follows: it must have a density lower than water and a melting point near or below the room temperature, a low solubility in water, a good chromatographic behavior, high extraction efficiency for the target analytes as

well as a good stability. To the best of our knowledge, just a few organic solvents fulfill the mentioned requirements. Among them, 1-dodecanol (density:  $0.8309 \text{ g mL}^{-1}$ ; melting point:  $22\text{--}24^\circ\text{C}$ ), 1-undecanol (density:  $0.8298 \text{ g mL}^{-1}$ ; melting point:  $13\text{--}15^\circ\text{C}$ ), and *n*-tetradecane (density:  $0.756 \text{ g mL}^{-1}$ ; melting point:  $4\text{--}6^\circ\text{C}$ ) are the most available ones. However, it should be noted that when *n*-tetradecane was used, the phase separation was not well done. Consequently, 1-undecanol and 1-dodecanol were considered as the extraction solvents. As it can be seen in Fig. 2, both solvents offer approximately the same extraction efficiency. From a practical point of view, it is easier to work with 1-undecanol and so, it was selected as the organic extraction solvent.

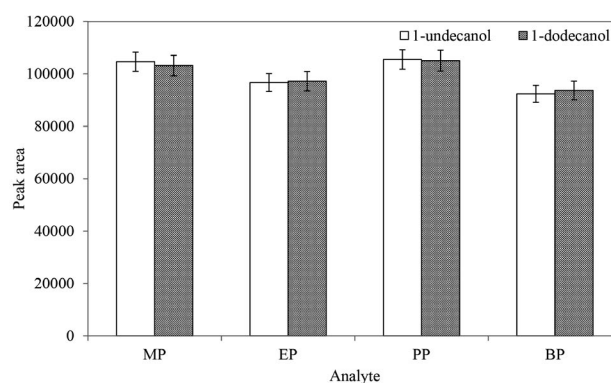
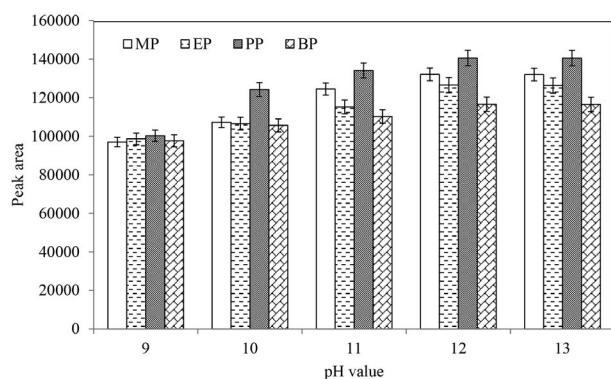


Figure 2. The effect of extraction solvent type on the extraction efficiency. Extraction conditions: sample volume of 10.0 mL ( $100.0 \mu\text{g L}^{-1}$  of mixed PBs), pH 13.0; volume of each organic solvent  $75 \mu\text{L}$ ; 10 times of the aspiration-dispersion cycles and the flow rate of the sample solution through NaCl column of  $2.0 \text{ mL min}^{-1}$ .

#### 3. 2. The pH of the Sample Solution

The adjustment of the sample solution pH is another key parameter to accelerate the extraction process and en-

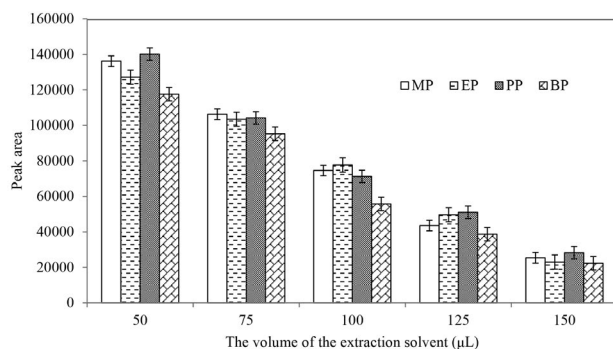
hance its efficiency in LPME methods.<sup>32,33</sup> In this work, as the target compounds are basic ( $pK_a \approx 8.5$ ), the sample solution pH was adjusted in the proper basic range (preferably 3 units over the  $pK_a$ ), so that the analytes could remain in their undissociated forms and so decrease their solubility in the sample solution. The dependence of the extraction performance on pH was evaluated in the range of 9–13 with the addition of NaOH 4 mol L<sup>-1</sup> by a micropipette. Based on Fig. 3, the maximum analytical signals were achieved at pH 12 and remained constant thereafter; hence, it was chosen as the optimum value for the subsequent studies.



**Figure 3.** The effect of the sample solution pH on the extraction efficiency. Extraction conditions: sample volume of 10.0 mL (100.0  $\mu\text{g L}^{-1}$  of mixed PBs), 1-undecanol as the extraction solvent; volume of the organic solvent 75  $\mu\text{L}$ ; 10 times of aspiration-dispersion cycles and the flow rate of the sample solution through NaCl column of 2.0 mL min<sup>-1</sup>.

### 3. 3. The Volume of the Extraction Solvent

In LPME techniques, the volume of the extracting solvent is usually chosen as low as possible to reach greater enrichment factors along with having lower toxicity.<sup>34</sup> In contrast, it should be satisfactory for the extraction of target analytes and handling the microextraction proce-

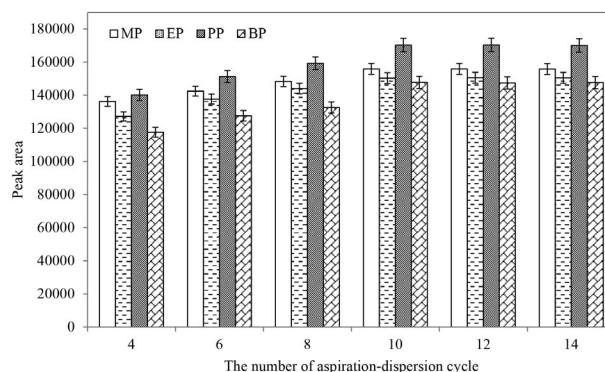


**Figure 4.** The effect of the volume of the extraction solvent on the method performance. Extraction conditions: sample volume of 10.0 mL (100.0  $\mu\text{g L}^{-1}$  of mixed PBs), 1-undecanol as the extraction solvent; pH 12.0; 10 times of aspiration-dispersion cycles and the flow rate of the sample solution through NaCl column of 2.0 mL min<sup>-1</sup>.

dure as well as practically possible for the injection into an analytical instrument.<sup>35</sup> The effect of the extractant volume on the extraction efficiency was investigated in the range of 50 to 150  $\mu\text{L}$ . As can be observed in Fig. 4, the peak area drops when the volume rises; it is noticeable that the dilution is the predominant factor for this phenomenon. On the whole and to gain the highest possible sensitivity, 50  $\mu\text{L}$  of the extractant solvent was chosen as an optimum value.

### 3. 4. The Number of Aspiration-Dispersion Cycles

The number of aspiration-dispersion cycles plays a major role for achieving the highest extraction efficiency along with the least time period.<sup>36</sup> To obtain the best performance, the parameter was investigated in the range of 4–14 while the other ones were kept constant. It is demonstrated that the analytical signals for all the target analytes were increased with the increase of cycles, up to the 10 and stayed approximately constant afterwards (Fig. 5). Therefore, to obtain satisfactory precision, 12 times of the aspiration-dispersion cycles were selected in the following experiments.

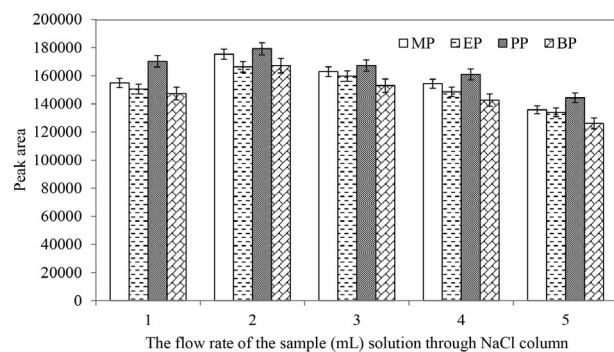


**Figure 5.** The effect of the number of aspiration-dispersion cycles on the extraction efficiency. Extraction conditions: sample volume of 10.0 mL (100.0  $\mu\text{g L}^{-1}$  of mixed PBs), 1-undecanol as the extraction solvent and its volume of 50  $\mu\text{L}$ ; pH 12.0 and the flow rate of the sample solution through NaCl column of 2.0 mL min<sup>-1</sup>.

### 3. 5. The Flow Rate of the Sample Solution Through NaCl Column

The flow rate of the sample solution through the barrel filled with NaCl influences the extraction performance and controls the extraction time. It should be high enough to fairly shorten the extraction time and low enough to amplify the ionic strength and consequently, improves the extraction efficiency owing to the salting-out effect.<sup>37</sup> This effect has been accounted for decline in the solubility of the target analytes in the aqueous phase and increased partitioning into the organic phase.<sup>38</sup> The effect of this parameter on the extraction efficiency was examined in the range

of 1–5 mL min<sup>-1</sup> by passing a 10.0 mL of the sample solution through the column applying a peristaltic pump. As shown in Fig. 6, due to the incomplete salting-out effect at the flow rate above 2.0 mL min<sup>-1</sup>, the extraction efficiency is almost starting to decrease. Therefore, 2.0 mL min<sup>-1</sup> was chosen as the optimum flow rate value to get the best possible efficiency.



**Figure 6.** The effect of the flow rate (mL) of the sample solution through NaCl column on the extraction efficiency. Extraction conditions: sample volume of 10.0 mL (100.0 µg L<sup>-1</sup> of mixed PBs), 1-undecanol as the extraction solvent and its volume of 50 µL; pH 12.0 and 12 times of aspiration-dispersion cycles.

### 3. 6. The Analytical Figure of Merits

To assess the applicability of the method, calibration curves were plotted at the optimum conditions using different concentration levels of the analytes. The limit of detection (LOD) based on the signal-to-noise ratio (S/N) of 3, the limit of quantitation (LOQ), determination coefficient ( $r^2$ ) and the linear range (LR) were calculated. As shown in Table 1, LODs and LOQs for the PBs were in the range of 2.5–5.0 µg L<sup>-1</sup> and 5.0–10.0 µg L<sup>-1</sup>, respectively, while LRs varied in the range of 5.0–250 µg L<sup>-1</sup> with  $r^2$  of 0.996 to 0.997.

**Table 1.** Some quantitative data achieved using salting-out based centrifugeless DLLME and HPLC-UV for the determination of PBs.

Analyte	MP	EP	PP	BP
LOD (µg L <sup>-1</sup> ) <sup>a</sup>	5.0	5.0	2.5	2.5
$r^2$	0.996	0.997	0.996	0.997
LOQ (µg L <sup>-1</sup> ) <sup>b</sup>	10.0	10.0	5.0	5.0
LR (µg L <sup>-1</sup> ) <sup>c</sup>	10.0–250	10.0–250	5.0–250	5.0–250

<sup>a</sup> Limit of detection for S/N = 3. <sup>b</sup> Limit of quantitation. <sup>c</sup> Linear range.

### 3. 7. The Precision and Accuracy

The intra-day and inter-day precision at three concentration levels of each analyte were performed and the results are summarized in Table 2. As can be seen, intra-assay precision was studied by measuring the samples at 7 runs a day and provided the relative standard deviation (RSD) values within the range of 2.8–3.7%. In addition, the inter-assay precision was determined on the 3-day period at a total run of 9 and RSDs were achieved in the range of 3.8–4.7%. In all experiments, the relative errors as the accuracy of the method were less than 6.4%. The results confirmed that the developed method is quite reliable and repeatable.

### 3. 8. The Comparisons With Other Methods

A comparison of the developed method with other formerly reported methods for the determination of PBs in the same media is provided in Table 3. According to the data shown, the present work has reasonable RSDs and adequate LRs compared with the other given methods. The table illustrates that the other methods require special devices or absorbents together with extra sample preparation steps which can be performed by skillful operators. It is important to note that by applying the mass spectrometer,

**Table 2.** Intra-day and inter-day precision and accuracy for the determination of PBs.

Compound	Concentration (µg L <sup>-1</sup> )	Intra-day, n = 7			Inter-day, n = 9 (three days)		
		Found value (µg L <sup>-1</sup> ) <sup>a</sup>	RSD (%)	Accuracy (%)	Found value (µg L <sup>-1</sup> ) <sup>a</sup>	RSD (%)	Accuracy (%)
MP	10	10.3	3.7	103	10.4	4.7	104
	100	94.1	3.5	94	103.3	4.3	103
	200	211.6	3.1	106	210.7	4.0	105
EP	10	10.5	3.6	105	10.6	4.5	106
	100	104.2	3.2	104	95.5	4.1	96
	200	191.2	2.8	104	207.7	3.9	104
PP	10	9.6	3.4	96	10.6	3.8	106
	100	105.6	3.3	106	96.3	4.6	96
	200	193.4	2.9	97	189.7	4.2	95
BP	10	9.4	3.7	94	10.5	4.6	105
	100	105.7	3.4	106	106.4	4.5	106
	200	209.3	3.0	105	192.8	4.0	96

<sup>a</sup> The average of three independent measurements.



**Table 3.** The comparison of the current method with the other methods for the determination of PBs.

Method	Sample matrix	LOD ( $\mu\text{g L}^{-1}$ )	LR ( $\mu\text{g L}^{-1}$ )	RSD%	Extraction time (minute)	Reference
SA-D- $\mu$ -SPE-GC-PID <sup>(a)</sup>	Water	0.05–0.3	0.2–50	6.0–8.0	20	39
AME-HPLC-DAD <sup>(b)</sup>	Water	1.0–6.5	3.2–500	3.0–22	90	40
VA-D- $\mu$ -SPE-HPLC-DAD <sup>(c)</sup>	Water	0.1–0.6	1.0–147	1.7–16	20	41
RDSE-GC-MS/MS <sup>(d)</sup>	Water	0.02–0.05	0.06–250	2.0–9.0	85	42
Salting-out based centrifugeless-DLLME-HPLC-UV <sup>(e)</sup>	Water	2.5–5.0	5.0–250	2.8–4.7	7.5	Presented method

<sup>(a)</sup> Solvent-assisted dispersive micro solid phase extraction and gas chromatography-photoionization detector <sup>(b)</sup> Adsorptive microextraction and high performance liquid chromatography-diode array detection <sup>(c)</sup> Vortex-assisted dispersive micro solid-phase extraction and high performance liquid chromatography-diode array detection <sup>(d)</sup> Rotating disk sorptive extraction and gas chromatography-tandem mass spectrometry <sup>(e)</sup> Dispersive liquid-liquid microextraction and high performance liquid chromatography-ultraviolet detection

the LODs would significantly decrease whereas the analysis cost remarkably increase. The most obvious point is that when it comes to the comparison of the extraction time, the presented method stands in the first order.

### 3. 9. Analysis of the Environmental Water Samples

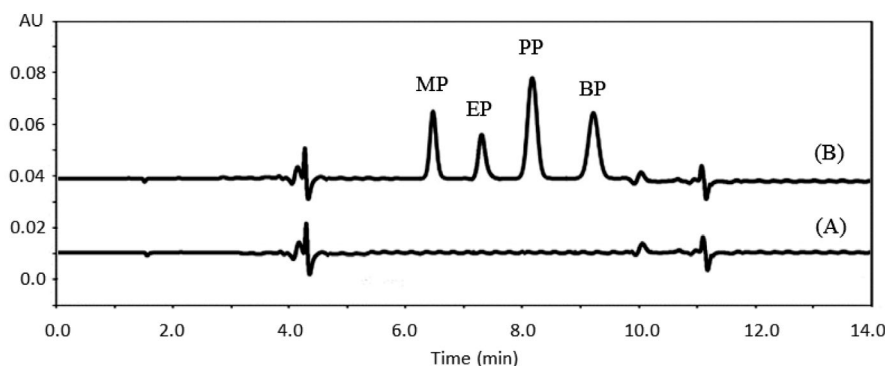
Set at the optimum conditions, the method performance was tested by analyzing the PBs in the four different environmental water samples. The results are presented in Table 4 and showed that they were free of PBs contamination. It is worth noting that the method is a non-exhaustive extraction procedure and therefore the relative recovery (determined as the ratio of the concentrations found in the

real sample and the pure water sample, spiked with a same quantity of the analytes), rather than the absolute recovery (applied in exhaustive extraction methods), was employed. Therefore, as to evaluate the matrix effects all the real samples were spiked with PBs standards at different concentration levels and the relative recovery experiments of the analytes are calculated (Table 4). The obtained recoveries were between 93–106%, indicating that the method is not influenced by the matrix in actual applications, while the RSD values were below than 3.9% ( $n = 7$ ). An overlay of two chromatograms obtained by applying the method for the Persian Gulf (Bandar Khamir Coast, Iran) sample before and after PBs spiking are shown in Fig. 7 and demonstrated no significant interference through the analytical procedure.

**Table 4.** The results obtained from the analysis of the natural water samples.

Sample	MP	EP	PP	BP
Caspian Sea (Noushahr Coast, Iran), (10.0 $\mu\text{g L}^{-1}$ added)				
PBs concentration ( $\mu\text{g L}^{-1}$ )	ND <sup>a</sup>	ND	ND	ND
Found after spike ( $\mu\text{g L}^{-1}$ )	10.4	9.5	9.3	9.7
Relative recovery%	104	95	93	97
RSD% ( $n = 7$ )	3.1	3.6	3.0	3.9
Persian Gulf (Bandar Khamir Coast, Iran), (25.0 $\mu\text{g L}^{-1}$ added)				
PBs concentration ( $\mu\text{g L}^{-1}$ )	ND	ND	ND	ND
Found after spike ( $\mu\text{g L}^{-1}$ )	26.2	24.1	23.7	26.5
Relative recovery%	105	96	95	106
RSD% ( $n = 7$ )	3.8	3.3	3.6	3.4
Jajroud River (Tehran, Iran), (50.0 $\mu\text{g L}^{-1}$ added)				
PBs concentration ( $\mu\text{g L}^{-1}$ )	ND	ND	ND	ND
Found after spike ( $\mu\text{g L}^{-1}$ ) 51.7	52.1	48.3	50.9	
Relative recovery%	103	104	97	102
RSD% ( $n = 7$ )	3.4	3.5	3.9	3.7
Amir Kabir Dam (Tehran, Iran), (100.0 $\mu\text{g L}^{-1}$ added)				
PBs concentration ( $\mu\text{g L}^{-1}$ )	ND	ND	ND	ND
Found after spike ( $\mu\text{g L}^{-1}$ ) 104.1	94.9	97.2	96.4	
Relative recovery%	104	95	97	96
RSD% ( $n = 7$ )	3.7	3.1	3.6	3.2

<sup>a</sup> Not detected.



**Figure 7.** An overlay of two HPLC chromatograms obtained by performing salting-out based centrifugeless DLLME and HPLC-UV for the Persian Gulf water sample (Bandar Khamir Coast, Iran), before (A) and after PBs spiking (B).

## 4. Conclusions

The aim of the present study was to develop and validate a rapid, robust and reliable method combined with HPLC-UV for the determination of the PBs in environmental water samples. The satisfactory extraction efficiency, sufficient sensitivity, and repeatability along with significant accuracy and linearity were achieved, almost independent of the complex matrix in the real sample analysis. Moreover, it needs just a little volume of organic extractants, being consequently an environmentally friendly approach of the sample preparation. The entire analytical procedure presents a cost-effective and quick way for screening purposes. Therefore, putting all the advantages together, the developed method possesses a great potential to be applied in the other applications.

## Disclosure statement

The authors declare no conflicts of interest.

## 5. References

1. D. Błędzka, J. Gromadzińska, W. Wąsowicz, *Environ. Int.*, **2014**, 67, 27–42. DOI:10.1016/j.envint.2014.02.007
2. E. P. Hines, P. Mendola, O. S. von Ehrenstein, X. Ye, A. M. Calafat, S. E. Fenton, *Reprod. Toxicol.*, **2015**, 54, 120–128. DOI:10.1016/j.reprotox.2014.11.006
3. S. Pan, C. Yuan, A. Tagmount, R. A. Rudel, J. M. Ackerman, P. Yaswen, C. D. Vulpe, D. C. Leitman, *Environ. Health Perspect.*, **2015**, 124, 563–569. DOI:10.1289/ehp.1409200
4. F. Artacho-Cordón, M. F. Fernández, H. Frederiksen, L. M. Iribarne-Durán, I. Jiménez-Díaz, F. Vela-Soria, A. M. Andersson, P. Martin-Olmedo, F. M. Peinado, N. Olea, J. P. Arrebola, *Environ. Int.*, **2018**, 119, 203–211. DOI:10.1016/j.envint.2018.05.052
5. L. Quirós-Alcalá, J. P. Buckley, M. Boyle, *Int. J. Hyg. Environ. Health*, **2018**, 221, 652–660. DOI:10.1016/j.ijheh.2018.03.006
6. L. Kolatorova, J. Vitku, R. Hampel, K. Adamcova, T. Skodova, M. Simkova, A. Parizek, L. Starka, M. Duskova, *Environ. Res.*, **2018**, 163, 115–122. DOI:10.1016/j.envres.2018.01.031
7. C. Haman, X. Dauchy, C. Rosin, J. F. Munoz, *Water Res.*, **2015**, 68, 1–11. DOI:10.1016/j.watres.2014.09.030
8. R. Karthikraj, A. K. Vasu, K. Balakrishna, R. K. Sinha, K. Kannan, *Sci. Total Environ.*, **2017**, 593, 592–598. DOI:10.1016/j.scitotenv.2017.03.173
9. X. Ye, L. J. Tao, L. L. Needham, A. M. Calafat, *Talanta*, **2008**, 76, 865–871. DOI:10.1016/j.talanta.2008.04.034
10. X. Ye, A. M. Bishop, L. L. Needham, A. M. Calafat, *Anal. Chim. Acta*, **2008**, 622, 150–156. DOI:10.1016/j.aca.2008.05.068
11. G. Shanmugam, B. R. Ramaswamy, V. Radhakrishnan, H. Tao, *Microchem. J.*, **2010**, 96, 391–396. DOI:10.1016/j.microc.2010.07.005
12. B. R. Ramaswamy, G. Shanmugam, G. Velu, B. Rengarajan, D. J. Larsson, *J. Hazard. Mater.*, **2011**, 186, 1586–1593. DOI:10.1016/j.jhazmat.2010.12.037
13. L. Labat, E. Kummer, P. Dallet, J. P. Dubost, *J. Pharm. Biomed. Anal.*, **2000**, 23, 763–769. DOI:10.1016/S0731-7085(00)00358-7
14. U. D. Uysal, T. Güray, *J. Anal. Chem.*, **2008**, 63, 982–986. DOI:10.1134/S1061934808100109
15. N. Cabaleiro, I. De La Calle, C. Bendicho, I. Lavilla, *Anal. Methods*, **2013**, 5, 323–340. DOI:10.1039/C2AY25830G
16. X. Ye, Z. Kuklenyik, A. M. Bishop, L. L. Needham, A. M. Calafat, *J. Chromatogr. B*, **2006**, 844, 53–59. DOI:10.1016/j.jchromb.2006.06.037
17. I. Márquez-Sillero, E. Aguilera-Herrador, S. Cárdenas, M. Valcárcel, *J. Chromatogr. A*, **2010**, 1217, 1–6. DOI:10.1016/j.chroma.2009.11.005
18. S. Mitra (Ed.): *Sample Preparation Techniques in Analytical Chemistry*, John Wiley & Sons, **2003**. ISBN: 978-0-471-32845-2
19. C. L. Arthur, J. Pawliszyn, *Anal. Chem.*, **1990**, 62, 2145–2148. DOI:10.1021/ac00218a019
20. H. Piri-Moghadam, F. Ahmadi, J. Pawliszyn, *TrAC, Trends Anal. Chem.*, **2016**, 85, 133–143. DOI:10.1016/j.trac.2016.05.029
21. Y. Yan, X. Chen, S. Hu, X. Bai, *J. Chromatogr. A*, **2014**, 1368, 1–17. DOI:10.1016/j.chroma.2014.09.068

22. A. Spietelun, Ł. Marcinkowski, M. de la Guardia, J. Namieśnik, *Talanta*, **2014**, *119*, 34–45. DOI:10.1016/j.talanta.2013.10.050
23. S. Kapitány, E. Sóki, J. Posta, Á. Béni, *Acta Chim. Slov.*, **2017**, *64*, 248–255. DOI:10.17344/acs.2017.3137
24. J. Vichapong, Y. Santaladchaiyakit, R. Burakham, S. Srijaranai, S., *Acta Chim. Slov.*, **2017**, *64*, 590–597. DOI:10.17344/acs.2017.3336
25. M. Rezaee, Y. Assadi, M. R. M. Hosseini, E. Aghaee, S. Berijani, *J. Chromatogr. A*, **2006**, *1116*, 1–9. DOI:10.1016/j.chroma.2006.03.007
26. E. L. Ç. İ. Latif, A. Hol, A. A. Kartal, A. Akdogan, E. L. Ç. İ. Aydan, T. Arslan, *Acta Chim. Slov.*, **2014**, *62*, 196–203. DOI:10.17344/acs.2014.897
27. E. Kupcová, K. Reiffová, *J. Sep. Sci.*, **2017**, *40*, 2620–2628. DOI:10.1002/jssc.201700123
28. E. Mirparizi, M. Rajabi, M. Bazregar, A. Asghari, *Anal. Bioanal. Chem.*, **2017**, *409*, 3007–3016. DOI:10.1007/s00216-017-0246-5
29. M. Bazregar, M. Rajabi, Y. Yamini, S. Arghavani-Beydokhti, A. Asghari, *Food Chem.*, **2018**, *244*, 1–6. DOI:10.1016/j.foodchem.2017.10.006
30. A. Sarafraz-Yazdi, A. Amiri, *TrAC, Trends Anal. Chem.*, **2010**, *29*, 1–14. DOI:10.1016/j.trac.2009.10.003
31. E. Psillakis, N. Kalogerakis, *TrAC, Trends Anal. Chem.*, **2003**, *22*, 565–574. DOI:10.1016/S0165-9936(03)01007-0
32. S. Dadfarnia, A. M. H. Shabani, *Anal. Chim. Acta*, **2010**, *658*, 107–119. DOI:10.1016/j.aca.2009.11.022
33. S. Pedersen-Bjergaard, K. E. Rasmussen, *J. Chromatogr. B*, **2005**, *817*, 3–12. DOI:10.1016/j.jchromb.2004.08.034
34. F. Pena-Pereira, I. Lavilla, C. Bendicho, *TrAC, Trends Anal. Chem.*, **2010**, *29*, 617–628. DOI:10.1016/j.trac.2010.02.016
35. E. Stanisz, J. Werner, A. Zgoła-Grześkowiak, *TrAC, Trends Anal. Chem.*, **2014**, *61*, 54–66. DOI:10.1016/j.trac.2014.06.008
36. S. Arghavani-Beydokhti, M. Rajabi, M. Bazregar, A. Asghari, *Anal. Methods*, **2017**, *9*, 1732–1740. DOI:10.1039/C6AY03477B
37. J. Liu, M. Jiang, G. Li, L. Xu, M. Xie, *Anal. Chim. Acta*, **2010**, *679*, 74–80. DOI:10.1016/j.aca.2010.09.013
38. G. G. Noche, M. E. F. Laespada, J. L. P. Pavón, B.M. Cordero, S. M. Lorenzo, *J. Chromatogr. A*, **2011**, *1218*, 6240–6247. DOI:10.1016/j.chroma.2011.06.112
39. M. Abbasghorbani, A. Attaran, M. Payehghadr, *J. Sep. Sci.*, **2013**, *36*, 311–319. DOI:10.1002/jssc.201200556
40. A. Neves Dias, A. Cristine da Silva, V. Simão, J. Merib, E. Carasek, *Anal. Chim. Acta*, **2015**, *888*, 59–66. DOI:10.1016/j.aca.2015.07.011
41. P. Rocío-Bautista, C. Martínez-Benito, V. Pino, J. Pasán, J. H. Ayala, C. Ruiz-Pérez, A. M. Afonso, *Talanta*, **2015**, *139*, 13–20. DOI:10.1016/j.talanta.2015.02.032
42. M. Becerra-Herrera, V. Miranda, D. Arismendi, P. Richter, *Talanta*, **2018**, *176*, 551–557. DOI:10.1016/j.talanta.2017.08.071

## Povzetek

Uspešno smo razvili preprosto, učinkovito in hitro disperzivno mikroekstrakcijo s topili brez centrifugiranja, osnovano na izsoljevanju, ki smo jo skupaj z visokoločljivostno tekočinsko kromatografijo z UV detekcijo (HPLC-UV) uporabili za določanje izbranih parabenov v okoljskih vodnih vzorcih. Po disperziji ekstrakcijskega topila (1-undekanol) s tališčem blizu sobne temperature v vzorec se motno zmes spusti skozi epruveto, napolnjeno s trdnim natrijevim kloridom. Slednji deluje kot separacijsko sredstvo na osnovi izsoljevanja. Potem se epruveto potopi v ledeno kopel, pri čemer se drobne kapljice ekstrakcijskega topila strdijo in se jih da zlahka pobrati in po ponovnem utekočinjenju injicirati v HPLC-UV. Meje zaznave so bile v območju 2,5–5,0 µg L<sup>-1</sup>, medtem ko je bila ponovljivost znotraj dneva ( $n = 7$ ) pod 3,7% in med dnevi ( $n = 9$ , trije dnevi) pod 4,7%. Metoda je imela zadovoljivo linearnost ( $0,997 \geq r^2 \geq 0,996$ ) in dokaj široko linearno območje (5,0–250 µg L<sup>-1</sup>). Relativna napaka pri točnosti je bila pod 6,4% v vseh poskusih. Metodo smo na koncu uporabili za predkoncentracijo in določitev analitov v različnih vzorcih naravnih vod ter dobili sprejemljive rezultate.



Except when otherwise noted, articles in this journal are published under the terms and conditions of the Creative Commons Attribution 4.0 International License

Scientific paper

# Synthesis of Copper-Doped $\text{MnO}_2$ Electrode Materials by One-Step Hydrothermal Method for High Performance

Dongxia An,<sup>1</sup> Yu Zhang,<sup>1</sup> Hong Zhang,<sup>1</sup> Gang Ma,<sup>1</sup> Cuimiao Zhang<sup>1</sup>  
and Zhiguang Ma<sup>1,2,\*</sup>

<sup>1</sup> College of Chemistry and Environmental Science, Hebei University, Baoding 071002, China

<sup>2</sup> Key Laboratory of Chemical Biology of Hebei Province, Hebei University, Baoding 071002, China

Tel.: +86-312-5079359 Fax: +86-312-5079525

Received: 01-06-2019

## Abstract

By adjusting the amount of  $\text{Cu}(\text{NO}_3)_2 \cdot 3\text{H}_2\text{O}$ ,  $\text{Cu}^{2+}$ -doped birnessite  $\delta\text{-MnO}_2$  spherical substances were synthesized by a simple hydrothermal synthesis process without any templates and surfactants. The structure, morphology, and specific surface area were characterized by XRD, SEM, TEM and BET. Further study shows that the 0.25 mmol Cu-doped  $\text{MnO}_2$  sample is expected to provide higher specific capacitance ( $636.3 \text{ F g}^{-1}$  at  $1 \text{ A g}^{-1}$  current density) compared with pure  $\delta\text{-MnO}_2$  ( $335.6 \text{ F g}^{-1}$  at the current density of  $1 \text{ A g}^{-1}$ ) and long-term cyclic stability (105.01% capacitance retention after 1500 cycles at current density of  $5 \text{ A g}^{-1}$ ). Electrochemical impedance spectroscopy proved the low resistance characteristics of the prepared samples. All the results show that the copper-doped  $\text{MnO}_2$  material is not only low cost, but also of excellent electrochemical performance, thus possesses great potential in future energy development.

**Keywords:** Copper-doped  $\text{MnO}_2$ ; hydrothermal method; supercapacitor

## 1. Introduction

The increasing environmental problems and the consumption of natural energy resources such as coal, natural gas and oil have created the need to develop green and sustainable energy sources that have the capacity to convert and store energy. Researchers have been focused on the development of energy storage devices, such as capacitors, batteries, supercapacitors and batteries.<sup>1–5</sup> Among various energy storage devices, supercapacitors (SCs) is a new type of environmentally friendly energy storage device with high power density (more than  $10 \text{ kW kg}^{-1}$ ), fast charge and discharge speed, long cycle life ( $>10^5$  cycles),<sup>6–9</sup> etc. Yet, in order to meet the requirements of rapid growing technology, supercapacitor also faces some challenges, such as low energy density and short lifespan.<sup>10–13</sup> There are two types of energy storage mechanisms for supercapacitors, double-layer capacitors and pseudo-capacitors. The common electrode material used for double-layer capacitors is carbon material. Whereas, transition metal oxides are the most commonly used materials for pseudo-capacitors.<sup>7,14,15</sup> Many researchers have been working on transition metal

oxides, which exhibit high specific capacitance and good stability for pseudocapacitors.<sup>16–19</sup> So far, various transition metal oxides have been used as electrode materials in pseudocapacitors, including  $\text{Co}_3\text{O}_4$ ,<sup>20</sup>  $\text{MnO}_2$ ,<sup>21</sup>  $\text{NiO}$ ,<sup>22,23</sup>  $\text{RuO}_2$ ,<sup>24</sup>  $\text{V}_2\text{O}_5$ ,<sup>25</sup> etc. Compared with other transition metal oxides,  $\text{MnO}_2$  has the advantages of low cost, high natural abundance, high theoretical capacity ( $1370 \text{ F g}^{-1}$ ), high voltage window, etc.<sup>26–31</sup> It is considered to be the most promising electrode material. However, its capacitance is much lower and its conductivity and structural stability are also relatively poor which restricts its application in real world.<sup>32</sup> In order to improve these problems,  $\text{MnO}_2$  has been combined with other materials to obtain good electrochemical performance, such as  $\text{graphene@MnO}_2$ ,<sup>33</sup>  $\text{carbon nanotubes@MnO}_2$ ,<sup>34,35</sup>  $\text{CuO@MnO}_2$ ,<sup>36</sup>  $\text{Co}_3\text{O}_4\text{@MnO}_2$ ,<sup>37,38</sup> nanocomposites. Moreover, cationic doping has been proved to be an effective way to improve the conductivity of materials. As an effective doped cation, copper cations are considered as one of the most suitable candidates for cationic doping to improve electrochemical performance.<sup>39</sup> However, it is still a challenge to obtain high-performance  $\text{MnO}_2$  electrode materials with a simple and low cost preparation

process. In addition, Cu-doped  $\text{MnO}_2$  is also used in other applications, such as the nanostructured copper manganese oxide (CMO) thin films<sup>40</sup> and selective absorbers.<sup>41</sup>

In this work, we designed and prepared  $\text{Cu}^{2+}$ -doped  $\text{MnO}_2$  by a simple one-step hydrothermal method. X-ray powder diffraction (XRD), scanning electron microscopy (SEM) and transmission electron microscopy (TEM) were used to analyze the morphology and microstructure of the samples. The electrochemical test results showed that the capacitance of 0.25 mmol  $\text{Cu}^{2+}$ -doped  $\text{MnO}_2$  mixed electrode was  $636.3 \text{ F g}^{-1}$  at  $1 \text{ A g}^{-1}$  current density and the capacitance retention was 105.01% after 1500 cycles at current density of  $5 \text{ A g}^{-1}$ .

## 2. Experimental

### 2. 1. Synthesis of $\text{Cu}^{2+}$ Doped $\text{MnO}_2$

All chemicals used in this experiment were analytical grade.  $\text{MnO}_2$  was synthesized using a typical hydrothermal method. Firstly,  $\text{KMnO}_4$  and  $\text{MnSO}_4$  (the molar ratio of 3:1) were added into deionized water (25 mL) respectively and stirred continuously. Then,  $\text{Cu}(\text{NO}_3)_2 \cdot 3\text{H}_2\text{O}$  salt of various doping contents (0.1, 0.25, 0.35, 0.45 mmol) was added into the above potassium permanganate solution during the stirring stage. Then, the manganese sulfate solution was slowly poured into the mixture. The mixture was stirred continuously until the solid was completely dissolved at room temperature, and a piece of the pretreated foam nickels were put vertically into the autoclave. The resultant product was transferred into a Teflon-lined stainless-steel auto-clave and heated to  $80^\circ$  for 3 h. Lastly, the vessel was allowed to be cooled to room temperature naturally and the NFs substrate with the active materials were taken out and labeled as M1, the brown precipitates were collected and washed with distilled water and ethanol for several times, then the filtrate were dried at  $60^\circ$  for 12 h under vacuum.

### 2. 2. Characterization

The surface morphology and microstructure of samples were characterized by field emission scanning electron microscope (SEM, JSM-7500F) and transmission electron microscopy (TEM, Tecnai G2 F20 S-TWIN). The X-ray powder diffraction (XRD) measurements were performed on Bruker D8 Advance.  $\text{N}_2$  absorption-desorption were performed with a Micromeritics TristarII 3020. The surface area was computed from the Brunauer–Emmett–Teller (BET) equation, and the pore size distribution was calculated from desorption curve by the Barrette–Joyner–Halenda (BJH) model.

### 2. 3. Electrochemical Measurement

Electrochemical properties were measured in a three electrode system employing the Electrochemical Worksta-

tion (INTERFACE 1000, GAMRY, US) in which the NF- $\text{Cu-MnO}_2$  was used as working electrode, saturated calomel electrode (SCE) as a reference electrode and a platinum wire as counter electrode. Cyclic voltammetry (CV), galvanostatic charge–discharge (GCD) and electrochemical impedance spectra (EIS) were performed using workstation in  $1 \text{ mol L}^{-1}$  KOH electrolyte. The capacitance formula is:

$$C_m = \frac{I\Delta t}{m\Delta V} \quad (1)$$

where  $I/m$  is the current density,  $t$  is the discharge time,  $V$  is the potential window, and  $m$  is the mass of the  $\text{MnO}_2$  material.

## 3. Results and Discussion

### 3. 1. Structure and Morphology

The X-ray diffraction (XRD) patterns of the two samples are shown in Figure. 1 to determine the phase composition of the product, in which curve A represents the pure  $\text{MnO}_2$  sample and B represents the 0.25 mmol  $\text{Cu}^{2+}$ -doped  $\text{MnO}_2$  sample. It can be clearly seen from curve A that the main characteristic peaks are located at  $12.9^\circ$ ,  $37.3^\circ$  and  $65.6^\circ$  which correspond to the (001) ( $-111$ ) and (020) planes of  $\text{MnO}_2$ , respectively. These characteristic peaks indicate that the sample belongs to the birnessite  $\delta\text{-MnO}_2$  structure. The wide and weak reflection peaks can be seen from the XRD patterns, indicating that the structure of pure  $\text{MnO}_2$  is amorphous. The XRD pattern is in good agreement with the diffraction peaks reported in JCPDS card no. 80–1098.<sup>42</sup> In addition, it can be clearly seen from curve B that it also shows peaks at  $26.1^\circ$  and  $55.9^\circ$  of the plane corresponding to the (011), (0–24) planes of  $\text{CuSO}_4 \cdot \text{H}_2\text{O}$  (JCPDS 21–0269). At the same

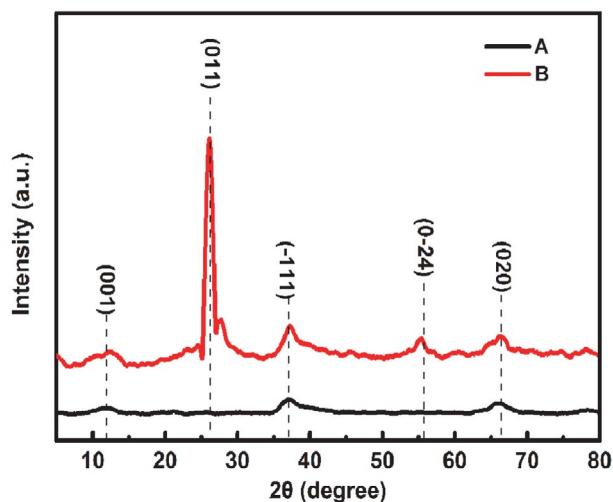


Fig1. XRD patterns of the samples.



time, it can be seen that the peak at 011 corresponds to the crystal structure of  $\text{CuSO}_4 \cdot \text{H}_2\text{O}$  formed in amorphous manganese dioxide.  $\delta\text{-MnO}_2$  has a two-dimensional (2D) layered structure, which is considered to be a convenient structure to promote the migration of metal ions or water molecules and to allow ions and water molecules to exist in the inter-laminar region.<sup>43</sup> Due to the relatively open layered structure,  $\text{Cu}^{2+}$  and  $\text{SO}_4^{2-}$  are embedded in the structure of  $\text{MnO}_2$ .

The morphologies of pure  $\text{MnO}_2$  and 0.25 mmol  $\text{Cu}^{2+}$  doped- $\text{MnO}_2$  electrodes were investigated by scanning electron microscopy (SEM) and transmission electron microscopy (TEM). Figure 2 shows the SEM and TEM images of  $\text{MnO}_2$  and 0.25 mmol  $\text{Cu}^{2+}$ -doped  $\text{MnO}_2$  electrodes. As can be seen from Figure 2a and 2b, the synthesized pure  $\text{MnO}_2$  and 0.25 mmol  $\text{Cu}^{2+}$ -doped  $\text{MnO}_2$  showed a surface morphology similar to that of a micro-flower consisting of a stack of vertically aligned thin nanosheets. It can be seen that there is no difference between the morphology of the two samples, which may be due to the fact that the amount of  $\text{Cu}^{2+}$  doped is too small to affect the morphology of  $\text{MnO}_2$ . Figures 2c and 2d show TEM images of  $\text{MnO}_2$  and 0.25 mmol  $\text{Cu}^{2+}$  doped  $\text{MnO}_2$ . As can be seen from the figure, the internal structure of the gate of the synthetic material is that the ultrathin nanosheets are connected to each other to form a layered and porous 3D structure. However, compared to  $\text{MnO}_2$  (Fig. c), the internal structure of  $\text{MnO}_2$  doped with  $\text{Cu}^{2+}$  (Fig. d) is made by more compact ultrathin nanosheets.

Figure 3 shows the  $\text{N}_2$  adsorption-desorption isotherms of  $\text{MnO}_2$  and 0.25 mmol  $\text{Cu}^{2+}$  doped  $\text{MnO}_2$ . It can be seen from the diagram that the isotherm can be identi-

fied as type III, which can be attributed to the slit pores formed by the self-assembled nanocrystals. There is no obvious narrow hysteresis ring between the two substances at relatively low pressure which also indicates that the porous characteristics of the sample are open and the capillary condensation of nitrogen has no significant delay. However, 0.25 mmol  $\text{Cu}^{2+}$  doped  $\text{MnO}_2$  has obvious hysteresis loops in the region of relative high pressure ( $P / P_0$

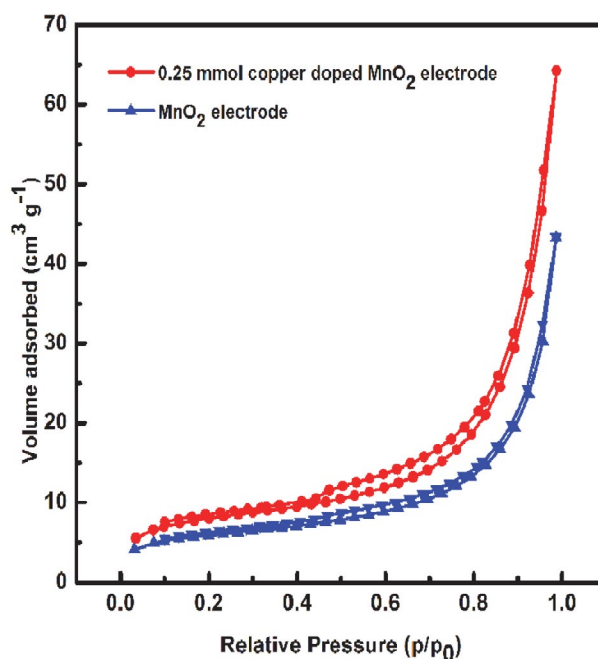


Fig. 3. Nitrogen adsorption-desorption isotherms of  $\text{MnO}_2$  and 0.25 mmol  $\text{Cu}^{2+}$  doped  $\text{MnO}_2$  electrode

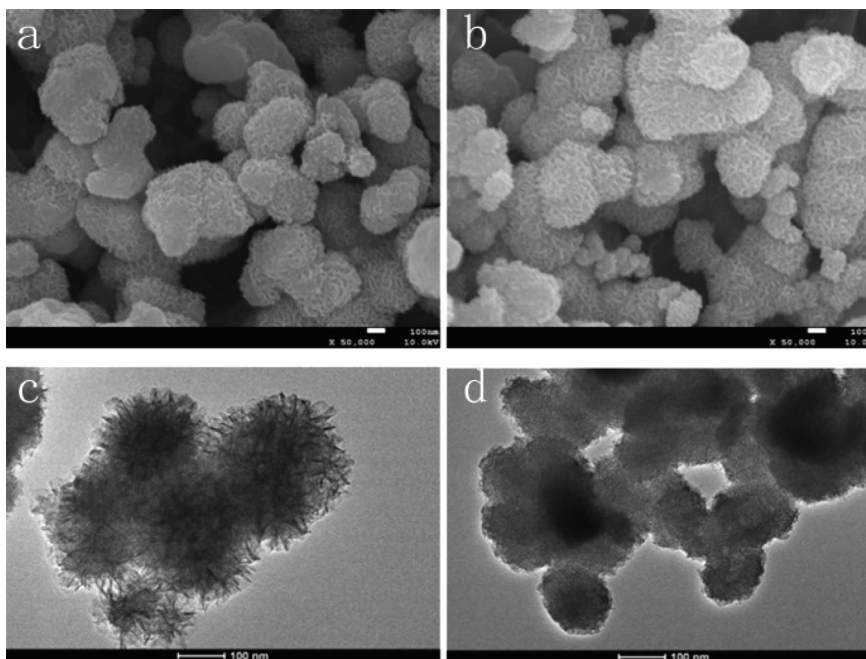


Fig. 2. SEM and TEM images of  $\text{MnO}_2$  (a and c) and 0.25 mmol  $\text{Cu}^{2+}$ -doped  $\text{MnO}_2$  (b and d)

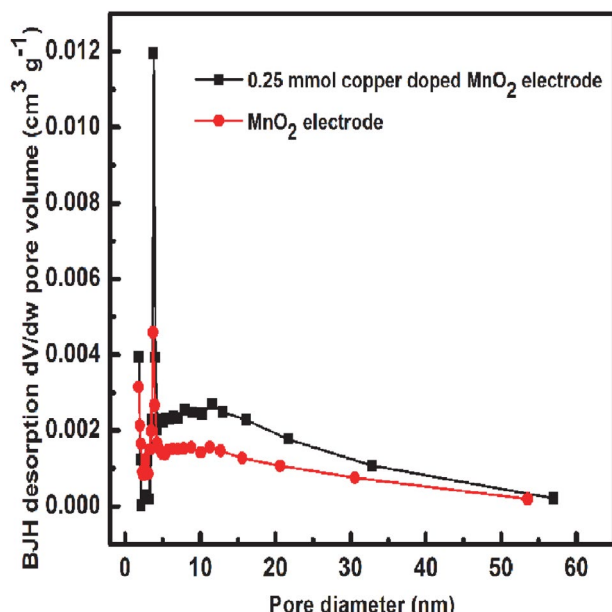


Fig. 4. BJH pore size distribution plot from the desorption branch of the  $\text{MnO}_2$  and 0.25 mmol  $\text{Cu}^{2+}$  doped  $\text{MnO}_2$  electrode.

$\geq 0.45$ ). The Brunauer-Emmett-Teller (BET) surface area of  $\text{MnO}_2$  and 0.25 mmol  $\text{Cu}^{2+}$  doped  $\text{MnO}_2$  is calculated to be 20.0 and 26.8  $\text{m}^2 \text{g}^{-1}$ , so the  $\text{MnO}_2$  doped with  $\text{Cu}^{2+}$  can exhibit better electrochemical performance due to its larger surface area which can provide more electroactive sites for electrochemical reaction.<sup>44</sup> In addition, the Barrete-Joyner-Halenda (BJH) method was used to further determine the pore size distribution of the two samples by desorption isotherms (Figure. 4). The pore volumes of  $\text{MnO}_2$  and 0.25 mmol  $\text{Cu}^{2+}$  doped  $\text{MnO}_2$  are 0.067 and 0.10  $\text{cm}^3 \text{g}^{-1}$ , respectively. According to the pore size distribution of the corresponding desorption branches of the nitrogen adsorption isotherm, the average pore sizes of the two samples are 13.4 and 14.8 nm, indicating that they are mesoporous. Therefore, it is shown that the doping of copper ions has an effect on the surface area and pore size of  $\text{MnO}_2$ , thus improving the electrochemical performance.

### 3. 2. Electrochemical Performance

To investigate its electrochemical performance thoroughly, the electrochemical behavior of pure  $\text{MnO}_2$  and  $\text{Cu}^{2+}$ -doped  $\text{MnO}_2$  solid electrodes was studied by cyclic voltammograms (CV), galvanostatic charge-discharge (GCD), and electrochemical impedance spectroscopy (EIS). Figure 5 demonstrates the CV curves for  $\text{MnO}_2$  and  $\text{Cu}^{2+}$ -doped  $\text{MnO}_2$  with different proportions at the scan rate of 5  $\text{mV s}^{-1}$  in the potential window of 0 to 0.6 V in 1 M KOH electrolyte. This figure shows that 0.25 mmol  $\text{Cu}^{2+}$ -doped  $\text{MnO}_2$  exhibits the largest coverage area and the highest current, which indicates its ideal pseudo-capacitance properties and rapid charging and discharge processes. Figure. 6 shows the GCD curves of  $\text{MnO}_2$  and

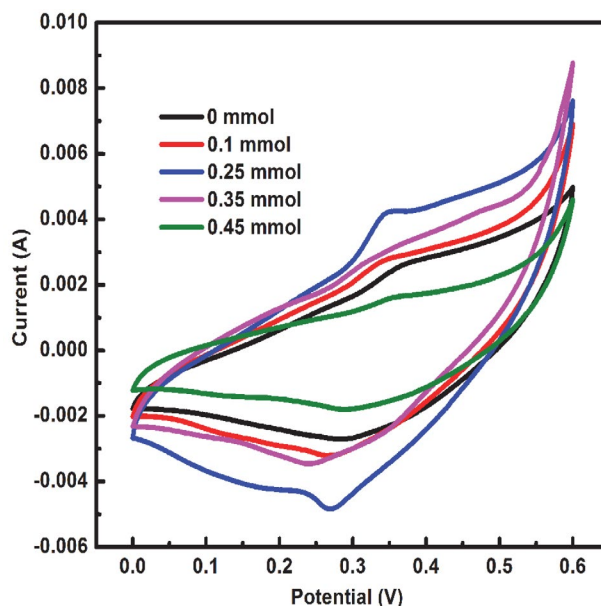


Fig. 5. CV curves of the as-prepared electrodes at 5  $\text{mV s}^{-1}$ .

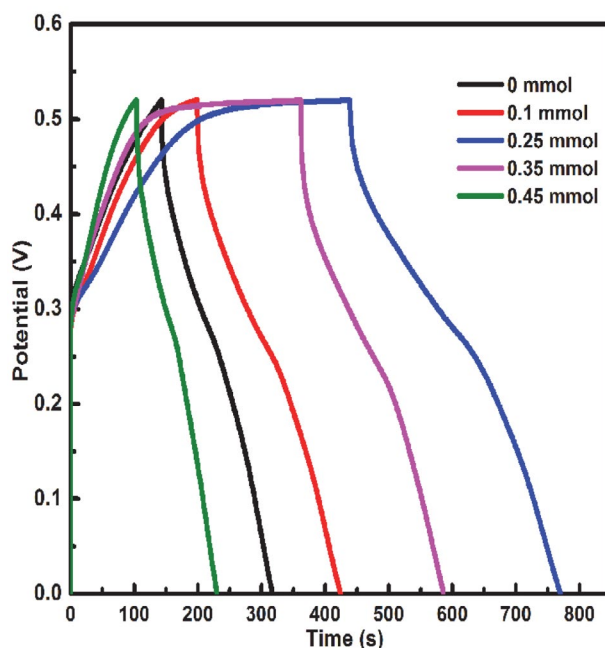


Fig. 6. Galvanostatic charge-discharge curves of as-prepared electrodes at a current density of 1  $\text{A g}^{-1}$ .

$\text{Cu}^{2+}$ -doped  $\text{MnO}_2$  electrodes with current density ranging from 1 to 10  $\text{A g}^{-1}$  in the 0-0.52 V voltage window. It shows that the electrode has the longest discharge time when the amount of doped copper is 0.25 mmol. The specific capacitance of the corresponding  $\text{MnO}_2$  electrode calculated from this GCD curves is shown in Figure. 7. The results show that the specific capacitance of the electrodes by pure  $\text{MnO}_2$  and  $\text{Cu}^{2+}$ -doped  $\text{MnO}_2$  with different copper contents are 335.6, 433.5, 636.3, 431.9 and 243.7  $\text{F g}^{-1}$  at current density of 1  $\text{A g}^{-1}$ , respectively.

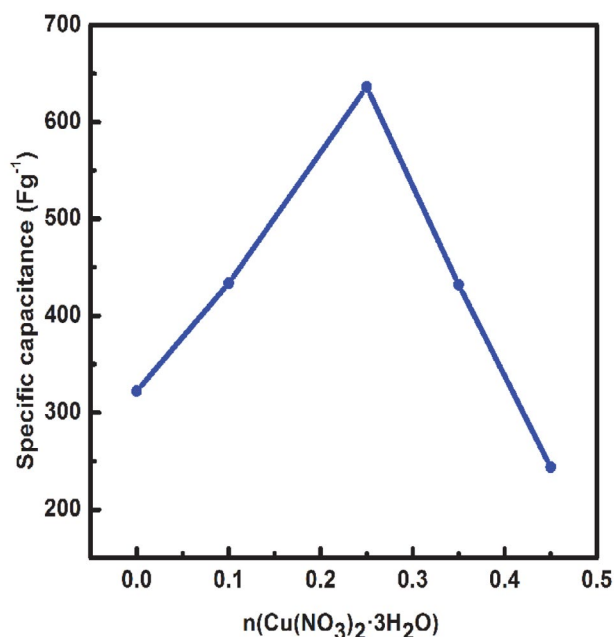


Fig. 7. Capacitance comparison curve of  $\text{MnO}_2$  electrode doped with  $\text{Cu}^{2+}$  with different copper proportions.

Figure 8 shows the CV curves of 0.25 mmol  $\text{Cu}^{2+}$ -doped  $\text{MnO}_2$  at the scan rate of  $5 \text{ mV s}^{-1}$  at a potential window of 0 to 0.6 V. It can be seen that the  $\text{MnO}_2$  with 0.25 mmol  $\text{Cu}^{2+}$  has regular and symmetrical shape, which proves that it has the typical pseudo-capacitance properties in the process of rapid charging and discharging. When the scanning rate is increased from  $5 \text{ mV s}^{-1}$  to  $100 \text{ mV s}^{-1}$ , the specific capacitance tends to decrease gradually. The CV curve is nearly symmetrical in the voltage window from 0 to 0.6 V without noticeable deflection, indicating its desirable reversibility and stability. This proportionality corresponds to the behavior of ideal capacitors.<sup>45</sup> Figure 9 shows the GCD process of 0.25 mmol  $\text{Cu}^{2+}$ -doped  $\text{MnO}_2$  electrodes. As the current density increases, the discharge time decreases, so the capacitance becomes smaller. Moreover, when the current density is  $1 \text{ A g}^{-1}$ , the capacitance of 0.25 mmol  $\text{Cu}^{2+}$ -doped  $\text{MnO}_2$  electrode is  $636.3 \text{ F g}^{-1}$ , which is nearly twice as high as that of pure  $\text{MnO}_2$  ( $335.6 \text{ F g}^{-1}$  at the current density of  $1 \text{ A g}^{-1}$ ). The almost symmetrical charge / discharge curves further confirm the ideal charge-discharge characteristics and excellent reversibility, which is in good agreement with the CV curves. The charge-discharge curve deviates from the straight line obviously, especially the curves obtained at low currents, indicating the pseudo-capacitance behavior of the composite material. When the current density is low, the ions have enough time to penetrate and enter the interior. However, under the condition of high current density, due to the rapid charge / discharge time, the internal components cannot be used effectively, resulting in weaker electrochemical performance.<sup>46</sup> In order to further understand the transport kinetics of electrochemical be-

havior, the EIS spectra of  $\text{MnO}_2$  and 0.25 mmol  $\text{Cu}^{2+}$ -doped  $\text{MnO}_2$  electrode shown in Figure 10 were obtained at open circuit potential in the frequency range from 0.01 Hz to 100 kHz. Typically,  $R_s$  (the composite resistance of electrolyte resistance, inherent resistance of substrate and contact resistance at active material / collector interface) can be obtained from the point where high frequency semicircle intersects crosses real resistance axis. And the Warburg impedances can be obtained from the slope of the diagram near the straight line in the low frequency region, and the larger the slope is, the smaller the resistance

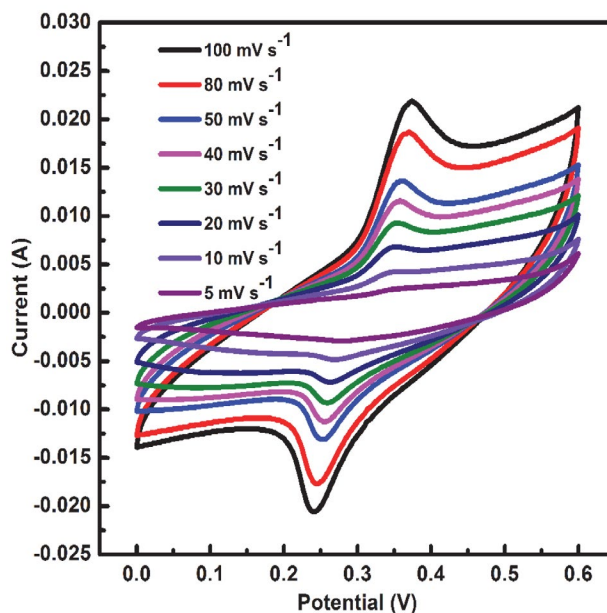


Fig. 8. CV curves of 0.25 mmol  $\text{Cu}^{2+}$ -doped  $\text{MnO}_2$  electrode at various scan rates.

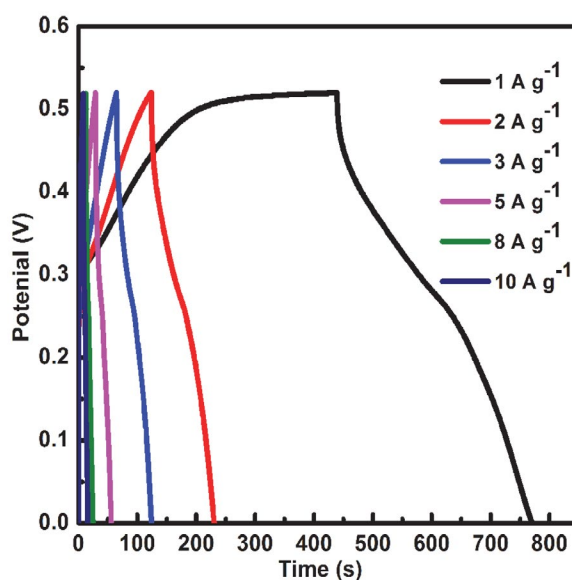


Fig. 9. Charge-discharge curves of the 0.25 mmol  $\text{Cu}^{2+}$ -doped  $\text{MnO}_2$  electrode at different current density.

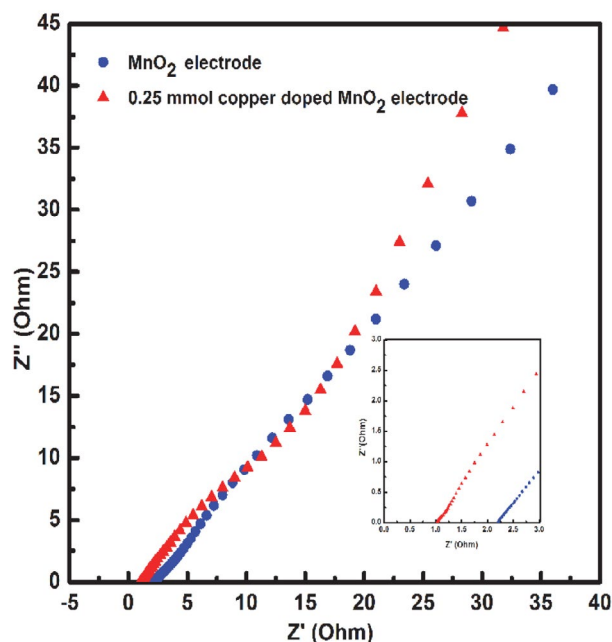


Fig. 10. Nyquist plots of the as-prepared electrodes.

is.<sup>47,48</sup> As shown in figure 10, the intersection point between  $\text{Cu}^{2+}$ -doped  $\text{MnO}_2$  electrode and point axis is smaller than that of  $\text{MnO}_2$ , so the  $R_s$  of  $\text{Cu}^{2+}$ -doped  $\text{MnO}_2$  is lower than that of  $\text{MnO}_2$ . In addition, the slope of  $\text{Cu}^{2+}$ - $\text{MnO}_2$  electrode is larger than that of  $\text{MnO}_2$  electrode, so the Weinberg impedance is smaller. Since the electrolyte solution resistance of the two electrodes and the intrinsic resistance of NF should be the same, it can be concluded that the doping of  $\text{Cu}^{2+}$  reduces the  $R_s$  and Weinberg impedance of the  $\text{MnO}_2$  electrode and decreases the contact resistance between the  $\text{MnO}_2$  / NF interfaces.

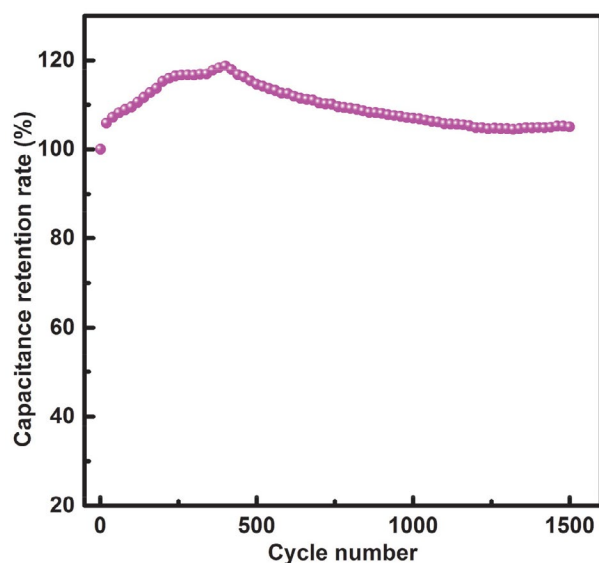


Fig. 11. Cycling stability of the 0.25 mmol  $\text{Cu}^{2+}$ -doped  $\text{MnO}_2$  electrodes at  $5 \text{ A g}^{-1}$ .

In order to further demonstrate the superior performance of the as-synthesized 0.25 mmol copper doped  $\text{MnO}_2$  electrode, as shown in Figure. 11, the long-term stability test of the 1500 cycles at the current density of  $5 \text{ A g}^{-1}$  was carried out. From figure 11, it can be seen that the capacitance retention ratio of 1 to 500 cycles increases as the capacitance increases with the number of cycles. This is because the  $\text{Cu}^{2+}$ -doped  $\text{MnO}_2$  is in an activated state during this process, and the activity gradually increases. After 500 cycles, the capacitance began to decrease slowly. Yet, even after 1500 cycles, the capacitance was still very good, showing a capacitance retention rate of 105.01% compared with the initial capacitance (100%) showing a good cycle stability.

## 4. Conclusions

In this work,  $\text{Cu}^{2+}$ -doped  $\text{MnO}_2$  were synthesized by hydrothermal method and the optimum doping amount of  $\text{Cu}^{2+}$  was investigated. The results of XRD, SEM, TEM, BET test showed that the prepared samples' structure, morphology and pore distributions. The experimental results show that the 0.25 mmol  $\text{Cu}^{2+}$ -doped  $\text{MnO}_2$  sample is expected to provide higher specific capacitance ( $636.3 \text{ F g}^{-1}$  at  $1 \text{ A g}^{-1}$  current density) compared with pure  $\delta\text{-MnO}_2$  ( $335.6 \text{ F g}^{-1}$  at the current density of  $1 \text{ A g}^{-1}$ ) and long-term cyclic stability (105.01% capacitance retention after 1500 cycles at current density of  $5 \text{ A g}^{-1}$ ). The EIS proved the lower resistance characteristics of the prepared electrodes. All the results show that the doping of  $\text{Cu}^{2+}$  has great influence on the improvement of  $\text{MnO}_2$  electrochemical performance. The results are expected to pave the way for the development of low-cost and high-performance supercapacitors and other energy storage devices.

## 5. Acknowledgment

This work was supported by the National Natural Science Foundation of China [grant numbers 51302062].

## 6. References

1. M. Armand and J. M. Tarascon, *Nature* **2008**, 451, 652–657. DOI:10.1038/451652a
2. M. M. Vadiyar, S. C. Bhise, S. S. Kolekar, J. Y. Chang, K. S. Ghule and A. V. Ghule, *Journal of Materials Chemistry A* **2016**, 4, 3504–3512. DOI:10.1039/C5TA09022A
3. V. Augustyn, P. Simon and B. Dunn, *Energy & Environmental Science* **2014**, 7, 1597–1614. DOI:10.1039/c3ee44164d
4. Q. Yang, Q. Li, Z. Yan, X. Hu, L. Kang, Z. Lei and Z. H. Liu, *Electrochimica Acta* **2014**, 129, 237–244. DOI:10.1016/j.electacta.2014.02.113



5. G. A. Ferrero, M. Sevilla and A. B. Fuertes, *Sustainable Energy & Fuels* **2017**, *1*, 127. DOI:10.1039/C6SE00047A
6. P. Simon and Y. Gogotsi, *Nature Materials* **2008**, *7*, 845–854. DOI:10.1038/nmat2297
7. G. Wang, L. Zhang and J. Zhang, *Chemical Society Reviews* **2012**, *43*, 797–828. DOI:10.1039/C1CS15060J
8. R. Kötz and M. Carlen, *Electrochimica Acta* **2000**, *45*, 2483–2498. DOI:10.1016/S0013-4686(00)00354-6
9. C. Liu, F. Li, L. P. Ma and H. M. Cheng, *Advanced Materials* **2010**, *22*, E28–E62. DOI:10.1002/adma.200903328
10. L. Yuan, X. H. Lu, X. Xiao, T. Zhai, J. Dai, F. Zhang, B. Hu, X. Wang, L. Gong and J. Chen, *Acs Nano* **2012**, *6*, 656. DOI:10.1021/nn2041279
11. C. Meng, C. Liu, L. Chen, C. Hu and S. Fan, *Nano Letters* **2010**, *10*, 4025–4031. DOI:10.1021/nl1019672
12. P. Yang, Y. Ding, Z. Lin, Z. Chen, Y. Li, P. Qiang, M. Ebrahimi, W. Mai, C. P. Wong and Z. L. Wang, *Nano Letters* **2014**, *14*, 731. DOI:10.1021/nl404008e
13. L. Peng, X. Peng, B. Liu, C. Wu, Y. Xie and G. Yu, *Nano Letters* **2013**, *13*, 2151–2157. DOI:10.1021/nl400600x
14. Y. Wang and Y. Xia, *Advanced Materials* **2013**, *25*, 5336–42. DOI:10.1002/adma.201301932
15. M. Zhi, C. Xiang, J. Li, M. Li and N. Wu, *Nanoscale* **2013**, *5*, 72–88. DOI:10.1039/C2NR32040A
16. C. C. Hu, K. H. Chang, M. C. Lin and Y. T. Wu, *Nano Letters* **2006**, *6*, 2690–2695. DOI:10.1021/nl061576a
17. D. Han, P. Xu, X. Jing, J. Wang, P. Yang, Q. Shen, J. Liu, D. Song, Z. Gao and M. Zhang, *Journal of Power Sources* **2013**, *235*, 45–53. DOI:10.1016/j.jpowsour.2013.01.180
18. Y. Xiao, C. Hu and M. Cao, *Journal of Power Sources* **2014**, *247*, 49–56. DOI:10.1016/j.jpowsour.2013.08.069
19. Y. Wei, C. W. Ryu and K. B. Kim, *Journal of Power Sources* **2007**, *165*, 386–392. DOI:10.1016/j.jpowsour.2006.12.016
20. M. M. Vadiyar, S. S. Kolekar, J. Y. Chang, A. A. Kashale and A. V. Ghule, *Electrochimica Acta* **2016**, *222*, 1604–1615. DOI:10.1016/j.electacta.2016.11.146
21. R. B. Rakhi, B. Ahmed, D. Anjum and H. N. Alshareef, *Acs Applied Materials & Interfaces* **2016**, *8*, 18806. DOI:10.1021/acsami.6b04481
22. Y. Han, S. Zhang, N. Shen, D. Li and X. Li, *Materials Letters* **2017**, *188*, 1–4. DOI:10.1016/j.matlet.2016.09.051
23. Q. X. Xia, J. M. Yun, R. S. Mane, L. Li, J. Fu, J. H. Lim and K. H. Kim, *Sustainable Energy & Fuels* **2017**, *1*, 529–539. DOI:10.1039/C6SE00085A
24. Z. Peng, X. Liu, H. Meng, Z. Li, B. Li, Z. Liu and S. Liu, *Acs Applied Materials & Interfaces* **2016**, *9*, 4577–4586. DOI:10.1021/acsami.6b12532
25. Y. Zhang, J. Zheng, Y. Zhao, T. Hu, Z. Gao and C. Meng, *Applied Surface Science* **2016**, *377*, 385–393. DOI:10.1016/j.apsusc.2016.03.180
26. W. Zhong, L. Lin, J. M. Yan and X. B. Zhang, *Advanced Science* **2017**, *4*, 1600382. DOI:10.1002/advs.201600382
27. J. Song, H. Li, S. Li, H. Zhu, Y. Ge, S. Wang, X. Feng and Y. Liu, *New Journal of Chemistry* **2017**, *41*, 3750–3757. DOI:10.1039/C6NJ04118C
28. W. Li, K. Xu, L. An, F. Jiang, X. Zhou, J. Yang, Z. Chen, R. Zou and J. Hu, *Journal of Materials Chemistry A* **2014**, *2*, 1443–1447. DOI:10.1039/C3TA14182A
29. Z. Song, W. Liu, M. Zhao, Y. Zhang, G. Liu, C. Yu and J. Qiu, *Journal of Alloys & Compounds* **2013**, *560*, 151–155. DOI:10.1016/j.jallcom.2013.01.117
30. W. HY, X. FX, Y. L, L. B and L. XW, *Small* **2014**, *10*, 3181–3186. DOI:10.1002/smll.201303836
31. W. Li, K. Xu, B. Li, J. Sun, F. Jiang, Z. Yu, R. Zou, Z. Chen and J. Hu, *Chemelectrochem* **2014**, *1*, 1003–1008. DOI:10.1002/celc.201400006
32. W. Wei, X. Cui, W. Chen and D. G. Ivey, *Chemical Society Reviews* **2011**, *40*, 1697–1721. DOI:10.1039/C0CS00127A
33. J. Chang, M. Jin, F. Yao, T. H. Kim, V. T. Le, H. Yue, F. Gunes, B. Li, A. Ghosh and S. Xie, *Advanced Functional Materials* **2013**, *23*, 5074–5083. DOI:10.1002/adfm.201301851
34. M. Huang, R. Mi, H. Liu, F. Li, X. L. Zhao, W. Zhang, S. X. He and Y. X. Zhang, *Journal of Power Sources* **2014**, *269*, 760–767. DOI:10.1016/j.jpowsour.2014.07.031
35. H. Ye, Y. Cheng, T. Hobson and L. Jie, *Nano Letters* **2010**, *10*, 2727. DOI:10.1021/nl101723g
36. M. Huang, Y. Zhang, F. Li, Z. Wang, Alamusi, N. Hu, Z. Wen and Q. Liu, *Sci Rep* **2014**, *4*, 4518. DOI:10.1038/srep04518
37. W. Li, G. Li, J. Sun, R. Zou, K. Xu, Y. Sun, Z. Chen, J. Yang and J. Hu, *Nanoscale* **2013**, *5*, 2901–8. DOI:10.1039/c3nr34140b
38. M. Huang, Y. Zhang, F. Li, L. Zhang, Z. Wen and Q. Liu, *Journal of Power Sources* **2014**, *252*, 98–106. DOI:10.1016/j.jpowsour.2013.12.030
39. D. J. Davis, T. N. Lambert, J. A. Vigil, M. A. Rodriguez, M. T. Brumbach, E. N. Coker and S. J. Limmer, *Journal of Physical Chemistry C* **2014**, *118*, 17342–17350. DOI:10.1021/jp5039865
40. S. Falahatgar, F. Ghodsi, F. Tepehan, G. Tepehan, I. Turhan, *Applied Surface Science* **2014**, *289*, 289–299. DOI:10.1016/j.apsusc.2013.10.153
41. R. Bayon, G.S. Vicente, A. Morales, *Solar Energy Materials and Solar Cells* **2010**, *94*, 998–1004. DOI:10.1016/j.solmat.2010.02.006
42. R. Chen, J. Yu and W. Xiao, *Journal of Materials Chemistry A* **2013**, *1*, 11682–11690. DOI:10.1039/c3ta12589k
43. V. Subramanian, H. Zhu and B. Wei, *Journal of Power Sources* **2006**, *159*, 361–364. DOI:10.1016/j.jpowsour.2006.04.012
44. S. Lu, D. Yan, L. Chen, G. Zhu, H. Xu and A. Yu, *Materials Letters* **2016**, *168*, 40–43. DOI:10.1016/j.matlet.2016.01.021
45. Z. Cheng, G. Tan, Y. Qiu, B. Guo, F. Cheng and H. Fan, *Journal of Materials Chemistry C* **2015**, *3*, 6166–6171. DOI:10.1039/C5TC00645G
46. L. Ren, J. Chen, X. Wang, M. Zhi, J. Wu and X. Zhang, *Rsc Advances* **2015**, *5*, 30963–30969. DOI:10.1039/C5RA02663F
47. Y. C. Hsieh, K. T. Lee, Y. P. Lin, N. L. Wu and S. W. Donne, *Journal of Power Sources* **2008**, *177*, 660–664. DOI:10.1016/j.jpowsour.2007.11.026
48. C. W. Huang and H. Teng, *Salud Publica De Mexico* **2008**, *46*, 132–140.



## Povzetek

S prilagajanjem množine dodanega  $\text{Cu}(\text{NO}_3)_2 \cdot 3\text{H}_2\text{O}$  smo s preprostim hidrotermalnim sinteznim postopkom sintetizirali birnesite  $\delta\text{-MnO}_2$  dopiran z  $\text{Cu}^{2+}$ . Strukturo, morfologijo in specifično površino smo določili z naslednjimi metodami: rentgensko praškovno difrakcijo (XRD), vrstično elektronsko mikroskopijo (SEM), presewno elektronsko mikroskopijo (TEM) in meritvami specifične površine (BET). Nadaljnje študije so pokazale, da naj bi se pri vzorcu  $\text{MnO}_2$ , dopiranem z 0,25 mmol  $\text{Cu}^{2+}$ , zvišala specifična kapacitivnost ( $636,3 \text{ F g}^{-1}$  pri gostoti toka  $1 \text{ A g}^{-1}$ ) v primerjavi s čistim  $\delta\text{-MnO}_2$  ( $335,6 \text{ F g}^{-1}$  pri gostoti toka  $1 \text{ A g}^{-1}$ ) in dolgoročno ciklično stabilnost (105,01 % zadrževanje kapacitivnosti po 1500 ciklih pri gostoti toka  $5 \text{ A g}^{-1}$ ). Z elektrokemijsko impedančno spektroskopijo (EIS) smo določili nizke upornosti pripravljenih vzorcev. Vsi rezultati kažejo, da je  $\text{MnO}_2$  material, dopiran z bakrom mogoče pripraviti z razmeroma nizkimi stroški. Material pa ima tudi odlične elektrokemijske lastnosti in posledično velik potencial v prihodnjem razvoju energetike.



Except when otherwise noted, articles in this journal are published under the terms and conditions of the Creative Commons Attribution 4.0 International License

# Synthesis, Labeling and Biological Evolution of New Thiopyrano[2,3-*b*]Pyridine Derivatives as Potential Anticancer Agents

Mamdouh Abdel-Monem Sofan,<sup>1,\*</sup> Wafaa Salama Hamama,<sup>2</sup>  
Ibrahim Ibrahim EL-Hawary,<sup>1</sup> Ismail Taha Ibrahim<sup>3</sup>  
and Hanafi Hassan Zoorob<sup>2</sup>

<sup>1</sup> Chemistry Department, Faculty of Science, Damietta University, Egypt

<sup>2</sup> Chemistry Department, Faculty of Science, Mansoura University, Egypt

<sup>3</sup> Hot Laboratories Center, Atomic Energy Authority, Cairo, Egypt

\* Corresponding author: E-mail: masofan1953@du.edu.eg

Received: 01-12-2019

## Abstract

The new thiopyrano[2,3-*b*]pyridines **4–9** could be synthesized from the nicotinonitrile derivative **1**. The cytotoxicity activity of the selected compounds **5**, **6** and **8** was tested against MCF-7 and HCT-116 cell lines. The compound **5** (TP<sub>5</sub>) exhibited significant inhibitory activity and displayed the most potent activity, more than **6** and **8**. The compound **5** with potent inhibitory activity in tumor growth inhibition would be a potential anticancer agent. In the light of this result, the labeled <sup>125</sup>I-compound **5** (<sup>125</sup>I-TP<sub>5</sub>) was prepared and its cytotoxicity against ascites tumor in mice has been evaluated. The results show that compound **5** (TP<sub>5</sub>) may be potentially used as a radiopharmaceutical for tumor diagnosis when labeled with <sup>125</sup>I.

**Keywords:** Nicotinonitrile; thiopyrano[2,3-*b*]pyridine; cytotoxic activity; ascites tumor.

## 1. Introduction

Cancer is one of the main leading causes of death in both developing and developed countries.<sup>1</sup> Cancer treatment has been a major research and development effort in academia and the pharmaceutical industry for numerous years.<sup>2,3</sup> Despite the fact that there is a large amount of information available dealing with the clinical aspects of cancer chemotherapy, there was a clear requirement for an updated treatment from the point of view of medicinal chemistry and drug design.<sup>4</sup> Another major goal for developing new anticancer agents is to overcome cancer resistance to drug treatment, which has made many of the currently available chemotherapeutic agents ineffective.<sup>5</sup> The pyridine nucleus is an integral part of anti-inflammatory and anticancer agents.<sup>6,7</sup> Some of 4-oxothiopyrano[2,3-*b*]pyridines were reported as potential antihypertensive agents.<sup>8,9</sup>  $\alpha,\beta$ -Unsaturated compounds have also exhibited excellent antitumor, anti-inflammatory, antimalarial and

other pharmacological effects.<sup>10–13</sup> In recent years, the synthesis and antifungal activities of 3-substituted methylene-4-oxothiopyrano[2,3-*b*]pyridines were published.<sup>14,15</sup> A number of the spiropyrazolo-3,3'-thiopyrano[2,3-*b*]pyridines and new tetra- and penta-heterocycles, which could be obtained by treating 3-(*N,N*-dimethylamino) methylene derivatives with nitrilimines and aminoazoles, respectively, showed high antifungal and anti-bacterial activities.<sup>15</sup>

Motivated by the above literature observations and our own previous reports,<sup>16–18</sup> herein we describe the use of the 4,6-dimethylnicotinonitrile-2-thiol (**1**) for the synthesis of thiopyranopyridine heterocyclic ring systems (Schemes 1–3) to investigate their antitumor activities. In addition, we were able to perform the iodine labeling of the new compound **5** using NBS as an oxidizing agent and examined the factors affecting the labeling yield. Bio-distribution of the labeled compound in normal and ascites bearing mice was also studied.

## 2. Experimental

### 2.1. Synthesis Procedures of the New Compounds

All melting points are uncorrected and were determined on Gallenkamp electric melting point device. The completion of the reactions and the purity of the compounds were determined by TLC on silica gel pre-coated aluminum sheets (Type 60 F254, Merck, Darmstadt, Germany) and spots were visualized under UV light (254 nm). The infrared (IR) spectra were recorded on a Jasco 4100 FTIR spectrophotometer as KBr discs ( $\nu_{\max}$  in  $\text{cm}^{-1}$ ).  $^1\text{H}$  NMR spectra were recorded on a Bruker Avance 400 spectrometer operating at 400 MHz and  $^{13}\text{C}$  NMR spectra on the same instrument at 75 MHz. Deuterated DMSO- $d_6$  was used as the solvent, tetramethylsilane (TMS) was used as the internal standard and chemical shifts were measured on  $\delta$  scale, given in ppm. The mass spectra were recorded on a Shimadzu GCMS-QP 1000 EX mass spectrometer at 70 eV. Elemental analyses were performed on Perkin-Elmer 2400 elemental analyzer at the Micro-analytical Center at Cairo University, Cairo, Egypt.

#### *Synthetic Procedure for Ethyl 3-(3-Cyano-4,6-dimethylpyridin-2-ylthio)propanoate (2)*

A mixture of compound **1** (3.28 g, 0.02 mol), ethyl bromopropanoate (3.6 g, 0.02 mol) and sodium carbonate (2.12 g, 0.02 mol) in DMF (50 mL) was heated under reflux with stirring for 4 h. The mixture was left to cool to room temperature, poured into water (50 mL), extracted with dichloromethane ( $3 \times 50$  mL). The organic layer was dried over anhydrous sodium sulfate, filtered off, and the solvent was stripped under vacuum. The precipitate formed was dried and recrystallized from methanol to give compound **2** (4.2 g, 80%).

White powder; mp 77–78 °C; IR (KBr):  $\nu/\text{cm}^{-1}$  2215.81 (CN); 1727.91 (CO, ester);  $^1\text{H}$  NMR (400 MHz, DMSO- $d_6$ )  $\delta$  (ppm) 1.29 (t, 3H,  $\text{CH}_3$ -ester), 2.50 (s, 3H,  $\text{CH}_3$ -4), 2.53 (s, 3H,  $\text{CH}_3$ -6), 2.82 (t, 2H,  $\text{CH}_2$ -CO), 3.50 (t, 2H,  $\text{CH}_2$ -S), 4.18 (q, 2H  $\text{CH}_2$ -O, ester), 6.85 (s, 1H,  $\text{C}_5$ -H pyridine);  $^{13}\text{C}$  NMR (75 MHz, DMSO- $d_6$ )  $\delta$  (ppm) 14.43, 20.35, 25.44, 25.94, 34.65, 60.95, 108.09, 115.71, 120.74, 152.15, 161.61, 161.62, 172.03; MS (EI, 70 eV)  $m/z$  = 264( $\text{M}^+$ ). Anal. Calcd for  $\text{C}_{13}\text{H}_{16}\text{N}_2\text{O}_2\text{S}$  (264.09): C, 59.07; H, 6.10; N, 10.60. Found: C, 60.54; H, 6.19; N, 10.75.

#### *Synthetic Procedure for Ethyl 3,4-Dihydro-5,7-dimethyl-4-oxo-2H-thiopyrano[2,3-b]pyridine-3-carboxylate (3)*

A solution of **2** (2.64 g, 0.01 mol) in THF (25 mL) was added dropwise to sodium hydride (1.2 g, 60%, 0.03 mol) in THF (50 mL) during 30 min with stirring under nitrogen at room temperature. The reaction mixture was heated under reflux for 6 h and left to cool to room temperature. After cooling in an ice bath, absolute ethanol (10 mL) was dropwise added and then cold water (50 mL). Af-

ter neutralization, to the mixture diluted HCl (50 %) was added, it was extracted with dichloromethane ( $3 \times 50$  mL). The organic layer was dried over anhydrous sodium sulfate, filtered off and the solvent was removed in vacuum. The solid residue was triturated with water and the precipitate formed was filtered, dried and recrystallized from ethanol to give title compound **3** (1.9 g, 72%).

Yellowish powder; mp 80–81 °C; IR (KBr):  $\nu/\text{cm}^{-1}$  1714.3 and 1666.2 ( $2 \times \text{C}=\text{O}$ ).  $^1\text{H}$  NMR (400 MHz, DMSO- $d_6$ )  $\delta$  (ppm) 1.30 (t, 3H,  $\text{CH}_3$ - ester), 2.52 (s, 3H,  $\text{CH}_3$ -5), 2.58 (s, 3H,  $\text{CH}_3$ -7), 2.78 (d, 2H,  $\text{CH}_2$ -2), 4.28 (q, 2H,  $\text{CH}_2$ -ester), 5.41 (br., 1H,  $\text{C}_3$ -H), 7.19 (s, 1H,  $\text{C}_6$ -H);  $^{13}\text{C}$  NMR (75 MHz, DMSO- $d_6$ )  $\delta$  (ppm) 14.29, 20.02, 22.48, 38.81, 40.06, 60.12, 122.26, 123.30, 147.66, 149.56, 157.25, 158.02, 164.50; MS (EI, 70 eV)  $m/z$  = 265( $\text{M}^+$ ). Anal. Calcd for  $\text{C}_{13}\text{H}_{15}\text{NO}_3\text{S}$  (265.11): C, 58.85; H, 5.70; N, 5.28. Found: C, 58.18; H, 5.32; N, 5.22.

#### *Synthetic Procedure for 2,3-Dihydro-5,7-dimethylthiopyrano[2,3-b]pyridin-4-one (4)*

A solution of  $\beta$ -ketoester **3** (1.25 g, 0.005 mol) in acetic acid (20 mL) and conc. HCl (10 mL) was heated under reflux for 4 h. After cooling to room temperature, the mixture was poured into cold water and solid formed was filtered off. This solid was left to dry and recrystallized from methanol to give the pure product **4** (0.7 g, 80%).

White powder; mp 95–96 °C; IR (KBr):  $\nu/\text{cm}^{-1}$  1666.8 (CO).  $^1\text{H}$  NMR (400 MHz, DMSO- $d_6$ )  $\delta$  (ppm) 2.51(s, 3H,  $\text{CH}_3$ -3), 2.53 (s, 3H,  $\text{CH}_3$ -7), 3.33 (t, 2H,  $\text{CH}_2$ -2), 3.01 (t, 2H,  $\text{CH}_2$ -3), 7.11 (s, 1H,  $\text{C}_6$ -H pyridine);  $^{13}\text{C}$  NMR (75 MHz, DMSO- $d_6$ )  $\delta$  (ppm) 19.00, 23.29, 24.99, 40.01, 118.91, 128.02, 145.01, 158.34, 161.99, 195.10; MS (EI, 70 eV)  $m/z$  = 193( $\text{M}^+$ ). Anal. Calcd for  $\text{C}_{10}\text{H}_{11}\text{NOS}$  (193.06): C, 62.15; H, 5.74; N, 7.25. Found: C, 62.10; H, 5.79; N, 7.28.

#### *Synthetic Procedure for Ethyl 2-(3,4-Dihydro-5,7-dimethyl-4-oxo-2H-thiopyrano[2,3-b]pyridin-3-yl)-2-oxoacetate (5)*

A mixture of thiopyranopyridin-4-one **4** (1.93 g, 0.01 mol) with diethyl oxalate (1 mL) in ethanol (20 mL) in the presence of sodium ethoxide was heated with stirring for 3 h. After cooling, the reaction mixture was poured into ice-cold water, acidified with dil. HCl. The formed precipitate was filtered off, dried and recrystallized from aqueous ethanol to give compound **5** (2.37 g, 81%).

White powder; mp 99–100 °C; IR (KBr):  $\nu/\text{cm}^{-1}$  1714.3 and 1666.2 (CO);  $^1\text{H}$  NMR (400 MHz, DMSO- $d_6$ )  $\delta$  (ppm) 1.29 (t, 3H,  $\text{CH}_3$ -ester), 2.52 (s, 3H,  $\text{CH}_3$ -5), 2.58 (s, 3H,  $\text{CH}_3$ -7), 2.78 (s, 2H,  $\text{CH}_2$ -2), 4.29 (2H, q,  $\text{CH}_2$ , ester), 5.41 (br., 1H,  $\text{C}_3$ -H), 7.19 (H, s,  $\text{CH}$ -6);  $^{13}\text{C}$  NMR (75 MHz, DMSO- $d_6$ )  $\delta$  (ppm) 14.29, 20.03, 22.48, 60.13, 38.81, 94.12, 122.26, 123.30, 147.66, 149.56, 157.25, 158.02, 164.51; MS (EI, 70 eV)  $m/z$  = 293 ( $\text{M}^+$ ). Anal. Calcd for  $\text{C}_{14}\text{H}_{15}\text{NO}_4\text{S}$  (293.07): C, 57.32; H, 5.15; N, 4.77. Found: C, 57.39; H, 5.22; N, 4.70.

**Synthetic Procedure for 5',7'-Dimethyl-2,3'-dihydro-spiro[imidazolidine-4,4'-thiopyrano[2,3-b]pyridine]-2,5-dione (6)**

A mixture of compound 4 (1.93 g, 0.01 mol), potassium cyanide (0.975 g, 0.015 mol) and ammonium carbonate (0.5 g) was dissolved in 30 mL of water – ethanol (2:1) solution. The reaction mixture was heated under reflux at 60 °C for 48 h. The reaction mixture was kept in refrigerator overnight. The formed precipitate was filtered off, dried and recrystallized from aqueous ethanol to give compound 6 (2.26 g, 86%).

White powder; mp 91–92 °C; IR (KBr):  $\nu/\text{cm}^{-1}$  3414.3 (NH) and 1666.2 (CO);  $^1\text{H}$  NMR (400 MHz, DMSO- $d_6$ )  $\delta$  (ppm) 2.42 (s, 3H, CH<sub>3</sub>-5'), 2.50 (s, 3H, CH<sub>3</sub>-7'), 2.99 (t, 2H, CH<sub>2</sub>-3'), 3.50 (t, 2H, CH<sub>2</sub>-2'), 6.69 (s, 1H, NH-3), 7.15 (s, 1H, CH-6'), 13.80 (s, 1H, NH-1);  $^{13}\text{C}$  NMR (75 MHz, DMSO- $d_6$ )  $\delta$  (ppm) 17.57, 18.73, 19.58, 25.08, 104.13, 116.15, 120.69, 152.49, 156.75, 159.26, 161.61, and 177.42; MS (EI, 70 eV)  $m/z$  = 263 ( $\text{M}^+$ ). Anal. Calcd for C<sub>12</sub>H<sub>13</sub>N<sub>3</sub>O<sub>2</sub>S (263.07): C, 54.74; H, 4.98; N, 15.96. Found: C, 54.70; H, 4.91; N, 15.90.

**Synthetic Procedure for (Z)-3-((Dimethylamino)methylene)-2,3-dihydro-5,7-dimethylthiopyrano[2,3-b]pyridine-4-one (7)**

A mixture of precursor 4 (1.93 g, 0.01 mol) with DMFDMA (1 mL) in dioxane (20 mL) in the presence of freshly prepared sodium ethoxide (0.23 g in 0.66 mL of absolute ethanol) was heated with stirring for 3 h. After cooling to room temperature, the reaction mixture was poured into ice-cold water then the formed precipitate was filtered off, dried and recrystallized from aqueous ethanol to give compound 7 (1.9 g, 77%).

White powder; mp 76–77 °C; IR (KBr):  $\nu/\text{cm}^{-1}$  1666.2 (CO).  $^1\text{H}$  NMR (400 MHz, DMSO- $d_6$ )  $\delta$  (ppm) 2.41 (s, 3H, CH<sub>3</sub>), 2.54 (s, 3H, CH<sub>3</sub>), 3.23 (m, 6H, N(CH<sub>3</sub>)<sub>2</sub>), 3.28 (s, 2H, CH<sub>2</sub>-2), 6.41 (s, 1H, CH-6), 7.27 (s, 1H, =CH);  $^{13}\text{C}$  NMR (75 MHz, DMSO- $d_6$ )  $\delta$  (ppm) 17.59, 24.07, 43.55, 28.9, 111.73, 181.16, 120.43, 125.30, 142.48, 160.48, 162.95; MS (EI, 70 eV)  $m/z$  = 248 ( $\text{M}^+$ ). Anal. Calcd for C<sub>13</sub>H<sub>16</sub>N<sub>2</sub>OS (248.10): C, 62.87; H, 6.49; N, 11.28. Found: C, 62.80; H, 6.42; N, 11.23.

**Synthetic Procedure for (Z)-3-(Ethoxymethylene)-2,3-dihydro-5,7-dimethylthiopyrano[2,3-b]pyridine-4-one (8)**

A mixture of compound 4 (1.93 g, 0.01 mol) with triethyl orthoformate (1 mL) in DMF (20 mL) was heated with stirring for 3 h in the presence of piperidine as the catalyst. The reaction mixture was left overnight at room temperature, poured into ice-cold water and acidified with dil. HCl. The formed precipitate was filtered off, dried and recrystallized from aqueous ethanol to give compound 8 (1.69 g, 68%).

Yellow powder; mp 86–87 °C; IR (KBr):  $\nu/\text{cm}^{-1}$  1714.3 (CO- ester) and 1666.2 (CO).  $^1\text{H}$  NMR (400 MHz, DMSO- $d_6$ )  $\delta$  (ppm) 1.23 (t, 3H, CH<sub>3</sub>- ester), 2.52 (m, 6H,

2CH<sub>3</sub>), 3.65 (s, 2H, S-CH<sub>2</sub>), 4.11 (q, 2H, CH<sub>2</sub>- ester), 6.51 (s, 1H, O-CH), 6.93 (s, 1H, pyridyl);  $^{13}\text{C}$  NMR (75 MHz, DMSO- $d_6$ )  $\delta$  (ppm) 15.39, 17.86, 23.04, 26.54, 62.83, 107.21, 120.69, 126.11, 142.45, 160.92, 163.02, 162.7, 179.85; MS (EI, 70 eV)  $m/z$  = 249 ( $\text{M}^+$ ). Anal. Calcd for C<sub>13</sub>H<sub>15</sub>NO<sub>2</sub>S (249.08): C, 62.62; H, 6.06; N, 5.62. Found: C, 62.68; H, 6.01; N, 5.67.

**Synthetic Procedure for 2,7,9-Trimethyl-2,4-dihdropyr-azolo[3',4':4,5]thiopyrano[2,3-b]pyridine (9)**

A mixture of 7 (2.48 g, 0.01 mol) and/or 8 (2.49 g, 0.01 mol) with methylhydrazine (0.46g, 2 mL, 0.01 mol) in DMF (20 mL) was stirred for 1 h. The reaction mixture was heated under reflux for 4 h. The reaction mixture was left to cool to room temperature and poured into ice-cold water. The formed precipitate was filtered off, dried and recrystallized from ethanol to give compound 9 (1.57 g, 68%).

Yellow powder; mp 77–78 °C;  $^1\text{H}$  NMR (400 MHz, DMSO- $d_6$ )  $\delta$  (ppm) 2.53 (s, 3H, CH<sub>3</sub>-9), 2.58 (s, 3H, CH<sub>3</sub>-7), 3.87 (s, 3H, CH<sub>3</sub>-2), 4.29 (s, 2H, S-CH<sub>2</sub>), 6.56 (s, 1H, CH-8), 7.93 (s, 1H, CH-3);  $^{13}\text{C}$  NMR (75 MHz, DMSO- $d_6$ )  $\delta$  (ppm) 18.73, 21.54, 40.36, 23.69, 116.01, 118.10, 128.36, 131.10, 145.16, 156.00, 160.09; MS (EI, 70 eV)  $m/z$  = 231 ( $\text{M}^+$ ). Anal. Calcd for C<sub>12</sub>H<sub>13</sub>N<sub>3</sub>S (231.32): C, 62.31; H, 5.66; N, 18.17. Found: C, 62.39; H, 5.72; N, 18.11.

## 2. 2. Cytotoxic Activity

### 2. 2. 1. Determination of the Anticancer Activity

**Material and Method:** (i) MCF-7 (Breast Carcinoma Cell Line) (ii) HCT-116 (Colon Carcinoma Cell line).

#### Measurement of Potential Cytotoxicity:

The potential cytotoxicity of the tested compounds was evaluated using the MTT assay. The cell lines were plated in 96-multiwell plates (10<sup>4</sup> cells/well) for 24 h before treatment with the prepared compounds to allow the attachment of cells to the wall of the plate. The tested compounds were dissolved in dimethyl sulphoxide (DMSO) and diluted 1000-fold in the assay. Different concentrations of the tested compound were added to the cell monolayer; triplicate wells were prepared for each individual dose. Monolayer cells were incubated with the compounds for 48 h at 37 °C, in atmosphere of 5% CO<sub>2</sub>. After 48 h, cells were fixed, washed and stained for 30 min with 0.4% (wt/vol) Sulfo-Rhodamine-B stain (SRB). The excess stain was washed with 1% acetic acid and attached stain was recovered with Tris EDTA buffer. The color intensity was measured in an ELISA reader. The relation between cell viability and drug concentration was plotted to get the survival curve of tumor cell line and the IC<sub>50</sub> was calculated. The relation between cell viability, inhibitory effect and drug concentration is shown in Tables 1 and 2.

### 2. 2. 2. The Cytotoxicity of $^{125}\text{I}$ -Compound 5 (Synthesis of $^{125}\text{I}$ -TP<sub>5</sub>)

**Materials.** NBS (*N*-bromosuccinimide) used as oxidizing agent, Aldrich chemical company, Germany. Sodium metabisulfite ( $\text{Na}_2\text{S}_2\text{O}_5$ ): molar mass 190.107 g/mol, The British drug house (BDH) LTD, England. Chloroform ( $\text{CHCl}_3$ ): molar mass 119.38 g/mol, Merck, Darmstadt, Germany. Sodium chloride ( $\text{NaCl}$ ): molar mass 58.44 g/mol, Adwic, Egypt. Ammonium hydroxide ( $\text{NH}_4\text{OH}$ ): 98%, Riedel-De Haen Ag., Seelze (Germany). Ethanol (97%) the British Drug House (BDH) Chemicals LTD, England.

**Animals.** Female Swiss Albino mice weighing 20–25 g were purchased from the Institute of Eye Research, Cairo, Egypt. The environmental and nutritional conditions were kept constant throughout the experimental period. The mice were kept at room temperature ( $22 \pm 2^\circ\text{C}$ ) with a 12 h on/off light schedule. Female mice were used in this study because their susceptibility to Ehrlich ascites carcinoma was higher than that of the male mice.<sup>19</sup> Animals were kept with free access to food and water throughout the experiment.

**EAC:** (Ehrlich ascites carcinoma) cells were obtained from Egyptian national cancer institute, Cairo University. The line was transplanted in mice by intraperitoneal injection of cells derived EAC bearing mice after 10 days post inoculation. The cells were injected intraperitoneally to produce ascites (liquid tumor) in the peritoneal cavity and intramuscularly in the right leg to produce solid tumor and leaving the left leg as control.<sup>20</sup>

**Radioactive Materials:** Sodium iodide ( $\text{Na}^{125}\text{I}$ ) was delivered from Institute of Isotopes Co., Ltd as a carrier free and reluctant free solution, Budapest, Hungary.

**Synthetic Procedure for Labeling of Compound 5 (TP<sub>5</sub>) Using  $\text{Na}^{125}\text{I}$ .** The  $^{125}\text{I}$ -TP<sub>5</sub> was synthesized according to the following procedure: 200  $\mu\text{L}$  of compound 5 solution (1 mg in 1 mL ethanol) in amber colored V-shaped bottom reaction vial. Then, 100  $\mu\text{L}$  of freshly prepared NBS solution (1 mg in 1 mL ethanol) was added. Then, 10  $\mu\text{L}$  of  $^{125}\text{I}$  (3.7 MBq) was added to the reaction mixture. The pH of the reaction mixture was adjusted to pH 3. The reaction mixture was shaken by electric vortex and left at ambient temperature ( $25 \pm 1^\circ\text{C}$ ) for 15 min, after that 20  $\mu\text{L}$  of saturated sodium metabisulfite solution (30 mg/mL,  $\text{H}_2\text{O}$  w/v) was added to inhibit the oxidation of the radioiodide.<sup>21</sup>

**Ascending Paper Chromatography:** On Whatman paper No. 1 sheet (1.5 cm width and 14 cm length), 2  $\mu\text{L}$  of the reaction mixture was placed 2.5 cm above the lower edge. For development a fresh mixture of solvent (chloroform, methanol) in a ratio of 9:1 (v/v) was used as the mobile phase. After complete development, the paper sheet was removed, dried and cut into strips. Each strip (1 cm width) was counted in a well type  $\gamma$ -counter where radio iodide ( $\text{I}^-$ ) remained near the origin ( $R_f = 0-0.1$ ), while the  $^{125}\text{I}$ -TP<sub>5</sub> moved with the solvent front ( $R_f = 0.8$ ).

**Paper Electrophoresis:** On Whatman No. 1 paper sheet (1.5 cm width and 48 cm length), 1–2  $\mu\text{L}$  of the reaction mixture was placed 10 cm away from the cathode. Electrophoresis was carried out for 1.5 h at voltage of 300 V using phosphate buffer (0.5 M) as electrolytes source solution. After complete development, the paper was removed, dried, and cut into strips. Each strip (1 cm width) was counted in a well type  $\gamma$ -counter.<sup>22</sup> Free radioiodide and  $^{125}\text{I}$ -TP<sub>5</sub> moved to different distances away from the spotting point towards the anode depending on the charge and the molecular weight of each one (distance from spotting point = 14 and 2 cm, respectively) as shown in Figure 1.

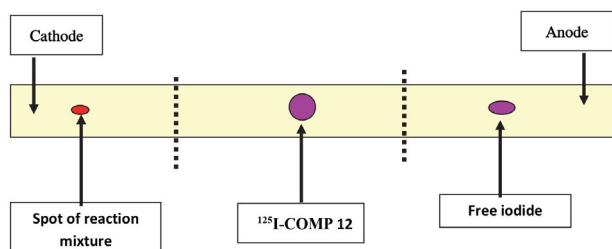


Figure 1: Paper electrophoresis for  $^{125}\text{I}$ -TP<sub>5</sub> and free iodide.

#### Factors Affecting the Labeling Yield:

**In-vitro Stability of the  $^{125}\text{I}$ -TP<sub>5</sub>.** The reaction mixture was prepared at the conditions, which gave the highest radiochemical yield. The mixture was left at ambient temperature and 1–2  $\mu\text{L}$  samples were taken at different time intervals ranged from 1 up to 24 h. Paper chromatography and electrophoresis was used to determine the *in vitro* stability of the labeled  $^{125}\text{I}$ -TP<sub>5</sub>.

**Bio-Distribution Study: Tumor Transplantation in Mice.** Ehrlich ascites carcinoma cells (EAC) were one of the excellent models for studying the biological behavior of malignant tumors and drugs assumed to produce effect at these sites. A line of EAC cells was maintained in female Swiss albino mice through weekly IP transplantation of  $2.0 \times 10^6$  tumor cells per mouse. EAC cells were obtained by needle aspiration with aseptic condition. The ascetic fluid was diluted with sterile saline so that 0.1 mL contained  $2.0 \times 10^6$  cells counted microscopically using a haemocytometer. Thus, 0.2 mL solution was then injected intraperitoneally to produce ascites and intramuscularly in the right thigh to produce solid tumor.<sup>23</sup>

**General Procedure for Bio-Distribution of the  $^{125}\text{I}$ -TP<sub>5</sub> in Ascites Bearing Mice.** This experiment was carried out using 24 ascites bearing mice. The mice were injected with 0.2 mL (70 KBq)  $^{125}\text{I}$ -TP<sub>5</sub> in the tail vein and then divided to 4 groups, 6 mice each. The mice were kept in metabolic cages for the recommended times (15, 30, 60 or 180 min) after injection of labeled drug. Mice were sacrificed by cervical dislocation at various time intervals. Organs and tissues of interest were removed, weighted and counted for its uptake of activity. The counting tubes con-



tained a standard equivalent to 100% percent of the injected dose, were assayed in gamma counter and the results were calculated as percentages of injected dose (ID) per gram tissue or organ.<sup>24</sup> The weights of blood, bone and muscles were assumed to be 7, 10 and 40 percent of the total body weight, respectively. Ascites were withdrawn using 20 cm plastic syringe, collected, weighted and counted.

**General Procedure for Bio-Distribution of the <sup>125</sup>I-TP<sub>5</sub> in Solid Tumor Bearing Mice.** This experiment was carried out using 24 solid tumor bearing mice. Same procedures were done as in ascites bearing mice. In addition tumor muscle was removed and counted for its uptake of activity and compared with that of normal muscle.

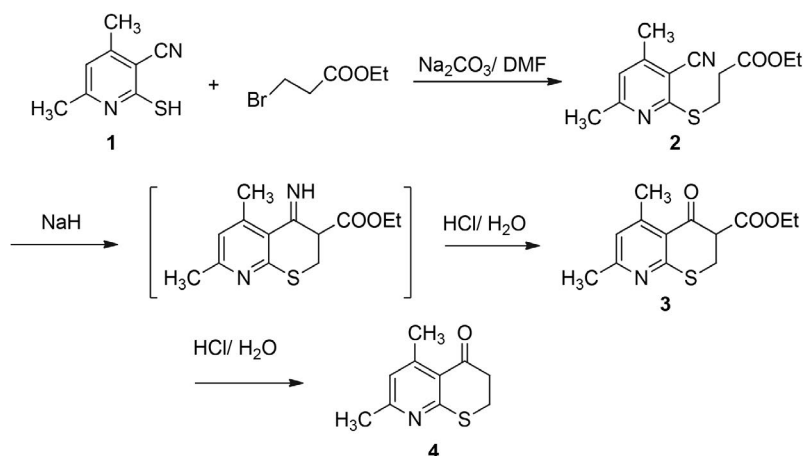
### 3. Result and Discussion

#### 3. 1. Chemistry

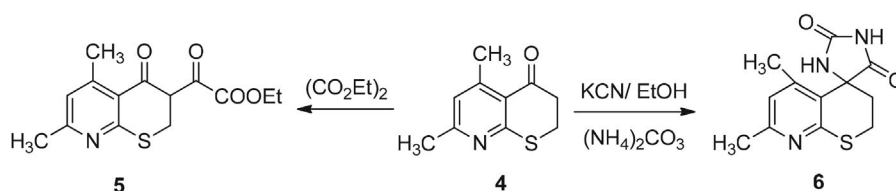
The key step in this trial to explore an anticancer drug is the synthesis of 5,7-dimethyl-4-oxothiopyrano[3,4-*b*]pyridine (**4**) from 2-mercapto-4,6-dimethylnicotinitrile (**1**). Thus, refluxing of the starting material **1** with ethyl 3-bromopropionate in DMF as a solvent and sodium carbonate afforded the *S*-alkylated derivative **2**. The IR spectrum of **2** revealed the presence of the absorption bands for CN and ester's CO functional groups at 2215.81 and 1727.91 cm<sup>-1</sup>, respectively. While its <sup>1</sup>H NMR indicated the presence of ethyl ester protons at  $\delta$  1.29 and 4.18 ppm and the propyl protons at  $\delta$  2.82 and 3.50 ppm. Cyclization of **2** by sodium hydride in tetrahydrofuran as a

solvent, followed by an acidic hydrolysis for the imine intermediate produced the corresponding thiopyrano[2,3-*b*]pyridine **3** in quantitative yield. The <sup>1</sup>H NMR spectrum data for compound **3** declared the presence of ethyl ester protons at  $\delta$  1.30 and 4.28 ppm. Its IR spectrum also showed the presence of the absorption bands due to the ester and cyclic ketonic carbonyl groups at 1714.3 and 1666.2 cm<sup>-1</sup>, respectively. The acidic hydrolysis of **3** led to the formation of the cyclic ketone **4** as a target precursor to synthesize the new thiopyranopyridines of pharmaceutical interest. The IR spectrum of **4** indicated the disappearance of the ester's CO group, while <sup>1</sup>H NMR showed the absence of ester's ethyl group and appearance of the signal of protons of CH<sub>2</sub>-3 group at  $\delta$  3.01 ppm (Scheme 1).

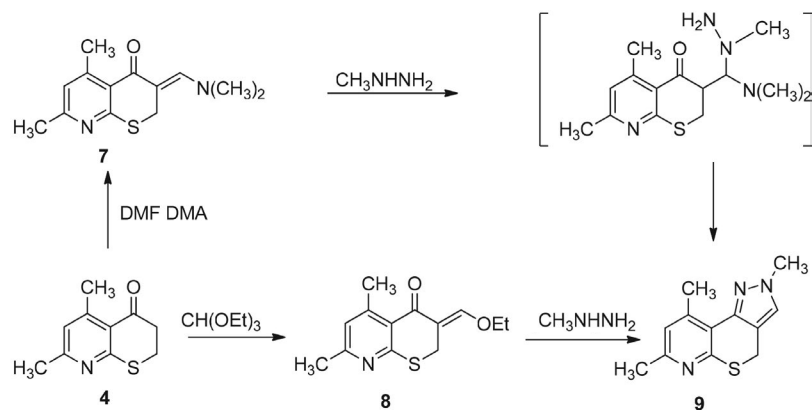
In turn, the precursor **4** was treated with diethyl oxalate under Claisen reaction conditions to produce the corresponding ethyl 4-oxothiopyranopyridine derivative **5**. The IR spectrum indicated the absorption band of the oxalo-carbonyls at 1714.3 cm<sup>-1</sup> as a broad band and <sup>1</sup>H NMR spectrum revealed the signals of the ethyl protons at  $\delta$  1.29 and 4.29 ppm. Also, the compound **4** was reacted with potassium cyanide and ammonium carbonate in ethanol under standard conditions of Bucherer–Berger reaction to get the 5,7'-dimethyl-2,3'-dihydrospiro[imidazolidine-4,4'-thiopyrano[2,3-*b*]pyridine]-2,5-dione (**6**). The IR spectrum of **6** revealed the presence of the absorption bands of NH and CO groups at 3414.3 and 1666.2 cm<sup>-1</sup>. Its <sup>1</sup>H NMR spectrum indicated the presence of the protons signals of the two NH groups at  $\delta$  6.69 and 13.80 ppm (Scheme 2).



Scheme 1. Synthesis of compounds **2**, **3** and **4**.



Scheme 2. Synthesis of compounds **5** and **6**.



Scheme 3. Synthesis of compounds 7–9.

The pyrazolothienopyrano[2,3-*b*]pyridine **9** was obtained by reacting 3-dimethylaminomethylene-2,3-dihydro-5,7-dimethylthiopyrano[2,3-*b*]pyridine-4-one (**7**) or 3-ethoxymethylene-2,3-dihydro-5,7-dimethylthiopyrano[2,3-*b*]pyridine-4-one (**8**) with methylhydrazine in ethanol. The enamine **7** and the enether **8** were synthesized by condensing the precursor **4** with DMFDMA in dioxane and/or triethyl orthoformate in DMF, respectively. The structure elucidation was based on elemental analysis and spectral data. The  $^1\text{H}$  NMR spectrum of **9** revealed singlet signals of the protons of the  $\text{CH}_2$ -4 group at  $\delta$  4.20 ppm and  $\text{CH}$ -3 proton at  $\delta$  8.97 ppm, in addition to the three methyl groups at  $\delta$  2.53, 2.58 and 3.87 ppm. Formation of **9** takes place *via* the initial addition of the most nucleophilic NH of the methylhydrazine to exocyclic enamine moiety of **7** followed by elimination of dimethyl amine and water molecules<sup>15</sup> (Scheme 3).

### 3. 2. Cytotoxicity Evaluation against the MCF-7 and HCT-116 Cell Lines

Three selected new compounds **5**, **6** and **8** were tested for cytotoxic activity against the MCF-7 (Breast Carci-

noma Cell Line) and HCT-116 (Colon Carcinoma Cell line) in the Regional Centre for Mycology and Biotechnology, Al-Azher University (Egypt). All new compounds tested were dissolved in DMSO in different concentrations (Tables 1 and 2).

The compound **5** showed a dramatic inhibitory effect on the growth of MCF-7 cell line and  $\text{IC}_{50}$  was  $3.45 \pm 0.2$   $\mu\text{g/mL}$ . Such inhibitory effect was a dose-dependent manner. The same effect was reported when such compound was tested for its ability to inhibit the growth of HCT-116 cell line with  $\text{IC}_{50}$   $13.2 \pm 0.9$   $\mu\text{g/mL}$ . The compound **6** displayed moderately potent toxicity against both MCF-7 and HCT-116 cell lines. Its  $\text{IC}_{50}$  values were  $29.43 \pm 1.1$  and  $44.1 \pm 1.8$   $\mu\text{g/mL}$ , respectively. The inhibitory activities of compound **8** against MCF-7 and HCT-116 cell lines were detected under the experimental conditions with  $\text{IC}_{50}$   $235 \pm 8.9$  and  $\text{IC}_{50}$   $305 \pm 9.2$   $\mu\text{g/mL}$ , respectively and showed low potent toxicity against the two cell lines.

The data indicated to the fact that the compound **5** with potent inhibitory activity in tumor growth inhibition would be a potential anticancer agent. The compound **6** has more potent toxicity against both MCF-7 and

Table 1. Cytotoxic activity against the MCF-7 of tested compounds

Sample Conc. ( $\mu\text{g/mL}$ )	Compound 5			Compound 6			Compound 8		
	Viability %	Inhibitory %	S.D. ( $\pm$ )	Viability %	Inhibitory %	S.D. ( $\pm$ )	Viability %	Inhibitory %	S.D. ( $\pm$ )
500	3.78	96.22	0.16	5.94	94.06	0.28	31.93	68.07	0.95
250	6.32	93.68	0.06	11.73	88.27	0.19	46.28	53.72	1.86
125	10.86	89.32	0.11	20.46	79.54	0.74	78.14	21.86	2.35
62.5	16.41	83.59	0.38	32.89	67.11	0.98	92.36	7.64	0.72
31.25	23.89	76.11	0.26	47.28	52.72	2.34	99.43	0.57	0.14
15.6	30.75	69.25	0.13	69.41	30.59	1.85	100	0	0
7.8	39.43	60.57	0.61	88.75	11.25	0.61	100	0	0
3.9	46.92	53.08	0.89	98.03	1.97	0.15	100	0	0
2	58.17	41.83	1.24	100	0	0	100	0	0
1	74.89	25.11	0.53	100	0	0	100	0	0
0	100	0	0	100	0	0	100	0	0

Inhibitory activity against Breast carcinoma cells was detected under the experimental conditions with  $\text{IC}_{50}$  of compound **5** =  $3.45 \pm 0.2$ ;  $\text{IC}_{50}$  of compound **6** =  $29.3 \pm 1.1$ ;  $\text{IC}_{50}$  of compound **8** =  $235 \pm 8.9$   $\mu\text{g/mL}$ .

**Table 2.** Cytotoxic activity against the HCT-116 of tested compounds

Sample Conc. (µg/mL)	Compound 5			Compound 6			Compound 8		
	Viability %	Inhibitory %	S.D. (±)	Viability %	Inhibitory %	S.D. (±)	Viability %	Inhibitory %	S.D. (±)
500	4.86	95.14	0.21	7.43	92.57	0.31	38.60	61.4	2.32
250	8.97	91.03	0.39	14.68	85.32	0.76	53.19	46.81	0.97
125	13.45	86.55	0.43	28.12	71.88	0.45	80.72	19.28	0.32
62.5	20.63	79.37	0.19	40.96	59.04	1.28	97.85	2.15	0.03
31.25	31.78	68.22	0.64	56.13	43.69	1.37	100	0	0
15.6	45.60	54.4	1.82	78.28	21.72	0.54	100	0	0
7.8	59.72	40.28	0.96	91.87	8.13	0.09	100	0	0
3.9	71.38	28.62	0.34	99.25	0.75	0.11	100	0	0
2	85.44	14.56	0.12	100	0	0	100	0	0
1	97.29	2.71	0.05	100	0	0	100	0	0
0	100	0	0	100	0	0	100	0	0

Inhibitory activity against Colon carcinoma cells was detected under the experimental conditions with  $IC_{50}$  of compound **5** =  $13.2 \pm 0.9$ ;  $IC_{50}$  of compound **6** =  $44.1 \pm 1.8$ ;  $IC_{50}$  of compound **8** =  $305 \pm 9.2$  µg/mL.

HCT-116 cell lines when compared to compound **8**. It seems appropriate to further study the compound **6** *in vivo* and *in vitro* using different cancer cell lines.

### 3. 3. The Cytotoxicity Evaluation of the Compound 5 (TP<sub>5</sub>) Labeled with <sup>125</sup>I (Synthesis of <sup>125</sup>I-TP<sub>5</sub>)

In the light of the above results of cytotoxicity of compounds **5**, **6** and **8** it was interesting for us to radiolabel the ethyl 2-(5,7-dimethyl-4-oxo-3,4-dihydro-2H-thiopyrano[2,3-*b*]pyridin-3-yl)-2-oxoacetate (**5**) and evaluate the cytotoxicity of the produced labeled compound against ascites tumor in mice to complete the aim of this study for exploring a new antitumor drug. Thus, the <sup>125</sup>I-compound **5** (<sup>125</sup>I-TP<sub>5</sub>) was synthesized by direct electrophilic substitution with Na<sup>125</sup>I under oxidative conditions in the presence of NBS. The radiochemical yield of <sup>125</sup>I-TP<sub>5</sub> was determined using paper chromatography and electrophoresis. The influence of different factors on the labeling yield, such as the substrate content, NBS content, pH, reaction time and reaction temperature must be determined. Each factor was optimized by the trial and error method. Bio-distribution of the <sup>125</sup>I-TP<sub>5</sub> in normal and ascites bearing mice was also studied.

#### Results of the Synthesis of <sup>125</sup>I-TP<sub>5</sub>

*Effect of substrate amount on the labeling yield of <sup>125</sup>I-TP<sub>5</sub>* using NBS as oxidizing agent at pH 3 was studied and the results are shown in Table 3. The results showed that the radiochemical yield of <sup>125</sup>I-TP<sub>5</sub> was low (45.5%) at small substrate amount (10 µg) and reached to maximum labeling value (87.9%) at 75 µg of compound **5**. At substrate amounts higher than the optimum amounts, the labeling yield reached plateau. This may be attributed to the fact that the yield reaches the saturation value because the entire generated iodonium ions [I<sup>+</sup>] in the reaction were captured at concentration of 0.5 mg.<sup>25</sup>

**Table 3.** Effect of TP<sub>5</sub> amount on the % labeling yield of <sup>125</sup>I-TP<sub>5</sub>

TP <sub>5</sub> (µg)	% Labeled compound	% Free iodide
10	45.5 ± 0.36*	54.5 ± 0.31
25	65.5 ± 0.6*	34.5 ± 0.6
50	75.1 ± 0.36*	24.9 ± 0.25
75	87.9 ± 0.40*	12.1 ± 0.35
100	87.5 ± 0.26*	12.5 ± 0.30
200	87.1 ± 0.40*	12.9 ± 0.35
500	86.7 ± 0.26*	13.3 ± 0.30

Values represent the mean ± SEM, *n* = 6 \* Significantly different from the initial values using unpaired student's t-test (*P* < 0.05) † Significantly different from the previous values using unpaired student's t-test (*P* < 0.05).

*Effect of the oxidizing agent amount* (Table 4). Radioiodination of compound **5** has been performed by using NBS as a mild oxidizing agent to transform iodide (I<sup>-</sup>) to iodonium ion (I<sup>+</sup>), which allows a spontaneous electrophilic substitution on aromatic ring.<sup>26</sup> At low NBS amount (5 µg), the radiochemical yield of <sup>125</sup>I-TP<sub>5</sub> was 53.5%. Low labeling yield was noted at a low NBS concentration apparently because of incomplete oxidation of iodide to iodonium ions.<sup>25</sup> A high radiochemical yield of 87.5% was achieved by increasing the amount of NBS to 50 µg. The

**Table 4.** Effect of NBS content on the radiochemical yield of <sup>125</sup>I-TP<sub>5</sub>

NBS (µg)	% Labeled compound	% Free iodide
5	53.5 ± 0.40	46.5 ± 0.3
10	78.1 ± 0.40	21.9 ± 0.3
25	82.2 ± 0.40*	17.8 ± 0.3
50	87.5 ± 0.50*†	12.5 ± 0.75
100	87.3 ± 0.04*	12.7 ± 0.06
200	81.2 ± 0.32*	18.8 ± 0.35

Values represent the mean ± SEM, *n* = 6 \* Significantly different from the initial values using student's t-test (*P* < 0.05). † Significantly different from the previous values using student's t-test (*P* < 0.05).

NBS amount above the maximum labeling value led to decrease in the radiochemical yield. This may be due to the formation of undesirable oxidative by-products *via* process such as bromination,<sup>27</sup> polymerization and denaturation of this compound. The formation of these impurities may be attributed to the reactivity and quantity of NBS.<sup>28</sup> Consequently, the use of optimum concentration of NBS is highly recommended in order to avoid the formation of by-products and to obtain high yield and purity.

**Effect of pH.** The nature of active oxidizing species of NBS depends on the pH of the medium and the reaction condition.<sup>29</sup> The influence of pH of the reaction mixture on the radiochemical yield of <sup>125</sup>I-TP<sub>5</sub> is shown in Table 5.

Table 5. Effect of pH on the radiochemical yield of <sup>125</sup>I-TP<sub>5</sub>

pH value	% Labeled compound	% Free iodide
1	25.2 ± 0.30*	74.8 ± 0.30*
2	80.2 ± 0.30*	19.5 ± 0.20
4	87.7 ± 0.44*†	12.3 ± 0.25
5	80.5 ± 0.20*†	19.5 ± 0.4
7	75.5 ± 0.20*†	24.5 ± 0.4

Values represent the mean ± SEM, *n* = 6 \* Significantly different from the initial values using unpaired student's t-test (*P* < 0.05) † Significantly different from the previous values using unpaired student's t-test (*P* < 0.05)

**Effect of reaction time.** The labeling yield is strongly dependent on reaction time in the range from 1 to 60 min.<sup>30</sup> It is clear from Table 6 that the radiochemical yield of <sup>125</sup>I-TP<sub>5</sub> is significantly increased by increasing the reaction time from 1 to 15 min, at which maximum radiochemical yield obtained (87.5%) and was constant till 15 min. Increasing the reaction time beyond 15 min caused slight decrease in the radiochemical yield and this may be due to exposing the substrate to highly reactive NBS for long reaction time which can result in oxidative side reactions.

Table 6. Effect of reaction time on the % labeling yield of <sup>125</sup>I-TP<sub>5</sub>

Time (min)	% Labeled compound	% Free iodide
1	75.5 ± 0.36	24.5 ± 0.55
5	80.5 ± 0.5*	19.5 ± 0.15
15	87.5 ± 0.3*	13.5 ± 0.2
30	84.7 ± 0.4*	15.3 ± 0.1
60	80.1 ± 0.25*	19.9 ± 0.15

Values represent the mean ± SEM, *n* = 6 \* Significantly different from the initial values using unpaired student's t-test (*P* < 0.05)

**In-vitro stability of <sup>125</sup>I-TP<sub>5</sub>.** It was observed that <sup>125</sup>I-TP<sub>5</sub> was stable for at least 3 h and the stability was decreased by time to reach 75.2% at 12 h post labeling (Table 7).

Table 7. In-vitro stability of <sup>125</sup>I-TP<sub>5</sub>

Time (h)	% Labeled compound	% Free iodide
1	85.5 ± 0.36	14.5 ± 0.55
3	85.1 ± 0.5*	14.9 ± 0.15
6	80.2 ± 0.3*	19.8 ± 0.2
12	75.2 ± 0.4*	24.8 ± 0.1

Values represent the mean ± SEM, *n* = 6 \* Significantly different from the initial values using unpaired student's t-test (*P* < 0.05)

Table 8. Effect of reaction temperature on the % labeling yield of <sup>125</sup>I-TP<sub>5</sub>

Temperature (°C)	% Labeled compound	% Free iodide
25	87.5 ± 0.36	12.5 ± 0.55
40	87.5 ± 0.5*	12.5 ± 0.15
50	87.5 ± 0.3*	12.5 ± 0.2
75	80.7 ± 0.4*	19.3 ± 0.1
80	65.1 ± 0.25*	34.9 ± 0.15

Values represent the mean ± SEM, *n* = 6 \* Significantly different from the initial values using unpaired student's t-test (*P* < 0.05)

Table 9. Biodistribution of <sup>125</sup>I-TP<sub>5</sub> in normal mice

Organs & Body fluids	% injected dose/gram tissue at different time intervals			
	15 min	30 min	60 min	180 min
Blood	18.0 ± 0.2	11.0 ± 0.5*	5.2 ± 0.3*	1.2 ± 0.03*
Bone	1.2 ± 0.05	2.1 ± 0.03*	3.2 ± 0.2*	0.9 ± 0.01*
Muscle	1.3 ± 0.04	2.3 ± 0.04*	2.7 ± 0.1	1.1 ± 0.09*
Liver	7.2 ± 0.3	9.8 ± 0.15*	14.2 ± 0.2*	3.7 ± 0.1
Stomach	2.3 ± 0.9	4.1 ± 0.4	3.1 ± 0.16*	1.1 ± 0.2*
Intestine	4.5 ± 0.50	6.2 ± 0.3*	2.7 ± 0.1*	2.2 ± 0.03*
Lung	1.2 ± 0.08	1.1 ± 0.12*	0.9 ± 0.2*	1.2 ± 0.01*
Heart	3.1 ± 0.1	2.9 ± 0.3*	1.2 ± 0.01*	0.3 ± 0.04*
Spleen	0.9 ± 0.01	1.1 ± 0.1*	1.2 ± 0.02	0.9 ± 0.05*
Kidney	4.2 ± 0.4	8.2 ± 0.6*	5.6 ± 0.3*	2.3 ± 0.06*
Thyroid	0.8 ± 0.4	1.2 ± 0.6*	2.7 ± 0.3*	5.9 ± 0.06*
Urine	8.9 ± 0.4	15.4 ± 0.6*	20.7 ± 0.3*	40.1 ± 0.06*

Values represent mean ± SEM. \* Means significantly differ from the previous each value using unpaired student's t-test (*P* < 0.05).

Table 10. Biodistribution of  $^{125}\text{I}$ -TP<sub>5</sub> in ascites bearing mice

Organs & Body fluids	% $^{125}\text{I}$ -TP <sub>5</sub> /gram organ Time post injection			
	15 min	30 min	60 min	180 min
Ascites	3.50 ± 0.4	5.7 ± 0.6*	7.6 ± 0.3*	5.8 ± 0.06*
Blood	16.1 ± 1.1	12.5 ± 0.2*	6.5 ± 0.04*	2.2 ± 0.3*
Bone	1.1 ± 0.05	1.2 ± 0.1*	0.9 ± 0.1*	0.3 ± 0.1*
Muscle	1.3 ± 0.01	2.3 ± 0.02*	1.7 ± 0.1	1.1 ± 0.02*
Liver	9.6 ± 0.05	11.8 ± 0.15*	10.42 ± 0.06*	3.9 ± 0.02
Stomach	3.5 ± 0.9	6.2 ± 0.6	9.1 ± 0.16*	2.3 ± 0.2*
Intestine	4.1 ± 0.50	8.2 ± 0.3*	6.3 ± 0.1*	2.1 ± 0.03*
Lung	1.2 ± 0.1	1.1 ± 0.12*	0.9 ± 0.2*	1.2 ± 0.01*
Heart	3.1 ± 0.8	2.1 ± 0.3*	1.7 ± 0.01*	0.9 ± 0.04*
Spleen	0.8 ± 0.3	0.9 ± 0.1*	0.7 ± 0.02	0.2 ± 0.05*
Kidney	6.1 ± 0.4	7.8 ± 0.6*	8.2 ± 0.3*	4.2 ± 0.06*
Thyroid	1.1 ± 0.4	2.3 ± 0.6*	3.1 ± 0.3*	4.1 ± 0.06*
Urine	4.3 ± 0.4	9.8 ± 0.6*	20.1 ± 0.3*	42.2 ± 0.06*

Values represent the mean ± SEM,  $n = 6$  \* Significantly different from the initial value of each organ using unpaired student's t-test ( $P < 0.05$ )

**Effect of reaction temperature.** The labeling yield was optimal (87.5%) at ambient temperature, 25 °C and decreased by increasing temperature and this may be due to the thermal decomposition of the  $^{125}\text{I}$ -TP<sub>5</sub>.<sup>31</sup>

**Biodistribution of  $^{125}\text{I}$ -TP<sub>5</sub> in normal mice.** As cleared from Table 9, biodistribution study in mice showed that  $^{125}\text{I}$ -TP<sub>5</sub> was distributed rapidly in blood, liver, intestine and kidney at 15 min post injection. After 30 min,  $^{125}\text{I}$ -TP<sub>5</sub> uptake was significantly decreased in organs like blood. However,  $^{125}\text{I}$ -TP<sub>5</sub> uptake was significantly increased in liver, kidney and intestine after 30 min. At 60 and 180 min post injection, the majority of tissues showed significant decrease in  $^{125}\text{I}$ -TP<sub>5</sub> uptake. Thyroid gland showed significant increase in  $^{125}\text{I}$ -TP<sub>5</sub> uptake at 6 and 180 min post injection.

#### Biodistribution of $^{125}\text{I}$ -TP<sub>5</sub> in ascites bearing mice.

The sites of greatest uptake of  $^{125}\text{I}$ -TP<sub>5</sub> after 15 min post injection were the blood, liver, kidney and intestine (16%, 9.6%, 6% and 4.1%), respectively. Table 10 shows that the accumulation of  $^{125}\text{I}$ -TP<sub>5</sub> was low in spleen, thyroid, bone and muscle at 15 min post injection. The uptake of  $^{125}\text{I}$ -TP<sub>5</sub> in ascetic fluid was rapidly taking place as each mL of ascetic fluid received 3.5% of total activity. The uptake of ascetic fluid/mL was significantly increased at 30 and 60 min and reached 5.7% and 7.6%, respectively. Thyroid uptake was increased by time post injection mainly due to *in vivo* deiodination of  $^{125}\text{I}$ -TP<sub>5</sub>.<sup>32</sup> Urine uptake of  $^{125}\text{I}$ -TP<sub>5</sub> increased with time, which confirms its excretion through renal pathway.

Table 11. Biodistribution of  $^{125}\text{I}$ -TP<sub>5</sub> in solid tumor bearing mice.

Organs & body fluids	Percent I.D./gram organ Time post injection			
	15 min	30 min	60 min	180 min
Blood	15.70 ± 1.10	12.02 ± 0.02*	7.9 ± 0.04*	4.95 ± 0.04*
Bone	0.70 ± 0.01	0.8 ± 0.01*	0.90 ± 0.01*	0.60 ± 0.01*
Control muscle	0.74 ± 0.01	0.8 ± 0.02*	0.560 ± 0.002	0.5 ± 0.002
Tumor muscle	1.50 ± 0.01	1.90 ± 0.02*	1.960 ± 0.002	1.75 ± 0.002
Liver	13.30 ± 0.5	19.20 ± 0.15*	12.50 ± 0.16*	4.90 ± 0.16*
Lung	2.20 ± 0.10	4.92 ± 0.12*	3.93 ± 0.02*	2.30 ± 0.02*
Heartw	6.05 ± 0.05	4.51 ± 0.05*	2.50 ± 0.01*	1.20 ± 0.01*
Stomachw	4.80 ± 0.09	6.51 ± 0.30	3.30 ± 0.16*	2.30 ± 0.16*
Intestine	3.5 ± 0.50	5.10 ± 0.30	6.10 ± 0.9*	3.10 ± 0.19*
Kidney (urine)	6.90 ± 0.40	12.04 ± 0.60	24.20 ± 0.30*	35.80 ± 0.30*
Spleen	0.90 ± 0.02	1.60 ± 0.04*	0.80 ± 0.02	0.50 ± 0.02
Normal leg	1.80 ± 0.02	3.60 ± 0.04*	3.40 ± 0.02	2.20 ± 0.02
Tumor leg	3.10 ± 0.40	8.04 ± 0.60	9.90 ± 0.30*	8.10 ± 0.30*

Values represent mean ± SEM,  $n = 6$  \* Means significantly differ from the previous each value using unpaired student's t-test ( $p \leq 0.05$ ).



**Biodistribution of  $^{125}\text{I}$ -TP<sub>5</sub> in solid tumor bearing mice.** Table 11 shows the biodistribution of  $^{125}\text{I}$ -TP<sub>5</sub> in important body organs and fluids in the solid tumor mice models at 15, 30, 60 and 180 min post injection. The amount of accumulated activity in left thigh tumor tissue was 3.1, 8.1, 9.9 and 8.1% at 15, 30, 60 and 180 min post injection, respectively. The maximum solid tumor uptake observed after 60 min post injection of  $^{125}\text{I}$ -TP<sub>5</sub>. Excretion of  $^{125}\text{I}$ -TP<sub>5</sub> goes mainly through the kidney. The compound has shown that the decline of  $^{125}\text{I}$ -TP<sub>5</sub> is slow from tumor site, which may be due to its interaction with DNA of tumor cells. These results showed that TP<sub>5</sub> may be potentially used as a radiopharmaceutical for tumor diagnosis when labeled with  $^{125}\text{I}$ .

## 4. Conclusions

Trying to get a new anticancer drug, the thiopyrano[2,3-*b*]pyridine derivatives **4–9** were prepared starting from 2-mercapto-4,6-dimethylnicotinonitrile (**1**). The cytotoxicity activity of compounds **5**, **6** and **8** was tested against MCF-7 and HCT-116 cell lines. The compound **5** showed dramatic effects against MCF-7 and HCT-116 cell lines, much better than **6** and **8**. The compound **5** with potent inhibitory activity in tumor growth inhibition would be a potential anticancer agent. The incorporation of an Auger emitter ( $^{125}\text{I}$ ) into a tumor site was achieved by labeling of the compound **5** (TP<sub>5</sub>) with  $^{125}\text{I}$ . The appropriate conditions for synthesis of  $^{125}\text{I}$ -TP<sub>5</sub> (87.5 % yield) are as follows: 75 µg of TP<sub>5</sub> as substrate, 50 µg of NBS as oxidizing agent, pH 4, room temperature, 15 min. High incorporation of  $^{125}\text{I}$ -TP<sub>5</sub> in tumor sites (ascites tumor) facilitates tumor imaging.  $^{125}\text{I}$ -TP<sub>5</sub> is convenient to transport  $^{125}\text{I}$  to the nucleus of tumor cells. The decline of  $^{125}\text{I}$ -TP<sub>5</sub> is slow from the tumor site and its excretion has been confirmed to go mainly through the renal pathway. The results showed that compound **5** (TP<sub>5</sub>) may be potentially used as a radiopharmaceutical for tumor diagnosis when labeled with  $^{125}\text{I}$ .

## 5. References

1. J. Y. Zhang, *Nat. Rev. Drug Discov.* **2002**, *1*, 101–102. DOI:10.1038/nrd726
2. G. S. Hassan, H. H. Kadry, S. M. Abou-Seri, M. M. Ali, A. E. E. Mahmoud, *Bioorg. Med. Chem.* **2011**, *19*, 6808–6817. DOI:10.1016/j.bmc.2011.09.036
3. A. T. Taher, H. H. Georgey, H. I. El-Subbagh, *Eur. J. Med. Chem.* **2012**, *47*, 445–451. DOI:10.1016/j.ejmech.2011.11.013
4. A. I. Carmen, M. Carlos, *Medicinal Chemistry of Anticancer Drugs*, 1st ed.; Elsevier: Amsterdam, The Netherlands, **2008**; pp. 1–8.
5. E. Borowski, M. M. Bontemps-Gracz, A. Piwkowska, *Acta Biochim. Pol.* **2005**, *52*, 609–627.
6. J.-K. Son, L. X. Zhao, A. Basnet, P. Thapa, R. Karki, Y. Na, Y. Jahng, T. C. Jeong, B.-S. Jeong, C.-S. Lee, E.-S. Lee *Eur. J. Med. Chem.* **2008**, *43*, 675–682. DOI:10.1016/j.ejmech.2007.05.002
7. A. G. Amr, M. M. Abdulla, *Bioorg. Med. Chem.* **2006**, *14*, 4341–4352. DOI:10.1016/j.bmc.2006.02.045
8. A. D. Settimo, A. M. Marini, G. Primofiore, F. D. Settimo, S. Salerno, C. L. Motta, G. Pardi, P. L. and Ferrarini, *J. Heterocycl. Chem.* **2000**, *37*, 379–382. DOI:10.1002/jhet.5570370224
9. P. L. Ferrarini, C. Mori, M. Badwanch, V. Galderone, R. Greco, C. Manera, A. Martinelli, P. Nieva, G. Saccomanni, *Eur. J. Med. Chem.* **2000**, *35*, 815. DOI:10.1016/S0223-5234(00)00173-2
10. T. Al. Nakibl, V. Bezjakl, M. J. Meeganz, *Eur. J. Med. Chem.* **1990**, *25*, 455–462. DOI:10.1016/0223-5234(90)90010-Z
11. D. Prithwiraj, B. Michel, L. Delphine, *Bioorg. Med. Chem.* **2010**, *18*, 2537–2548. DOI:10.1016/j.bmc.2010.02.041
12. K. Bimal, B. Indrani, F. Frederick, *Eur. J. Med. Chem.* **2010**, *45*, 846–848. DOI:10.1016/j.ejmech.2009.11.024
13. G. Damia, M. D'Incalci, *Eur. J. Cancer* **2009**, *45*, 2768–2781. DOI:10.1016/j.ejca.2009.08.008
14. Y. Zheng, Z. Ma, X. Zhang, N. Yang, G. Yang, *Int. J. Chem.* **2011**, *3(1)*, 42. DOI:10.5539/ijc.v3n1p42
15. K. M. Dawood, *J. Heterocycl. Chem.* **2005**, *42*, 211–225. DOI:10.1016/j.wavemoti.2005.02.002
16. M. A. Waly, I. I. EL-Hawary, W. S. Hamama, H. H. Zoorob, *J. Heterocycl. Chem.* **2013**, *50*, E12–E17. DOI:10.1002/jhet.1020
17. W. S. Hamama, M. A. Waly, I. I. EL-Hawary, H. H. Zoorob, *J. Heterocycl. Chem.* **2016**, *53*, 953–957. DOI:10.1002/jhet.1631
18. M. A. Waly, I. I. EL-Hawary, T. M. El-gogary, *Med. Chem. Res.* **2013**, *22*, 1674–1678. DOI:10.1007/s00044-012-0161-4
19. J. Mester, K. De Goeij, M. Sluysen, *Eur. J. Cancer*, **1996**, *32*, 1603. DOI:10.1016/0959-8049(96)00117-7
20. A. Abd El-Bary, A. M. Amin, A. El-Wetery, S. Saad, M. Shoukry, *Pharmacol. Pharm.* **2012**, *3*, 97–102. DOI:10.4236/pp.2012.31014
21. A. M. Amin, S. E. Soliman, H. A. El-Aziz, S. Abo-El Enein, *Int. J. Chem.*, **2014**, *6(1)*, 17–25. DOI:10.5539/ijc.v6n1p17
22. D. L. Bailey, D. W. Townsend, P. E. Valk, M. N. Maissey, “Positron Emission Tomography: Basic Sciences”. Secaucus, NJ: Springer-Verlag London. **2005**, *62(5)*, 779–784. DOI:10.1007/b136169
23. C. H. Cheng, C. F. Meares, D. A. Goodwin, In: “Application of nuclear and radiochemistry”, (R. M. Lambrecht, N. Morcos, Eds.), Pergamon, New York, **1983**, p. 103–114. DOI:10.1016/B978-0-08-027544-4.50016-2
24. K. M. El-Azony, *J. Radioanal. Nucl. Chem.* **2010**, *285*, 315–320. DOI:10.1007/s10967-010-0583-8
25. N. Greenwood, A. Earnshaw, *Origin of the elements, isotopes and atomic weighs. In: “Chemistry of the Elements”. Second Edition, Elsevier Ltd. Oxford, 1997*, pp: 1–20. DOI:10.1016/B978-0-08-030712-1.50004-1
26. K. M. El-Azony, A. A. El-Mohty, H. M. Killa, U. Seddik, S. I. Khater, *J. Labelled Comp. Radiopharm.*, **2009**, *52(1)*, 1–5. DOI:10.1002/jlcr.1556
27. I. T. Ibrahim, M. A. Motaleb, K. M. Attalah, *J. Radioanal. Nucl. Chem.* **2010**, *285*, 431–436. DOI:10.1007/s10967-010-0607-4

28. L. L. Johnson, L. Schofield, T. Donahay, P. J. Mastrofranceso, *J. Nucl. Med.* **2000**, 41(7), 1237–1243.
29. B. Johannsen, H. Spies: “Chemistry of Radiopharmacology of Technetium Complexes”, *Workshop on generator and cyclotron produced radiopharmaceuticals, Riyadh, Saudi Arabia*, Oct. **1991**, 13–31.
30. P. Krogsaard-Larsen, T. Liljefors, U. Madsen, Radiotracers: Synthesis and use in imaging. In: *Textbook of Drug Design and Discovery, Third Edition*, **2003**, 205–232.
31. M. A. Motaleb, M. T. El-Kolaly, H. M. Rashed, A. Abd El-Bary *J. Radioanal. Nucl. Chem.* **2012**, 292, 629–635.  
DOI:10.1007/s10967-011-1499-7
32. M. A. Motaleb, M. E. Moustapha, I. T. Ibrahim, *J. Radioanal. Nucl. Chem.* **2011**, 289(7), 239–245.  
DOI:10.1007/s10967-011-1069-z

## Povzetek

Iz nikotinonitrilnih derivatov **1** smo lahko sintetizirali nove tiopirano[2,3-*b*]piridine **4–9**. Citotoksično aktivnost izbranih spojin **5**, **6** in **8** smo testirali na celičnih linijah MCF-7 in HCT-116. Spojina **5** (TP<sub>5</sub>) je izkazala opazno inhibitorno aktivnost in je bila najbolj učinkovita, bolj kot spojini **6** in **8**. Spojina **5**, z močno inhibitorno aktivnostjo na rast tumorjev, bi lahko bila potencialna protirakava učinkovina. V luči naših rezultatov smo pripravili <sup>125</sup>I-radiooznačeno spojino **5** (<sup>125</sup>I-TP<sub>5</sub>) in preučili njeno citotoksičnost proti ascitnim tumorjem pri miših. Rezultati kažejo, da je spojina **5** (TP<sub>5</sub>) potencialno uporabna kot radiofarmacevtska spojina za diagonozo tumorjev, kadar je označena s <sup>125</sup>I.



Except when otherwise noted, articles in this journal are published under the terms and conditions of the Creative Commons Attribution 4.0 International License

Scientific paper

# Crystal Structure, Hirshfeld Surface Analysis and Biological Activities of *trans*-Dipyridinebis (3-Acetyl-2-Oxo-2*H*-Chromen-4-Olato)Cobalt(II)

Linda Bejaoui,<sup>1</sup> Jan Rohlíček,<sup>2</sup> Vaclav Eigner,<sup>2</sup> Amel Ismail,<sup>3</sup> Monia El Bour<sup>3</sup> and Rached Ben Hassen<sup>1,\*</sup>

<sup>1</sup> Laboratoire des Matériaux et de l'Environnement pour le Développement Durable, LR18ES10, Université de Tunis El Manar, 9, Avenue Dr. Zoheir Safi, 1006 Tunis, Tunisie.

<sup>2</sup> Institute of Physics AS CR, v.v.i., Na Slovance 2, 182 21 Prague 8, Czech Republic.

<sup>3</sup> National Institute of Marine Sciences and Technologies (INSTM), Salammbô, Tunisia.

\* Corresponding author: E-mail: rached.benhassen@issbat.utm.tn

Received: 01-28-2019

## Abstract

The novel cobalt(II) complex, *trans*-dipyridinebis(3-acetyl-2-oxo-2*H*-chromen-4-olato)cobalt(II), was synthesized in ethanol. The coordination sphere of the cobalt cation was elucidated using single-crystal X-ray diffraction analysis and spectroscopic techniques (FT-IR, UV-Visible and fluorescence). Hirshfeld surface analysis indicates that hydrogen bond interactions, such as C–H...O hydrogen bonding between the oxygen of lactone group and the pyridine appear as a primary interaction between the complex's molecules. The presence of  $\pi$ - $\pi$  stacking was evident by the shape index and curvature. Analysis of 2D fingerprint plots confirm that intermolecular H...H, C...H and H...O interactions are well dominated and are in complement to the Hirshfeld surface. The metal-ligand coordination strongly influences the fluorescence intensity (the fluorescence quenching) and the offset of the emission wavelength. The metal complex was monitored for antimicrobial activity using the disk diffusion method and showed significant activity compared to the coumarin ligand.

**Keywords:** Coumarin; cobalt Complex; fluorescence quenching; hirshfeld surfaces; antimicrobial activity

## 1. Introduction

In recent decades, the new coumarin derivatives have received increased attention due of their important biological activities.<sup>1</sup> Coumarins exhibit biochemical and physical properties. So, they are used as improver's agents in cosmetics products,<sup>2</sup> fluorescent probes,<sup>3</sup> and indicators for biological research and as medicaments,<sup>4</sup> for the treatment of various clinical conditions.<sup>5</sup> Research has also demonstrated the selective cytotoxicity of coumarins for tumor cells as well as their influence on the regulation of immune response, cell growth and differentiation.<sup>6,7</sup> The physical, pharmacological and therapeutic properties of coumarins are adjusted by the substitution of a heterocyclic moiety as a substituent or as a fused component in the coumarin skeleton.<sup>8</sup>

The investigations of metal-based drugs have become an interesting subject for bioinorganic chemists.<sup>9,10</sup> They are used as therapeutic agents for the treatment of

different diseases.<sup>11–14</sup> The scientific research in this field has proven that the binding of a drug to a metal increases its activity. In some cases, the complex has an even more interesting activity than the parent compound.<sup>15,16</sup> In particular, several metal-coumarin complexes have also been prepared and some show a biological activity superior to that of coumarin itself.<sup>17,18</sup>

Cobalt complexes have attracted the attention in the medical field because cobalt is an essential trace element in all animals. It is mainly present as vitamin B<sub>12</sub> which plays an important role in many biological processes. Thus, cobalt may be less toxic to the human body than other metals.<sup>19,20</sup>

New studies are based on the investment of protocols for the synthesis of new coumarin derivatives prepared from 3-acetyl-4-hydroxycoumarin, in the form of complexes,<sup>21</sup> chalcones,<sup>22,23</sup> aminocoumarines,<sup>24</sup> Schiff bases,<sup>25,26</sup> and their complexes.<sup>15,26</sup> We always try to highlight them through structural studies, physical properties and

biological evaluation. In this context, we continue our studies on the synthesis of new Co(II) complexes from 3-acetyl-4-hydroxycoumarin and we succeeded to prepare *trans*-dipyridinebis(3-acetyl-2-oxo-2H-chromen-4-olato) cobalt(II), a new complex which was characterized by spectroscopic techniques such as FT-IR, UV-Visible and fluorescence. Its three-dimensional structure is determined by single-crystal X-ray diffraction. Characterization and quantification of its intermolecular interactions are performed by Hirshfeld surface analysis. This new complex was evaluated by its antioxidant and antimicrobial activities.

## 2. Experimental

### 2.1. Analyses and Instrumentation

All analytical grade chemicals and solvent were commercially available purchased and used as received without further purification. The starting organic compound 3-acetyl-4-hydroxycoumarin was prepared as previously described.<sup>27</sup> The IR spectra of ligand and its metal complex were recorded on a Bruker FT-IR spectrophotometer Tensor 27 by KBr pellet technique in the range 4000–400 cm<sup>-1</sup>. The electronic absorption spectra were recorded on double beam UVD-3500 UV-Vis spectrometer in ethanol and dimethylsulfoxide (DMSO) in the region 200–900 nm. The fluorescence study of the complex was recorded on a SHIMADZU RF-5301PC spectrophotometer. Solutions of different concentrations ( $c_1 = 0.6 \cdot 10^{-3}$  mol/L,  $c_2 = 0.7 \cdot 10^{-4}$  mol/L,  $c_3 = 1.6 \cdot 10^{-5}$  mol/L,  $c_4 = 0.26 \cdot 10^{-5}$  mol/L,  $c_5 = 0.4 \cdot 10^{-6}$  mol/L) were prepared in DMSO and the experiments were carried out at room temperature.

### 2.2. Synthesis and Crystallization

Hot ethanolic solution of ligand 3-acetyl-4-hydroxycoumarin (0.50 mmol, 0.102 g) was added to previously heated aqueous solution of cobalt(II) acetate tetrahydrate Co(OAc)<sub>2</sub> · 4H<sub>2</sub>O (0.25 mmol, 0.062 g). The mixture was heated for a few minutes, and then the pyridine (0.5 mmol) was added to the solution. The reaction was refluxed at 70° C for 1 h and then cooled down to room temperature (Scheme 1). After cooling, a purple powder was settled down and the precipitate was filtered off, washed several times with ethanol. Yield: 0.18 g, 59%. The successive recrystallization from ethanol produces transparent purple-color crystals of shape and size suitable for single-crystal X-ray diffraction with a decomposition temperature  $T_{\text{decomp}} > 643$  K. FT-IR ( $\nu_{\text{max}}$  (KBr, 4000–400) /cm<sup>-1</sup>): 3065 (C–H, aromatic), 1613 (C=O, ketone), 473 Co–O (coumarin), 430 Co–N(pyridine).

The purity of the sample was also checked by the X-ray powder diffraction analysis. When the crystal structure was solved from the single crystal, the simple comparison of the measured with calculated powder diffraction

pattern was made. It confirmed the phase purity of the synthesized sample.

### 2.3. X-Ray Diffraction

The single-crystal X-ray diffraction data were collected on a Supernova Atlas S2 CCD diffractometer with mirror-monochromated Cu-K $\alpha$  radiation at 120 K. Crysalis PRO software was used for data reduction and correction of absorption.<sup>28</sup> The crystal data, the data collection and the details of the structure are summarized in Table 1. The structure was solved by the direct method using Superflip software,<sup>29</sup> and was refined by least-squares calculations on  $F^2$  with Jana2006.<sup>30</sup> All hydrogen atoms present in the structure model were discernible in difference Fourier maps and could be refined to reasonable geometry. According to common practice, H atoms bonded to C were kept in ideal positions with C–H bond equals to 0.96 Å. and with  $U_{\text{iso}}(\text{H}) = 1.2U_{\text{eq}}$ . All non-hydrogen atoms were refined using harmonic refinement. The molecular and packing diagrams of new complex were generated using the software DIAMOND Version 3.<sup>31</sup> The ORTEP of the molecule with thermal ellipsoids was also generated.<sup>32</sup>

**Table 1.** Crystallographic details and structure refinement of complex

Chemical formula	C <sub>32</sub> H <sub>24</sub> CoN <sub>2</sub> O <sub>8</sub>
$M_r$	623.46
Crystal system, space group	Monoclinic, C2/c
$T$ (K)	120
$a, b, c$ (Å)	16.1109(3),
	14.4864(3), 11.4281(3)
$\beta$ (°)	98.3873(18)
$V$ (Å <sup>3</sup> )	2638.67(10)
$Z$	4
No. of measured, independent and observed [ $I > 3\sigma(I)$ ] reflections	20921, 2679, 2509
$R_{\text{int}}$	0.028
$R[F^2 > 3\sigma(F^2)], wR(F^2), S$	0.026, 0.083, 1.15
No. of parameters	197
$\Delta\rho_{\text{max}}, \Delta\rho_{\text{min}}$ (e Å <sup>-3</sup> )	0.29, -0.21
CCDC number	1891314

### 2.4. Antimicrobial Assay

The antibacterial test was carried out by using standard paper disc method according to Ismail *et al.* 2010,<sup>33</sup> with slight modification. Briefly, 2 mg of each crude extract dissolved in 1 mL of sterile dimethyl sulfoxide (DMSO) was applied to sterile filter paper discs (6 mm). Then, discs were placed on tryptic soy agar (TSA, BIO RAD) plates, which were inoculated with 18 h cultured of the tested pathogen (10<sup>6</sup> bacteria/mL) in tryptic soy broth (TSB, BIO RAD). As negative control, a disc loaded with DMSO was simultaneously prepared. Plates were incubated overnight at 30 °C. After 24 h incubation, inhibition

diameter was measured in mm. All assays were carried out in triplicate.

Bacterial type strains (8 strains) used for the antimicrobial activity evaluation of chemical compounds were: *Escherichia coli* ATCC 25922, *Pseudomonas fluorescens* (Danish Institute for Fisheries Research, Denmark), *Pseudomonas aeruginosa* ATCC 27853, *Salmonella typhimurium* C52 (Laboratoire Hydrobiologie Marine et Continentale, Université de Montpellier II, France), *Staphylococcus aureus* ATCC 25923, *Vibrio anguillarum* ATCC 12964T, *Vibrio alginolyticus* ATCC 17749T and the yeast *Candida albicans* ATCC 10231.

### 3. Results and Discussion

Co(II) complex, *trans*-dipyridinebis(3-acetyl-2-oxo-2H-chromen-4-olato)cobalt(II), was obtained by mixing 3-acetyl-4-hydroxycoumarin with  $\text{Co}(\text{OAc})_2 \cdot 4\text{H}_2\text{O}$  and pyridine (py) in 2:1:2 ration in absolute ethanol.

#### 3. 1. Infrared Spectra

The comparison of the infrared absorption spectrum of the complex (Fig. 1) with that of the ligand shows the absence of frequency of the stretching vibration  $\nu(\text{OH})$  which appears around  $3435\text{ cm}^{-1}$  in the spectrum of the uncoordinated coumarin ligand. This indicates that the carbonyl groups of the ligand were deprotonated during coordination with the cobalt(II) cations. The band around  $1613\text{ cm}^{-1}$  is less intense and less wide compared to the analogous band in the coumarin ligand spectrum, this band corresponds to the lactone-carbonyl fragment which is a superposition of two stretching bands of the conjugated  $\text{C}=\text{C}$  and  $\text{C}=\text{O}$ . A decrease in the frequency of the stretch band of the  $\text{C}=\text{O}$  acetyl group is observed with respect to the starting coumarin ligand which is may be caused by the engagement of this group in the coordination sphere of cobalt(II) cation. The low frequency region shows the appearance of new low intensity bands in the spectrum of the cobalt complex at frequencies  $473\text{ cm}^{-1}$  and  $430\text{ cm}^{-1}$ , attributed to the vibration of the bonds  $\text{Co}-\text{O}(\text{coumarin})$  and  $\text{Co}-\text{N}(\text{pyridine})$ .

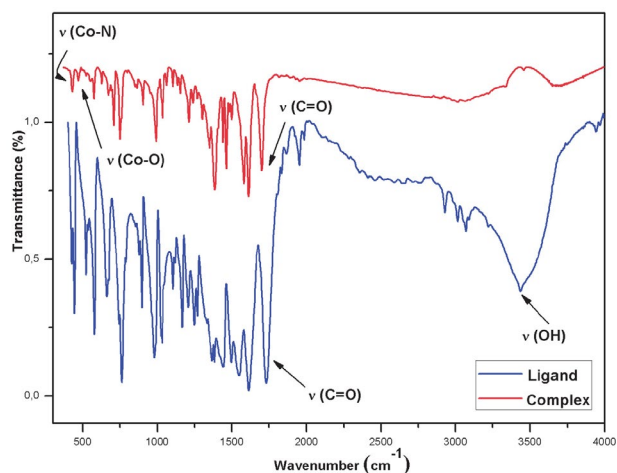
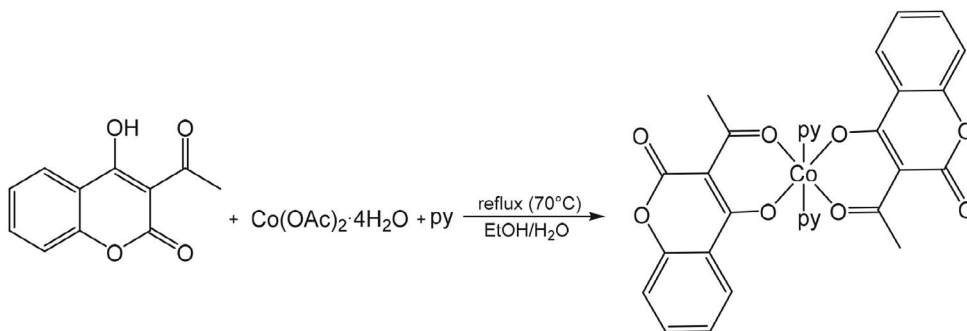


Figure 1. Comparison of the two IR spectra of the complex and ligand.

#### 3. 2. UV-Visible Spectra

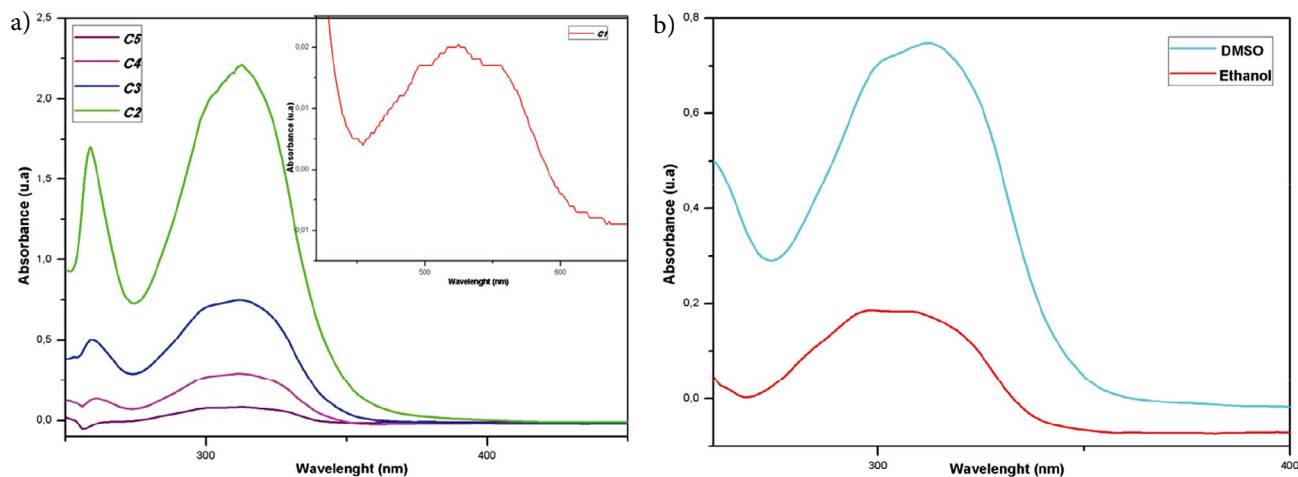
The UV-Vis spectra of the cobalt(II) complex were recorded at different concentrations in DMSO in Figure 2 (a). For high concentrations, these spectra display a large absorption band between 440 nm and 610 nm with maxima at 509 nm, this corresponds to the electronic transition  $d \rightarrow d^*$ . The position of the maximum is compatible with the octahedral configurations of cobalt(II) complexes.<sup>34</sup> We also observed that the progressive decrease in the concentration of the complex is accompanied by a hypsochromic displacement in the low wavelength range of the absorption bands located between 270 nm and 350 nm, which are attributed to the  $\pi \rightarrow \pi^*$  electronic transition of coumarin as well as hypochromic effect on the intensity of absorption.

The electron absorption spectra of the complex in different solvents with different polarities ((DMSO) and ethanol) in order to examine the influence of the surrounding environment on the spectroscopic properties of the complex are presented in Fig. 2 (b). The absorption spectrum of the complex in DMSO solvent shows a red-shift of the absorption maximum of the  $\pi \rightarrow \pi^*$  transition with  $\lambda_{\text{max}} = 314\text{ nm}$  compared to the spectrum recorded in ethanol ( $\lambda_{\text{max}} = 302\text{ nm}$ ) and a hyperchromic effect. This is manifested by the dipole interaction between the complex



Scheme 1: Synthesis of *trans*-dipyridinebis(3-acetyl-2-oxo-2H-chromen-4-olato)cobalt(II).



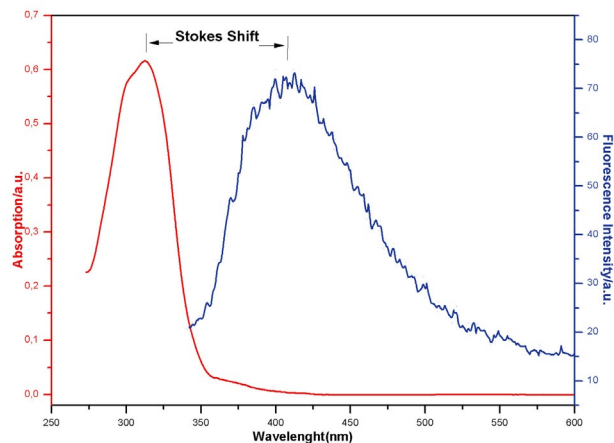


**Figure 2.** (a) Absorption spectra of complex recorded in DMSO at different concentrations  $c_2 = 0.7 \cdot 10^{-4}$  M,  $c_3 = 1.6 \cdot 10^{-5}$  M,  $c_4 = 0.26 \cdot 10^{-5}$  M and  $c_5 = 0.4 \cdot 10^{-6}$  M. The inset shows the spectrum at  $c_1 = 0.6 \cdot 10^{-3}$  M. (b) UV-Visible spectra of complex Co(II) at different solvents (EtOH and DMSO) at  $1.6 \cdot 10^{-5}$  M concentration.

molecules and the surrounding molecules of the polar solvent, which causes a decrease of the energy difference of the HOMO-LUMO of electronic transition  $\pi \rightarrow \pi^*$  and consequently an increase of the wavelength. This result is evident when comparing the spectra of the complex studied in ethanol and DMSO.

### 3. 3. Fluorescence Spectra

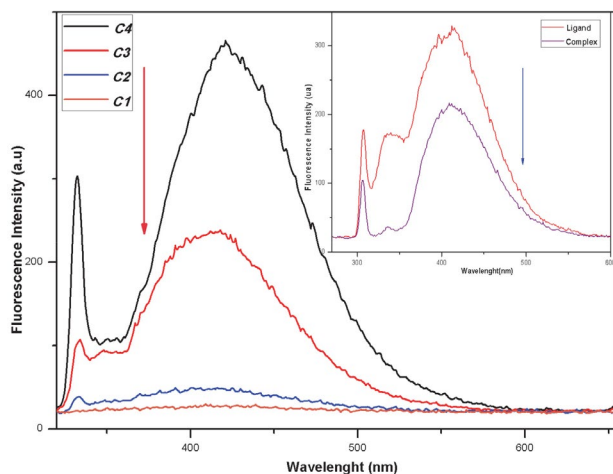
The analysis of the fluorescence spectrum of the complex in DMSO at concentration of  $10^{-5}$  M shows that the excitation peak of its possible fluorescent center is almost identical to its corresponding absorption band (recorded under the same conditions) and that the emission spectrum is approximately an inverted image of the absorption spectrum with a slight red shift (Fig. 3). The wavelength interval between the peak position of the absorption spectrum and the peak of the fluorescence spectrum of the same electron transition  $\pi \rightarrow \pi^*$  is called the Stokes shift. Indeed, the probability that an electron re-



**Figure 3.** The absorption and emission spectra of the complex in DMSO at  $10^{-5}$  M.

turns to a particular vibrational energy level in the ground state is similar to the probability that this electron is in the ground state before excitation. That is, the same electronic transitions are the most favorable for absorption and emission. This concept is known as the mirror image rule.

The analysis of the emission spectra of the complex at different concentrations (Fig. 4) in the DMSO for a 330 nm excitation corresponding to the  $\pi \rightarrow \pi^*$  transition shows a broad band of fluorescence in the blue-green region with a maximum emission at about 416 nm. The increase in the concentration of the complex solution resulted in a significant decrease in the intensity of photoluminescence and a hypochromic shift towards the low wavelengths. This decrease is due to the solvation phenomenon, to the interaction between the solvent and the solute, as well as to the coordination effect of the co-



**Figure 4.** Fluorescence spectra of the complex (recorded in DMSO at  $\lambda_{\text{ex}} = 330$  nm) at different concentrations  $c_1 = 0.7 \cdot 10^{-4}$  M,  $c_2 = 1.6 \cdot 10^{-5}$  M,  $c_3 = 0.26 \cdot 10^{-5}$  M,  $c_4 = 0.4 \cdot 10^{-6}$  M. The inset shows the spectra of complex and ligand (in DMSO at  $\lambda_{\text{ex}} = 303$  nm) at concentration  $1.6 \cdot 10^{-5}$  M.

balt(II) ions. This effect has been observed in other cobalt(II) complexes.<sup>21</sup> This phenomenon is known as fluorescence quenching. The comparison of the fluorescence spectra of the coordinated complex and uncoordinated coumarin (Fig. 4), recorded in the same solvent (DMSO) at concentration of  $1.6 \cdot 10^{-5}$  M and an excitation at 303 nm reveals a significant decrease in emission intensity and a slight hypsochromic shift of the complex. Indeed, there seems to be a transfer of intramolecular photoinduced electrons (PeT) from coumarin to the cobalt(II) cation. The photoluminescence properties of the cobalt complex result mainly from the coumarin ligand. During excitation, an electron transfer takes place from the coumarin fluorophore excited at the LUMO energy level of the cobalt(II) complex, which leads to the quenching of the fluorescence. The decrease in the fluorescence intensity also indicates that the Co(II) ions have a quality of fluorescent quenching. The results of our study are consistent with works reports of Singh et al.<sup>35</sup>

### 3. 4. Structural Study

In the asymmetric unit of the crystal structure (Fig. 5), the Co(II) cation is coordinated by two O atoms (O<sub>1</sub>, O<sub>2</sub>) and two N atoms (N4, N5). The octahedral environment of cobalt(II) consists of 3-acetyl-2-oxo-2H-chromen-4-olato in equatorial sites in *trans* configuration and two pyridine molecules occupying the axial sites. The cobalt(II) atom exhibits an axially elongated octahedral CoN<sub>2</sub>O<sub>4</sub> coordination geometry. Compared to the other crystal structures in the literature (Table 2)<sup>36</sup>, the Co–O and Co–N distances as well as the O–Co–O, O–Co–N and N–Co–N

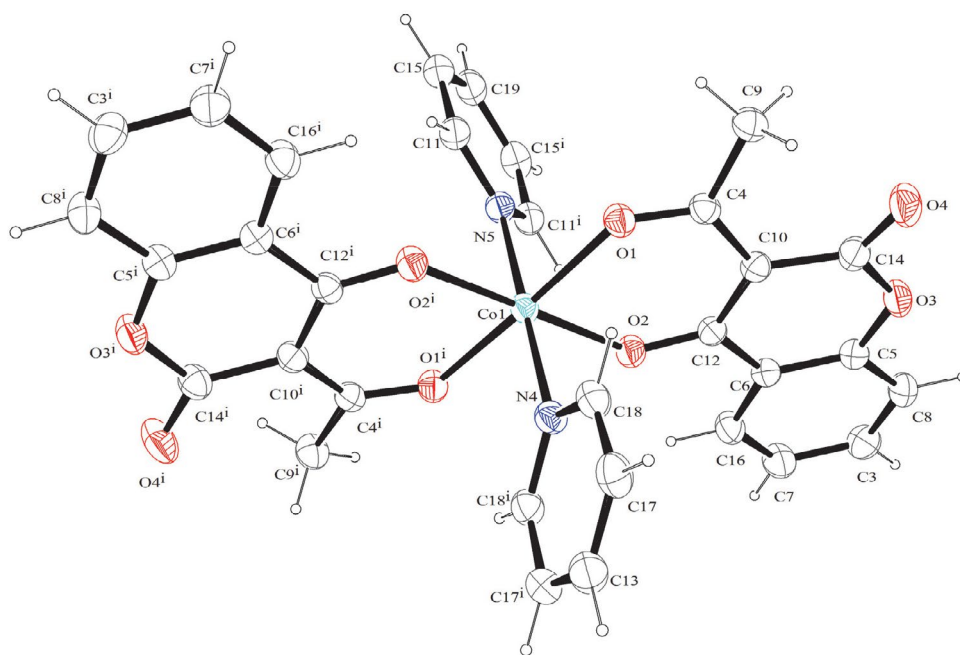
**Table 2.** Selected bond length (Å) and bond angle (°) for complex

Distance	(Å)	Angle	(°)
Co1–O1	2.0562(10)	O1–Co1–O1 <sup>i</sup>	176.57(4)
Co1–O2	2.0407(11)	O1–Co1–O2	84.42(4)
Co1–N4	2.1596(16)	O1–Co1–O2 <sup>i</sup>	95.59(4)
Co1–N5	2.1585(16)	O2–Co1–O2 <sup>i</sup>	179.60(4)
O1–C4	1.2536(18)	N5–Co1–O1	88.28(4)
O2–C12	1.2610(17)	N4–Co1–O2	89.80(4)
N4–C18	1.3477(14)	N5–Co1–O2 <sup>i</sup>	90.20(4)
N5–C11	1.3441(15)	N4–Co1–O1 <sup>i</sup>	91.72(4)

Symmetry code: (i)  $-x, y, \frac{1}{2} - z$

angles are considered as the expected values of a cobalt(II) complex coordinated by four oxygen atoms in the equatorial plane and two nitrogen atoms in axial positions.

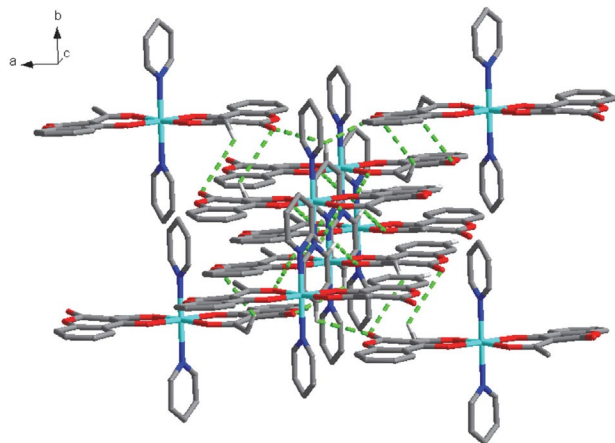
However, the angle between the equatorial plane (Co1–O1–O2) and the coumarin ligand (O1–O2–C12) is 2.67° which is smaller compared to the previously published compounds.<sup>21</sup> In addition, the angle between the two planes of pyridine in the axial position, plane 1 (C15/C11/N5/C11<sup>i</sup>/C15<sup>i</sup>/C19) and plane 2 (C18/N4/C18<sup>i</sup>/C17/C13/C17<sup>i</sup>) with symmetry code: (ii)  $(-x, -y, -z)$  is 53.81°. In the packing of crystal lattice, all the complex molecules are connected by an extensive network of hydrogen bonds (Table 3) and by interactions of type C–H  $\cdots$   $\pi$  and  $\pi$ – $\pi$ . In fact, the intermolecular bond between the coumarin lactone group and the pyridine C15–H1c15  $\cdots$  O4, C18–H1c18  $\cdots$  O4 and C19–H1c19  $\cdots$  O3 creates a network of interactions of type C–H  $\cdots$   $\pi$  which can be seen in the packing diagram where the complexes are connected in chains parallel to the axis [001] (Fig. 6).



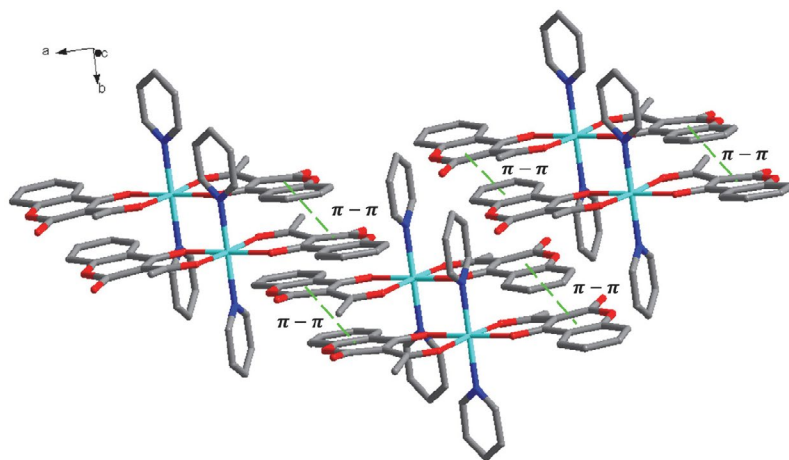
**Figure 5.** A perspective view of complex showing the atom-labelling scheme and displacement ellipsoids at the 50% probability level, symmetry code: (i)  $-x, y, \frac{1}{2} - z$ .

**Table 3.** Hydrogen-bond geometry (Å, °) for complex

<i>D</i> –H... <i>A</i>	<i>D</i> –H	H... <i>A</i>	<i>D</i> ... <i>A</i>	<i>D</i> –H... <i>A</i>
C15–H1c15...O4 <sup>iv</sup>	0.96	2.67	3.3905 (19)	132.34
C18–H1c18...O4 <sup>v</sup>	0.96	2.44	3.1600 (15)	132.04
C19–H1c19...O3 <sup>iv</sup>	0.96	2.66	3.2105 (14)	116.53

Symmetry codes: (iv)  $\frac{1}{2} + x, \frac{1}{2} + y, z$ ; (v)  $-\frac{1}{2} - x, \frac{1}{2} - y, -z$ .**Figure 6.** Crystal packing of complex showing the formation of a chain along [001], showing the intermolecular C–H...O hydrogen bonds as thin green lines. Hydrogen atoms not involve in hydrogen bonding has been omitted for the sake of clarity.

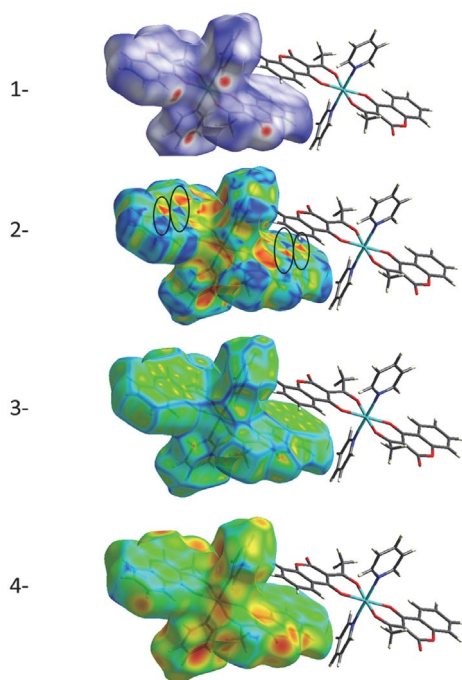
These hydrogen bonds also connect the complexes in parallel layers to the *a*-axis. In the plane (110), we can also find layers that are weakly connected by offset  $\pi$ - $\pi$  interactions between coumarin ligands (Fig. 7). The benzene ring and the coumarinic lactone ring are in contact with the neighboring molecule via  $\pi$ -forces at the symmetry code (iii:  $-\frac{1}{2} - x, \frac{1}{2} - y, 1 - z$ ) with intercentroid separations of 3.9533 (9) Å (Cg3...Cg6<sup>iii</sup>) and 3.6177 (10) Å (Cg6...Cg6<sup>iii</sup>).

**Figure 7.** Crystal packing of complex showing a weak offset  $\pi$ - $\pi$  stacking interactions between coumarin ligands in (110) plane. The green dotted line represents  $\pi$ - $\pi$  stacking interactions. Hydrogen atoms have been omitted for clarity.

### 3. 5. Hirshfeld Surface Analysis

The Hirshfeld surfaces were used for exploring intermolecular interactions in the studied crystal.<sup>37, 38</sup> The molecular Hirshfeld surfaces calculations were performed using the CrystalExplorer 3.1 program,<sup>39</sup> which accepts a structure input file in the CIF format. The Hirshfeld surfaces of the title compound are illustrated in Fig.8. This figure is showing surfaces that have been mapped over  $d_{\text{norm}}$  (normalized contact distance) (Fig. 8 (1)), shape index (Fig. 8 (2)), curvedness (Fig. 8 (3)) and  $d_e$  (distance from a point on the surface to the nearest nucleus outside the surface) (Fig. 8 (4)). The Hirshfeld surfaces of cobalt(II) complex were generated using a standard (high) surface resolution with 3D  $d_{\text{norm}}$  surfaces mapped to a ranges  $-0.1829$  to  $1.0550$ . The  $d_{\text{norm}}$  mapping indicates that strong hydrogen bond interactions, such as C–H...O hydrogen bonding between the oxygen of the lactone group and the pyridine appear as a primary interaction between the complex's molecules, seen as a bright red zone in the Hirshfeld surfaces (Fig. 8 (1)).

The size and shape of the Hirshfeld surface allow the qualitative and quantitative study and visualization of intermolecular close contacts in molecular crystals. The shape index and the curvature were used to identify packaging modes (planar stacking arrangements). In fact, the presence of  $\pi \cdots \pi$  stack is evident as a flat region down on both sides of the molecules and is clearly visible on the curve surface. The pattern of the red and blue triangles on

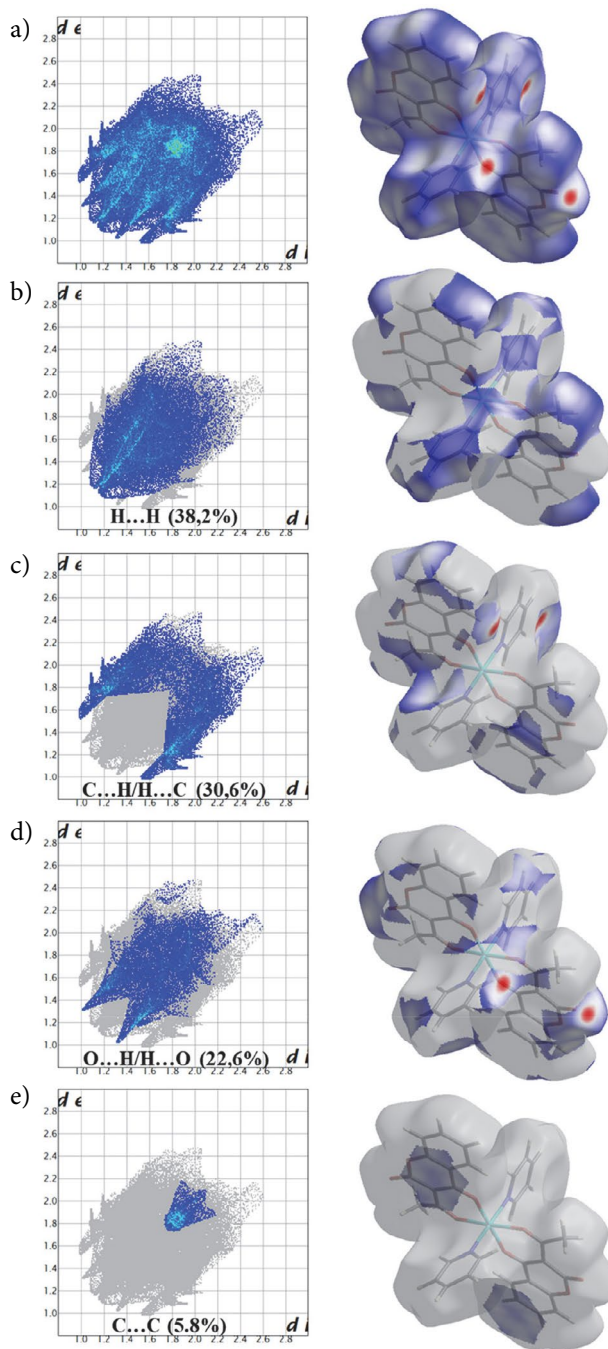


**Figure 8.** Hirshfeld surfaces of complex: (1) 3D  $d_{\text{norm}}$  surface, (2) surface index, (3) curvedness, (4)  $d_e$ .

the area of the shape index surface (Fig. 8 (2)) is characteristic of the  $\pi \cdots \pi$  stacking. The blue triangles exhibit the convex regions due to the carbon atoms of the molecule inside the surface, while the red triangles represent the concave regions because of the carbon atoms of the stacked molecule  $\pi$  above.<sup>40,41</sup> The C–H  $\cdots \pi$  contact in the crystal shows a bright-orange spots on the  $d_e$  surface (Fig. 8 (4)),<sup>38</sup> directly above the center of the C=C bonds and generates a distinct pattern of a pair of wings in the two-dimensional fingerprint plot (Fig. 9), it will become obvious that this is a characteristic feature of all C–H  $\cdots \pi$  interactions.

The 2D fingerprint plots are deconstructed to highlight particular atom pair contacts. This allows the separation of the contributions of different types of overlapping interaction in the complete fingerprint. The analysis of 2D fingerprint plots for the title compound (Fig. 9) confirm that intermolecular H  $\cdots$  H, C  $\cdots$  H and H  $\cdots$  O interactions are well dominated and are in complement to the Hirshfeld surface. The first main interaction of type H  $\cdots$  H were represented by the largest region in the fingerprint plot with contribution 38.2%. A second main interaction of type C  $\cdots$  H is due to hydrogen bonds C8  $\cdots$  H1c17–C17, and appears at the top left of the plot in the form of the characteristic wings with a contribution of 30.6%, these can also be identified by C–H  $\cdots \pi$  type interactions. This deduction is compatible with the qualitative  $d_e$  surface analysis. A third principal interaction of type H  $\cdots$  O is manifested in the molecular structure by the C15–H1c15  $\cdots$  O4, C18–H1c18  $\cdots$  O4 and C19–H1c19  $\cdots$  O3 hydrogen bonds between axial pyridine and coumarin plane.

This type of interaction is presented as two sharp points pointing to the lower left of the plot which contributes 22.6% of the total. The interactions C  $\cdots$  C exist in the 2D plot with a low contribution of 5.9%. This contact corresponds to the parallel  $\pi \cdots \pi$  stacks between the coumarin cycles. It's compatible with the surfaces of the shape index and the curvature.



**Figure 9.** Two-dimensional fingerprint plots of the complex showing percentages of contacts contributing to the total Hirshfeld surface area of the molecule: (a) all interactions, and delineated into (b) H  $\cdots$  H, (c) C  $\cdots$  H/H  $\cdots$  C, (d) O  $\cdots$  H/H  $\cdots$  O and (e) C  $\cdots$  C interactions.



### 3. 6. Antioxidant Activity

The antiradical activity of the extracts is determined by the method of reduction of the free radical of DPPH (1,1-diphenyl-2-picrylhydrazyl).<sup>42</sup> The DPPH radical is a stable organic free radical with an adsorption band at 515–518 nm. The free radical scavenging mechanism is the transfer of the hydrogen atom from the test compound to DPPH, which is transformed into a stable molecule DPPH.<sup>43</sup> The ability to reduce the DPPH radicals was determined by the decrease in its absorbance at 515 nm induced by antioxidants. The  $IC_{50}$  (scavenging concentration 50%) allowing calculate the extract concentration needed to trap 50% of the DPPH radicals. It is determined graphically by linear regression. The graph was plotted with percent scavenging effects (% IDPPH) according to concentration ( $\mu\text{mol/L}$ ) (Fig. 10). The metal complex showed good activities as a radical scavenger with  $IC_{50} = 0.0195 \mu\text{mol/L}$ . A lower  $IC_{50}$  value indicates greater antioxidant activity, compared to ascorbic acid (vitamin C) as a reference that has an  $IC_{50}$  value of  $21 \mu\text{mol/L}$ ,<sup>44</sup> it is considered a good free radical trapper. In addition, it possesses significant antioxidant activity relative to its coumarin ligand,<sup>21</sup> and other similar cobalt(II) complexes. It is difficult to draw general conclusions about antioxidant structure-activity relationships with the limited number of antioxidant molecules. It may

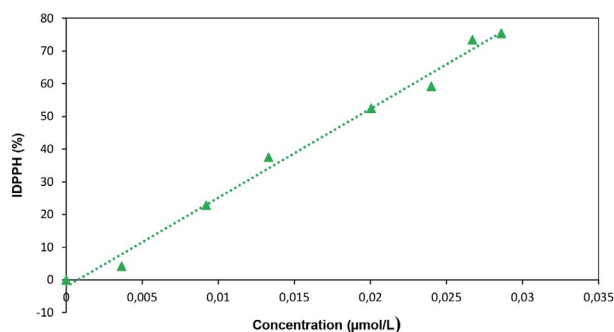


Figure 10. DPPH inhibition percentage curves of the coumarin complex.

be suggested that metal ions significantly change the chemical properties of coumarin ligand. The complexation with the transition metal was carried out *via* the carboxylate and phenol groups of the two ligands of coumarin in equatorial positions, this can improve the antiradical activity.<sup>45</sup>

### 3. 7. Antimicrobial Activity

The antimicrobial activities of ligand and complex were screened against six Gram-negative bacteria: *Escherichia coli*, *Pseudomonas aeruginosa*, *Salmonella typhimurium*, *Vibrio alginolyticus*, *Pseudomonas fluorescens* and *Vib-*

Table 4. Antimicrobial activities of the synthesized coumarin ligand and complex

Microorganisms	<i>E. coli</i>	<i>P. aeruginosa</i>	<i>S. typhimurium</i>	<i>V. alginolyticus</i>	<i>P. fluorescens</i>	<i>C. albicans</i>	<i>V. anguillarum</i>	<i>S. aureus</i>
Compound (2 mg/mL)	INHIBITION ZONES (mm)							
Coumarin ligand	11.33	11	11.66	11	11.33	12.66	10.33	11
Complex	11.66	8	9.33	13.33	8.33	8.66	12	8.66
Control (DMSO)	0	0	0	0	0	0	0	0

All data are the averages of the measurements in triplicate

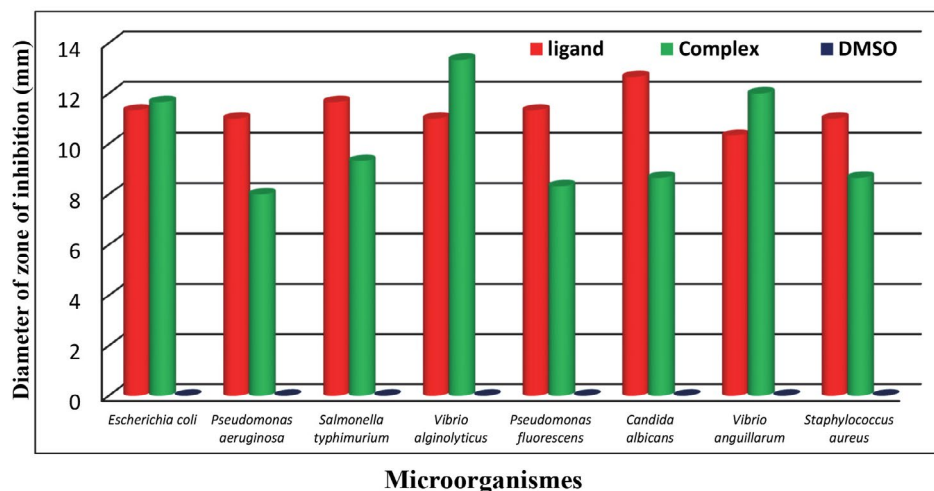


Figure 11. Antibacterial activity spectrum of the complex.



*rio anguillarum* and a Gram-positive bacterium: *Staphylococcus aureus* and against a fungus, ie *Candida albicans*, to evaluate their potential as an antimicrobial agent.

The antimicrobial activities of the complex and its coumarin ligand under test against different strains of bacteria are shown in Table 4 and Figure 11. The most sensitive microorganisms to the Co complex were *Escherichia coli*, *Vibrio alginolyticus* and *Vibrio anguillarum* (gram negative) with inhibition diameters of 11.66, 13.33 and 12 mm, respectively. This complex also showed low activity against *Pseudomonas aeruginosa*, *Salmonella typhimurium*, *Pseudomonas fluorescens*, *Candida albicans* and *Staphylococcus aureus*. In contrast, the coumarin ligand 3-acetyl-4-hydroxycoumarin exhibits a broad antibacterial activity against all strains tested but was more active against *Escherichia coli*, *Pseudomonas aeruginosa*, *Salmonella typhimurium*, *Pseudomonas fluorescens*, *Candida albicans* and *Staphylococcus aureus* with inhibition diameters of 11.33, 11, 11.66, 12.66, 11.33, and 11 mm, respectively. This relatively high antibacterial activity of uncoordinated coumarin may be due to its flat molecular structure that contributes to penetration across the membrane or bacterial cell wall.<sup>46</sup> It is clear that the zones of inhibition may be larger or weak for metal chelates than for the coumarin ligand for certain microorganisms. In addition, the antibacterial actions of coumarin ligand can be significantly improved upon chelation with cobalt(II) ions.<sup>47</sup> In particular cases, the increase in antimicrobial activity is due to the faster diffusion of metal complexes as a whole across the cell membrane or to the combined activity of the metal and the ligand.<sup>48</sup>

The minimum inhibitory concentration (MIC) was determined by the micro-dilution method according to the standard reference method for bacteria.<sup>49</sup> Various concentrations of metal complex solutions (62.5, 125, 250, 500  $\mu\text{g/mL}$ , and 1  $\text{mg/mL}$ ) were obtained by dissolving the compound in DMSO (2%) and then diluted to give serial two-fold dilutions. These solutions were added to each medium in the 96-well plates. The bacterial suspensions are added at the rate of 180  $\mu\text{L}$  in suspension of  $10^6$  bacteria/mL to each well. The purpose of this method was to determine the exact concentration of the compound under study which will have an inhibitory effect on growth selected microorganisms. This concentration was considered as minimal inhibition concentration (MIC). The MIC values was determined against *Escherichia coli*, *Vibrio algi-*

*nolyticus* and *Vibrio anguillarum* bacteria which have an inhibition diameter greater than 10 mm. As a negative control, DMSO did not affect the growth of bacterial strains at the concentrations used in this study. Values of MIC of complex are shown in Table 5. It should be noted that the cobalt(II) complex exhibited a good MIC result against Gram negative bacteria.

## 4. Conclusion

In this paper, a novel Co(II) complex *trans*-dipyridinbis(3-acetyl-2-oxo-2H-chromen-4-olato)cobalt(II) was synthesized and characterized by different spectroscopic techniques. The bonding of ligand to metal ion is confirmed by spectral studies (UV-Vis, IR, and fluorescence). The IR spectral analysis shows a decrease in the frequency of the stretch band of the C=O acetyl group with respect to the coumarin which may be due to the donor-acceptor interaction of this group with the cobalt(II) cation. The UV-Vis spectral studies suggested an octahedral geometry for the Co(II) complex. The metal-ligand coordination causes a decrease in the fluorescence intensity (the fluorescence quenching) and an offset of the emission wavelength. The crystal structure of the Co complex was studied by single-crystal X-ray diffraction; the cobalt(II) atom exhibits an axially elongated octahedral  $\text{CoN}_2\text{O}_4$  coordination geometry. In the packing of crystal lattice, all the complex molecules are connected by an extensive network of C–H  $\cdots$  O hydrogen bonds and by interactions of type C–H  $\cdots$   $\pi$  and  $\pi$ – $\pi$ . The molecular Hirshfeld surface and 2D fingerprint plots were used for quantitative mapping out of molecular interactions, revealing that close contacts are dominated by H  $\cdots$  H, C  $\cdots$  C and C  $\cdots$  H interactions, these relatively weak contacts have clear signatures in the fingerprint plots. The new coumarin complex reveal potentially important antioxidant activity against free radicals DPPH compared to the coumarin derivative ligand and vitamin C. The antimicrobial studies suggested that the coumarin derivative ligand is biologically active and its metal complex exhibits significantly enhanced antimicrobial activity against some microbial strains in comparison to the free ligand. Thus, this new cobalt(II) complex can be used further in the pharmaceutical industry, as an antioxidant and antimicrobial agent, after testing its toxicity to humans.

## 5. Supplementary Material

CCDC reference number 1891314 for the cobalt complex contain the supplementary crystallographic data for this paper. These data can be obtained free of charge at [www.ccdc.cam.ac.uk](http://www.ccdc.cam.ac.uk), or from Cambridge Crystallographic Data Center, 12, Union Road, Cambridge CB2 1EZ, UK; Fax: +44 1223 336 033; e-mail: [deposit@ccdc.cam.ac.uk](mailto:deposit@ccdc.cam.ac.uk).

**Table 5.** Minimum Inhibitory Concentration assay of metal complex against bacterial pathogens

Microorganisms	<i>Escherichia coli</i>	<i>Vibrio alginolyticus</i>	<i>Vibrio anguillarum</i>
	MIC (mg/mL)		
Complex	0.250	0.125	0.125
Control (DMSO)	0	0	0

## Acknowledgements

Financial support from the Ministry of Higher Education and Scientific Research of Tunisia is gratefully acknowledged. The authors gratefully also acknowledge the ICDD for financial support (Grant number: 09-04). The crystallographic part was supported by the project LO1603 under the Ministry of Education, Youth and Sports National sustainability program I of Czech Republic, using instruments of the ASTRA laboratory established within the Operation program Prague Competitiveness - project CZ.2.16/3.1.00/24510.

## 6. References

1. D. Egan, R. O'Kennedy, E. Moran, D. Cox, E. Prosser, R. D. Thornes, *Drug Metab. Rev.* **1990**, 22, 503–529. DOI:10.3109/03602539008991449
2. H. Xiong, L. Lvye, X. Qun, J. Rohrer, *Thermo Fisher Scientific Application Note*. **2016**, pp. 1128.
3. L. Hongqi, C. Li, C. Zhen, *Adv. Chem. Sensors*. **2012**, pp. 121–150. DOI:10.5772/33157
4. E. Guardado Yordi, M. J. Matos, A. Pérez-Martínez, C. Tornes, L. Santana, E. Molina Pérez, E. Uriarte, *Food Funct.* **2017**, 8, 2958–2966. DOI:10.1039/C7FO00402H
5. P. K. Jain, H. Joshi, *J. Appl. Pharm. Sci.* **2012**, 2, 236–240. DOI:10.7324/JAPS.2012.2643
6. Y. Bansal, P. Sethi, G. Bansal, *Med. Chem. Res.* **2013**, 22, 3049–3060. DOI:10.1007/s00044-012-0321-6
7. D. R. Vianna, L. Hamerski, F. Figueiró, A. Bernardi, L. C. Visentin, *Eur. J. Med. Chem.* **2012**, 57, 268–274. DOI:10.1016/j.ejmech.2012.09.007
8. K. Rohini, P. S. Srikumar, *J. Biofertilizers Biopestic.* **2014**, 5, 5–7. DOI:10.4172/2157-7544.1000130
9. I. P. Kostova, I. I. Manolov, I. N. Nicolova, N. D. Danchev, *Farmaco*. **2001**, 56, 707–713. DOI:10.1016/S0014-827X(01)01109-0
10. D. N. Kanthecha, D. B. Raval, V. R. Thakkar, M. N. Patel, *Acta Chim. Slov.* **2018**, 65, 333–343. DOI:10.17344/acsi.2017.4018
11. S. J. S. Franchi, R. A. de Souza, A. E. Mauro, I. Z. Carlos, L. C. de Abreu Ribeiro, F. V. Rocha, A. V. de Godoy-Netto, *Acta Chim. Slov.* **2018**, 65, 547–553. DOI:10.17344/acsi.2017.4112
12. I. Sheikhsheia, A. Badiei, M. Ghazizadeh, *Der Chem. Sin.* **2012**, 3, 24–28.
13. A. S. Munde, V. A. Shelke, S. M. Jadhav, A. S. Kirdan, S. R. Vaidya, S. G. Shankarwar, T. K. Chondhekar, *Adv. Appl. Sci. Res.* **2012**, 3, 175–182.
14. D. Lai Peng, N. Sun, *Acta Chim. Slov.* **2018**, 65, 895–901. DOI:10.17344/acsi.2018.4543
15. I. Ketata, T. Bouzaïene, T. Ben Ayed, R. Ben Hassen, *Mediterr. J. Chem.* **2014**, 3, 767–779. DOI:10.13171/mjc.3.1.2014.08.04.14
16. L. W. Xue, H. J. Zhang, P. P. Wang, *Acta Chim. Slov.* **2019**, 66, 190–195. DOI:10.17344/acsi.2018.4773
17. A. Karaliota, O. Kretsi, C. Tzougraki, *J. Inorg. Biochem.* **2001**, 84, 33–37. DOI:10.1016/S0162-0134(00)00214-2
18. G. Kokotos, V. Theodorou, C. Tzougraki, D. L. D. Deforce, E. G. Van Den Eckhout, *Bioorganic Med. Chem. Lett.* **1997**, 7, 2165–2168. DOI:10.1016/S0960-894X(97)00384-3
19. C. R. Munteanu, K. Suntharalingam, *Dalton Trans.* **2015**, 1–19. DOI:10.1039/C5DT02101D
20. N. Shahabadi, S. Kashanian, F. Darabi, *Eur. J. Med. Chem.* **2010**, 45, 4239–4245. DOI:10.1016/j.ejmech.2010.06.020
21. L. Bejaoui, J. Rohlicek, R. Ben Hassen, *J. Mol. Struct.* **2018**, 1173, 574–582. DOI:10.1016/j.molstruc.2018.07.017
22. A. Ghouili, R. Ben Hassen, *Acta Crystallogr. Sect. E Struct. Reports Online*. **2011**, 67, 6–13. DOI:10.1107/S160053681102980
23. A. Ghouili, M. Dusek, V. Petricek, T. Ben Ayed, R. Ben Hassen, *J. Phys. Chem. Solids*. **2014**, 75, 188–193. DOI:10.1016/j.jpcs.2013.09.011
24. A. Brahmia, T. Ben Ayed, R. Ben Hassen, *Acta Crystallogr. Sect. E Struct. Reports Online*. **2013**, 69, 1296. DOI:10.1107/S160053681301934X
25. J. Rohlíček, I. Ketata, T. Ben Ayed, R. Ben Hassen, *J. Mol. Struct.* **2013**, 1051, 280–284. DOI:10.1016/j.molstruc.2013.08.031
26. I. Ketata, L. Mechi, T. Ben Ayed, M. Dusek, V. Petricek, R. Ben Hassen, *Open J. Inorg. Chem.* **2012**, 2, 33–39. DOI:10.4236/ojic.2012.22006
27. A. Ghouili, A. Brahmia, R. Ben Hassen, *Acta Crystallogr. Sect. C*. **2015**, 71, 873–877. DOI:10.1107/S2053229615016083
28. *CrysAlis PRO* version 1.17.1.38.43, Rigaku Oxford Diffraction: Yarnton, UK, **2015**.
29. L. Palatinus, G. Chapuis, *J. Appl. Crystallogr.* **2007**, 40, 786–790. DOI:10.1107/S0021889807029238
30. V. Petricek, M. Dusek, L. Palatinus, *Jana*. The crystallographic computing system, Institute of Physics. Praha, Czech Republic, **2006**.
31. K. Brandenburg, H. Putz, “DIAMOND Version 3”, Crystal Impact GbR, Postfach 1251, D-53002 Bonn, Germany, **2005**.
32. L. J. Farrugia, *J. Appl. Cryst.* **2012**, 45, 849–854. DOI:10.1107/S0021889812029111
33. A. Ismail, L. Ktari, A. Boudabbous, M. El Bour, *Bull. Inst. Natn. Scien. Tech. Mer de Salammbô*. **2010**, 37, 127–132.
34. A. Bernalte-Garcia, F. J. Garcia-Barros, F. J. Higes-Rolando, F. Luna-Giles, *Bioinorg. Chem. Appl.* **2004**, 2, 307–316. DOI:10.1155/S1565363304000184
35. K. Singh, Y. Kumar, P. Puri, G. Singh, *Bioinorg. Chem. Appl.* **2012**, 2012, 1–9. DOI:10.1155/2012/729708
36. R. Kirchmaier, E. Altinand, A. Lentz, *Z. Krist.* **2004**, 219, 29–30.
37. M. A. Spackman, D. Jayatilaka, *CrystEngComm*. **2009**, 11, 19–32. DOI:10.1039/B818330A
38. J. J. McKinnon, M. A. Spackman, A. S. Mitchell, *Acta Crystallogr. Sect. B* **2004**, 60, 627–668. DOI:10.1107/S0108768104020300
39. S. K. Wolff, D. J. Grimwood, J. J. McKinnon, D. Jayatilaka, M. A. Spackman, *Crystal Explorer 3.1*, University of Western Australia, Perth, Australia, **2012**.
40. Y. H. Luo, G. G. Wu, S. L. Mao, B. W. Sun, *Inorg. Chim. Acta* **2013**, 397, 1–9. DOI:10.1016/j.ica.2012.11.010

41. I. Bennour, M. Haukka, F. Teixidor, C. Viñas, A. Kabadou, *J. Organomet. Chem.* **2017**, 846, 74–80. DOI:10.1016/j.jorganchem.2017.05.047
42. W. Brand-Williams, M. E. Cuvelier, C. Berset, *Food Sci. Technol.* **1995**, 28, 25–30. DOI:10.1016/S0023-6438(95)80008-5
43. P. Molyneux, *Songklanakarin J. Sci. Technol.* **2004**, 26, 211–219.
44. Y. C. F. Ladoh, S. D. Dibong, M. A. Nyegue, T. R. P. Djembissi, N. B. Lenta, M. E. Mpondo, J. Yinyang, J. D. Wansi, *J. Appl. Biosci.* **2014**, 84, 7636–7643. DOI:10.4314/jab.v84i1.9
45. M. Rajeshirke, R. Shah, P. Yadav, N. V. Purohit, *Der Pharmacia Sinica.* **2012**, 3, 239–248.
46. O. Kayser, H. Kolodziej, *Z. Naturforsch.* **1999**, 54c, 169–174. DOI:10.1515/znc-1999-3-405
47. N. K. Singh, M. S. Agrawal, R. C. Aggarwal, *Synth. React. Inorg. Met. Chem.* **1985**, 15, 75–92. DOI:10.1080/00945718508059368
48. N. Fahmi, R. V. Singh, *Transit. Met. Chem.* **1994**, 19, 12–16. DOI:10.1007/BF00139327
49. V. Duraipandiyar, S. Ignacimuthu, *J. Ethnopharmacol.* **2009**, 123, 494–498. DOI:10.1016/j.jep.2009.02.020

## Povzetek

V etanolu smo sintetizirali nov kobaltov(II) kompleks *trans*-dipiridinbis(3-acetil-2-okso-2*H*-kromen-4-olato)kobalt(II). Koordinacijska sfera kobaltovega kationa je bila določena z monokristalno rentgensko difrakcijo in spektroskopskimi tehnikami (FT-IR, UV-Vis in fluorescenca). Hirshfeldova analiza površine kaže, da predstavljajo vodikove vezi, kot je C–H...O vodikova vez med kisikovim atomom laktonske skupine in piridinom, najpomembnejše interakcije med molekulami. Prisotnost  $\pi$ - $\pi$  interakcij je razvidna na podlagi indeksa oblike in ukrivljenosti. Analiza 2D diagramov potrjuje, da dominirajo intermolekularne H...H, C...H in H...O interakcije, kar je v soglasju s Hirshfeldovo površino. Koordinacija kovina-ligand močno vpliva na intenziteto fluorescence in na zamik emisijske valovne dolžine. Kompleks smo testirali tudi na antimikrobno aktivnost z uporabo difuzijske metode na disku in kaže znatno aktivnost v primerjavi s kumarinom.



Except when otherwise noted, articles in this journal are published under the terms and conditions of the Creative Commons Attribution 4.0 International License

*Scientific paper*

# The Influence of Cardboard Dust on Structural, Morphological and Mechanical Properties of Biocomposite PLA and HDPE Filaments for 3D Printing

Diana Gregor-Svetec,\* Urška Stankovič Elesini, Raša Urbas,  
Mirjam Leskovšek and Urška Vrabič Brodnjak

University of Ljubljana, Faculty of Natural Sciences and Engineering, Department of Textiles, Graphic Arts and Design,  
Snežniška ulica 5, Ljubljana, Slovenia

\* Corresponding author: E-mail: diana.gregor@ntf.uni-lj.si;  
Tel: +386 1 200 32 72

Received: 02-05-2019

## Abstract

In the material extrusion of the thermoplastic filaments, known as Fused Deposition Modelling, usually, pure thermoplastic polymers are used. Recently, the focus of the research is given to the development of new biocomposite thermoplastic materials. In our research, 3D printable biocomposite filaments, made with the addition of 50 wt.% of cardboard dust to the HDPE and PLA polymer matrix were studied. The influence of the added cardboard dust on structural, morphological and mechanical properties of the 3D printable biocomposite filaments was investigated. With the addition of the corrugated cardboard dust into the HDPE and PLA polymer matrix the changes in density, uniformity, chemical structure and transition temperatures of the samples were detected. The addition of the cardboard dust into the HDPE polymer matrix lead to low tenacity, toughness, deformability resulting in brittleness of the 3D printable biocomposite filament, whereas the addition of the cardboard dust into the PLA polymer matrix lowered tensile properties, but didn't affected bending toughness and has even improved compression strength of the 3D printable filament.

**Keywords:** 3D printing; filaments; PLA; HDPE; biocomposite

## 1. Introduction

The production of cardboard is a continuous process. Layers of paper are glued together into long, continuous strips of cardboard and are automatically cut, while the waste (small shreds) falls alongside the line. This waste needs to be removed as quickly as possible.

The corrugated cardboard industry is primarily using shredders to destroy and or to air handling their scrap material. These shredders use a rip and tear technology, to break apart the cardboard. This process is noisy and at the same time causes formation of the waste – the cardboard dust. Bigger part of unused waste cardboard is recycled and waste cardboard dust is incinerated.<sup>1</sup> Incineration is an expensive, rigid and technology-dependend waste management strategy.<sup>1</sup> Burning the cardboard waste and the dust is wasteful, because incineration captures only one fifth of calories in these materials.<sup>2</sup>

However, another possibility is to recycle the cardboard dust by using it as a filler in polymer filaments for

3D printing. The most spread 3D printing technology is the Fused Deposition Modelling (FDM), in which thermoplastic polymer is melted into a semi-liquid state and extruded through the head onto the build platform.<sup>3</sup> Materials that are used in the FDM 3D printing must have suitable heat transfer characteristics and rheology i.e. behaviour of liquid flow. Thus, the most appropriate are some of the thermoplastic polymers, such as polylactic acid (PLA), acrylonitrile butadiene styrene (ABS), polyamide (PA) etc.<sup>4</sup>

In our research, two thermoplastic polymer filaments were used, polylactic acid (PLA) and high-density polyethylene (HDPE). The PLA is mostly amorphous. It is produced from renewable resources (i.e. corn starch or sugarcane) and is biodegradable under the suitable conditions. Since the PLA has low toughness and thermal stability, different reinforcements are used to improve its disadvantages. Regarding mentioned, the PLA matrix was, through various studies reinforced with different materi-

als, such as hemp, flax, jute, sisal and bamboo fibres, cellulose nanofibres etc.<sup>5–11</sup> The PLA is the most common polymer for FDM 3D printing. Properties of the PLA filament loaded with the wood particles in different levels from 0–50% were investigated by Kariza et al.<sup>12</sup> Results have shown that the increase of wood particles, decreased the density of the composite filaments for 3D printing. The tensile strength of the filaments increased with an addition of 10% wood, but decreased with higher wood content. At the same time, the storage modulus decreased with higher wood content, although the glass transition temperature did not change.

The composite filament from PLA, ABS, HDPE, as well as other matrices reinforced with carbon, glass or natural fibres, core-shell rubber, organic and inorganic particles, are also used in FDM application.<sup>13</sup>

The HDPE is highly crystalline, low density and flexible recyclable and eco-friendly material, and as shown by Kreiger et al., it has potential also in the in-home recycling of post-consumer plastic.<sup>12</sup> Its drawbacks are high thermal expansion, poor temperature capability, low toughness and ductility. To improve some of those drawbacks, the HDPE as matrix was reinforced with different materials such as kenaf and jute fibres, treated argan-nut shell particles, pinecone, coconut and snail shell powder, pineapple fibres etc.<sup>14–22</sup> Recently, the impact of addition of thermo-mechanical (TMP) pulp fibers (0–30% w/w) on the mechanical properties of bio-polyethylene was researched by Tarrés et al.<sup>23</sup>

The HDPE filaments are also used for FDM 3D printing, though not as often as the PLA.

For the purpose of our research the PLA and the HDPE polymers were reinforced with 50 wt.% cardboard dust. The aim of our research was to determine the influence of the addition, of the cardboard dust on the structure and the properties of 3D printable filaments.

## 2. Materials and Methods

### 2.1. Materials

Two 3D printable biocomposite filaments were produced with adding of the 50 wt.% cardboard dust into the PLA and the HDPE polymer matrix. The cardboard dust was obtained from a paper mill, as a residue in a cardboard production. The pure PLA and the HDPE 3D printable filaments were produced from commercial pellets (producer

Plastika Trček, Slovenia). As a reference, 3D printable filaments made from the pure PLA and HDPE were used.

### 2.2. Testing Methods

3D printable filaments were qualitatively analysed with the FT-IR spectrometer Spectrum GX I (Perkin Elmer). Spectra were recorded over the range 4000–800 cm<sup>-1</sup>, with the resolution of 4 cm<sup>-1</sup>.

The density of 3D printable filaments was calculated as a ratio of mass per unit volume. The time of sound wave propagation through the 3D printable filaments in the longitudinal direction was measured using a Pulse Propagation Meter PPM-5R (H. Morgan, Co.), at a frequency of 160 Hz. The velocity of the sound waves was calculated as a ratio of the distance and the time of the pulse propagation. The thermal stability of the 3D printable filaments was measured with the Hot-stage microscopy, using the Mettler FP84HT microscopy system. Temperature measuring range was between 30–200 °C, and the rate of heating was 5 °C/min.

The analysis of the 3D printable filaments cross-section was performed by the Scanning electron microscope (SEM) JSM-6060 LV (Jeol), at different magnifications.

The dynamic Mechanical Analysis (DMA) was performed using a Q800 DMA analyser (TA Instruments). The measurements were performed in a dual cantilever bending mode on the 3D printable filaments, with the sample length of 35 mm. Measurements were performed at the frequency from 1 to 10 Hz of oscillation and temperature range 0–160 °C, with the temperature step of 3 °C/min rising to 160 °C. Depending on the temperature and the frequency, the transition temperatures, bending storage modulus ( $E'$ ), bending loss modulus ( $E''$ ) and tan delta ( $\tan \delta$ ) of the 3D printable polymer filaments were determined.

The mechanical properties were determined using a tensile testing machine Instron 5567 (Instron). The tensile properties of the 3D printable filaments were determined according to the ASTM D2256. The bending resistance was determined with the 2-point bending test and the compression load was measured by compressing the filament to half its thickness.

## 3. Results and Discussion

### 3.1. Structural Characteristics

For composite materials, changes in chemical composition or interactions between the 3D printable filaments can be observed as changes in the peak intensities.<sup>24,25</sup>

Figure 1 shows spectra of the analysed pure PLA and the biocomposite PLA/cardboard dust 3D printable filaments in the range of wavenumber from 4000 to 800 cm<sup>-1</sup>. More detailed insight into spectra can be seen in the range

Table 1: Notation of 3D printable filaments

Sample	Polymer matrix	Added filler
PLA	PLA	/
PLA/50 c.d.	PLA	Cardboard dust (50 wt.%)
HDPE	HDPE	/
HDPE/50 c.d.	HDPE	Cardboard dust (50 wt.%)



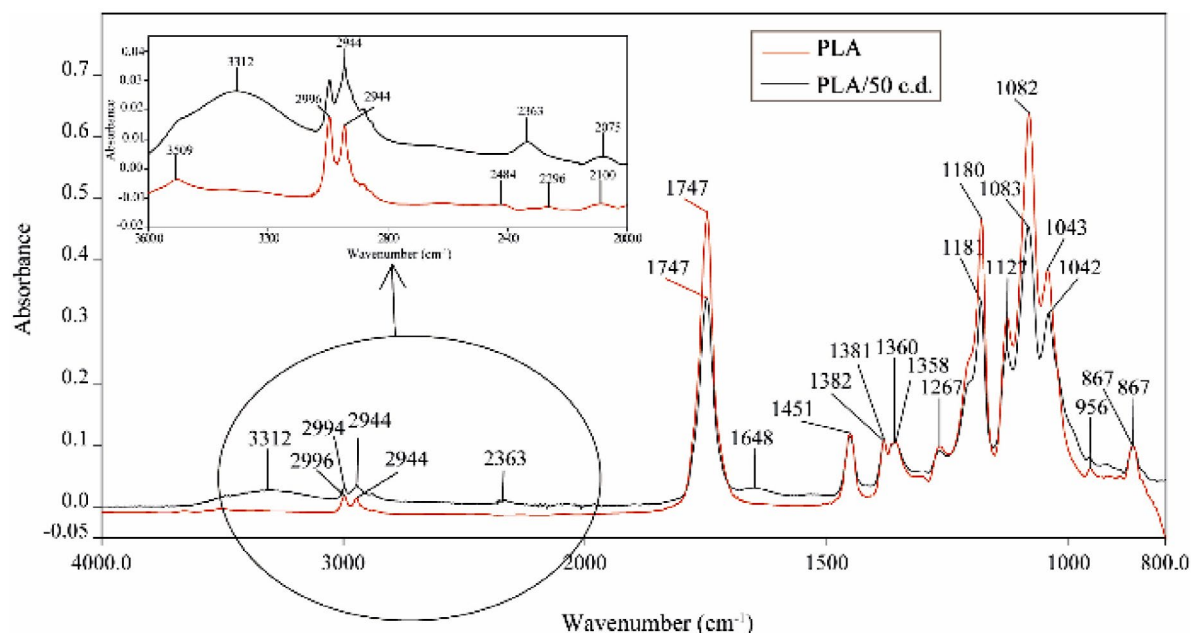


Figure 1: ATR FTIR spectra of pure PLA (PLA) and 50 wt.% PLA/ cardboard dust (PLA/50 c.d.) 3D printable filaments

of 3600 and 2000  $\text{cm}^{-1}$ , where the differences due to the addition of the 50 wt. % cardboard dust can be observed. The peaks at 2996 and 2944  $\text{cm}^{-1}$  are typical for the PLA, and present the stretching of the hydroxyl groups and the symmetrical and the asymmetrical stretching of the C-H groups.<sup>26</sup> In the sample PLA/50 c.d., the peak at 3312  $\text{cm}^{-1}$  can be detected.<sup>27</sup> This confirms the presence of the cellulose in the sample, because it shows the vibration of the -OH group.<sup>28</sup> At pure PLA 3D printable filament, the peak at 3509  $\text{cm}^{-1}$  can be assigned to the asymmetrical stretch-

ing of the C-H group in the PLA. This peak was also detected for the biocomposite PLA/cardboard dust 3D printable filament, but with lower intensity. In the range between 1800 and 800  $\text{cm}^{-1}$ , PLA spectra had higher absorbance, compared to the biocomposite filament sample. In this range no significant peaks were detected, only the peak at 1648  $\text{cm}^{-1}$ , which presents the vibrations of the  $\text{CH}_2$  group and the vibrations of the hydrogen bonds in the cellulose. This again confirms the presence of the cellulose, though, despite the addition of the 50 wt.% corrugat-

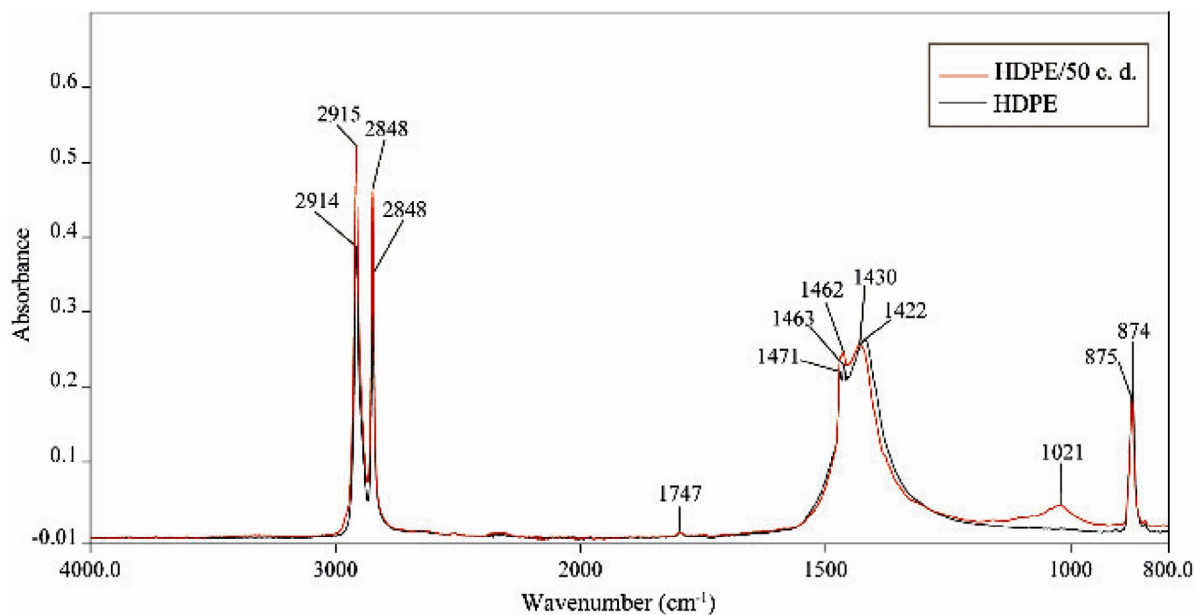


Figure 2: ATR FTIR spectra of pure HDPE (HDPE) and 50 wt.% HDPE/cardboard dust (HDPE/50 c.d.) 3D printable filaments

ed cardboard dust, the content of the PLA component stands out.

Figure 2 shows spectra of the analysed pure HDPE and the 50 wt.% HDPE/cardboard dust 3D printable filaments in the range of wavenumber from 4000 to 800  $\text{cm}^{-1}$ . It unites the absorption bands of the polyethylene matrix and the characteristic absorption bands of the cellulose (cardboard dust). Characteristic peaks for the HDPE are in the range of 2915 and 2848  $\text{cm}^{-1}$ , and can be assigned to the symmetrical and the asymmetrical vibrations of the  $\text{CH}_2$  groups in the HDPE. The same is with the peaks at 875 and 874  $\text{cm}^{-1}$ , which present the bending of the  $\text{CH}_2$ . The assigned peak at 1720  $\text{cm}^{-1}$  corresponds to the carbonyl groups, which is the main result of the polyethylene. The peak at 1021  $\text{cm}^{-1}$  confirmed the addition of the cellulose in the sample.<sup>27,28</sup> This peak corresponds to the asymmetrical vibrations of the glycosidic rings of the cellulose. From the presented spectra it can be seen that the major peaks are from the HDPE component, meaning that the filament's surface is composed mainly from the HDPE polymer.

**Table 2:** Density, sound wave velocity and melting temperature of 3D printable filaments

Sample	Density ( $\text{g/cm}^3$ )	Sound wave velocity (km/s)	Melting temperature ( $^{\circ}\text{C}$ )
PLA	1.260	1.77	172
PLA/50 c.d.	0.961	2.45	150
HDPE	0.995	2.05	132
HDPE/50 c.d.	0.501	1.31	150

Results presented in table 2 show that after the cardboard dust was added into the PLA polymer matrix the density of the 3D printable filament decreased for 25%, while the longitudinal speed of the sound waves traveling through the filament increased almost for 40%. The later applies that the structure of the biocomposite PLA/cardboard dust 3D printable filament (PLA/50 c.d.) is more oriented in direction of the filament axes, compared to the pure PLA 3D printable filament. The density of the 50 wt.% biocomposite HDPE/cardboard dust 3D printable filament (HDPE/50 c.d.) reduced to half its value, compared to the pure HDPE 3D printable filament. In this sample also, the sound wave velocity decreased substantially, implying that the structure is more porous with lower uniformity.

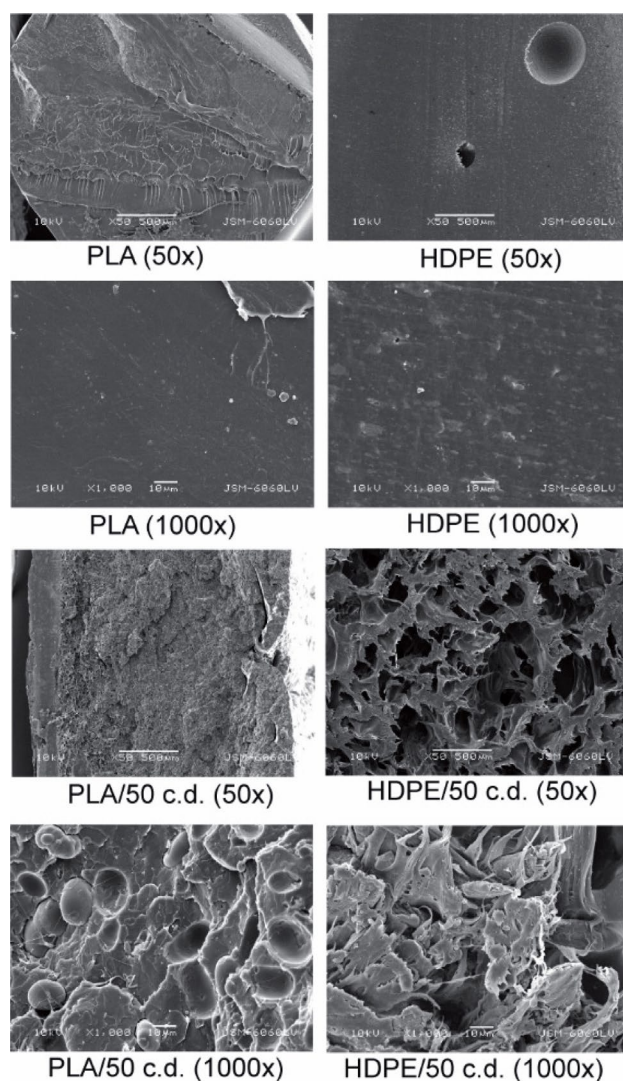
Thermal analysis has shown, that the first changes in the structure of the pure PLA 3D printable filament occurred at 147  $^{\circ}\text{C}$ , while the melting was completed at 172  $^{\circ}\text{C}$ . In the 50 wt.% biocomposite PLA/cardboard dust 3D printable filament the first changes were noticed at 120  $^{\circ}\text{C}$ . The cardboard dust part of the biocomposite firstly turned yellow, and later melted at 140  $^{\circ}\text{C}$ , whereas the PLA component completely melted at 150  $^{\circ}\text{C}$ .

On the other hand, the addition of the cardboard dust increased thermal stability of the 50 wt.% biocomposite HDPE/cardboard dust 3D printable filament for about 15%. The first change was noticed at 132  $^{\circ}\text{C}$ , where the HDPE matrix starts to melt, and the cellulose starts yellowing.

Cross-section images of the pure PLA 3D printable filament revealed relatively uniform structure without any seen additives or pores in the structure. On the other hand, the cardboard dust in the biocomposite filament (Figure 3) acts as a filler in the PLA polymer matrix, thus leaving the structure a bit more porous, less uniform and with visible particles of the cardboard dust, due to which the surface of the filament was rougher and more brittle. The pure HDPE 3D printable filament has some holes in the structure, resulting from the filament production process. The addition of 50 w.t.% of cardboard dust has profound effect on the structure of polymer matrix. With the addition the structure becomes highly porous, with visible small particles of cardboard dust in the matrix. SEM analysis has revealed better inclusion of the cardboard dust particles to the PLA matrix as to the HDPE matrix. The cross section of PLA/cardboard dust 3D printable filament (PLA/50 c.d.) shows numerous voids, caused by cardboard particles, whereas cross section of the sample HDPE/50 c.d. shows much more disrupted structure with lot of cavities present.

### 3. 2. Mechanical Characteristics

Mechanical properties of analysed 3D printable filaments under tensile, bending and compression load are shown in Table 3. The addition of the cardboard dust into the PLA matrix influenced the mechanical properties differently. Both PLA filaments, pure and biocomposite, are tough, thus bending filament till 15 $^{\circ}$  didn't reveal noticeable difference in the bending load. The biocomposite PLA/cardboard dust 3D printable filament is weaker at loads acting in direction of filament axes, as the tensile strength was 5-times, strain at break 3-times and elastic modulus for almost 50% lower compared to the pure PLA 3D printable filament, which is in agreement with the morphological study of the filament cross-section. SEM image analysis has revealed more porous structure for the biocomposite PLA/cardboard dust 3D printable filament, compared to the pure PLA 3D printable filament, which is also confirmed with its lower density. The tensile force acting on the filament is not transported from the matrix to the filler effectively, which leads to lower strength and modulus, and also lowers the plasticity of the biocomposite. This suggests that the cardboard dust, as a filler, is not bonded enough to the polymer matrix. On the other hand, the addition of the cardboard dust improves the compression toughness of the filament. By compressing the filament to half its thickness, a higher load was determined for the PLA/50 c.d. filament, because of the stiffness of the cardboard dust particles, which are imbedded in the more or



**Figure 3:** Cross-sections of 3D printable filaments (SEM; 50× and 1000× magnification)

less amorphous polymer matrix. A bit higher sound wave velocity propagation in the biocomposite PLA/cardboard dust 3D printable filament also suggest, that mainly amorphous structure of the polymer matrix is more oriented in the longitudinal direction of the filament, because of the filler.

The HDPE 3D printable filament is weaker compared to the PLA 3D printable filament. It has lower strength and is much more extensible. The HDPE behaves differently than the PLA under the influence of tensile load. It reaches the maximum load (198 N) at lower strain (9.94%) compared to the PLA, but then deforms under the same load (155 N) without breakage until the strain of 191% is reached. For the PLA, and both biocomposite 3D printable filaments the break occurs at maximum load. A high deterioration of the mechanical properties was determined for the biocomposite HDPE/cardboard dust 3D printable filament. This is due to the low miscibility of the HDPE polymer with the cardboard dust, thus resulting in highly porous, non-homogenous structure. The biocomposite HDPE/cardboard dust 3D printable filament is ductile, with low tensile strength, which is 8-times lower, compared to the pure HDPE 3D printable filament. It has lower toughness and resistance to bending and compression.

The reason for the higher deterioration of the mechanical properties for the biocomposite HDPE/cardboard dust 3D printable filament compared to the PLA/cardboard dust 3D printable filament is in the much weaker interfacial bonding between the filler and the matrix, and much more porous structure. The presence of the cavities confirms that the interfacial bonding between the filler and the matrix polymer is poor and weak (Figure 3). It also appears that the cardboard dust is not well distributed in the polymer matrix, especially in the sample HDPE/50 c.d. where the polymer matrix is no longer continuously distributed, and localised bundles of the cardboard dust are present, leading to poor bonding between them and to the polymer matrix. These causes stress concentration and without efficient transporting the stress between the polymer matrix and the filler, resulting in a substantially lower strength of the HDPE/cardboard dust 3D printable filament. Compounding and surface modification of the polymer matrix could improve the interfacial bonding between the filler and the polymer matrix leading to better response to stress and less deterioration of the mechanical properties.

### 3. 3. Dynamic Mechanical Characteristics

The dynamic mechanical properties of the samples as a function of a temperature are shown in Figures 4 to 6, while the glass relaxation transition temperatures are shown in Table 4.

**Table 3:** Mechanical properties of 3D printable filaments

	Tensile strength (MPa)	Strain at break (%)	Elastic modulus (GPa)	Load at bending (N)	Load at compression (kN)
PLA	56.46	12.46	1.45	2.71	8.85
PLA/50 c.d.	11.57	4.12	0.84	2.73	10.19
HDPE	16.76	191 (9.94*)	0.39	1.97	5.75
HDPE/50 c.d.	2.05	7.60	0.12	0.71	1.50

\* strain at maximum force

As can be seen from Figure 4, the biocomposite HDPE and PLA filaments respond differently to dual cantilever bending in the temperature relaxation interval due to the very different structural characteristics. The curve slope of the bending storage modulus  $E'$  of the pure HDPE sample slowly decreases through the wider temperature interval (from 0 to 140 °C) and thus implies on semi-crystalline viscoelastic polymer structure. During heating, the bending storage modulus decreases due to the movement of the macromolecules in the amorphous region (5). In the case of the pure PLA sample, the rapid drop of the storage modulus  $E'$  curve through very narrow temperature interval (from 50 to 60 °C) characterises the amorphous nature of the polymer. The movement of the molecular segments, which leads to their equilibrium conformations and increase in free volume, are achieved in very narrow relaxation interval. The storage modulus  $E'$  of the HDPE filament is much higher as in the case of the PLA through the whole temperature scale, suggesting that the HDPE filament has more ordered structure with greater interactions among the molecular chains compared to the PLA filament structure. The PLA filament is thus more prone to deformation (more flexible), while the HDPE filament is stiffer with higher elasticity.

After the cardboard dust is mixed into the HDPE polymer (HDPE/50 c.d.), the bending storage modulus  $E'$  drastically decreases for 91.1% and stay low through the whole temperature range. The noticed decrease of the storage modulus is more intensive for the pure HDPE filament compared to the biocomposite HDPE/50 c.d. sample. The pure HDPE sample dissipated more energy influenced by the macromolecules movement, which resulted in the higher plastic deformation of the HDPE filament (Figure 5), with decreased elasticity and increased flexibility.

In contrary, the biocomposite PLA/50 c.d. shows very similar elastic response as the pure PLA (as can be seen from the Figure 4), which suggests that the cardboard dust does not have any significant influence on the con-

nection between the PLA molecular chains, only that the drop of the elasticity, influenced by the heating, occurred earlier. The elasticity of both the PLA and the PLA/50 c.d. filament is still low, indicating lower stiffness than the pure HDPE filament, but higher than the biocomposite filament HDPE/50 c.d.

Table 4: Glass transition temperature of the 3D printing filament

Sample	Relaxation transition temperature* $T_g$ [°C]
PLA	59.39
PLA/50 c.d.	58.04
HDPE	55.89
HDPE/50 c.d	42.71

\*  $T_g$  was determined from the curves of the bending storage modulus.

The relaxation transition temperatures ( $T_g$ ) of the pure PLA and HDPE filaments are higher as for their biocomposite PLA/50 c.d. and HDPE/50 c.d. filaments. The temperature of relaxation transition decreases just slightly in the case of the PLA filaments (from 59.4 °C for the pure PLA to 58.0 °C for the PLA/50 c.d.), while apparent decrease was detected in the case of the HDPE filaments (from 55.9 °C for the pure HDPE to 42.7 °C for the HDPE/50 c.d.). By adding the cardboard dust, the free volume between the adjacent molecular chains increases, which contributes to easier and earlier slippage of the structure segments, required less energy to gain the relaxation state.

The curves of bending loss modulus  $E''$  (Figure 5) for the HDPE and the PLA filaments are different in shape according to the mentioned semicrystalline and amorphous structure of both filaments, respectively. The curve of loss modulus  $E''$  of the pure HDPE filaments is wider, which suggests that movement of the macromolecules took more time and caused the dissipate energy to take place at wider

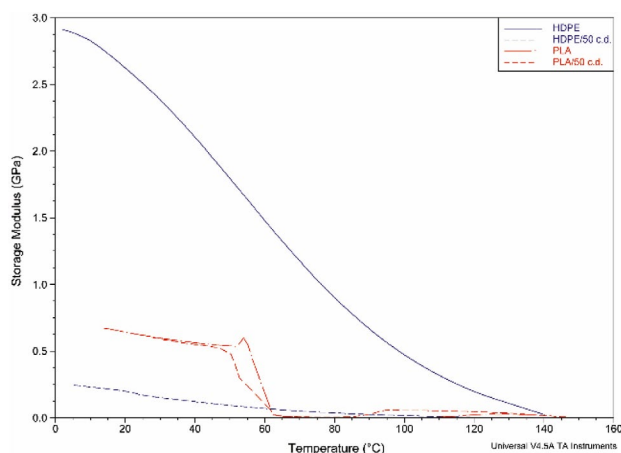


Figure 4: Bending storage modulus of 3D printing filaments at 10 Hz of oscillation

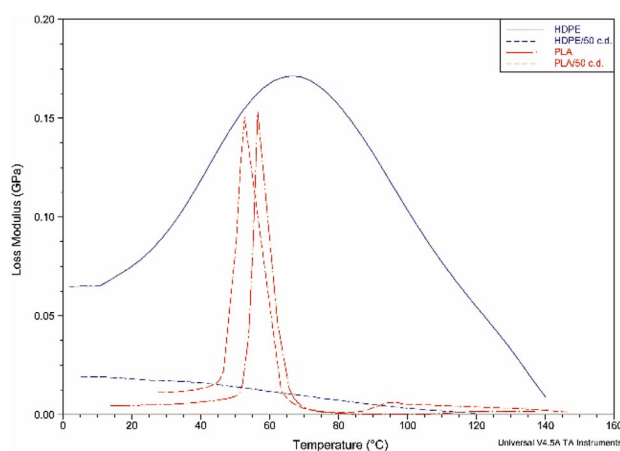
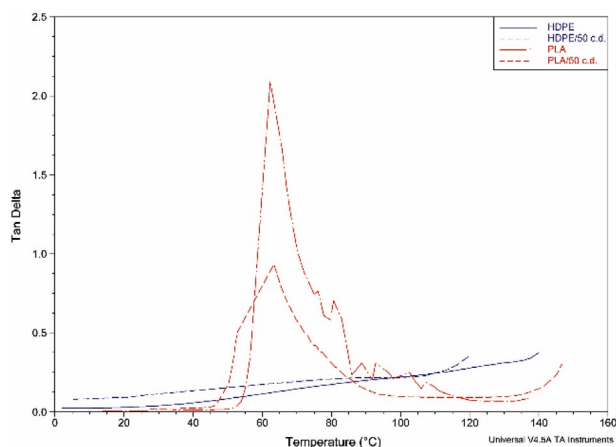


Figure 5: Bending loss modulus of 3D printing filaments at 10 Hz of oscillation



temperature interval. With elevated temperature, the curve of the loss modulus increased and reached the peak at 65 °C. After that, the loss modulus starts to decrease. After the cardboard dust is mixed with the HDPE, the value of the loss modulus decreased drastically, with no noticeable peak in modulus. According to the values of the loss modulus, the biocomposite filament HDPE/50 c.d. is less prone to the plastic deformations as the pure and more rigid HDPE filament. The peaks of the loss modulus  $E''$  for both PLA filaments are more prominent and were reached at 56.6 °C and 52.7 °C for the pure PLA and the biocomposite filament PLA/50 c.d., respectively. Both curves are narrow in the interval of relaxation transition because of the dominant amorphous regions.



**Figure 6:** Loss factor ( $\tan \delta$ ) of 3D printing filaments at 10 Hz of oscillation

The damping properties of the filaments are shown in Figure 6. From the diagram can be seen that the value of the loss factor ( $\tan \delta$ ) was significantly higher in the case of the pure PLA filament, compared to the PLA/50 c.d. and the HDPE filaments. Since the pure PLA has loss factor ( $\tan \delta$ ) above 1, the filament shows more viscous than elastic properties, while the pure HDPE with loss factor far below 1 is more elastic, due to its higher crystallinity. In the pure PLA filament, the movement of the molecular segments is more intensive as in the PLA/50 c.d. in which incorporated cardboard dust reduced the intensity of macromolecules movement. The PLA/50 c.d. filament exhibits lower damping properties and with loss factor ( $\tan \delta$ ) around 1 that implies approx. equal share of the plastic and the elastic component in the structure. Comparing to the HDPE/50 c.d. filament, the pure HDPE has lower  $\tan \delta$  values, influenced by the greater elastic response of the structure, as seen in Figure 4.

## 4. Conclusions

The structural, the morphological and the mechanical properties of two biocomposite 3D printable filaments

(the 50 wt.% HDPE/cardboard dust and the 50 wt.% PLA/cardboard dust) were compared with the properties of the pure HDPE and the PLA 3D printable filaments. Behaviour of the 3D printable filaments under tensile, bending and compression load was evaluated.

The morphology of filaments is mainly nonhomogeneous and porous. SEM image analyses evidenced a heterogeneous distribution of the cardboard dust and the pores in the polymer matrix. It was established that the biocomposite 3D printable filaments have lower density, thermal stability and inferior mechanical properties in comparison to the pure filaments. With the FTIR analysis the changes in morphology, due to the addition of the cardboard dust has been confirmed. The addition of the 50 wt.% cardboard dust into the HDPE polymer matrix leads to low tenacity, toughness, deformability resulting in brittleness of the biocomposite filament, whereas the addition into the PLA polymer matrix didn't affect bending toughness and has even improved the compression strength of the 3D printable filament. When viscoelastic properties are discussed, the pure HDPE shows higher stiffness with greater elastic response than the pure PLA. With the addition of the 50 wt.% carbon dust the stiffness of the HDPE filament is significantly lowered, while it does not have any significant influence on the stiffness of the PLA/cardboard biocomposite. It follows, that PLA and HDPE 3D printed objects, both pure and composite, will be stiff when handling at ambient temperature. With increased temperature above 30 °C, the structure of the HDPE sample and therefore 3D objects will become more flexible (when used). Above this region, it is of big of importance that the 3D objects are not exposed to greater mechanical deformation, which can result in irreversible plastic deformation of the material. In the case of the PLA samples, this region is found to be above 45 °C.

Considering that most of the mechanical properties deteriorate with the addition of the 50 wt.% cardboard dust into the HDPE, it is recommended to use smaller fraction of the carbon dust, which is also cited in the references as in the research of Kariza et al.<sup>12</sup>

Their research confirmed the 50% of wood content decreased the tensile properties of composite filament with PLA. When smaller amount of wood parts (10%) were used, tensile properties and storage modulus increased.

Therefore the goal of the future researches is also to find the optimal (critical) portion of the cardboard dust, which does not have the significant influence on the mechanical behaviour of the material, especially the HDPE (or might even improve it).

## Acknowledgement

Research is a part of the project *Cel.Cycle, Discarded potentials of biomass. Programme »Potential of biomass for development of advanced materials and bio-based products«* is co-financed by EU Structural Funds in Slovenia.



## 5. References

1. C. K. Thomas, D. Fullerton, Garbage: Recycling, and Illicit Burning or Dumping. In *The Economics of Residential Solid Waste Management*, Routledge, London, Great Britain, 2017, pp. 81–94. DOI:10.4324/9781315240091-5
2. A. M. Omer, *Renew. Sust. Energ. Rev.* **2008**, 12(9), 2265–2300.
3. D. Muck, I. Križanovskij. *3D printing*. Ljubljana, Pasadena, 2015. DOI:10.1016/j.rser.2007.05.001
4. H. N. Chia, B. M. Wu, *J. Biol. Eng.* **2015**, 9(1), 4. DOI:10.1186/s13036-015-0001-4
5. M. A. Sawpan, K. L. Pickering, A. Fernyhough, *Compos. Part A-Appl. S.* **2011**, 42(3), 310–319.
6. B. Bax, J. Müssig, *Compos. Sci. Technol.* **2008**, 68, 1601–1607. DOI:10.1016/j.compscitech.2008.01.004
7. S. H. Lee, T. Ohkita, K. Kitagawa, *Holzforchung.* **2004**, 58(5), 529–536.
8. C. Miao, W. Y. Hamad, *Cellulose.* **2013**, 20(5), 2221–2262. DOI:10.1007/s10570-013-0007-3
9. M. Jonoobi, J. Harun, A. P. Mathew, K. Oksman, *Compos. Sci. Technol.* **2010**, 70(12), 1742–1747. DOI:10.1016/j.compscitech.2010.07.005
10. T. Mokhena, J. Sefadi, E. Sadiku, M. John, M. Mochane, A. Mtibe, *Polymers* **2018**, 10(12), 1363. DOI:10.3390/polym10121363
11. R. Gunti, A. V. Ratna Prasad, A. V. S. S. K. S. Gupta, *Polym Composite.* **2018**, 39(4), 1125–1136. DOI:10.1002/pc.24041
12. M. Kariza, M. Serneka, M. Obućinab, M. Kitek Kuzman, *Materials Today Communications* **2018**, 14, 135–140. DOI:10.1016/j.mtcomm.2017.12.016
13. P. U. Chris-Okafor, C. C. Okonkwo, M. S. Ohaeke, *Am J Polym Sci.* **2018**, 8(1), 17–21.
14. M. A. Kreiger, M. L. Mulder, A. G. Glover, J. M. Pearce, *J. Clean. Prod.* **2014**, 70, 90–96. DOI:10.1016/j.jclepro.2014.02.009
15. F. M. Salleh, A. Hassan, R. Yahya, A. D. Azzahari, *Compos. Part B-Eng.* **2014**, 58, 259–266. DOI:10.1016/j.compositesb.2013.10.068
16. S. Mohanty, S. K. Verma, S. K. Nayak, *Compos. Sci. Technol.* **2006**, 66(3–4), 538–547. DOI:10.1016/j.compscitech.2005.06.014
17. H. Essabir, M. El Achaby, R. Bouhfid, A. Qaiss, *J. Bionic. Eng.* **2015**, 12, 129–141. DOI:10.1016/S1672-6529(14)60107-4
18. J. George, S. S. Bhagawan, S. Thomas, *J. Therm. Anal. Calorim.* **1996**, 47(4), 1121–1140. DOI:10.1007/BF01979452
19. S. Agayev, O. Ozdemir, *Mater Res Express.* **2019**, 6(4), 1–10. DOI:10.1088/2053-1591/aafc42
20. I. O. Eze1, I. O. Igwe1, O. Ogbobe1, E. E. Anyanwu, I. Nwachukwu, *International Journal of Engineering and Technologies* **2016**, 9, 13. DOI:10.18052/www.scipress.com/IJET.9.13
21. A. T. Vasu, C. Reddy, S. Danaboyina, G. K. Manchala, M. Chavali, *J Polym Sci Appl.* **2017**, 1:2.
22. N. A. Patel, J. R. Shah, S. J. Thanki, *International Journal of Creative Research Thoughts (IJCRT).* **2018**, 6, 1244–1254.
23. Q. Tarrés, J. K. Melbø, M. Delgado-Aguilara, F. X. Espinach, P. Mutjé, G. Chinga-Carrasco, *Composites Part B.* **2018**, 153, 70–77. DOI:10.1016/j.compositesb.2018.07.009
24. I. H. Kim, S. C. Lee, Y. G. Jeong, *Fiber. Polym.* **2009**, 10(5), 687–693. DOI:10.1007/s12221-010-0687-6
25. S. Inkinen, M. Hakkarainen, A. C. Albertsson, A. Södergård, *Biomacromolecules.* **2011**, 12(3), 523–532. DOI:10.1021/bm101302t
26. D. Edith, J. L. Six, *Appl. Surf. Sci.* **2006**, 253, 2758–2764. DOI:10.1016/j.apsusc.2006.05.047
27. S. Tsuchikawa, M. Schwanninger, *Appl. Spectrosc. Rev.* **2013**, 48(7), 560–587. DOI:10.1080/05704928.2011.621079
28. J. R. Riba, T. Canals, R. Cantero, *Applied spectroscopy.* **2015**, 69(4), 442–450. DOI:10.1366/14-07611

## Povzetek

Pri ekstrudiranju termoplastičnih filamentov, se po postopku modeliranja s spajanjem slojev, običajno uporabljajo čisti termoplastični polimeri. V zadnjem času so raziskave osredotočene na razvoj novih, biokompozitnih termoplastičnih materialov. V raziskavi smo proučili biokompozitne filamente za 3D tisk, izdelane z dodatkom 50 % kartonskega prahu v HDPE in PLA polimerno matrico. Preučevali smo vpliv dodanega kartonskega prahu na strukturne, morfološke in mehanske lastnosti biokompozitnih filamentov, namenjenih za 3D tisk. Z dodajanjem kartonskega prahu v polimerno matrico HDPE in PLA, smo zaznali spremembe gostote, enakomernosti, kemijske strukture in temperaturnih prehodov vzorcev. Dodajanje le-tega v polimerno matrico HDPE, je povzročilo znižanje trdnosti, žilavosti in deformabilnosti, kar je povzročilo krhkost biokompozitnega filamenta. Kljub temu, da je dodatek kartonskega prahu v PLA znižal natezne lastnosti, pa ni vplival na upogibno togost filamentov in vzorci imajo celo izboljšano kompresijsko trdnost.



Except when otherwise noted, articles in this journal are published under the terms and conditions of the Creative Commons Attribution 4.0 International License

# Synthesis, Crystal Structures and Antimicrobial Activity of Oxidovanadium(V) Complexes with Hydrazone and Pyrone Ligands

Ling-Wei Xue,<sup>1,2,\*</sup> Yong-Jun Han<sup>1</sup> and Xiao-Qiang Luo<sup>1</sup>

<sup>1</sup> School of Chemical and Environmental Engineering, Pingdingshan University, Pingdingshan Henan 467000, P.R. China

<sup>2</sup> Henan Key Laboratory of Research for Central Plains Ancient Ceramics, Pingdingshan University, Pingdingshan Henan 467000, P.R. China

\* Corresponding author: E-mail: pdsuchemistry@163.com

Received: 02-08-2019

## Abstract

A pair of oxidovanadium(V) complexes, [VOLL<sup>1</sup>] (1) and [VOLL<sup>2</sup>] (2), where L is the dianionic form of the hydrazone ligand *N*'-(5-chloro-2-hydroxybenzylidene)pivalohydrazide (H<sub>2</sub>L), L<sup>1</sup> and L<sup>2</sup> are the deprotonated forms of 3-hydroxy-2-methyl-4*H*-pyran-4-one (HL<sup>1</sup>; maltol) and 2-ethyl-3-hydroxy-4*H*-pyran-4-one (HL<sup>2</sup>; ethyl maltol), respectively, have been prepared and characterized by elemental analyses, IR and UV-Vis spectroscopy, and single-crystal X-ray crystallographic determination. The V atoms in the complexes are in octahedral coordination, with the hydrazone ligand coordinated to the V atoms through the phenolate O, imino N and enolate O atoms, and with the pyrone ligands coordinated to the V atoms through two O atoms. The effect of the compounds on the antimicrobial activity against *Staphylococcus aureus*, *Escherichia coli*, and *Candida albicans* was studied.

**Keywords:** Hydrazone; Pyrone; Vanadium complex; Crystal structure; Antimicrobial activity

## 1. Introduction

Schiff bases are important ligands in coordination chemistry.<sup>1</sup> In recent years, metal complexes of Schiff bases have attracted remarkable attention due to their versatile biological activity, such as antifungal, antibacterial and antitumor.<sup>2</sup> Schiff base complexes derived from salicylaldehyde and its derivatives with primary amines, bearing the NNO, NNS, NOO or NSO donor sets, have particular biological activities.<sup>3</sup> Hydrazones, bearing the typical functional group CH=N–NH–C(O), are a kind of Schiff base compounds. Hydrazones show interesting and remarkable biological activities, especially antimicrobial application.<sup>4</sup> Pyrone compounds are bidentate ligands in various metal complexes.<sup>5</sup> Most complexes with pyrone ligands have interesting biological properties.<sup>6</sup> The search of literature indicates that vanadium complexes with pivalol substituted hydrazones are limited. In the present work, two oxidovanadium(V) complexes, [VOLL<sup>1</sup>] (1) and [VOLL<sup>2</sup>] (2), where L is the dianionic form of the hydrazone ligand *N*'-(5-chloro-2-hydroxybenzylidene)pivalohydrazide (H<sub>2</sub>L), L<sup>1</sup> and L<sup>2</sup> are the deprotonated form of 3-hydroxy-2-methyl-4*H*-pyran-4-one (HL<sup>1</sup>; maltol)

and 2-ethyl-3-hydroxy-4*H*-pyran-4-one (HL<sup>2</sup>; ethyl maltol), respectively, are reported.

## 2. Experimental

### 2.1. Material and Methods

5-Chlorosalicylaldehyde, pivalohydrazide, 3-hydroxy-2-methyl-4*H*-pyran-4-one (maltol) and 2-ethyl-3-hydroxy-4*H*-pyran-4-one (ethyl maltol) were purchased from Fluka. Other reagents and solvents were analytical grade and used without further purification. Elemental (C, H, and N) analyses were made on a Perkin-Elmer Model 240B automatic analyser. Infrared (IR) spectra were recorded on an IR-408 Shimadzu 568 spectrophotometer. UV-Vis spectra were recorded on a Lambda 35 spectrometer. X-ray diffraction was carried out on a Bruker SMART 1000 CCD area diffractometer.

### 2.2. Synthesis of H<sub>2</sub>L

5-Chlorosalicylaldehyde (0.156 g, 1.0 mmol) and pivalohydrazide (0.116 g, 1.0 mmol) were dissolved in

methanol (30 mL). The mixture was stirred at ambient temperature for 1 h to give a colorless solution. The solvent was removed to give colorless solid product of  $H_2L$ , which was re-crystallized from ethanol. The yield is 93%. IR data (KBr,  $cm^{-1}$ ): 1623 (C=N). UV-Vis data in methanol [ $10^{-3}$  mol  $L^{-1}$ ;  $\lambda_{max}$  (nm),  $\epsilon$  (L mol $^{-1}$  cm $^{-1}$ )]: 230, 15,570; 290, 14,310; 366, 10,205. Anal. Calcd. (%) for  $C_{12}H_{15}ClN_2O_2$ : C, 56.6; H, 5.9; N, 11.0. Found (%): C, 56.4; H, 6.0; N, 11.1.

### 2. 3. Synthesis of Complex 1

5-Chlorosalicylaldehyde (15.6 mg, 0.10 mmol) was dissolved in methanol (10 mL) and methanol solution (10 mL) of pivalohydrazide (11.6 mg, 0.10 mmol) was added dropwise. Mixture was stirred at ambient temperature for 1 h. Then, 3-hydroxy-2-methyl-4*H*-pyran-4-one (12.6 mg, 0.10 mmol) and VO(acac) $_2$  (26.5 mg, 0.10 mmol) dissolved in methanol (10 mL) was added. The mixture was stirred for 1 h at ambient temperature to give a deep brown solution. Brown block-shaped single crystals suitable for X-ray diffraction were formed by slow evaporation of the solution in air for several days. The yield is 45%, 20.0 mg (based on V). IR data (KBr,  $cm^{-1}$ ): 1612 (C=N), 973 (V=O). UV-Vis data in methanol [ $10^{-3}$  mol  $L^{-1}$ ;  $\lambda_{max}$  (nm),  $\epsilon$  (L mol $^{-1}$  cm $^{-1}$ )]: 275, 16,230; 330, 5,230; 470, 1,575. Anal. Calcd. (%) for  $C_{18}H_{18}ClN_2O_6V$ : C, 48.6; H, 4.1; N, 6.3. Found (%): C, 48.7; H, 4.0; N, 6.2.

### 2. 4. Synthesis of Complex 2

Complex 2 was prepared by the same method as described for complex 1, with 3-hydroxy-2-methyl-4*H*-pyran-4-one replaced by 3-hydroxy-2-ethyl-4*H*-pyran-4-one (14.0 mg, 0.10 mmol). The yield is 51%, 23.4 mg (based on V). IR data (KBr,  $cm^{-1}$ ): 1612 (C=N), 980 (V=O). UV-Vis data in methanol [ $10^{-3}$  mol  $L^{-1}$ ;  $\lambda_{max}$  (nm),  $\epsilon$  (L mol $^{-1}$  cm $^{-1}$ )]: 275, 17,530; 330, 6,020; 470, 4,225. Anal. Calcd. (%) for  $C_{19}H_{20}ClN_2O_6V$ : C, 49.7; H, 4.4; N, 6.1. Found (%): C, 49.9; H, 4.3; N, 6.2.

### 2. 5. X-Ray Structure Determination

Data were collected from selected crystals mounted on glass fibres. The data for the two complexes were processed with SAINT<sup>7</sup> and corrected for absorption using SADABS.<sup>8</sup> Multi-scan absorption corrections were applied with  $\psi$ -scans.<sup>9</sup> The structures were solved by direct methods using the program SHELXS-97 and were refined by full-matrix least-squares techniques on  $F^2$  using anisotropic displacement parameters. The structures were refined by SHELXL-97 program.<sup>10</sup> All hydrogen atoms were placed at the calculated positions. Idealized H atoms were refined with isotropic displacement parameters set to 1.2 (1.5 for methyl groups) times the equivalent isotropic  $U$  values of the parent atoms. The structure of complex 1 contains large solvent accessible void which might accommodate a disordered methanol molecule. The crystallo-

Table 1. Crystallographic data and refinement parameters for complexes 1 and 2

Parameters	1	2
Habit, color	Block, brown	Block, brown
Molecular formula	$C_{18}H_{18}ClN_2O_6V$	$C_{19}H_{20}ClN_2O_6V$
Formula weight	444.73	458.76
Temperature, K	298(2)	298(2)
Radiation ( $\lambda$ , Å)	MoK $_{\alpha}$ (0.71073)	MoK $_{\alpha}$ (0.71073)
Crystal system	Hexagonal	Triclinic
Space group	$R\bar{3}$	$P\bar{1}$
Unit cell dimensions:		
$a$ , Å	40.9930(12)	10.2988(6)
$b$ , Å	40.9930(12)	10.5588(7)
$c$ , Å	7.3018(9)	11.3944(7)
$\alpha$ , °	90	63.0460(10)
$\beta$ , °	90	75.2270(10)
$\gamma$ , °	120	71.1960(10)
$V$ , Å $^3$	10626.2(14)	1036.77(11)
$Z$	18	2
$\rho_{calcd}$ , g cm $^{-3}$	1.251	1.470
$F(000)$	4104	472
Reflections collected	18661	5504
Independent reflections	4387	3812
Data/parameters	2809/253	3123/266
Final $R$ indices ( $I > 2\sigma(I)$ )	$R_1 = 0.0512$ , $wR_2 = 0.1215$	$R_1 = 0.0393$ , $wR_2 = 0.1100$
$R$ indices (all data)	$R_1 = 0.0951$ , $wR_2 = 0.1437$	$R_1 = 0.0497$ , $wR_2 = 0.1188$
Goodness-of-fit on $F^2$	1.050	1.044

**Table 2.** Selected bond lengths (Å) and bond angles (°) for complexes **1** and **2**

<b>1</b>			
V1–O1	1.8563(18)	V1–O2	1.9256(19)
V1–O3	1.8715(16)	V1–O4	2.2710(18)
V1–O6	1.5782(19)	V1–N1	2.0905(19)
O6–V1–O1	97.55(10)	O6–V1–O3	97.92(9)
O1–V1–O3	107.93(8)	O6–V1–O2	101.02(10)
O1–V1–O2	152.43(9)	O3–V1–O2	89.55(8)
O6–V1–N1	95.84(9)	O1–V1–N1	83.99(8)
O3–V1–N1	160.34(8)	O2–V1–N1	74.04(7)
O6–V1–O4	173.68(9)	O1–V1–O4	81.16(8)
O3–V1–O4	76.72(7)	O2–V1–O4	82.44(7)
N1–V1–O4	90.19(7)		
<b>2</b>			
V1–O1	1.848(3)	V1–O2	1.927(2)
V1–O3	1.863(2)	V1–O4	2.258(2)
V1–O6	1.582(3)	V1–N1	2.098(3)
O6–V1–O1	100.45(13)	O6–V1–O3	97.37(12)
O1–V1–O3	96.71(10)	O6–V1–O2	94.86(13)
O1–V1–O2	155.01(11)	O3–V1–O2	100.81(10)
O6–V1–N1	100.20(12)	O1–V1–N1	83.22(11)
O3–V1–N1	162.15(11)	O2–V1–N1	74.66(11)
O6–V1–O4	172.57(12)	O1–V1–O4	85.42(11)
O3–V1–O4	77.29(9)	O2–V1–O4	81.25(10)
N1–V1–O4	84.93(10)		

graphic data for the complexes are listed in Table 1, selected bond lengths and bond angles for complexes **1** and **2** are given in Table 2.

## 2. 6. Antimicrobial Assay

Qualitative determination of antimicrobial activity was done using the disk diffusion method as described in the literature.<sup>11</sup> Suspensions in sterile peptone water from 24-h cultures of microorganisms were adjusted to 0.5 McFarland. Muller-Hinton Petri dishes of 90 mm were inoculated using these suspensions. Paper disks (6 mm in diameter) containing 10 µL of the substance to be tested (at a concentration of 2048 µg mL<sup>-1</sup> in DMSO) were placed in a circular pattern in each inoculated plate. Incubation of the plates was done at 37 °C for 18–24 h. Reading of the results was done by measuring the diameters of the inhibition zones generated by the test substance. Tetracycline was used as a reference substance. Determination of MIC was done using the serial dilutions in liquid broth method. The materials used were 96-well plates, suspensions of microorganism (0.5 McFarland), Muller-Hinton broth (Merck) and stock solutions of each substance to be tested (2048 µg mL<sup>-1</sup> in DMSO). The following concentrations of the substances to be tested were obtained in the 96-well plates: 1024, 512, 256, 128, 64, 32, 16, 8, 4 and 2 µg mL<sup>-1</sup>. After incubation at 37 °C for 18–24 h, the MIC for each tested substance was determined by microscopic observation of

microbial growth. It corresponds to the well with the lowest concentration of the tested substance where microbial growth was clearly inhibited.

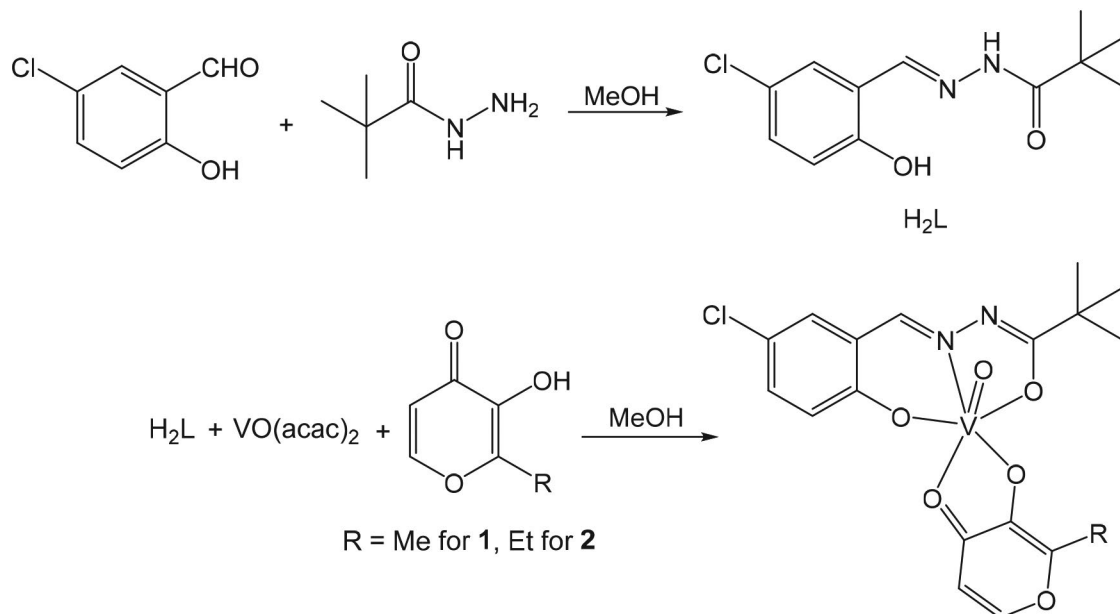
## 3. Results and Discussion

### 3. 1. Chemistry

The hydrazone compound H<sub>2</sub>L was prepared by the condensation of equimolar quantities of 5-chlorosalicylaldehyde with pivalohydrazide in methanol. Complexes **1** and **2** were readily synthesized by reaction of the hydrazone with VO(acac)<sub>2</sub> in methanol in the presence of 3-hydroxy-2-methyl-4H-pyran-4-one and 2-ethyl-3-hydroxy-4H-pyran-4-one, respectively (Scheme 1). All the compounds are very stable at room temperature in the solid state, and soluble in common organic solvents, such as methanol, ethanol, and acetonitrile. The results of the elemental analyses are in accord with the composition suggested for the Schiff base and the complexes.

### 3. 2. IR and UV-Vis Spectra

For the IR spectrum of H<sub>2</sub>L (Fig. S1), the typical band indicative of the azomethine group was observed at 1623 cm<sup>-1</sup>, while in the complexes (Figs. S2 and S3), it was observed at 1612 cm<sup>-1</sup>. The weak absorption at 3450 cm<sup>-1</sup> for H<sub>2</sub>L can be attributed to the vibration of O–H group. The bands indicative of the V=O groups of the complexes



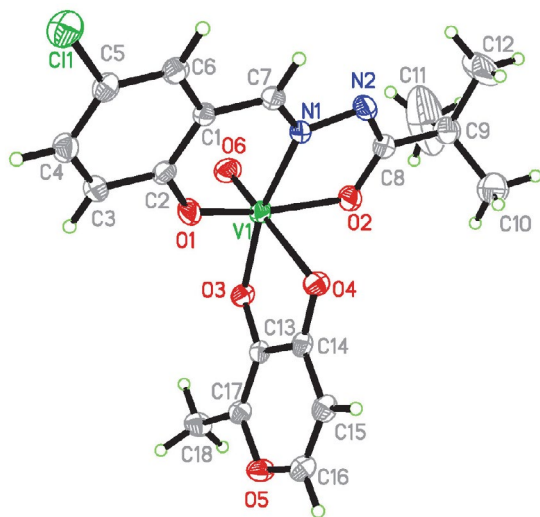
**Scheme 1.** The synthetic procedure of the complexes.

are observed at 973–980  $\text{cm}^{-1}$ . UV-Vis spectra of  $\text{H}_2\text{L}$  and the complexes were measured in methanol. In the spectrum of the hydrazone (Fig. S4), the band centered at 365 nm is attributed to the azomethine chromophore  $\pi\text{--}\pi^*$  transition. The band at higher energy (292 nm) is associated with the benzene  $\pi\text{--}\pi^*$  transition. In the spectra of the complexes (Figs. S5 and S6), the bands at 470 nm are attributed to the intramolecular charge transfer transitions from the  $p_\pi$  orbital on the phenolate O to the empty  $d$  orbitals of the V atoms.<sup>12</sup>

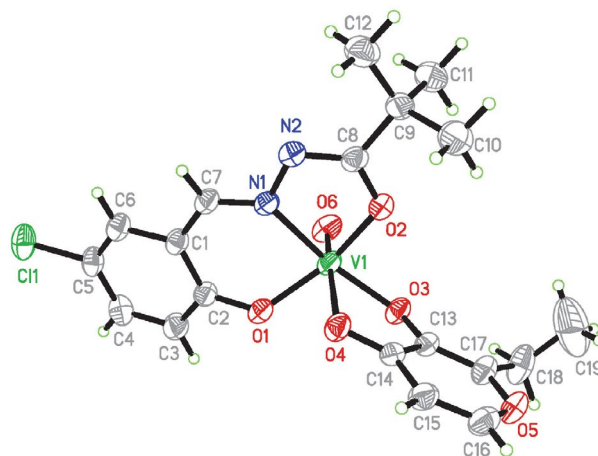
### 3. 3. Structure Description of the Complexes

The molecular structures of complexes **1** and **2** are shown in Figs. 1 and 2, respectively. The V atoms are coor-

minated by one hydrazone ligand, one pyrone ligand, and one oxo O group. The hydrazone ligand coordinated to the V atom through the phenolate O, imino N, and enolate hydroxyl O atoms. The pyrone ligands are coordinated to the V atoms through the deprotonated hydroxyl O and carbonyl O atoms. The V atoms are in octahedral coordination, with the three donor atoms of the hydrazone ligand, and the hydroxyl O atom of the pyrone ligand defining the equatorial plane, and with the carbonyl O atom of the pyrone ligand, and the oxo O group occupying the axial positions. In both complexes, the corresponding bond distances around the V atoms are comparable to each other, and also similar to the corresponding bonds observed in the similar vanadium complexes with hydrazones or pyrones.<sup>13</sup> The *cis* and *trans* coordinate bond angles in the equatorial planes are range from 74.66(11) to 100.81(10)° and from 155.01(11) to 162.15(11)° for complex **1**, and



**Fig. 1.** Perspective view of complex **1** with 30% probability thermal ellipsoids.



**Fig. 2.** Perspective view of complex **2** with 30% probability thermal ellipsoids.



from 74.04(7) to 107.93(8)° and from 152.43(9) to 160.34(8)° for complex **2**, respectively. In addition, the values for the axial *trans* O–V–O angles are 172.57(12)° and 173.68(9)°, respectively, for complexes **1** and **2**. All the above bond values indicating the distortion of the octahedral coordination from ideal geometry.

### 3. 4. Antimicrobial Activity

The antimicrobial activity results are summarized in Table 3. A comparative study of minimum inhibitory concentration (MIC) values of the hydrazone and the complexes indicates that the complexes have better activity than the free hydrazone. Generally, this is caused by the greater lipophilic nature of the complexes than the ligand. Such increased activity of the metal chelates can be explained on the basis of chelating theory.<sup>14</sup> On chelating, the polarity of the metal atoms will be reduced to a greater extent due to the overlap of the ligand orbital and partial sharing of positive charge of the metal atoms with donor atoms. Further, it increases the delocalization of *p*-electrons over the whole chelate ring and enhances the lipophilicity of the complexes. This increased lipophilicity enhances the penetration of the complexes into lipid membrane and blocks the metal binding sites on enzymes of microorganisms.

From the results, it is obvious that the two complexes have higher antibacterial and antifungal activities against *Staphylococcus aureus*, *Escherichia coli*, and *Candida albicans* when compared to the free hydrazone. This phenomenon is in accordance with those reported in literature.<sup>15</sup> The two complexes have in general the same activities against all the bacteria and fungi strains. The complexes have strong activity against *Escherichia coli*, with MIC value of 1.0 µg/mL, which is superior to tetracycline. The complexes have strong activity against *Staphylococcus aureus*, yet, they are weaker than tetracycline. It is interesting that both complexes have medium activity against *Candida albicans*, which is rarely seen in metal complexes.<sup>16</sup>

**Table 3.** MIC values (µg/mL) for the antimicrobial activities of the tested compounds

Compounds	<i>Staphylococcus aureus</i>	<i>Escherichia coli</i>	<i>Candida albicans</i>
H <sub>2</sub> L	64	16	> 512
<b>1</b>	2.0	1.0	64
<b>2</b>	2.0	1.0	64
Tetracycline	0.32	2.12	> 1024

### 4. Material

CCDC 1896231 for **1**, and 1896233 for **2** contain the supplementary crystallographic data for this paper. These

data can be obtained free of charge at <http://www.ccdc.cam.ac.uk/const/retrieving.html> or from the Cambridge Crystallographic Data Centre, 12 Union Road, Cambridge CB2 1EZ, UK; fax: +44(0)1223-336033 or email: [deposit@ccdc.cam.ac.uk](mailto:deposit@ccdc.cam.ac.uk).

### 5. Acknowledgments

This research was supported by the Top-class foundation of Pingdingshan University (no. PXY-BSQD-2018006 and PXY-PYJJ-2018002).

### 6. References

- (a) X. W. Zhu, *Russ. J. Coord. Chem.* **2018**, *44*, 421–424; DOI:10.1134/S1070328418070084  
(b) D. L. Peng, *Russ. J. Coord. Chem.* **2017**, *43*, 189–195; DOI:10.1134/S1070328417030058  
(c) D.-L. Peng, *J. Struct. Chem.* **2018**, *59*, 589–594; DOI:10.1134/S0022476618030125  
(d) X.-W. Zhu, *Acta Chim. Slov.* **2018**, *65*, 939–945; DOI:10.17344/acsi.2018.4607  
(e) D.-L. Peng, *Transit. Met. Chem.* **2016**, *41*, 843–848; DOI:10.1007/s11243-016-0086-8  
(f) D.-L. Peng, *Russ. J. Coord. Chem.* **2017**, *43*, 404–410. DOI:10.1134/S1070328417060045
- (a) Z.-C. Liu, B.-D. Wang, Z.-Y. Yang, Y. Li, D.-D. Qin, T.-R. Li, *Eur. J. Med. Chem.* **2009**, *44*, 4477–4484; DOI:10.1016/j.ejmech.2009.06.009  
(b) D.-D. Qin, Z.-Y. Yang, G.-F. Qi, T.-R. Li, *Transition Met. Chem.* **2009**, *34*, 499–505; DOI:10.1007/s11243-009-9222-z  
(c) Y.-Y. Yu, H.-D. Xian, J.-F. Liu, G.-L. Zhao, *Molecules* **2009**, *14*, 1747–1754. DOI:10.3390/molecules14051747
- (a) Y.-T. Li, J.-W. Dong, Y. Lu, Y.-T. Gu, C.-N. Shang, F.-Y. Liu, Y. Xin, C.-L. Jing, Z.-L. You, *Chinese J. Inorg. Chem.* **2018**, *34*, 1192–1198;  
(b) Z. You, H. Yu, Z. Li, W. Zhai, Y. Jiang, A. Li, S. Guo, K. Li, C. Lv, C. Zhang, *Inorg. Chim. Acta* **2018**, *480*, 120–126; DOI:10.1016/j.ica.2018.05.020  
(c) L. W. Xue, G. Q. Zhao, Y. J. Han, Y. X. Feng, *Russ. J. Coord. Chem.* **2011**, *37*, 262–269; DOI:10.1134/S1070328411030110  
(d) Z. You, H. Yu, B. Zheng, C. Zhang, C. Lv, K. Li, L. Pan, *Inorg. Chim. Acta* **2018**, *469*, 44–50; DOI:10.1016/j.ica.2017.09.011  
(e) L. W. Xue, Y. J. Han, G. Q. Zhao, Y. X. Feng, *Russ. J. Coord. Chem.* **2012**, *38*, 24–28. DOI:10.1134/S1070328411120104
- (a) M. B. Labib, J. N. Philoppes, P. F. Lamie, E. R. Ahmed, *Bioorg. Chem.* **2018**, *76*, 67–80; DOI:10.1016/j.bioorg.2017.10.016  
(b) A. Erguc, M. D. Altintop, O. Atli, B. Sever, G. Iscan,

- G. Gormus, A. Ozdemir, *Lett. Drug Des. Discov.* **2018**, *15*, 193–202;
- (c) M. A. Abdelgawad, M. B. Labib, M. Abdel-Latif, *Bioorg. Chem.* **2017**, *74*, 212–220;  
DOI:10.1016/j.bioorg.2017.08.014
- (d) A. A. Zakeyah, J. Whitt, C. Duke, D. F. Gilmore, D. G. Meeker, M. S. Smeltzer, M. A. Alam, *Bioorg. Med. Chem. Lett.* **2018**, *28*, 2914–2919;
- (e) M. A. Abdelrahman, I. Salama, M. S. Gomaa, M. M. Elaasser, M. M. Abdel-Aziz, D. H. Soliman, *Eur. J. Med. Chem.* **2017**, *138*, 698–714;  
DOI:10.1016/j.ejmech.2017.07.004
- (f) P. Sridhar, M. Alagumuthu, S. Arumugam, S. R. Reddy, *RSC Advances* **2016**, *6*, 64460–64468.  
DOI:10.1039/C6RA09891F
5. (a) B. Song, K. Saatchi, G. H. Rawji, C. Orvig, *Inorg. Chim. Acta* **2002**, *339*, 393–399;  
DOI:10.1016/S0020-1693(02)00961-1
- (b) W. Y. Hsieh, S. Liu, *Synth. React. Inorg. Met.-Org. Nano-Met. Chem.* **2005**, *35*, 61–70;
- (c) W. Y. Hsieh, C. M. Zaleski, V. L. Pecoraro, P. E. Fanwick, S. A. Liu, *Inorg. Chim. Acta* **2006**, *359*, 228–236;
- (d) V. Vrdoljak, B. Prugovečki, M. Cindrić, D. Matković-Čalogović, A. Brbot-Šaranović, *Acta Chim. Slov.* **2008**, *55*, 828–833;
- (e) S. Guo, N. Sun, Y. Ding, A. Li, Y. Jiang, W. Zhai, Z. Li, D. Qu, Z. You, *Z. Anorg. Allg. Chem.* **2018**, *644*, 1172–1176. DOI:10.1002/zaac.201800060
6. (a) M. Rangel, A. Tamura, C. Fukushima, H. Sakurai, *J. Biol. Inorg. Chem.* **2001**, *6*, 128–132;  
DOI:10.1007/s007750000180
- (b) C.-T. Yang, S. G. Sreerama, W.-Y. Hsieh, S. Liu, *Inorg. Chem.* **2008**, *47*, 2719–2727;  
DOI:10.1021/ic7022506
- (c) D. Sanna, L. Biro, P. Buglyo, G. Micera, E. Garribba, *J. Inorg. Biochem.* **2012**, *115*, 87–99;  
DOI:10.1016/j.jinorgbio.2012.04.020
- (d) E. A. Enyedy, O. Domotor, E. Varga, L. Kiss, R. Trondl, C. G. Hartinger, B. K. Keppler, *J. Inorg. Biochem.* **2012**, *117*, 189–197.  
DOI:10.1016/j.jinorgbio.2012.08.005
7. SMART and SAINT. Area Detector Control and Integration Software, Madison (WI, USA): Bruker Analytical X-ray Instruments Inc., 1997.
8. G. M. Sheldrick, SADABS, Program for Empirical Absorption Correction of Area Detector Data, Göttingen (Germany): Univ. of Göttingen, 1997.
9. A. C. T. North, D. C. Phillips, F. S. Mathews, *Acta Crystallogr. A* **1968**, *24*, 351–359.  
DOI:10.1107/S0567739468000707
10. G. M. Sheldrick, *Acta Crystallogr.* **2015**, *C71*, 3–8.
11. (a) A. Barry, *Procedures and Theoretical Considerations for Testing Antimicrobial Agents in Agar Media*, In: Antibiotics in Laboratory Medicine, Lorian, V. (Ed.), Baltimore: Williams and Wilkins, 1991;
- (b) T. Rosu, M. Negoiu, S. Pasculescu, E. Pahontu, D. Poirier, A. Gulea, *Eur. J. Med. Chem.* **2010**, *45*, 774–781.  
DOI:10.1016/j.ejmech.2009.10.034
12. G. Asgedom, A. Sreedhara, J. Kivikoski, E. Kolehmainen, C. P. Rao, *J. Chem. Soc. Dalton Trans.* **1996**, 93–97.  
DOI:10.1039/dt9960000093
13. (a) L.-Y. He, X.-Y. Qiu, J.-Y. Cheng, S.-J. Liu, S.-M. Wu, *Polyhedron* **2018**, *156*, 105–110;  
DOI:10.1016/j.poly.2018.09.017
- (b) S. D. Kurbah, M. Asthana, I. Syiemlieh, A. A. Lywait, M. Longchar, R. A. Lal, *J. Organomet. Chem.* **2018**, *876*, 10–16;  
DOI:10.1016/j.jorgchem.2018.08.025
- (c) M. A. Naziri, E. Sahin, N. Seferoglu, B. Shaabani, *J. Coord. Chem.* **2018**, *71*, 89–103;  
DOI:10.1080/00958972.2018.1432857
- (d) H. Y. Qian, *Russ. J. Coord. Chem.* **2017**, *43*, 780–786; DOI:10.1134/S1070328417110070
- (e) P. Adak, B. Ghosh, B. Pakhira, R. Sekiya, R. Kuroda, S. K. Chattopadhyay, *Polyhedron* **2017**, *127*, 135–143;  
DOI:10.1016/j.poly.2017.01.054
- (f) X.-F. Chen, T.-R. Wang, Z. Ma, Y. Yu, L. Tang, L.-Y. Jin, G.-H. Sheng, H.-L. Zhu, *Polyhedron* **2017**, *137*, 321–324. DOI:10.1016/j.poly.2017.05.011
14. J. W. Searl, R. C. Smith, S. Wyard, *J. Proc. Phys. Soc.* **1961**, *78*, 1174–1181.  
DOI:10.1088/0370-1328/78/6/311
15. (a) X. W. Zhu, *Russ. J. Coord. Chem.* **2018**, *44*, 335–339;  
DOI:10.3103/S1068367418040213
- (b) H. Y. Qian, *Russ. J. Coord. Chem.* **2018**, *44*, 32–38;  
DOI:10.1134/S1070328418010074
- (c) D.-L. Peng, N. Sun, *Acta Chim. Slov.* **2018**, *65*, 895–901. DOI:10.17344/acsi.2018.4543
16. (a) B. Thati, A. Noble, R. Rowan, B. S. Creaven, M. Walsh, M. McCann, D. Egan, K. Kavanagh, *Toxicol. Vitro* **2007**, *21*, 801–808;  
DOI:10.1016/j.tiv.2007.01.022
- (b) D. C. Menezes, F. T. Vieira, G. M. de Lima, J. L. Wardell, M. E. Cortes, M. P. Ferreira, M. A. Soares, A. V. Boas, *Appl. Organometal. Chem.* **2008**, *22*, 221–226;  
DOI:10.1002/aoc.1375
- (c) B. Chudzik, I. B. Tracz, G. Czernel, M. J. Fiolka, G. Borsuk, M. Gagos, *Eur. J. Pharm. Sci.* **2013**, *49*, 850–857. DOI:10.1016/j.ejps.2013.06.007

## Povzetek

Sintetizirali smo dva oksidovanadijeva(V) kompleksa  $[\text{VOLL}^1]$  (**1**) in  $[\text{VOLL}^2]$  (**2**), kjer je L dianion hidrazona  $N'$ -(5-kloro-2-hidroksibenziliden)pivalohidrazida ( $\text{H}_2\text{L}$ ),  $\text{L}^1$  in  $\text{L}^2$  sta deprotonirani obliki 3-hidroksi-2-metil-4*H*-pyran-4-ona ( $\text{HL}^1$ ; maltol) in 2-etil-3-hidroksi-4*H*-piran-4-ona ( $\text{HL}^2$ ; etil maltol), ter ju okarakterizirali z elementno analizo, IR in UV-Vis spektroskopijo in monokristalno rentgensko analizo. V kompleksih ima vanadijev atom oktaedrično koordinacijo s hidrazonskim ligandom koordiniranim na V atom preko fenolatnega O, iminskega N in enolatnega O atoma ter s pironskim ligandom koordiniranim preko dveh O atomov. Določili smo tudi protimikrobno aktivnost obeh spojin proti *Staphylococcus aureus*, *Escherichia coli* in *Candida albicans*.



Except when otherwise noted, articles in this journal are published under the terms and conditions of the Creative Commons Attribution 4.0 International License

Scientific paper

# DFT/TDDFT Investigation on the Electronic Structure and Spectroscopic Properties of Cis-Dioxomolybdenum (VI) Complexes

Imane Seghir, Nadia Nebbache,\* Yazid Meftah, Salah Eddine Hachani and Samira Maou

Laboratory of Applied chemistry LCA, Faculty of Sciences, University of Biskra,  
B.P. 145, R.P. 07000 Biskra, Algeria

\* Corresponding author: E-mail: nadianebbache1@gmail.com; nadia\_nebbache@yahoo.fr  
Telephone/Fax: (+213)33543318

Received: 02-11-2019

## Abstract

In this contribution, two mononuclear molybdenum complexes with  $H_2L$  tridentate (ONO) Schiff base ligand are characterized using computational techniques. Density functional theory (DFT) and its time extension (TD-DFT) calculations are performed to study the electronic structure in ground and excited state and to interpret the electronic absorption spectra in gas and aqueous phases. TDDFT calculations affirm that the LMCT charge transfer dominates for both complexes and a hypochromic effect on absorption properties is observed according to solvent substitution. All theoretical results compare nicely with available experimental data.

**Keywords:** Mo complexes; schiff base; electronic absorption spectra; DFT; TD-DFT

## 1. Introduction

Transition metal complexes have attracted considerable attention in the development of coordination chemistry; due to their high stability and their important properties in different oxidation state.<sup>1–3</sup> These inorganic compounds exhibit a broad range of antiviral,<sup>4</sup> antibacterial,<sup>5–8</sup> antifungal agents,<sup>9</sup> anti-inflammatory activities,<sup>10</sup> transporting layer in organic light-emitting diodes<sup>11</sup> and hold promise to be used in various chemical and physical fields. The interest on the mentioned compounds increases during the last two decades, particularly for complexes containing functional groups with lone electron pairs such as studied Schiff base molybdenum complexes.<sup>12–14</sup>

Molybdenum complexes with general formula  $[MoO_2(H_2L)]$ <sup>15–17</sup> are used for their excellent properties as a stimulator in the enzymatic reactions.<sup>18,19</sup> According to two studies (Rayati et al and Jain et al.),<sup>20,21</sup> molybdenum complexes with O and N donor ligands are seen as very strong and potential catalysts for both homogeneous and heterogeneous reactions. They are also used in some industrial processes such as epoxidation of olefins and ammoxidation of propene.<sup>22</sup>

In fact, laboratory techniques, such as spectroscopic analysis, are used to understand the properties of metal complexes but these techniques are expensive, time-consuming, and in some cases not convincing to explain some molecular phenomena. Resort to theoretical chemistry, Density Functional Theory (DFT) and its time dependent extension, Time-Dependent Density Functional Theory (TD-DFT) are very solicited due to their ability to give accurate results of the electronic structures and molecular properties.<sup>23</sup>

In a recent research, two types of mononuclear metallic complexes  $[MoO_2(L)(H_2O)]$  and  $[MoO_2(L)(MeOH)]$  containing L tridentate (ONO) Schiff base ligand, where L ( $H_2L$ ) = 2,4-dihydroxybenzaldehyde and benzoylhydrazone, were synthesized. They were characterized using various spectroscopic and structural techniques including UV-Vis, FTIR and XRD and an octahedral structural arrangement was observed. The electrochemical properties of the resulting metal complexes have been investigated by using cyclic voltammetry measurements.<sup>24</sup>

Although all their important experimental results of these complexes were reported, no theoretical background has been proposed yet to provide supplementary insights for the experimental data.

The current contribution represents a theoretical study of structural, electronic and spectroscopic properties of these two complexes by using quantum calculations based on DFT and TDDFT approaches.

## 2. Computational Details

The ground state geometry of molybdenum complexes was fully optimized using density functional theory (DFT) calculations<sup>25–28</sup> based on CAM-B3LYP exchange-correlation functional<sup>29</sup> with the double- $\zeta$  quality basis set LANL2DZ<sup>30,31</sup> associated to a pseudopotential on Mo atom. The 6-311G\* basis set<sup>32,33</sup> was used for N, C, O, and H atoms. The electronic absorption spectra were simulated by using time-dependent density functional theory

(TD-DFT)<sup>34</sup> in gas and aqueous phase combined with polarized continuum model (PCM)<sup>35</sup>. The CAM-B3LYP exchange-correlation functional is known, because of its long-range corrections, to be well adapted to the calculations of charge-transfer spectra in complexes. All DFT/TDDFT calculations were performed using GAUSSIAN 09 Rev: D.01 program package.<sup>36</sup>

## 3. Results and Discussion

### 3.1. Optimized Geometry

X rays diffraction (XRD) data of the molybdenum complexes revealed that the studied systems have a distorted octahedral geometry with ONO deprotonated ligand via two phenolic oxygen and iminic nitrogen atoms. The

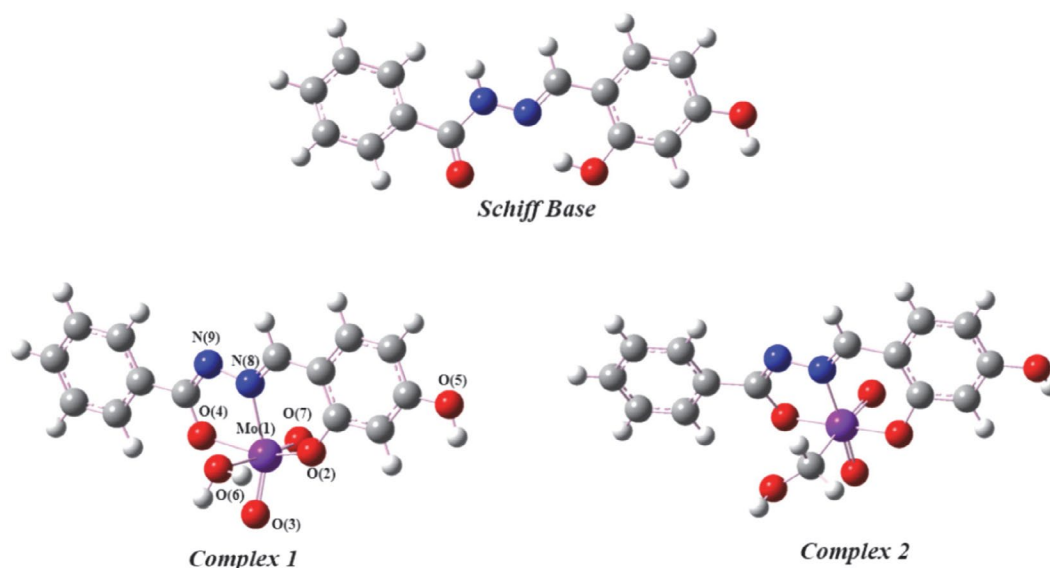


Figure 1. Optimized molecular structures of Schiff base and the two Mo complexes at CAM-B3LYP/LANL2DZ/6-311G\* level

Table 1. Selected experimental and theoretical geometric parameters at CAM-B3LYP/LANL2DZ/6-311G\* level of complex 1.

Bond length (Å°)			Angle (°)		
	Theo	Exp <sup>24</sup>		Theo	Exp <sup>24</sup>
Mo(1)-O(3)	1.711(0)	1.7162	O(2)-Mo(1)-O(4)	145.21(5)	150.058
Mo(1)-O(7)	1.694(3)	1.6842	O(3)-Mo(1)-N(8)	152.77(2)	155.208
Mo(1)-O(6)	2.488(2)	2.3782	O(6)-Mo(1)-O(7)	173.88(5)	173.589
Mo(1)-O(4)	2.001(6)	2.0082	O(3)-Mo(1)-O(7)	107.46(6)	105.539
Mo(1)-O(2)	1.976(3)	1.9202	O(4)-Mo(1)-N(8)	70.80(6)	71.307
Mo(1)-N(8)	2.250(6)	2.2402	O(3)-Mo(1)-O(4)	96.48(1)	96.848
N(8)-N(9)	1.379(6)	1.4033	O(2)-Mo(1)-O(3)	101.35(5)	103.768
N(9)-C(11)	1.289(2)	1.3093	O(2)-Mo(1)-N(8)	79.98(3)	83.278
N(8)-C(16)	1.285(4)	1.2823	O(4)-Mo(1)-O(6)	78.86(2)	97.608
O(4)-C(11)	1.319(2)	1.3213	O(4)-Mo(1)-O(7)	101.79(8)	96.691
O(2)-C(12)	1.330(6)	1.3503	O(7)-Mo(1)-N(8)	98.82(9)	97.608
C(12)-C(15)	1.409(9)	1.4113	O(2)-Mo(1)-O(7)	100.95(6)	98.431
C(15)-C(16)	1.434(6)	1.4223	O(3)-Mo(1)-O(6)	78.41(0)	79.957
C(10)-C(11)	1.473(2)	1.4583	O(6)-Mo(1)-N(8)	75.57(2)	76.497



optimized ground state geometries of complex 1, complex 2 and Schiff base ligand at CAM-B3LYP level of theory are shown in Figure 1. The main optimized geometry parameters associated to the complex 1 are collected in Table 1 (complex 2 calculated structural parameters are given in supporting information file). It can be seen that the optimized structure parameters are generally in good agreement with the available experimental data.<sup>24</sup> Slight differences between the calculated bond lengths and angles values and those given by the refinement of X-ray results are observed, these differences are within 0.02 Å for bonds and 2.1° for angles, respectively. This discrepancy may be partially assigned to the neglect of lattice interactions during DFT calculations. The largest difference occurs for O(4)-Mo(1)-O(6) angle which differs by 18° with the experimental value, a discrepancy probably due to the effect of neighboring molecules.

### 3. 2. Frontier Molecular Orbitals Analysis

Frontier molecular orbitals (FMO) have an important role for giving an insight into the chemical reactivities and some of the physical properties. The spectral properties of transition metal complexes are strongly related to the energy of these orbitals. According to Fukui's theory,<sup>37,38</sup> the reactivity of the complexes can be estimated using the energy gap ( $\Delta E_{H-L}$ ), the highest occupied molecular orbital (HOMO) could act as an electron donor while lowest unoccupied molecular orbital (LUMO) could be an electron acceptor, knowing that when the corresponding energy gap decreases, the reactivity of the complex increases and vice versa. The DFT molecular orbital diagram corresponding to the studied complexes are

shown in Figure 2. It can be seen from this Figure that the energy gap of complex 1 (5.89 eV) is considerably higher than the energy gap of complex 2 (2.83 eV), which indicates that the complex 2 is more reactive compared to the complex 1.

The contribution rate values of Mo central atom and the ligands are given in Table 2. The HOMO eigenvalue decreases from -7.43 eV in complex 1 to -11.22 eV in complex 2. The HOMO orbitals are mainly localized on ligands. The value of the contribution for non-metal atoms in HOMO, HOMO-1 and HOMO-2 are between 98% and 100% in complex 1 and between 89% and 100% in complex 2. These results predict that the electronic transitions are predominantly occurred via a ligand-metal charge transfer (LMCT).

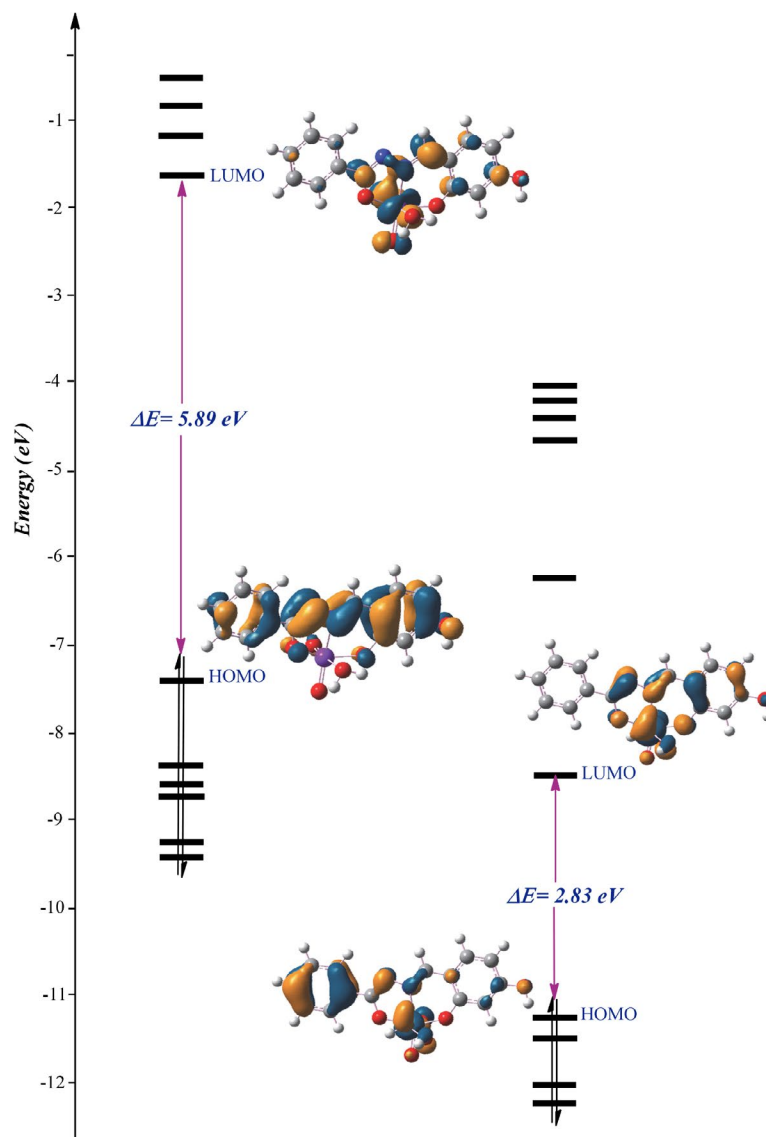
Furthermore, the difference between LUMO and LUMO+1 is of 0.26 eV in complex 1, suggesting that LUMO+1 can also easily contribute to electronic transition between HOMO and LUMO+1 whereas in the complex 2, the energy difference between LUMO and LUMO+1 is about of 3.04 eV, which confirms that LUMO+1 can't participate in the electronic transfer.

### 3. 3. Absorption Properties

The electronic transitions in metal complexes involve electron transfer between metal atom and ligands. If the transfer occurs from ligand to the metal, the transition is called a ligand-to-metal charge-transfer (LMCT). If the electronic charge shifts from the ligand to another ligand, the transition is named ligand-to-ligand charge-transfer (LLCT). Intra ligand charge transfer (ILCT) arises from the transfer of electrons in the same ligand.

Table 2. Energy and composition of some selected MOs of Mo complexes.

	MO	Energy (eV)	% of composition		
			Mo	Oxo	Schiff base
Complex 1	LUMO+3	-0.51	43	14	43
	LUMO+2	-0.78	48	21	31
	LUMO+1	-1.21	66	18	16
	LUMO	-1.56	35	44	21
	HOMO	-7.43	0	0	100
	HOMO-1	-8.44	0	2	98
	HOMO-2	-8.58	0	0	100
	HOMO-3	-8.72	0	1	99
	HOMO-4	-9.26	0	19	81
Complex 2	LUMO+3	-4.38	36	17	47
	LUMO+2	-4.79	66	21	13
	LUMO+1	-5.33	24	16	60
	LUMO	-8.38	2	11	87
	HOMO	-11.22	2	9	89
	HOMO-1	-11.68	0	0	100
	HOMO-2	-12.00	1	6	93
	HOMO-3	-12.31	0	3	96
	HOMO-4	-12.84	1	38	61



**Figure 2.** Frontier molecular orbital (FMO) diagram of complex 1 (left) and complex 2 (right)

**Table 3.** The experimental and theoretical electronic absorption wavelengths and important contributions for Mo complexes.

	$\lambda_{\text{Exp}}^{24}(\text{nm})$	$\lambda_{\text{Theo}}(\text{nm})$	Energy(eV)	f	Important contributions	Nature
Complex 1	418	402.34	3.08	0.23	H→L (89.78%)	LMCT/LLCT/ILCT
	329	323.36	3.83	0.14	H→L+1 (85.34%)	LMCT/LLCT/ILCT
	304	301.30	4.11	0.64	H-1→L (40.98%) H→L+2 (40.41%)	LMCT/LLCT/ILCT LMCT/LLCT/ILCT
		251.58	4.92	0.17	H-2→L (27.49%) H-1→L+2 (21.86%)	LMCT/LLCT/ILCT LMCT/LLCT/ILCT
	408	397.68	3.11	0.16	H→L (89.21%)	ILCT
Complex 2		321.59	3.85	0.08	H→L+2(82.06%)	LMCT
	324	310.87	3.98	0.01	H-6→L (39.14%)	LMCT/LLCT/ILCT
					H-4→L (17%)	LMCT/LLCT/ILCT
					H-6→L+1(10.13%)	LMCT/LLCT/ILCT

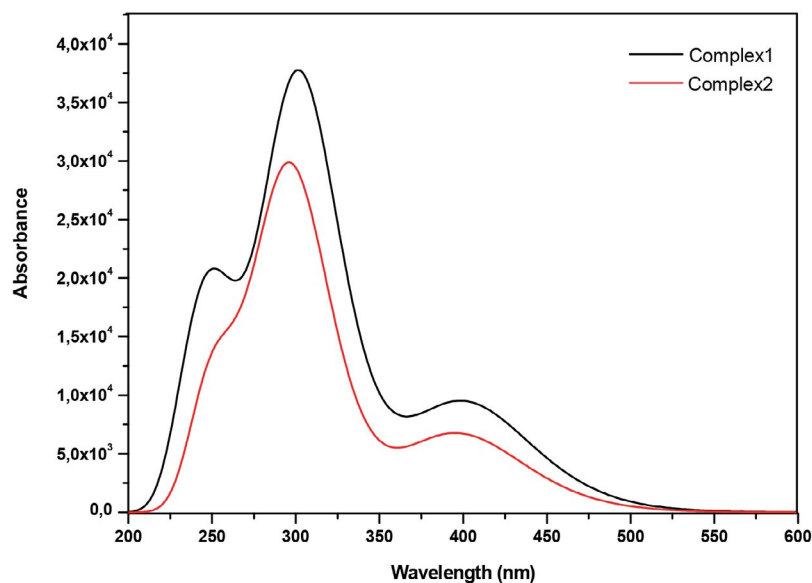


Figure 3. The theoretical UV-Vis spectra for two Mo complexes.

Time-dependent density functional theory (TD-DFT) calculations combined with CAM-B3LYP method have been performed in liquid phase to investigate the absorption properties of the two Mo complexes. The calculated absorption parameters with experimental data are listed in Table 3. The UV spectrum of complex 1 monitored in Figure 3 shows four bands located at 402.34, 323.36, 311.12 and 301.30 nm. The important contributions of orbitals in different transitions reported in table 3 attribute these bands respectively to HOMO→LUMO, HOMO→LUMO+1, HOMO-1→LUMO, and HOMO→LUMO+2 due to  $\pi(\text{H}_2\text{L}) \rightarrow d(\text{Mo})$  charge transfer (LMCT) mixed with both  $\pi \rightarrow \pi^*$  and  $n \rightarrow \pi^*$  transitions (ILCT/LLCT). Regarding the UV spectrum of complex 2 (Figure

3), two principal bands were observed at 397.68 and 321.59 nm attributed to  $\pi(\text{H}_2\text{L}) \rightarrow d(\text{Mo})$  charge transfer (LMCT). The decrease detected in the absorption intensity gives a hypochromic effect. It's due to the substitution of the ligand.

### 3. 4. Solvent Effect on Absorption Properties

TD-DFT calculations have been performed in order to predict the effect of different solvents on absorption properties in the UV range of complex1. Figure 4 are illustrate maximum absorption bands ( $\lambda_{\text{max}}$ ) in the obtained spectra of the studied compound in vacuum and in differ-

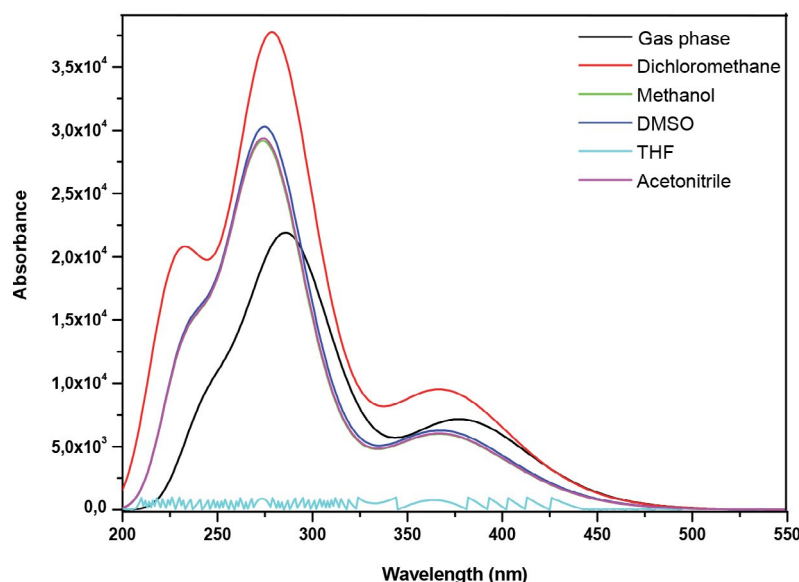


Figure 4. The theoretical UV-Vis spectra for complex1 in different solvents

ent solvents: dichloromethane ( $\text{CH}_2\text{Cl}_2$ ), methanol ( $\text{CH}_2\text{OH}$ ), dimethyl sulfoxide DMSO ( $\text{C}_2\text{H}_6\text{OS}$ ), tetrahydrofuran THF ( $(\text{CH}_2)_4\text{O}$ ) and acetonitrile ( $\text{CH}_3\text{CN}$ ). It can be seen that the complex 1 exhibits two bands of maximum absorption between 400 and 225 nm for all solutions and the spectra look the same. The decrease in absorption intensity indicates that the used solvents have simultaneously hypochromic effect on the absorption properties of the examined compound. Compared to those of complex 1 in vacuum the absorption shift to a longer wavelength (red shift) indicates that bathochromic shift is observed. Similar trends are observed in DMSO, methanol and acetonitrile solvents but with lower band intensities compared to dichloromethane. In the case of THF, no band appeared, indicating that the tested complex dissolved in THF does not exhibit typical absorption bands in UV range.

### 3. 5. Infrared Spectra

Fourier transformed infrared spectroscopy analysis is mainly used to identify the functional groups in the molecules. In the case of our study, vibrational frequency calculations<sup>39,40</sup> were performed at the same theoretical level to compare between the calculated IR spectrum of the complex 1 and the experimental one. The absence of imaginary frequencies in the calculated vibrational modes indicates that the obtained optimized geometry corresponds to a minimum on the potential energy surface. The theoretical infrared spectra of the complex 1 and its ligand are shown in Figure 5 and 6 respectively. The experimental and theoretical vibrational wavenumbers and intensities for the complex 1 and the ligand are reported in Table 4. The com-

parison of the results displayed reveals that the experimental and the theoretical values of the vibrational wavenumbers are approximately close.

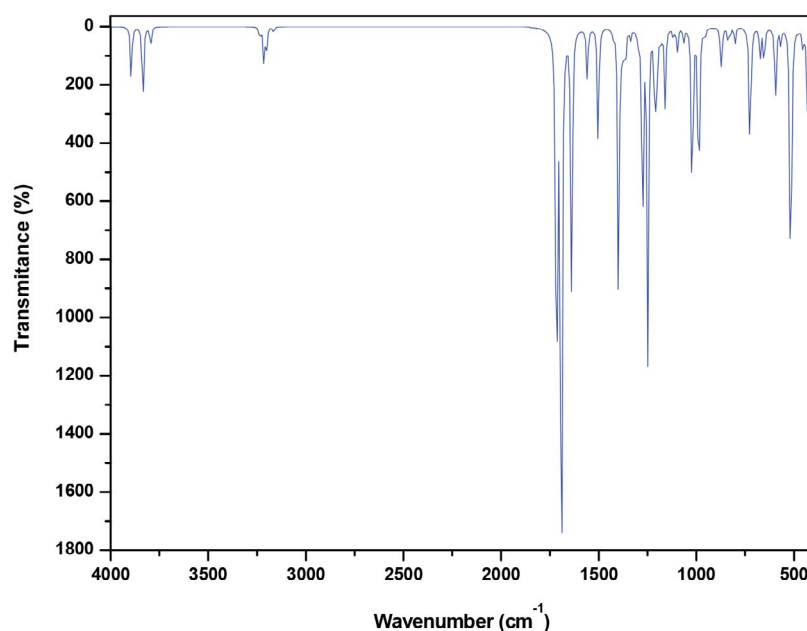
Regarding the IR signals of the ligand, two intense bands are observed at 1672.30 and 1765.66  $\text{cm}^{-1}$  corresponding to  $\nu(\text{C}=\text{O})$  and  $\nu(\text{C}=\text{N})$  stretching of the imine group,<sup>41</sup> respectively. Thin bands were observed in the range of 3160–3360  $\text{cm}^{-1}$ , assigned to the presence of hydrogen bonded  $\nu(\text{NH})$  and  $\nu(\text{OH})$ .<sup>42,43</sup> The existence of the above bands confirms that the ligand of the studied compound is a Schiff base with a hydroxyl substituent.

As represented in Figure 5 and reported in Table 4, the dioxidomolybdenum (VI) complex with a cis  $\text{MoO}_2$  part has two strong bands at 987.75 and 1023.18  $\text{cm}^{-1}$ , assigned to a symmetrical and asymmetrical  $\nu(\text{O}-\text{M}-\text{O})$  vibrations respectively.<sup>44, 45</sup>

The absence of NH vibration in IR spectra of the complex indicates that a nitrogen atom N coordinates Mo center by the free lone electron pair.

**Table 4.** The experimental and theoretical vibrational wavenumbers and intensities for the ligand and its Mo (VI) complex.

Assignments	FTIR freq ( $\text{cm}^{-1}$ )	
	Exp <sup>24</sup>	Cal
$\nu(\text{H}_2\text{O})$	3512	3794.93
$\nu(\text{OH})$	3300	3834.65
$\nu(\text{CN})$	1614	1633.91
$\nu(\text{N}_2)$	1132	1097.66
$\nu(\text{CO})$	1240	1248.9
$\nu(\text{MO})$	565	594.12
$\nu(\text{MN})$	441	382.05
$\nu(\text{MO}_2)$	946	1023.18



**Figure 5.** Theoretical IR spectra for complex 1

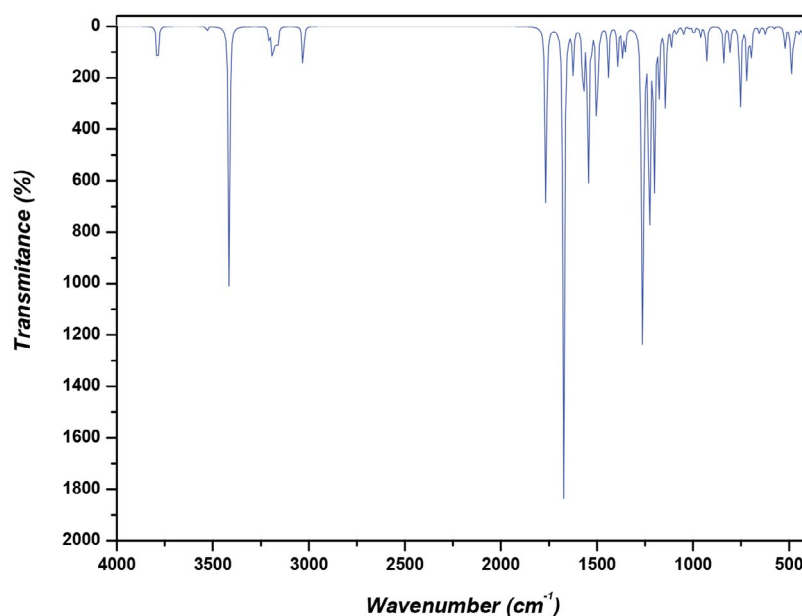


Figure 6. Theoretical IR spectra for ligand

## 4. Conclusion

In this paper, we investigated the structural parameters, electronic structures and spectroscopic properties of two cis-dioxomolybdenum (VI) complexes using DFT and TDDFT calculations. The optimized geometries in the ground state show that the structural parameters are in agreement with the experimental values. The predominant transitions are governed by a ligand-metal charge transfer (LMCT) due to the electronic configuration of the metal atom Mo (VI) in the complex, which is equal to zero ( $d^0$ ), therefore, the d-d excited state is unavailable usually referred as metal-centered (MC) transition. UV-Vis spectra of complex 1 calculated in gas and in liquid phase solvents show a decrease in absorption intensity indicating that the used solvents have simultaneously hypochromic effect on the absorption properties. The complex dissolved in THF does not exhibit typical absorption bands in UV range. According to IR spectra, the observed bands confirm that the ligand of the studied compound is a Schiff base with a hydroxyl substituent. The disappearance of NH vibration indicates that the nitrogen atom N coordinates Mo center by the free lone electron.

## 5. Acknowledgments

The authors wish to thank Professor Henry Chermette (Institute of Analytical Sciences, UMR 5280, Lyon, FRANCE) for technical support, for its fruitful discussion and for the careful proofreading of the article.

**Conflict of interest:** The authors declare that they have no conflict of interest.

## Supporting Information Available

Selected theoretical geometric parameters of complex 2 are reported in Table S1 and the Frontier molecular orbitals (FMO) of Mo complexes are given in Figure S1.

## 6. References

1. C. J. Windorff, G. P. Chen, J. N. Cross, W. J. Evans, F. Furche, A. J. Gaunt, M. T. Janicke, S. A. Kozimor and B. L. Scott, *Journal of the American Chemical Society*. **2017**, 139, 3970–3973. DOI:10.1021/jacs.7b00706
2. S. Sangeeta, K. Ahmad, N. Noorussabah, S. Bharti, M. K. Mishra, S. R. Sharma and M. Choudhary, *Journal of Molecular Structure*. **2018**, 1156, 1–11. DOI:10.1016/j.molstruc.2017.11.062
3. O. V. Nesterova, D. S. Nesterov, A. Krogul-Sobczak, M. F. C. Guedes da Silva and A. J. L. Pombeiro, *Journal of Molecular Catalysis A: Chemical*. **2017**, 426, 506–515. DOI:10.1016/j.molcata.2016.09.005
4. K. S. Kumar, S. Ganguly, R. Veerasamy and E. De Clercq, *European journal of medicinal chemistry*. **2010**, 45, 5474–5479. DOI:10.1016/j.ejmech.2010.07.058
5. I. Sheikhshoaie, S. Y. Ebrahimipour, M. Sheikhshoaie, H. A. Rudbari, M. Khaleghi and G. Bruno, *Spectrochimica Acta Part A: Molecular and Biomolecular Spectroscopy*. **2014**, 124, 548–555. DOI:10.1016/j.saa.2014.01.043
6. H. M. Mehdi, Z. Niklas, G. Golar, B. Ferdinand, B. Mojtaba, S. J. A. and M.-Z. N. C., *European Journal of Inorganic Chemistry*. **2018**, 2018, 2549–2556.
7. S. Y. Ebrahimipour, M. Khosravan, J. White and S. Fekri, *Applied Organometallic Chemistry*. **2018**, 32, 1–11. DOI:10.1002/aoc.4233



8. S. P. Sovilj, D. Mitić, B. J. Drakulić and M. Milenković, *Journal of the Serbian Chemical Society*. **2012**, 77, 53–66.  
DOI:10.2298/JSC110328160S
9. S. Pasayat, S. P. Dash, P. K. Majhi, Y. P. Patil, M. Nethaji, H. R. Dash, S. Das and R. Dinda, *Polyhedron*. **2012**, 38, 198–204.  
DOI:10.1016/j.poly.2012.03.007
10. G. L. Parrilha, R. P. Vieira, A. P. Rebolledo, I. C. Mendes, L. M. Lima, E. J. Barreiro, O. E. Piro, E. E. Castellano and H. Beraldo, *Polyhedron*. **2011**, 30, 1891–1898.  
DOI:10.1016/j.poly.2011.04.024
11. W.-J. Shin, J.-Y. Lee, J. C. Kim, T.-H. Yoon, T.-S. Kim and O.-K. Song, *Organic Electronics*. **2008**, 9, 333–338.  
DOI:10.1016/j.orgel.2007.12.001
12. L. H. Abdel-Rahman, N. M. Ismail, M. Ismael, A. M. Abu-Dief and E. A.-H. Ahmed, *Journal of Molecular Structure*. **2017**, 1134, 851–862. DOI:10.1016/j.molstruc.2017.01.036
13. R. N. Egekenze, Y. Gultneh and R. Butcher, *Inorganica Chimica Acta*. **2018**, 478, 232–342.  
DOI:10.1016/j.ica.2018.01.027
14. D. Majumdar, J. K. Biswas, M. Mondal, M. S. Babu, R. K. Metre, S. Das, K. Bankura and D. Mishra, *Journal of Molecular Structure*. **2018**, 1155, 745–757.  
DOI:10.1016/j.molstruc.2017.11.052
15. Ö. Şahin, Ü. Ö. Özdemir, N. Seferoğlu, Z. K. Genc, K. Kaya, B. Aydın, S. Tekin and Z. Seferoğlu, *Journal of Photochemistry and Photobiology B: Biology*. **2018**, 178, 428–439.  
DOI:10.1016/j.jphotobiol.2017.11.030
16. M. Chakraborty, S. Roychowdhury, N. R. Pramanik, T. K. Raychaudhuri, T. K. Mondal, S. Kundu, M. G. Drew, S. Ghosh and S. S. Mandal, *Polyhedron*. **2013**, 50, 602–611.  
DOI:10.1016/j.poly.2012.12.006
17. J. M. Mir, S. Roy, P. K. Vishwakarma and R. C. Maurya, *Journal of the Chinese Advanced Materials Society*. **2018**, 6, 1–19.
18. A. Magalon, J. G. Fedor, A. Walburger and J. H. Weiner, *Coordination chemistry reviews*. **2011**, 255, 1159–1178.  
DOI:10.1016/j.ccr.2010.12.031
19. C. J. Doonan, H. L. Wilson, K. Rajagopalan, R. M. Garrett, B. Bennett, R. C. Prince and G. N. George, *Journal of the American Chemical Society*. **2007**, 129, 9421–9428.  
DOI:10.1021/ja071402a
20. S. Rayati, N. Rafiee and A. Wojtczak, *Inorganica Chimica Acta*. **2012**, 386, 27–35. DOI:10.1016/j.ica.2012.02.005
21. K. R. Jain, W. A. Herrmann and F. E. Kühn, *Coordination Chemistry Reviews*. **2008**, 252, 556–568.  
DOI:10.1016/j.ccr.2007.10.018
22. A. Rezaeifard, M. Jafarpour, H. Raissi, M. Alipour and H. Stoeckli-Evans, *Zeitschrift für anorganische und allgemeine Chemie*. **2012**, 638, 1023–1030.  
DOI:10.1002/zaac.201200079
23. R. G. Parr: *Horizons of Quantum Chemistry*, Springer, **1980**, pp. 5–15.
24. S. A. Aboafia, S. A. Elsayed, A. K. El-Sayed and A. M. El-Hendawy, *Journal of Molecular Structure*. **2018**, 1158, 39–50.  
DOI:10.1016/j.molstruc.2018.01.008
25. P. Hohenberg, *Phys. Rev.* **1964**, 136, B864.  
DOI:10.1103/PhysRev.136.B864
26. C. Lee, W. Yang and R. G. Parr, *Physical review B*. **1988**, 37, 785. DOI:10.1103/PhysRevB.37.785
27. X.-W. Fan, X.-H. Ju and H.-M. Xiao, *Journal of hazardous materials*. **2008**, 156, 342–347.  
DOI:10.1016/j.jhazmat.2007.12.024
28. T. Wei, W. Zhu, J. Zhang and H. Xiao, *Journal of hazardous materials*. **2010**, 179, 581–590.
29. T. Yanai, D. P. Tew and N. C. Handy, *Chemical Physics Letters*. **2004**, 393, 51–57. DOI:10.1016/j.cplett.2004.06.011
30. P. J. Hay and W. R. Wadt, *The Journal of chemical physics*. **1985**, 82, 270–283. DOI:10.1063/1.448799
31. P. J. Hay and W. R. Wadt, *The Journal of Chemical Physics*. **1985**, 82, 299–310. DOI:10.1063/1.448975
32. A. Petersson, A. Bennett, T. G. Tensfeldt, M. A. Al-Laham, W. A. Shirley and J. Mantzaris, *The Journal of chemical physics*. **1988**, 89, 2193–2218. DOI:10.1063/1.455064
33. W. J. Hehre, R. Ditchfield and J. A. Pople, *The Journal of Chemical Physics*. **1972**, 56, 2257–2261.  
DOI:10.1063/1.1677527
34. T. Helgaker and P. Jørgensen, *The Journal of chemical physics*. **1991**, 95, 2595–2601. DOI:10.1063/1.460912
35. E. Cancès, B. Mennucci and J. Tomasi, *The Journal of chemical physics*. **1997**, 107, 3032–3041. DOI:10.1063/1.474659
36. R. A. Gaussian09, Inc., Wallingford CT **2009**.
37. K. Fukui, T. Yonezawa and H. Shingu, *The Journal of Chemical Physics*. **1952**, 20, 722–725. DOI:10.1063/1.1700523
38. K. Fukui, T. Yonezawa, C. Nagata and H. Shingu, *The Journal of Chemical Physics*. **1954**, 22, 1433–1442.  
DOI:10.1063/1.1740412
39. F. Perakis, L. De Marco, A. Shalit, F. Tang, Z. R. Kann, T. D. Kühne, R. Torre, M. Bonn and Y. Nagata, *Chemical reviews*. **2016**, 116, 7590–7607.  
DOI:10.1021/acs.chemrev.5b00640
40. D. Ojha, K. Karhan and T. D. Kühne, *Scientific reports*. **2018**, 8, 16888. DOI:10.1038/s41598-018-35357-9
41. M. Ocak, T. Ak, A. Aktaş, N. Özbek, O. C. Çağlıcı, A. Güm-rükçüoğlu, H. Kantekin, Ü. Ocak and H. Alp, *Journal of fluorescence*. **2017**, 27, 59–68. DOI:10.1007/s10895-016-1934-9
42. Y. Tan, N. Zhao, J. Liu, P. Li, C. N. Stedwell, L. Yu and N. C. Polfer, *Journal of The American Society for Mass Spectrometry*. **2017**, 28, 539–550. DOI:10.1007/s13361-016-1575-x
43. S. T. El-Sayed, A. M. Ali, E. El-Sayed, W. G. Shousha and N. I. Omar, *J. Appl. Pharm. Sci*. **2017**, 7, 6–12.
44. R. Takjoo, A. Hashemzadeh, H. A. Rudbari and F. Nicolo, *Journal of Coordination chemistry*. **2013**, 66, 345–357.  
DOI:10.1080/00958972.2012.748191
45. N. Maheswari and G. Muralidharan, *Applied Surface Science*. **2017**, 416, 461–469. DOI:10.1016/j.apsusc.2017.04.094

## Povzetek

V tem prispevku smo z uporabo računskih tehnik opredelili dva enojedra molibdenova kompleksa s Schiffovo bazo  $H_2L$  tridentatnim (ONO) ligandom. Teorija gostotnega funkcionala (DFT) in njeni časovno podaljšani (TD-DFT) izračuni so bili izvedeni v namen preučevanja elektronske strukture osnovnega in vzbujenega stanja ter za interpretacijo elektronskih absorpcijskih spektrov v plinski in vodni fazi. Izračuni TDDFT potrjujejo, da je LMCT prenos naboja prevladujoč za oba kompleksa. Opazili smo hipokromni učinek na absorpcijske lastnosti glede na substitucijo topila. Vsi teoretični rezultati se dobro ujemajo z razpoložljivimi eksperimentalnimi podatki



Except when otherwise noted, articles in this journal are published under the terms and conditions of the Creative Commons Attribution 4.0 International License

# Effect of Swelling of Chemical Reagents and the Sulfuric-Chromic Acid Bath on Surface Texturizing of Poly(Acrylonitrile-Butadiene-Styrene)

Lorena Magallón Cacho,<sup>1,3</sup> José de Jesús Pérez Bueno,<sup>1,\*</sup> Yunny Meas Vong<sup>1</sup>  
and Guy Stremsdoerfer<sup>2</sup>

<sup>1</sup> Centro de Investigación y Desarrollo Tecnológico en Electroquímica, S.C. Parque Tecnológico Querétaro s/n Sanfandila, Pedro Escobedo, Qro., México. 76703.

<sup>2</sup> Laboratory of Tribology and Dynamics of the Systems UMR 5513 Ecole Central de Lyon. 36 Avenue Guy de Collongue B P 163 69131, Ecully Cedex, France.

<sup>3</sup> CONACYT - Instituto Nacional de Electricidad y Energías Limpias, Av. Reforma 113, Col. Palmira. Cuernavaca, Mor. C.P. 62490.

\* Corresponding author: E-mail: jperez@cideteq.mx;  
+52(442) 2116090, +52(442)2116001

Received: 02-21-2019

## Abstract

The surface modification of copolymer substrates of Acrylonitrile-Butadiene-Styrene (ABS) is significant for the electroplating industry. The sulfuric-chromic acid bath, used in the Electroless process, conditioning the ABS surface by selective oxidation of poly(butadiene) creating interconnected micro-holes, which allows an excellent mechanical adherence between the metallic film and the substrate. The chromium in its hexavalent form Cr(VI) is harmful to human beings and the environment being a carcinogenic element. This work shows a surface alteration effect with different types of chemical reagents on ABS surface and its treatment with the sulfuric-chromic acid bath in concentrations below those of the normal process, to analyze the possible application of the electroless process. The use of the different chemical reagents studied favored the alteration of the ABS surface causing various types of surface reactions, which could be shown spontaneously or during the conditioning step.

**Keywords:** Electroless; ABS; Chromium Trioxide; Surface Modification

## 1. Introduction

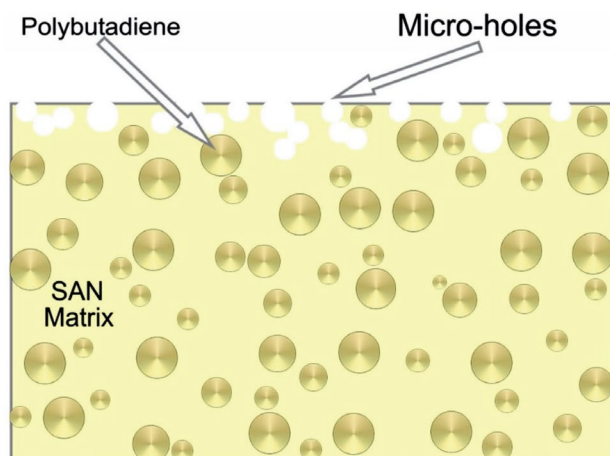
The metallizing of plastic materials has great industrial importance worldwide. The capability of metallizing plastic substrates represents a significant reduction of costs in both production and transport of materials due to a lower weight compared to metallic products. Metallization of plastics can be obtained by different methods as PVD, CVD, electric arc spraying,<sup>1</sup> and other chrome (VI)-free methods.<sup>2</sup> The most used process of metallizing non-conductive materials is known as “Electroless,” which allows metallizing autocatalytically, in the absence of electric current, non-conductive materials that cannot be directly metallized by a conventional electrolytic process.<sup>3,4</sup> Once it has formed a thin conductive layer (Ni or Cu), an electrolytic deposit grows a metallic film and provides the final

finishing. ABS metallized pieces even can be reprocessed by chemical pickling.<sup>5</sup>

The surface of the piece has to be conditioned so that an excellent adherence exists between the foil and the substrate. With this purpose, in the Electroless process, there is the etching stage, which creates favorable conditions to carry on the surface metallization in a correct way and has the desired adhesion. The etching is performed with a mixture of CrO<sub>3</sub> and H<sub>2</sub>SO<sub>4</sub>, which in certain conditions of temperature and elevated concentrations of Cr(VI), modifies the surface of the substrate.<sup>3</sup>

The most used not-conductive substrate for metallizing is the thermoplastic copolymer Acrylonitrile-Butadiene-Styrene (ABS). Its conformation consists of a continuous matrix of the copolymer poly(styrene-co-acrylonitrile) and a phase segregated throughout the volume in the form

of microspheres of poly(butadiene). The superficial spheres of poly(butadiene) being in contact with the sulfuric-chromic acid bath are oxidized selectively, leaving empty sites (microvoids) interconnected with the frequency that the poly(butadiene) sites had (Figure 1). Subsequently, the growth of the metallic film is performed from inside the voids outward promoting mechanical adhesion.<sup>6–8</sup>



**Figure 1.** Schematic representation of the poly(butadiene) distribution in the matrix of poly(styrene-acrylonitrile) (SAN) and micro-voids formation due to selective etching with the sulfuric-chromic acid bath.

Numerous approaches were reported for metallization of ABS, polyimide and other polymers with surface modification by different methods such as photocatalysis,<sup>9,10</sup> plasma,<sup>11–13</sup> molecules grafted,<sup>14</sup> and silane coupling.<sup>15</sup>

Although the use of the sulfuric-chromic acid bath results in an excellent appearance and adhesion of the metallic deposit, reason for which it has been used on a large scale per decades, it has major disadvantages. The Cr (VI) is carcinogenic, which represents serious risks to humans and the environment.<sup>16,17</sup> Also, special handling of this type of residues involves additional costs to industrial processes, especially in the effluent treatment systems and optimal control of the manufacturing process to prevent labor hazards. Therefore, it is of primary importance the study of alternatives to create a conductive layer on the surface of ABS with an environmentally acceptable process, doing a partial or total replacement of the current method.

The use of electroless plating has been extended to these objects designed and then 3D printed using ABS. Stages of surface preparation for the process such as aluminum paint paste and aluminum epoxy paste have been used for electroless coating varying temperature and deposition time.<sup>18</sup>

The electroless process have been combined with other techniques such as Laser Direct Structuring (LDS)<sup>19</sup>

or Selective Surface Activation Induced by Laser (SSAIL)<sup>20</sup> using organocopper compounds for portable electronics. This allows obtaining precise metallized patterns with selective fabrication onto ABS finished with electroless copper plating (ECP).

In the last decade, there have been a very intensive quest for improving the etching treatment for ABS especially for copper and nickel plating.<sup>19,21,22</sup> There are many different alternatives proposed in these studies and all of them with the same target, avoid the use of Cr<sup>6+</sup> in metallization of ABS and other polymers.<sup>22</sup> The studies focused in substituting the sulfuric-chromic acid bath, and among many different procedures, the use of KMnO<sub>4</sub> have been one of the more important points of reference.<sup>21,23</sup>

Nowadays, the swelling of substances into polymers are mainly used in hydrogels for making of them superabsorbent composites<sup>24</sup> and conferring them some characteristics by the swelling of substances such as ionic,<sup>25,26</sup> anti-microbial,<sup>27</sup> fuels,<sup>28</sup> fertilizers.<sup>29</sup> There are other works focused in the humidity absorption into polymers.<sup>26,30,31</sup>

In the case of the swelling for electroless process, recent works reported the use of swelling for increase the adhesion strength of a polymer such as polyimide and an electroless copper layer with a TiO<sub>2</sub> photocatalytic treatment.<sup>32</sup>

There is a proposal of a surface swelling-induced strategy-based facile electroless deposition method to prepare copper circuits on various polymer substrates such as ABS, polyimide, and silicon rubber.<sup>33</sup> There are reports of an Ag catalytic process using swelling impregnation pretreatment method for electroless nickel deposition on Kevlar fiber, which show both corrosion resistance and high tensile strength.<sup>34</sup>

There are some works that, as an alternative to swelling, use voids on the surface to trap water and cause an effect of hydrophilicity and self-cleaning by a direct contact of external drops with the water already on the surface.<sup>35</sup>

There are works related to the deposition of some layers on a swelling polymer that leads to the formation of uniform wrinkles after the release of polymer strain because of isotropic polymer elongation. Particularly, conductive silver wrinkles have been grown on an elastomer by combining polymer swelling with electroless deposition for ultrasensitive pressure sensors.<sup>36</sup>

For such a reason, this work presents the study of various chemical reagents that pre-treat, through a chemical stage, the surface modification of ABS with subsequent treatment with the sulfuric-chromic acid bath at low concentrations. This pretreatment is performed as a stage before that of conditioning within the Electroless process. The final objective, using chemical reagents before the sulfuric-chromic acid bath, is obtaining a rough surface using low concentrations of Cr(VI) that allows having an excellent adherence between the substrate and the autocatalytic

cally obtained plating through the Electroless process.

The selection criteria for the chemical reagents were based on the dissolution times of the polymers, their flash-points and chemical resistance presented by the ABS in the presence of the selected reagents, for a 48 h period. Saubestre<sup>37</sup> mentioned that the use of nitric acid and methanol favors solvation of the polymer surfaces, favoring its oxidation when performing the etching with the sulfuric-chromic acid bath at lower concentrations (75 g/L  $\text{CrO}_3$ ) than required by the usual process (350 g/L  $\text{CrO}_3$ ).

## 2. Experimental

The two different types of ABS used in this study were A) oval ABS pieces from the brand Nacobre (without dye – without white powder of  $\text{TiO}_2$  in rutile form) and B) ABS plates from the brand Senosan, AA50 White 1000 (with dye, having rutile  $\text{TiO}_2$  for provide a white appearance). The reason for including two types of ABS, with or without white titania powder and both broadly used in the industry, was the expected change or influence on the swelling and metallization process.

The characterization of the ABS was done by Infra-red Spectroscopy (FT-IR) with a Thermo Nicolet FT-IR model Nexus was used identifying the bands corresponding to the ABS, according to each of the functional groups.

A dissolution using industrial grade acetone was prepared for identification of the dye present in the ABS Senosan AA50 White 1000. The obtained precipitate was left to dry and was subsequently milled. Later, it was characterized by X-ray Diffraction (XRD), with a Bruker AXS, model D8Advance using a 40 mA and 40 kV, which allowed to obtain the diffractograms of the crystalline components.

The analysis of molecular weights for both types of ABS was performed using the technique of Gel Permeation Chromatography (GPC) with 20 mg of sample in 10 mL of HPLC grade THF. The temperature in the oven was 40 °C and kept under mechanical stirring for 2 h. Standards of poly(styrene) were used and the equipment utilized was a Chromatograph of Permeation in Gel of the brand Waters.

The conventional etching tests were performed by dipping ABS (without dye) in the sulfuric-chromic acid bath. The concentration was 350 g/L of  $\text{CrO}_3$  (99.2%, JT Baker) and 22% v/v  $\text{H}_2\text{SO}_4$  (98.4%, JT Baker). The mixture was stirred and heated to an average temperature of 75 °C and, to determine the degree of attack on the plastic surface, tests were performed at three different times: 4, 10 and 15 minutes, which served as references of industry-wide standard procedure in conditioning the surface of ABS.

The ABS pieces (without dye) were submerged in 30 mL of four different organic solvents separately: Diethyl oxalate (99 +%, Aldrich) for 7 min, phenetole (99%, Aldrich) for 5, 10, 20 and 30 s, industrial grade acetone at

10, 30, 50 and 80% v/v with methanol (99.9%, JT Baker), and 30 mL of nitric acid (65.6%, JT Baker), all these tests at room temperature. Likewise, tests were conducted dipping ABS (with dye) in a solution of  $\text{KMnO}_4$  (99.8%, JT Baker) at a concentration of 0.5 M with a time of experimentation of 15 min. The solution was subjected to heating with an average temperature of 78 °C and stirring during the tests. The pieces were rinsed with deionized water and allowed to dry at room temperature. Subsequently, treatments were performed using the sulfuric-chromic acid bath at  $\text{CrO}_3$  concentrations of 350 g/L and 75 g/L.

Hardness measurements were performed with Vickers micro-indentation technique on substrates of ABS (without dye) having as pretreatment immersion into phenetole, diethyl oxalate, Acetone, and the sulfuric-chromic etching, and on a substrate without pretreatment which served as a reference. We used a Digital Alpha MXT-Microhardness Tester brand Matsuzawa with a load of 200 g.

The contact angle measurements were performed with a Digidrop GBX, Scientific Instruments. The surface images were obtained by Scanning Electron Microscopy (SEM) with a JEOL equipment, model JSM-5400LV at a magnification of 5000X and voltage of 20 kV. Adhesion measurements were performed using the “Cross-Cut Tape Test” according to ASTM method D-3359, using a kit manufactured by Precision Gage & Tool Co. The measurement of reflectance was done with an Ocean Optics spectrometer, Inc. Model USB2000 with fiber extension and an integrating sphere suspended approximately 4 mm over an ABS plate immersed into a solution of electroless Ni.

## 3. Results and Discussion

### 3. 1. Characterization of ABS (FT-IR)

The ABS has the following four characteristic bands: a) 2240  $\text{cm}^{-1}$  corresponding to the vibration of the nitrile groups (C–N) present in the acrylonitrile; b) 970  $\text{cm}^{-1}$  belonging to the deformation of the CH groups trans-R H C = C H R present in the poly (butadiene); c) 760  $\text{cm}^{-1}$  and d) 700  $\text{cm}^{-1}$  characteristic of the vibrational modes of the benzene ring monosubstituted, present in the styrene. Figure 2 shows the spectra obtained resulting from the characterization of the two different types of ABS studied in this work, where the characteristic bands were identified for the three constituent monomers.

Figure 3 shows the X-ray powder diffractogram for the analysis of a solution of ABS Senosan AA50 White 1000, where the peaks are identified for the 100%  $\text{TiO}_2$  as a rutile phase. It is widely known that the rutile phase has a lower photocatalytic activity compared to the anatase phase,<sup>38</sup> which added to the encapsulating polymer by photo-oxidation restricts and prevents the formation of OH radicals with water. Therefore, it is possible to discard the material used in this conformation for photocatalysis in the case that the pieces would be illuminated with UV.



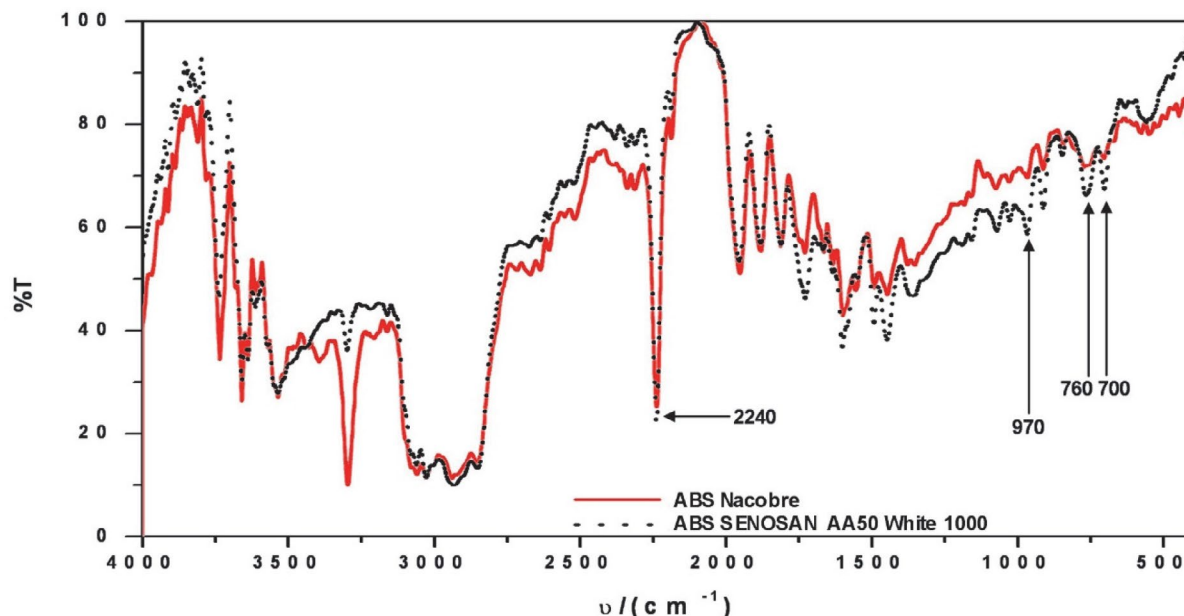


Figure 2. FT-IR spectra of ABS from Nacobre and SENOSAN AA50 White 1000.

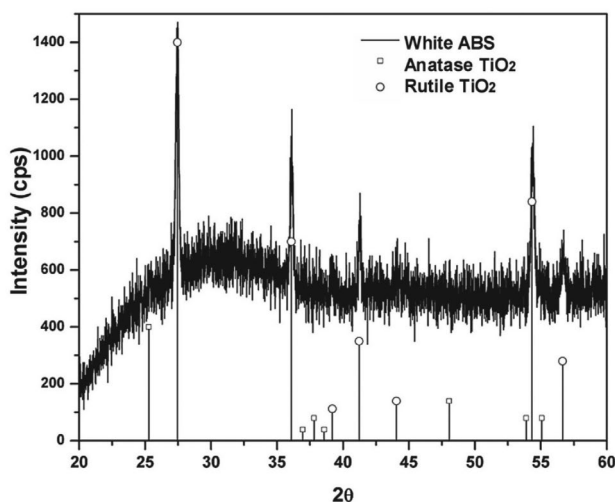


Figure 3. X-ray diffractogram of ABS dissolution with dye.

The molecular weight measured by GPC technique for ABS without dye was about 136.26 Daltons and for the ABS with dye was about 169.13 Daltons. It is important to know that there is not a marked difference in molecular weights between the polymers, which have been studied comparing their behavior with organic solvents, as there is a significant dependence of this parameter.

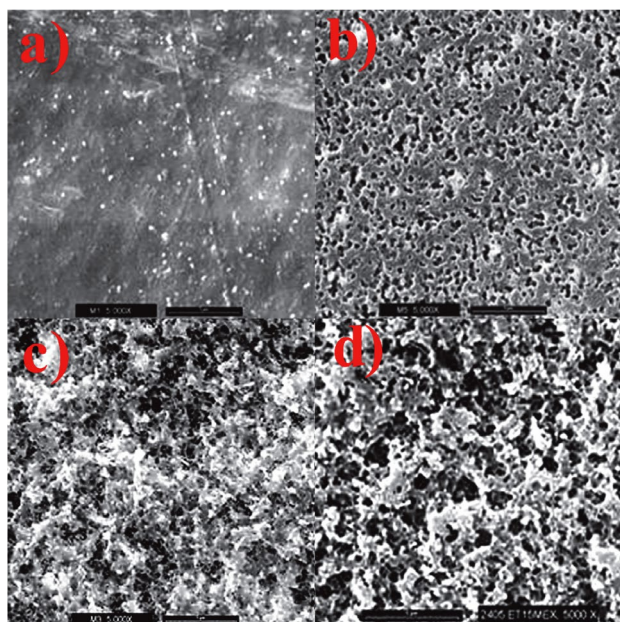
### 3. 2. Conditioning Tests with the Sulfuric-Chromic Acid Bath

The sulfuric-chromic acid bath is influenced by two factors, the concentration of the bath and the immersion

time. The combination of which has resulted in varying degrees of attack on the substrate surface. Figure 4 (a) shows the micrograph corresponding to the surface for one piece without coloring and without treatment, which was taken as a reference to the original substrate conditions. Figure 4 (b, c, d) shows the effect caused by etching at different times. The formation of micro-holes in the samples was notorious, which had an average size of about 0.26  $\mu\text{m}$  for the sample with 4 minutes of treatment. Comparing the images reveal the severity of the surface modification for longer times of treatment (10 and 15 min) with an average hole size of about 0.51  $\mu\text{m}$ . The etching of the polybutadiene domains was caused by the sulfuric-chromic acid bath. This bath is highly oxidant and the chrome reacts with the polymer by the oxidation reaction of  $-\text{C}=\text{C}-$  bonds in the polybutadiene  $[-\text{CH}_2-\text{CH}=\text{CH}-\text{CH}_2]_n-$  leaving some polar groups in the surface such as  $-\text{OH}$  and  $-\text{COOH}$ .<sup>39</sup> The polybutadiene is washed away from the surface leaving voids as shown in Fig 4b, 4c, 4d. Polybutadiene is very sensitive to oxidative degradation. There are many works showing details about the oxidation and foto-oxidation processes of polybutadiene,<sup>40</sup> polystyrene,<sup>41</sup> polyacrylonitrile,<sup>41</sup> and other polymers.<sup>42,43</sup>

### 3. 3. Test for Surface Texturizing with the Sulfuric-Chromic Acid Bath

When the mixture had been used continuously, the concentration may vary due to the reduction of  $\text{Cr}^{+6}$  to  $\text{Cr}^{+3}$  causing that its oxidizing power was diminished. Table 1 shows the contact angle values obtained for different treatments. The value of the contact angle for the sulfuric-chromic treatment increases considerably, comparing



**Figure 4.** ABS SEM micrographs of (a) untreated; (b) and (c) etching with the sulfuric-chromic acid bath (350g/L),  $T_{\text{avg}} = 75\text{ }^{\circ}\text{C}$ ,  $t_{\text{imm}} = 4$  and 10 min of undyed parts, respectively; (d) 350 g / L,  $T_{\text{avg}} = 75\text{ }^{\circ}\text{C}$ , 15 min  $t_{\text{imm}}$  = white ABS samples. The scale bars in all cases were 1  $\mu\text{m}$  at 5000X.

it to an untreated substrate, which was attributable to the influence of the formation of a highly rough surface. However, the factor that the water droplet can be held in a smaller number of points is not the only factor, which is only the physical aspect. There is also a chemical modification factor, which is susceptible to changes over time due to interaction with the environment. This is evidenced by the affectation of the adhesion and the homogeneity of the metal layer deposited with the Electroless process, in the cases that the samples were stored after pretreatment.

### 3. 4. Tests with Chemical Reagents

#### 3. 4. 1. Diethyl Oxalate

Diethyl Oxalate is an excessively aggressive solvent for the ABS structure. The tests resulted in a generalized softening of the ABS plates and loss of shape of the parts. Also, a white precipitate product from the dissolution of ABS in the solvent was observed. Subsequently, the pre-treated substrate was introduced into the sulfuric-chromic acid bath. However, all the absorbed solvent reacted abruptly, showing an effervescence effect and causing the samples to become semi-transparent and olive-colored (Fig. 5 (b)) as compared to an untreated substrate (Fig. 5 (a)). The effect of deformation on the ABS structure, with the use of this type of solvent and its reaction with the sulfuric-chromic acid bath, makes it difficult to be used as an ABS pretreatment system.

#### 3. 4. 2. Phenetole

The pieces treated with the solvent at different treatment times showed a slight softening of the surface proportional to the immersion time, there were not discoloration, surface wear or deformation. However, the solvent remained adsorbed on the piece, giving off a very intense characteristic odor. It was observed that the softening effect of the surface remained even 24 hours after the treatment was done. This effect may help to reduce the usage time of the sulfuric-chromic acid bath since the surface was previously softened. However, the obtained effect when conducting the chemical treatment on the piece with 30 s by dipped was extremely severe. After a few seconds, the solvent adsorbed on the surface violently reacted with the sulfuric-chromic acid bath, leaving the surface with a burnt appearance and an olive green color (Fig. 5 (c)).

**Table 1.** The contact angles of ABS pieces for different surface treatments.

ABS substrate	$\theta$	Image
(a) Without treatment	57.9°	
(b) Sulfuric-chromic acid bath 10 min	113°	
(c) Sulfuric-chromic acid bath 15 min	119.8°	
(d) $\text{KMnO}_4$	68°	

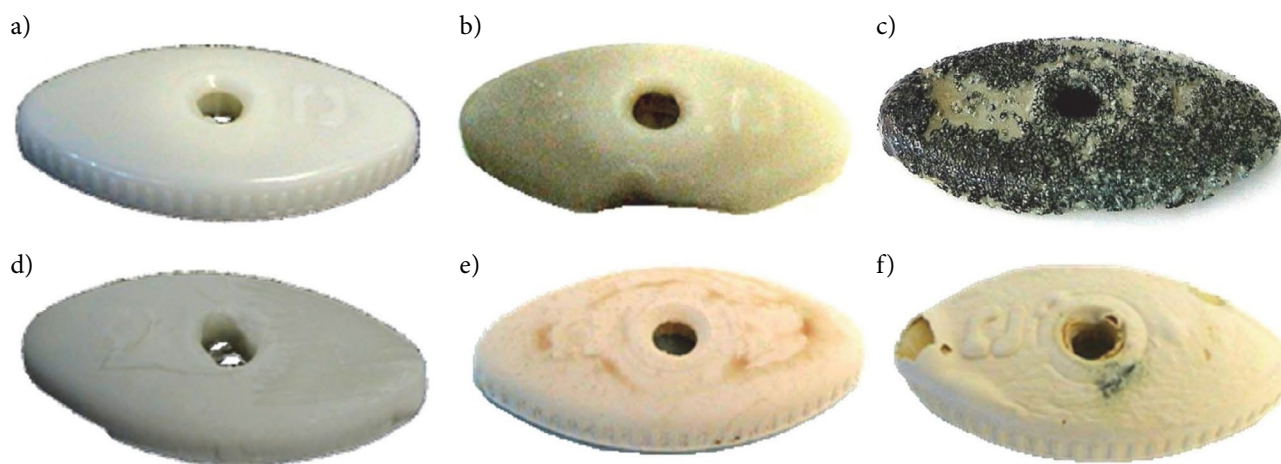
### 3. 4. 3. Acetone

The dipping of ABS in industrial grade acetone, results in a rapid softening, deformation and dissolution of it, resembling a plastic being melt with a sticky consistency. The piece loses its original semi-transparent yellow color. ABS residues were observable in the solvent due to the surface wear. The results were similar in very short immersion times and rapid drying of the acetone on the surface. Even with this result, it was decided to continue with the chemical pretreatment of the sulfuric-chromic conventional treatment. As with the other cases, acetone adsorbed on the surface reacted quickly when in contact with the conventional etching bath, causing a change of appearance on the substrate. A thin white film was formed on the surface which was easily removed (Fig. 5

(d)). The ABS is completely soluble in acetone with an immediate effect.

### 3. 4. 4. Methanol

The use of methanol was not visibly aggressive for ABS and the treatment did not show color changes or modification of the substrate. However, when testing the etching with the sulfuric-chromic acid bath, it was observed that the surface rapidly reacted, which was indicative that the methanol was adsorbed on the surface of the ABS. As in other cases, there was a change from the original color to a dull color on the surface and in the back of the piece were observed bubbles formed by the plastic as a result of the reaction (Fig. 5 (e)).



**Figure 5.** A piece of ABS without dye: (a) without treatment, with chemical treatment, and conditioning with the sulfuric-chromic acid bath (350 g/L): (b) Diethyl Oxalate; (c) phenetole; (d) Acetone; (e) Methanol; with chemical treatment and conditioning with sulfuric-chromic mixture (75g/L): (f) nitric acid.



**Figure 6.** White-ABS premetalized with Ni-JetMetal® and electrolytic deposition of Cu-Ni-Cr: (a) sulfuric-chromic bath for 10 min; (B) sulfuric-chromic bath for 15 min; (C)  $\text{KMnO}_4$  for 15 min.



### 3. 4. 5. Nitric Acid

The ABS pieces without dye were immersed in nitric acid and showed a slight softening of the surface, only for as long as it remained wet, losing this feature when dried. It was observed the discoloration and swelling of the substrate. After the pretreatment with nitric acid, the etching was carried out using the sulfuric-chromic acid bath but at a lower concentration (75g / L). In this case, the adsorbed nitric acid reacted causing a cracked surface and with the formation of small lumps, accompanied again by a color change. Figure 5 (f) shows sequentially the physical effects on each of the pretreatment steps, beginning with an untreated piece, which was then treated with nitric acid and subsequently with the sulfuric-chromic acid bath.

### 3. 4. 6. Potassium Permanganate (KMnO<sub>4</sub>)

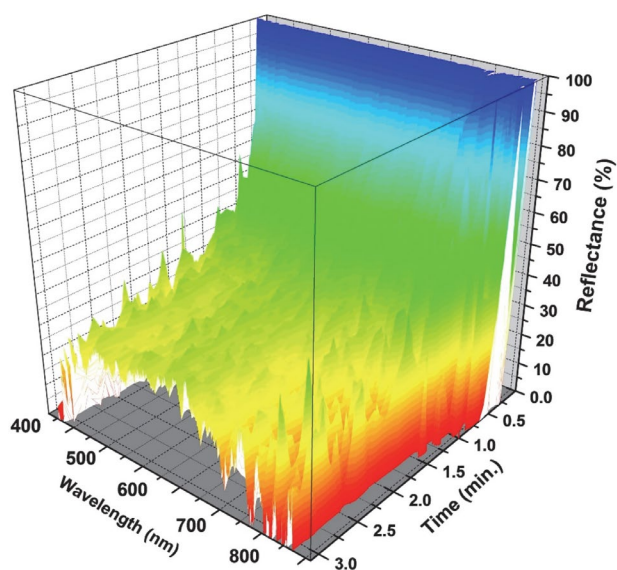
Treatment of ABS with KMnO<sub>4</sub> showed a noticeable color change on the substrate. It did not show a softening of the surface as in the previous cases. The contact angle value obtained for the pretreated surface with potassium permanganate was slightly larger than for the untreated piece. This could be due to the existence of a small modification of the surface, which increased by the increase of surface roughness as in the case of the contact angle values for the sulfuric-chromic acid bath treatment. Unlike the other pretreatments, the pieces after potassium permanganate were not treated with the sulfuric-chromic acid bath. The premetallized with nickel under JetMetal Technologies' technique and subsequently performed the electrodeposition of Copper-Nickel-Chromium (Fig. 6 (c)). However, in the adhesion tests by cross-cut adhesive tape done according to ASTM method D-3359, the adhesion rating obtained was 0B. This value indicates that even though the contact angle for this pretreatment is higher than that of a normal substrate, the possible modification of the surface is not sufficient for obtaining a bond similar to the sulfuric-chromic acid bath (Table 2). Figure 6 (a) and Figure 6 (b) show the comparison between two ABS pieces with the sulfuric-chromic acid bath pretreatment for 10 and 15 min, respectively. Both were metallized conventionally. Compared to potassium permanganate substrate (Fig. 6 (c)), it is notorious the influence of the pretreatment before metallization in both appearance and adhesion.

Figure 7 shows a reflectance graph of an ABS sample acquired *in situ* during the nickel deposition process by the Electroless conventional process. The decrease in intensity of reflected light on the ABS pretreated surface can notoriously observe as it grows a dark layer of nickel. The nickel deposit takes a few seconds to be perceptible, which is reflected in the measurement. Electroless nickel solution, with a characteristic green hue, slightly contributes to the absorption of light, particularly at the ends of the graph.

**Table 2.** Adhesion results for coatings on surfaces with different treatments (ASTM D-3359).

ABS substrate	Adhesion classification
Sulfuric-chromic, 10 min. + Ni, Electroless + Cu-Ni-Cr Electrolytic	5B
Sulfuric-chromic, 10 min. + Ni, JetMetal <sup>+</sup> + Cu-Ni-Cr Electrolytic	4B
Sulfuric-chromic, 15 min. + Ni, JetMetal <sup>+</sup> + Cu-Ni-Cr Electrolytic	4B
KMnO <sub>4</sub> 0.5 M, 15 min. + Ni, JetMetal <sup>+</sup> + Cu-Ni-Cr Electrolytic	0B

The characterization results of Vickers hardness (Table 3) shows the influence of different chemical pretreatments hardness values for the ABS substrate. The acetone was the chemical that affects more the substrate with a decrement of 3.7 HV<sub>200</sub> comparing to the reference value for the ABS without treatment (11.5 HV<sub>200</sub>). The sulfuric-chromic acid bath pretreatment did not significantly affect the hardness value of the ABS. However, the solvent adsorbed on the surface significantly reduce the hardness of the material due to structural changes that suffer the polymer surface by reaction with such solvents. The severity of the attack on substrates with Diethyl oxalate pretreatment with nitric acid and subsequent attack of the sulfuric-chromic acid bath (Fig. 5 (b) and 5 (f)), blocked the hardness measurement since the surface characteristics not allowed to obtain the trace formed by the indentation tip on the substrate surface.



**Figure 7.** Reflectance graph for the growth of a nickel film on ABS.

**Table 3.** Vickers hardness measurements on ABS surfaces with different treatments.

ABS substrate	HV <sub>200</sub>
Without treatment	11.5
Sulfuric-chromic acid bath	11.3
Diethyl Oxalate	12.9
Phenetole	9.6
Acetone	7.8

## 4. Conclusions

The simple reduction of the concentration of Cr (VI) in industrial baths may represent a major environmental and economic impact. However, the results of the experimentation show that the nitric acid and methanol are not viable chemical treatments before conditioning with the sulfuric-chromic acid bath at low concentrations, contrary to what reported in the literature. The main reason for this to happens is due to the adsorption of these chemical reagents on the surface of the polymer, which on contact with chromium-sulfuric mixture react violently, causing the surface modification of the material but without complying with the requirements to have the desired final appearance. The same effect was presented by using diethyl oxalate, phenetole, and acetone.

The swelling of solvents is not propitious before the use of the sulfuric-chromic acid bath. It could be used a chemical treatment that involves adsorption of molecules on the surface of the treated parts, either before other conventional or novel plating process, for example, JetMetal Technologies<sup>®</sup>. This because of possible deformation after effects such as samples or loss of adhesion of the deposit.

In the case of KMnO<sub>4</sub>, although it has been reported as an excellent pretreatment system to replace CrO<sub>3</sub> for the conditioning step of the Electroless process. The adhesion results indicate that there is not enough modification of the substrate for obtaining an excellent adhesion in accordance with the ASTM D-3359 method.

There are two contribution to the observed contact angle results. First, the chemical composition of the surface may change for the measurements in Table 1 but this was not possible to been proved by the FTIR technique. Second, the surface morphology was severely changed becoming coarse. The separation among the high points in these new surfaces going to conditioning the increase of the contact angle, especially when comparing with the water drop size. We propose that when few of these high points support the drop, the contact angle increases making the surface more hydrophobic, such as in the case of the sample with sulfuric-chromic acid bath with 15 min, or in some sections even superhydrophobic.

All the samples showed swelling of the tested solvents. The effect of acetone resulted as the most notorious change. Since the effect of the sulfuric-chromic acid bath

was severe on most of the samples, there was not a direct observed difference between the two types of ABS (without or with 2 wt% of white powder of TiO<sub>2</sub> in rutile form).

## Acknowledgments

This work was done under the auspices of the Mexican Council for Science and Technology CONACYT, through the projects CEMIE-Sol No. 207450 P18, P62, P96; Graphenic Materials National Laboratory No. 293371. Thanks to The World Bank and the Energy Secretariat for the grant of the PRODETES Price, No. 002/2017/PRODETES-PLATA. Also, the first author acknowledges CONACYT for his graduate fellowship.

## 5. References

1. S. Nigam, S. S. Mahapatra, S. K. Patel, *Materials Today: Proceedings* **2018**, 5, 8446–8453. DOI:10.1016/j.matpr.2017.11.540
2. D. Lehmann, J. Nagel, P. Zimmermann, P. Schlenstedt, K. Galvanotechnik **2018**, 109, 43–48.
3. A. Fares Karam, G. Stremsdoerfer, in: K. L. Mittal (Ed.): *Metallized Plastics 5 & 6: Fundamental and Applied Aspects*, CRC Press, London, **1998**, pp. 137–144. DOI:10.1201/b11958
4. P. C. Rodríguez, in: *Galvanoplastia Aplicada Teoría y Práctica*, Alsina, Buenos Aires, Argentina, **1998**, pp. 7.
5. A. P. Kurek, R. G. Moll, G. Herbst, M. E. R. Dotto, N., *J. Appl. Poly. Sci.* **2018**, 135, 46131. DOI:10.1002/app.46131
6. J. J. Kuzmick, in: O. Glenn Mallory, J. B. Hajdu (Eds.): *Electroless Plating: Fundamentals and Applications*, American Electroplaters and Surface Finishers Society, Orlando, Florida, **1990**, chapter 14.
7. N. Platzter, in: American Society of Electroplated Plastics, *Standard and Guidelines for Electroplated Plastics*, Prentice-Hall, Englewood Cliffs, N. J., **1972**, chapter 1. DOI:10.1002/pol.1982.130200910
8. J. B. Hajdu, G. Krulik, in: L. J. Durney, Van Nostrand Reinhold (Eds.): *Electroplating Engineering Handbook*, New York, **1984**, pp. 202–205.
9. L. Magallón Cacho, J. J. Pérez Bueno, Y. Meas Vong, G. Stremsdoerfer, F. J. Espinoza Beltrán. *Surf. Coat. Tech.* **2011**, 206, 1410–1415. DOI:10.1016/j.surfcoat.2011.09.005
10. X. Geng, Q. Qiang, J. Zhao, J. Yang, Z. Wang, *J. Adhes. Sci. Tech.* **2015**, 29, 705–715. DOI:10.1080/01694243.2014.1001960
11. N. Inagaki, K. Narushima, M. Morita, *J. Adhes. Sci. Tech.* **2006**, 20, 917–938. DOI:10.1163/15685610677657797
12. J. R. Bartoli, I. Y. Abbe, M. N. P. Carreño, I. Pereyra, E. G. Fernandes, *AIP Conference Proceedings 1981, International Conference on Times of Polymers and Composites: From Aerospace to Nanotechnology* **2018**, 020162. DOI:10.1063/1.5046024



13. G. Rozovskis, J. Vinkevičius, J. Jačiauskiene, *J. Adhes. Sci. Tech.* **1996**, *10*, 399–406. DOI:10.1163/156856196X00490
14. H. Zhang, Z. Kang, J. Sang, H. Hirahara, *Surf. Coat. Tech.* **2018**, *340*, 8–16. DOI:10.1016/j.surfcoat.2018.02.005
15. N. Inagaki, S. Tasaka, T. Baba, *J. Adhes. Sci. Tech.* **2001**, *15*, 749–762. DOI:10.1163/15685610152540821
16. M. Sitting, in: *Handbook of Toxic and Hazardous Chemicals and Carcinogens*, Noyes Publications, William Andrew Publishing, LLC, Norwich, New York, U.S.A., **1991**, p. 440–444.
17. WHO Regional Office for Europe, Air Quality Guidelines, Copenhagen, Denmark, **2000**, chapter 6.4.
18. N. K. Dixit, R. Srivastava, R. Narain, *Proceedings of the Institution of Mechanical Engineers, Part L: Journal of Materials: Design and Applications* **2019**, *233*, 942–954. DOI:10.1177/1464420717719920
19. J. Zhang, J. Feng, L. Jia, H. Zhang, G. Zhang, S. Sun, T. Zhou, *ACS Applied Materials and Interfaces* **2019**, *11*, 13714–13723. DOI:10.1021/acsami.9b01856
20. K. Ratautas, A. Jagminiene, I. Stankeviciene, E. Norkus, G. Raciukaitis, *2018 13<sup>th</sup> International Congress Molded Interconnect Devices* **2018**, 8526970. DOI:10.1109/ICMID.2018.8526970
21. S. Chen, Q. Zhu, Y. Zhao, J. He, G. Wang, *Materials and Corrosion* **2019**, *70*, 720–725. DOI:10.1002/maco.201810485
22. X. Han, G. Wang, Y. He, Y. Wang, Y. Qiao, L. Zhang, *Journal of Adhesion Science and Technology* **2018**, *32*, 2481–2493. DOI:10.1080/01694243.2018.1488460
23. X. Han, G. Wang, J. He, J. Guan, Y. He, *Surface and Interface Analysis* **2019**, *51*, 177–183. DOI:10.1002/sia.6560
24. I. Anil, S. T. Gunday, O. Alagha, A. Bozkurt, *Journal of Polymers and the Environment* **2019**, *27*, 1086–1095. DOI:10.1007/s10924-019-01415-0
25. J. Li, S. Wang, F. Liu, X. Wang, H. Chen, T. Mao, Z. Wang, *Journal of Membrane Science* **2019**, *581*, 303–311. DOI:10.1016/j.memsci.2019.03.025
26. K. Kang, D. Kim, *Journal of Membrane Science* **2019**, *578*, 103–110. DOI:10.1016/j.memsci.2019.02.043
27. E. A. M. Azmy, H. E. Hashem, E. A. Mohamed, N. A. Negm, *Journal of Molecular Liquids* **2019**, *284*, 748–754. DOI:10.1016/j.molliq.2019.04.054
28. A. Blivernitz, T. Förster, S. Eibl, *Polymer Testing* **2019**, *76*, 261–272. DOI:10.1016/j.polymertesting.2019.03.009
29. X. Yu, Z. Wang, J. Liu, H. Mei, D. Yong, J. Li, *Materials Today Communications* **2019**, *19*, 124–130. DOI:10.1016/j.mtcomm.2018.12.015
30. R. Kessentini, O. Klinkova, I. Tawfiq, M. Haddar, *Polymer Testing* **2019**, *75*, 159–166. DOI:10.1016/j.polymertesting.2019.01.013
31. S. H. Kamarul Bahrain, J. Mahmud, *Materials Letters* **2019**, *242*, 32–34. DOI:10.1016/j.matlet.2019.01.100
32. Q. Qiang, X. Geng, Z. Wang, *Journal of Adhesion Science and Technology* **2019**, *33*, 371–381. DOI:10.1080/01694243.2018.1507318
33. X. Sun, L. Zhang, S. Tao, Y. Yu, S. Li, H. Wang, J. Qiu, *Advanced Materials Interfaces* **2017**, *4*, 1700052. DOI:10.1002/admi.201700052
34. H. Pang, R. Bai, Q. Shao, Y. Gao, A. Li, Z. Tang, *Applied Surface Science* **2015**, *359*, 280–287. DOI:10.1016/j.apsusc.2015.10.100
35. S. M. Simon, A. Chandran, G. George, M. S. Sajna, P. Valparambil, E. Kumi-Barmiah, G. Jose, P. R. Biju, C. Joseph, N. V. Unnikrishnan, *ACS Omega*, **2018**, *3*, 14924–14932. DOI:10.1021/acsomega.8b01940
36. N. Gao, X. Zhang, S. Liao, H. Jia, Y. Wang, *ACS Macro Letters* **2016**, *5*, 823–827. DOI:10.1021/acsmacrolett.6b00338
37. E. B. Saubestre, in: F. A. Lowenheim (Ed.): *Modern Electroplating*, Wiley-Interscience Publication, New York, **1995**, chapter 28.
38. R. K. Wahi, W. W. Yu, Y. Liu, M. L. Mejia, J. C. Falkner, W. Nolte, V. L. Colvin, *J. Molecular Catal. A: Chem. A* **2005**, *242*, 48–56. DOI:10.1016/j.molcata.2005.07.034
39. W. Zhao, J. Ding, Z. Wang, *Langmuir* **2013**, *29*, 5968–5973. DOI:10.1021/la400321k
40. M. Piton, A. Rivaton, *Polymer degradation and stability* **1996**, *53*, 343–359. DOI:10.1016/0141-3910(96)00093-6
41. J. L. Gardette, B. Mailhot, J. Lemaire, *Polymer degradation and stability* **1995**, *48*, 457–470. DOI:10.1016/0141-3910(95)00113-Z
42. M. Piton, A. Rivaton, *Polymer degradation and stability* **1997**, *53*, 147–157. DOI:10.1016/S0141-3910(96)00116-4
43. J. F. Rabek, *Polymer photodegradation: Mechanisms and experimental methods*. Chapman and Hall, London, UK, **1995**, Chapter 2.

## Povzetek

Površinska modifikacija kopolimernih substratov iz akrilonitril-butadien-stirena (ABS) je pomembna za industrijo galvanizacije. Kopel mešanice žveplove kisline in kromovega(VI) oksida, ki se uporablja v postopku priprave površine ABS s selektivno oksidacijo polibutadiena ustvarja med seboj povezane mikro pore, kar omogoča odlično mehansko adhezijo med kovinsko folijo in podlago. Šestvalentni krom (Cr (VI)) je škodljiv za ljudi in okolje in je kancerogen. V prispevku raziskujemo spremembe površine z različnimi tipi kemijskih reagentov na površino ABS in njegovo obdelavo v kopeli mešanice žveplove kisline in kromovega(VI) oksida v koncentracijah, ki so nižje od uporabljenih v običajnih procesih. Z uporabo različnih preučevanih kemijskih reagentov se je površina ABS spreminjala, kar je povzročilo različne vrste reakcij na površini, ki so lahko potekale spontano ali med postopkom priprave površine.



Except when otherwise noted, articles in this journal are published under the terms and conditions of the Creative Commons Attribution 4.0 International License

Scientific paper

# Adsorptive Removal of Remazol Brilliant Violet-5R Dye from Aqueous Solutions using Calcined Eggshell as Biosorbent

Eszter Rápó,<sup>1,2</sup> Katalin Posta,<sup>2</sup> Maria Suciu,<sup>3</sup> Robert Szép<sup>4</sup>  
and Szende Tonk<sup>1,\*</sup>

<sup>1</sup> Environmental Science Department, Sapientia Hungarian University of Transylvania,  
Calea Turzii 4, 400193 Cluj-Napoca, RO

<sup>2</sup> Plant Protection Institute, Szent István University, Páter K. 1, H-2100 Gödöllő, HU

<sup>3</sup> National Institute for Research and Development of Isotopic and Molecular Technologies, Electron Microscopy Integrated  
Laboratory, Donath 67-103, 400293 Cluj-Napoca, RO

<sup>4</sup> Faculty of Economics, Sapientia Hungarian University of Transylvania, Piața Libertății 1, 530104 Miercurea-Ciuc, RO\*

Corresponding author: E-mail: tonk.szende@sapientia.ro

Received: 02-25-2019

## Abstract

As a result of industrial development water pollution has become a major issue. Providing clean water of sufficient quality and quantity is essential. According to literature, 100 000 different dyes are used worldwide in the printing, food and textile industries. Remazol Brilliant Violet-5R belongs to the group of azo dyes used in the textile industry. The purpose of this paper is to study the removal of anionic dye RBV-5R using calcined eggshell. We investigated the effect of initial dye concentration (20–100 mg/L RBV-5R), biomass amount, contact time, temperature, and pH on the adsorption process. We calculated the amounts of adsorbed material in equilibrium and the efficiency of the adsorption process. Various studies were performed on the adsorption process and the adsorbent morphology (EDX, SEM, FTIR, Raman), as well as isotherm (Langmuir, Freundlich, Temkin and Dubinin-Radushkevich), kinetic and diffusion models were used to characterize the process. Calcined eggshell was also characterized by thermogravimetric, BET surface methods. Based on the results obtained, it can be said that the calcined eggshell can be used effectively to remove the dye from the aqueous solution.

**Keywords:** Adsorption; calcined eggshell; Remazol Brilliant Violet-5R

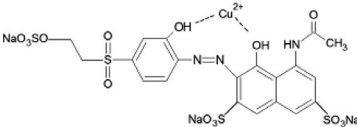
## 1. Introduction

Water is the source of life, our existence, and our civilization depends to a great extent on the presence of good quality water.<sup>1</sup> Today, about 232 million inhabitants in 26 countries live in water scarcity, mainly in the African and Middle Eastern countries, but also in the Netherlands, Belgium and Hungary.<sup>2,3</sup> Several cities around the world are struggling with water crisis. For instance, the population of Cape Town can use 50 liters of water per day. A similar albeit somewhat less urgent problem faces Mexico and Melbourne as well. According to an article in The New York Times, Jakarta has become so dry that the city is sinking due to the extraction of the huge amount of groundwa-

ter. In Brazil's most populous city (São Paulo), water was pumped out of sludge in 2015, since it was enough only for 20 days for the population.<sup>4–6</sup> Humanity has used materials since ancient times that are capable of staining other materials, initially working with natural colors of animal and vegetable origin. Modern industries, however, use synthetic dyes instead. Remazol Brilliant Violet-5R (Table 1), one of the most important dyes in the textile industry, is an organic dye that can be classified as reactive dye, as well as azo dye. Reactive dyes are typically anionic in nature, highly soluble in water, and resistant to light.<sup>7</sup> RBV-5R is often used as a starting material in the manufacturing process of polymer dyes.<sup>8</sup> In residual industrial wastewater, reactive dyes are highly toxic, characterized by a high

chemical and biological oxygen demand, by high, suspended solids and strong, vivid colors.<sup>9</sup> When RBV-5R enters the aquatic environment, not least because of its Cu<sup>2+</sup> content, it can be toxic to aquatic life because it prevents photosynthesis by blocking the entry of light into deeper layers.

**Table 1.** Properties of the studied RBV-5R textile dye

Dye name	Remazol Brilliant Violet-5R (RBV-5R)
Molecular formula	C <sub>20</sub> H <sub>16</sub> N <sub>3</sub> Na <sub>3</sub> O <sub>15</sub> S <sub>4</sub>
Colour Index Number	18097
Molecular Weight	735.58 g/mol
Maximum absorption	$\lambda_{\max} = 553 \text{ nm}$
Chemical structure	

The adsorption processes have been widely researched in the context of water pollution and several alternative biosorbents have been tested for efficacy. These biosorbents can be household or industrial wastes: orange- and banana peel<sup>10</sup> tea/coffee filter<sup>11,12</sup> grape-, potato- and apple peel<sup>13</sup> dead and dried mushrooms<sup>14,15</sup> sawdust,<sup>16</sup> bentonite<sup>17–19</sup> clay.<sup>20</sup>

Eggshells from household waste can also be used as an adsorbent. The eggshell is a porous, uneven, granular structure with high surface area. It contains approximately 17 000 pores. 95–97% of the eggshell is made up of calcium carbonate (CaCO<sub>3</sub>), calcite crystals and fewer organic materials such as proteins, fats and sugars.<sup>21,22</sup> Eggshell as an adsorbent can be used to remove many organic and inorganic substances: heavy metals<sup>23,24</sup> phenols,<sup>25</sup> cyanide,<sup>26</sup> drug residues,<sup>27</sup> dyes.<sup>28–30</sup>

The aim of this study is to investigate the removal of Remazol Brilliant Violet-5R dye from aqueous solutions using calcined chicken (*Gallus Gallus domesticus*) eggshell household waste as biosorbent. This study covers a niche by focusing more specifically on the elemental analysis of the biosorbent material before and after adsorption (with EDX, Raman and FTIR analyses), calculating the biosorbents' bioconcentration factor and studying the morphological changes of the adsorbent using SEM images. Calcined eggshell was also characterized by thermogravimetric, BET surface methods.

## 2. Materials and Methods

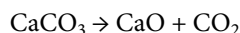
### 2.1. Adsorbate

The analytical grade dye, Remazol Brilliant Violet-5R, selected for the purposes of the adsorption experiments in the present study, was purchased from DyeStar Singapore Pte. Ltd. It was used without any purification.

The dye stock solution of 2 g/L was prepared by dissolving the dye powder with deionized (MilliQ) water. During adsorption studies, stock solution was diluted to the needed concentration (20, 40, 60, 80, 100 mg/L).

### 2.2. Adsorbent

Chicken eggshell (*Gallus Gallus domesticus*) samples were collected from kitchen waste. In order to remove pollutants and impurity from its surface, they were repeatedly washed with tap water and ultrapure MilliQ deionized water. After drying (Memmert UN75PLUS dried at 85 °C) the chicken eggshell was crushed and sieved to 160 µm particle size. Finally, it was calcined at 1000 °C for 4 hours.



### 2.3. Batch Adsorption and Studies of Initial Parameters' Change

The biosorption of azo-dye RBV-5R on the surface of calcined eggshell was carried out in 250 mL Berzelius flask using 100 mL dye in aqueous solution.

During batch equilibrium experiments, the concentration of the dye was measured by Agilent Cary 60 UV-VIS spectrophotometer at  $\lambda_{\max} = 553 \text{ nm}$ . The concentration was calculated by using calibration curve quantitative measuring technique. Results listed below are the means and standard deviations from 9 different measurements.

To achieve maximum adsorption capacity and efficiency, various initial parameters (such as initial dye concentration, biomass weight, aqueous solution pH and temperature) affecting the RBV-5R dye removal process on calcined eggshell were studied and optimized.

The effect of initial dye concentration on adsorption with calcined eggshell (160 µm particle size) was studied using constantly rotating (700 rpm) 1.5 g calcined eggshell in a 100 mL aqueous solution of RBV-5R azo-dye between 20–100 mg/L concentrations at 20 °C without pH adjustment (pH = 6).

To examine the effect of calcined eggshells weight, 100 mL volumes of 20 mg/L concentration RBV-5R dye (pH = 6) was constantly (700 rpm) mixed with 0.5–1–1.5–2 g eggshell (160 µm particle size) at 20 °C.

Due to the fact that dye adsorption is pH dependent, the effect of pH was also studied between pH = 2–11 by mixing 20 mg/L dye solution at 700 rpm with 1.5 g calcined eggshell (160 µm particle size) at 20 °C. In each case 1M HCl and NaOH was used as pH adjuster (Hanna HI4521 pH/mV/ISE/temperature Bench Meter with dual channel electrode). First, the dye solutions were prepared, then the Berzelius flask containing the solution was put on a magnetic stirrer, and the wished pH was adjusted with 1M NaOH and 1M HCl. IKA C-MAG HS7 digital magnetic shakers were used to investigate the effect of temperature (20, 30, 40 °C) on the adsorption process, where con-

stant parameters were:  $c = 20$  mg/L, particle size = 160  $\mu\text{m}$ , biomass weight = 1.5 g, 700 rpm agitation speed, pH = 6.

## 2. 4. Analytical Methods

For the characterization of calcined eggshell, thermal analysis was carried out using a DTA-TG differential heat analyzer, Model: STA 449 F5 Jupiter, Manufacturer: Netzsch GmbH, Germany, with graphite furnace, with a possibility of analysis of up to 1600  $^{\circ}\text{C}$ . The heat treatment temperature of the samples was 1200  $^{\circ}\text{C}$  at a heating rate of 10 K/min under a nitrogen atmosphere.

Total surface area ( $S_t$ ), pore volume ( $V_p$ ) and pore radius ( $R_m$ ) were obtained from  $\text{N}_2$  adsorption-desorption isotherms (measured at  $-196$   $^{\circ}\text{C}$ ), using the BET model for  $S_t$  determination, and Dollimore – Heal method for  $V_p$  and  $R_m$ . The isotherms were recorded using Sorptomatic 1990 apparatus (Thermo Electron Corporation). For prior determination, the samples were degassed at 150  $^{\circ}\text{C}$  in vacuum (around 1 Pa) for 3 hours, in order to remove the physically adsorbed impurities from the surface. No pressure variation was observed at the end of the 1 hour samples degassing process.<sup>31–33</sup>

The powdered calcined eggshell surface was studied by scanning electron microscopy (JEOL (USA) JSM 5510 LV SEM) at various magnifications before and after ad-

sorption. During the test, eggshell particle sizes of 160  $\mu\text{m}$  were used (control, 2 g/L RBV-5R solution). To improve the quality of the images and to increase the electrical conductivity of the surface, the surface of the samples was covered with a thin layer (10nm) of  $1.33 \times 10^{-6}$  mBar vacuum.

Scanning Jeol JEM 5510 JV and Oxford Instruments EDS Analysis System Inca 300 (UK) were used to examine the elemental composition of the calcined eggshell on the control and the dye adsorbed samples (2 g/L RBV-5R). Elemental distribution was studied and enrichment factors were calculated. The value obtained gives the percentage of elements in the dye-„contaminated” sample relative to the control sample.

$$\delta = \frac{R_{\text{sample}} - R_{\text{control}}}{R_{\text{control}}} \cdot 100$$

Where:  $\delta$  – enrichment factor,  $R_{\text{sample}}$  – the EDX results for eggshells in the 2 g/L solution, – the amount of elements in the control eggshell obtained during EDX measurement.

FTIR spectroscopy was used to identify the functional groups of calcined eggshells before and after RBV-5R dye adsorption, which was performed by JASCO 615FTIR at 500–4000  $\text{cm}^{-1}$  wavelength.

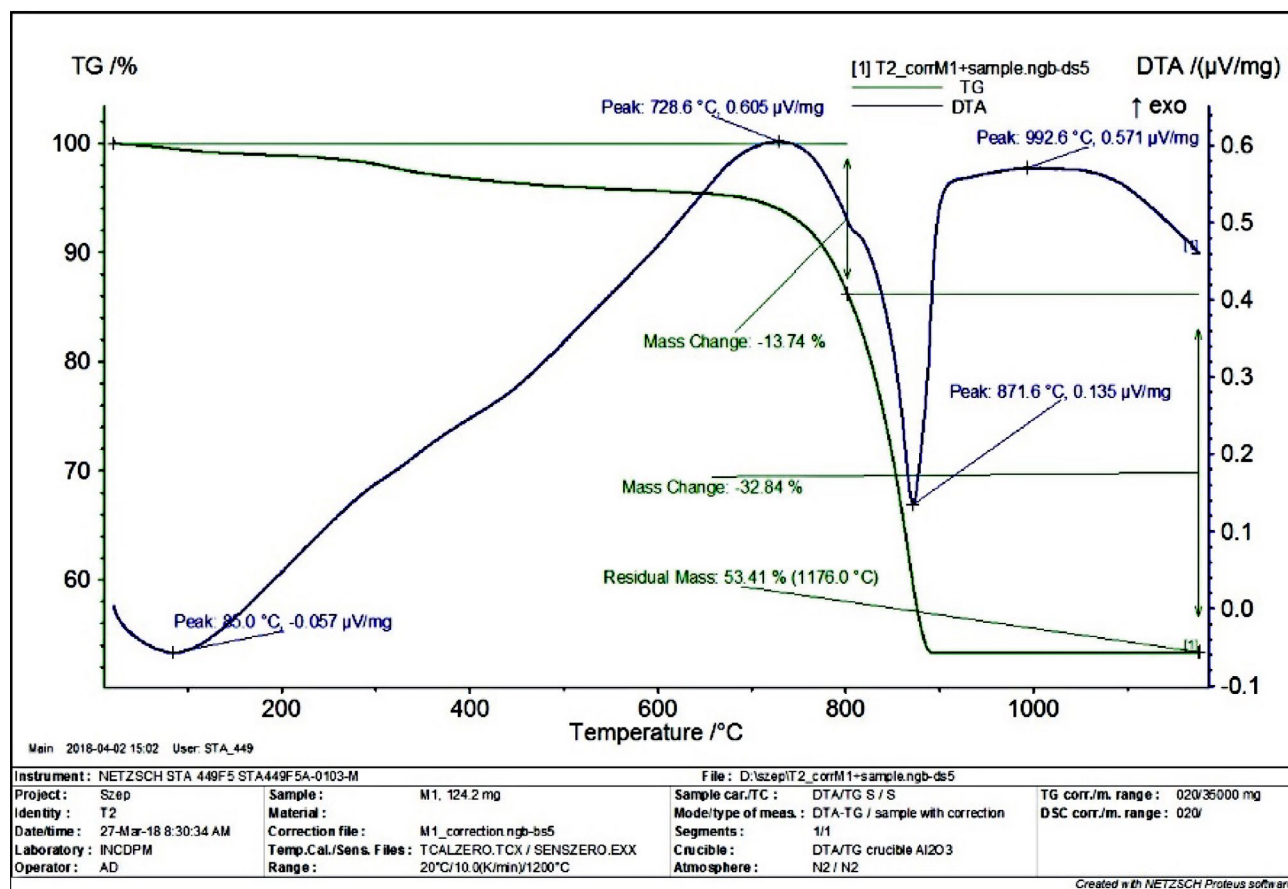


Figure 1. Thermogravimetric measurements (Created with NETZSCH Proteus software): TG – Thermogravimetry, DTA – Differential Thermoanalytics



HORIBA JobinYvon LabRAM HR Raman Spectrophotometer, with a 532 nm wavelength green laser (with a laser point diameter of 1.5  $\mu\text{m}$ , an optic lattice of 1800 lines/mm, and 100x objective) was used to study the material assays of calcined eggshell (powdered form), RBV-5R dye.

### 3. Results and discussion

#### 3.1. Thermogravimetry

Materials can change their physical and chemical properties due to heat, and thermal analyses can be used to test these properties. During the process, the eggshell bio-sorbent properties were investigated as a function of elapsed time or temperature variation. The most important ingredient of eggshell is calcite with a known decomposition temperature of 900  $^{\circ}\text{C}$ .<sup>31</sup> But at this temperature we found gray/black residues in the sample. Figure 1 made with Proteus software shows the TG-thermogravimetric curve and the DTA differential thermal analysis curve (which gives the heat flow at the temperature).

Based on the TG curve (green curve), there are two main mass losses owing to temperature, below 800  $^{\circ}\text{C}$  and in the range 800–900  $^{\circ}\text{C}$ . In the first case, mass loss can be explained with the disappearance of adsorbed water molecules and organic compounds. In the second case, the main weight loss corresponds to 32.84% by weight when the  $\text{CaCO}_3$  phase is transformed into a  $\text{CaO}$  phase.

Since the mass of the sample remained constant after 900  $^{\circ}\text{C}$ , we can assume that the transformation is complete.<sup>32,33</sup>

According to the DTA curve, decomposition occurs at 728.6  $^{\circ}\text{C}$ , which is the maximum temperature at which exothermic phenomenon or decomposition occurs.

#### 3.2. BET surface

Based on the values obtained in the BET surface and Dollimore–Heal method, listed in Table 2, it can be observed that after the adsorption the surface area ( $S_t$ ) of the calcined eggshell decreased, thus dye molecules had become incorporated into the pores. Moreover, we can see that the pore volume ( $V_p$ ) also decreased after dye adsorption.

Table 2. Eggshell surface area and pore volume

Sample	$S_t$ ( $\text{m}^2/\text{g}$ )	$V_p$ ( $\text{cm}^3/\text{g}$ )
Control calcined eggshell	3.0	0.015
Dye adsorbed calcined eggshell	1.7	0.012

The size distribution of the pore bars of the two samples is shown in Figure 2. Figure 2.1 shows the multimodal mesoporous and macroporous structure of untreated calcined eggshell having three main ranges for the pore radii-

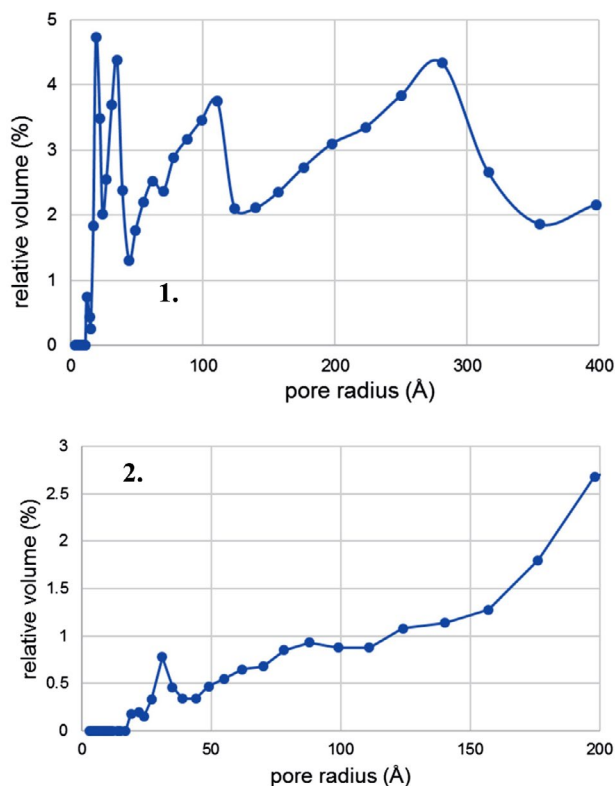


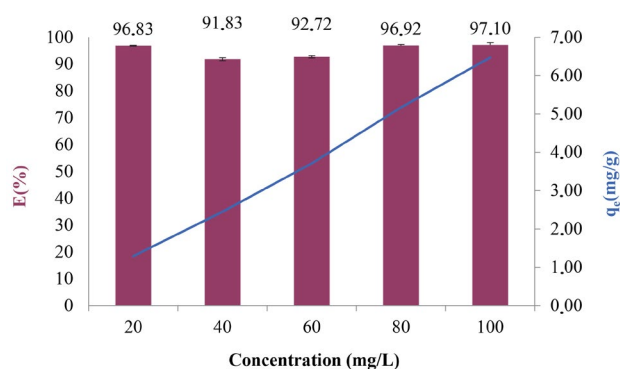
Figure 2. Pore size distribution (1) control (2) dye adsorbed calcined eggshell

us: 21–20  $\text{\AA}$ , 110  $\text{\AA}$  and 280  $\text{\AA}$ . The first two are located in the mesoporous region and the last one is in the small macroporous region.

As for the sample after the adsorption, due to the small value of the surface, the pore size analysis is not very accurate, but there are two types of pores with radius of about 30  $\text{\AA}$  and 90  $\text{\AA}$ . For values above 150  $^{\circ}\text{C}$ , the pore radius cannot be calculated due to the nitrogen condensation between the material particles.

#### 3.3. Effect of the Initial RBV-5R Dye Concentration

Five different studies ( $C_i = 20\text{--}100$   $\text{mg/L}$ ) were made for the adsorption process at a constant 700 rpm at room temperature, 1.5 g of biomass (1000  $^{\circ}\text{C}$  calcined eggshell) without adjusting the pH of the aqueous medium. The equilibrium values obtained at the end of the adsorption were used to calculate the efficiency of the bio-sorption and the maximum amount of material in equilibrium. Figure 3 graphically illustrates the calculated values. Here we can observe that the efficiency achieved is in all cases greater than 90%. Compared to our previous study (untreated eggshell adsorption), no clear trend was observed regarding the increase in concentration. But for subsequent comparison, studies were performed on the 20  $\text{mg/L}$  solution.

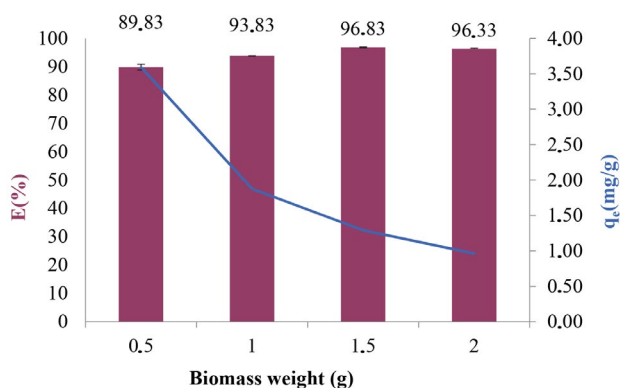


**Figure 3.** Effect of the initial RBV-5R dye concentration, standard deviations calculated from measurements from nine parallel results, where E-efficiency of adsorption, q<sub>e</sub>-maximum adsorption capacities at equilibrium (C<sub>i</sub> = 20–100 mg/L, 1.5 g biomass, 160 μm, 700 rpm, pH = 6.0 ± 0.2, T = 20 ± 1 °C).

### 3. 4. Effect of the Amount of Biosorbent

The amount of biomass is an important factor in the adsorption process. In theory, the higher the amount of adsorbent present in the aqueous medium, the more binding sites are available to the dye molecules. Nonetheless, after a while, the binding dye molecules are depleted in the solution. In our research we investigated the adsorption parameters of four different initial amounts of calcined eggshells (0.5; 1; 1.5; 2 g).

We studied the dye's adsorption on untreated eggshell, it can be observed in Figure 4 that the increase as the amount of calcined eggshell increases, the removal efficiency increases, but the quantity in equilibrium exhibits a decreasing tendency. Based on the results, the highest efficiency was obtained (E% = 96.83) for 1.5 g of calcined eggshell.

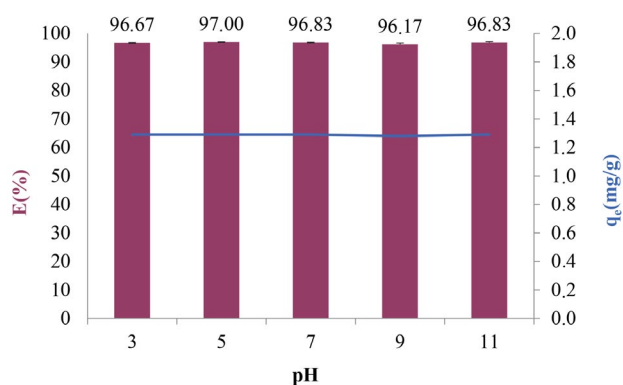


**Figure 4.** Effect of the initial biomass weight, standard deviations calculated from measurements from nine parallel results, where E-efficiency of adsorption, q<sub>e</sub>-maximum adsorption capacities at equilibrium (C<sub>i</sub> = 20 mg/L, 160 μm, 700 rpm, pH = 6.0 ± 0.2, T = 20 ± 1 °C).

### 3. 5. Effect of the pH of an Aqueous Medium

The pH of the aqueous medium can influence the bi-adsorption of the dyes: changes in sorbent properties, adsorption mechanism, dissociation of the dye molecules, and the chemical structure of the dye. Changing the pH may cause surface charge as well. Reactive dyes and thus RBV-5R dressing dyes are anionic in nature. This property implies that the dye may be adsorbed in acidic medium with greater efficiency. The pH of the prepared 20 mg/L dye solutions was adjusted using 1M NaOH and 1M HCl solutions. In practice, adding HCl to the aqueous solution protonates the surface of the biosorbent in the solution (acidic medium), so that the anionic dye is willing to bound to the surface of the adsorbent. In the basic medium, by adding NaOH, there is a repulsive force between the dye and the adsorbent, so that the surface of the calcined eggshell is deprotonated; therefore, the adsorption is less efficient.

The calcined eggshell used in our research contains CaO, which is alkaline, highly influencing the pH of the aqueous medium. At the end of the adsorption experiments, the solutions were filtered and the pH of the filtrate was checked. All solutions showed a pH of around 11. Figure 5 shows the results in equilibrium, the constant values of quantity in equilibrium and efficiency were the consequence of the similar pH.



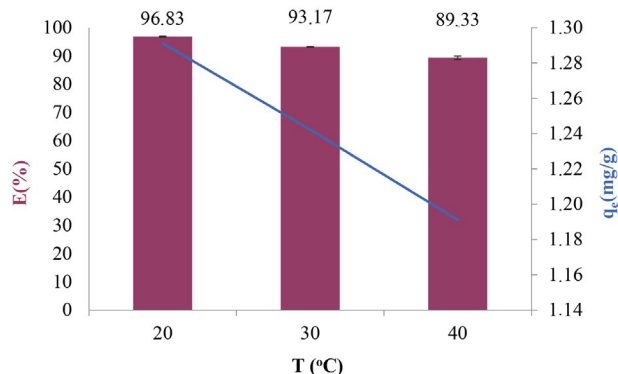
**Figure 5.** Effect of the pH of an aqueous medium, standard deviations calculated from measurements from nine parallel results, where E-efficiency of adsorption, q<sub>e</sub>-maximum adsorption capacities at equilibrium (C<sub>i</sub> = 20 mg/L, 1.5 g, 160 μm, 700 rpm, pH = 2–11, T = 20 ± 1 °C).

### 3. 6. Effect of Solution Temperature

In our research, the adsorption properties of the calcined eggshell were studied by changing the temperatures (20, 30, 40 °C) of the dye solution.

Figure depicts the effect of temperature dependence on the efficiency and the quantity in equilibrium. It can be observed that the efficiency and the quantity in equilibrium decreases with the increase in the temperature of the aqueous medium. Similar results were obtained in our previous

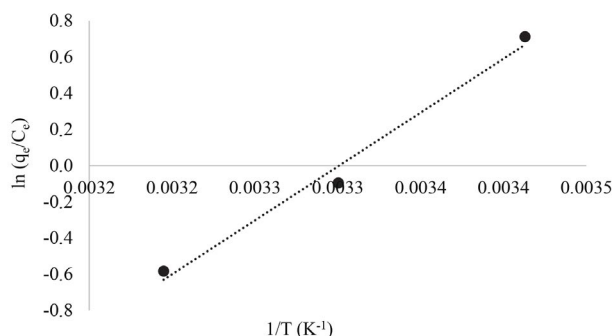
study for untreated eggshells, but with lower efficiency (20 °C: 94.39, 30 °C: 92.36, 40 °C: 89.65). This was anticipated because the molecules' thermal movement increases with the increase of temperature, and thus adsorption decreases.



**Figure 6.** Effect of the temperature, standard deviations calculated from measurements from nine parallel results, where E-efficiency of adsorption,  $q_e$ -maximum adsorption capacities at equilibrium ( $C_i = 20$  mg/L, 1.5 g, 160  $\mu$ m, 700 rpm, pH =  $6.0 \pm 0.2$ , T =  $20\text{--}40 \pm 1$  °C).

### 3. 7. Thermodynamics

In our research we investigated the effect of temperature (239K, 303K and 313K) on the adsorption process. Based on the results obtained,  $\ln(q_e/C_e)$  was plotted against  $1/T$ , and the thermodynamic parameters were determined on the basis of the equation of the obtained straight line.



**Figure 7.** van't Hoff plot for the biosorption of RBV-5R dye, where slope ( $-\Delta H^\circ/R$ ) = 5952, intercept( $\Delta S^\circ/R$ ) = -19.65 and  $R^2$ -coefficient = 0.985.

Table 3 shows the thermodynamic parameters calculated on the basis of equation, namely enthalpy, entropy

and free energy of Gibbs. In line with the results of our untreated eggshell experiments,  $\Delta H$ , enthalpy is less than 84 kJ/mol but positive. According to literature data, it can be concluded that adsorption is an endothermic process and physical adsorption ( $\Delta H < 84$  KJ/mole physical adsorption;  $\Delta H$  84–420 kJ/mol of chemical adsorption), and the positive value of  $\Delta S$  entropy indicates the randomness of the adsorption process. Gibbs' free energy is reduced by the effect of temperature. The lower the temperature, the higher the spontaneity of the process, so it is inversely proportional.<sup>34–37</sup>

In summary, based on thermodynamic data, it can be said that biosorption is a spontaneous and endothermic process. Physical adsorption occurs between the dye molecules and the surface of the calcined eggshell.

**Table 3.** Calculated thermodynamic parameters

$\Delta S$ (J/mol K)	$\Delta H$ (kJ/mol)	$\Delta G$ (kJ/mol)		
		293 K	303 K	313 K
0.2	49.6	1.8	0.2	-1.5

### 3. 8. Adsorption Isotherm Models

In order to characterize the adsorption process, the four most frequently used isotherm models (Langmuir, Freundlich, Temkin, Dubinin-Radushkevich) were used. In each case, the linear regression coefficients and characteristic parameters were calculated based on equations received from linearized forms.<sup>24</sup> The calculated parameters lead us to state that adsorption is physical in nature (Table 4). Weak van der Waals bonds are formed between the biosorbent and the dye, because the B-Temkin constant is less than 20 kJ/mol and the E-energy is less than 8 kJ/mol. Since the correlation coefficient of the Langmuir isotherm is the highest in our experimental conditions, the Langmuir isotherm model describes the process, assuming that the adsorption is reversible, monolayer. The surface of the adsorbent, in this case calcined eggshell, has a homogeneous, uniform strength with a constant number of binding centers that incorporate only one molecule into a binding site.

### 3. 9. Adsorption Kinetic and Diffusion Models

Kinetic and diffusion models can be used to study the adsorption mechanisms between biosorbent, calcined

**Table 4.** Parameters of isotherm models ( $C_i = 20\text{--}100$  mg/L, 1.5 g biomass, 160  $\mu$ m, 700 rpm, pH =  $6.0 \pm 0.2$ , T =  $20 \pm 1$  °C, P = 1atm)

Langmuir		Freundlich			Dubinin-Radushkevich			Temkin			
K <sub>L</sub> (l/mg)	q <sub>max</sub> (mg/g)	R <sup>2</sup>	n	K <sub>f</sub> (mg <sup>(1-1/n)</sup> l <sup>1/n</sup> /g)	R <sup>2</sup>	β (mol <sup>2</sup> kJ <sup>2</sup> )	E (kJ/mol)	R <sup>2</sup>	A <sub>T</sub> (l/g)	B (J/mol)	R <sup>2</sup>
0.133	16.949	0.924	1.388	2.31	0.678	2 × 10 <sup>-7</sup>	1.58	0.833	2.4	3 × 10 <sup>-5</sup>	0.282

**Table 5.** Parameters of kinetic models ( $C_i = 20\text{--}100$  mg/L, 1.5 g biomass, 160  $\mu\text{m}$ , 700 rpm,  $\text{pH} = 6.0 \pm 0.2$ ,  $T = 20 \pm 1$  °C,  $P = 1$  atm)

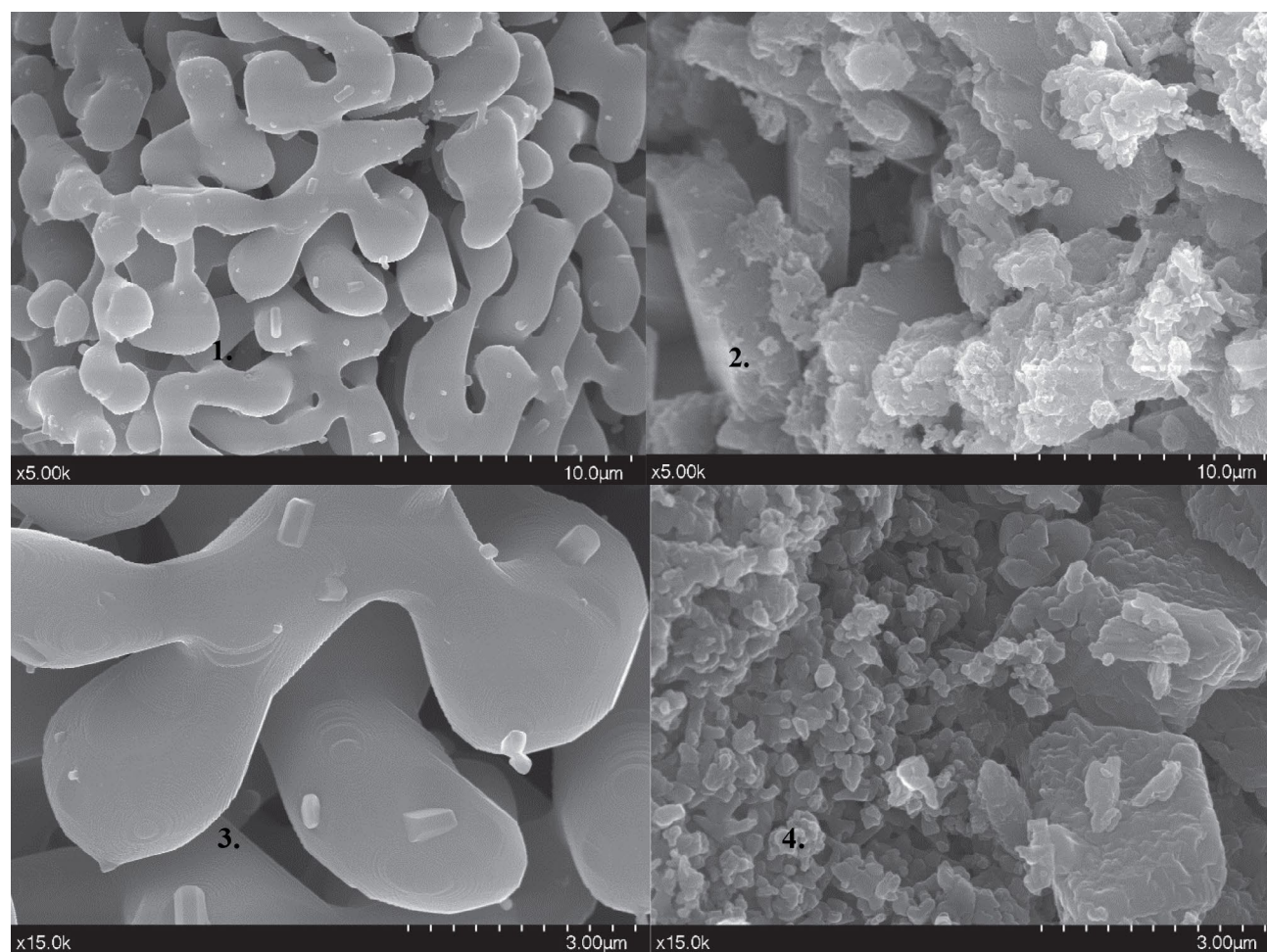
RBV-5R		I. order kinetic model			II. order kinetic model		
C (mg/L)	$q_e$ (exp) (mg/g)	$k_1$ (1/min)	$q_e$ (calc) (mg/g)	$R^2$	$k_2$ (g/mg $\times$ min)	$q_e$ (calc) (mg/g)	$R^2$
20	1.290	0.534	1.43	0.839	6.842	1.946	0.9999
40	2.450	0.019	1.67	0.459	0.553	3.678	0.9997
60	3.710	0.014	2.12	0.521	0.174	5.571	0.9997
80	5.710	0.052	1.07	0.453	0.246	7.806	0.9999
100	6.470	0.022	1.64	0.519	0.133	9.728	0.9999

**Table 6.** Parameters of diffusion models ( $C_i = 20\text{--}100$  mg/L, 1.5 g biomass, 160  $\mu\text{m}$ , 700 rpm,  $\text{pH} = 6.0 \pm 0.2$ ,  $T = 20 \pm 1$  °C,  $P = 1$  atm)

RBV-5R		Intra-particle diffusion			Liquid film diffusion		
C (mg/L)	D (cm <sup>2</sup> /s)	$k_{ip}$ (mg/g $\cdot$ min <sup>1/2</sup> )	Intercept	$R^2_{ip}$	$k_{fd}$ (1/min)	Intercept	$R^2_{fd}$
20	$9.09 \times 10^{-8}$	0.060	1.088	0.746	0.399	−2.08	0.841
40	$1.39 \times 10^{-8}$	0.012	2.287	0.218	0.018	−2.86	0.666
60	$6.60 \times 10^{-9}$	0.028	3.326	0.334	0.001	−2.59	0.508
80	$1.31 \times 10^{-8}$	0.151	3.776	0.375	0.059	−2.31	0.819
100	$8.86 \times 10^{-9}$	0.169	4.579	0.418	0.019	−2.19	0.506

egg shells, and adsorbents, RBV-5R. The correlation coefficient of first order and second order kinetic models was

determined by the linear regression method. The calculated parameters for each model are shown in Table 5. Since

**Figure 8.** SEM (1, 3) control and (2, 4) 2 g/L RBV-5R dye adsorbed calcined eggshell



the calculations show that the linear regression coefficient is higher for the second order kinetic model, in addition to our experimental conditions, the adsorption process is described more precisely by the second order kinetic model developed by Ho and McKay.<sup>24,38</sup>

The intraparticle diffusion rate or the liquid film diffusion rate can control the biosorption of the RBV-5R clothing dye on the surface of the calcined eggshell.

Table 6 summarizes the calculated parameters for each diffusion model (intraparticle, liquid film), namely the linear regression coefficients, intersects, velocity values, and particle diffusion coefficient (D). The pore diffusion coefficients range from  $6.60 \times 10^{-9}$  to  $9.09 \times 10^{-8}$  cm<sup>2</sup>/s by varying the concentration. It can also be observed that none of the incisions pass through the origin of any diffusion model. It can be concluded that during the binding of the dye on the surface of the eggshell, the intra-particle section is not rate-determining, nor does the liquid film diffusion affect the adsorption process.<sup>34–37</sup>

In summary, the speed of the process is only determined by biosorption.

### 3. 10. Scanning Electron Microscopy

The morphological properties and texture of the surface of the calcined eggshell used during the adsorption were studied by scanning electron microscopy, both for the control and the dye adsorbed eggshells. Figure 8 shows the captured images at 5 000x and 15 000x magnifications. In the figures (Figures 8.1 and 8.3), the porous structure of the calcined eggshell is observed between the irregular shaped structures. Moreover, on the surface some small crystals of about 300 nm can be found. Following the adsorption (Figures 8.2 and 8.4), this porous and irregular structure disappears, with the molecules of the dye filling the “gaps”.

### 3. 11. Energy Dispersive Spectroscopy, Enrichment Factors

To determine the elemental composition of calcined eggshell (control and dye adsorbed), energy-dispersive X-ray spectroscopy was performed where the dye-adsorbed biomass was in a 2 g/L solution. The table below shows (Table 7) that there were two main elements in the control sample, Ca and O – since calcined eggshells composition is CaO – and in small percentage N, Mg, C, and Pb. Gold was also present, but is not listed in the table because of its small value (it was attached to the specimen in vacuum to increase conductivity). After adsorption, the amount of C and the amount of N increased by more than 500%, which is typically derived from the dye, being an azo dye.

Table 7. Results of EDX analyses

Elements	Wt(%) calcined eggshell	Wt(%)calcined eggshell + RBV-5R	Enrichment factor (%)
C	3.33	9.89	197.49
N	0.32	2.09	554.17
O	35.97	36.04	0.19
Mg	0.76	0.67	–11.84
Ca	59.63	51.29	–13.99

### 3. 12 Fourier Transformation Infrared Spectroscopy

Functional groups of calcined eggshell before and after adsorption were determined using Fourier transformations infrared spectroscopy in a wavelength range of 500 and 4000 cm<sup>–1</sup> (Figure 9). Typical peaks of calcite and CaO are found at 874, 1442, 1795 cm<sup>–1</sup> wavelengths, 713 and 1050 cm<sup>–1</sup> typically exhibit peaks of R-SO<sub>2</sub>, functional groups on 2923 and 2853 cm<sup>–1</sup> represent CH.<sup>21,38–40</sup>

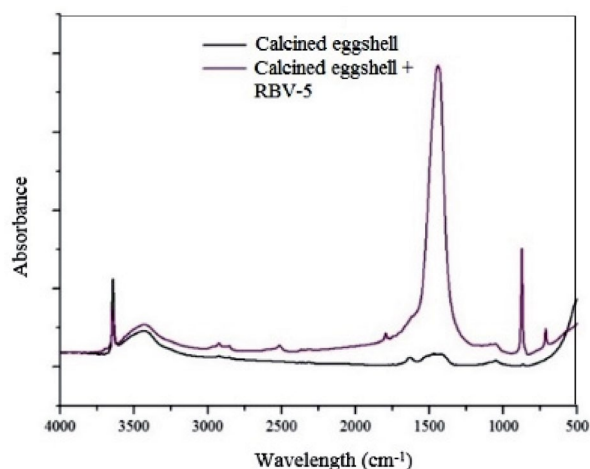


Figure 9. FTIR spectrum for control and 2 g/L RBV-5R dye adsorbed calcined eggshell

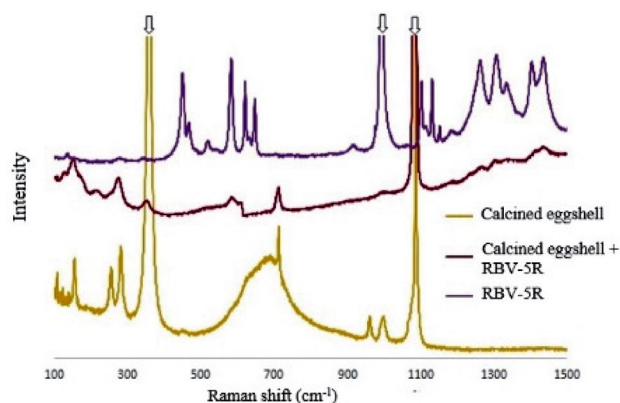
### 3. 13. Raman Spectroscopy

Raman spectroscopic measurements were performed in the Litosphere Fluidum Research Laboratory of the Eötvös Loránd University, Faculty of Science. Figure illustrates the spectra obtained in the Raman Shift interval between 100 and 1500 cm<sup>–1</sup>. The figure from top to bottom includes the calcined eggshell, RBV-5R dye adsorbed biomass and RBV-5R fabric dye spectra.

Spectrums of the control and the dye adsorbed calcined eggshells contained peaks of calcite described in literature<sup>41,42</sup> at 150–154, 712–711, 1087–1086 cm<sup>–1</sup>. Peaks at 281–274 and 3618 cm<sup>–1</sup> represent Ca(OH)<sub>2</sub>. We also observe the characteristic peaks of the dye on the dye-adsorbed biomass sample: 582, 1261–1262, 1307–1306,



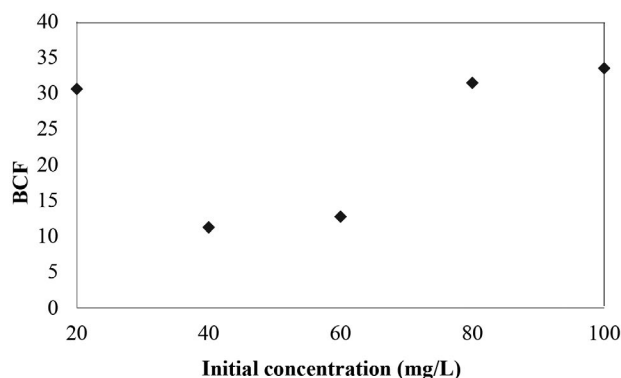
1437–1435  $\text{cm}^{-1}$ . Newly emerging peaks may be suitable for aliphatic C-S, N = N bonds.<sup>43</sup>



**Figure 10.** Raman spectrum for control, 2 g/L RBV-5R dye adsorbed calcined eggshell and RBV-5R dye

### 3. 14. Bioconcentration Factor

Based on the equilibrium concentrations, the bioconcentration factor (BCF) was determined. It indicates how many times the calcined eggshell can accumulate the concentration of RBV-5R. BCF was calculated based on the concentration of the aqueous solution in equilibrium and the concentration of paint on the surface of the calcined eggshell. According to the work of Milinki,<sup>44</sup> bio-sorbents can be grouped according to their bioconcentration value as:  $\text{BCF} > 3$  large,  $1.5 < \text{BCF} < 3$  medium,  $\text{BCF} < 1.5$  small tendency. Five different concentrations (20–100 mg/L) were determined for the BCF (Figure 11). The highest BCF value was obtained for the 100 mg/L solution where  $\text{BCF} = 33.48$ . It can be observed that the change in the BCF value shows a tendency similar to the efficiency of removing the initial dye concentration. Since the BCF has exceeded the value 3 for all concentrations, the calcined eggshell biomass has a high bioaccumulation tendency.



**Figure 11.** Bioconcentration factor  
( $C_i = 20$ –100 mg/L, 1.5 g adsorbent, 160  $\mu\text{m}$ , 700 rpm,  $\text{pH} = 6.0 \pm 0.2$ ,  $T = 20 \pm 1^\circ\text{C}$ )

## 4. Conclusion

This study proves that calcined is suitable for removing RBV-5R dye from sewage.

We have shown that the decomposition of the eggshell occurs at  $728.6^\circ\text{C}$ . The total surface area of the eggshell decreased after the adsorption.

Changing the initial parameters leads to the following conclusions:

- by changing the initial dye concentration results show an efficiency higher than 90% in each case;
- as the amount of biomass increases, the amount of bound dye decreases; the highest efficiency is reached at 1.5 g (96.8%);
- in our case, the pH of the aqueous solution did not influence the potency of the binding because the sorbent used in it provided a strong alkaline pH ( $\text{pH} = 11$ ); in each case the efficiency was higher than 95%;
- the increase in the temperature of the aqueous solution reduces the efficiency of adsorption, the process is spontaneous, endothermic.

Mathematical modeling of equilibrium data leads to the following conclusions:

- in addition to our experimental conditions, the adsorption processes are most accurately described by the Langmuir isotherm;
- second order kinetic model characterizes the adsorption process;
- the results of the diffusion models prove that neither the intraparticle model nor the liquid film influences the rate of the adsorption process; only the adsorption is decisive;
- thermodynamic measurements further confirm the physical nature of adsorption, the spontaneity of the process, because as the temperature increases, the amount of adsorption decreased.

SEM images of calcined eggshell powder confirm that the dye molecules fill the porous structure. EDX measurements confirm the adsorption resulting in increased C and N and decreased Ca and Mg. Based on the peaks of control and dye adsorbed samples of FTIR and Raman spectra, functional groups and bonds specific to each component can be found.

## Acknowledgements

This work was funded by the Sapientia Hungariae Foundations' Collegium Talentum scholarship program. Research would not have been possible without support from the Research and Instrument Core Facility (RICF) of the Faculty of Science of the Eötvös University, Budapest (Dr. Csaba Szabó, László Aradi).

## 6. References

1. P. Juuti, T. Katko, H. Vuorinen, 'Environmental History of Water - Global view on community water supply and sanitation', 2007.

2. C. Pregun, C. Juhász, 'Vízminőségvédelem', Debreceni Egyetem Agrár- És Gazdálkodástudományok Centruma (AGTC) Mezőgazdaság-, Élelmiszertudományi És Környezetgazdálkodási Kar Víz- És Környezetgazdálkodási Intézet.
3. Török S., 'Vízellátás és szennyvízkezelés [Digitális Tankönyvtár]', Szent István Egyetem, 2011.
4. Day Zero, <http://coct.co/water-dashboard/>, accessed April 2, 2018.
5. M. Kimmelman, *N. Y. Times* 2017.
6. Why Cape Town Is Running Out of Water, and Who's Next, <https://news.nationalgeographic.com/2018/02/cape-town-running-out-of-water-drought-taps-shutoff-other-cities/>, accessed March 30, 2018.
7. S. K. Chinta, S. Vijaykumar, *I.J.E.M.S.* 2013, 4, 308.
8. O. S. Bello, T. T. Siang, M. A. Ahmad, *Asia-Pac. J. Chem. Eng.* 2012, 7, 378. DOI:10.1002/apj.557
9. H. Zollinger, 'Color Chemistry: Syntheses, Properties, and Applications of Organic Dyes and Pigments', John Wiley & Sons, 2003.
10. G. Annadural, R. S. Juang, D. J. Lee, *Water Sci. Technol. J. Int. Assoc. Water Pollut. Res.* 2003, 47, 185. DOI:10.2166/wst.2003.0049
11. M. Hirata, N. Kawasaki, T. Nakamura, K. Matsumoto, M. Kabayama, T. Tamura, S. Tanada, *J. Colloid Interface Sci.* 2002, 254, 17. DOI:10.1006/jcis.2002.8570
12. M. T. Uddin, M. A. Islam, S. Mahmud, M. Rukanuzzaman, *J. Hazard. Mater.* 2009, 164, 53. DOI:10.1016/j.jhazmat.2008.07.131
13. F. Kaymak-Ertekin, A. Gedik, *LWT - Food Sci. Technol.* 2004, 37, 429. DOI:10.1016/j.lwt.2003.10.012
14. C. Majdik, S. Burca, A. Maicaneanu, M. Stanca, S. Tonk, P. Mezey, *Rev. Roum. Chim.* 2010, 55, 871.
15. B. Nagy, A. Măicăneanu, C. Indolean, C. Mânzatu, L. Silaghi-Dumitrescu, C. Majdik, *J. Taiwan Inst. Chem. Eng.* 2014, 45, 921. DOI:10.1016/j.jtice.2013.08.013
16. B. Nagy, A. Maicaneanu, C. Indolean, S. Burca, L. Silaghi-Dumitrescu, C. Majdik, *Acta Chim. Slov.* 2013, 60, 263.
17. R. Fabryanty, C. Valencia, F. E. Soetaredjo, J. N. Putro, S. P. Santoso, A. Kurniawan, Y.-H. Ju, S. Ismadji, *J. Environ. Chem. Eng.* 2017, 5, 5677. DOI:10.1016/j.jece.2017.10.057
18. N. Georgieva, Z. Yaneva, D. Dermendzhieva, *Water Sci. Technol.* 2017, 76, 1065. DOI:10.2166/wst.2017.283
19. Z. Huang, Y. Li, W. Chen, J. Shi, N. Zhang, X. Wang, Z. Li, L. Gao, Y. Zhang, *Mater. Chem. Phys.* 2017, 202, 266. DOI:10.1016/j.matchemphys.2017.09.028
20. A. Kausar, M. Iqbal, A. Javed, K. Aftab, Z.-H. Nazli, H. N. Bhatti, S. Nouren, *J. Mol. Liq.* 2018, 256, 395. DOI:10.1016/j.molliq.2018.02.034
21. R. Slimani, I. El Ouahabi, F. Abidi, M. El Haddad, A. Regti, M. R. Laamari, S. E. Antri, S. Lazar, *J. Taiwan Inst. Chem. Eng.* 2014, 45, 1578. DOI:10.1016/j.jtice.2013.10.009
22. P. S. Guru, S. Dash, *Adv. Colloid Interface Sci.* 2014, 209, 49. DOI:10.1016/j.cis.2013.12.013
23. J. V. Flores-Cano, R. Leyva-Ramos, J. Mendoza-Barron, R. M. Guerrero-Coronado, A. Aragón-Piña, G. J. Labrada-Delgado, *Appl. Surf. Sci.* 2013, 276, 682. DOI:10.1016/j.apsusc.2013.03.153
24. S. Tonk, C. Majdik, S. Robert, M. Suci, E. Rápó, B. Nagy, A. Gabriella Niculae, *Rev. Chim. - Buchar. - Orig. Ed.* 2017, 68, 1951.
25. L. Giraldo, J. C. Moreno-Piraján, *J. Anal. Appl. Pyrolysis* 2014, 106, 41. DOI:10.1016/j.jaap.2013.12.007
26. O. A. A. Eletta, O. A. Ajayi, O. O. Ogunleye, I. C. Akpan, *J. Environ. Chem. Eng.* 2016, 4, 1367. DOI:10.1016/j.jece.2016.01.020
27. J. Li, D. H. L. Ng, R. Ma, M. Zuo, P. Song, *Chem. Eng. Res. Des.* 2017, 126, 123. DOI:10.1016/j.cherd.2017.07.005
28. N. Pramanpol, N. Nitayapat, *Kasetsart J. - Nat. Sci.* 2006, 40, 192.
29. A. Mittal, M. Teotia, R. K. Soni, J. Mittal, *J. Mol. Liq.* 2016, 223, 376. DOI:10.1016/j.molliq.2016.08.065
30. E. Rápó, R. Szép, Á. Keresztesi, M. Suci, S. Tonk, *Acta Chim. Slov.* 2018, 65, 709. DOI:10.17344/acsi.2018.4401
31. Y.-B. Wang, J.-M. Jehng, *Chem. Eng. J.* 2011, 175, 548. DOI:10.1016/j.cej.2011.09.126
32. Nuchnapa Tangboriboon, Ruksapong Kunanurukapong, A. Srivat, *J. Ceram. Process. Res.* 2012, *Journal of Ceramic Processing Research* 13(4):413-419, 413.
33. G. RAMESH, D. JAYABALAKRISHNAN, C. RAMESHKUMAR, *J. Optoelectron. Biomed. Mater.* 2018, 10, 21.
34. R. Mohadi, K. Anggraini, F. Riyanti, A. Lesbani, *Sriwij. J. Environ.* 2016, 1, 32. DOI:10.22135/sje.2016.1.2.32-35
35. H. J. Park, S. W. Jeong, J. K. Yang, B. G. Kim, S. M. Lee, *J. Environ. Sci.* 2007, 19, 1436. DOI:10.1016/S1001-0742(07)60234-4
36. T. Wittoon, *Ceram. Int.* 2011, 37, 3291. DOI:10.1016/j.ceramint.2011.05.125
37. O. S. Bello, M. A. Ahmad, *Chem. Ecol.* 2011, 27, 481. DOI:10.1080/02757540.2011.600696
38. H. Patel, *Fresenius Environ. Bull.* 2011, 20.
39. P. C. N. Ejikeme, E. M. Ejikeme, G. N. Okonkwo, *Int. J. Tech. Res. Appl.* 2014, 2, 96.
40. Subramani S.E., Thinakaran N., *Process Saf. Environ. Prot.* 2017, 106. DOI:10.1016/j.psep.2016.11.024
41. Y. S. Ho, G. McKay, *Process Biochem.* 1999, 34, 451. DOI:10.1016/S0032-9592(98)00112-5
42. B. P. Vinayan, Z. Zhao-Karger, T. Diemant, V. S. Kiran Chakravadhanula, N. I. Schwarzbürger, M. Ali Cambaz, R. Jürgen Behm, C. Kübel, M. Fichtner, *Nanoscale* 2016, 8, 3296. DOI:10.1039/C5NR04383B
43. G. A. C. Ribeiro, D. S. A. Silva, C. C. dos Santos, A. P. Vieira, C. W. B. Bezerra, A. A. Tanaka, S. A. A. Santana, G. A. C. Ribeiro, D. S. A. Silva, C. C. dos Santos, A. P. Vieira, C. W. B. Bezerra, A. A. Tanaka, S. A. A. Santana, *Polímeros* 2017, 27, 16. DOI:10.1590/0104-1428.2386
44. A. V. Borhade, A. S. Kale, *Appl. Water Sci.* 2017, 1. DOI:10.1007/s13201-017-0558-9
45. S. K. Sharma, *Spectrochim. Acta. A. Mol. Biomol. Spectrosc.* 2007, 68, 1008. DOI:10.1016/j.saa.2007.06.047
46. D. B. Thomas, M. E. Hauber, D. Hanley, G. I. N. Waterhouse, S. Fraser, K. C. Gordon, *J. Exp. Biol.* 2015, 218, 2670. DOI:10.1242/jeb.124917
47. Raman Spectroscopy for Analysis and Monitoring, <http://www.horiba.com/fileadmin/uploads/Scientific/Documents/Raman/bands.pdf>.

48. Ecotoxicology and Enviromental Protection|Digitális Tankönyvtár, [http://www.tankonyvtar.hu/hu/tartalom/tam-op412A/2011-0038\\_28\\_milinki\\_en/ix01.html](http://www.tankonyvtar.hu/hu/tartalom/tam-op412A/2011-0038_28_milinki_en/ix01.html), accessed November 26, 2017.

## Povzetek

Onesnaženje vode je postalo z razvojem industrije pereč problem, zato je še bolj pomembno zagotavljanje vode ustrezne čistosti v zadostnih količinah. Po literaturnih podatkih je za tiskanje, živila in tekstilno industrijo uporabljano 100 000 različnih barvil. Remazol briljantno vijolično -5R (RBV-5R) spada v skupino azo barvil uporabljenih v tekstilni industriji. Namen raziskave je bil preučitev odstranjevanja anionskega barvila RBV-5R s kalciniranimi jajčnimi lupinami. Preučili smo vpliv začetne koncentracije barvila (20–100 mg/L RBV-5R), količine biomase, kontaktnega časa, temperature in pH vrednosti na proces adsorpcije. Določili smo ravnotežno adsorbirano količino barvila in učinkovitost procesa. Pri tem smo uporabili različne tehnike za določanje morfologije adsorbenta (EDX, SEM, FTIR, Raman), različne adsorpcijske modele za opis adsorpcijske izoterme (Langmuir, Freundlich, Temkin in Dubinin-Radushkevich) ter kinetične in difuzijske matematične modele za karakterizacijo procesa. Prav tako smo kalcinirane jajčne lupine okarakterizirali gravimetrično in z BET. Na osnovi rezultatov lahko zaključimo, da kalcinirane jajčne lupine učinkovito odstranjujejo barvilo iz vodnih raztopin.



Except when otherwise noted, articles in this journal are published under the terms and conditions of the Creative Commons Attribution 4.0 International License

*Scientific paper*

# Assessment of the 14- and 15-Year-Old Students' Understanding of the Atmospheric Phenomena

Janja Majer,<sup>1\*</sup> Miha Slapničar<sup>2</sup> and Iztok Devetak<sup>2\*</sup>

<sup>1</sup> University of Maribor, Faculty of Natural Sciences and Mathematics, Koroška 160, 2000 Maribor, Slovenia

<sup>2</sup> University of Ljubljana, Faculty of Education, Kardeljeva pl. 16, 1000 Ljubljana, Slovenia

\* Corresponding author: E-mail: janja.majer@um.si  
iztok.devetak@pef.uni-lj.si

Received: 02-27-2019

## Abstract

The main purpose of this study was to identify understanding of atmospheric pollution phenomena such as acid rain, global warming, ozone layer depletion and photochemical smog among grade 9 lower secondary school students (aged 14 to 15), in all Slovenian regions. The research involves the development of a three-tier multiple-choice diagnostic test entitled the Atmospheric Pollution Phenomena Diagnostic Test (APPDiT). APPDiT is a 15-item diagnostic test comprising items for assessing students' understanding and self-confidence of atmospheric pollution problems. The results reveal that the majority of the participants demonstrated a lack of knowledge or misconception about atmosphere pollution since the overall success rate on the APPDiT was 39.6%. In particular, only 36.7%, 5.1%, 42.7% or 19.1% of the students have adequate knowledge regarding understanding of the formation, consequences, and strategies to reduce acid rain, global warming, ozone layer depletion and photochemical smog, respectively. This shows a substantial students' knowledge deficits related to atmosphere pollution at the end of the compulsory education in Slovenia.

**Keywords:** Three-tier diagnostic test; atmospheric pollution; adequate knowledge; lack of knowledge; misconception; self-confidence

## 1. Introduction

Across the globe, both the extent and the impact of air pollution are highly variable.<sup>1</sup> Air pollution is induced by the presence of toxic substances in the atmosphere, mainly produced by human activities in recent years,<sup>2</sup> which generate a number of phenomena that affect the ecosystem and living beings. Acid rain, global warming, ozone layer depletion and photochemical smog are the major ecological phenomena of air pollution.<sup>3</sup> Therefore, air pollution control is vital and should be top of the priority list of governments.<sup>4</sup> What is even more important than control is the knowledge and understanding of the formation of air pollution and their impact on health, because with suitable environmental awareness people can significantly reduce intentional environmental damage. One way to make this happen is through education, in particular science and environmental education. In addressing environmental issues, it is imperative to begin with youngsters in order that they become more concerned about the environment and also engaged in actions to protect it, since this is contribu-

ting to sustaining the environment for generations to come.<sup>5,6</sup> For that reason, teachers are responsible for developing students' environmental awareness and knowledge in the classroom. All major environmental education documents and International Conferences recognize explicitly the importance of knowledge and understanding of general environmental principles.<sup>7</sup> Researchers are convinced that education is an effective strategy for preparing young people to learn about environmental issues. Some research reveals that disinterest toward environmental issues is due to a lack of knowledge, while those students that are well informed about environmental issues also showed interest in them.<sup>8–10</sup> If we want to achieve lifelong understanding of environmental phenomena, environmental learning must be included throughout the entire vertical of the curricula, as this would also encourage cross-curricula integration.<sup>11</sup>

Recently, it has been shown that students of all ages have many misconceptions regarding environmentally-related content, as they poorly distinguish between general environmental problems.<sup>12,13</sup> For example, the majority

think that the “hole” in the ozone layer contributes to global warming by allowing greater penetration of the sun rays resulting the increase of the Earth’s temperature. Recently, Yazdanparast et al.<sup>14</sup> identified significant misconceptions among 12 and 18 years old students regarding atmosphere composition, as 45.1% of students think that the most common gas in an unpolluted atmosphere is oxygen, while only 23.7% of respondents know that this gas is nitrogen. Valeiras et al.<sup>15</sup> found similar results with Argentinean students, where 87.0% of students identified that the atmosphere is composed mostly of oxygen. Sah et al.<sup>16</sup> reported that around 71.0% students between 12 to 15 years identify the burning of coal as the main atmospheric pollutant and around 2.0% of students identified other fossil fuels, e.g. oil, as the important atmospheric pollutants. Other studies show that most students identify industry and energy as the main causes of pollution, followed by the use of deodorants, fertilizers and pesticides.<sup>17,18</sup> However, Dove et al.<sup>19</sup> found that most students recognize industry and transport as the main sources of acid rain formation, but they are not aware of the primary pollutants such as nitride and sulphur oxides that enter the atmosphere and cause the formation of acid rain. Furthermore, students think that atmospheric phenomena such as acid rain, ozone depletion and the global warming are caused by the same pollutants.<sup>20</sup> Other researchers have shown that misconceptions about many environmental issues, climate change included, are not only held by students but by teachers as well.<sup>21</sup> Due to the complex relationship between different atmospheric phenomenon, not only teachers’ but also the media and literature have referred to them in synonymous ways in spite of their entirely different meanings. This and many other misconceptions concerning the causes of atmospheric phenomenon probably affect peoples’ ideas about the actions that need to be taken to alleviate them. If these misconceptions can be identified and addressed already at primary school level, students’ conceptual understanding of environmental issues can be further developed. And for this reason, there has lately been significant interest in educating students about atmospheric phenomenon, so as to enable them to successfully cope with atmospheric pollution.

Common approaches to identifying misconceptions are the use of open-ended questions, multiple choice questions, multi-tier diagnostic questions (3-tier or 4-tier items), and interviews.<sup>22</sup> In the 3-tier format, the first tier requires a fact-based response (Tier 1; a multiple-choice answer tier). The second tier is reasoning for that response (Tier 2; a multiple-choice reason tier) and the third tier is a confidence scale (Tier 3; e.g. a six-point confidence scale) to indicate how confident respondents are in the correctness of their responses to the answer and reason tiers. The addition of a confidence scale helps to overcome some of the limitations of the 2-tier format, wherein, it is not easy to differentiate whether a correct response can be attributed to a high level of understanding or whether it is due to guess-

ing.<sup>23</sup> For example, if the responses to both tiers are incorrect but confidence is high, it is an indication of a misconception. On the other hand, if the responses to both tiers are correct but confidence is low, it could mean a lack of knowledge, rather than good understanding.<sup>22</sup> A more detailed probing of students’ concepts understanding can be executed by applying 4-tier items, but for the purposes of this study a simpler version of the 3-tier items was used. The main reason for this decision was the students’ age (14-years-olds solve items more effectively when they are not too complicated) and the fact that the 3-tier items can also be valid enough to identify students’ conceptions.

## 2. Research Problem and Research Questions

Knowledge of environmental problems and pollution-related phenomena has grown over the last two decades especially in basic schools, as the environmental crisis is the greatest threat mankind collectively has ever faced, even beyond the threat of nuclear warfare according to Pikhala et al.<sup>24</sup> In Slovenia, there is little attention paid to environmental education.<sup>25,26</sup> In the contemporary education, students do not learn much about environmental issues.<sup>27</sup> Although the environmental concepts are present in the primary and secondary school science curriculum, but there are usually not enough lessons to include environmental education into actual classroom activities, so that the adequate students’ environmental literacy could develop.<sup>28</sup> In chemistry and biology, students should be taught the main causes of air, water and soil pollution and their effects on people’s health and lives, but we do not have enough data to evaluate students’ basic understanding of environmental issues.<sup>29</sup>

The aim of the present research is to identify the level of 9 grade primary school students’ understanding of atmospheric phenomenon, such as acid rain, global warming, ozone layer depletion and photochemical smog. For that purpose, two research questions were formed:

- (1) What is 14- and 15-year-old students’ current level of knowledge regarding the atmospheric phenomena?
- (2) Do students understand the reasons for atmospheric phenomenon such as acid rain, global warming, ozone layer depletion and photochemical fog?

## 3. Method

A cross-sectional non-experimental and descriptive research approach was used in this research.<sup>30</sup>

### 3.1. Participants

Altogether, 1012 lower secondary school (grade 9; last year of compulsory basic education in Slovenia) stu-



dents participated in this research. The sample represented 5.8% of the whole population of 9-grade students (17,475 students) in the school year 2017<sup>31</sup> in Slovenia. Students were from 24 schools (representing 5.3% of all 452 lower secondary schools in Slovenia). Schools were sampled from eight different regions of Slovenia; 20.8% were from Primorska, 2.5% from Notranjska, 9.7% from Dolenjska, 22.7% from Osrednjeslovenska, 24.0% from Gorenjska, 12.4% from Savinjska, 3.8% from Posavska and 4.2% from the Pomurska region. The sample consisted of 474 (46.8%) male and 538 (53.2%) female students. The students' average school grade in biology is 3.8, in chemistry 3.7 and in physics 3.5 (grades' scale from 1 to 5; 1 meaning insufficient and 5 meaning excellent).

Purposive sampling was used to select participants for this research. However, all eleven statistical regions of Slovenia were included in the sampling. The nine grade students were selected according to their expressed interest to participate in the research, and also according to the interest of students' chemistry teachers, school principals and their parents/caregivers. Before applying the instruments, students' parents/caregivers granted all necessary permissions for students' participation in the research.

### 3. 2. Instruments

The data was collected using two instruments: the information about participants (IP) and a diagnostic in-

strument entitled Atmospheric Pollution Phenomena Diagnostic Test (APPDiT) to measure students' understanding of atmospheric phenomenon as the result of the pollution because of human activities. The content validity of the instrument was confirmed by six independent experts in chemical and environmental education. Both instruments were designed specifically for this study. The full texts of the instruments can be obtained by request from the corresponding author.

The IP questionnaire comprises of general information about the participants (e.g. gender, school, region, and grades in biology, chemistry, and physics. The APPDiT comprise of 15 three-tier multiple-choice items. Each task measures students' understanding of specific environmental phenomena such as: acid rain, global warming, ozone layer depilation, and photochemical fog. Each item, as presented in Figure 1, includes three-tiers: a multiple-choice answer tier (Tier 1), a reasoning tier (Tier 2) describing an expected reason for the students' answer selected in Tier 1 and a six-point confidence scale (Tier 3) – the answers obtained in the six-point confidence scale correspond to "1-just guessing", "2-very unconfident", "3-unconfident", "4-confident", "5-very confident" and "6-absolutely confident" and expresses the students' confidence in giving the answer and the reason for it (Tiers 1 and 2). In order to simplify the discussion, the following answers from the confidence scale were merged as follows: "Not Sure", when students choose "1" or "2" on the confidence scale, fol-

#### 8. Which compounds are responsible for the global warming?

- A Chlorofluorocarbons.
- B Sulphur dioxide.
- C Carbon dioxide.
- D Carbon dioxide, Methane and Chlorofluorocarbons.**

#### 8.1 Why did you choose such an answer in the above question No. 8?

- A CFCs (chlorofluorocarbons or freons) that can be found in deodorants are responsible for the increase of greenhouse gases.
- B Sulphur dioxide (SO<sub>2</sub>) reacts with water droplets in the air, and the resulting precipitation affects the increases of greenhouse gases.
- C Carbon dioxide (CO<sub>2</sub>) that is generated through burning of fossil fuels is the only gas that affects the global warming.
- D Gaseous molecules with at least three atoms can absorb heat and emit it back into the atmosphere, which increases the greenhouse effect.**

#### 8.2 How confident are you in the correct answer?

1	2	3	4	5	6
<i>Just</i>	<i>Very</i>				
<i>guessing</i>	<i>unconfident</i>	<i>Unconfident</i>	<i>Confident</i>	<i>Very confident</i>	<i>Absolutely</i>
					<i>confident</i>

**Figure 1.** An example of the task no. 8 in APPDiT; 1<sup>st</sup> tier (8), 2<sup>nd</sup> tier (8.1); 3<sup>rd</sup> tier (8.2.); the correct answer and the correct reason are presented in bold.

lowed by "Sure", which corresponds to "3" or "4" and "Very Sure" when students pick "5" or "6" on the confidence scale. The overall response possibilities in the APPDiT (first, second, and third tiers together) resulted in the following categories: (i) a combination of correct (tier 1) and correct (tier 2) and very sure or sure (tier 3) answers was treated as *Adequate knowledge* (ii) a combination of incorrect (tier 1) and incorrect (tier 2) and not sure or sure (tier 3) answers was treated as *Lack of knowledge* and (iii) a combination of correct or incorrect (tier 1) and incorrect or correct (tier 2) and either not sure, sure or very sure (tier 3) answers was treated as *Misconception*.<sup>32</sup> The answer to an item was considered to be correct if both first and second tiers were correctly answered. According to Chandrasegaran et al.,<sup>33</sup> such decisions decrease the percentage of students that obtain a correct answer by chance. The Cronbach alpha reliability coefficient of the APPDiT was calculated to be 0.86 for tier 1 and tier 2, while 0.92 for tier 3. Thus the APPDiT is a reliable test not only in that it identifies but also differentiates 15-year old students' misconceptions from a lack of knowledge regarding the atmospheric phenomena. Students' could achieve maximum 30 points solving the tasks on APPiDT (15 for answer tier, 15 for reason tier).

### 3. 3. Research Design

The research was conducted in April 2017. The IP and APPDiT were applied anonymously in groups and all the participants had similar classroom conditions while fulfilling both instruments. They spent 45 minutes on completing both instruments on average. The participants were informed that the data would be used for research purposes only, and the main objective of the study was explained. School principals, teachers, students and their parents/caregivers agreed to their participation in the research. The data analysis shows normal data distribution for all items on the answer tier (Skewness is 0.34; Kurtosis is 0.02) and reason tier (Skewness is 0.44; Kurtosis is 0.16). For that reason, descriptive statistics (mean *M*, standard deviations *SD*) were applied to reveal the level of students' understanding of atmospheric phenomena and self-confidence while solving the specific tasks in APPDiT, data were analysed using SPSS Statistics. Moreover, McNemar's test to determine if there are significant differences on a dichotomous dependent variable between two related tiers of APPiDT was applied. This statistical test was applied on the data because students were divided into four groups according to their achievements in APPiDT; incorrect answer & incorrect reason, incorrect answer & correct reason, correct answer & incorrect reason and correct answer & correct reason. Taking into account that  $2 \times 2$  contingency tables can be formed for each APPDiT item this test was the most reasonable selection. The research was conducting according to ethical standards for educational research.

## 4. Results and Discussion

### 4. 1. Students' Knowledge About Atmospheric Phenomena

The answer and reason responses (i.e. tier 1 and tier 2 responses) of the APPDiT indicated low levels of students understanding of environmental pollution through the atmospheric phenomena, since the overall success rate students achieved on average was only 39.8%, i.e. 11.9 points out of 30. The answer was considered correct when both tiers of the particular item (tier 1 and tier 2) were correctly answered. McNemar's test, which was used to determine if there are differences between students' achievements in solving two related tiers of APPiDT, shows statistically significant differences in solving tasks in most items ( $p \leq 0.05$ ), except in items 9, 10, 11 in 15 ( $p \geq 0.05$ ) (see Table 1).

The first three tasks in the APPDiT, the composition of the unpolluted air, air pollutants and their state of matter, referred to general knowledge on atmospheric pollution. The results show that 58.5% of the students have adequate knowledge regarding the main air pollutants, but on the other hand, almost the same percentage of students demonstrated a lack of knowledge regarding the state of matter of air pollutants. Student's knowledge about particular atmospheric phenomena such as acid rain, global warming, ozone layer depletion and photochemical smog was further tested. The average students achievements related to the specific items are presented in Table 1. 36.7% of the students responded correctly to both tier 1 and tier 2 regarding acid rain related items (4, 5 and 6), while only a small percentage of students (just between 7.4% to 22.0%) gave an incorrect reason along with the correct answer. The results imply that only 36.7% of students have adequate knowledge and understanding of acid rain formation, its consequences, and strategies to reduce it; however, all others may have learned facts without an adequate understanding, which leads either to misconceptions (11.5%) or lack of knowledge (34.0%). The highest level of lack of knowledge concerned global warming. More than a half of the whole respondents in the APPDiT did not understand the causes and consequences of global warming, while a very small percentage (5.1%) showed adequate knowledge with a level of self-confidence below 14.3%. 83.1% of students have a lack of knowledge about the actions that should be undertaken to reduce global warming, which is even more worrying as this shows a very low environmental awareness of students. Students' knowledge on the items related to ozone layer depletion (11, 12 and 13) was on the same level as those with global warming. 43.4% of students gave an incorrect response to both tier 1 and tier 2 regarding the importance of the ozone layer. Accordingly, the significant lack of knowledge was identified for these items, where 69.4% and 51.4% of students did not know either the causes of ozone layer depletion on the consequences of the reduction of the pro-

**Table 1.** The success of students' responses for the APPDiT diagnostic test.

The content of specific item in the APPDiT test	The first (content) and the second (reason) tiers					The third tier (students' level of confidence)				
	Incorrect answer & incorrect reason [f%]	Incorrect answer & correct reason [f%]	Correct answer & incorrect reason [f%]	Correct answer & correct reason [f%]	Mc-Nemar [X <sup>2</sup> ]	Not sure [f%]	Sure [f%]	Very sure [f%]	M	SD
1. Content of the nonpolluted air	31.4	17.3	21.5	29.8	0.034	23.3	49.8	26.9	3.3	1.8
2. Air pollutants	24.2	2.2	14.9	58.5	0.000	15.9	55.0	29.1	3.6	1.7
3. Physical properties of air pollutants	53.1	5.6	12.7	28.6	0.000	30.7	55.1	14.1	2.8	1.6
4. Understanding on formation of an acid rain	34.0	17.9	11.5	36.7	0.000	41.2	41.9	16.9	2.7	1.7
5. The possible effects of acid rain deposition	44.9	9.4	6.8	38.7	0.051	32.8	45.3	21.9	3.0	1.8
6. Strategies to reduce acid rain	35.5	7.7	20.3	36.7	0.000	40.3	44.4	15.3	2.7	1.7
7. Understanding the causes of global warming	61.0	12.0	22.0	5.1	0.000	37.5	48.2	14.3	2.7	1.6
8. Substances responsible for the occurrence of global warming	46.8	4.3	21.8	27.0	0.000	51.5	37.5	11.1	2.3	1.6
9. The consequences of global warming	56.3	10.8	8.2	24.7	0.071	40.6	42.0	17.4	2.7	1.8
10. Actions to reduce global warming	83.1	4.4	4.5	7.8	1.00	37.4	43.0	19.7	2.9	1.8
11. The importance of the ozone layer	43.4	4.4	7.4	42.7	0.447	38.1	35.7	26.3	3.0	2.0
12. Causes of the ozone layer depletion	69.4	5.4	12.4	12.8	0.000	51.7	35.5	12.8	2.4	1.7
13. Consequences of the reduction of protective ozone layer	51.4	4.0	7.4	37.3	0.001	41.5	38.6	19.9	2.8	1.8
14. Factors impact ground-level ozone development	46.4	12.8	21.5	19.1	0.000	52.1	37.6	10.3	2.3	1.6
15. Action to reduce photochemical smog	49.4	10.8	8.1	31.9	0.060	48.6	38.9	12.5	2.4	1.6

protective ozone layer. Items 14 and 15 dealt with the tropospheric ozone, which is associated with photochemical smog. Here, students were expected to understand the importance of the stratospheric ozone to human health, e.g. lung and heart diseases with chronic patients, etc. and other environmental problems e.g. damaging plants, diminishing crops produce, etc. However, only 19.1% of the students have adequate knowledge regarding the stratospheric ozone, while 46.4% or 49.4% of students choose incorrect tier 1 and incorrect tier 2 combinations for items 14 and 15, respectively, which again shows a lack of knowledge. All-in-all, the mean values of tier 3, which measures the students' level of confidence, were between 2.3 – 3.6 out of 6, indicating a low level of student confidence when answering questions in APPDiT.

Based on the low level of confidence and low achievements in APPDiT, we might conclude that students had difficulties understanding the basic concepts regarding pollution of the atmosphere, its effects and consequences. As students should learn about these phenomena, the curriculums for the following subjects were analysed: learning

about the environment (1<sup>st</sup> to 3<sup>rd</sup> grade), science and technology (4<sup>th</sup> and 5<sup>th</sup> grade), natural sciences (6<sup>th</sup> and 7<sup>th</sup>) and biology (8<sup>th</sup> and 9<sup>th</sup>). We anticipated that curriculum analysis could shed some light on the problems we found from the APPDiT (Table 2). Analysis revealed that students are acquainted with pollution concepts in the first grade of compulsory education already, when discussing environmental education.<sup>28</sup> In the third grade of lower secondary school, students deal with the pollution of air, water and soil that is caused by traffic. For the first time they get to know the exhaust gases and the formation of acid rain. Science and technology curriculum for 5<sup>th</sup> grade includes knowledge about air, the atmosphere and the composition of unpolluted air, the causes of air pollution and actions to reduce the effects of air pollution. After, we found that in the science curriculum for 7<sup>th</sup> grade, content such as unpolluted air, global warming, ozone depletion, acid rain and photochemical smog, are explained. Moreover, according to the curriculum, students also need to recognise the consequences and propose action on the aforementioned causes of air pollution. However, in che-

**Table 2.** Curricula analysis of subjects in compulsory education in Slovenia and learning content connected with the environmental pollution

School Subject	Hours per year	Learning themes	Learning themes related to the environmental pollution	Grade	Learning content related to environmental pollution
Environmental studies	105	Time, Space, States of Matter, Force and Motion, Natural Phenomena, Living things, Human, Community, Relationships, Traffic, Environmental education	Traffic, Environmental education	1 <sup>st</sup> 2 <sup>nd</sup> 3 <sup>rd</sup>	Environmental pollution Consequences of pollution for living beings The impact of traffic on the environment Water, soil and air pollutants
Science and technology	105	States of matter, Force and Motion, Natural Phenomena, Human, Living things,	States of matter	4 <sup>th</sup> 5 <sup>th</sup>	/ Air and water pollution Actions for cleaner air
Science	70 105	States of Matter, Energy, Living Nature, Human impact on the environment	Human impact on the environment	6 <sup>th</sup> 7 <sup>th</sup>	Atmospheric pollution Thermal water pollution /
Biology	52 64	Introduction to Biology, Research and Experiments, Cell, Human Body Structure Introduction to Biology and Society, Research and Experiments, Chemistry of living systems, Genetics, Biotechnology, Evolution, Biodiversity, Biomes and Biosphere, Human impact on the environment	/	8 <sup>th</sup>	/
			Human impact on the environment	9 <sup>th</sup>	Global warming Ozone depletion
Chemistry	70 64	Introduction to Chemistry, Atoms, Chemical Bonds, Chemical Reactions, Periodic Table, Acids/Bases/Salts, Hydrocarbons, Oxygen and Nitrogen Organic Compounds	Hydrocarbons	8 <sup>th</sup> 9 <sup>th</sup>	/ Impact of hydrocarbons on the environment
Physics	70 64	Introduction to Physics, Light, Space, Motion, Forces, Pressure and Buoyancy, Newtons' laws, Work and Energy, Heat, Electrical current, Magnetic Forces, Physics and Environment	Physics and Environment	8 <sup>th</sup> 9 <sup>th</sup>	/ Ecology

mistry curriculum for 8<sup>th</sup> and 9<sup>th</sup> grade we did not find any direct connection with the atmospheric phenomena as the result of pollution. Instead, we found content such as acids/bases/salts, the products that are formed as a consequence of complete and incomplete burning of hydrocarbons, impact of hydrocarbons and their derivatives on the environment and action to reduce them. Since there is no direct connection to the environmental problems proposed by the chemistry curriculum in 8<sup>th</sup> and 9<sup>th</sup> grade (13–15-years olds) of lower secondary school in Slovenia, it is a responsibility of the teachers to connect this specific content from science and technology and chemistry curricula as mentioned above. Hence, it can be assumed that

the lack of knowledge we found in APPDiT (Table 1) in 8<sup>th</sup> and 9<sup>th</sup> grade is most probably a consequence of confusion acquired in lower grades on atmospheric phenomenon. Simply put, students lose the connections between concepts learned from 5<sup>th</sup> up to 9<sup>th</sup> grade of lower secondary school about atmospheric pollution and teachers are responsible for linking these specific concepts so that students acquire a broader picture of these problems in the environment. Therefore, the question is why teachers do not upgrade student knowledge on atmospheric phenomenon from lower grades. Is the problem in the curriculum or do teachers themselves need to acquire a better and deeper understanding of the subject. Some studies

have indicated that teachers hold prevalent misconceptions on these particular topics, similar to students' misconceptions.<sup>30</sup> In order for teachers to be able to teach students properly about climate change and not to pass their own misconceptions to students, they themselves should acquire a deeper understanding of the subject. It is also important to emphasise that pre-service chemistry teachers have a course Fundamentals of Environmental Chemistry in Slovenia, but obviously they do not integrate these topics into their teaching. It is also reasonable to suggest, that additional professional development courses in environmental chemistry should be available for in-service chemistry, biology and physics teachers.

It can be concluded that the average Slovenian 9<sup>th</sup> grade student does not recognize or understand the reasons for atmospheric phenomenon, such as acid rain, global warming, ozone layer depletion and photochemical fog since their score on the APPDiT was insufficient and demonstrated low level of confidence. Hence, more emphasis should be placed on developing an understanding of particular atmospheric pollution factors, as the main misconceptions and lack of knowledge were connected with global warming and ozone layer depletion. Since we found specific environmental topics about air composition and pollution already in the curricula for 5<sup>th</sup> and 7<sup>th</sup> grades but not in later grades, it is reasonable to assume that students tend to forget basic concepts on this topic. It is also important to emphasize that teachers should present global warming more clearly to their students, as this phenomenon is the most important one in the last decade, and student's knowledge about it, the weakest. However, it should also be stressed that textbooks used by students while learning specific concepts should be developed in a way that stimulate learning with understanding and that textual and pictorial material would be presented in a way that enables adequate learning processes.<sup>34</sup>

## 5. Conclusions

The purpose of this study was to determine whether Slovenian 14- and 15-year-old students have sufficient knowledge about pollution of the atmosphere, its effects and consequences (both on the environment and on people). The 3-tier APPDiT instrument was used to obtain information about their understanding of the composition of the atmosphere and of basic atmospheric phenomenon such as acid rain, global warming, ozone layer depletion and photochemical smog at the basic school level. An additional instrument to gather students' background information was also used. It can be concluded that only a small percentage of students, 36.7%, 5.1%, 42.8% and 19.1% recognise and understand the reasons of acid rain, global warming, ozone layer depletion and photochemical smog formation, respectively. Moreover, only 33.0% of students know appropriate actions that should be undertaken in or-

der to diminish the consequences of air pollution and, surprisingly, while only 7.8% of students know about the actions to diminish global warming. From here, it is clear that students' overall knowledge of particular atmospheric phenomenon is very low with the lowest level of concerning understanding on global warming.

The present research highlights important issues in current basic school curricula and points to directions in further research into the content of atmospheric pollution phenomena. We must be aware that it is too late if one starts tackling these problems and seeking solutions only when they become obvious. Therefore, it is essential to include environmental topics about acid rain, global warming, ozone layer depletion and photochemical smog into the school curriculum in the upper grades, which, however, would require a change at the national level. The introduction of such changes may be chaotic at the beginning and thus demand high level of cooperation among all the stakeholders involved, however it would lead to a number of positive impacts such as enhancing students' critical thinking skills, developing personal growth or life-building skills, including confidence, autonomy, and leadership.<sup>35</sup>

There are some limitations of this research. The first one can be found in the analysis of the students' responses on all three tiers identifying the proportion of specific misconceptions about atmospheric phenomena at the end of the contemporary education in Slovenia. The more in-depth analysis will be done and submitted for publication later on. The second limitation lies in the fact that the APPDiT as applied only at one level of education and it can be also implemented at the end of secondary education as well as at the beginning or/and at the end of university teacher education. These data can provide more detailed picture of students' and teachers' understanding of specific environmental issues. Taking into account the limitation of this research some further research on this topic can be conducted. For instance, the analysis of the correlations between answer, reason and confidence tier need to be provided. The level of teachers' environmental literacy, how they apply environmental issues in their teaching even when the specific curriculum aim is suggested can be studied. More detailed textbooks analysis regarding environmental issues is necessary to interpret the data in more detail. The bottom-up approach of teaching and learning modules development to present science concepts in the environmental context is obligatory and their research-based implementation is necessary.

## 6. References

1. M. K. Hill, *Understanding Environmental Pollution*, 2nd Edition, Cambridge University Press, Cambridge, UK, **2005**.
2. Air pollution sources, <https://www.eea.europa.eu/themes/air/air-pollution-sources>, (Accessed: May 31, 2017).



3. S. H. Schneider, *Science* **1989**, 243, 771–781.  
DOI:10.1126/science.243.4892.771
4. J. D. Sachs, *Lancet* **2012**, 379, 2206–2211.  
DOI:10.1016/S0140-6736(12)60685-0
5. C. Y. Fook, G. K. Sidhu, S. Narasuman, L. L. Fong, S. B. Abdul Rahman (Eds.), 7<sup>th</sup> International Conference on University Learning and Teaching (InCULT 2014) Proceedings: Educate to Innovate, Springer, **2015**.  
DOI:10.1007/978-981-287-664-5
6. J. C. Bradley, T. M. Waliczek, J. M. Zajicek, *J. Environ. Educ.* **1999**, 30, 17–21. DOI:10.1080/00958969909601873
7. S. Koutalidi, M. Scoullou, *Chem. Educ. Res. Pract.* **2016**, 17, 10–23. DOI:10.1039/C5RP00151J
8. V. Papadimitriou, *J. Sci. Educ. Technol.* **2004**, 13, 299–307.  
DOI:10.1023/B:JOST.0000031268.72848.6d
9. M. Mohiuddin, A. Muhammad, M. Masud, Z. Su, *Sustainability* **2018**, 10, 1534–1582. DOI:10.3390/su10051534
10. V. Papadimitriou, *J. Sci. Educ. Technol.* **2004**, 13, 299–307.  
DOI:10.1023/B:JOST.0000031268.72848.6d
11. M. Kışoğlu, H. Gürbüz, M. Erkol, M. Akilli, *Int. Electron. J. Elementary Educ.* **2010**, 2, 217–230.
12. M. Karpudewan (Ed.), A. N. Md. Zain (Ed.), A. Chandrasegaran (Ed.), *Overcoming Students' Misconceptions in Science: Strategies and Perspectives from Malaysia, Singapur, Springer*, **2017**. DOI:10.1007/978-981-10-3437-4
13. K. A. Walz, S. C. Kerr, *J. Chem. Educ.* **2007**, 84, 1693–1696.  
DOI:10.1021/ed084p1693
14. T. Yazdanparast, S. Salehpour, M. R. Masjedi, S. A. Azin, S. M. Seyedmehdi, E. Boyes, M. Stanisstreet, M. Attarchi, *Acta Med. Iran.* **2013**, 5, 487–493.
15. N. Valerias, L. A. Godoy, *Int. J. Environ. Pollut.* **2007**, 31, 342–358. DOI:10.1504/IJEP.2007.016501
16. J. K. Sah, A. A. Bellad, *Al Ameen J. Med. Sci.* **2015**, 8, 230–234.
17. A. Dimitriou, V. Christidou, *Biologist* **2007**, 42, 24–29.  
DOI:10.1080/00219266.2007.9656103
18. (a) G. Myers, E. Boyes, M. Stanisstreet, *Int. Res. Geogr. Environ. Educ.* **1999**, 8, 108–119.  
DOI:10.1080/10382049908667600  
(b) G. Myers, E. Boyes, M. Stanisstreet, *Res. Sci. Technol. Educ.* **2004**, 22, 133–152. DOI:10.1080/0263514042000290868
19. J. Dove, *Environ. Educ. Res.* **1996**, 2, 89–100.  
DOI:10.1080/1350462960020108
20. D. Marinopoulos, H. Stavridou, *J. Biol. Educ.* **2002**, 37, 18–25.  
DOI:10.1080/00219266.2002.9655841
21. F. Groves, A. Pugh, *J. Sci. Educ. Technol.* **1999**, 8, 75–81.  
DOI:10.1023/A:1009433705790
22. Y. K. Yan, R. Subramaniam, *Chem. Educ. Res. Pract.* **2018**, 19, 213–226. DOI:10.1039/C7RP00143F
23. I. Caleon, R. Subramaniam, *Int. J. Sci. Educ.* **2010**, 32, 939–961. DOI:10.1080/09500690902890130
24. P. Pihkala, *Global Discourse* **2017**, 7, 1–19.  
DOI:10.1080/23269995.2017.1300412
25. S. A. Glažar, M. Vrtačnik, A. Bačnik, *Environ. Educ. Res.* **1998**, 4, 299–308. DOI:10.1080/1350462980040305
26. A. Šorgo, A. Kamenšek, *Energy Educ. Sci. Technol., Part B* **2012**, 4, 1067–1076.
27. M. Rickinson, *Environ. Educ. Res.* **2001**, 3, 207–317.  
DOI:10.1080/13504620120065230
28. M. Kolar, D. Krnel, A. Velkavrh, Program osnovna šola, učni načrt spoznavanje okolja, Ministrstvo za šolstvo in šport, Ljubljana, **2011**.
29. S. Nava, F. Becherini, A. Bernardi, A. Bonazza, M. Chiari, I. García-Orellana, F. Lucarelli, N. Ludwig, A. Migliori, C. Sabbioni, R. Udisti, G. Valli, R. Vecchi, *Sci. Total Environ.* **2010**, 408, 1403–1413. DOI:10.1016/j.scitotenv.2009.07.030
30. E. A. Stuart, D. B. Rubin, Best practices in quasi-experimental designs: matching methods for causal inference. In: J. Osborne (Ed.): *Best Practices in Quantitative Methods*, Thousand Oaks, CA: SAGE Publications, **2008**, pp. 155–176.  
DOI:10.4135/9781412995627.d14
31. <https://www.stat.si> (Accessed: October 10, 2017).
32. H. Ozge Arslana, C. Cigdemoglu, C. Moseley, *Int. J. Sci. Educ.* **2012**, 34, 1667–1686.  
DOI:10.1080/09500693.2012.680618
33. A. L. Chandrasegaran, D. F. Treagust, M. Mocerino, *Chem. Educ. Res. Pract.* **2007**, 8, 293–307.  
DOI:10.1039/B7RP90006F
34. Š. Hrast, V. Ferko Šavec, *Acta Chim. Slov.* **2017**, 64, 959–967.  
DOI:10.17344/acsi.2017.3657
35. N. M. Ardoin, A. W. Bowers, N. Wyman Roth, *J. Environ. Educ.* **2018**, 49, 1–17. DOI:10.1080/00958964.2017.1366155

## Povzetek

Članek predstavlja rezultate raziskave, ki je med slovenskimi osmo- in devetošolci ugotavljala razumevanje atmosferskih pojavov kot so kisle padavine, globalno segrevanje, zmanjševanje koncentracije stratosferskega ozona in fotokemični smog. Raziskava vključuje razvoj tristopenjskega diagnostičnega inštrumenta sestavljenega iz petnajstih vprašanj z naslovom Diagnostično preverjanje poznavanja pojavov onesnaženja atmosfere (APPDiT). V raziskavi je sodelovalo skupno 1012 učencev iz vse Slovenije. Podatki pridobljeni z APPDiT so omogočili proučevanje razumevanja in prepričanosti učencev o vzrokih in posledicah onesnaževanja atmosfere. Rezultati kažejo, da učenci 8. in 9. razreda osnovne šole sicer poznajo nekatere osnovne pojme atmosferskih pojavov, medtem ko imajo precejšnje pomanjkanje znanja v zvezi z onesnaževanjem in pojavi, ki nastanejo kot posledica onesnaževanja atmosfere. V povprečju so učenci dosegli le 39 % vseh točk na APPDiT. 42,7 % učencev ima ustrezno razumevanje pojmov povezanih z zmanjševanjem stratosferskega ozona. Razumevanje pojavov povezanih s kislimi padavinami ima le 36,7 %, fotokemični smog razume le 19,1 %, kar pa je najbolj presenetljivo le 5,1 % učencev razume nastanek in pomen globalnega segrevanja. Iz rezultatov je mogoče sklepati, da imajo učenci ob koncu osnovne šole velike težave z razumevanjem pojavov v ozračju, saj več kot polovica učencev atmosferskih pojavov, ki so posledica onesnaženja, bodisi ne pozna ali pa napačno razume.



Except when otherwise noted, articles in this journal are published under the terms and conditions of the Creative Commons Attribution 4.0 International License

# Fluorescent Membrane Probes Based on a Coumarin-Thiazole Scaffold

Stane Pajk,<sup>1,2,\*</sup> Maja Garvas<sup>2,3</sup> and Janez Štrancar<sup>2</sup>

<sup>1</sup> Faculty of pharmacy, University of Ljubljana, Ljubljana, Slovenia

<sup>2</sup> Laboratory of biophysics, Jožef Stefan Institute, Ljubljana, Slovenia

<sup>3</sup> Jožef Stefan International Postgraduate School, Ljubljana, Slovenia

\* Corresponding author: E-mail: stane.pajk@ffa.uni-lj.si

Received: 02-28-2019

## Abstract

Biological functions of cell membranes and their correlation to the heterogeneity of the latter's lipid composition are still poorly understood. Fluorescence provides one of the most versatile tools for studying biological membranes. However, few bright and photostable fluorescent probes for labeling plasma membranes are available. We have designed and synthesized two such probes, **8** and **9**, that are based on the thiazole-coumarin scaffold. Both are environment sensitive and exhibit similar shifts of emission spectra in a variety of solvents as probes based on 7-nitrobenz-2-oxa-1,3-diazol-4-yl (NBD). In particular, the second, positively charged probe **9** labels the plasma membrane selectively with limited redistribution to other membranes of the cell. Unfortunately, compared to the other two probes tested, **8** and **6-NBD-PC**, it exhibits the highest rate of photobleaching. Nevertheless, these new thiazole-coumarin based membrane probes provide a viable approach to the design of novel membrane probes.

**Keywords:** Fluorophore; microscopy; coumarin; photobleaching; membrane

## 1. Introduction

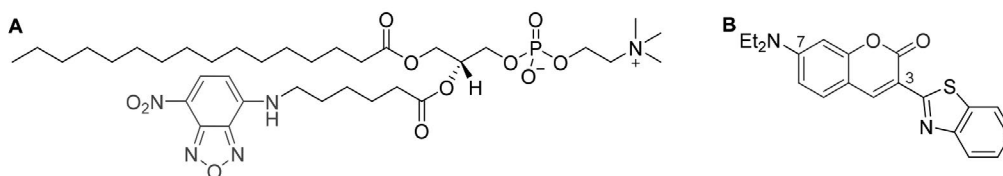
The biological functions of cell membranes are strongly related to the heterogeneity of their lipid composition.<sup>1</sup> However, the underlying mechanisms responsible for membrane heterogeneity remain poorly understood and are therefore a hot topic of research.<sup>1</sup> Membrane heterogeneity is essentially that of lipid distribution, identifiable by distinct physicochemical properties measurable by an array of techniques.<sup>2</sup> Fluorescence techniques stand out of this array, because of their high sensitivity and ability to operate in systems of varied complexity.<sup>2</sup> Because of this advantages fluorescence techniques became practically indispensable in the fields relevant to physical, chemical, biological and medical sciences.<sup>3</sup>

Especially fluorescence microscopy techniques revolutionized our understanding of life at cellular level. With appropriate probes we are able to visualize selected structures, view on-going processes or measure numerous parameters *e.g.* intracellular concentration of a selected ion.<sup>3–5</sup> However, new technologies based on fluorescence phenomena continually emerge, while the development of new fluorophores and fluorescent probes lags behind.<sup>6</sup> This

problem is especially pronounced in fluorescence imaging of membranes in live cells, since not many suitable membrane probes are available. Although most of such probes work well in model membranes, they are frequently unsuitable for experiments on living cells, because, for example, of their internalization, photobleaching and toxicity.<sup>7</sup>

Differences in lipid composition are reflected in small differences in polarity of the membrane. The latter can be detected by solvatochromic dyes, a subclass of environment-sensitive probes.<sup>7</sup> In principle, environment-sensitive probes do not need selective partitioning in the membrane, since changes in local polarity result in changes of quantum yield and shifts of their emission maxima.<sup>7</sup> The latter can be observed by several fluorescence microspectroscopy techniques (spectral imaging) that enable very small shifts of emission maximum position, down to 1 nm, to be detected.<sup>8</sup>

7-Nitrobenz-2-oxa-1,3-diazol-4-yl (NBD) is one of the environment-sensitive fluorophores widely used for studying membrane heterogeneity (Figure 1, A). However, it has a number of downsides, photobleaching being one of the most pronounced.<sup>9,10</sup> Fluorophores based on the cou-



**Figure 1.** (A) Structure of the phospholipid analog **C6-NBD-PC**, *N*-(7-nitrobenz-2-oxa-1,3-diazol-4-yl) (NBD) is in green. (B) Coumarin 6 dye with coumarin scaffold highlighted in blue and with marked positions 3 and 7.

marin scaffold (Figure 1, B) are also environment sensitive and, usually, more photostable than NBD.<sup>11</sup> Moreover, there are well established structure–spectra relationships that enable the design of coumarin-based probes with predictable photophysical properties.<sup>12</sup>

In this work, we report on the synthesis of two fluorescent membrane probes based on the coumarin-thiazole scaffold. The aim was to produce probes for selective labeling of plasma membranes of living cells. The synthesized probes were compared to **6-NBD-PC** regarding labeling properties, environment-sensitivity and photostability.

## 2. Experimental

### 2.1. Materials and Methods

Chemicals from Sigma-Aldrich and Acros were used without further purification. All reactions were performed under argon atmosphere unless otherwise stated. Analytical TLC was performed on Merck silica gel (60 F<sub>254</sub>) plates (0.25 mm) and visualized with ultraviolet light and detected with 20% sulphuric acid in ethanol. Melting points were determined on a Reichert hot stage microscope. <sup>1</sup>H and <sup>13</sup>C NMR spectra were recorded on a BRUKER AVANCE III 400 MHz NMR spectrometer in CDCl<sub>3</sub>, DMSO-*d*<sub>6</sub>, MeOH-*d*<sub>4</sub>, and pyridine-*d*<sub>5</sub> solution, with TMS or residual solvent signals as the internal standards. Mass spectra were recorded using an ADVION expression CMS and a VG-Analytical Q-TOF Premier mass spectrometer, the later for determination of high resolution masses (HRMS). Fluorescence spectra were measured with Perkin Elmer LS 55 fluorescence spectrophotometer or Biotec Synergy H4 Hybrid Microplate reader. Absorption spectra were measured with Varian Cary 50 UV-Vis spectrophotometer. Inverted Nikon TE-2000 E fluorescence microscope, equipped with a confocal unit Carv II (BD Biosciences) and Rolera-MGi camera was used for fluorescence microscopy observations.

### 2.2. Synthesis and Characterization

**3-(Benzyloxy)-*N,N*-dioctylaniline (1).** An oven-dried pressure tube equipped with a magnetic stirring bar was charged with Pd<sub>2</sub>dba<sub>3</sub> (69.6 mg, 1 mol %), RuPhos (35.4 mg, 1 mol %), KOtBu (1.53 g, 13.7 mmol, 1.8 equiv.), 1-(benzyloxy)-3-bromobenzene (2 g, 7.6 mmol, 1 equiv.) and activated molecular sieves of 4 Å (300 mg). The vessel was flushed well with argon. Dry toluene (10 mL) and di-

octylamine (3.2 mL, 1.4 equiv.) were added, and the pressure tube was sealed with a Teflon screw cap and placed into an oil bath at 110 °C for 3 h. The reaction mixture was then cooled to room temperature and filtered. The solvent was removed under reduced pressure and the crude product was purified by flash chromatography (EtOAc:hexane, 1:6), to give the desired product (95%) as a light yellow oil. <sup>1</sup>H NMR (400 MHz, CDCl<sub>3</sub>): δ (ppm) 7.49–7.28 (m, 5H), 7.10 (dd, *J*<sub>1,2</sub> = 8.0 Hz, 1H), 6.30–6.22 (m, 2H), 5.04 (s, 2H), 3.25–3.15 (m, 4H), 1.60–1.48 (m, 4H), 1.35–1.15 (m, 20H), 0.88 (t, *J* = 8.0 Hz, 6H). <sup>13</sup>C NMR (100 MHz, CDCl<sub>3</sub>): δ 160.31, 149.68, 137.66, 129.92, 128.69, 127.95, 127.66, 105.24, 100.85, 99.14, 70.02, 51.26, 31.99, 29.66, 29.50, 27.41, 27.33, 22.81, 14.26. MS (ESI): *m/z* calcd. for C<sub>29</sub>H<sub>46</sub>NO: 424.3 (M+H)<sup>+</sup>, found 424.1.

**3-(Dioctylamino)phenol (2).** Compound **1** (3.26g, 7.7 mmol) was dissolved in EtOAc (100 mL). Argon was passed through the solution, followed by addition of Pd/C (350 mg). Hydrogen was passed through the reaction mixture and the reaction mixture was then stirred at room temperature with hydrogen atmosphere for 15 h. Argon was passed through the reaction mixture, Pd/C was filtered off and the solvent was removed under reduced pressure, to yield the desired product as dark oil (99%). The crude product was used in the next step without further purification. MS (ESI): *m/z* calcd. for C<sub>22</sub>H<sub>38</sub>NO: 332.3 [M–H]<sup>–</sup>, found 332.2.

**4-(Dioctylamino)-2-hydroxybenzaldehyde (3).** POCl<sub>3</sub> (1.26 mL, 13.5 mmol, 3 equiv.) was added dropwise to dry DMF (3 mL) at 0 °C (ice bath). Reaction mixture was stirred on an ice bath for 30 minutes, followed by dropwise addition of phenol **2** dissolved in dry DMF (2 mL). Reaction mixture was then stirred at 80 °C for 2 h. Reaction mixture was cooled to room temperature, diluted with EtOAc (50 mL) and transferred to a flask with saturated solution of NaHCO<sub>3</sub> (100 mL). The mixture was stirred for 1 h at room temperature. Upper organic layer was collected, washed with brine (50 mL) and dried over Na<sub>2</sub>SO<sub>4</sub>. The solvent was evaporated under reduced pressure and the crude product was purified by flash chromatography (DCM), to give the desired product (41%) as light brown oil. <sup>1</sup>H NMR (400 MHz, CDCl<sub>3</sub>): δ (ppm) 11.65 (s, 1H), 9.48 (d, *J* = 0.4 Hz, 1H), 7.25 (d, *J* = 8.8 Hz, 1H), 6.22 (dd, *J*<sub>1</sub> = 8.8 Hz, *J*<sub>2</sub> = 1.6 Hz, 1H), 6.03 (s, *J* = 1.6 Hz, 1H), 3.35–3.25 (m, 4H), 1.66–1.50 (m, 4H), 1.37–1.20 (m, 20H), 0.89 (t, *J* = 8.0 Hz, 6H). <sup>13</sup>C NMR (100 MHz, CDCl<sub>3</sub>): δ (ppm)

191.97, 164.39, 154.57, 135.38, 111.51, 104.75, 97.01, 51.42, 31.90, 29.52, 29.38, 27.37, 27.13, 22.75, 14.21. MS (ESI):  $m/z$  calcd. for  $C_{23}H_{40}NO_2$ : 362.3  $[M+H]^+$ , found 362.2.

**7-(Diocetyl amino)-2-oxo-2H-chromene-3-carboxamide (4).** The aldehyde **3** (643 mg, 1.8 mmol, 1 equiv.) and diethylmalonate (822  $\mu$ L, 4.5 mol, 2.5 equiv.) was dissolved in dry ethanol (30 mL) followed by the addition of piperidine (50  $\mu$ L, 0.5 mol, 0.28 equiv.). Reaction mixture was refluxed for 15 h. Methanol (20 mL) was added to cooled (0 °C) reaction mixture and ammonia gas was bubbled through for 15 min. Yellow precipitate started to form and the reaction mixture was stirred at room temperature for 3 days. Water (20 mL) was added to the reaction mixture and the desired product was collected by filtration as a yellow precipitate (87%). M.p. 90–93 °C.  $^1H$  NMR (400 MHz, DMSO- $d_6$ ):  $\delta$  (ppm) 8.66 (s, 1H), 8.02 (d,  $J$  = 3.6 Hz, 1H), 7.66 (d,  $J$  = 8.8 Hz, 1H), 7.61 (d,  $J$  = 3.6 Hz, 1H), 6.77 (dd,  $J_1$  = 8.8 Hz,  $J_2$  = 2.4 Hz, 1H), 6.56 (d,  $J$  = 2.4 Hz, 1H), 3.46–3.34 (m, 4H), 1.60–1.48 (m, 4H), 1.38–1.20 (m, 20H), 0.86 (t,  $J$  = 6.8 Hz, 6H).  $^{13}C$  NMR (100 MHz, DMSO- $d_6$ ):  $\delta$  (ppm) 163.64, 161.70, 157.34, 152.83, 148.10, 131.51, 110.19, 109.65, 107.65, 95.95, 50.36, 31.25, 28.84, 28.73, 26.74, 26.23, 22.10, 13.96. MS (ESI):  $m/z$  calcd. for  $C_{26}H_{40}N_2O_3Na$ : 451.3  $[M+Na]^+$ , found 451.0.

**7-(Diocetyl amino)-2-oxo-2H-chromene-3-carbothioamide (5).** The amide **4** (609 mg, 1.9 mmol, 1 equiv.) and Lawesson's reagent (395 mg, 0.98 mmol, 0.51 equiv.) were dissolved in dry dioxane (20 mL) and the reaction mixture was refluxed overnight. The solvent was evaporated under reduced pressure and the residue dissolved in EtOAc (50 mL). EtOAc solution was washed with water (2×50 mL), saturated aqueous solution of  $NaHCO_3$  (2×50 mL), brine (50 mL) and dried over  $Na_2SO_4$ . The solvent was evaporated under reduced pressure and the crude product was purified by flash chromatography (EtOAc:hexane, 1:2), to give the desired product (61%) as a brown solid.  $^1H$  NMR (400 MHz,  $CDCl_3$ ):  $\delta$  (ppm) 10.37 (d,  $J$  = 5.6 Hz, 1H), 9.32 (s, 1H), 7.92 (d,  $J$  = 5.6 Hz, 1H), 7.47 (d,  $J$  = 9.2 Hz, 1H), 6.64 (dd,  $J_1$  = 9.2 Hz,  $J_2$  = 2.4 Hz, 1H), 6.44 (d,  $J$  = 2.4 Hz, 1H), 3.45–3.32 (m, 4H), 1.70–1.56 (m, 4H), 1.40–1.22 (m, 20H), 0.89 (t,  $J$  = 7.2 Hz, 6H). MS (ESI):  $m/z$  calcd. for  $C_{26}H_{40}N_2O_2SNa$ : 467.3  $[M+Na]^+$ , found 467.2.

**3-(4-(Chloromethyl)thiazol-2-yl)-7-(diocetyl amino)-2H-chromen-2-one (6).** The thioamide **5** (515 mg, 1.16 mmol, 1 equiv.) was dissolved in DMF (5 mL), followed by addition of 1,3-dichloropropan-2-one (177 mg, 1.4 mmol, 1.2 equiv.). The reaction mixture was stirred at room temperature for 3 days. Solvent was removed under reduced pressure and the residue was dissolved in DCM (50 mL), washed with saturated solution of  $NaHCO_3$  (2×30 mL), water (2×30 mL) and brine (2×50 mL), and dried over  $Na_2SO_4$ . The solvent was evaporated under reduced pressure and the crude product was purified by flash chromatogra-

phy (DCM), to give the desired product (69%) as an orange solid. M.p. 57–60 °C.  $^1H$  NMR (400 MHz,  $CDCl_3$ ):  $\delta$  (ppm) 8.23 (s, 1H), 7.43 (d,  $J$  = 8.8 Hz, 1H), 7.35 (s, 1H), 6.62 (dd,  $J_1$  = 8.8 Hz,  $J_2$  = 2.4 Hz, 1H), 6.51 (d,  $J$  = 2.4 Hz, 1H), 4.75 (d,  $J$  = 0.8 Hz, 2H), 3.35 (t,  $J$  = 8.0 Hz, 4H), 1.68–1.56 (m, 4H), 1.40–1.22 (m, 20H), 0.89 (t,  $J$  = 6.8 Hz, 6H).  $^{13}C$  NMR (100 MHz,  $CDCl_3$ ):  $\delta$  (ppm) 161.81, 161.09, 156.63, 152.20, 151.71, 140.53, 130.47, 118.81, 118.79, 112.32, 110.10, 108.50, 97.16, 97.14, 51.55, 41.26, 31.88, 29.52, 29.38, 27.29, 27.13, 22.74, 14.20. MS (ESI):  $m/z$  calcd. for  $C_{29}H_{41}ClN_2O_2SNa$ : 539.3  $[M+Na]^+$ , found 539.0.

**Diethyl ((2-(7-(diocetyl amino)-2-oxo-2H-chromen-3-yl)thiazol-4-yl)methyl)phosphonate (7).** Thiazol **6** (206 mg, 0.4 mmol, 1.1 equiv.) was dissolved in triethyl phosphite (3 mL) and the solution was stirred at 130 °C for 15 h. Triethyl phosphite was distilled off under reduced pressure and the crude product was purified by flash chromatography (DCM:MeOH, 50:1 to 25:1), to give the desired product (81%) as an orange oil.  $^1H$  NMR (400 MHz,  $CDCl_3$ ):  $\delta$  (ppm) 8.69 (s, 1H), 7.42 (d,  $J$  = 8.8 Hz, 1H), 7.29–7.26 (m, 1H), 6.62 (dd,  $J_1$  = 8.8 Hz,  $J_2$  = 2.4 Hz, 1H), 6.51 (d,  $J$  = 2.4 Hz, 1H), 4.15–4.05 (m, 4H), 3.46 (d,  $J$  = 21.2 Hz, 2H), 3.40–3.29 (m, 4H), 1.69–1.55 (m, 4H), 1.42–1.19 (m, 26H), 0.98–0.81 (m, 6H).  $^{13}C$  NMR (100 MHz,  $CDCl_3$ ):  $\delta$  (ppm) 161.11, 160.48, 156.55, 152.05, 146.22 (d,  $^2J_{PC}$  = 8.0 Hz), 140.03, 130.31, 117.79 (d,  $^3J_{PC}$  = 7.2 Hz), 112.79, 110.03, 108.59, 97.22, 62.38 (d,  $^2J_{PC}$  = 6.6 Hz), 51.55, 31.89, 29.80 (d,  $^1J_{PC}$  = 140.6 Hz), 29.38, 29.10, 27.30, 27.15, 22.74, 16.52 (d,  $^3J_{PC}$  = 6.1 Hz), 14.21. HRMS (ESI):  $m/z$  calcd. for  $C_{33}H_{52}N_2O_5PS$ : 619.3335  $[M-H]^-$ , found 619.3346.

**((2-(7-(Diocetyl amino)-2-oxo-2H-chromen-3-yl)thiazol-4-yl)methyl)phosphonic acid (8).** To a solution of diethyl phosphonate **7** (190 mg, 0.31 mmol, 1 equiv.) in dry  $CH_2Cl_2$  (7.5 mL) cooled in an ice bath, TMSBr (1.5 mL) was added dropwise. The reaction mixture was left to react for 3 days at room temperature. The solvent was evaporated under reduced pressure and 5 mL of a mixture of THF and water (1:1) was added and the reaction mixture was stirred for 1 day. Solvents were removed under reduced pressure and product was re-crystallized from  $CH_3CN$  to give an orange solid (84%). M.p. 106–109 °C.  $^1H$  NMR (400 MHz, pyridine- $d_5$ ):  $\delta$  (ppm) 8.89 (s, 1H), 7.78 (d,  $J$  = 3.2 Hz, 1H), 7.54 (d,  $J$  = 9.2 Hz, 1H), 6.82 (dd,  $J_1$  = 9.2 Hz,  $J_2$  = 1.6 Hz, 1H), 6.65 (d,  $J$  = 1.6 Hz, 1H), 4.02 (d,  $J$  = 20.4 Hz, 2H), 3.37 (t,  $J$  = 7.6 Hz, 4H), 1.67–1.54 (m, 4H), 1.35–1.15 (m, 20H), 0.87 (t,  $J$  = 7.2 Hz, 6H).  $^{13}C$  NMR (100 MHz, pyridine- $d_5$ ):  $\delta$  (ppm) 161.21, 160.11, 157.17, 152.67, 151.15 (d,  $^2J_{PC}$  = 7.6 Hz), 140.42, 131.13, 117.93 (d,  $^3J_{PC}$  = 6.3 Hz), 113.48, 110.84, 109.15, 97.52, 51.63, 33.76 (d,  $^1J_{PC}$  = 134.0 Hz), 32.34, 30.01, 29.87, 27.83, 27.49, 23.23, 14.60. HRMS (ESI):  $m/z$  calcd. for  $C_{29}H_{44}N_2O_5PS$ : 563.2709  $[M+H]^+$ , found 563.2705.

**1-(2-(7-(Diocetyl amino)-2-oxo-2H-chromen-3-yl)thiazol-4-yl)-N,N,N-trimethylmethanaminium chloride**



(9). Compound **6** (106 mg, 0.20 mmol, 1 equiv.) was dissolved in 4.2 M solution of trimethylamine (5 mL). The reaction mixture was left to react for 3 days at room temperature. The solvent was evaporated under reduced pressure and the solid residue was suspended in a mixture of diethyl ether and hexane (1:1) (5 mL), filtered and washed with diethyl ether and hexane (1:1) (10 mL), to give the desired product as an orange solid (85%). M.p. 152–155 °C.  $^1\text{H}$  NMR (400 MHz, MeOD):  $\delta$  (ppm) 8.73 (s, 1H), 7.89 (s, 1H), 7.52 (d,  $J = 9.2$  Hz, 1H), 6.75 (dd,  $J_1 = 9.2$  Hz,  $J_2 = 1.6$  Hz, 1H), 6.51 (d,  $J = 1.6$  Hz, 1H), 4.70 (s, 2H), 3.42 (t,  $J = 7.6$  Hz, 4H), 3.25 (s, 9H), 1.72–1.58 (m, 4H), 1.45–1.25 (m, 20H), 0.90 (t,  $J = 7.2$  Hz, 6H).  $^{13}\text{C}$  NMR (100 MHz, MeOD):  $\delta$  (ppm) 164.03, 162.66, 158.19, 154.35, 145.04, 142.61, 132.20, 127.05, 112.54, 111.93, 109.77, 97.92, 65.45, 54.03, 52.38, 33.15, 30.73, 30.61, 28.45, 28.14, 23.89, 14.61. HRMS (ESI):  $m/z$  calcd. for  $\text{C}_{32}\text{H}_{50}\text{N}_3\text{O}_2\text{S}$ : 540.3624  $[\text{M}]^+$ , found 540.3637.

## 2. 3. Cell Culture and Parameters of Fluorescence Microscopy

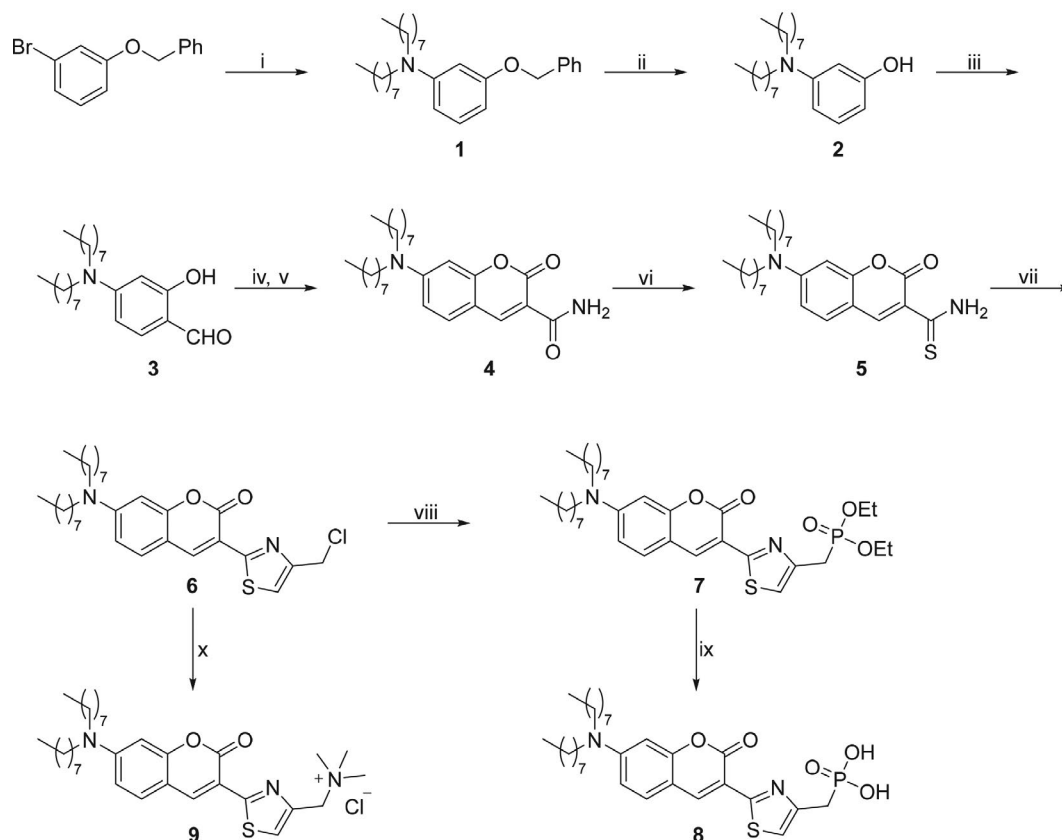
Mouse lung epithelial cell line LA-4 was cultured in cell medium (F12K medium, 15% FCS, both from ATCC, 1% P/S (antibiotics), 1% NEAA (nonessential amino acids)

from Sigma). The cells were cultured at 37 °C in a humidified 5%  $\text{CO}_2$  atmosphere. For the fluorescence microscopy observation, cells were plated on 8 well glass-bottom cell culture dish (Lab-Tek Chambered Coverglass) for an additional day. Cell medium was replaced with fluorescent dye in a phosphate buffer saline at final concentration  $10^{-7}$  M or  $10^{-8}$  M (0.1% DMSO), incubated for a few minutes than fluorescence at different time points was measured or wide field fluorescence images were taken. Samples were excited by nonpolarized light from a Xe-Hg source (Sutter Lambda LS, Novato, CA) through broad-band filters (all band-pass filters and dichroic were BrightLine from Semrock, Rochester, NY). Fluorescence was detected through matching broadband filters. Objective with 60 $\times$  (water immersion) magnification was used with high numerical aperture (NA = 1.27, working distance 0.17 mm). Set of filters used in experiments was following: 415–455 nm excitation filter, 458 nm dichroic, and 468–552 nm emission filter.

## 3. Results and Discussion

### 3. 1. Design and Synthesis

Coumarins have been used as the basis of membrane probes, but the probes presented in this paper are the first



**Scheme 1.** Reagents and conditions: (i) dioctylamine,  $\text{Pd}_2\text{dba}_3$ , RuPhos, KOTBu, toluene, 110 °C, 95%; (ii)  $\text{H}_2$ , Pd/C, EtOAc, RT, 99%; (iii)  $\text{POCl}_3$ , DMF, 80 °C, 41%; (iv) diethyl malonate, piperidine, EtOH, 95 °C; (v)  $\text{NH}_3(\text{g})$ , EtOH, RT, 87% (over two steps); (vi) Lawesson's reagent, dioxane, reflux, 61%; (vii) 1,3-dichloropropan-2-one, DMF, RT, 69%; (viii)  $\text{P}(\text{OEt})_3$ , 130 °C, 81%; (ix) TMSBr, DCM, RT, 84%; (x)  $\text{Me}_3\text{N}$ , EtOH, RT, 85%.

to mimic the amphiphilic properties of membrane lipids, by possessing aliphatic tails and a polar head incorporated in the coumarin core.<sup>13–15</sup> Thiazole at position 3 of the coumarin scaffold is known to produce marked red-shifts of the excitation and emission spectra and, in addition, to result in higher molar absorptivities and quantum yields than those of the 3-unsubstituted derivative.<sup>16</sup> In our case it also provided the opportunity for introducing a polar head group.<sup>17</sup> Probes were designed with a permanently charged polar head at physiological pH, since this reduces the likelihood of flip-flop and further redistribution to other membranes of the cell. The lipophilic part of the probe comprises two aliphatic tails attached to the amino group at position 7 of the coumarin scaffold.

Since the synthesized probes differ only in their head groups, the first six synthetic steps were the same for both probes. Synthesis commenced with palladium-catalyzed N-arylation of diethylamine with 1-(benzyloxy)-3-bromobenzene, giving compound **1** in high yield (Scheme 1).<sup>18</sup> The benzyl protective group was removed with hydrogen in the presence of Pd/C to afford compound **2**. In the next step, a formyl group was introduced under Vilsmeier–Haack conditions to yield salicylaldehyde **3**. This was followed by two reaction steps in one pot; first, Knoevenagel condensation between salicylaldehyde **3** and diethyl malonate to yield 7-diethylaminocoumarin-3-carboxylic acid ethyl ester and, second, aminolysis of the ester with ammonia to give amide **4**. The amide **4** was, in the next step and using Lawesson's reagent, converted to thioamide **5**.<sup>16</sup> Reaction between thioamide **5** and 1,3-dichloroacetone in DMF gave thiazole **6**. The latter conversion was first attempted in THF instead of DMF and with the 1.5 equiv. of Et<sub>3</sub>N, as used successfully with aliphatic thioamides,<sup>19</sup> but the initial attempts did not produce the desired product. Only after replacing the THF by DMF and omitting the base was the desired product, thiazole **6**, obtained.<sup>16</sup> Thiazole **6** was further reacted with P(OEt)<sub>3</sub> to yield diethylphosphonate **7**. In the next step, both ester groups were cleaved with TMSBr to yield probe **8** having a negatively charged headgroup.<sup>20,21</sup> To obtain a probe with

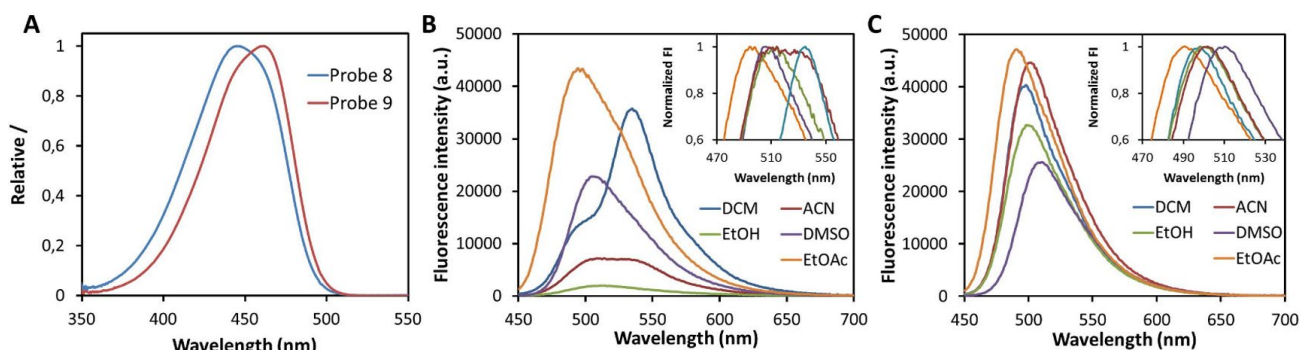
a positively charged headgroup, thiazole **6** was reacted with Me<sub>3</sub>N to give probe **9**.<sup>22</sup>

### 3. 2. Absorption and Emission Spectra

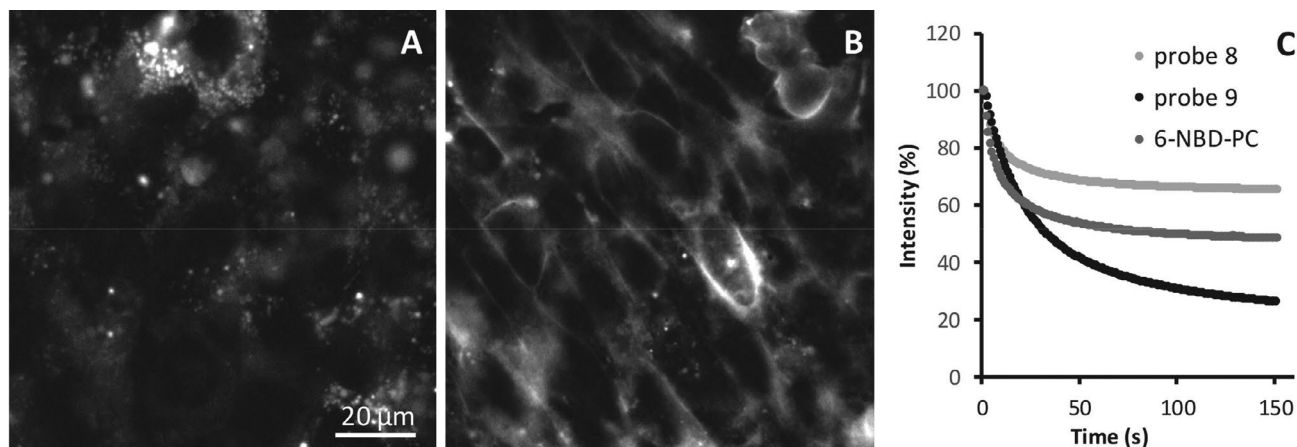
Absorption spectra of ethanol solutions of probes **8** and **9** were recorded (Figure 2, A). Absorption maximum for probe **8** was 445 nm and 461 nm for probe **9**. This is a relatively large difference in position of absorption maxima for probes with the same fluorescent core. To further characterize the photophysical properties, the fluorescence spectra of probes **8** and **9** were recorded in solvents of different polarities (Figure 2, B and C). Shifts in emission maxima and differences in overall shape of spectra in different solvents were more pronounced with probe **8** than with probe **9**. In the case of probe **8**, type of solvent also had more significant influence on emission intensity as compared to probe **9**. Phosphonic acid of probe **8** can form hydrogen bonds with the solvent and we assume this is how solvent influences the shape and intensity of emission spectrum. This may also explain the difference in absorption spectra of probes **8** and **9**, since both probes differ only in the type of polar headgroup.

### 3. 3. Fluorescence Microscopy

LA4 cells were labeled with probes **8** and **9** and observed under a fluorescence microscope. Labeling was carried out by addition of dyes dissolved in DMSO. Both probes labeled cells rapidly and, at the concentrations used, evenly and without apparent induction of toxicity. Strikingly, probe **8** was internalized rapidly into intracellular membranes, whereas probe **9** remained localized mostly on the plasma membrane (Figure 3, A and B). This is in accordance with general observations that positively charged membrane probes are internalized to a lesser extent.<sup>7</sup> For future development of probe **9** a zwitterion configuration or an additional positive charge at the head-group should increase localization of the probe at the plasma membrane.<sup>7</sup>



**Figure 2.** (A) Normalized absorption spectra of probes **8** (blue) and **9** (red). Absorption spectra were recorded with  $8 \cdot 10^{-6}$  M solutions of each in ethanol. (B and C) Emission spectra for probes **8** (B) and **9** (C) in different solvents at concentrations of  $5 \cdot 10^{-7}$  M ( $\lambda_{\text{ex}} = 420$  nm). Inset: normalized emission spectra for probes **8** (B) and **9** (C) in different solvents.



**Figure 3.** LA4 cells labeled with (A) probe **8** and (B) probe **9** for 5 min at 10 nM concentration. (C) Bleaching of probes with time; probe **8** (light grey circles), probe **9** (black circles) and commercial 6-NBD-PC from Avanti Polar Lipids (dark grey circles). The concentration of the probes on cells, where the bleaching characteristics of probes are presented, was 100 nM.

In a study of photostability, probes **8** and **9** were compared to commercially available 6-NBD-PC in labeled LA4 cells (Figure 3, C). Internalized probe **8** proved to be more photostable than 6-NBD-PC while, surprisingly, probe **9** was more prone to photobleaching than probe **8** or 6-NBD-PC. This is interesting, since probes **8** and **9** possess the same coumarin-thiazole scaffold, differing only in the polar headgroup. As well as small differences in chemical structure, different environment, such as lipid composition, oxygen and antioxidant concentration, can influence the rate of photobleaching.<sup>23,24</sup> This and the influence of polar headgroup can explain different rates of photobleaching for probes **8** and **9**. The initially planned microspectroscopy, *i.e.* recording of emission spectra in each voxel, was not possible due to the high rate of photobleaching of probe **9**, even when using bleaching-corrected fluorescence microspectroscopy.<sup>25</sup> This limiting factor will be addressed in any future development by incorporating design features that increase photostability.<sup>26,27</sup>

## 4. Conclusion

The plasma membrane remains in the focus of research, with fluorescent techniques, in particular the numerous types of fluorescence microscopy, being the most versatile tool for its study. The full potential of fluorescence microscopy is, however, limited by the lack of bright and photostable fluorescent probes. We have designed and synthesized two membrane probes, **8** and **9**, both based on the thiazole-coumarin scaffold. Both probes are environment sensitive, especially probe **8** exhibits significant shifts of emission maxima and fluorescence intensity depending on the solvent. Both probes quickly labeled cell membranes, in particular, the positively charged probe **9** labeled the plasma membrane selectively, with slow redistribution to other intracellular membranes. Nevertheless, it had the

highest rate of photobleaching of all the probes tested, *i.e.* probes **8** and 6-NBD-PC. Because of the low photostability of probe **9**, a microspectroscopy study was not possible. However, we have proved that the use of coumarin-based membrane probes constitutes a viable approach to the design of novel membrane probes.

## 5. References

1. E. Sezgin, I. Levental, S. Mayor, C. Eggeling, *Nat. Rev. Mol. Cell Biol.* **2017**, 18, 361–374. DOI:10.1038/nrm.2017.16
2. A. P. Demchenko, Y. Mély, G. Duportail, A. S. Klymchenko, *Biophys. J.* **2009**, 96, 3461–3470. DOI:10.1016/j.bpj.2009.02.012
3. B. Valeur, J.-C. Brochon (Ed.): *New trends in fluorescence spectroscopy: applications to chemical and life science*, Springer, New York, **2001**. DOI:10.1007/978-3-642-56853-4
4. S. Yuan, W. Su, E. Wang, *Acta Chim. Slov.* **2017**, 64, 638–643. DOI:10.17344/acsi.2017.3442
5. Y. Deng, Y. Chen, X. Zhou, *Acta Chim. Slov.* **2018**, 65, 271–277. DOI:10.17344/acsi.2017.3620
6. S. W. Hell, *Angew. Chem.* **2015**, 54, 8054–8066. DOI:10.1002/anie.201504181
7. S. Klymchenko Andrey, R. Kreder, *Chem. Biol.* **2014**, 21, 97–113. DOI:10.1016/j.chembiol.2013.11.009
8. Z. Arsov, I. Urbančič, M. Garvas, D. Biglino, A. Ljubetič, T. Koklič, J. Štrancar, *Biomed. Opt. Express.* **2011**, 2, 2083–2095. DOI:10.1364/BOE.2.002083
9. I. Urbančič, A. Ljubetič, Z. Arsov, J. Štrancar, *Biophys. J.* **2013**, 105, 919–927. DOI:10.1016/j.bpj.2013.07.005
10. D. M. C. Ramirez, W. W. Ogilvie, L. J. Johnston, *Biochim. Biophys. Acta.* **2010**, 1798, 558–568. DOI:10.1016/j.bbamem.2009.12.005
11. S. Pajk, *Tetrahedron Lett.* **2014**, 55, 6044–6047. DOI:10.1016/j.tetlet.2014.09.019
12. H. Schill, S. Nizamov, F. Bottanelli, J. Bierwagen, V. N. Belov,

- S. W. Hell, *Chem. Eur. J.* **2013**, 19, 16556–16565.  
DOI:10.1002/chem.201302037
13. C. Wolff, B. Fuks, P. Chatelain, *J. Biomol. Screen.* **2003**, 8, 533–543. DOI:10.1177/1087057103257806
14. O. García-Beltrán, O. Yañez, J. Caballero, A. Galdámez, N. Mena, M. T. Nuñez, B. K. Cassels, *Eur. J. Med. Chem.* **2014**, 76, 79–86. DOI:10.1016/j.ejmech.2014.02.016
15. P. Jurkiewicz, L. Cwiklik, P. Jungwirth, M. Hof, *Biochimie.* **2012**, 94, 26–32. DOI:10.1016/j.biochi.2011.06.027
16. H. Takechi, Y. Oda, N. Nishizono, K. Oda, M. Machida, *Chem. Pharm. Bull.* **2000**, 48, 1702–1710.  
DOI:10.1248/cpb.48.1702
17. N. Nishizono, K. Oda, Y. Kato, K. Ohno, M. Minami, M. Machida, *Heterocycles.* **2004**, 63, 1083–1091.  
DOI:10.3987/COM-04-10021
18. B. P. Fors, S. L. Buchwald, *J. Am. Chem. Soc.* **2010**, 132, 15914–15917. DOI:10.1021/ja108074t
19. S. Pajk, M. Živec, R. Šink, I. Sosič, M. Neu, C. Chung, M. Martínez-Hoyos, E. Pérez-Herrán, D. Álvarez-Gómez, E. Álvarez-Ruiz, A. Mendoza-Losana, J. Castro-Pichel, D. Barros, L. Ballell-Pages, R. J. Young, M. A. Convery, L. Encinas, S. Gobec, *Eur. J. Med. Chem.* **2016**, 112, 252–257.  
DOI:10.1016/j.ejmech.2016.02.008
20. K. C. Nicolaou, D. Rhoades, Y. Wang, R. Bai, E. Hamel, M. Auja, J. Sandoval, J. Gavriluk, *J. Am. Chem. Soc.* **2017**, 139, 7318–7334. DOI:10.1021/jacs.7b02655
21. P. Lassaux, M. Hamel, M. Gulea, H. Delbrück, P. S. Mercuri, L. Horsfall, D. Dehareng, M. Kupper, J. Frère, K. Hoffmann, M. Galleni, C. Bebrone, *J. Med. Chem.* **2010**, 53, 4862–4876.  
DOI:10.1021/jm100213c
22. B. Wang, W. Sun, F. Bu, X. Li, H. Na, C. Zhao, *Int. J. Hydrog. Energy.* **2016**, 41, 3102–3112.  
DOI:10.1016/j.ijhydene.2015.12.123
23. O. Woodford, A. Harriman, W. McFarlane, C. Wills, *ChemPhotoChem.* **2017**, 1, 317–325.  
DOI:10.1002/cptc.201600061
24. C. E. Aitken, R. A. Marshall, J. D. Puglisi, *Biophys. J.* **2008**, 94, 1826–1835. DOI:10.1529/biophysj.107.117689
25. I. Urbančič, Z. Arsov, A. Ljubetič, D. Biglino, J. Štrancar, *Opt. Express.* **2013**, 21, 25291–25306. DOI:10.1364/OE.21.025291
26. J. B. Grimm, B. P. English, J. Chen, J. P. Slaughter, Z. Zhang, A. Revyakin, R. Patel, J. J. Macklin, D. Normanno, R. H. Singer, T. Lionnet, L. D. Lavis, *Nat. Methods.* **2015**, 12, 244–250.  
DOI:10.1038/nmeth.3256
27. J. B. Grimm, A. K. Muthusamy, Y. Liang, T. A. Brown, W. C. Lemon, R. Patel, R. Lu, J. J. Macklin, P. J. Keller, N. Ji, L. D. Lavis, *Nat. Methods.* **2017**, 14, 987–994.  
DOI:10.1038/nmeth.4403

## Povzetek

Biološke funkcije celičnih membran in njihove korelacije s heterogenostjo njihove lipidne sestave so še vedno slabo raziskane. Fluorescenca omogoča enega izmed najbolj vsestranskih pristopov k raziskovanju bioloških membran, vendar je za označevanje plazemskih membran na voljo le malo svetlih in fotostabilnih fluorescenčnih označevalcev. Načrtovali in sintetizirali smo dve novi tovrstni fluorescenci barvili, spojini **8** in **9**, ki temeljita na tiazolo-kumarinskem ogrodju. Obe izkazujeta občutljivost na okolje in kažeta podobne premike v emisijskih spektrih v različnih topilih kot je bilo opaženo pri 7-nitrobenz-2-oksa-1,3-diazol-4-ilu (NBD). Drugo, pozitivno nabito barvilo **9**, obarva plazemsko membrano selektivno in z omejenim prerazporejanjem v ostale celične membrane. Žal pa **9**, za razliko od preostalih dveh testiranih barvil, torej **8** in **6-NBD-PC**, zelo hitro fotoblede. Ne glede na to, razvoj dveh novih tiazolo-kumarinskih membranskih barvil predstavlja smislen pristop k načrtovanju novih membranskih barvil.



Except when otherwise noted, articles in this journal are published under the terms and conditions of the Creative Commons Attribution 4.0 International License

# Synthesis, Characterization and Crystal Structures of Cobalt(II), Zinc(II) and Cadmium(II) Complexes Derived from 2-Hydroxy-*N'*-(pyridin-2-ylmethylene)benzohydrazide with Antimicrobial Activity

Li-Hang Wang,<sup>1</sup> Xiao-Yang Qiu<sup>1,2,\*</sup> and Shu-Juan Liu<sup>1</sup>

<sup>1</sup> College of Science & Technology, Ningbo University, Ningbo 315212, P.R. China

<sup>2</sup> State Key Laboratory of Structural Chemistry, Fujian Institute of Research on the Structure of Matter, Chinese Academy of Sciences, Fuzhou, Fujian 350002, P.R. China

\* Corresponding author: E-mail: xiaoyang\_qiu@126.com

Received: 03-08-2019

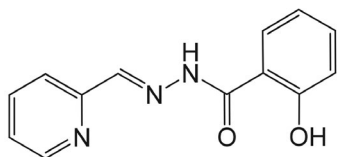
## Abstract

Three new cobalt(II), zinc(II) and cadmium(II) complexes,  $[\text{CoL}_2] \cdot 2\text{CH}_3\text{OH} \cdot \text{H}_2\text{O}$  (**1**),  $[\text{ZnL}_2]$  (**2**) and  $[\text{Cd}(\text{HL})_2(\text{NO}_3)]\text{N}_3$  (**3**), were prepared from 2-hydroxy-*N'*-(pyridin-2-ylmethylene)benzohydrazide (HL). The complexes have been characterized by IR, UV-Vis and single-crystal X-ray diffraction techniques. X-ray analysis indicates that the complexes are mononuclear species, with the metal atoms in octahedral coordination. The hydrazone compound and its complexes were evaluated for their antibacterial (*Bacillus subtilis*, *Staphylococcus aureus*, *Escherichia coli*, and *Pseudomonas fluorescence*) and antifungal (*Candida albicans* and *Aspergillus niger*) activities. The complexes have effective activities against the bacteria.

**Keywords:** Hydrazone; Mononuclear complex; Crystal structure; Antimicrobial activity

## 1. Introduction

Hydrazones are a kind of Schiff base compounds, bearing typical functional group,  $\text{CH}=\text{N}-\text{NH}-\text{C}(\text{O})$ . Compounds have attracted tremendous attention due to their interesting and versatile biological properties like antibacterial,<sup>1</sup> antifungal,<sup>2</sup> as well as antitumor.<sup>3</sup> Cobalt, zinc and cadmium complexes derived from Schiff base ligands have been widely studied for their potential antibacterial activities.<sup>4</sup> As a further exploration of novel complex based antimicrobial agents, in the present work, three new cobalt(II), zinc(II) and cadmium(II) complexes,  $[\text{CoL}_2] \cdot 2\text{CH}_3\text{OH} \cdot \text{H}_2\text{O}$  (**1**),  $[\text{ZnL}_2]$  (**2**) and  $[\text{Cd}(\text{HL})_2(\text{NO}_3)]\text{N}_3$  (**3**), respectively, where L is the anion of 2-hydroxy-*N'*-(pyridin-2-ylmethylene)benzohydrazide (HL; Scheme 1), are presented.



Scheme 1. HL

## 2. Experimental

### 2. 1. Materials and Instruments

All the organic compounds and inorganic salts with AR grade were obtained from Sigma-Aldrich and used without further purification. The ligand HL was prepared according to the literature method.<sup>5</sup> Elemental analyses (C, H, N) were carried out with a Perkin-Elmer 2400II analyzer. FT-IR spectra were recorded on a Perkin-Elmer 377 spectrometer with KBr pellets. UV-Vis spectra were recorded on a Lambda 900 spectrometer. <sup>1</sup>H and <sup>13</sup>C NMR data were recorded on a Bruker 500 MHz spectrometer. X-ray diffraction was carried out on a Bruker APEX II CCD diffractometer.

### 2. 2. Synthesis of Complex 1

HL (1.0 mmol, 0.24 g) and  $\text{Co}(\text{NO}_3)_2 \cdot 6\text{H}_2\text{O}$  (1.0 mmol, 0.29 g) were dissolved in 50 mL MeOH. The mixture was heated to reflux for 1 h. Then, it was cooled to room temperature. Single crystals of the complex were generated after 5 days following the slow evaporation of the solvent. Yield 27%. IR data ( $\text{cm}^{-1}$ ): 3454 (OH), 1600 (C=N). UV-Vis data ( $\text{CH}_3\text{OH}$ ,  $\lambda_{\text{max}}$ , nm): 276, 380, 390.

Elemental analysis found: C, 54.25; H, 4.72; N, 13.46%,  $C_{26}H_{20}CoN_6O_4 \cdot 2CH_3OH \cdot H_2O$  calcd: C, 54.11; H, 4.87; N, 13.52%.

### 2. 3. Synthesis of Complex 2

HL (1.0 mmol, 0.24 g) and  $Zn(CH_3COO)_2 \cdot 2H_2O$  (1.0 mmol, 0.22 g) were dissolved in 50 mL MeOH. The mixture was heated to reflux for 1 h. Then, it was cooled to room temperature. Single crystals of the complex were generated after 7 days following the slow evaporation of the solvent. Yield 45%. IR data ( $cm^{-1}$ ): 3450 (OH), 3387 (NH), 1596 (C=N). UV-Vis data ( $CH_3OH$ ,  $\lambda_{max}$ , nm): 269, 305, 323, 370. Elemental analysis found: C, 57.38; H, 3.77; N, 15.26%,  $C_{26}H_{20}N_6O_4Zn$  calcd: C, 57.21; H, 3.69; N, 15.40%.

### 2. 4. Synthesis of Complex 3

HL (1.0 mmol, 0.24 g),  $NaN_3$  (1.0 mmol, 0.065 g) and  $Cd(NO_3)_2 \cdot 4H_2O$  (1.0 mmol, 0.31 g) were dissolved in 50 mL MeOH. The mixture was heated to reflux for 1 h. Then, it was cooled to room temperature. Single crystals of the complex were generated after 3 days following the slow evaporation of the solvent. Yield 33%. IR data ( $cm^{-1}$ ): 3450 (OH), 2072 ( $N_3$ ), 1638 (C=O), 1601 (C=N), 1456, 1311, 1072 ( $NO_3$ ). UV-Vis data ( $CH_3OH$ ,  $\lambda_{max}$ , nm): 280, 368. Elemental analysis found: C, 44.52; H, 3.31; N, 19.92%,  $C_{26}H_{22}CdN_{10}O_7$  calcd: C, 44.68; H, 3.17; N, 20.04%.

### 2. 5. X-ray Crystallography

The collected data were reduced with SAINT,<sup>6</sup> and multi-scan absorption correction was applied by using SADABS.<sup>7</sup> Structures of the three complexes were solved by direct method and refined against  $F^2$  by full-matrix least-squares method with SHELXTL.<sup>8</sup> The non-hydrogen atoms were refined anisotropically. The hydroxyl and amino hydrogen atoms were located from electronic density maps and refined isotropically. The remaining hydrogen atoms were placed in calculated positions and constrained to ride on their parent atoms. The atoms O5, O6, O7, C27 and C28 of the solvent molecules in complex 1, and the azide anion in complex 2 are disordered, which were refined with isotropic behavior. The hydrogen atoms of the disordered methanol molecules in complex 1 are not added, but included in the formula. The crystallographic data and refinement parameters for the compounds are listed in Table 1. Selected bond lengths and angles are listed in Table 2.

## 3. Results and Discussion

### 3. 1. Chemistry

HL was prepared from the condensation reaction of 2-pyridinecarboxaldehyde with 2-hydroxybenzohydrazide in MeOH. The complexes were prepared from the self-assembly of hydrazone compound with cobalt nitrate, zinc acetate, and cadmium nitrate and sodium azide, respec-

**Table 1.** Crystallographic and refinement data for HL and its metal complexes.

	HL	1	2	3
Formula	$C_{13}H_{11}N_3O_2$	$C_{28}H_{28}CoN_6O_7$	$C_{26}H_{20}N_6O_4Zn$	$C_{26}H_{22}CdN_{10}O_7$
Formula weight	241.25	618.49	545.85	698.94
T (K)	298(2)	298(2)	298(2)	298(2)
Crystal system	Monoclinic	Monoclinic	Monoclinic	Monoclinic
Space group	$P2_1/c$	$P2_1/n$	$C2/c$	$P2_1/n$
a (Å)	4.8050(6)	11.208(1)	18.215(2)	13.056(2)
b (Å)	22.413(3)	18.930(2)	24.601(2)	8.275(1)
c (Å)	10.875(2)	13.124(2)	11.556(1)	13.056(2)
$\beta$ (°)	102.399(2)	98.426(2)	103.588(2)	104.100(3)
V (Å <sup>3</sup> )	1143.8(3)	2754.4(5)	5033.2(9)	1368.1(4)
Z	4	4	8	2
$D_{calc}$ (g cm <sup>-3</sup> )	1.401	1.491	1.441	1.697
$\mu$ (Mo K $\alpha$ ) (mm <sup>-1</sup> )	0.098	0.682	1.020	0.865
F(000)	504	1280	2240	704
Measured reflections	10430	15995	13037	5483
Unique reflections	2026	5124	4588	2038
Observed reflections ( $I \geq 2\sigma(I)$ )	1388	4299	3057	1427
Parameters	167	381	340	205
Restraints	1	32	2	14
GOF on $F^2$	1.032	1.116	0.993	1.015
$R_1, wR_2$ [ $I \geq 2\sigma(I)$ ] <sup>a</sup>	0.0468, 0.0953	0.0700, 0.2230	0.0496, 0.1254	0.0535, 0.1302
$R_1, wR_2$ (all data) <sup>a</sup>	0.0819, 0.1124	0.0806, 0.2345	0.0786, 0.1436	0.0853, 0.1435

<sup>a</sup>  $R_1 = F_o - F_c/F_o$ ,  $wR_2 = [\sum w(F_o^2 - F_c^2)/\sum w(F_o^2)^2]^{1/2}$



**Table 2.** Selected bond distances (Å) and angles (°) for the complexes

<b>1</b>			
Co(1)–O(1)	1.905(3)	Co(1)–O(3)	1.923(3)
Co(1)–N(1)	1.926(4)	Co(1)–N(2)	1.856(4)
Co(1)–N(4)	1.933(4)	Co(1)–N(5)	1.852(4)
N(5)–Co(1)–N(2)	178.44(18)	N(5)–Co(1)–O(1)	96.03(16)
N(2)–Co(1)–O(1)	82.50(16)	N(5)–Co(1)–O(3)	82.26(16)
N(2)–Co(1)–O(3)	97.18(16)	O(1)–Co(1)–O(3)	89.85(14)
N(5)–Co(1)–N(1)	98.42(17)	N(2)–Co(1)–N(1)	83.04(17)
O(1)–Co(1)–N(1)	165.49(16)	O(3)–Co(1)–N(1)	90.71(16)
N(5)–Co(1)–N(4)	82.78(17)	N(2)–Co(1)–N(4)	97.76(17)
O(1)–Co(1)–N(4)	91.27(16)	O(3)–Co(1)–N(4)	165.04(16)
N(1)–Co(1)–N(4)	91.93(17)		
<b>2</b>			
Zn(1)–O(1)	2.162(3)	Zn(1)–O(3)	2.110(2)
Zn(1)–N(1)	2.230(3)	Zn(1)–N(2)	2.052(3)
Zn(1)–N(4)	2.265(3)	Zn(1)–N(5)	2.047(3)
N(5)–Zn(1)–N(2)	169.45(10)	N(5)–Zn(1)–O(3)	75.49(9)
N(2)–Zn(1)–O(3)	115.05(9)	N(5)–Zn(1)–O(1)	105.23(9)
N(2)–Zn(1)–O(1)	74.78(10)	O(3)–Zn(1)–O(1)	93.20(11)
N(5)–Zn(1)–N(1)	105.21(10)	N(2)–Zn(1)–N(1)	75.15(11)
O(3)–Zn(1)–N(1)	95.16(11)	O(1)–Zn(1)–N(1)	149.55(9)
N(5)–Zn(1)–N(4)	74.64(10)	N(2)–Zn(1)–N(4)	94.81(10)
O(3)–Zn(1)–N(4)	149.95(9)	O(1)–Zn(1)–N(4)	91.46(10)
N(1)–Zn(1)–N(4)	95.71(11)		
<b>3</b>			
Cd(1)–N(1)	2.379(6)	Cd(1)–O(3)	2.396(5)
Cd(1)–N(2)	2.417(5)		
N(1)–Cd(1)–N(1A)	101.9(3)	N(1)–Cd(1)–O(3A)	149.79(19)
N(1)–Cd(1)–O(3)	105.20(18)	O(3)–Cd(1)–O(3A)	53.2(2)
N(1)–Cd(1)–N(2A)	95.1(2)	N(1)–Cd(1)–N(2)	67.7(2)
O(3)–Cd(1)–N(2A)	122.10(19)	O(3)–Cd(1)–N(2)	83.20(18)
N(1)–Cd(1)–N(2A)	95.08(19)	O(3)–Cd(1)–N(2A)	122.10(19)
N(2)–Cd(1)–N(2A)	153.3(3)		

tively, in MeOH. The C, H, N content determined from the elemental analyses agree well with those determined by single-crystal X-ray diffraction techniques.

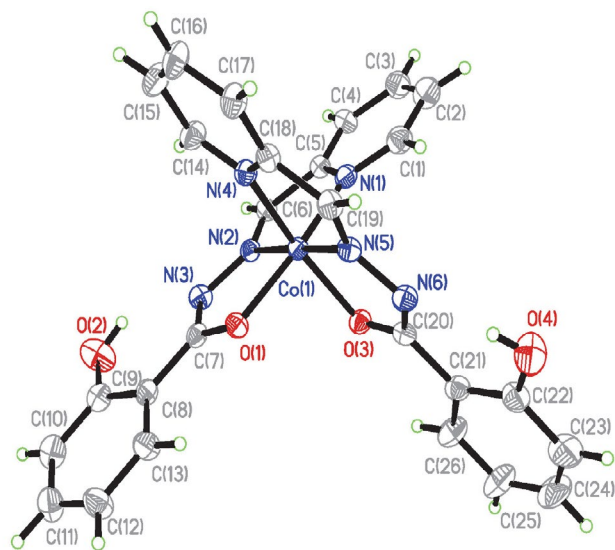
### 3. 2. IR Spectra

The weak and broad absorptions centered at 3420–3454  $\text{cm}^{-1}$  are attributed to the stretching vibration of the O–H bonds. The sharp bands observed at 3241  $\text{cm}^{-1}$  of HL and at 3387  $\text{cm}^{-1}$  of complex **3** are attributed to the stretching vibration of the amino N–H bonds. The strong bands at 1628  $\text{cm}^{-1}$  of the hydrazone HL and at 1638  $\text{cm}^{-1}$  of complex **3** are due to the  $\nu(\text{C}=\text{O})$  stretching vibrations, and the bands at 1596–1607  $\text{cm}^{-1}$  due to the  $\nu(\text{C}=\text{N})$  stretching vibrations. The absence of the  $\nu(\text{C}=\text{O})$  bands in the spectra of complexes **1** and **2** suggests the enolization of the amide functionality upon coordination to the metal atoms. For the spectrum of complex **3** typical band for  $\nu(\text{C}=\text{O})$  indicates that the carbonyl group is free. The typical bands for the nitrate ligand for complex **3** are observed

at 1456, 1311 and 1072  $\text{cm}^{-1}$ , and that for the azide anion is at 2072  $\text{cm}^{-1}$ .<sup>9</sup>

### 3. 3. Structure Description of Complex 1

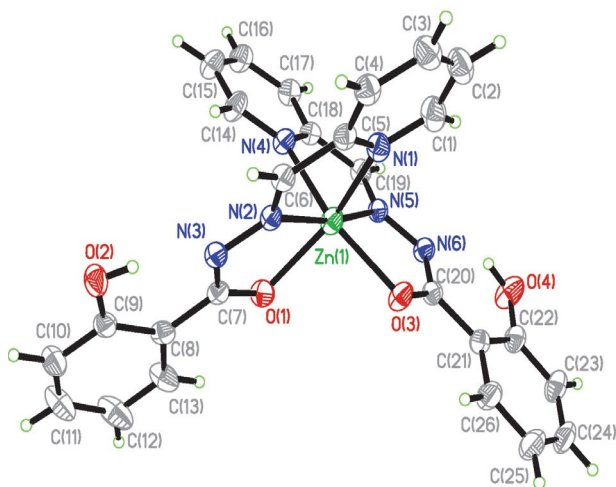
The structure of complex **1** is presented in Figure 1. The asymmetric unit comprises of a cobalt complex molecule, two methanol molecules and one water molecule. The coordination sphere of the Co atom is a distorted octahedral, with the tridentate hydrazone ligands coordinated in a meridional mode, generating five membered chelate rings with angles in the range 82.26(16)–83.04(17)°. The coordinate bond angles are within normal values.<sup>9</sup> The hydrazone coordinates to the Co atom with the pyridine nitrogen, enolate oxygen and imino nitrogen atoms. Ligand L is nearly coplanar, with the dihedral angles between the benzene and pyridine rings of 10.7(5) and 13.2(5)°, respectively. The bond lengths are similar to the cobalt complexes containing the enolate form of this ligand type.<sup>5,10,11</sup>



**Figure 1.** A perspective view of complex 1 with the atom labeling scheme. Thermal ellipsoids are drawn at the 30% probability level.

### 3. 4. Structure Description of Complex 2

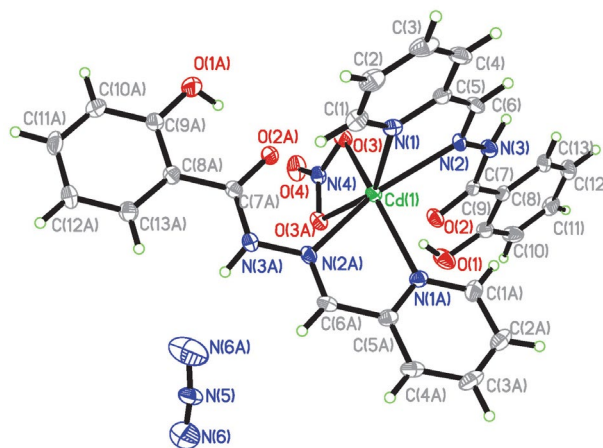
The structure of complex 2 is presented in Figure 2. The coordination sphere of the Zn atom is a distorted octahedral, with the tridentate hydrazone ligands coordinated in a meridional mode, generating five membered chelate rings with angles in the range 74.78(10)–75.49(9)°. The coordinate bond angles are within normal values.<sup>12</sup> The hydrazone coordinates to the Zn atom with the pyridine nitrogen, imino nitrogen and enolate oxygen atoms. Ligand L is somewhat deviated from planarity, with dihedral angles between the benzene and pyridine rings of 19.1(6) and 11.1(6)°, respectively. The bond lengths are similar to the zinc complexes containing the enolate form of this ligand type.<sup>12,13</sup>



**Figure 2.** A perspective view of complex 2 with the atom labeling scheme. Thermal ellipsoids are drawn at the 30% probability level.

### 3. 5. Structure Description of Complex 3

The structure of complex 3 is presented in Figure 3. The asymmetric unit comprises of a cadmium complex cation and an azide anion. The cadmium complex cation possesses a crystallographic two-fold rotation axis symmetry, with the axis passing through the line of Cd(1)–N(4)–O(4). The coordination sphere of the Cd atom can be described as a severely distorted octahedral, with the bidentate hydrazone ligands coordinated in a meridional mode, generating five a membered chelate ring with angle of 67.7(2)°. The coordinate bond angles are within normal values.<sup>14</sup> The hydrazone coordinates to the Cd atom through the pyridine nitrogen, imino nitrogen and enolate oxygen atoms. Hydrazone ligand is nearly coplanar, with dihedral angles between the benzene and pyridine rings of 7.9(5)°. The nitrate ligand coordinates to the Cd atom through two oxygen atoms. The coordinate bond lengths are comparable to the cadmium complexes containing this ligand type.<sup>14,15</sup>



**Figure 3.** A perspective view of complex 3 with the atom labeling scheme. Thermal ellipsoids are drawn at the 30% probability level.

### 3. 6. Antibacterial Activity

The MIC (Minimum Inhibitory Concentration,  $\mu\text{g mL}^{-1}$ ) values of the compounds were determined by a colorimetric method using the dye MTT.<sup>16</sup> HL and the three complexes were screened for antibacterial activities against two Gram (+) bacterial strains (*B. subtilis* and *S. aureus*) and two Gram (–) bacterial strains (*E. coli* and *P. fluorescence*). The MIC values of the compounds against four bacteria are listed in Table 3. Penicillin G was used as a reference. The hydrazone HL has medium activity against *S. aureus*, weak activity against *B. subtilis*, and no activity against *E. coli* and *P. fluorescence*. The complexes have in general stronger activities against the bacterial strains than the free hydrazone. Complex 1 has strong activity against *B. subtilis* and *S. aureus*, and weak activity against *E. coli* and *P. fluorescence*. Complex 2 has medium

activity against *B. subtilis* and *S. aureus*, weak activity against *P. fluorescence*, and no activity against *E. coli*. Complex **3** has strong activity against all the bacterial strains. The MIC values of complex **3** on *B. subtilis* and *S. aureus* are 2.3 and 1.2  $\mu\text{g mL}^{-1}$ , which are better than penicillin G. However, the free hydrazone and the complexes have no activity against two fungal strains *Candida albicans* and *Aspergillus niger*.

Table 3. Antimicrobial activities of the compounds

Tested material	Minimum inhibitory concentrations ( $\mu\text{g mL}^{-1}$ )			
	<i>B. subtilis</i>	<i>S. aureus</i>	<i>E. coli</i>	<i>P. fluorescence</i>
HL	37.5	18.8	> 150	> 150
<b>1</b>	4.7	9.4	37.5	37.5
<b>2</b>	18.8	18.8	> 150	37.5
<b>3</b>	2.3	1.2	9.4	4.7
Penicillin G	2.3	4.7	>150	>150
DMSO	> 150	> 150	> 150	> 150

## 4. Conclusion

In summary, three new cobalt(II), zinc(II) and cadmium(II) complexes derived from 2-hydroxy-*N'*-(pyridin-2-ylmethylene)benzohydrazide were prepared and structurally characterized. The metal atoms in the complexes are in octahedral coordination. The cobalt and cadmium complexes have effective antibacterial activities against *Bacillus subtilis*, *Staphylococcus aureus*, *Escherichia coli*, and *Pseudomonas fluorescence*.

## 5. Supplementary Material

CCDC 1875732 (HL), 1875733 (**1**), 1875734 (**2**), and 1875735 (**3**) contain the supplementary crystallographic data for this paper. These data can be obtained free of charge at <http://www.ccdc.cam.ac.uk/const/retrieving.html> or from the Cambridge Crystallographic Data Centre (CCDC), 12 Union Road, Cambridge CB2 1EZ, UK; fax: +44(0)1223-336033 or e-mail: [deposit@ccdc.cam.ac.uk](mailto:deposit@ccdc.cam.ac.uk).

## 6. Acknowledgments

This work was financially supported by K.C. Wong Magna Fund in Ningbo University, Ningbo Natural Science Fund (Project no. 201701HJ-B01019) and College Students of Science and Technology Innovation Projects in Zhejiang province and Ningbo city (Project no. 2017R405008 and 2017YZD001).

## 7. References

- (a) U. P. Singh, H. R. Bhat, A. Verma, M. K. Kumawat, R. Kaur, S. K. Gupta, R. K. Singh, *RSC Advances* **2013**, 3, 17335–17348; DOI:10.1039/c3ra41604f  
(b) F. Zhi, N. Shao, Q. Wang, Y. Zhang, R. Wang, Y. Yang, *J. Struct. Chem.* **2013**, 54, 148–154; DOI:10.1134/S0022476613010216  
(c) S. Naseem, M. Khalid, M. N. Tahir, M. A. Halim, A. A. C. Braga, M. M. Naseer, Z. Shafiq, *J. Mol. Struct.* **2017**, 1143, 235–244. DOI:10.1016/j.molstruc.2017.04.093
- (a) C. Loncle, J. M. Brunel, N. Vidal, M. Dherbomez, Y. Le-tourneux, *Eur. J. Med. Chem.* **2004**, 39, 1067–1071; DOI:10.1016/j.ejmech.2004.07.005  
(b) E. N. Nfor, A. Husian, F. Majoumo-Mbe, I. N. Njah, O. E. Offiong, S. A. Bourne, *Polyhedron* **2013**, 63, 207–213. DOI:10.1016/j.poly.2013.07.028
- (a) H. F. He, X. Y. Wang, L. Q. Shi, W. Y. Yin, Z. W. Yang, H. W. He, Y. Liang, *Bioorg. Med. Chem. Lett.* **2016**, 26, 3263–3270; DOI:10.1016/j.bmcl.2016.05.059  
(b) R. M. Mohareb, D. H. Fleita, O. K. Sakka, *Molecules* **2011**, 16, 16–27; DOI:10.3390/molecules16010016  
(c) H.-Q. Chang, L. Jia, J. Xu, W.-N. Wu, T.-F. Zhu, R.-H. Chen, T.-L. Ma, Y. Wang, Z.-Q. Xu, *Trans. Met. Chem.* **2015**, 40, 485–491; DOI:10.1007/s11243-015-9938-x  
(d) D. A. Megger, K. Rosowski, C. Radunsky, J. Koster, B. Sitek, J. Muller, *Dalton Trans.* **2017**, 46, 4759–4767; DOI:10.1039/C6DT04613D  
(e) L. M. Wang, S. J. Zhao, G. L. Bao, Y. Zhang, S. C. Xi, G. L. Zhou, X. Zhai, P. Gong, *Med. Chem.* **2016**, 12, 621–630. DOI:10.2174/1573406412666160106154551
- (a) P. Bera, P. Brandao, G. Mondal, H. Jana, A. Jana, A. Santra, P. Bera, *Polyhedron* **2017**, 134, 230–237; DOI:10.1016/j.poly.2017.06.024  
(b) R. R. Zaky, K. M. Ibrahim, I. M. Gabr, *Spectrochim. Acta A* **2011**, 81, 28–34;  
(c) M. V. Angelusiu, S. F. Barbuceanu, C. Draghici, G. L. Al-majan, *Eur. J. Med. Chem.* **2010**, 45, 2055–2062. DOI:10.1016/j.ejmech.2010.01.033
- P. Zhou, Y.-G. Zhao, Y. Bai, K.-L. Pang, C. He, *Inorg. Chim. Acta* **2007**, 360, 3965–3970. DOI:10.1016/j.ica.2007.05.038
- Bruker, SMART (Version 5.625) and SAINT (Version 6.01). Bruker AXS Inc., Madison, Wisconsin, USA, 2007.
- G. M. Sheldrick, SADABS. Program for Empirical Absorption Correction of Area Detector, University of Göttingen, Germany, 1996.
- G. M. Sheldrick, *Acta Crystallogr.* **2015**, A71, 3–8. DOI:10.1107/S2053273314026370
- (a) S. Chandra, A. K. Sharma, *J. Coord. Chem.* **2009**, 62, 3688–3700; DOI:10.1080/00958970903121305  
(b) S. S. Massoud, F. A. Mautner, *Inorg. Chim. Acta* **2005**, 358, 3334–3340. DOI:10.1016/j.ica.2005.05.007
- B. Samanta, J. Chakraborty, S. Shit, S. R. Batten, P. Jensen, J. D. Masuda, S. Mitra, *Inorg. Chim. Acta* **2007**, 360, 2471–2484. DOI:10.1016/j.ica.2006.12.019
- (a) M. Mishra, K. Tiwari, S. Shukla, R. Mishra, V. P. Singh, *Spectrochim. Acta A* **2014**, 132, 452–464;

- DOI:10.1016/j.saa.2014.05.007
- (b) A. Sousa-Pedrares, N. Camina, J. Romero, M. L. Duran, J. A. Garcia-Vazquez, A. Sousa, *Polyhedron* **2008**, 27, 3391–3397. DOI:10.1016/j.poly.2008.08.011
12. (a) P. Singh, D. P. Singh, V. P. Singh, *Polyhedron* **2014**, 81, 56–65; DOI:10.1016/j.poly.2014.05.066
- (b) P. Domiano, C. Pelizzi, G. Predieri, *Polyhedron* **1984**, 3, 281–286; DOI:10.1016/S0277-5387(00)88108-5
- (c) B. Samanta, J. Chakraborty, S. Shit, S. R. Batten, P. Jensen, J. D. Masuda, S. Mitra, *Inorg. Chim. Acta* **2007**, 360, 2471–2484. DOI:10.1016/j.ica.2006.12.019
13. (a) S. Konar, A. Jana, K. Das, S. Ray, S. Chatterjee, S. K. Kar, *Polyhedron* **2012**, 47, 143–150; DOI:10.1016/j.poly.2012.07.080
- (b) C.-F. Chow, S. Fujii, J.-M. Lehn, *Chem. Asian J.* **2008**, 3, 1324–1335; DOI:10.1002/asia.200800101
- (c) D.-L. Peng, N. Sun, *Acta Chim. Slov.* **2018**, 65, 895–901. DOI:10.17344/acsi.2018.4543
14. F. X. Shen, W. Huang, X. C. Huang, S. Peng, D. Y. Wu, *Transit. Met. Chem.* **2015**, 40, 681–689. DOI:10.1007/s11243-015-9962-x
15. (a) K. Das, S. Konar, P. Pal, A. Jana, S. Chatterjee, S. Mukhopadhyay, *Polyhedron* **2015**, 85, 172–180; DOI:10.1016/j.poly.2014.08.043
- (b) F. A. Afkhami, A. A. Khandar, G. Mahmoudi, W. Maniukiewicz, J. Lipkowski, J. M. White, R. Waterman, S. Garcia-Granda, E. Zangrando, A. Bauza, A. Frontera, *CrystEngComm* **2016**, 18, 4587–4596. DOI:10.1039/C6CE00877A
16. J. Meletiadis, J. F. G. M. Meis, J. W. Mouton, J. P. Donnelly, P. E. Verweij, *J. Clin. Microbiol.* **2000**, 38, 2949–2954.

## Povzetek

Tri nove spojine, in sicer kobaltov(II), cinkov(II) in kadmijev(II) kompleks  $[\text{CoL}_2] \cdot 2\text{CH}_3\text{OH} \cdot \text{H}_2\text{O}$  (**1**),  $[\text{ZnL}_2]$  (**2**) in  $[\text{Cd}(\text{HL})_2(\text{NO}_3)_2] \cdot \text{N}_3$  (**3**) smo sintetizirali z uporabo 2-hidroksi-*N'*-(piridin-2-ilmetilen)benzohidrazida (HL) ter jih okarakterizirali z IR, UV-Vis in monokristalno rentgensko difrakcijo. Rentgenska analiza je razkrila, da so kompleksi enojedrne zvrsti s kovinskim ionom v oktaedrični koordinaciji. Hidrazonu in njegovim kompleksom smo določili tudi antibakterijske (*Bacillus subtilis*, *Staphylococcus aureus*, *Escherichia coli*, *Pseudomonas fluorescens*) in antimikotične (*Candida albicans*, *Aspergillus niger*) lastnosti. Kompleksi imajo izražene protibakterijske lastnosti.



Except when otherwise noted, articles in this journal are published under the terms and conditions of the Creative Commons Attribution 4.0 International License

Scientific paper

# Alteration in the Chemical Composition of Immortelle, Silver Fir and Prickly Juniper Essential Oils Induced by Light

Ilijana Odak,<sup>1,\*</sup> Irena Škorić,<sup>2</sup> Daria Grbavac,<sup>1</sup> Ana Ratković<sup>2</sup> and Ivana Šagud<sup>2</sup>

<sup>1</sup> Department of Chemistry, Faculty of Science and Education, University of Mostar, Matice hrvatske bb, 88000 Mostar, Bosnia and Herzegovina.

<sup>2</sup> Department of Organic Chemistry, Faculty of Chemical Engineering and Technology, University of Zagreb, Marulićev trg 19, 10000 Zagreb, Croatia

\* Corresponding author: E-mail: [ilijana.odak@fpmoz.sum.ba](mailto:ilijana.odak@fpmoz.sum.ba)  
Tel: +38736445478, Fax: +38736355458

Received: 03-12-2019

## Abstract

The objective of this study was to evaluate impact of light and available oxygen on the chemical composition of three selected essential oils. Aliquots of immortelle (*Helichrysum italicum*), silver fir (*Abies alba*) and prickly juniper (*Juniperus oxycedrus*) essential oils were exposed to UV-A irradiation in the presence of atmospheric oxygen as well as in the presence of inert gas. The compositions of fresh and irradiated samples were studied by GC-MS. Each oil showed an individual response to the applied conditions. In immortelle oil, dominant process was phototransformation of  $\gamma$ -curcumene to italicene, isoitalicene and  $\alpha$ -curcumene. Since  $\gamma$ -curcumene is one of the major components of immortelle essential oil, exposure of this oil to light can cause significant changes in primary composition and thus quality. In silver fir and prickly juniper oil irradiation caused only slight changes among sesquiterpenes that are present as minor components. Both oils were found to be photostable and insensitive to the presence of atmospheric oxygen.

**Keywords:** Essential oil; photostability; phototransformation; cycloaddition; dehydrogenation; UV-Vis promoted deterioration

## 1. Introduction

Phytochemicals have long history of usage in nutrition, medicine and cosmetics due to the wide range of beneficial properties they possess. Nowadays, the interest in phytochemicals is continuously growing, whether for healthy food, natural pharmaceuticals or personal care and household products. This can be attributed to the consumer's increased awareness regarding the "green" products and an overall greater health consciousness. An important class of natural products in food and cosmetics industries as well as in folk medicine are essential oils. As defined by the International Organization for Standardization (ISO 9235, 2013) essential oil is a "product obtained from raw plant material by steam distillation, by mechanical processes from the epicarp of citrus fruits, or by dry distillation, after separation of the aqueous phase, if any, by physical processes." Usages of essential oils overcame the traditional medicinal practices and nowadays they are widely applied in the

cosmetics, pharmaceutical and food industries.<sup>1–3</sup> Such various areas of essential oils application result from the differences in their chemical composition which range from very simple to highly complex, containing more than 100 constituents. Specific features of essential oils, such as antioxidant properties or odor, do not depend only on the major components but also on the synergism between these components and the structure and properties of each. Terpenes well known for their pharmacological properties, also serve as lead compounds in synthesis of derivatives that might possess improved biological activity.<sup>4,5</sup>

Components of essential oils including terpenes, esters, aromatic hydrocarbons and phenols, may undergo changes when exposed to air, heat or light. They can be transformed into one another by oxidation, isomerization, cyclization or dehydrogenation or may be transformed into other products by the same reactions as well as by polymerization and degradation.<sup>6</sup> Changes in the composition of the starting material can lead to the decline in qual-

ity and its biological properties<sup>7</sup> and even lead to compounds that can cause harm to the user.<sup>8,9</sup> In order to develop efficient use of essential oils in various areas of applications, it is necessary to carry out research regarding their properties, chemical composition as well as photostability or changes in the composition during storage and usage. Ultraviolet and visible light is found to cause faster compositional changes through the reactions of oxidation, photocycloaddition and isomerization. Mieting *et al.*<sup>10</sup> found photoanethole in stored essential oil from anis, as a result of photocycloaddition between anethole and anisaldehyde. In sweet fennel oil, *trans*-anethole isomerizes to *cis*-anethole and oxidizes to anisaldehyde under the influence of light.<sup>11</sup> Turek and Stintzing<sup>12,13</sup> found degradation of some monoterpenes in rosemary oil under the influence of light while thyme oil does not show significant changes when exposed to daylight.

In this paper, three commercially available essential oils from Bosnia and Herzegovina (B&H) were studied in order to determine their photostability. Territory of B&H is characterized by high floristic diversity. A large number of medicinal and aromatic plant species are native to B&H and represent an important economic resource. B&H is covered with coniferous woods, which has resulted in widespread usage of products derived from this species. Essential oils from *Abies alba* is industrially one of the most important in B&H. Silver fir oil is used commercially in cosmetic and fragrance industries as well as household products.<sup>14</sup> Another important conifer is *Juniperus oxycedrus* (prickly juniper) and its essential oil which is used in many pharmaceutical skin preparations and veterinary medicine. One of the most cultivated aromatic plants in Herzegovina is *Helichrysum italicum* subsp. *italicum* (immortelle) due to the economic value of its essential oil. It is a highly valued oil with a complex chemical composition, used in perfume and cosmetics industry.<sup>15</sup>

The influence of light on the chemical changes of selected essential oils has been studied in the conditions that cause accelerated changes induced by light. Irradiated samples were analyzed by GC-MS and compared to the fresh ones in order to evaluate potential changes in chemical composition.

## 2. Experimental

### 2. 1. Plant Material and Chemicals

Fresh samples of immortelle, silver fir and prickly juniper essential oils were obtained from distillery plant Roing Ltd. (B&H, <http://www.essential-oils.ba/>). Oils were obtained by steam distillation of the corresponding plants, all harvested in Herzegovina region in 2017, and dried over anhydrous sodium sulphate. Pentane, DMSO and petroleum ether were obtained from Sigma-Aldrich (St. Louis, MO, USA). Silica gel (Fluka 0.063–0.2 mm) was used for chromatographic purifications.

### 2. 2. Photochemical Testing

Essential oil samples were prepared as follows: aliquots of 1 mL were filled in 2 mL clear glass vials and closed with sealing plugs with the air left in the headspace (conditions A). The second set of samples was prepared in the same way but flushed with pure nitrogen (conditions B). The sealed vials were irradiated for 48 hours (or more) at 25 °C in a Luzchem CCP-ICH2 photoreactor equipped with 16 lamps of the 366 nm wavelength. After irradiation, oil samples were analyzed using GC-MS system.

### 2. 3. Gas Chromatography–Mass Spectrometry Analysis

The analysis of the oils was carried out using Shimadzu GC-MS QP2010 system equipped with an AOC-20i autosampler, using fused silica capillary column Inert Cap (5% diphenyl – 95% dimethylpolysiloxane, 30 m × 0.25 mm i.d., film thickness 0.25 µm). 1.0 µL of solution diluted 1:500 v/v in pentane was injected in splitless mode with helium as carrier gas. For immortelle essential oil, the operating conditions were as follows: injection temperature 250 °C; helium flow rate, 1.15 mL/min; oven temperature program: 60 °C (1.5 min), 60–120 °C (5 °C/min), 120–240 °C (4 °C/min), 240 °C (2 min). MS (EI) conditions: ion source temperature: 250 °C, interface temperature: 250 °C, ionization voltage: 70 eV, mass range: *m/z* 40–400 u, scan time: 0.5 sec. For silver fir oil, the operating conditions were as follows: injection temperature 260 °C; helium flow rate, 1.11 mL/min; oven temperature program: 50 °C (5 min), 50–260 °C (3 °C/min), 260 °C (15 min). MS (EI) conditions: ion source temperature: 200 °C, interface temperature: 280 °C, ionization voltage: 70 eV, mass range: *m/z* 40–400 u, scan time: 0.5 sec. The operating conditions for prickly juniper oil were as follows: injection temperature 250 °C; helium flow rate, 1.06 mL/min; oven temperature program: 60 °C (2 min), 60–200 °C (3 °C/min), 200 °C (10 min). MS (EI) conditions: ion source temperature: 200 °C, interface temperature: 250 °C, ionization voltage: 70 eV, mass range: *m/z* 40–400 u; scan time: 0.5 sec. GCMSolution 2.5 (Shimadzu) was used to handle data. GC-MS analyses were performed in triplicate and the results are represented as mean values.

Identification of oil components was based on (a) retention indices on a non-polar column relative to a homologous series of *n*-alkanes (C<sub>8</sub>–C<sub>40</sub>); (b) on the comparison of their mass spectra and retention indices with the Wiley 7 and NIST spectra libraries and with those reported in the literature.<sup>16–19</sup>

### 2. 4. Fractionation and Irradiation of Immortelle Essential Oil

Sample of immortelle essential oil was subjected to vacuum distillation in order to remove α-pinene and oth-



er monoterpenes of lower boiling points. The residue was distributed by liquid-liquid extraction in DMSO – hexane system. After removal of hexane on rotary evaporator, nonpolar fraction was subjected to column chromatography on silica gel using petroleum ether as eluent, yielding a fraction with 80% of  $\gamma$ -curcumene. Two sets of samples were prepared, one with the air in a headspace of the vial and one flushed with nitrogen. Samples were irradiated in the photoreactor at 366 nm during 24 hours and analysed by GC-MS as described in part 2.3. for immortelle oil.

### 3. Results and Discussion

The influence of the light was assessed by brief irradiation in the photochemical reactor at a wavelength of 366 nm in order to imitate UV-A fraction of sunlight. Samples of fresh oils were kept in photoreactor under air (sample A) and under nitrogen (sample B) for 48 hours or longer. Table 1 shows compounds from particular oil whose percentage has changed during irradiation, while complete tables with full chemical composition of each freshly distilled oil can be found in Appendix. Changes higher than 0.2 in relative peak area were considered relevant.

#### 3. 1. Immortelle Oil

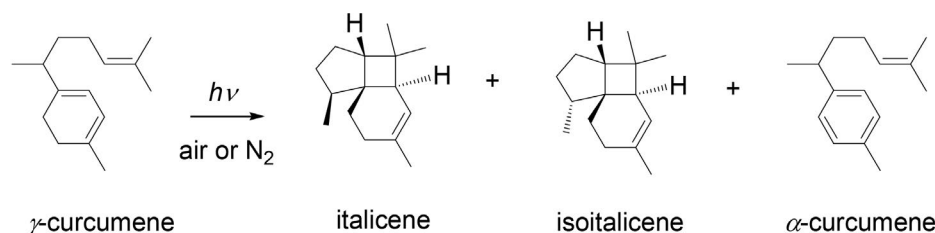
Essential oil of immortelle contained 70 components (Table A.1).  $\alpha$ -Pinene (28.5%),  $\gamma$ -curcumene (9.8%),  $\beta$ -selinene (6.3%) and italicene (5.0%) were the major components. Stability of immortelle essential oil was studied earlier by us under realistic storage conditions.<sup>20</sup> The samples were left during a period of 12 months in the dark and daylight in the presence and absence of oxygen. The only significant change was a decrease in  $\gamma$ -curcumene percentage. Test in the photoreactor confirmed photochemical transformations that occurred during realistic storage conditions. Irradiation causes the transformation of  $\gamma$ -curcumene mostly to italicene and isoitalicene as a result of [2+2]-photocycloaddition and to the  $\alpha$ -curcumene via dehydrogenation/aromatization (Scheme 1, Table 1). Dehydrogenation to  $\alpha$ -curcumene is more favored when the oxygen is present in the headspace. Changes induced by light are more pronounced when the oil is flushed with inert gas rather than left in the air atmosphere. Since UV and Vis light accelerate autoxidation<sup>21</sup> and polymerization processes, absence of oxygen allows photochemical transformations, such as cyclization, to take place to a greater extent.

To confirm this particular transformation, the fraction from the immortelle oil with the  $\gamma$ -curcumene as a major component was isolated by distillation, extraction

**Table 1.** Changes in GC-MS relative peak area of characteristic compounds during exposure of essential oils to various conditions

Compound	RI <sup>a</sup>	% Fresh	Changes in relative peak area	
<i>Immortelle oil</i>			A <sup>b</sup>	B <sup>b</sup>
Isoitalicene	1376	0.7	+0.3	+1.0
Italicene	1405	5.0	+2.4	+2.7
$\gamma$ -Curcumene	1477	9.8	–3.3	–3.7
$\alpha$ -Curcumene	1482	2.7	+0.6	+0.2
<i>Silver fir oil</i>			A <sup>c</sup>	B <sup>c</sup>
Caryophyllene	1413	2.7	–0.5	–0.3
Himachala-2,4-diene	1418	1.0	–0.5	–0.5
<i>Prickly juniper oil</i>			A <sup>b</sup>	B <sup>b</sup>
Bourbonene	1379	tr	+0.3	+0.4
Germacrene D	1476	1.9	–0.3	–0.4

<sup>a</sup> RI: retention indices. <sup>b</sup> Storage condition A: 48 h, air; B: 48 h, nitrogen. <sup>c</sup> Storage condition A: 146 h, air; B: 146 h, nitrogen.



**Scheme 1.** Photochemical transformations of  $\gamma$ -curcumene

and column chromatography. The GC-MS analysis of the irradiated fraction revealed that the  $\gamma$ -curcumene completely disappears and is transformed to the above-mentioned products. Among two cycloaddition products, italicene is formed in greater amount than isoitalicene because the conformation of  $\gamma$ -curcumene that leads to italicene by suprafacial [2+2]-photocycloaddition is more favorable than the conformation that leads to isoitalicene by the same suprafacial [2+2]-photocycloaddition.

### 3. 2. Silver Fir Oil

In fresh oil a total of 67 compounds was identified, representing 98.3% of the chemical composition (Table A.2). The major compounds present in silver fir oil were  $\beta$ -pinene (24.1%), limonene (23.6%),  $\alpha$ -pinene (17.8%), camphene (9.1%) and bornyl acetate (9.0%). After 48 hours of irradiation in the atmosphere of air or nitrogen (samples A and B) the oil kept its original composition. Prolonging irradiation to 146 hours caused decline in caryophyllene and himachala-2,4-diene amount (Table 1). A few new peaks appeared among sesquiterpenes which were difficult to identify due to small amount. Oxygen presence or absence does not play any role in photochemical stability, so the observed changes cannot be attributed to oxidations.

### 3. 3. Prickly Juniper Oil

Analysis of fresh prickly juniper oil identified 46 compounds, representing 98.2% of the total oil (Table A.3). The predominant components in prickly juniper were  $\beta$ -myrcene (48.0%),  $\alpha$ -pinene (24.7%) and limonene (9.0%). After 48 hours of irradiation the only noticeable change was a slight decrease of germacrene D, while other compounds were retained in their initial shares. This ten-membered ring with two double bonds is photochemically reactive as demonstrated by Bulow *et al.*<sup>22</sup> in photochemically induced rearrangement experiments with isolated germacrene D. Bourbonene is one of the main photoproducts, and it was detected in chromatogram with increased amount after irradiation (Table 1).

## 4. Conclusion

Photostability investigation on the three selected essential oils demonstrated individual character of these oils in response to irradiation.  $\gamma$ -Curcumene is rarely found in natural products in larger proportions due to its reactivity. Its relatively high content in immortelle oil makes this oil special in its chemical composition and contributes significantly to its odor and biological activity.<sup>23</sup> It is showed that this reactive sesquiterpene is sensitive to light and undergoes photochemical transformation to another interesting structure, that of italicenes that contain a rare

four-membered ring. Thus, if it is desired to maintain an original amount of  $\gamma$ -curcumene, it is necessary to keep this oil in the dark. Silver fir oil is photochemically stable regardless of oxygen availability. It is not necessary to store the oil in the dark and under the inert gas. Prickly juniper oil also showed good photostability, especially among monoterpenes that preserved their shares. The amount of change during exposure to UV light was very low under both sets of conditions.

## 5. Acknowledgement

This work was supported by Federal Ministry of Education and Science, Bosnia and Herzegovina [Grant No.05-39-3831-1/15].

## 6. Appendix

Chemical composition of the freshly distilled immortelle, silver fir and prickly juniper essential oils can be found in Appendix.

## 7. References

1. V. R. Preedy, *Essential Oils in Food Preservation, Flavor and Safety*, 1st Ed, Academic Press, Amsterdam, **2016**.
2. R. G. Berger, *Flavours and Fragrances: Chemistry, Bioprocessing and Sustainability*, Springer-Verlag, Berlin Heidelberg, **2007**. DOI:10.1007/978-3-540-49339-6
3. J. S. Raut, S. M. Karuppaiyil, *Ind. Crops Prod.* **2014**, 62, 250–264. DOI:10.1016/j.indcrop.2014.05.055
4. J. Lazarević, A. Kolarević, G. Stojanović, A. Smelčerović, P. Ciuffreda, E. Santaniello, *Acta Chim. Slov.* **2018**, 65, 801–810. DOI:10.17344/acsi.2018.4380
5. J. Lazarević, A. Kolarević, A. Đorđević, G. Stojanović, A. Smelčerović, P. Ciuffreda, E. Santaniello, *Acta Chim. Slov.* **2017**, 64, 603–612. DOI:10.17344/acsi.2017.3356
6. C. Turek, F. C. Stintzing, *Compr. Rev. Food Sci. Food Saf.* **2013**, 12, 40–53. DOI:10.1111/1541-4337.12006
7. K. H. Kubeczka, in: R. Carle (Ed.): *Atherosclerotic Ole – Anspruch und Wirklichkeit*, Wissenschaftliche Verlagsgesellschaft, Stuttgart, **1993**, 85–102.
8. M. Skold, L. Hagvall, A. T. Karlberg, *Contact Derm.* **2008**, 58, 9–14. DOI:10.1111/j.1600-0536.2007.01262.x
9. J. Brared-Christensson, M. Matura, B. Gruvberger, M. Bruze, A. T. Karlberg, *Contact Derm.* **2010**, 62, 32–41. DOI:10.1111/j.1600-0536.2009.01657.x
10. H. Miething, V. Seger, R. Hansel, *Phytother. Res.* **1990**, 4, 121–123. DOI:10.1002/ptr.2650040311
11. T. A. Misharina, A. N. Polshkov, *Appl. Biochem. Microbiol.* **2005**, 41, 693–702. DOI:10.1007/s10438-005-0111-8
12. C. Turek, F. C. Stintzing, *J. Food Sci.* **2011**, 76, 1365–1375. DOI:10.1111/j.1750-3841.2011.02416.x

13. C. Turek, F. C. Stintzing, *Food Res. Int.* **2012**, *46*, 341–353.  
DOI:10.1016/j.foodres.2011.12.028
14. A. Wajs-Bonikowska, M. Sienkiewicz, A. Stobiecka, A. Maciag, L. Szoka, E. Karna, *Chem. Biodivers.* **2015**, *12*, 407–418.  
DOI:10.1002/cbdv.201400167
15. D. A. Viegas, A. Palmeira-de-Oliveira, L. Salgueiro, J. Martin-ez-de-Oliveira, R. Palmeira-de-Oliveira, *J. Ethnopharm.* **2014**, *151*, 64–65.
16. R. P. Adams, Identification of Essential oil Components by Gas Chromatography/Mass Spectroscopy. 4th ed., Allured Publ. Corp, Carol Stream, IL, **2007**.
17. V. I. Babushok, P. J. Linstrom, I. G. Zenkevich, *J. Phys. Chem. Ref. Data* **2011**, *40*, 043101. DOI:10.1063/1.3653552
18. NIST Chemistry WebBook. <https://webbook.nist.gov/chemistry/> (20 December 2018)
19. A. Bianchini, P. Tomi, J. Costa, A.F. Bernardini, *Flavour Fragrance J.* **2001**, *16*, 30–34.  
DOI:10.1002/1099-1026(200101/02)16:1<30::AID-FFJ941>3.0.CO;2-F
20. I. Odak, T. Lukić, S. Talić, *J. Essent. Oil Bear. Pl.* **2018**, *21*, 614–622. DOI:10.1080/0972060X.2018.1489309
21. E. Choe, D. B. Min, *Compr. Rev. Food Sci. Food Saf.* **2006**, *5*, 169–186. DOI:10.1111/j.1541-4337.2006.00009.x
22. N. Bullock, W. A. König, *Phytochemistry*. **2000**, *55*, 141–168.  
DOI:10.1016/S0031-9422(00)00266-1
23. A. Sala, M. Recio, R. M. Giner, S. Manez, H. Tournier, G. Schinella, J. L. Rios, *J. Pharm. Pharmacol.* **2002**, *54*, 365–371.  
DOI:10.1211/0022357021778600

## Povzetek

Namen te študije je bil ugotoviti učinek svetlobe in kisika na kemijsko sestavo treh eteričnih olj. Alikvote olja iz laškega smilja (*Helichrysum italicum*), bele jelke (*Abies alba*) in vrste brina (*Juniperus oxycedrus*) smo izpostavili obsevanju z UV-A svetlobo v prisotnosti atmosferskega kisika in v prisotnosti inertnega plina. Sestavo svežih in obsevanih vzorcev smo raziskali z GC/MS. Vsako izmed olj je pokazalo drugačen odziv na uporabljene pogoje. Pri olju iz laškega smilja je bil glavni proces fototransformacija  $\gamma$ -kurkumena v italicen, izoitalicen in  $\alpha$ -kurkumen. Ker je  $\gamma$ -kurkumen ena izmed glavnih sestavin eteričnega olja laškega smilja, lahko izpostavljenost tega olja svetlobi povzroči bistvene spremembe v njegovi sestavi in s tem tudi kakovosti. Pri olju bele jelke in brina pa je obsevanje povzročilo zgolj majhne spremembe pri seskviterpenih, ki pa so prisotni samo v manjših deležih. Obe olji sta se torej izkazali kot fotostabilni in neobčutljivi na prisotnost atmosferskega kisika.



Except when otherwise noted, articles in this journal are published under the terms and conditions of the Creative Commons Attribution 4.0 International License

Scientific paper

# Micro and Nanostructure Surface and Interface Characterization of Anodized Zr in Two Different Electrolytes

Andrei Bogdan Stoian,<sup>1</sup> Maria Vardaki<sup>1</sup> and Ioana Demetrescu<sup>1,2\*</sup><sup>1</sup> Faculty of Applied Chemistry and Materials Science, Department of General Chemistry, University Politehnica of Bucharest, 1-7 Gheorghe Polizu str., 011061, Bucharest, Romania<sup>2</sup> Academy of Romanian Scientists, 54 Spaiul Independentei, 050094, Bucharest, Romania\* Corresponding author: E-mail: ioana\_demetrescu@yahoo.com; i\_demetrescu@chim.upb.ro  
Tel. +4 021 402 3930

Received: 03-13-2019

## Abstract

The present work reports on the morphologies and properties of anodized Zr in two different electrolytes. The Zr phosphates ( $\alpha$ -ZP) obtained in the inorganic electrolyte containing  $\text{H}_3\text{PO}_4 + \text{NaF}$  and zirconia ( $\text{ZrO}_2$ ) nanostructures formed in the organic glycerol-based electrolyte were investigated by SEM, FT-IR and AFM. The surface analysis was completed by contact angles measurements. It was found that the type of electrolyte along with the applied voltage influence the structure of the sample and being more precise, the anodic oxidation in  $\text{H}_3\text{PO}_4$  electrolyte promotes the evolution of flaky structures and eventually of pores by increasing the applied voltage, while the anodizing performed in glycerol-based electrolyte results in the formation of nanoporous structures that evolve into nanotubes as the applied voltage grows. Based on experimental data a film forming mechanism for  $\alpha$ -ZP and  $\text{ZrO}_2$  was proposed and correlated to analyzed surface properties.

**Keywords:** Zirconium phosphate; zirconia; anodizing; organic; inorganic; electrolyte

## 1. Introduction

Due to its remarkable physical, chemical and mechanical properties, zirconium (Zr) has been used in various fields including nuclear industry for having low neutron absorption and microelectronic industry for having high dielectric constant.<sup>1,2</sup> Zr is a strong, reactive valve metal that possesses physical and chemical properties similar to titanium (Ti) forming spontaneously a protective oxide film when it comes in contact with air. With a passive film, Zr presents an excellent resistance to corrosion in a variety of conditions, such as organic solutions, alkalis and acids and can be considered a promising and useful material that can be used in applications such as oxygen sensors,<sup>3</sup> protective coating materials in optical devices,<sup>4</sup> photocatalysts in environmental applications<sup>5</sup> and catalysts for fuel cells.<sup>6</sup> It is to mention that Zr is considered one of the most biocompatible elements and a good choice for restorative works in oral cavity,<sup>7–9</sup> being a competition for Ti and Ti alloys.<sup>10,11</sup> Oral cavity environ-

ments are very aggressive not only because of saliva, but for their varying pH content as well, and the excellent resistance to corrosion of Zr and Zr alloys especially in combination with Ti is a strong point for recommendation as biomaterial.<sup>12–14</sup> The present work reports on formation of zirconium phosphates ( $\alpha$ -ZP) as a result of anodizing in inorganic  $\text{H}_3\text{PO}_4 + \text{NaF}$  electrolyte. It is important to know that  $\alpha$ -ZP materials<sup>15</sup> thanks to their properties (thermal stability, ion exchange capability, good biological compatibility etc.) can be considered good candidates for a variety of applications, like for example to be used in catalysis<sup>16</sup> and photochemistry.<sup>17</sup> The ease of formation and modification along with the excellent properties makes  $\alpha$ -ZP an urgent topic of ongoing research aiming to the extension of their applications in various fields,<sup>18,19</sup> being considered an old material with a bright future. Regarding the anodizing of Zr in the organic electrolyte,  $\text{ZrO}_2$  nanostructures formed present desired qualities that proved to be useful for many applications, including biomedical field.<sup>20</sup> Further, it was found

that the way of self-organization of obtained  $\text{ZrO}_2$  nano-tubes appears to be very much alike to that proposed for  $\text{Ti}$ .<sup>21,22</sup> Zr anodic oxidation *via* electrochemical anodizing is a facile and inexpensive method for surface modification, providing the opportunity for obtaining a variety of different nanostructures based on the applied conditions (electrolyte, pH, applied voltage, post treatments etc.). In the present work is reported the fabrication of  $\alpha$ -ZP and  $\text{ZrO}_2$  nanostructures and shows how the used electrolyte and the applied electrochemical conditions during the anodizing process can affect the final structure, morphology and properties of the samples. Based on experimental data, a film forming mechanism for  $\alpha$ -ZP and  $\text{ZrO}_2$  was proposed and, as novelty, was direct correlated to analyzed surface properties.

## 2. Experimental

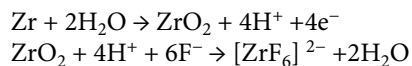
Zr samples (foil, thickness 0.1 mm, 99.98% – Sigma-Aldrich) were cleaned in an ultrasonic bath in distilled water and ethanol for 10 minutes each. The samples were then dried in atmosphere at room temperature. The surface modification was achieved by anodizing the samples with a Matrix MPS-7163 DC power supply. The anodizing was carried out for 60 minutes applying different voltages for each sample (5 V, 15 V, 45 V and 75 V) using the Zr sample as the anode and Pt foil as the cathode. Two sets of samples were produced by using different electrolytes. The first electrolyte (E1) containing 2M  $\text{H}_3\text{PO}_4$  (85 wt.% – Sigma-Aldrich) and 30 mM NaF (>98% – Sigma-Aldrich) was used to obtain Zr phosphates and the second electrolyte (E2) containing glycerol 15vol%  $\text{H}_2\text{O}$  + 0.2M  $\text{NH}_4\text{F}$  was used to obtain  $\text{ZrO}_2$  nanostructures.<sup>23</sup> The micro surface morphologies of the Zr samples were investigated with a Quanta 650 scanning electron microscope (SEM) from FEI in high vacuum at 10 kV. The coating thickness was evaluated by scratching the film and measuring the cross section with the SEM. The infrared spectra (FT-IR) were obtained with a Perkin-Elmer Spec-

trum 100 spectrometer in the range 4000–600  $\text{cm}^{-1}$ . Micro roughness and adhesion forces were evaluated using an A.P.E. Research A100-SGS atomic force microscope (AFM) from 5 measurements for each sample. The wettability of the samples was evaluated with a CAM100 equipment from KSV Instruments using ultra-pure water. The contact angle values represent the average of 5 measurements.

## 3. Results and Discussion

### 3.1. Surface Morphology

Fig. 1a shows the surface of Zr samples anodized in E1 at 5 V that are covered in two types of structures: the first type is represented by small semi-spheres with diameters of approximately 300 nm which form small clusters; the second type is represented by ridges with lengths of 1–3  $\mu\text{m}$  and widths of 30 to 400 nm. On the same sample there was observed a phenomenon of bubble formation (10–100  $\mu\text{m}$  diameter) and breaking, with the result of superficial stratum exfoliation. Outside the sites of former bubbles, a higher concentration of  $\alpha$ -ZP ridges was observed. This observed process of bubble forming and breaking was not completed during the anodizing time and on the surface are present sites in all development stages. Anodizing in E2 at the same voltage (Fig. 1b) led to the formation on the surface of the samples of an oxide layer with the thickness ranging between 200–400 nm. The oxide formation is the result of following reactions presented below<sup>7</sup>:



The role of fluoride ions in the oxide formation and in its stability has been reported in literature.  $\text{ZrO}_2$  nanostructures formation in  $\text{F}^-$  containing electrolytes is the result of the competition between the electrochemical oxide formation and the chemical dissolution of said oxide

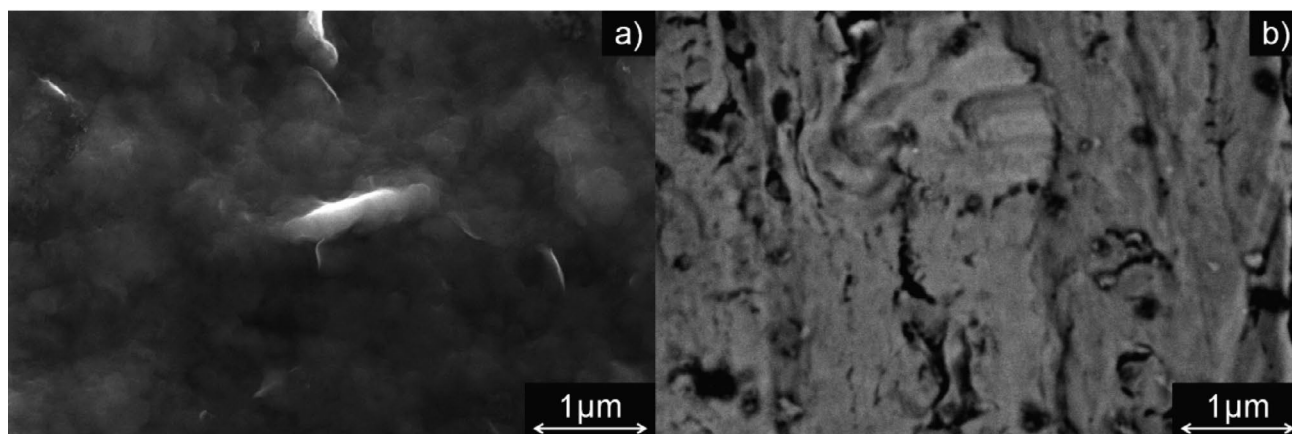


Fig. 1 SEM micrographies for Zr samples anodized at 5 V in a) E1; b) E2

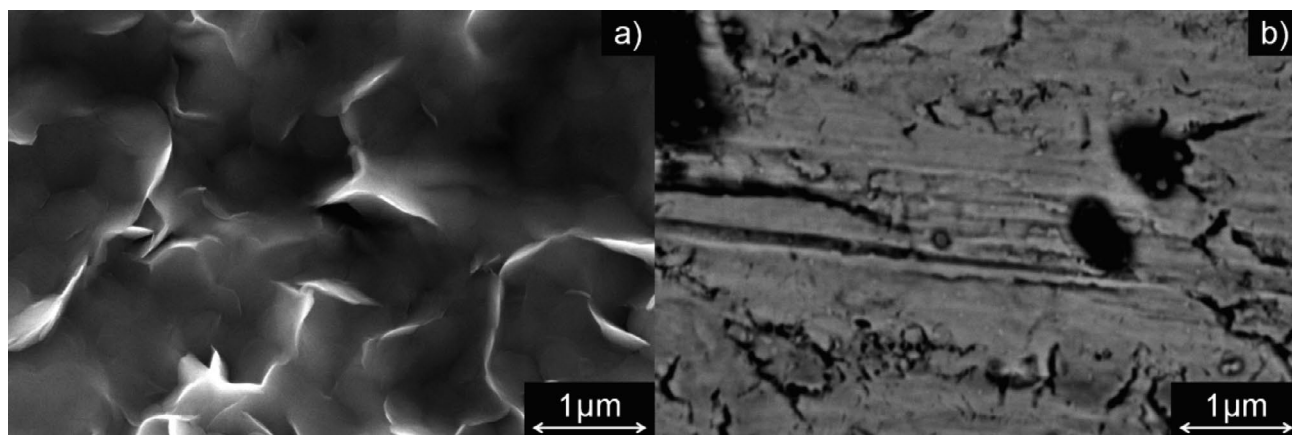


Fig. 2 SEM micrographies for Zr samples anodized at 15 V in a) E1; b) E2

through an intermediate stage where complex hexafluoro-zirconate anions form.

This oxide layer is covered in random cracks and incipient pores with diameters of around 100 nm start to appear.

At 15 V, anodizing in E1 led to a seemingly homogeneous surface shown in Fig. 2a. The two types of structures: semi-spheres (250 nm diameter) and ridges (length 300–800 nm and 60–100 nm width) are still present. However, in this case, the higher voltage led to an increased

process speed. As such, there are no remaining bubbles on the surface at the end of the anodizing process, although the sites are still observable. The bubbles, which formed on the surface, were smaller (around 10  $\mu\text{m}$  diameter) but denser. It is also evident that there are more  $\alpha$ -ZP structures formed and at this voltage, they begin to take their classical flaked, laminar and aggregated shapes. Electrolyte E2 produced at 15 V a surface similar to the one obtained at 5 V (Fig. 2b). The differences occur in the dimensions of the surface features. The oxide layer is similar in thickness,

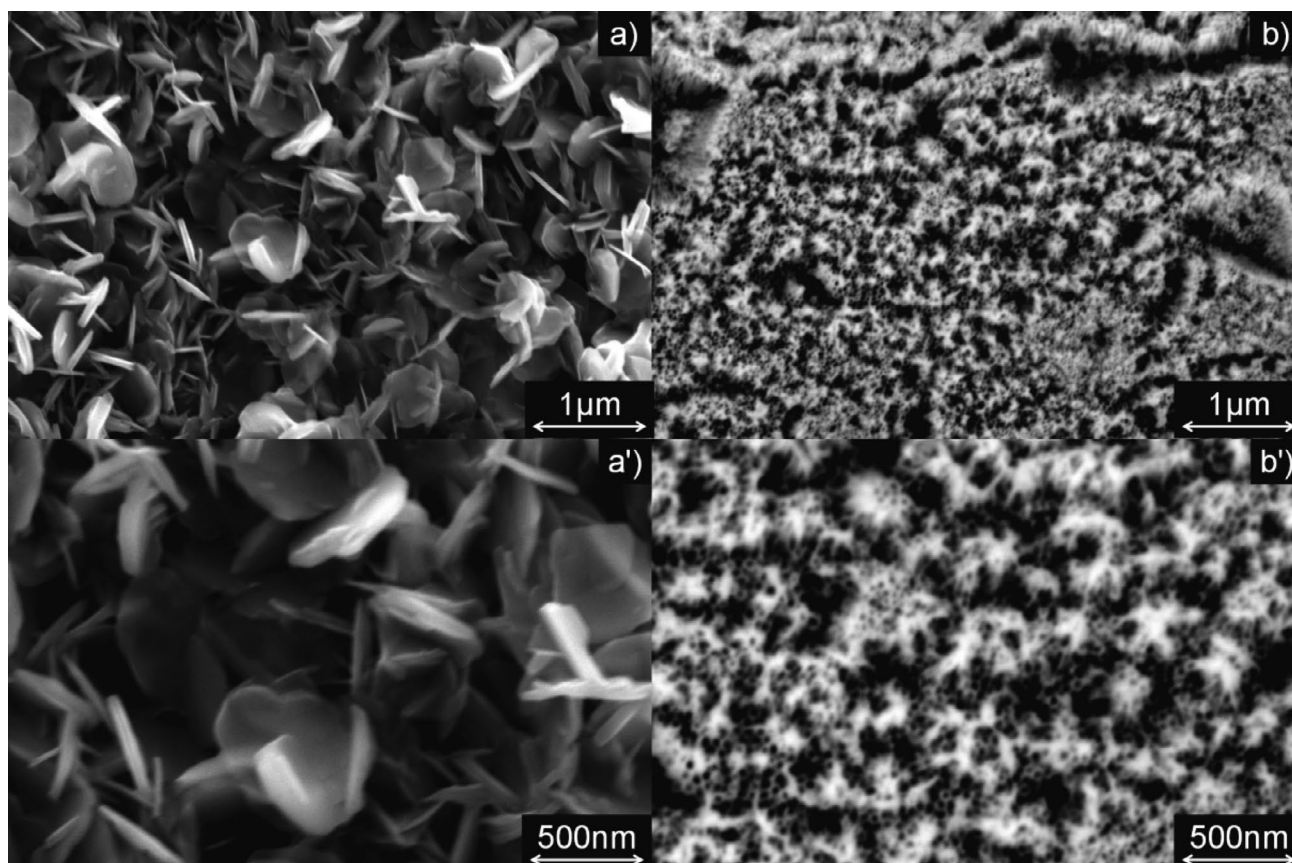


Fig. 3 SEM micrographies for Zr samples anodized at 45 V in a), a') E1; b), b') E2



but the cracks are deeper, wider, more numerous and the now well-formed pores have diameters between 100 nm and 4  $\mu\text{m}$ .

When the anodizing voltage was increased to 45 V the sample anodized in E1 was completely covered with  $\alpha$ -ZP structures (Fig. 3 a, a').

These quasi-hexagonal pellet structures had lengths of around 600 nm and thicknesses of around 80 nm and were not ordered in any particular direction. Underneath this stratum, a porous  $\text{ZrO}_2$  surface was found present, with uniform pores having diameters of around 200 nm. Anodizing in E2 led to the covering of the Zr sample with  $\text{ZrO}_2$  a mixture of nanopores, nanotubes and nanograss (Fig. 3 b, b'). Nanopores were observed on the thick initial oxide layer that hadn't dissolved totally at this voltage. The nanograss was found at the remaining boundary between the nanopore and nanotube layers and is probably a by-product of partial dissolution of the top porous layer. The nanotubes diameters range between 20 and 50 nm and the wall thickness is around 10 nm. Their length varies and are not particularly well organized. The tops of some of the nanotubes are covered and merge to form the nanograss.

At the highest studied anodizing voltage of 75 V, on the surface of the sample fabricated in E1 there are visible both  $\alpha$ -ZP structures and a  $\text{ZrO}_2$  surface covered with pores (Fig. 4a, a').

The  $\alpha$ -ZP structures are found in laminated aggregates formed by multiple pellets and have sizes from 0.17 to 1  $\mu\text{m}$  in length and 24 to 123 nm in thickness. The  $\text{ZrO}_2$  pores present on the surface have diameters of around 400 nm. Anodizing in E2 led to the formation of two surfaces covered in nanotubes (Fig. 4b, b'). The first surfaces is represented by the initial oxide layer that partially dissolved which is now covered with closely packed nanotubes with diameters around 28 nm and wall thicknesses around 10 nm. The second surface positioned just beneath the first is represented by new oxide formed and dissolved during the anodization process at equilibrium. This surface is covered with larger and better organized nanotubes with diameters of around 75 nm and wall thicknesses around 14 nm.

### 3. 2. FT-IR Analysis

The corresponding FT-IR spectra of the obtained samples are shown in Fig.5. For the sample anodized in E1, the spectra<sup>23</sup> exhibit the characteristics vibration bands from the phosphate group (Fig. 5a). The broad band around 3150  $\text{cm}^{-1}$  attributed to OH stretching of water molecules and the weak peak at around 1620  $\text{cm}^{-1}$  indicates the bending of the water molecules. More water seems to be present on samples obtained at lower voltages. The strong band centered around 960  $\text{cm}^{-1}$  corresponds to

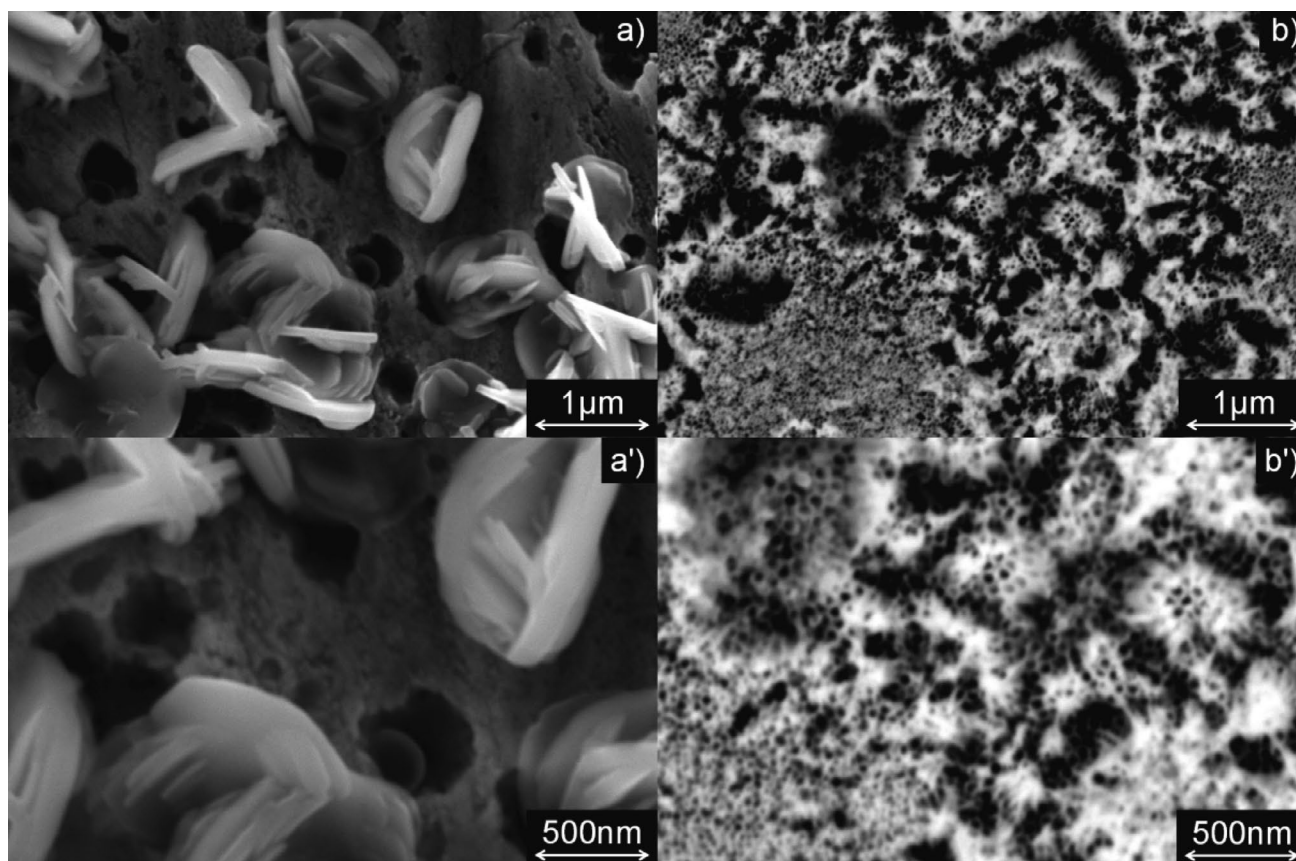


Fig.4 SEM micrographies for Zr samples anodized at 75 V in a), a') E1; b), b') E2

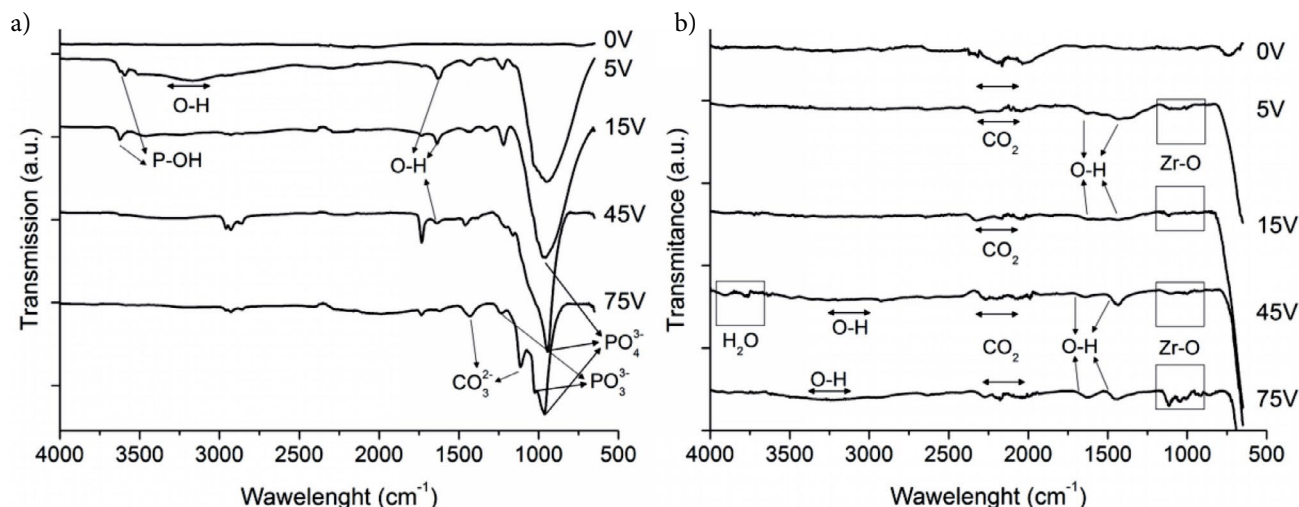


Fig. 5 FT-IR spectra for Zr samples covered with a) phosphates; b) oxides

some distorted tetrahedral phosphate groups in the nuclei of zirconium phosphates. The band at  $1126\text{ cm}^{-1}$  corresponds to the deformation vibrations of P-O bonding of the  $\text{PO}_3$  terminal groups. This band is only visible at the sample obtained at 75 V. Two bands at  $3660$  and  $3643\text{ cm}^{-1}$  are due to free and hydrogen bonded surface P-OH groups respectively and are more evident for samples obtained at 5V and 15V. In the region of phosphate vibrations spectra of all samples exhibits bands at  $1445$ ,  $1425$ ,  $1369$ ,  $1350$  and  $1208\text{ cm}^{-1}$ . These bands were observed in the FT-IR spectra of  $\alpha$ -ZP. The two weak, bands at  $1445$  and  $1425\text{ cm}^{-1}$  may be due to impurities of surface carbonate. The peaks attributed to phosphates become more well defined with the increase of the elaboration voltage.

The spectra anodized in E2 (Fig. 5b) show characteristic bands for  $\text{ZrO}_2$  covered surfaces. The band around  $3900\text{--}3600\text{ cm}^{-1}$  is characteristic for  $\text{H}_2\text{O}$ . The broad band around  $3150\text{ cm}^{-1}$  attributed to OH stretching of water molecules and the weak peak at around  $1620\text{ cm}^{-1}$  that indicates the bending of the water molecules is present on  $\text{ZrO}_2$  samples as well. At around  $2400\text{--}2200\text{ cm}^{-1}$  all samples show residues of  $\text{CO}_2$ . The absorption peaks of Zr-O vibrational bond are present for all the samples and the signal was found to be increasing with the anodizing voltage.

### 3. 3. Contact Angle Measurements

Contact angle measurements (Table 1) show that polished Zr is slightly hydrophilic. Samples covered with  $\alpha$ -ZP show a constant decrease of contact angle values with the increase of the anodizing voltage.  $\text{ZrO}_2$  samples show an increase of contact angle values at 5 V, reaching the limit of hydrophobicity, however, as the anodizing voltage increases, the contact angle values rapidly drop, reaching a state of super hydrophilicity at 75 V.

Table 1 Average contact angle values for Zr samples.

Applied voltage (V)	Contact angle ( $^\circ$ )	
	$\alpha$ -ZP	$\text{ZrO}_2$
0	$69.1 \pm 3.4$	$69.1 \pm 3.4$
5	$35.5 \pm 2$	$91 \pm 4.1$
15	$32.4 \pm 1.8$	$27.3 \pm 2.1$
45	$31.6 \pm 1.4$	$16 \pm 1.2$
75	$26.1 \pm 1.2$	$8.7 \pm 0.7$

### 3. 4. AFM Analysis

The roughness values (Ra) for the samples obtained in the two electrolytes are shown in Table 2.

Table 2 Average roughness values for Zr samples.

Applied voltage (V)	Ra (nm)	
	$\alpha$ -ZP	$\text{ZrO}_2$
0	$36 \pm 4$	$36 \pm 4$
5	$358 \pm 16.9$	$85 \pm 5.5$
15	$178 \pm 9.2$	$36 \pm 2.6$
45	$127 \pm 8.1$	$40 \pm 3.1$
75	$154 \pm 8.7$	$29 \pm 1.9$

As can be noticed, the values for the roughness of the samples covered with  $\alpha$ -ZP structures are around 4 times higher than those obtained for the samples covered with  $\text{ZrO}_2$  nanotubes. However, the trend is similar, both types of samples experiencing an increase of roughness at 5 V, followed by a steady decrease as the voltage rises. This phenomenon can be attributed to the balance between phosphate/oxide formation and dissolution on and from the

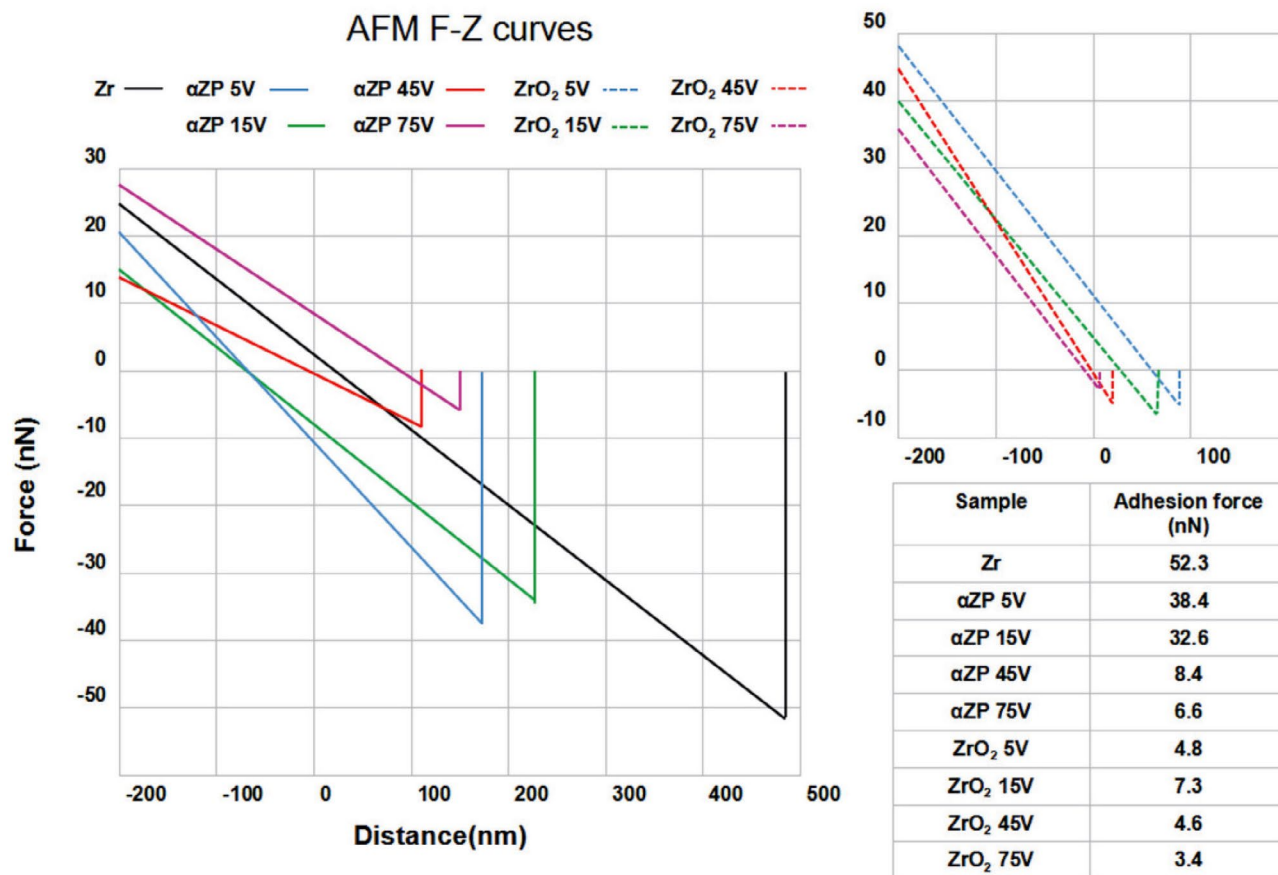


Fig. 6 Normalized median values for AFM tip adhesion forces (F-Z curves)

samples surfaces during anodizing that is dependent on the applied voltage.

The normalized median values for the adhesion force measured with the AFM are shown as F-Z diagrams in Fig. 6. Polished Zr has the highest adhesion force, probably given by the smooth surface. This force is also active a great distance from the surface, the AFM tip being affected at around 480 nm from the surface. Samples covered with α-ZP structures have smaller attraction forces than bare Zr. The forces values and action range decrease steadily with the voltage.

The adhesion force measured by AFM experienced a decreasing trend with the increase of the sample elaboration voltage, suggesting the formed phosphate was the primary responsible for the reduction of the adhesion forces. Thin crystalline phosphates are produced on the Zr surface, the phosphate coating reducing the frictional force produced through shaping, drawing or slip processes. ZrO<sub>2</sub> samples have the smallest forces that act only close to the surface. The capillaries on the surface provide better absorbent qualities, yielding different general surface qualities. The system formed by the SiC AFM tip and the surface of the samples experiences repulsive interactions mostly because of hydration forces which generate

a decrease in friction coefficients and adhesion forces. The two surfaces seem to have different hardness levels, ZrO<sub>2</sub> surfaces producing higher displacements of the AFM tip than α-ZP surfaces at the maximum indentation depth.

Fig. 7 shows the probable film forming mechanism for α-ZP and ZrO<sub>2</sub> structures covered surfaces. From the gathered data, we deduced that competing phenomena are occurring on the surface during the anodizing process in both cases. These processes are: forming of Zr phosphates and/or oxides (depending on the electrolyte), dissolution of  $\text{ZrF}_6^{2-}$  complexes from the surface and forming of auto-organized zirconium compound structures. Regardless of the used electrolyte, these phenomena are influenced by the anodizing voltage which changes the balance and the speeds at which these phenomena occur, leading to different results. As was largely described in the literature,<sup>22</sup> anodizing parameters such as time, voltage, temperature and most important anodizing electrolyte composition are critical for the resulting desired morphologies. The composition of the sample surface seems to be less affected by the anodizing potential, instead being directly affected by the electrolyte composition.

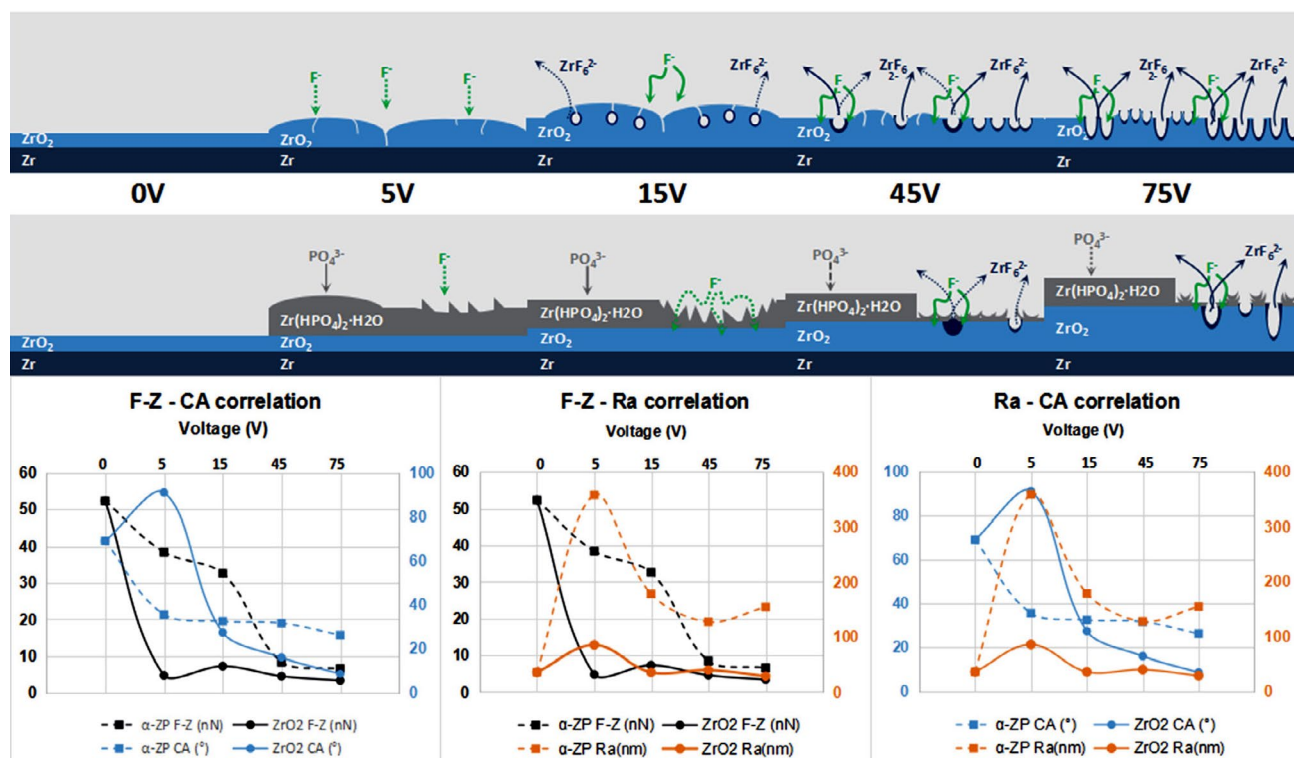


Fig. 7 Proposed film forming mechanism for  $\alpha$ -ZP and  $\text{ZrO}_2$  and correlation of analyzed surface properties

## 4. Conclusions

The SEM and AFM investigations revealed that structures with various sizes and shapes can be obtained by modifying the anodizing both the voltage and the electrolyte. On the surface of Zr anodized in  $\text{H}_3\text{PO}_4$   $\alpha$ -ZP flake structures were obtained. These structures became more organized with the increase of the voltage and, at higher voltages,  $\text{ZrO}_2$  pores began to form. When glycerol used, the formation of auto-organized nanotubes was found to be directly dependent on the applied voltage. The roughness is influenced by the type as well as by the degree of homogeneity of structures formed on the surfaces. The wettability and the AFM micro adhesion forces and roughness values can be correlated to some degree for both samples. In the case of orthopedic and dental implants it is usually reported that hydrophilic materials have higher biocompatibility, facilitating initial interaction between the biomaterial and the biofluids, thus promoting osseointegration. Roughness has a major role in the wettability of a biomaterial as well in the subsequent cell interaction with the implant surface. Based on all experimental data, a film forming mechanism for  $\alpha$ -ZP and  $\text{ZrO}_2$  was proposed and correlated to analyzed surface properties. From a physical concept, these results enable the understanding of the optimal properties needed for the development of damage-tolerant thin films leading to practical applications.

## Acknowledgments

This work was supported by the Romanian Government National Council of Scientific Research in Higher Education (CNCSIS) – Executive Unit for Financing Higher Education, Research, Development and Innovation (UEFISCDI), project number PN-III-P4-ID PCE 2016-0316.

## 5. References

1. B. Cox, *J. Nucl. Mater.* **2005**, 336, 331–368.
2. A. Gomez-Sanchez, M. Katunar, W. Schreiner, G. Duffó, S. Cere, D. J. Schiffrin, *Acta Chim. Slov.* **2014**, 61, 316–327. DOI:10.1016/j.jnucmat.2004.09.029
3. E. Ivers-Tiffée, K. H. Hardtl, W. Menesklou, J. Riegel, *Electrochim. Acta* **2001**, 47, 807–814. DOI:10.1016/S0013-4686(01)00761-7
4. Q. Zhang, J. Shen, Wang, G. Wu, L. Chen, *Int. J. Inorg. Mater.* **2000**, 2, 319–323. DOI:10.1016/S1466-6049(00)00037-4
5. A. I. Ahmed, S. A. El-Hakam, S. E. Samra, A. A. El-Khouly, A. S. Khder, *Colloids Surf. A Physicochem. Eng. Asp.* **2008**, 317, 62–70. DOI:10.1016/j.colsurfa.2007.09.043
6. H. J. Cho, G. M. Choi, *J. Power Sources* **2008**, 176, 96–101. DOI:10.1016/j.jpowsour.2007.09.118
7. D. E. Romonti, A. Gomez Sanchez, I. Milosev, I. Demetrescu, S. Cere, *Mater. Sci. Eng. C*, **2016**, 62, 458–466.

- DOI:10.1016/j.msec.2016.01.079
8. G. O. Buica, A. B. Stoian, D. Ionita, I. Demetrescu *Mater. Corros.* **2018**, 69, 1713–1719. DOI:10.1002/maco.201810277
  9. A. Gomez Sanchez, J. Ballarre, J. C. Orellano, G. Duffó, S. Cere, J. Mater. Sci. Mater. Med., **2013**, 24, 161–169. DOI:10.1007/s10856-012-4770-8
  10. M. Mindroiu, E. Cicek, F. Miculescu, I. Demetrescu, *Rev. Chim. Bucharest* **2007**, 58, 898–903.
  11. I. Milošev, B. Kapun, V. S. Šelih, *Acta Chim. Slov.* **2013**, 60, 543–555.
  12. C. Vasilescu, S. I. Drob, P. Osiceanu, J. M. Calderon Moreno, M. Prodana, D. Ionita, I. Demetrescu, M. Marcu, I. A. Popovici, E. Vasilescu *Metall and Mat. Trans. A*, **2017**, 48, 513–523. DOI:10.1007/s11661-016-3774-2
  13. A. B. Stoian, M. Vardaki, D. Ionita, M. Enachescu, O. Brancoveanu, I. Demetrescu, *Ceram. Int.*, **2018**, 44, 7026–7033. DOI:10.1016/j.ceramint.2018.01.137
  14. S. Minagar, C. C. Berndt, J. Wang, E. Ivanowa, C. Wen, *Acta Biomater.* **2012**, 8, 2875–2888. DOI:10.1016/j.actbio.2012.04.005
  15. T. Hanawa, Y. Tsutsumi, *Bioceram. Dev. Appl.*, **2010**, 1, DOI:10.1007/s11661-016-3774-2
  16. K. Segawa, S. Nakata, S. Asaoka, *Mater. Chem. Phys.* **1987**, 17, 181–200. DOI:10.1016/0254-0584(87)90055-1
  17. C. Kumar, A. Chaudhari, G. Rosenthal, *J. Am. Chem. Soc.* **1994**, 116, 403–404. DOI:10.1021/ja00080a059
  18. H. Xiao, S. Liu *Mater. Des.* **2018**, 155, 19–35. DOI:10.1016/j.matdes.2018.05.041
  19. M. Pica, A. Donnadio, M. Casciola, *Coord. Chem. Rev.* **2018**, 374, 218–235. DOI:10.1016/j.ccr.2018.07.002
  20. W. Jang, J. He, J. Zhong, J. Lu, S. Yuan, B. Liang, *Appl. Surf. Sci.*, **2014**, 307, 407–413. DOI:10.1016/j.apsusc.2014.04.047
  21. K. Yasuda, J. M. Macak, S. Berger, A. Ghicov, P. Schmuki, *J. Electrochem. Soc.* **2007**, 154, C472–C478. DOI:10.1149/1.2749091
  22. M. Kulkarni, A. Mazare, P. Schmuki, A. Iglic, *Adv. Mater. Lett.*, **2016**, 7, 23–28. DOI:10.5185/amlett.2016.6156
  23. F. Muratore, A. Baron-Wiechéc, T. Hashimoto, A. Gholinia, P. Skeldon, G. E. Thompson, *Electrochim. Acta*, **2011**, 56, 10500–10506. DOI:10.1016/j.electacta.2010.12.089
  24. X. g He, H. Xiao, H. Choi, A. Díaz, B. Mosby, A. Clearfield, H. Liang, *Colloids. Surf. A* **2014**, 452, 32–38. DOI:10.1016/j.colsurfa.2014.03.041

## Povzetek

Pričujoče delo obravnava morfologijo in lastnosti anodiziranega Zr v dveh različnih elektrolitih. Cirkonijev fosfat ( $\alpha$ -ZP) smo pripravili v anorganskem elektrolitu, ki je vseboval  $\text{H}_3\text{PO}_4$  in NaF. Nano cirkonijev oksid ( $\text{ZrO}_2$ ) smo pripravili v elektrolitu na osnovi glicerola. Spojini smo karakterizirali z naslednjimi metodami vrstično elektronsko mikroskopijo (SEM), infrardečo spektroskopijo (FT-IR) in mikroskopom na atomsko silo (AFM). Analizo površine smo preiskovali tudi z meritvami kontaktnih kotov. Ugotovili smo, da vrsta elektrolita skupaj z uporabljenjo napetostjo vpliva na strukturo vzorca. Anodna oksidacija v elektrolitu  $\text{H}_3\text{PO}_4$  pospešuje nastanek in razvoj luskastih struktur in sčasoma por s povečanjem uporabljene napetosti. Pri procesu anodne oksidacije v elektrolitu na osnovi glicerola pa nastajajo nanoporozne strukture, ki se pri naraščanju napetosti razvijajo v nanocevke. Na podlagi eksperimentalnih podatkov smo predlagali mehanizma za oblikovanje  $\alpha$ -ZP in  $\text{ZrO}_2$  v povezavi z analiziranimi lastnostmi površin.



Except when otherwise noted, articles in this journal are published under the terms and conditions of the Creative Commons Attribution 4.0 International License



# Synthesis, Crystal Structures and Catalytic Property of Dioxomolybdenum(VI) and Nickel(II) Complexes Derived from bis-Schiff Bases

Ling-Wei Xue,\* Qin-Long Peng, Pan-Pan Wang, Hui-Jie Zhang

College of Chemistry and Chemical Engineering, Pingdingshan University, Pingdingshan Henan 467000, P.R. China

\* Corresponding author: E-mail: pdsuchemistry@163.com

Received: 03-26-2019

## Abstract

A new mononuclear dioxomolybdenum(VI) complex,  $[\text{MoO}_2\text{L}^1]$ , and a new linear trinuclear nickel(II) complex,  $[\text{Ni}\{\text{NiL}^2(\mu_1\text{-}\eta^1\text{-}\eta^0\text{-OAc})(\mu_2\text{-}\eta^1\text{-}\eta^1\text{-OAc})\}_2] \cdot \text{H}_2\text{O}$ , where  $\text{L}^1$  is the dianionic form of *N,N'*-bis(5-fluorosalicylidene)-1,3-propanediamine ( $\text{H}_2\text{L}^1$ ),  $\text{L}^2$  is the dianionic form of *N,N'*-bis(5-fluoro-2-hydroxybenzylidene)-2-hydroxy-1,3-propanediamine ( $\text{H}_2\text{L}^2$ ), have been synthesized and characterized by elemental analysis, FT-IR spectroscopy, and single-crystal X-ray determination. The Mo atom in the molybdenum complex is coordinated by four donor atoms of the Schiff base ligand, and two oxo groups, forming an octahedral coordination. In the nickel complex, there are three bridges across the Ni-Ni atom pairs, involving two phenolate O atoms of a Schiff base ligand, and an O-C-O moiety of a  $\mu_2\text{-}\eta^1\text{-}\eta^1\text{-OAc}$  group. The central Ni atom is located on an inversion center and has octahedral coordination involving four bridging O atoms from two Schiff base ligands in the equatorial plane and two O atoms from two  $\mu_2\text{-}\eta^1\text{-}\eta^1\text{-OAc}$  ligands in the axial positions. The coordination around the terminal Ni atoms is also octahedral, with two imino N and two phenolate O atoms from a Schiff base ligand defining the equatorial plane, and with two O atoms respectively from a  $\mu_1\text{-}\eta^1\text{-}\eta^0\text{-OAc}$  and a  $\mu_2\text{-}\eta^1\text{-}\eta^1\text{-OAc}$  ligands occupying the axial positions. The molybdenum complex has excellent catalytic property for sulfoxidation reactions.

**Keywords:** Dioxomolybdenum complex; nickel complex; Schiff base; Crystal structure; Sulfoxidation

## 1. Introduction

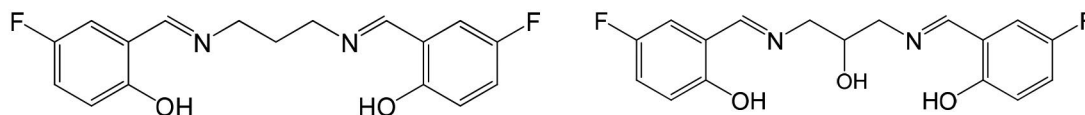
Molybdenum and nickel complexes with multi-dentate ligands have received remarkable attention in recent years for their catalytic properties<sup>1</sup> and molecular structures.<sup>2</sup> Salicylaldehyde and its derivatives have been widely used as ligands for the preparation of metal complexes with various applications.<sup>3</sup> A large number of molybdenum and nickel complexes with Schiff bases have been reported.<sup>4</sup> Some of the complexes have shown oxygen atom transfer properties as they were found to oxidize thiols, hydrazine, polyketones, and tertiary phosphines.<sup>5</sup> Recently, we have reported some molybdenum and manganese complexes derived from hydrazone type ligands, and show interesting catalytic properties.<sup>6</sup> We report in this paper the syntheses, crystal structures and catalytic property of a

new dioxomolybdenum(VI) complex,  $[\text{MoO}_2\text{L}^1]$ , and a new linear trinuclear nickel(II) complex,  $[\text{Ni}\{\text{NiL}^2(\mu_1\text{-}\eta^1\text{-}\eta^0\text{-OAc})(\mu_2\text{-}\eta^1\text{-}\eta^1\text{-OAc})\}_2] \cdot \text{H}_2\text{O}$ , where  $\text{L}^1$  is the dianionic form of *N,N'*-bis(5-fluorosalicylidene)-1,3-propanediamine ( $\text{H}_2\text{L}^1$ ),  $\text{L}^2$  is the dianionic form of *N,N'*-bis(5-fluoro-2-hydroxybenzylidene)-2-hydroxy-1,3-propanediamine ( $\text{H}_2\text{L}^2$ ; Scheme 1).

## 2. Experimental

### 2.1. Materials and Methods

5-Fluorosalicylaldehyde, propane-1,3-diamine and 2-hydroxy-1,3-propanediamine were purchased from Fluka. Other reagents and solvents were analytical grade



Scheme 1. The Schiff base ligands  $\text{H}_2\text{L}^1$  and  $\text{H}_2\text{L}^2$



and used without further purification. The Schiff bases  $H_2L^1$  was prepared according to the literature method.<sup>7</sup> Elemental (C, H, and N) analyses were made on a Perkin-Elmer Model 240B automatic analyzer. IR spectra were recorded on an IR-408 Shimadzu 568 spectrophotometer.  $^1H$  NMR spectra were recorded on a Bruker 300 MHz instrument.

## 2. 2. Synthesis of $H_2L^2$

5-Fluorosalicylaldehyde (2.0 mmol, 0.28 g) was dissolved in methanol (20 mL), to which was added dropwise a methanol solution (10 mL) of 2-hydroxy-1,3-propanediamine (1.0 mmol, 0.090 g) with stirring at room temperature. The mixture was stirred at room temperature for 30 min, and most of the solvent was removed by distillation. The yellow crystalline product was obtained by filtration. Yield: 93%. IR data ( $cm^{-1}$ , KBr): 3370m, 1638s, 1587s, 1492s, 1450w, 1387w, 1318w, 1263s, 1216m, 1142m, 1090w, 1040m, 966w, 878m, 822s, 784s, 673w, 577w, 456w.  $^1H$  NMR (300 MHz, DMSO)  $\delta$  12.72 (s, 2H, OH), 8.51 (s, 2H, CH=N), 7.35 (dd,  $J$  = 8.9, 3.1 Hz, 2H, ArH), 7.19 (td,  $J$  = 8.7, 3.2 Hz, 2H, ArH), 6.89 (dd,  $J$  = 9.0, 4.5 Hz, 2H, ArH), 4.04 (s, 1H, OH), 3.79 (dd,  $J$  = 12.1, 4.0 Hz, 2H,  $CH_2$ ), 3.61 (dd,  $J$  = 12.1, 6.6 Hz, 2H,  $CH_2$ ).  $^{13}C$  NMR (75 MHz, DMSO)  $\delta$  156.98, 156.12, 153.02, 119.32, 119.01, 118.81, 116.71, 69.22, 62.87. Anal. Calcd. (%) for  $C_{17}H_{16}F_2N_2O_3$ : C, 61.07; H, 4.82; N, 8.38. Found (%): C, 61.26; H, 4.73; N, 8.29.

## 2. 3. Synthesis of the Molybdenum Complex

$MoO_2(acac)_2$  (0.1 mmol, 33.5 mg) in methanol (10 mL) was added with stirring to  $H_2L$  (0.1 mmol, 31.8 mg) in methanol (10 mL). The mixture was stirred at refluxed for 30 min to give a yellow solution. The solution was left still at room temperature in air to give yellow block-shaped single crystals, which were collected by filtration and dried in vacuum containing anhydrous  $CaCl_2$ . Yield: 52%. IR data ( $\nu$ ,  $cm^{-1}$ ): 1621 s, 1547 m, 1471 s, 1381 m, 1266 s, 1153 s, 1076 w, 977 m, 895 m, 820 m, 743 w, 703 w, 659 w, 620 w, 571 w, 515 w, 449 w, 415 w. UV-vis data in methanol [ $\lambda_{max}$  (nm),  $\epsilon$  ( $L\ mol^{-1}\ cm^{-1}$ )]: 270, 12380; 325, 9310; 420, 2115. Anal. Calcd. (%) for  $C_{17}H_{14}F_2MoN_2O_4$ : C, 45.96; H, 3.18; N, 6.31. Found (%): C, 45.75; H, 3.27; N, 6.24.

## 2. 4. Synthesis of the Nickel Complex

$H_2L^2$  (0.3 mmol, 100.2 mg) was dissolved in methanol (20 mL), to which was added a methanol-water solution (20 mL, V:V = 10:1) of nickel acetate tetrahydrate (0.5 mmol, 124.5 mg) with stirring. The mixture was stirred at room temperature for 30 min to give a green solution, which was kept still to slow evaporate of the solvents. Green block-like single crystals suitable for X-ray diffraction were formed. Yield: 37%. IR data ( $\nu$ ,  $cm^{-1}$ ): 3426 w,

1634 s, 1563 s, 1472 s, 1425 m, 1398 m, 1302 m, 1252 w, 1213 w, 1147 m, 1059 w, 957 w, 862 w, 817 s, 679 w, 616 w, 574 w, 475 w. UV-vis data in methanol [ $\lambda_{max}$  (nm),  $\epsilon$  ( $L\ mol^{-1}\ cm^{-1}$ )]: 361, 41900; 255, 48010; 235, 49132. Anal. Calcd. (%) for  $C_{42}H_{42}F_4N_4Ni_3O_{15}$ : C, 46.07; H, 3.87; N, 5.12. Found (%): C, 45.88; H, 3.97; N, 5.26.

## 2. 5. X-ray Diffraction

Data were collected from selected crystals mounted on a glass fiber. The data for the complexes were processed with SAINT<sup>8</sup> and corrected for absorption using SADABS.<sup>9</sup> Multi-scan absorption corrections were applied with  $\omega$  scans.<sup>10</sup> The structures of the complexes were solved by direct method using SHELXS-97 program and refined by full-matrix least-squares techniques on  $F^2$  using anisotropic displacement parameters.<sup>11</sup> All non-hydrogen atoms were refined anisotropically. The water H atoms in the nickel complex were located in a difference Fourier map and refined isotropically, with O–H and H...H distances restrained to 0.85(1) and 1.37(2) Å, respectively. The remaining hydrogen atoms were placed at the calculated positions. The C8–C9–C10–O7 moiety in the nickel complex is disordered over two sites, with occupancies of 0.532(3) and 0.468(3). Crystallographic data for the complex are listed in Table 1. Selected bond lengths and angles are given in Table 2.

**Table 1.** Crystallographic data and structure refinement for the complexes

	The molybdenum complex	The nickel complex
Molecular formula	$C_{17}H_{14}F_2MoN_2O_4$	
$C_{42}H_{42}F_4N_4Ni_3O_{15}$		
Formula weight	444.24	1094.93
Crystal system	Monoclinic	Monoclinic
Space group	$P2_1/c$	$P2_1/n$
$a$ , Å	10.689(2)	12.548(1)
$b$ , Å	17.327(2)	13.188(1)
$c$ , Å	9.001(1)	15.065(1)
$\beta$ , °	103.175(2)	112.789(3)
$V$ , Å <sup>3</sup>	1623.2(4)	2298.3(4)
$Z$	4	2
$F(000)$	888	1124
$\mu(MoK\alpha)$ , mm <sup>-1</sup>	0.857	1.305
Collected reflections	14985	21744
Independent reflections	2885	4270
Observed reflections ( $I \geq 2\sigma(I)$ )	2494	3077
Restraints/parameters	0/235	17/342
Goodness of fit on $F^2$	1.063	1.056
$R_{int}$	0.0285	0.0439
$R_1$ , $wR_2$ ( $I \geq 2\sigma(I)$ ) <sup>*</sup>	0.0248, 0.0570	0.0588, 0.1660
$R_1$ , $wR_2$ (all data) <sup>*</sup>	0.0330, 0.0607	0.0876, 0.1914
$\Delta\rho_{max}$ , $\Delta\rho_{min}$ , $e\ \text{\AA}^{-3}$	0.303, -0.354	1.028, -0.665

<sup>\*</sup>  $R_1 = \sum ||F_o| - |F_c|| / \sum |F_o|$ ,  $wR_2 = [\sum w(F_o^2 - F_c^2)^2 / \sum w(F_o^2)^2]^{1/2}$ .

Table 2. Selected bond lengths (Å) and angles (°) for the complexes

The molybdenum complex			
Mo(1)–O(1)	1.9290(17)	Mo(1)–O(2)	2.0935(17)
Mo(1)–O(3)	1.7016(17)	Mo(1)–O(4)	1.7040(18)
Mo(1)–N(1)	2.317(2)	Mo(1)–N(2)	2.169(2)
O(3)–Mo(1)–O(4)	104.27(9)	O(3)–Mo(1)–O(1)	102.08(8)
O(4)–Mo(1)–O(1)	101.45(9)	O(3)–Mo(1)–O(2)	89.80(8)
O(4)–Mo(1)–O(2)	159.93(8)	O(1)–Mo(1)–O(2)	89.22(7)
O(3)–Mo(1)–N(2)	93.80(8)	O(4)–Mo(1)–N(2)	86.32(9)
O(1)–Mo(1)–N(2)	159.85(8)	O(2)–Mo(1)–N(2)	78.42(7)
O(3)–Mo(1)–N(1)	168.13(8)	O(4)–Mo(1)–N(1)	85.67(8)
O(1)–Mo(1)–N(1)	81.88(7)	O(2)–Mo(1)–N(1)	79.00(7)
N(2)–Mo(1)–N(1)	80.19(8)		
The nickel complex			
Ni(1)–O(1)	2.061(3)	Ni(1)–O(2)	2.053(3)
Ni(1)–O(6)	2.044(4)	Ni(2)–O(1)	1.995(3)
Ni(2)–O(2)	1.990(3)	Ni(2)–O(3)	2.177(5)
Ni(2)–O(5)	2.066(5)	Ni(2)–N(1)	2.014(4)
Ni(2)–N(2)	2.016(5)		
O(6)–Ni(1)–O(6A)	180	O(6)–Ni(1)–O(2)	89.0(2)
O(6)–Ni(1)–O(2A)	91.0(2)	O(2)–Ni(1)–O(2A)	180
O(6)–Ni(1)–O(1)	90.1(1)	O(6)–Ni(1)–O(1A)	89.9(1)
O(2)–Ni(1)–O(1)	79.4(1)	O(2)–Ni(1)–O(1A)	100.6(1)
O(1)–Ni(1)–O(1A)	180	O(2)–Ni(2)–O(1)	82.5(1)
O(2)–Ni(2)–N(1)	172.8(2)	O(1)–Ni(2)–N(1)	90.8(2)
O(2)–Ni(2)–N(2)	90.2(2)	O(1)–Ni(2)–N(2)	171.5(2)
N(1)–Ni(2)–N(2)	96.2(2)	O(2)–Ni(2)–O(5)	91.3(2)
O(1)–Ni(2)–O(5)	90.7(2)	N(1)–Ni(2)–O(5)	91.5(2)
N(2)–Ni(2)–O(5)	93.8(2)	O(2)–Ni(2)–O(3)	92.6(2)
O(1)–Ni(2)–O(3)	90.2(2)	N(1)–Ni(2)–O(3)	84.7(2)
N(2)–Ni(2)–O(3)	85.8(2)	O(5)–Ni(2)–O(3)	176.2(2)

## 2. 6. Catalytic Oxidation

The complexes ( $0.001 \text{ mol L}^{-1}$ ) and phenyl methyl sulfide ( $0.100 \text{ mol L}^{-1}$ ) were dissolved at room temperature in a mixture of  $\text{CH}_2\text{Cl}_2$  and  $\text{CH}_3\text{OH}$  (6:4) together with 1,3,5-trimethoxybenzene ( $0.100 \text{ mol L}^{-1}$ ) as internal standard. The resulting solution was cooled to 283 K and  $\text{H}_2\text{O}_2$  (35% w/w) added dropwise ( $0.125 \text{ mol L}^{-1}$ ). An aliquot of the reaction solution (2.0 mL) was quenched with 5.0 mL of a stock solution of  $\text{Na}_2\text{SO}_3$  ( $0.100 \text{ mol L}^{-1}$ ) and extracted with dichloromethane (three times 4 mL). From the collected organic phases the solvent was removed under reduced pressure to complete dryness and the residue redissolved in deuterated chloroform (0.60 mL) and analyzed by  $^1\text{H}$  NMR to determine the yield with reference to the internal standard 1,3,5-trimethoxybenzene.

## 3. Results and Discussion

### 3. 1. Chemistry

Reaction of the Schiff base  $\text{H}_2\text{L}^1$  with  $\text{MoO}_2(\text{acac})_2$ , and  $\text{H}_2\text{L}^2$  with  $\text{Ni}(\text{CH}_3\text{COO})_2$ , respectively, afforded the molybdenum and nickel complexes. The complexes are

soluble in DMF, DMSO, methanol, ethanol and acetonitrile. We have attempted to grow diffraction quality crystals from various solvents, however, well-shaped single crystals suitable for X-ray diffraction can only be obtained from methanol solution.

### 3. 2. Structure Description of the Molybdenum Complex

The molecular structure of the complex is shown in Fig. 1. The coordination geometry around the Mo atom in the complex is octahedrally distorted. The Schiff base ligand coordinates to the Mo atom through two phenolate O and two imino N atoms, forming three six-membered chelate rings with the Mo atom. The other two sites are coordinated by two oxo groups. Atoms O(1), N(1), N(2) and O(3) located at the equatorial plane show a high degree of planarity, with mean deviation from the plane of  $0.002(3) \text{ Å}$ . The Mo(1) atom deviates from the least-squares plane defined by the four equatorial donor atoms by  $0.185(2) \text{ Å}$  in the direction of the axial atom O(4). The angular distortion in the octahedral coordination comes from the bites O(2)–Mo(1)–O(4) [ $159.93(8)^\circ$ ] and O(1)–

Mo(1)–N(2) [159.85(8)°]. The dihedral angle between the two benzene rings of the Schiff base ligand is 112.0(5)°. In the complex, the coordinate bond lengths are comparable to those observed in molybdenum complexes with Schiff base ligands.<sup>12</sup> The Mo(1)–O(2) and Mo(1)–N(1) bonds are much longer than usual, which is caused by the *trans* effects of the Mo=O bonds. The Mo=O bonds are also longer than usual, which might be caused by the formation of hydrogen bonds with adjacent groups (Table 3). In the crystal of the complex, molecules are linked through intermolecular C–H...O hydrogen bonds (Table 3), to form a three-dimensional network (Fig. 2).

### 3. 3. Structure Description of the Nickel Complex

The molecular structure of the complex is shown in Fig. 3. The asymmetric unit of the compound contains a linear trinuclear nickel(II) complex molecule and a water molecule of crystallization. The molecule of the complex possesses crystallographic two-fold rotation axis symmetry, with the inversion center located at the site of Ni(1) atom. There are three bridges across the Ni...Ni atom pairs, involving two phenolate O atoms of a Schiff base ligand, and an O–C–O moiety of a  $\mu_2$ - $\eta^1$ : $\eta^1$ -OAc group. The acetate bridges linking the central and terminal nickel atoms are mutually *trans*. The trinuclear nickel complex molecule consists of two NiL units connected to each other by a completely encapsulated third metal atom, Ni(1). The adjacent Ni(1)...Ni(2) distance is 3.018(1) Å.

The cage of Ni(1) is formed by phenolate bridges, O(1) and O(2), from the Schiff base ligands, and by two O atoms from two  $\mu_2$ - $\eta^1$ : $\eta^1$ -OAc ligands that furthermore connect the central metal with the two outer metal atoms resulting in an octahedral environment. The coordination around Ni(1) atom displays only slight distortion. The bond distances Ni–O are relatively similar and range from 2.044(4) to 2.061(3) Å. The greatest deviation of the bond angles from those expected for an ideal octahedral geometry is found for O(1)–Ni(1)–O(2) with 79.4(1)°, and O(1)–Ni(1)–O(2A) with 100.6(1)°. The remaining bond angles are close to the ideal values for the octahedral coordination.

The coordination around the inversion-related terminal Ni atoms is also octahedral, with two imino N and

two phenolate O atoms from a Schiff base ligand defining the equatorial plane, and with two O atoms respectively from a  $\mu_1$ - $\eta^1$ : $\eta^0$ -OAc and a  $\mu_2$ - $\eta^1$ : $\eta^1$ -OAc ligands occupying the axial positions. The coordination around the terminal metal atoms also displays slight distortion. The greatest deviation of the bond angles from those expected for an ideal octahedral geometry is O(1)–Ni(2)–O(2) (82.5(1)°), which is caused by the strain created by the four-membered chelate ring Ni(1)–O(1)–Ni(2)–O(2).

The NiL units in the complex are butterfly-shaped, with the dihedral angles formed by the two benzene rings of the Schiff base ligands of 57.5(5)°. In the crystal structure of the complex (Fig. 4), the methanol molecules are linked to the nickel complex molecules through O–H...O hydrogen bonds (Table 3). In addition, there are  $\pi$ ... $\pi$  stacking interactions among the benzene rings defined by atoms C(1)/C(2)/C(3)/C(4)/C(5)/C(6) and C(12A)/C(13A)/C(14A)/C(15A)/C(16A)/C(17A) [symmetry code for A:  $-x, 1-y, 1-z$ ; centroid-centroid distance 4.873(3) Å, the angle between the planes 57°; the perpendicular distance between the planes 3.593(6) Å] in the complex.

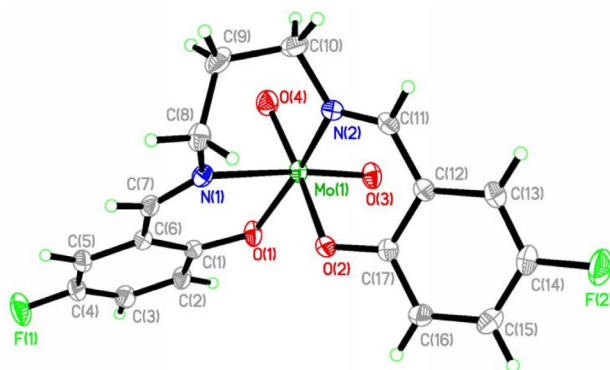


Fig. 1. Molecular structure of the molybdenum complex at 30% probability thermal ellipsoids.

### 3. 4. IR and UV-Vis Spectra

In the infrared spectra of the free Schiff bases, there showed stretching band attributed to C=N and OH at 1638–1645 and 3370  $\text{cm}^{-1}$ , respectively. In the spectra of the complexes, the  $\nu_{\text{C=N}}$  bands were observed at lower fre-

Table 3. Distances (Å) and angles (°) involving hydrogen bonding of the complexes

D–H...A	d(D–H)	d(H...A)	d(D...A)	Angle(D–H...A)
The molybdenum complex				
C(3)–H(3)...O(3) <sup>i</sup>	0.93	2.57(3)	3.1980(6)	125(4)
C(10)–H(10A)...O(4)	0.97	2.53(3)	2.8760(5)	101(5)
C(11)–H(11)...O(3) <sup>ii</sup>	0.93	2.48(4)	3.1287(6)	127(5)
C(13)–H(13)...O(4) <sup>ii</sup>	0.93	2.56(4)	3.2410(6)	131(5)
The nickel complex				
O(7)–H(7A)...O(8) <sup>iii</sup>	0.82	2.07(3)	2.77(2)	143(4)

Symmetry codes: i:  $1-x, -y, -z$ ; ii:  $2-x, -y, 1-z$ .

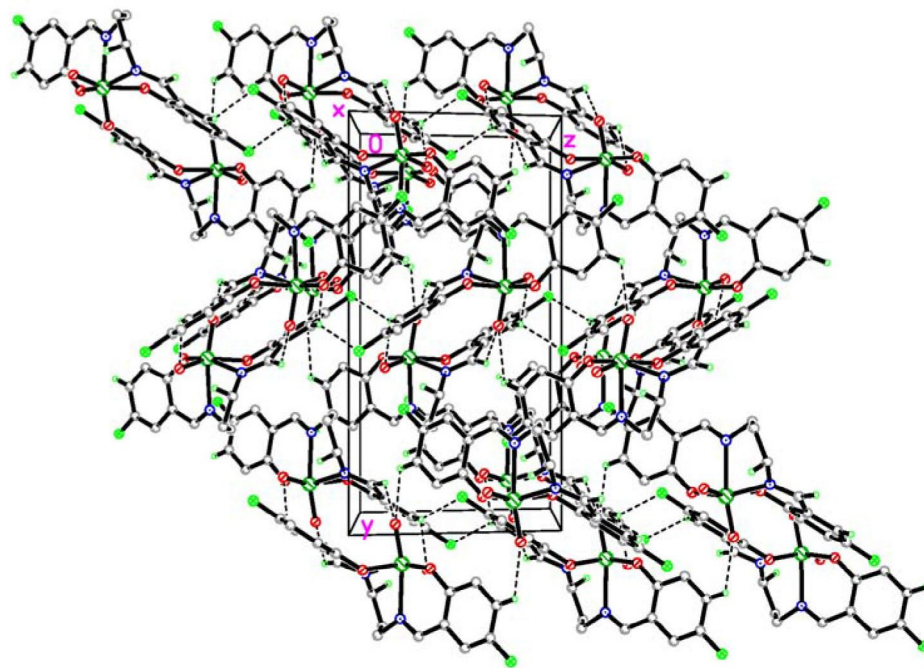


Fig. 2. Molecular packing structure of the molybdenum complex, viewed along the *x*-axis direction. Hydrogen bonds are drawn as dotted lines.

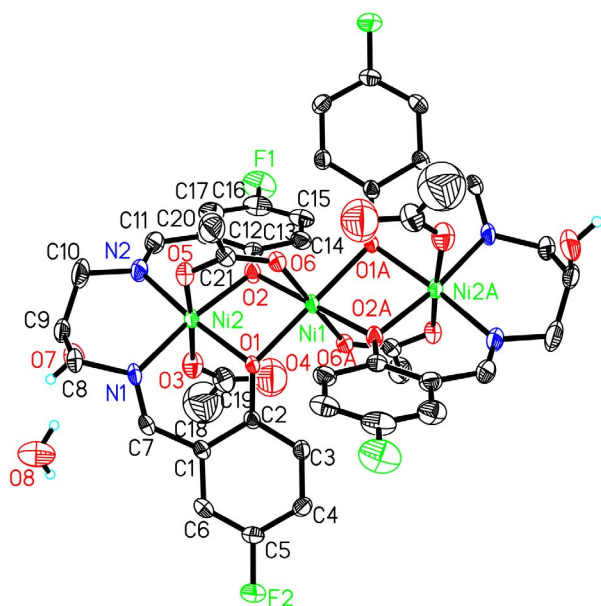


Fig. 3. Molecular structure of the nickel complex. Displacement ellipsoids are drawn at the 30% probability level and H atoms are shown as small spheres of arbitrary radii. Atoms labeled with the suffix A or unlabeled are related to the symmetry position  $-x, 1-y, 1-z$ .

quencies, viz.  $1621\text{--}1634\text{ cm}^{-1}$ .<sup>13</sup> In the spectrum of the molybdenum complex, there showed two prominent bands at  $977$  and  $895\text{ cm}^{-1}$ , which attributed to dioxomolybdenum groups.<sup>14</sup> In the spectrum of the nickel complex, there exhibits typical acetate vibrations  $\nu_{\text{asym}}(\text{OAc})$  at  $1563\text{ cm}^{-1}$  and  $\nu_{\text{sym}}(\text{OAc})$  at  $1450\text{ cm}^{-1}$ .<sup>15</sup> The bands due to  $\nu_{\text{C=O}}$  are absent in both the free Schiff bases and the complexes. This suggests the formation of the azomethine

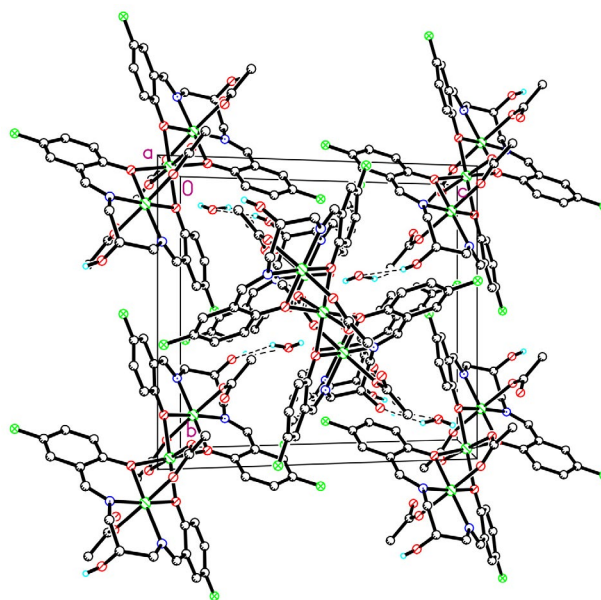


Fig. 4. Molecular packing diagram of the nickel complex, viewed along the *a* axis. Hydrogen bonds are drawn as dashed lines.

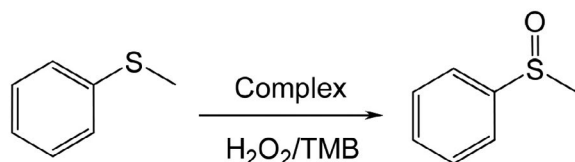
groups,  $\text{CH=N}$ , during the condensation reaction of the starting material. The weak bands in the low wave numbers are assigned to the Mo–O and Mo–N vibrations.

The electronic spectra of the complexes were recorded in methanol. In the molybdenum complex, there showed bands at  $325\text{ nm}$  and weak band at  $420\text{ nm}$ . The weak band is attributed to intra-molecular charge transfer transitions from the  $p_{\pi}$  orbital on the nitrogen and oxygen to the empty  $d$  orbitals of the metal. The intense band ob-

served at 270 nm is assigned to intra-ligand  $\pi$ - $\pi^*$  transitions. In the nickel complex, the azomethine chromophore  $\pi$ - $\pi^*$  transition is located at 361 nm. The broad non-symmetric band with absorption maximum at 420 nm can be assigned as LMCT.

### 3. 5. Catalytic Property of the Complexes

Catalytic oxidation test of the complexes on the oxidation of sulfides under homogeneous conditions in solution using methyl phenyl sulfide (thioanisole) as substrate is shown as Scheme 3. As oxidant hydrogen peroxide was used in a slight excess of 1.25 equivalents based on the sulfide substrate. Reactions were run with 1 mol% of catalyst based on the substrate at a temperature of 10 °C. NMR technique has been used to monitor the formation of the sulfoxides with 1,3,5-trimethoxybenzene (TMB) as internal standard to determine the yields. The reaction was started by the addition of hydrogen peroxide. A control reaction under the same condition without any complex present leads to less than 1% sulfide conversion within 4 h. In the presence of the molybdenum complex conversion of 94% of sulfide to the corresponding sulfoxide within 60 min reaction time was observed. After about 2 h in all cases the conversions of total amount of sulfide were completed. Under the given conditions no over oxidation to the sulfone could be detected. However, the nickel complex has no activity on the reaction. Thus, the molybdenum complex showed excellent catalytic property for the sulfoxidation reaction.



Scheme 2. The sulfoxidation process.

## 4. Supplementary Materials

CCDC-1870626 and 1465136 contain the supplementary crystallographic data for this paper. The data can be obtained free of charge at <http://www.ccdc.cam.ac.uk/const/retrieving.html> or from the Cambridge Crystallographic Data Centre (CCDC), 12 Union Road, Cambridge CB2 1EZ, UK; fax: +44(0)1223-336033 or e-mail: [deposit@ccdc.cam.ac.uk](mailto:deposit@ccdc.cam.ac.uk).

## Acknowledgements

This research was supported by the Top-class foundation of Pingdingshan University (no. PXY-BSQD-2018006 and PXY-PYJJ-2018002).

## 6. References

- (a) C. A. Gamelas, A. C. Gomes, S. M. Bruno, F. A. A. Paz, A. A. Valente, M. Pillinger, C. C. Romao, I. S. Goncalves, *Dalton Trans.* **2012**, 41, 3474–3484; DOI:10.1039/c2dt11751g  
(b) L. S. Feng, J. S. Maass, R. L. Luck, *Inorg. Chim. Acta* **2011**, 373, 85–92; DOI:10.1016/j.ica.2011.03.060  
(c) M. Bagherzadeh, M. Amini, A. Ellern, L. K. Woo, *Inorg. Chem. Commun.* **2012**, 15, 52–55; DOI:10.1016/j.inoche.2011.09.037  
(d) S. Rayati, N. Rafiee, A. Wojtczak, *Inorg. Chim. Acta* **2012**, 386, 27–35. DOI:10.1016/j.ica.2012.02.005
- (a) B. I. Ceylan, Y. D. Kurt, B. Ulkuseven, *J. Coord. Chem.* **2009**, 62, 757–766; DOI:10.1080/00958970802339669  
(b) M. N. Sokolov, M. A. Mikhailov, P. A. Abramov, V. P. Fedin, *J. Struct. Chem.* **2012**, 53, 197–201;  
(c) S.-P. Gao, *J. Coord. Chem.* **2011**, 64, 2869–2877. DOI:10.1080/00958972.2011.608163
- (a) S. Mandal, R. Saha, B. Mahanti, M. Fleck, D. Bandyopadhyay, *Inorg. Chim. Acta* **2012**, 387, 1–7; DOI:10.1016/j.ica.2011.12.035  
(b) M. A. Vazquez-Fernandez, M. I. Fernandez-Garcia, A. M. Gonzalez-Noya, M. Maneiro, M. R. Bermejo, M. J. Rodriguez-Douton, *Polyhedron* **2012**, 31, 379–385; DOI:10.1016/j.poly.2011.09.031  
(c) F. Habib, P.-H. Lin, J. Long, I. Korobkov, W. Wernsdorfer, M. Murugesu, *J. Am. Chem. Soc.* **2011**, 133, 8830–8833. DOI:10.1021/ja2017009
- (a) N. K. Ngan, K. M. Lo, C. S. R. Wong, *Polyhedron* **2012**, 33, 235–251; DOI:10.1016/j.poly.2011.11.057  
(b) S. Duman, I. Kizilcikli, A. Koca, M. Akkurt, B. Ulkuseven, *Polyhedron* **2010**, 29, 2924–2932; DOI:10.1016/j.poly.2010.07.022  
(c) R. D. Chakravarthy, K. Suresh, V. Ramkumar, D. K. Chand, *Inorg. Chim. Acta* **2011**, 376, 57–63; DOI:10.1016/j.ica.2011.05.033  
(d) C. P. Rao, A. Sreedhara, P. V. Rao, M. B. Verghese, K. Rissanen, E. Kolehmainen, N. K. Lokanath, M. A. Sridhar, I. S. Prasad, *J. Chem. Soc. Dalton Trans.* **1998**, 2383–2393.
- (a) M. Mancka, W. Plass, *Inorg. Chem. Commun.* **2007**, 10, 677–680; DOI:10.1016/j.inoche.2007.02.029  
(b) S. N. Rao, N. Kathale, N. N. Rao, K. N. Munshi, *Inorg. Chim. Acta* **2007**, 360, 4010–4016; DOI:10.1016/j.ica.2007.05.035  
(c) R. Dinda, S. Ghosh, L. R. Falvello, M. Tomas, T. C. W. Mak, *Polyhedron* **2006**, 25, 2375–2382. DOI:10.1016/j.poly.2006.02.002
- (a) L. Wang, Y. J. Han, Q. B. Li, L. W. Xue, *Russ. J. Coord. Chem.* **2017**, 43, 389–395; DOI:10.1134/S1070328417060094  
(b) Q.-B. Li, Y.-J. Han, G.-Q. Zhao, L.-W. Xue, *Acta Chim. Slov.* **2017**, 64, 500–505. DOI:10.17344/acsi.2017.3416
- (a) L. Shi, Z.-P. Xiao, Z. Zhuang, H.-L. Zhu, *Acta Crystallogr.* **2007**, E63, o4726;  
(b) L.-W. Xue, Y.-J. Han, G.-Q. Zhao, Y.-X. Feng, *J. Chem. Crystallogr.* **2011**, 41, 1599–1603. DOI:10.1007/s10870-011-0146-z

8. Bruker, SMART and SAINT. *Area Detector Control and Integration Software*; Bruker Analytical X-ray Instruments Inc.: Madison, WI, USA, 1997.
9. G. M. Sheldrick, SADABS. *Program for Empirical Absorption Correction of Area Detector Data*; University of Göttingen: Göttingen, Germany, 1997.
10. A. C. T. North, D. C. Phillips, F. S. Mathews, *Acta Crystallogr.* **1968**, A24, 351–355. DOI:10.1107/S0567739468000707
11. G. M. Sheldrick, SHELXL-97. *Program for the Refinement of Crystal Structures*; University of Göttingen: Göttingen, Germany, 1997.
12. (a) S. N. Rao, K. N. Munshi, N. N. Rao, M. M. Bhadbhade, E. Suresh, *Polyhedron* **1999**, 18, 2491–2497; (b) W.-X. Xu, W.-H. Li, *Synth. React. Inorg. Met.-Org. Nano-Met. Chem.* **2012**, 42, 160–164. DOI:10.1016/S0277-5387(99)00139-4
13. G. Romanowski, M. Wera, *Polyhedron* **2010**, 29, 2747–2754. DOI:10.1016/j.poly.2010.06.030
14. T. Głowiak, L. Jerzykiewicz, J. A. Sobczak, J. J. Ziolkowski, *Inorg. Chim. Acta* **2003**, 356, 387–392. DOI:10.1016/S0020-1693(03)00301-3
15. B.-H. Ye, X.-Y. Li, I. D. Williams, X.-M. Chen, *Inorg. Chem.* **2002**, 41, 6426–6431. DOI:10.1021/ic025806+

## Povzetek

Sintetizirali smo nov enojedrni dioksomolibdenov(VI) kompleks,  $[\text{MoO}_2\text{L}^1]$ , in nov linearni trijedrni nikljev(II) kompleks,  $[\text{Ni}\{\text{NiL}^2(\mu_1\text{-}\eta^1\text{:}\eta^0\text{-OAc})(\mu_2\text{-}\eta^1\text{:}\eta^1\text{-OAc})\}_2]\cdot\text{H}_2\text{O}$ , kjer je  $\text{L}^1$  dianionska oblika  $N,N'$ -bis(5-fluorosaliciliden)-1,3-propandiamina ( $\text{H}_2\text{L}^1$ ) in  $\text{L}^2$  dianionska oblika  $N,N'$ -bis(5-fluoro-2-hidroksibenziliden)-2-hidroksi-1,3-propandiamina ( $\text{H}_2\text{L}^2$ ). Kompleksa smo okarakterizirali z elementno analizo, FT-IR spektroskopijo in monokristalno rentgensko difrakcijo. V molibdenovem kompleksu je Mo atom oktaedrično koordiniran s štirimi donorskimi atomi Schiffove baze ter z dvema okso skupinama. V nikljevem kompleksu so prisotni trije mostovi med Ni-Ni pari atomov, ki vsebujejo dva fenolna O atoma Schiffove baze in O–C–O skupino  $\mu_2\text{-}\eta^1\text{:}\eta^1\text{-OAc}$  liganda. Sredinski Ni atom leži na centru inverzije in ima oktaedrično koordinacijo s štirimi mostovnimi O atomi dveh Schiffovih baz v ekvatorialni legi ter z dvema O atomoma z dveh  $\mu_2\text{-}\eta^1\text{:}\eta^1\text{-OAc}$  ligandov v aksialni legi. Koordinacija okoli terminalnih Ni atomov je tudi oktaedrična z dvema imino N atomoma in dvema fenolno O atomoma Schiffove baze v ekvatorialni legi ter z dvema O atomoma  $\mu_1\text{-}\eta^1\text{:}\eta^0\text{-OAc}$  in  $\mu_2\text{-}\eta^1\text{:}\eta^1\text{-OAc}$  ligandov v aksialni legi. Molibdenov kompleks ima odlične katalitične lastnosti pri reakciji sulfoksidacije.



Except when otherwise noted, articles in this journal are published under the terms and conditions of the Creative Commons Attribution 4.0 International License



Scientific paper

# Microwave-Assisted Synthesis and Anticancer Activity of Triazolyl Thiazolidine Derivatives of Pyrene

Avula Srinivas,<sup>1,\*</sup> Pulluri Karthik,<sup>1</sup> Malladi Sunitha<sup>2</sup>  
and Koduri Vasumathi Reddy<sup>3</sup>

<sup>1</sup> Department of Chemistry, Vaagdevi Degree & PG College

<sup>2</sup> Jayamukhi Institute of Technological Sciences, Narsampet, Warangal, Telangana

<sup>3</sup> Department of Zoology, Vaagdevi Degree & PG College

Kishanpura, Warangal, Telangana, India 506001

\* Corresponding author: E-mail: avula.sathwikreddy@gmail.com

Received: 03-29-2019

## Abstract

In a one pot procedure a series of (*R*)-2-((2*S*,3*S*)-3-((1-(4-chlorophenyl)-1*H*-1,2,3-triazol-4-yl)methoxy)-3,6-dihydro-2*H*-pyran-2-yl)-3-phenylthiazolidin-4-ones **9a–g** and 2-((2*R*)-2-((2*S*,3*S*)-3-((1-(4-chlorophenyl)-1*H*-1,2,3-triazol-4-yl)methoxy)-3,6-dihydro-2*H*-pyran-2-yl)-4-oxo-3-phenylthiazolidin-5-yl)acetic acids **10a–g** was prepared by condensation of (2*S*,3*S*)-3-((1-(4-chlorophenyl)-1*H*-1,2,3-triazol-4-yl)methoxy)-3,6-dihydro-2*H*-pyran-2-carbaldehyde with mercapto acids and primary amines in the presence of ZnCl<sub>2</sub> under both microwave irradiation and conventional heating conditions. Characterization of new compounds has been done by means of IR, NMR, MS and elemental analysis. The cytotoxicity was assessed against a panel of four different human tumor cell lines: A549 derived from human alveolar adenocarcinoma epithelial cells (ATCC No. CCL-185), Hela derived from human cervical cancer cells (ATCC No. CCL-2), MDA-MB-231 derived from human breast adenocarcinoma cells (ATCC No. HTB22) and HEK 293 (normal human embryonic kidney cell line) using the MTT assays. Among the tested compounds **9e** and **10e** showed the most potent activity against MCF-7 breast cancer cell line with IC<sub>50</sub> values of 1.91 and 1.95 μM, whereas **9b**, **10b**, **9g** and **10g** showed promising activity against MDA-MB-231 and Hela cell lines with IC<sub>50</sub> values of 5.84, 5.74, 7.89 and 7.65 μM, respectively.

**Keywords:** Glycosides; click reaction; cyclisation; thiazolidinones; anticancer activity

## 1. Introduction

Carbohydrates, besides being the most abundant class of bio-molecules, a vital source of energy and structural components, have an important role in biological processes, organic synthesis and chemical industries.<sup>1</sup> In the chemical industry they act as readily available raw materials for large scale applications and have been used in the pharmaceutical, food, cosmetic and detergent industries.<sup>2</sup> They have an important role in cell physiology in the form of glycoconjugates (glycolipids, glycoproteins and polysaccharides) and in many biological processes such as intercellular recognition, bacterial and viral infection, cancer metastasis, apoptosis and neuronal proliferation, etc.<sup>3</sup>

The introduction of a carbohydrate moiety into a system often imparts interesting properties, such as hydro-

philicity, lowered toxicity and enhanced bioactivities.<sup>4</sup> Organic chemists have linked carbohydrates to various biologically potent compounds to enhance their biological applications, such as steroids, aminoacids and other therapeutic agents.<sup>5</sup> One of the methods used to link a carbohydrate moiety with a potential compound is *via* a triazole ring using the well known click-chemistry reactions.<sup>6</sup> The versatility of the alkyne- azide cyclisation reaction and the introduction of a triazole ring makes this process an efficient method to obtain cyclized products with biological potential.<sup>7</sup> The strategy of linking a carbohydrate moiety with another species *via* a triazole ring is gaining importance in organic synthesis, natural products chemistry and biochemistry.<sup>8</sup> The stability, polar nature and possible hydrogen bonding ability of a triazole ring combined with the biocompatibility and presence of stereogenic centers of

a carbohydrate moiety makes glucal-based triazole very interesting for organic synthetic chemists.

1,2,3-Triazoles are one of the most important classes of heterocyclic organic compounds, which are reported to be involved in a plethora of biological activities and to be present in diverse therapeutic areas.<sup>9</sup> The 1,2,3-triazole motif is associated with diverse pharmacological activities such as antibacterial, antifungal, hypoglycemic, antihypertensive and analgesic properties. Polysubstituted five-membered aza heterocycles rank as the most potent glycosidase inhibitors.<sup>10</sup> Further, this nucleus in combination with or in linking with various other classes of compounds such as amino acids, steroids, aromatic compounds, carbohydrates *etc* became prominent in having various pharmacological properties.<sup>11</sup> 1,2,3-Triazole modified carbohydrates have become easily available after the discovery of the Cu(I) catalyzed azide-alkynes 1,3-dipolar cycloaddition reaction<sup>12</sup> and quickly became a prominent class of non-natural sugars. The chemistry and biology of triazole modified sugars is dominated by triazole glycosides.<sup>13</sup> Therefore, the synthesis and investigation of biological activity of 1,2,3-triazole glycosides is an important objective, which also received a considerable attention by the medicinal chemists.

Thiazolidinone and its derivatives are known to possess significant pharmacological<sup>14</sup> and biological activities,<sup>15</sup> like sedative,<sup>16</sup> anti inflammatory,<sup>17</sup> anti tubercular,<sup>18</sup> anticancer,<sup>19</sup> anti tumor,<sup>20</sup> anti-HIV,<sup>21</sup> anti bacterial,<sup>22</sup> anti fungal,<sup>23</sup> analgesic, hypotermic,<sup>24</sup> anesthetic,<sup>25</sup> nematocidal<sup>26</sup> and CNS stimulant.<sup>27</sup> Furthermore, thiazolidinones have been used for the treatment of cardiac diseases,<sup>28</sup> diabetic complications like cataract nephropathy, neuropathy,<sup>29</sup> and as selective anti platelet activating factor.<sup>30</sup>

Microwave irradiation is an alternative heating technique based on the transformation of electromagnetic energy into heat. Often this method increases the rate of chemical reactions<sup>31</sup> and results in higher yields. In recent years, multi component reactions (MCRs)<sup>32–36</sup> have received interesting attention due to their simplicity, efficiency, atom economy, shortened reaction times, and the possibility for diversity oriented synthesis.

Following the successful introduction, inspired by the biological profile of triazoles, thiazolidinones, and in the continuation of our work on biologically active heterocycles<sup>37–46</sup> we have developed a series of novel triazolyl thiazolidine derivatives of pyrene, and evaluated their anticancer activity.

## 2. Results and Discussion

The key intermediate **8** required for the synthesis of the title compound was prepared according to the procedure outlined in the Scheme 1. Diacetyl-D-glucal (**2**) prepared from 3,4,6-tri-O-acetyl-D-glucal by treating with

triethyl silane and boron trifluoride diethyl etherate, deacylation of **2**, with NaOMe in methanol at 0 °C for 1 h gave **3** (77%), which on subsequent treatment with TBDMSCl in dichloromethane in the presence of NEt<sub>3</sub> after 12 h afforded TBS ether **4** (80%), on treatment with propargyl bromide in toluene in the presence of tetrabutylammonium hydrogensulphate produced diether **5**. After deprotection of TBS ether, the propargyl ether was converted into triazole **7** (82%) by using 1,3-dipolar cycloaddition with *para*-chlorophenyl azide carried out at ambient temperature in the presence of CuSO<sub>4</sub> and sodium ascorbate in a mixture of 1:1 CH<sub>2</sub>Cl<sub>2</sub>–H<sub>2</sub>O. Oxidation of **7** with IBX in acetonitrile afforded compound **8**. Subsequently one-pot synthesis of triazole linked thiazolidenone glycosides was carried out by the condensation reaction between **8**, primary aromatic amine and a thioglycolic acid in the presence of ZnCl<sub>2</sub> under microwave irradiation/conventional heating (Scheme 2). In the classical method, the reactions were performed in dry toluene at reflux for a long time (2–4 h), often leading to degradation processes and consequent low yields of isolated products, whereas with the application of microwave assisted technology, the reactions were completed in only 5–10 minutes and the compounds were isolated by conventional work-up; products **9a–g** and **10a–g** were obtained in satisfactory yields, often higher than those achieved by traditional methods. The structures of synthesized compounds were confirmed by IR, NMR, MS and elemental analysis and evaluated for their anticancer activity.

## 3. In vitro Cytotoxicity

Cytotoxicity of all the synthesized compounds was determined on the basis of measurement of *in vitro* growth inhibition of tumor cell lines in 96 well plates by cell-mediated reduction of tetrazolium salt to water-insoluble formation of crystals using doxorubicin as a standard. The cytotoxicity was assessed against a panel of four different human tumor cell lines: A549 derived from human alveolar adenocarcinoma epithelial cells (ATCC No. CCL-185), Hela derived from human cervical cancer cells (ATCC No. CCL-2), MDA-MB-231 derived from human breast adenocarcinoma cells (ATCC No. HTB22) and HEK 293 (normal human embryonic kidney cell line) using the MTT assays.<sup>34</sup> The IC<sub>50</sub> values were calculated from the plotted absorbance data for the dose-response curves. IC<sub>50</sub> values (in μM) are indicated as means ±SD of three independent experiments. From the data reported in Table 2, most of the prepared compounds (note: the enantiomeric purity of the final products was not established) possessed significant cytotoxicity effect on all the tested cell lines and potencies of some of the compounds were comparable to the standard doxorubicin, the most widely used drug for the treatment of tumors. Among the tested compounds **9e** and **10e** showed the most potent activity against MCF-7 cell

line with IC<sub>50</sub> values of 1.91 and 1.95 μM, respectively, whereas **9b**, **10b**, **9g** and **10g** showed promising activity against MDA-MB-231 and Hela cell lines with IC<sub>50</sub> values of 5.84, 5.74, 7.89 and 7.65 μM, respectively.

## 4. Experimental

Commercial grade reagents were used as supplied. Solvents except analytical reagent grade were dried and purified according to literature when necessary. Reaction progress and purity of the compounds were checked by thin-layer chromatography (TLC) on pre-coated silica gel F254 plates from Merck and compounds visualized either by exposure to UV light or dipping in 1% aqueous potassium permanganate solution. Silica gel chromatographic columns (60–120 mesh) were used for separations. Optical rotations were measured on an Perkin–Elmer 141 polarimeter by using a 2 mL cell with a path length of 1 dm with CHCl<sub>3</sub> or CDCl<sub>3</sub> as the solvent. All melting points are uncorrected and were measured using Fisher–Johns apparatus. IR spectra were recorded as KBr disks on a Perkin–Elmer FT IR spectrometer. Microwave reactions were carried out in mini lab microwave catalytic reactor (ZZKD, WBFY-201). The <sup>1</sup>H NMR and <sup>13</sup>C NMR spectra were recorded on a Varian Gemini spectrometer (300 MHz for <sup>1</sup>H and 75 MHz for <sup>13</sup>C). Chemical shifts are reported as δ (ppm) against TMS as the internal reference and coupling constants (*J*) are reported in Hz units. Mass spectra were recorded on a VG micro mass 7070H spectrometer. Elemental analysis (C, H, N) were determined by a Perkin–Elmer 240 CHN elemental analyzer, and are within ±0.4% of theoretical values.

**((2*R*,3*S*)-3-Acetoxy-3,6-dihydro-2*H*-pyran-2-yl)methyl acetate (**2**).** Tri-*O*-acetyl-D-glucal (**1**) (3.0 g, 11.02 mmol)

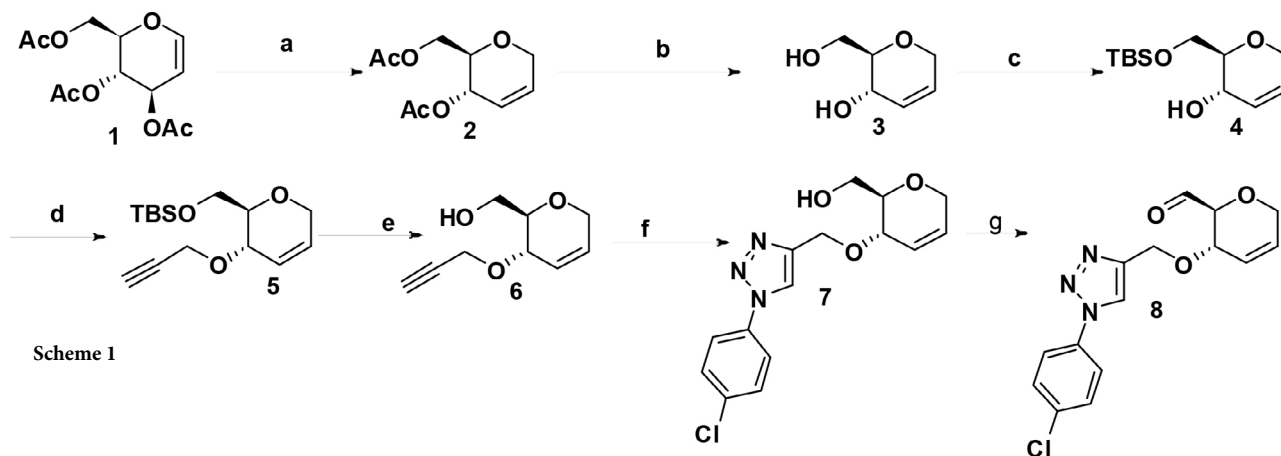
was dissolved in anhydrous dichloromethane (5 mL). The solution was cooled to 0 °C, triethylsilane (1.53 g, 13.22 mmol) was added and the mixture was stirred for five minutes. Next boron trifluoride diethyl etherate (690 μL of a 40% wt. solution in diethyl ether, 11.02 mmol) was added dropwise and the reaction mixture was stirred for 90 min. The mixture was poured into a saturated solution of NaHCO<sub>3</sub>. The organic layer was washed with water, dried over Na<sub>2</sub>SO<sub>4</sub> and concentrated under reduced pressure. Column chromatography on silica gel (PE–EtOAc, 3:1) yielded the title compound (2.24 g, 10.42 mmol, 95%) as a colourless syrup. [α]<sub>D</sub><sup>20</sup>: +115.5 (*c* = 1.00, CHCl<sub>3</sub>). <sup>1</sup>H NMR (300 MHz, CDCl<sub>3</sub>): δ 5.87–5.84 (m, 2H, =CH), 4.95 (t, 1H, OCH), 4.03–3.99 (m, 1H, CH), 4.12–4.09 (m, 4H, OCH<sub>2</sub>), 2.20 (s, 6H, COCH<sub>3</sub>); <sup>13</sup>C NMR (75 MHz, CDCl<sub>3</sub>): δ 170.2, 127.2, 125.8, 73.6, 65.1, 64.0, 62.5, 21.1; MS: *m/z* (M<sup>+</sup>+H) 215. Anal. Calcd for C<sub>10</sub>H<sub>14</sub>O<sub>5</sub>: C, 56.07; H, 6.59. Found: C, 55.82; H, 6.35.

**(2*R*,3*S*)-2-((*tert*-Butyldimethylsilyloxy)methyl)-3,6-dihydro-2*H*-pyran-3-ol (**4**).** Diacetate **2** (17.22 mmol) was treated by a catalytic amount of sodium methoxide in methanol (100 mL) at room temperature. After evaporation of the solvent, the free hydroxyl unsaturated glycoside was obtained in quantitative yield and used without further purification. This diol was treated with 2.50 equiv of TBDMSCl (3.14 g, 21.14 mmol), 2.6 equiv of NEt<sub>3</sub> (3.2 mL, 22.4 mmol), and 0.05 equiv of imidazole (30 mg, 0.43 mmol) in CH<sub>2</sub>Cl<sub>2</sub> (30 mL) at room temperature for *ca.* 24 h (until TLC analysis showed no more starting material). After addition of 25 mL of water and extraction with 3 × 30 mL of CH<sub>2</sub>Cl<sub>2</sub>, the organic layer was dried. After evaporation of the solvent under reduced pressure, the residue was purified by column chromatography using petroleum ether/ethyl acetate as the eluent yielding the title compound (1.94 g, 10.42 mmol, 85%) as a colourless syrup. <sup>1</sup>H

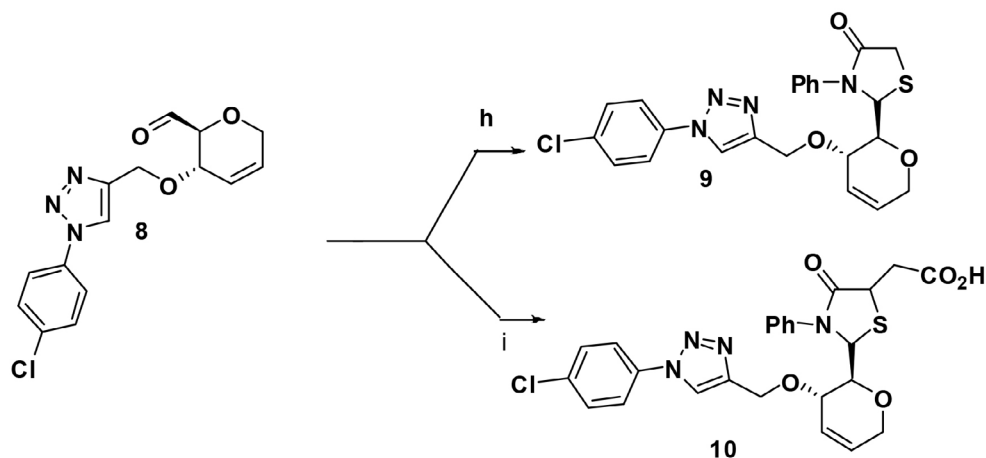
Table 1. Synthesis of compounds 9a–g and 10a–g

Compound	R	Mol. Formula	Reaction time		Yield	
			A (h)	B (min)	A	B
<b>9a</b>	C <sub>6</sub> H <sub>5</sub>	C <sub>23</sub> H <sub>21</sub> ClN <sub>4</sub> O <sub>3</sub> S	4.5	7	62	80
<b>9b</b>	4-Cl-C <sub>6</sub> H <sub>4</sub>	C <sub>23</sub> H <sub>20</sub> Cl <sub>2</sub> N <sub>4</sub> O <sub>3</sub> S	3.5	5	71	89
<b>9c</b>	4-NO <sub>2</sub> -C <sub>6</sub> H <sub>4</sub>	C <sub>23</sub> H <sub>20</sub> ClN <sub>5</sub> O <sub>5</sub> S	4.0	6	69	82
<b>9d</b>	2-CH <sub>3</sub> -C <sub>6</sub> H <sub>4</sub>	C <sub>24</sub> H <sub>23</sub> ClN <sub>4</sub> O <sub>3</sub> S	3.0	8	63	86
<b>9e</b>	4-CH <sub>3</sub> -C <sub>6</sub> H <sub>4</sub>	C <sub>24</sub> H <sub>23</sub> ClN <sub>4</sub> O <sub>3</sub> S	3.5	7	68	88
<b>9f</b>	3-OH - C <sub>6</sub> H <sub>4</sub>	C <sub>23</sub> H <sub>21</sub> ClN <sub>4</sub> O <sub>4</sub> S	4.0	6	79	86
<b>9g</b>	4-OH - C <sub>6</sub> H <sub>4</sub>	C <sub>23</sub> H <sub>21</sub> ClN <sub>4</sub> O <sub>4</sub> S	3.0	3	80	91
<b>10a</b>	C <sub>6</sub> H <sub>5</sub>	C <sub>25</sub> H <sub>23</sub> ClN <sub>4</sub> O <sub>5</sub> S	4.5	8	63	79
<b>10b</b>	4-Cl-C <sub>6</sub> H <sub>4</sub>	C <sub>25</sub> H <sub>22</sub> Cl <sub>2</sub> N <sub>4</sub> O <sub>5</sub> S	3.5	5	65	82
<b>10c</b>	4-NO <sub>2</sub> -C <sub>6</sub> H <sub>4</sub>	C <sub>25</sub> H <sub>22</sub> ClN <sub>5</sub> O <sub>7</sub> S	4.0	7	61	79
<b>10d</b>	2-CH <sub>3</sub> -C <sub>6</sub> H <sub>4</sub>	C <sub>26</sub> H <sub>25</sub> ClN <sub>4</sub> O <sub>5</sub> S	3.5	5	70	81
<b>10e</b>	4-CH <sub>3</sub> -C <sub>6</sub> H <sub>4</sub>	C <sub>26</sub> H <sub>25</sub> ClN <sub>4</sub> O <sub>5</sub> S	3.0	5	67	82
<b>10f</b>	3-OH - C <sub>6</sub> H <sub>4</sub>	C <sub>25</sub> H <sub>23</sub> ClN <sub>4</sub> O <sub>6</sub> S	4.0	8	77	87
<b>10g</b>	4-OH - C <sub>6</sub> H <sub>4</sub>	C <sub>25</sub> H <sub>25</sub> ClN <sub>4</sub> O <sub>6</sub> S	2.5	4	79	90

A: Conventional heating. B: microwave irradiation



Scheme 1



Scheme 2

**Reagents and conditions:** (a)  $\text{BF}_3$ ,  $\text{Et}_2\text{O}$ ,  $\text{Et}_3\text{SiH}$ ,  $\text{CH}_2\text{Cl}_2$ . (b)  $\text{MeOH}$ ,  $\text{NaOMe}$ . (c)  $\text{TBDMSCl}$ ,  $\text{Et}_3\text{N}$ ,  $\text{CH}_2\text{Cl}_2$ . (d) Propargyl bromide,  $\text{NaH}$ ,  $n\text{-Bu}_4\text{N}\text{-HSO}_4$ , 35%  $\text{NaOH}$ , toluene. (e)  $\text{TBAF}$ ,  $\text{THF}$ . (f)  $\text{PhN}_3$ ,  $\text{CuSO}_4$ , sodium ascorbate,  $\text{CH}_2\text{Cl}_2$ ,  $\text{H}_2\text{O}$  (1:1). (g)  $\text{IBX}$ ,  $\text{CH}_3\text{CN}$ . (h)  $\text{PhNH}_2$ ,  $\text{AcOH}$ ,  $\text{SHCH}_2\text{COOH}$ ,  $\text{ZnCl}_2$ ,  $\text{C}_6\text{H}_6$ . (i)  $\text{SHCHCOOHCH}_2\text{COOH}$ ,  $\text{ZnCl}_2$ ,  $\text{C}_6\text{H}_6$ .

**Table 2.**  $\text{IC}_{50}$  values of tested compounds 9a–g and 10a–g against four human cell lines and normal cell line (HEK 293)

Compound	$\text{IC}_{50}$ Values in $\mu\text{M}$				HEK293
	A549	Hela	MDA-MB-231	MCF-7	
9a	4.89	2.98	13.34	5.31	>100
9b	>100	>100	>5.84	>100	>100
9c	5.44	>100	>100	8.95	>100
9d	>100	>100	>100	>100	>100
9e	5.75	>100	>100	51.71	>100
9f	>100	7.89	>100	>100	>100
9g	>100	>100	13.39	1.91	>100
10a	4.67	3.03	13.56	5.62	>100
10b	>100	>100	>5.74	>100	>100
10c	5.56	>100	>100	8.65	>100
10d	>100	>100	>100	>100	>100
10e	5.89	>100	>100	52.09	>100
10f	>100	7.92	>100	>100	>100
10g	>100	>100	13.56	1.95	>100
Doxorubicin	0.459	0.509	0.91	1.07	>100

A549: Adeno carcinomic human alveolar basal epithelial cells; Hela: Immortal cell lines; MDA-MB-231: Epithelial human breast cancer cells, MCF-7: Michigan Cancer Foundation-7 breast cancer cell line.

NMR (300 MHz,  $\text{CDCl}_3$ ):  $\delta$  6.0–5.82 (m, 2H, =CH), 5.42 (d,  $J$  = 6.5 Hz, 1H, CH), 4.50 (brs, 1H, OH), 4.20–4.12 (m, 1H, CH), 3.91–3.80 (m, 4H,  $\text{CH}_2$ ), 0.98 (s, 9H, *t*-Bu), 0.24 (s, 6H,  $\text{CH}_3$ );  $^{13}\text{C}$  NMR (75 MHz,  $\text{CDCl}_3$ ):  $\delta$  127.5, 125.6, 84.6, 81.5, 73.6, 62.7, 25.6, 18.1; MS:  $m/z$  ( $\text{M}^+ + \text{Na}$ ) 267. Anal. Calcd for  $\text{C}_{12}\text{H}_{24}\text{O}_3\text{Si}$ : C, 58.97; H, 9.90. Found: C, 58.62; H, 9.75.

***tert*-Butyldimethyl(((2*R*,3*S*)-3-(prop-2-ynyloxy)-3,6-dihydro-2*H*-pyran-2-yl)methoxy)silane (5).** To a solution of alcohol 4 (400 mg, 1.63 mmol, 1.0 equiv) in toluene (1.6 mL) was added a 35% aqueous solution of NaOH (1.6 mL), propargyl bromide (80% solution in toluene, 363  $\mu\text{L}$ , 2.4 mmol, 1.5 equiv), and *n*- $\text{Bu}_4\text{NHSO}_4$  (280 mg, 0.82 mmol, 0.5 equiv). After 6 h of vigorous stirring at rt,  $\text{Et}_2\text{NH}$  (1.6 mL) was added. The reaction mixture was stirred for 1 h, poured into ice water, cautiously neutralized by addition of a 3M solution of hydrochloric acid, and extracted with EtOAc. The combined organic extracts were washed with brine, dried over  $\text{MgSO}_4$ , filtered, and concentrated under reduced pressure. The crude material was purified by flash chromatography on silica gel (hexane–EtOAc 85:15) to afford propargyl ether as a colorless oil (0.345 g, 75%).  $^1\text{H}$  NMR (300 MHz,  $\text{CDCl}_3$ ):  $\delta$  6.03–5.80 (m, 2H, =CH), 4.69 (t,  $J$  = 3.9 Hz, 1H, CH), 3.68 (dd,  $J$  = 8.9 Hz, 4.1 Hz, 1H, OCH), 3.99–3.89 (m, 6H,  $\text{CH}_2$ ), 3.20 (s, 1H, CH), 0.96 (s, 9H, *t*-Bu), 0.23 (s, 6H,  $\text{CH}_3$ );  $^{13}\text{C}$  NMR (75 MHz,  $\text{CDCl}_3$ ):  $\delta$  127.2, 124.9, 78.0, 76.2, 74.2, 64.2, 63.2, 58.5, 25.3, 18.5; MS:  $m/z$  ( $\text{M}^+ + \text{H}$ ) 283. Anal. Calcd for  $\text{C}_{15}\text{H}_{26}\text{O}_3\text{Si}$ : C, 63.78; H, 9.28. Found: C, 63.62; H, 8.95.

**((2*R*,3*S*)-3-(Prop-2-ynyloxy)-3,6-dihydro-2*H*-pyran-2-yl)methanol (6).** To a stirred solution of 5 (0.325 g) in tetrahydrofuran a catalytic amount of TBAF was added and stirred the reaction mixture at room temperature for 15 min, extracted the product with ethyl acetate (20 mL). The combined organic extracts were washed with brine, dried over  $\text{MgSO}_4$ , filtered, and concentrated under reduced pressure. The crude material was purified by flash chromatography on silica gel (60–120 mesh, hexane–EtOAc 70:30) to afford the title alcohol as yellow oil (0.285 g, 85%).  $^1\text{H}$  NMR (300 MHz,  $\text{CDCl}_3$ ):  $\delta$  5.95–5.75 (m, 2H, =CH), 4.65 (d,  $J$  = 3.9 Hz, 1H, CH), 4.52 (brs, 1H, OH), 4.09–4.11 (m, 4H,  $\text{OCH}_2$ ), 3.64 (dd,  $J$  = 4.1 Hz, 8.9 Hz, 1H, OCH), 3.76 (d,  $J$  = 6.8 Hz, 2H,  $\text{OCH}_2$ ), 3.28 (s, 1H, CH);  $^{13}\text{C}$  NMR (75 MHz,  $\text{CDCl}_3$ ):  $\delta$  127.2, 125.6, 78.3, 76.1, 74.1, 64.2, 61.4, 58.0; MS:  $m/z$  ( $\text{M}^+ + \text{H}$ ) 169. Anal. Calcd for  $\text{C}_9\text{H}_{12}\text{O}_3$ : C, 64.27; H, 7.10. Found: C, 64.02; H, 6.95.

**((2*R*,3*S*)-3-((1-(4-Chlorophenyl)-1*H*-1,2,3-triazol-4-yl)methoxy)-3,6-dihydro-2*H*-pyran-2-yl)methanol (7).** To a solution containing alkyne 6 (0.250 g, 0.778 mmol), *para*-chlorophenyl azide (0.130 g, 0.849 mmol) in dichloromethane (10 mL) and water (10 mL) were added  $\text{CuSO}_4 \cdot 5\text{H}_2\text{O}$  (0.110 g) and sodium ascorbate (0.114 g). The resulting suspension was stirred at room temperature for 6

h. After this time, the mixture was diluted with 5 mL dichloromethane and 5 mL water. The organic phase was separated, dried with sodium sulphate and concentrated at reduced pressure. The crude product was purified by column chromatography on silica gel (60–120 mesh, hexane–EtOAc 65:35) to afford 7 (0.290 g, 75%) as a white powder. M.p. 149–151 °C.  $^1\text{H}$  NMR (300 MHz,  $\text{CDCl}_3$ ):  $\delta$  8.05 (s, 1H, Ar-H), 7.56 (d,  $J$  = 9.2 Hz, 2H, Ar-H), 7.45 (d,  $J$  = 8.9 Hz, 2H, Ar-H), 5.85–5.79 (m, 2H, =CH), 4.59 (s, 2H,  $\text{OCH}_2$ ), 4.50 (brs, 1H, OH), 3.88–3.99 (m, 4H,  $\text{OCH}_2$ ), 3.8–3.75 (m, 2H, OCH);  $^{13}\text{C}$  NMR (75 MHz,  $\text{CDCl}_3$ ):  $\delta$  140.9, 134.5, 134.1, 128.4, 127.5, 125.4, 122.1, 121.5, 78.6, 68.5, 65.7, 64.2, 62.4; MS:  $m/z$  ( $\text{M}^+ + \text{H}$ ) 322. Anal. Calcd for  $\text{C}_{15}\text{H}_{16}\text{ClN}_3\text{O}_3$ : C, 55.90; H, 5.01; N, 13.06. Found: C, 55.65; H, 4.95; N, 12.86.

**(*R*)-2-((2*S*,3*S*)-3-((1-(4-Chlorophenyl)-1*H*-1,2,3-triazol-4-yl)methoxy)-3,6-dihydro-2*H*-pyran-2-yl)-3-phenylthiazolidin-4-ones 8a–g.** To a solution of alcohol 7 (0.120 g, 0.465 mmol) in  $\text{CH}_2\text{Cl}_2$  (5 mL), a catalytic amount of IBX was added at 0 °C and stirred at room temperature for 30 min. The reaction mixture was filtered and washed with  $\text{CH}_2\text{Cl}_2$  (2  $\times$  10 mL). It was dried ( $\text{Na}_2\text{SO}_4$ ) and evaporated to give aldehyde 7 (0.110 g) in quantitative yield as a yellow liquid, which was used as such for the next reaction.

To a stirred mixture of 8 (0.110 g, 0.373 mmol), aromatic amine (0.373 mmol) and anhydrous thioglycolic acid (0.140 g, 0.211 mmol) in dry toluene (5 mL),  $\text{ZnCl}_2$  (0.100 g, 0.751 mmol) was added after 2 min and irradiated in microwave bath reactor at 280 W for 4–7 minutes at 110 °C. After cooling, the filtrate was concentrated to dryness under reduced pressure and the residue was taken up in ethyl acetate. The ethyl acetate layer was washed with 5% sodium bicarbonate solution and finally with brine. The organic layer was dried over  $\text{Na}_2\text{SO}_4$  and evaporated to dryness at reduced pressure. The crude product thus obtained was purified by column chromatography on silica gel (60–120 mesh) with hexane–ethyl acetate as the eluent. Under conventional method the reaction mixture in toluene (10 mL) was refluxed at 110 °C for the appropriate time (Table 1).

**(*R*)-2-((2*S*,3*S*)-3-((1-(4-Chlorophenyl)-1*H*-1,2,3-triazol-4-yl)methoxy)-3,6-dihydro-2*H*-pyran-2-yl)-3-phenylthiazolidin-4-one (9a).** M.p. 157–159 °C, IR (KBr)  $\nu$  3100, 3010, 1750, 1620, 1602, 1440, 1350, 1340, 1210, 735  $\text{cm}^{-1}$ .  $^1\text{H}$  NMR (300 MHz,  $\text{CDCl}_3$ ):  $\delta$  8.04 (s, 1H, Ar-H), 7.50 (d,  $J$  = 9.2 Hz, 2H, Ar-H), 7.40 (d,  $J$  = 8.9 Hz, 2H, Ar-H), 7.10–6.20 (m, 5H, Ar-H), 5.80–5.71 (m, 2H, =CH), 4.90 (d,  $J$  = 5.2 Hz, 1H, CHS), 4.52 (s, 2H,  $\text{OCH}_2$ ), 4.09–3.94 (m, 2 $\times$ CH), 3.79 (d,  $J$  = 6.6 Hz, 2H,  $\text{OCH}_2$ ), 3.72 (s, 2H,  $\text{CH}_2$ ).  $^{13}\text{C}$  NMR (75 MHz,  $\text{CDCl}_3$ ):  $\delta$  170.4, 144.1, 141.8, 134.1, 128.2, 125.6, 122.4, 119.4, 85.6, 72.6, 66.4, 64.0, 51.4, 33.9; MS:  $m/z$  ( $\text{M}^+ + \text{H}$ ) 469. Anal. Calcd for  $\text{C}_{23}\text{H}_{21}\text{ClN}_4\text{O}_3\text{S}$ : C, 58.91; H, 4.51; N, 11.95. Found: C, 58.68; H, 4.35; N, 11.66.

**(R)-3-(4-Chlorophenyl)-2-((2S,3S)-3-((1-(4-chlorophenyl)-1H-1,2,3-triazol-4-yl)methoxy)-3,6-dihydro-2H-pyran-2-yl)thiazolidin-4-one (9b).** M.p. 226–228 °C. IR (KBr)  $\nu$  3190, 3018, 1756, 1616, 1609, 1430, 1340, 1320, 1208, 731  $\text{cm}^{-1}$ .  $^1\text{H}$  NMR (300 MHz,  $\text{CDCl}_3$ ):  $\delta$  8.05 (s, 1H, Ar-H), 7.54 (d,  $J$  = 9.4 Hz, 4H, Ar-H), 7.42 (d,  $J$  = 8.6 Hz, 4H, Ar-H), 5.84–5.75 (m, 2H, =CH), 4.94 (d,  $J$  = 5.2 Hz, CH-S), 4.50 (s, 2H,  $\text{OCH}_2$ ), 4.06–3.96 (m, 2H, 2 $\times$ CH), 3.80 (t, 2H,  $\text{OCH}_2$ ), 3.72 (s, 2H,  $\text{CH}_2$ );  $^{13}\text{C}$  NMR (75 MHz,  $\text{CDCl}_3$ ):  $\delta$  170.5, 144.2, 139.2, 134.2, 129.2, 125.5, 122.2, 119.4, 85.4, 72.8, 65.4, 63.4, 51.2, 34.1. MS:  $m/z$  ( $\text{M}^+\text{+Na}$ ) 525. Anal. Calcd for  $\text{C}_{23}\text{H}_{20}\text{Cl}_2\text{N}_4\text{O}_3\text{S}$ : C, 54.88; H, 4.00; N, 11.13. Found: C, 54.58; H, 3.75; N, 10.86.

**(R)-2-((2S,3S)-3-((1-(4-Chlorophenyl)-1H-1,2,3-triazol-4-yl)methoxy)-3,6-dihydro-2H-pyran-2-yl)-3-(4-nitrophenyl)thiazolidin-4-one (9c).** M.p. 211–213 °C. IR (KBr)  $\nu$  3112, 3020, 1746, 1626, 1619, 1560, 1435, 1344, 1324, 1218, 739  $\text{cm}^{-1}$ .  $^1\text{H}$  NMR (300 MHz,  $\text{CDCl}_3$ ):  $\delta$  8.26 (d,  $J$  = 8.7 Hz, 2H), 8.03 (s, 1H, Ar-H), 7.61 (d,  $J$  = 9.4 Hz, 4H, Ar-H), 7.46 (d,  $J$  = 8.5 Hz, 4H, Ar-H), 6.84 (d,  $J$  = 9.8 Hz, 2H, Ar-H), 5.86–5.79 (m, 2H, =CH), 4.96 (d,  $J$  = 5.2 Hz, CH-S), 4.55 (s, 2H,  $\text{OCH}_2$ ), 4.05–3.95 (m, 2H, 2 $\times$ CH), 3.85 (d,  $J$  = 6.9 Hz, 2H,  $\text{OCH}_2$ ), 3.82 (s, 2H,  $\text{CH}_2$ ).  $^{13}\text{C}$  NMR (75 MHz,  $\text{CDCl}_3$ ):  $\delta$  171.5, 144.0, 141.8, 134.2, 128.5, 125.4, 119.5, 85.4, 72.4, 65.9, 63.6, 51.5, 34.6. MS:  $m/z$  ( $\text{M}^+\text{+H}$ ) 514. Anal. Calcd for  $\text{C}_{23}\text{H}_{20}\text{ClN}_5\text{O}_5\text{S}$ : C, 53.75; H, 3.92; N, 13.63. Found: C, 53.58; H, 3.75; N, 13.39.

**(R)-2-((2S,3S)-3-((1-(4-Chlorophenyl)-1H-1,2,3-triazol-4-yl)methoxy)-3,6-dihydro-2H-pyran-2-yl)-3-ortho-tolylthiazolidin-4-one (9d).** M. p. 191–193 °C. (IR) KBr  $\nu$  3116, 3024, 1741, 1622, 1615, 1450, 1439, 1348, 1321, 1218, 749  $\text{cm}^{-1}$ .  $^1\text{H}$  NMR (300 MHz,  $\text{CDCl}_3$ ):  $\delta$  8.08 (s, 1H, Ar-H), 7.56 (d,  $J$  = 9.2 Hz, 2H, Ar-H), 7.49 (d,  $J$  = 8.7 Hz, 2H, Ar-H), 7.45–7.39 (m, 4H, Ar-H), 5.76 (m, 2H, =CH), 4.93 (d,  $J$  = 5.2 Hz, 1H, CHS), 4.60 (s, 2H,  $\text{OCH}_2$ ), 4.05–3.96 (m, 2H, CH), 3.90 (t, 2H,  $\text{OCH}_2$ ), 3.81 (s, 2H,  $\text{CH}_2$ ), 2.1 (s, 3H,  $\text{CH}_3$ ).  $^{13}\text{C}$  NMR (75 MHz,  $\text{CDCl}_3$ ):  $\delta$  170.5, 144.2, 138.2, 134.2, 130.7, 128.6, 125.6, 122.0, 119.5, 116.5, 85.4, 72.6, 65.8, 63.4, 52.0, 32.3, 17.5. MS:  $m/z$  ( $\text{M}^+\text{+H}$ ) 483. Anal. Calcd for  $\text{C}_{24}\text{H}_{23}\text{ClN}_4\text{O}_3\text{S}$ : C, 59.68; H, 4.80; N, 11.60. Found: C, 59.48; H, 4.55; N, 11.49.

**(R)-2-((2S,3S)-3-((1-(4-Chlorophenyl)-1H-1,2,3-triazol-4-yl)methoxy)-3,6-dihydro-2H-pyran-2-yl)-3-para-tolylthiazolidin-4-one (9e).** M. p. 195–198 °C. IR (KBr)  $\nu$  3126, 3014, 1746, 1632, 1625, 1442, 1434, 1341, 1331, 1228, 740  $\text{cm}^{-1}$ .  $^1\text{H}$  NMR (300 MHz,  $\text{CDCl}_3$ ):  $\delta$  8.05 (s, 1H, Ar-H), 7.51 (d,  $J$  = 9.2 Hz, 2H, Ar-H), 7.45 (d,  $J$  = 8.7 Hz, 2H, Ar-H), 7.25 (d,  $J$  = 8.2 Hz, 2H, Ar-H), 6.84 (d,  $J$  = 9.4 Hz, 2H, Ar-H), 5.72–5.68 (m, 2H, =CH), 4.95 (s, 1H, CHS), 4.59 (s, 2H,  $\text{OCH}_2$ ), 4.04–3.99 (m, 2H, CH), 3.98 (t, 2H,  $\text{OCH}_2$ ), 3.90 (s, 2H,  $\text{CH}_2$ ), 2.32 (s, 3H,  $\text{CH}_3$ ).  $^{13}\text{C}$  NMR (75 MHz,  $\text{CDCl}_3$ ):  $\delta$  170.5, 144.2, 138.6, 136.2, 134.1, 133.2, 129.4, 127.5, 122.5, 119.5, 85.4, 72.0, 66.4,

63.5, 51.5, 34.0, 21.4. MS:  $m/z$  ( $\text{M}^+\text{+H}$ ) 483. Anal. Calcd for  $\text{C}_{24}\text{H}_{23}\text{ClN}_4\text{O}_3\text{S}$ : C, 59.68; H, 4.80; N, 11.60. Found: C, 59.58; H, 4.65; N, 11.43.

**(R)-2-((2S,3S)-3-((1-(4-Chlorophenyl)-1H-1,2,3-triazol-4-yl)methoxy)-3,6-dihydro-2H-pyran-2-yl)-3-(3-hydroxyphenyl)thiazolidin-4-one (9f).** M. p. 218–219 °C. IR (KBr)  $\nu$  3116, 3024, 1746, 1622, 1615, 1424, 1346, 1336, 1228, 1201, 749  $\text{cm}^{-1}$ .  $^1\text{H}$  NMR (300 MHz,  $\text{CDCl}_3$ ):  $\delta$  9.40 (brs, 1H, Ph-OH), 8.08 (s, 1H, Ar-H), 7.58 (d,  $J$  = 9.3 Hz, 2H, Ar-H), 7.49 (d,  $J$  = 8.6 Hz, 2H, Ar-H), 6.83–6.76 (m, 4H, Ar-H), 5.72–5.68 (m, 2H, =CH), 4.94 (d,  $J$  = 5.2 Hz, 1H, CHS), 4.64 (s, 2H,  $\text{OCH}_2$ ), 4.12 (t, 2H,  $\text{OCH}_2$ ), 4.01–3.94 (m, 2H, CH), 3.92 (s, 2H,  $\text{CH}_2$ ).  $^{13}\text{C}$  NMR (75 MHz,  $\text{CDCl}_3$ ):  $\delta$  170.5, 158.2, 143.8, 134.5, 130.4, 128.6, 125.6, 122.4, 119.5, 114.8, 106.5, 85.4, 72.5, 66.4, 63.4, 51.5, 34.1. MS:  $m/z$  ( $\text{M}^+\text{+Na}$ ) 507. Anal. Calcd for  $\text{C}_{23}\text{H}_{21}\text{ClN}_4\text{O}_4\text{S}$ : C, 59.96; H, 4.36; N, 11.55. Found: C, 59.28; H, 4.65; N, 11.43.

**(R)-2-((2S,3S)-3-((1-(4-Chlorophenyl)-1H-1,2,3-triazol-4-yl)methoxy)-3,6-dihydro-2H-pyran-2-yl)-3-(4-hydroxyphenyl)thiazolidin-4-one (9g).** M. p. 273–275 °C. IR (KBr)  $\nu$  3119, 3028, 1741, 1619, 1611, 1420, 1336, 1326, 1218, 1213, 769  $\text{cm}^{-1}$ .  $^1\text{H}$  NMR (300 MHz,  $\text{CDCl}_3$ ):  $\delta$  9.42 (brs, 1H, Ph-OH), 8.05 (s, 1H, Ar-H), 7.56 (d,  $J$  = 9.2 Hz, 2H, Ar-H), 7.46 (d,  $J$  = 8.4 Hz, 2H, Ar-H), 7.32 (d,  $J$  = 8.6 Hz, 2H, Ar-H), 7.02 (d,  $J$  = 8.8 Hz, 2H, Ar-H), 5.89–5.80 (m, 2H, =CH), 4.96 (d,  $J$  = 5.4 Hz, 1H, CHS), 4.66 (s, 2H,  $\text{OCH}_2$ ), 4.09 (d,  $J$  = 2H,  $\text{OCH}_2$ ), 4.04–3.98 (m, 2H, CH), 3.94 (s, 2H,  $\text{CH}_2$ ).  $^{13}\text{C}$  NMR (75 MHz,  $\text{CDCl}_3$ ):  $\delta$  170.9, 154.1, 144.4, 134.9, 134.8, 128.8, 127.2, 125.6, 123.2, 119.4, 116.4, 85.4, 72.6, 66.5, 64.0, 51.6, 34.5. MS:  $m/z$  ( $\text{M}^+\text{+H}$ ) 485. Anal. Calcd for  $\text{C}_{23}\text{H}_{21}\text{ClN}_4\text{O}_4\text{S}$ : C, 59.96; H, 4.36; N, 11.55. Found: C, 59.38; H, 4.75; N, 11.33.

**General procedure for the synthesis of 10a–g.** To a solution of alcohol 7 (0.120 g, 0.465 mmol) in  $\text{CH}_2\text{Cl}_2$  (5 mL), a catalytic amount of IBX was added at 0 °C and stirred at room temperature for 30 min. The reaction mixture was filtered and washed with  $\text{CH}_2\text{Cl}_2$  (2  $\times$  10 mL). It was dried ( $\text{Na}_2\text{SO}_4$ ) and evaporated to give aldehyde 7 (0.110 g) in quantitative yield as a yellow liquid, which was used as such for the next reaction.

To a stirred mixture of 7 (0.110 g, 0.373 mmol), aromatic amine (0.373 mmol) and anhydrous thiomalic acid (0.140 g, 0.211 mmol) in dry toluene (5 mL),  $\text{ZnCl}_2$  (0.100 g, 0.751 mmol) was added after 2 min and irradiated in microwave bath reactor at 280 W for 4–7 minutes at 110 °C. After cooling, the filtrate was concentrated to dryness under reduced pressure and the residue was taken up in ethyl acetate. The ethyl acetate layer was washed with 5% sodium bicarbonate solution and finally with brine. The organic layer was dried over  $\text{Na}_2\text{SO}_4$  and evaporated to dryness at reduced pressure. The crude product thus obtained was purified by column chromatography on silica



gel (60–120 mesh) with hexane–ethyl acetate as the eluent. Under conventional method the reaction mixture in toluene (10 mL) was refluxed at 110 °C for the appropriate time (Table 1).

**2-((2R)-2-((2S,3S)-3-((1-(4-Chlorophenyl)-1H-1,2,3-triazol-4-yl)methoxy)-3,6-dihydro-2H-pyran-2-yl)-4-oxo-3-phenylthiazolidin-5-yl)acetic acid (10a).** M. p. 221–223 °C. IR (KBr)  $\nu$  3114, 3004, 1740, 1724, 1610, 1600, 1430, 1330, 1320, 1219, 755  $\text{cm}^{-1}$ .  $^1\text{H}$  NMR (300 MHz,  $\text{CDCl}_3$ ):  $\delta$  11.50 (s, 1H,  $\text{CO}_2\text{H}$ ), 8.09 (s, 1H, ArH), 7.58 (d,  $J = 9.2$  Hz, 2H, ArH), 7.49 (d,  $J = 8.9$  Hz, 2H, Ar-H), 7.41–6.76 (m, 5H, Ar-H), 6.10 (s, 1H, CHS), 5.84–5.79 (m, 2H, =CH), 4.65 (t, 1H, CH), 4.52 (s, 2H,  $\text{OCH}_2$ ), 4.10–4.08 (m, 2H, OCH), 3.98 (d,  $J = 6.2$  Hz, 2H,  $\text{OCH}_2$ ), 2.36 (d, 2H,  $\text{CH}_2$ ).  $^{13}\text{C}$  NMR (75 MHz,  $\text{CDCl}_3$ ):  $\delta$  175.2, 173.0, 144.4, 141.5, 134.5, 128.5, 125.6, 122.4, 119.4, 86.4, 72.5, 66.4, 49.5, 46.4, 38.6. MS:  $m/z$  ( $\text{M}^+ + \text{H}$ ) 527. Anal. Calcd for  $\text{C}_{25}\text{H}_{23}\text{ClN}_4\text{O}_4\text{S}$ : C, 56.98; H, 4.40; N, 10.65. Found: C, 56.78; H, 4.25; N, 10.43.

**2-((2R)-3-(4-Chlorophenyl)-2-((2S,3S)-3-((1-(4-chlorophenyl)-1H-1,2,3-triazol-4-yl)methoxy)-3,6-dihydro-2H-pyran-2-yl)-4-oxothiazolidin-5-yl)acetic acid (10b).** M. p. 269–271 °C. IR (KBr)  $\nu$  3106, 3021, 1752, 1729, 1606, 1619, 1440, 1330, 1310, 1212, 741  $\text{cm}^{-1}$ .  $^1\text{H}$  NMR (300 MHz,  $\text{CDCl}_3$ ):  $\delta$  11.62 (s, 1H,  $\text{CO}_2\text{H}$ ), 8.12 (s, 1H, Ar-H), 7.54–7.49 (m, 6H, Ar-H), 7.30 (d,  $J = 8.3$  Hz, 2H, Ar-H), 6.13 (s, 1H, CHS), 5.5–5.48 (m, 2H, =CH), 4.59 (t, 1H, CH), 4.5 (s, 2H,  $\text{OCH}_2$ ), 4.09–4.05 (m, 2H, OCH), 3.96 (d,  $J = 6.5$  Hz, 2H,  $\text{OCH}_2$ ), 2.34 (d, 2H,  $\text{CH}_2$ ).  $^{13}\text{C}$  NMR (75 MHz,  $\text{CDCl}_3$ ):  $\delta$  175.2, 173.2, 144.1, 139.6, 134.5, 134.1, 129.0, 127.4, 125.8, 122.4, 119.5, 86.5, 73.0, 66.8, 63.5, 49.3, 46.5, 39.1. MS:  $m/z$  ( $\text{M}^+ + \text{H}$ ) 561. Anal. Calcd for  $\text{C}_{25}\text{H}_{22}\text{Cl}_2\text{N}_4\text{O}_5\text{S}$ : C, 53.48; H, 3.95; N, 9.98. Found: C, 53.18; H, 3.65; N, 9.78.

**2-((2R)-2-((2S,3S)-3-((1-(4-Chlorophenyl)-1H-1,2,3-triazol-4-yl)methoxy)-3,6-dihydro-2H-pyran-2-yl)-3-(4-nitrophenyl)-4-oxothiazolidin-5-yl)acetic acid (10c).** M. p. 257–259 °C. IR (KBr)  $\nu$  3104, 3026, 1736, 1728, 1616, 1601, 1550, 1425, 1324, 1314, 1208, 769  $\text{cm}^{-1}$ .  $^1\text{H}$  NMR (300 MHz,  $\text{CDCl}_3$ ):  $\delta$  11.42 (s, 1H,  $\text{CO}_2\text{H}$ ), 8.20 (d,  $J = 8.4$  Hz, 2H, Ar-H), 8.02 (s, 1H, ArH), 7.48 (d,  $J = 9.2$  Hz, 2H, Ar-H), 7.42 (d,  $J = 8.6$  Hz, 2H, Ar-H), 6.75 (d,  $J = 9.6$  Hz, 2H, Ar-H), 6.15 (s, 1H, CHS), 5.56–5.49 (m, 2H, =CH), 4.62 (s, 2H,  $\text{OCH}_2$ ), 4.56 (t, 1H, CH), 2.30 (d, 2H,  $\text{CH}_2$ ).  $^{13}\text{C}$  NMR (75 MHz,  $\text{CDCl}_3$ ):  $\delta$  175.2, 173.2, 143.6, 135.2, 134.2, 131.5, 128.9, 127.4, 125.6, 124.1, 122.5, 119.4, 86.1, 72.8, 66.5, 63.9, 49.3, 46.5, 39.0. MS:  $m/z$  ( $\text{M}^+ + \text{H}$ ) 573. Anal. Calcd for  $\text{C}_{25}\text{H}_{22}\text{ClN}_5\text{O}_7\text{S}$ : C, 52.50; H, 3.88; N, 12.24. Found: C, 52.38; H, 3.65; N, 12.01.

**2-((2R)-2-((2S,3S)-3-((1-(4-Chlorophenyl)-1H-1,2,3-triazol-4-yl)methoxy)-3,6-dihydro-2H-pyran-2-yl)-4-oxo-3-ortho-tolylthiazolidin-5-yl)acetic acid (10d).** M.

p. 243–245 °C. IR (KBr)  $\nu$  3111, 3014, 1731, 1719, 1626, 1625, 1458, 1449, 1368, 1331, 1238, 729  $\text{cm}^{-1}$ .  $^1\text{H}$  NMR (300 MHz,  $\text{CDCl}_3$ ):  $\delta$  11.60 (s, 1H,  $\text{CO}_2\text{H}$ ), 8.09 (s, 1H, Ar-H), 7.50 (d,  $J = 9.4$  Hz, 2H, Ar-H), 7.45 (d,  $J = 8.5$  Hz, 2H, Ar-H), 6.86–7.10 (m, 4H, Ar-H), 6.20 (s, 1H, CHS), 5.51–5.46 (m, 2H, =CH), 4.65 (s, 2H,  $\text{OCH}_2$ ), 4.45 (t, 1H, CH), 4.10–4.05 (m, 2H, OCH), 3.95 (d,  $J = 6.5$  Hz, 2H,  $\text{OCH}_2$ ), 2.35 (d, 2H,  $\text{CH}_2$ ), 2.10 (s, 3H,  $\text{CH}_3$ ).  $^{13}\text{C}$  NMR (75 MHz,  $\text{CDCl}_3$ ):  $\delta$  175.4, 173.5, 144.5, 138.6, 135.0, 134.5, 130.5, 129.5, 126.0, 122.0, 119.4, 116.5, 86.5, 73.0, 67.0, 64.0, 49.6, 46.5, 38.5, 17.5; MS:  $m/z$  ( $\text{M}^+ + \text{Na}$ ) 563. Anal. Calcd for  $\text{C}_{26}\text{H}_{25}\text{ClN}_4\text{O}_5\text{S}$ : C, 57.72; H, 4.66; N, 10.36. Found: C, 57.58; H, 4.55; N, 10.21.

**2-((2R)-2-((2S,3S)-3-((1-(4-Chlorophenyl)-1H-1,2,3-triazol-4-yl)methoxy)-3,6-dihydro-2H-pyran-2-yl)-4-oxo-3-para-tolylthiazolidin-5-yl)acetic acid (10e).** M. p. 207–209 °C. IR (KBr)  $\nu$  3136, 3024, 1756, 1729, 1612, 1605, 1432, 1424, 1331, 1321, 1248, 757  $\text{cm}^{-1}$ .  $^1\text{H}$  NMR (300 MHz,  $\text{CDCl}_3$ ):  $\delta$  11.42 (s, 1H,  $\text{CO}_2\text{H}$ ), 8.06 (s, 1H, Ar-H), 7.55 (d,  $J = 9.5$  Hz, 2H, Ar-H), 7.46 (d,  $J = 8.5$  Hz, 2H, Ar-H), 7.30 (d,  $J = 9.2$  Hz, 2H, Ar-H), 6.84 (d,  $J = 9.6$  Hz, 2H, Ar-H), 6.15 (s, 1H, CHS), 4.63 (s, 2H,  $\text{OCH}_2$ ), 4.45 (t, 1H, CH), 4.14–4.09 (m, 2H, OCH), 3.93 (d,  $J = 6.9$  Hz, 2H,  $\text{OCH}_2$ ), 2.30 (d, 2H,  $\text{CH}_2$ ), 2.24 (s, 3H,  $\text{CH}_3$ ).  $^{13}\text{C}$  NMR (75 MHz,  $\text{CDCl}_3$ ):  $\delta$  175.2, 173.8, 144.5, 138.5, 136.5, 134.0, 133.5, 129.4, 127.4, 125.6, 122.0, 119.4, 86.5, 73.0, 66.5, 64.0, 49.5, 46.1, 39.0, 21.5; MS:  $m/z$  ( $\text{M}^+ + \text{H}$ ) 541. Anal. Calcd for  $\text{C}_{26}\text{H}_{25}\text{ClN}_4\text{O}_5\text{S}$ : C, 57.72; H, 4.66; N, 10.36. Found: C, 57.52; H, 4.65; N, 10.19.

**2-((2R)-2-((2S,3S)-3-((1-(4-Chlorophenyl)-1H-1,2,3-triazol-4-yl)methoxy)-3,6-dihydro-2H-pyran-2-yl)-3-(3-hydroxyphenyl)-4-oxothiazolidin-5-yl)acetic acid (10f).** M. p. 217–219 °C. IR (KBr)  $\nu$  3126, 3014, 1748, 1730, 1720, 1612, 1605, 1414, 1336, 1316, 1218, 1211, 779  $\text{cm}^{-1}$ .  $^1\text{H}$  NMR (300 MHz,  $\text{CDCl}_3$ ):  $\delta$  11.42 (s, 1H, OH), 8.03 (s, 1H, Ar-H), 7.56 (d,  $J = 9.4$  Hz, 2H, Ar-H), 7.48 (d,  $J = 8.3$  Hz, 2H, Ar-H), 7.14–6.95 (m, 4H, Ar-H), 6.16 (s, 1H, CHS), 5.40 (s, 1H, OH), 4.65 (s, 1H,  $\text{OCH}_2$ ), 4.10–4.03 (m, 2H, OCH), 3.98 (t, 1H, CH), 2.35 (d, 2H,  $\text{CH}_2$ ).  $^{13}\text{C}$  NMR (75 MHz,  $\text{CDCl}_3$ ):  $\delta$  175.3, 173.2, 158.3, 144.5, 134.9, 130.5, 128.5, 127.5, 125.6, 122.0, 119.5, 114.6, 106.3, 86.5, 72.8, 66.5, 64.0, 49.5, 46.5, 39.0; MS:  $m/z$  ( $\text{M}^+ + \text{H}$ ) 543. Anal. Calcd for  $\text{C}_{25}\text{H}_{23}\text{ClN}_4\text{O}_6\text{S}$ : C, 55.30; H, 4.26; N, 10.32. Found: C, 55.12; H, 4.05; N, 10.09.

**2-((2R)-2-((2S,3S)-3-((1-(4-Chlorophenyl)-1H-1,2,3-triazol-4-yl)methoxy)-3,6-dihydro-2H-pyran-2-yl)-3-(4-hydroxyphenyl)-4-oxothiazolidin-5-yl)acetic acid (10g).** M. p. 246–248 °C. IR (KBr)  $\nu$  3149, 3038, 1751, 1728, 1629, 1615, 1440, 1346, 1316, 1228, 1203, 739  $\text{cm}^{-1}$ .  $^1\text{H}$  NMR (300 MHz,  $\text{CDCl}_3$ ):  $\delta$  11.39 (s, 1H,  $\text{CO}_2\text{H}$ ), 8.05 (s, 1H, Ar-H), 7.58 (d,  $J = 9.5$  Hz, 2H, Ar-H), 7.48 (d,  $J = 8.5$  Hz, 2H, Ar-H), 7.32 (d,  $J = 8.8$  Hz, 2H, Ar-H), 6.90 (d,  $J = 9.7$  Hz, 2H, Ar-H), 6.08 (s, 1H, CHS), 5.50–5.48 (m, 2H,

=CH), 5.42 (s, 1H, OH), 4.60 (s, 2H, OCH<sub>2</sub>), 4.15–4.10 (m, 2H, OCH), 3.95 (d, *J* = 6.9 Hz, 2H, OCH<sub>2</sub>), 3.91 (t, 1H, CH), 2.30 (d, 2H, CH<sub>2</sub>). <sup>13</sup>C NMR (75 MHz, CDCl<sub>3</sub>): δ 175.5, 173.8, 154.5, 144.5, 135.0, 134.5, 129.0, 127.5, 125.7, 123.5, 119.5, 116.5, 86.5, 73.0, 67.0, 64.0, 49.5, 46.5, 39.0. MS: *m/z* (M<sup>+</sup>+Na) 565. Anal. Calcd for C<sub>25</sub>H<sub>23</sub>ClN<sub>4</sub>O<sub>6</sub>S: C, 55.30; H, 4.26; N, 10.32. Found: C, 55.09; H, 4.02; N, 10.19.

## 5. Conclusion

A series of novel triazole linked thiazolidinone derivatives **9a–g** and **10a–g** was prepared and evaluated for their anticancer activity against four human cell lines and normal cell line (HEK 293). The screened compounds **9f** and **10f** exhibited potent anticancer activity compared to standard drug at the tested concentrations and **9b**, **10b**, **9g** and **10g** exhibited potent anticancer activity compared to standard drug at the tested concentrations.

## 6. Acknowledgements

The authors are thankful to CSIR- New Delhi for the financial support (Project funding 02/247/15/EMR-II), Director, CSIR-IIT, Hyderabad, India, for NMR and MS spectral analysis.

## 7. References

- (a) A. Farran, C. Cai, M. Sandoval, *Chem. Rev.* **2015**, *115*, 6811–6853. DOI:10.1021/cr500719h  
(b) A. Varki, *Glycobiology*. **1993**, *3*, 97–130. DOI:10.1093/glycob/3.2.97
- N. Galonde, K. Nott, A. Debuigne, *J. Chem. Tech. Biotechnol.* **2012**, *87*, 451–471. DOI:10.1002/jctb.3745
- (a) M. E. Caines, H. Zhu, M. Vuckovic, *J. Bio. Chem.* **2008**, *283*, 31279–31283. DOI:10.1074/jbc.C800150200  
(b) H. Shirato, S. Ogawa, H. Ito, *J. Virol.* **2008**, *82*, 10756–10767. DOI:10.1128/JVI.00802-08  
(c) S. Nagaraj, K. Gupta, V. Pisarev, *Nat. Med.* **2007**, *13*, 828–835. DOI:10.1038/nm1609  
(d) K. E. Niederer, D. Morrow, J. L. Gettings, M. Irick, A. Krawiecki, J. L. Brewster, *CellSignal.* **2005**, *17*, 177–186. DOI:10.1016/j.cellsig.2004.06.009  
(e) H. Yagi, M. Yanagisawa, Y. Suzuki, *J. Bio. Chem.* **2010**, *285*, 37293–37301. DOI:10.1074/jbc.M110.157081
- (a) C. R. Bertozzi, L. L. Kiessling, *Chem. Glyc. Bio. Sci.* **2001**, *291*, 2357–2364. DOI:10.1126/science.1059820  
(b) T. Angata, A. Varki, *Chem. Rev.* **2002**, *102*, 439–469. DOI:10.1021/cr000407m  
(c) R. R. Schmidt, W. Kinzy, *Adv. Carbohydr. Chem. Biochem.* **1994**, *50*, 21–123. DOI:10.1016/S0065-2318(08)60150-X  
(d) V. K. Tiwari, B. B. Mishra, *Research Signpost, Trivandrum. India.* **2011**, *41*, 1–45
- (a) V. K. Tiwari, R. C. Mishra, A. Sharma, R. P. Tripathi, *Mini Rev. Med. Chem.* **2012**, *12*, 1497–1519. DOI:10.2174/138955712803832654  
(b) V. K. Tiwari, B. B. Mishra, K. B. Mishra, N. Mishra, A. S. Singh, X. Chen, *Chem. Rev.* **2016**, *116*, 3086–3240. DOI:10.1021/acs.chemrev.5b00408  
(c) K. B. Mishra, B. B. Mishra, V. K. Tiwari, *Carbohydr. Res.* **2014**, *399*, 2–7. DOI:10.1016/j.carres.2014.09.001  
(d) D. Kumar, K. B. Mishra, B. B. Mishra, V. K. Tiwari, *Steroids*, **2014**, *80*, 71–79. DOI:10.1016/j.steroids.2013.11.022
- R. Huisgen, G. Szeimies, L. Moebius, *Chem. Ber.* **1967**, *100*, 2494–2507. DOI:10.1002/cber.19671000806
- (a) R. Huisgen, *Angew. Chem. Int. Ed.* **1963**, *2*, 565–598. DOI:10.1002/anie.196305651  
(b) R. Huisgen, *Angew. Chem. Int. Ed.* **1963**, *2*, 633–696. DOI:10.1002/anie.196306961  
(c) R. Huisgen, 1,3-Dipolar cycloadditions – introduction, survey, mechanism. In 1,3-Dipolar Cycloaddition Chemistry, Ed. A. Padwa. New York: Wiley. **1984**, 1–176. DOI:10.1002/chin.198518341  
(d) V. V. Rostovtsev, L. G. Green, V. V. Fokin, K. B. Sharpless, *Angew. Chem. Int. Ed.* **2002**, *412*, 2596–2599. DOI:10.1002/1521-3773(20020715)41:14<2596::AID-ANIE2596>3.0.CO;2-4
- (a) F. G. Heras, R. Alonso, G. Alonso, *J. Med. Chem.* **1979**, *22*, 496–501. (b) J. C. Morris, J. Chiche, C. Grellier, *J. Med. Chem.* **2011**, *54*, 6905–6918. (c) S. B. Ferreira, A. C. R. Sodero, M. F. C. Cardoso, *J. Med. Chem.* **2010**, *53*, 2364–2375.
- (a) K. D. Hani, D. A. Leigh, *Chem. Soc. Rev.* **2010**, *39*, 1240–1251. DOI:10.1039/B901974J  
(b) C. O. Kappe, E. van der Eycken, *Chem. Soc. Rev.* **2010**, *39*, 1280–1290. DOI:10.1039/B901973C  
(c) A. H. El-Sagheer, T. Brown, *Chem. Soc. Rev.* **2010**, *39*, 1388–1405. DOI:10.1039/b901971p  
(d) A. Qin, J. W. Y. Lam, B. Z. Tang, *Chem. Soc. Rev.* **2010**, *39*, 2522–2544. DOI:10.1039/b909064a  
(e) M. Meldal, C. W. Tornøe, *Chem. Rev.* **2008**, *108*, 2952–3015. DOI:10.1021/cr0783479  
(f) H. Nandivada, X. Jiang, J. Lahann, *Adv. Mater.* **2007**, *19*, 2197–2208. DOI:10.1002/adma.200602739  
(g) Y. L. Angell, K. Burgess, *Chem. Soc. Rev.* **2007**, *36*, 1674–1689. DOI:10.1039/b701444a  
(h) D. Fournier, R. Hoogenboom, U. S. Schubert, *Chem. Soc. Rev.* **2007**, *36*, 1369–1380. DOI:10.1039/b700809k  
(i) J. E. Moses, A. D. Moorhouse, *Chem. Soc. Rev.* **2007**, *36*, 1249–1262. DOI:10.1039/B613014N  
(j) J. F. Lutz, *Angew. Chem. Int. Ed.* **2007**, *46*, 1018–1025. DOI:10.1002/anie.200604050  
(k) A. Dondoni, *Chem. Asian J.* **2007**, *2*, 700–708. DOI:10.1002/asia.200700015  
(l) H. C. Kolb, K. B. Sharpless, *Drug Dis. Today*, **2003**, *8*, 1128–1137. DOI:10.1016/S1359-6446(03)02933-7
- A. Brick, J. Muldoon, Y.-C. Lin, J. H. Elder, D. S. Goodsell,

- A. J. Olson, V. V. Fokin, K. B. Sharpless, C.-H. Wong, *Chem-BioChem* **2003**, 4, 1246–12148. (b) M. J. Soltis, H. J. Yeh, K. A. Cole, N. Whittaker, R. P. Wersto, E. C. Kohn, *Drug Metab. Dispos.* **1996**, 24, 799–806. DOI:10.1002/cbic.200300724
11. (a) W.-Q. Fan, A. R. Katritzky, 1, 2,3-Triazoles, In *Comprehensive Heterocyclic Chemistry II*. Ed. A. R. Katritzky, C. W. Rees, V. Scriven, Elsevier, Oxford, **1996**, 4, 1–126, pp. 905–1006. DOI:10.1016/B978-008096518-5.00079-4  
(b) M. Whiting, J. Muldoon, Y.-C. Lin, S. M. Silverman, W. Lindstrom, A. J. Olson, H. C. Kolb, M. G. Finn, K. B. Sharpless, J. H. Elder, V. V. Fokin, *Angew. Chem. Int. Ed.* **2006**, 45, 1435–1439. DOI:10.1002/anie.200502161  
(c) Y. Bourne, H. C. Kolb, Z. Radić, K. B. Sharpless, P. Taylor, P. Marchot, *Proc. Natl. Acad. Sci. U. S. A.* **2004**, 101, 1449–1454. DOI:10.1073/pnas.0308206100  
(d) W. G. Lewis, G. Green, F. Z. Grynszpan, Z. Radić, P. R. Carlier, P. Taylor, M. G. Finn, K. B. Sharpless, *Angew. Chem. Int. Ed.* **2002**, 41, 1053–1057. DOI:10.1002/1521-3773(20020315)41:6%3C1053::AID-ANIE1053%3E3.0.CO;2-4
12. R. Huisgen, A. Padwa, *1,3-Dipolar Cycloaddition Chemistry*, Wiley, New York, **1984**, 1, 1–176.
13. (a) N. A. Al-Maoudi, A. Y. Al-Soud, *Tetrahedron Lett.* **2002**, 43, 4021–4022. DOI:10.1016/S0040-4039(02)00733-5  
(b) B. H. M. Kuijpers, S. Groothuys, A. B. R. Keereweere, P. J. L. M. Quaedflieg, R. H. Blaauw, F. L. van Delft, F. P. J. T. Rutjes, *Org. Lett.* **2004**, 6, 3123–3126. DOI:10.1021/ol048841o  
(c) C. Srinivas, X. Fang, Q. Wang, *Tetrahedron Lett.* **2005**, 46, 2331–2334. DOI:10.1016/j.tetlet.2005.01.175  
(d) S. Hotha, R. I. Anegundi, A. A. Natu, *Tetrahedron Lett.* **2005**, 46, 4585–4588. DOI:10.1016/j.tetlet.2005.05.012  
(e) S. Hotha, S. Kashyap, *J. Org. Chem.* **2006**, 71, 364–367. DOI:10.1021/jo051731q
14. (a) R. B. Patel, P. S. Desai, K. R. Desai, K. H. Chikalia, *Indian J. Chem., Sect. B* **2006**, 45B, 773–778.  
(b) A. Bishnoi, S. Krishna, C. K. M. Tripathi, *Indian J. Chem., Sect. B* **2006**, 45B, 2136–2139.
15. C. V. Dave, M. C. Shukla, *Indian J. Chem., Sect. B* **2000**, 39B, 210–214.
16. W. J. Doran, H. A. Shoukly, *J. Org. Chem.* **1939**, 93, 626–633.
17. J. S. Biradar, S. Y. Manjunath, *Indian J. Chem., Sect. B* **2004**, 43B, 389–392.
18. (a) N. P. Buu-Hoi, N. D. Young, F. Binon, *J. Chem. Soc.* **1948**, 70, 3436–3439. DOI:10.1021/ja01190a064  
(b) A. Gangjee, G. Adaer, *J. Med. Chem.* **1999**, 42, 2447–2455. DOI:10.1021/jm990079m  
(c) T. Srivastava, K. G. Anil, H. Wahajul, S. Sudhir, B. K. Setu, *Arkivoc* **2005**, (ii), 120–130.
19. B. R. Shah, N. C. Desai, P. B. Trivedi, *Indian J. Heterocycl. Chem., Sect. B* **1993**, 2, 249–252.
20. L. L. Chijavasakaya, I. Gopnovich, R. S. Chelchenko, *Chem Abstr.* **1969**, 70, 10641y.
21. (a) A. Chimmiri, S. Grasso, A. M. Monforte, P. Monforte, M. Zappala, *Il Farmaco* **1991**, 46, 817–823.  
(b) A. Chimmiri, S. Grasso, A. M. Monforte, P. Monforte, M. Zappala, *Il Farmaco* **1991**, 46, 925–933.  
(c) A. Chimmiri, S. Grasso, C. Molica, A. M. Monforte, P. Monforte, M. Zappala, *Il Farmaco*, **1996**, 51, 279–282.
22. V. M. Barot, *Asian J. Chem.* **1996**, 100, 8802–8806. DOI:10.1021/jp952984y
23. M. H. Khan, Nizamuddin, *J. Food Agric. Chem.* **1995**, 43, 2719–2729.
24. V. K. Ahulwalia, C. Gupta, *Heterocycles* **1991**, 32, 907–914.
25. (a) H. D. Trautmen, L. M. Longe, *J. Am. Chem. Soc.* **1948**, 70, 3434–3436. DOI:10.1021/ja01190a063  
(b) A. R. Surray, *J. Am. Chem. Soc.* **1949**, 71, 3354–3356. DOI:10.1021/ja01178a023
26. M. R. Manrao, J. Monika, V. K. Kaul, *Pl. Dis. Res.* **1997**, 12, 94–96.
27. T. Saini, S. Kumar, B. Narsimhan, *Cent. Nerv. Syst. Agents. Med. Chem.* **2015**, 16, 19–28. DOI:10.2174/1871524915666150608103224
28. T. Kato, T. Ozaki, N. Ohi, *Tetrahedron Asymmetry* **1999**, 10, 3963–3968. DOI:10.1016/S0957-4166(99)00441-3
29. (a) R. B. Desyk, B. S. Zimenskowsky, *Current. Org. Chem.* **1992**, 35, 2712–2719.  
(b) A. Usha, O. Swathi, B. Dinesh, L. T. Ganpat, *Arkivoc* **2006**, (xiii), 83–89. DOI:10.3998/ark.5550190.0007.709
30. Y. Tanabe, H. Yamamoto, M. Murakami, I. K. Yanag, Y. Kubota, Y. Sanimistu, G. Suzukamo, *J. Chem. Soc. Perkin Trans. 1* **1975**, 7, 935–938.
31. (a) C. O. Kappe, *Angew. Chem. Int. Ed.* **2004**, 43, 6250–6284. DOI:10.1002/anie.200400655  
(b) C. O. Kappe, D. Dallinger, *Nat. Rev. Drug Discovery* **2006**, 5, 51–63. DOI:10.1038/nrd1926
32. Y. Kumar, V. Bahadur, A. K. Singh, V. S. Parmer, E. V. van der Eycken, B. K. Singh, *Beilstein J. Org. Chem.* **2014**, 10, 113–118.
33. V. Sharma, P. K. Jaiswal, D. K. Yadav, M. Saran, J. Prikhodko, M. Mathur, A. K. Swami, I. V. Mashevskaya, S. Chaudhary, *Acta Chim. Slov.* **2017**, 64, 988–1004. DOI:10.17344/acsi.2017.3709
34. B. Prek, B. Stanovnik, *Acta Chim. Slov.* **2017**, 64, 798–803.
35. B. L. Turek, M. Kočevr, K. Kranjc, F. Perdih, *Acta Chim. Slov.* **2017**, 64, 737–746.
36. L. Moradi, M. A. Sadegh, *Acta Chim. Slov.* **2017**, 64, 506–512. DOI:10.17344/acsi.2017.3417
37. A. Srinivas, M. Sunitha, P. Karthik, G. Nikitha, K. Raju, B. Ravinder, S. Anusha, T. Rajasri, D. Swapna, D. Swaroopa, K. Srinivas, K. Vasumathi Reddy, *J. Heterocycl. Chem.* **2017**, 54, 3250–3257. DOI:10.1002/jhet.2943
38. A. Srinivas, M. Sunitha, P. Karthik, K. V. Reddy, *Acta Chim. Slov.* **2017**, 64, 1030–1041. DOI:10.17344/acsi.2017.3805
39. A. Srinivas, M. Sunitha, K. Raju, B. Ravinder, S. Anusha, T. Rajasri, P. Swapna, D. Sushmitha, D. Swaroopa, G. Nikitha, C. G. Rao, *Acta Chim. Slov.* **2017**, 64, 319–331. DOI:10.17344/acsi.2016.3153
40. A. Srinivas, *Acta Chim. Slov.* **2016**, 63, 173–179.
41. A. Srinivas, M. Sunitha, *Indian J. Chemistry, Sect. B* **2016**, 55B, 102–109.
42. A. Srinivas, M. Sunitha, *Indian J. Chemistry, Sect. B* **2016**, 55B, 231–239.

43. C. S. Reddy, A. Srinivas, M. Sunitha, A. Nagaraj, *J. Heterocycl. Chem.* 2010, 47, 1303–1309. DOI:10.1002/jhet.474
44. A. Srinivas, C. S. Reddy, A. Nagaraj, *Chem. Pharm. Bull.* 2009, 57, 685–693.
45. C. S. Reddy, A. Srinivas, A. Nagaraj, *J. Heterocycl. Chem.* 2009, 46, 497–502. DOI:10.1002/jhet.100
46. C. S. Reddy, A. Srinivas, A. Nagaraj, *J. Heterocycl. Chem.* 2008, 45, 1121–1125. DOI:10.1002/jhet.5570450428
47. T. Mossamen, *J. Immunol. Methods* 1983, 65, 55–63. DOI:10.1016/0022-1759(83)90303-4

## Povzetek

S kondenzacijo (2S,3S)-3-((1-(4-klorofenil)-1H-1,2,3-triazol-4-il)metoksi)-3,6-dihidro-2H-piran-2-karbaldehida z merkaptokislinami in primarnimi amini v prisotnosti  $\text{ZnCl}_2$  smo pod pogoji obsevanja z mikrovalovi in klasičnim segrevanjem pripravili seriji (R)-2-((2S,3S)-3-((1-(4-klorofenil)-1H-1,2,3-triazol-4-il)metoksi)-3,6-dihidro-2H-piran-2-il)-3-feniltiazolidin-4-onov **9a–g** in 2-((2R)-2-((2S,3S)-3-((1-(4-klorofenil)-1H-1,2,3-triazol-4-il)metoksi)-3,6-dihidro-2H-piran-2-il)-4-okso-3-feniltiazolidin-5-il)ocetnih kislin **10a–g**. Nove spojine smo karakterizirali z IR, NMR, MS in elementno analizo. Raziskali smo citotoksičnost na seriji štirih različnih človeških tumorskih celičnih linij: A549 iz človeških alveolarnih adenokarcinomskih epiteljskih celic (ATCC No. CCL-185), Hela iz človeških rakastih celic materničnega vratu (ATCC No. CCL-2), MDA-MB-231 iz človeških adenokarcinomskih celic dojke (ATCC No. HTB22) in HEK 239 (normalne človeške embrionske celice ledvic) s pomočjo MTT analize. Izmed testiranih spojin sta **9e** in **10e** pokazali največjo učinkovitost proti MCF-7 celični liniji raka dojke z  $\text{IC}_{50}$  vrednostmi 1.91 in 1.95  $\mu\text{M}$ , spojine **9b**, **10b**, **9g** in **10g** pa so pokazale obetavno aktivnost proti MDA-MB-231 in Hela celicam z  $\text{IC}_{50}$  vrednostmi 5.84, 5.74, 7.89 in 7.65  $\mu\text{M}$ .



Except when otherwise noted, articles in this journal are published under the terms and conditions of the Creative Commons Attribution 4.0 International License

Scientific paper

# Spectroscopic Determination of Metal-Ligand Coordination by Biologically Active 2-Picolinehydroxamic Acid with Iron(III) and Oxidovanadium(IV) in Aqueous Solutions

Magdalena Woźniczka,<sup>1,\*</sup> Mirosława Świątek,<sup>1</sup> Joanna Gądek-Sobczyńska,<sup>1</sup>  
Beata Pasternak<sup>2</sup> and Aleksander Kufelnicki<sup>1</sup>

<sup>1</sup> Department of Physical and Biocoordination Chemistry, Faculty of Pharmacy, Medical University of Lodz, Muszyńskiego 1, 90-151 Lodz, Poland

<sup>2</sup> Department of Organic Chemistry, Faculty of Chemistry, University of Lodz, Tamka 12, 91-403 Lodz, Poland

\* Corresponding author: E-mail: magdalena.wozniczka@umed.lodz.pl

Received: 04-11-2019

## Abstract

The complexing properties of 2-picolinehydroxamic acid towards iron(III) as well as oxidovanadium(IV) were characterized in aqueous solutions by the UV-Vis spectrophotometric method. The speciation models have been confirmed and even extended by electrospray-ionization mass spectrometry (ESI-MS) studies. For both systems, mononuclear complexes were formed below a pH of 1 and coordination by {O,O'} chelation mode leading to the formation of five-membered rings was confirmed. The overall stability constant values were determined and compared with other similar systems, indicating more effective binding of the ligand by Fe(III) than VO(IV). The acidic medium of the reaction in the VO(IV) – 2-picolinehydroxamic acid system prevented the oxidation of VO(IV) to V(V). 2-Picolinehydroxamic acid was chosen because of its previously evidenced biological properties. As a result of acidification, reversible dissociation of the complexes in both systems was observed, indicating the action of 2-picolinehydroxamic acid as a potential siderophore.

**Keywords:** Iron(III) complexes; oxidovanadium(IV) complexes; 2-picolinehydroxamic acid; UV/Vis spectroscopy; ESI-MS spectroscopy

## 1. Introduction

Metal ions and their complexes have a significant impact on biological systems. Therefore, it is extremely important to analyze the detailed structure and composition of these compounds, especially since their application as therapeutic agents is constantly increasing.<sup>1</sup> The iron is important ion for catalyzing oxidoreductase reactions<sup>2,3</sup> and playing a key role in cellular respiration.<sup>4</sup> This metal is found in many essential metalloproteins<sup>5</sup> and is a nutrient of microorganisms, provided in the form of iron(III)-siderophore complex.<sup>6,7</sup>

Not any less interesting transition metal is vanadium, present mainly in the body as the oxidovanadium(IV) ion, potentially an inhibitor of phosphatases, phosphotransferases, nucleases and kinases,<sup>8–10</sup> acting as an essential cofactor in two classes of enzymes, haloperoxidases

and nitrogenases, probably also in a third class, vanabins.<sup>4,5</sup> Based on vanadium as an insulin mimetic agent, the drugs have been proposed for treatment of diabetes.<sup>11–13</sup>

The potentially toxic effects of iron and vanadium led to a permanent search for ligands binding excess metal ions.<sup>5,11</sup> A characteristic feature of most of the hydroxamic acids is their ability to form very stable complexes with iron(III)<sup>15,16</sup> and oxidovanadium(IV).<sup>17</sup> As a result, the determination of formation constants is often impossible by pH-potentiometry, particularly when complexation occurs in a strongly acidic medium. However, the metal-hydroxamic acid interaction might be quite well characterized by UV-Vis electronic absorption bands and is supported by ESI-MS spectroscopy. Some natural hydroxamic acids exist as siderophores and are responsible for iron transport to microbial cells.<sup>18–20</sup> In addition, hydroxamic acids showing a strong interaction with metal ions have

been used to treat anemia, remove excess iron ions and serve as inhibitors.<sup>15,21–24</sup> They also arouse clinical interest related to the possible treatment of lung silicosis, and can be used as antimalarials and antibacterial agents.<sup>25</sup> Deferoxamine B, a siderophore produced by microorganisms, has been recognized as a strong vanadium chelator.<sup>26</sup>

The present study examines the complexation equilibria for the iron(III) and oxidovanadium(IV) ions with 2-picolinehydroxamic acid (PicHA) (Fig. 1) in aqueous solution, which have not been described until now. Recent studies indicate that 2-picolinohydroxamic acid alone, as well coordinated by the cobalt(II) ion, exhibits antimicrobial properties, especially against *Candida*, *Pseudomonas aeruginosa* and *Bacillus subtilis*, and activates non-specific immune cells that indirectly promote the eradication of infection.<sup>27</sup>

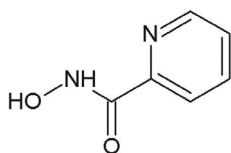


Fig. 1. The ligand 2-picolinehydroxamic acid structure (PicHA, LH).

## 2. Experimental

### 2.1. Materials

2-Picolinehydroxamic acid (PicHA) was synthesized by a team at the Department of Chemistry, National Taras Shevchenko University of Kiev, according to the procedure described in.<sup>28</sup> Iron(III) chloride from Fluka and oxidovanadium(IV) sulfate oxide hydrate from Alfa Aesar were used as standard solutions. The carbonate-free 1.0 mol L<sup>-1</sup> NaOH solution, HPLC-grade water and methanol were purchased from J.T. Baker. Hydrochloric acid solution from Avantor Performance Materials was standardized alkalimetrically and determined by the Gran method.<sup>29</sup> The standard solution of sodium chloride (Chempur) was used to adjust the ionic medium without further purification. Argon of high purity (Linde) was used.

### 2.2. Spectrophotometric Measurements

UV-Vis absorption spectra were recorded on a Cary 50 Bio spectrophotometer with the slit width of 1.5 nm. The spectrophotometer was equipped with a fiber-optic device allowing simultaneous recording of spectrophotometric scans with pH values. Measurements were controlled by a Titrando 905 automatic titrator system (Metrohm) with a combined polymer microelectrode In-Lab Semi-Micro (METTLER TOLEDO). The fiber-optic probe, 5 mm long, corresponding to a path length of 1 cm, was dipped directly into the thermostatted titration vessel. The electrode was calibrated with buffers at pH 4.00 and 7.00 before use. All the experiments were accomplished in

aqueous solution at a constant temperature of  $25.0 \pm 0.1$  °C and ionic strength  $I = 1.0$  mol L<sup>-1</sup> adjusted by NaCl. A stream of pure argon was passed over the surface of a 10 mL sample to obtain solutions free of oxygen and carbon dioxide. The pH values, changing after the addition of each base aliquot, were controlled by the Titrando 905 titrator and a time delay was given to equilibrate the system. The spectrum was recorded with a slow scan (300 nm min<sup>-1</sup>) at selected pH values.

The studies of Fe(III) complexation with PicHA were performed at ligand-to-metal molar ratios 4:1, 6:1 and 10:1 (total metal concentration of  $5.0 \times 10^{-4}$  mol L<sup>-1</sup>). A large excess of ligand in relation to the metal ion was used to avoid precipitation from Fe(III) aqua-hydroxido complexes which could occur at a pH above 1.<sup>30</sup> Formation constants of the Fe(III) aqua-hydroxido complexes were determined under the same conditions as the complexation equilibria with the ligand. In turn, the titrations in the presence of VO(IV) were carried out at ligand-to-metal molar ratios 1:1 and 2:1 (at constant concentration of metal ions  $5.0 \times 10^{-3}$  mol L<sup>-1</sup>). For VO(IV), under the present experimental conditions (pH about 3), the hydroxylated forms could be neglected in comparison with the vanadyl aqua-ion.<sup>31,32</sup> The initial pH appeared below 1.0 in all the experiments due to acidification by 1.0 mol L<sup>-1</sup> HCl. The pH values in the range of 0.90–1.30 were calculated directly from acid contents. The carbonate-free 1.0 mol L<sup>-1</sup> NaOH was used as a titrant. Such a high concentration of the titrant was associated with necessity of neutralize a large excess of acid and avoid excessive dilution of the sample. The titrations were continued until precipitation.

The HypSpec program, part of the Hyperquad 2008 suite (Protonic Software)<sup>33</sup> was used to calculate the molar absorption coefficients of the individual species and to determine the equilibrium constants resulting from spectrophotometric data. Overall concentration formation constants were calculated by a fitting procedure according to the formula:  $\beta_{mlh} = [M_m L_l H_h] / [M]^m [L]^l [H]^h$ . Based on these constants, the graphical simulation of the complex species distribution was carried out by HySS 2009.<sup>34</sup>

### 2.3. Electrospray-Ionization Mass Spectrometry (ESI-MS) Measurements

The ESI-MS and MS/MS spectra were recorded using a Varian 500-MS LC hexapole ion-trap mass spectrometer (Palo Alto, CA, USA). The study was performed for the ligand, as well as both iron(III) and oxidovanadium(IV) systems with PicHA in 50/50% (v/v) methanol/water mixture without the addition of a background electrolyte. The ESI response is higher when methanol/water mixture is used because methanol provides a more stable spray and produces smaller initial droplets than water alone or highly aqueous solvent.<sup>35</sup>

The ligand spectra were determined at the concentration of  $1.0 \times 10^{-2}$  mol L<sup>-1</sup>. For iron(III) – ligand system, the



molar ligand-metal ratio was equal to 4:1 at the concentration of Fe(III) ion  $2.5 \times 10^{-4} \text{ mol L}^{-1}$ . The spectra recorded in the presence of oxidovanadium(IV) and PicHA were carried out at a ligand-to-metal molar ratio 2:1 (concentration of VO(IV) ion  $2.5 \times 10^{-3} \text{ mol L}^{-1}$ ). The samples containing metal-ligand systems were adjusted to various pH values, selected for maximization formation of individual complexes (according to the species distribution graphs). The test samples were introduced into the ESI-MS source by continuous infusion using an instrument syringe pump at a rate of  $10 \mu\text{L min}^{-1}$ . The ESI-source was operated at 5.00 kV and the capillary heater was set to  $350^\circ\text{C}$ . The cone voltage was within the range of 40–120 V. The experiments were carried out in the positive and negative ion-mode.

### 3. Results and Discussion

#### 3. 1. UV-Vis Spectra

##### 3. 1. 1. Fe(III) Complexes

The electronic absorption spectra of PicHA in the presence of the iron(III) ion were recorded within the range of 300–800 nm (Fig. 2a). The tested pH range allowed for the maximum molar absorption coefficients and for the overall stability constants (Fig. 2b, Table 1) to be calculated by the HypSpec deconvolution procedure for the accepted  $[\text{FeL}]^{2+}$  and  $[\text{FeL}_2]^+$  species (Fig. 3). The mixed hydroxido complexes with ligand, complexes with protonated ligand [LH], as well as the polynuclear complexes, observed for transition metal ion – PicHA systems,<sup>27,36,37</sup> have not been confirmed in the equilibrium model during the refinement procedure. Dissociation constants of PicHA (Fig. 1) used in the model were taken from own data.<sup>27</sup> The first step of ligand dissociation for  $[\text{LH}_2]^+$  form concerns the protonated pyridyl group ( $\text{pK}_{\text{a}1}$  1.80)

and the second one is assigned to the dissociation of the hydroxamic group proton ( $\text{pK}_{\text{a}1}$  8.22) of the [LH] form. Molar absorption coefficients of iron(III) ion, calculated on the basis of the electronic absorption spectra (Fig. S1a,b), were used in HypSpec procedure. The hydrolysis of the iron(III) ion was already observed above pH 1 (Fig. S1c). The separately determined formation constants of the aqua-hydroxido complexes:  $[\text{Fe}(\text{OH})]^{2+}$  and  $[\text{Fe}(\text{OH})_2]^+$  were equal to  $\log_{10} \beta_{10-1} = -2.68(2)$  and  $\log_{10} \beta_{10-2} = -6.48(10)$ , respectively, and corresponded to the literature data.<sup>30,38–40</sup> During the calculations, the potential polynuclear hydrolysis species ( $[\text{Fe}_2(\text{OH})_2]^{4+}$  or  $[\text{Fe}_3(\text{OH})_4]^{5+}$ )<sup>38</sup> were not accepted by the HypSpec fitting procedure under the present experimental conditions. As indicated by the reference data,<sup>30,38</sup> a low concentration of iron ions, adapted to the experiment, results in the trace amount or absence of polynuclear complexes in the solution. In addition, the presence of chloride ions and the way they form relatively strong complex with iron(III) affects the lower hydrolysis effect, especially in the formation of polynuclear complexes.<sup>38,41</sup>

The high stability constants values obtained in the Fe(III) – PicHA system (Table 1), correspond to the reference data for other hydroxamic acids<sup>22</sup> and confirm the possibility of the formation of very stable iron(III) chelates with the ligand. Chelation in the  $[\text{FeL}]^{2+}$  species is possible by the oxygen atoms of the ligand, forming a stable five-membered ring (Fig. 3a), just as reported for X-ray crystal forms.<sup>21</sup> Natural trihydroxamic acids also chelate the iron(III) ion using oxygen atoms,<sup>25</sup> thus it could be assumed that the same coordination mode occurs for the  $[\text{FeL}_2]^+$  complex (Fig. 3b) with a high value of the stepwise stability constant  $\log_{10} K_{\text{FeL}_2}^{\text{FeL}} = 9.93$  (base on Table 1 and theoretically supported in the literature<sup>42,43</sup>). The distribution curves of the complex species as a function of pH are shown in Fig. 4.

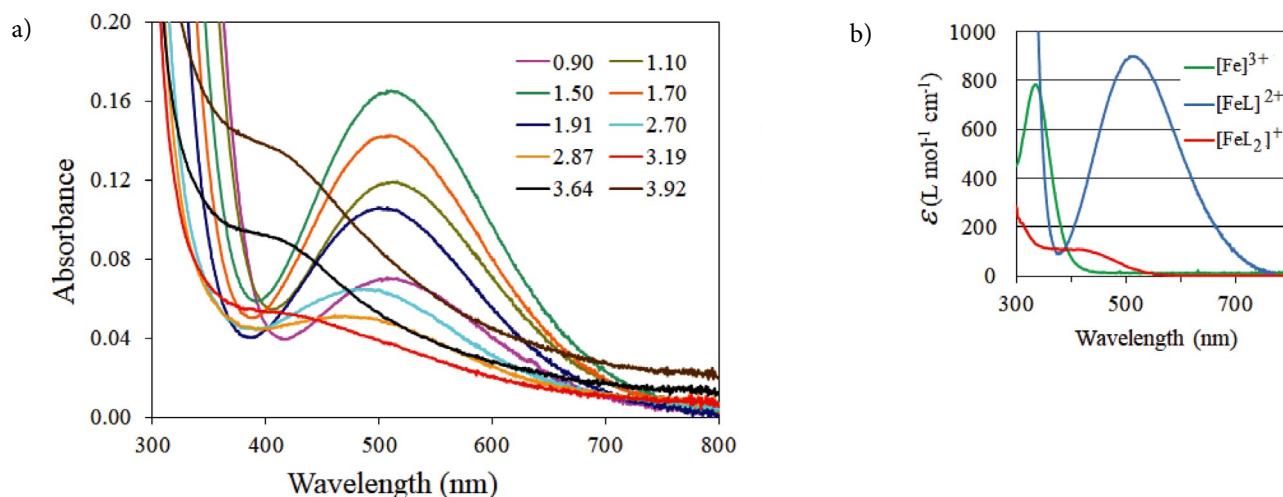


Fig. 2. (a) UV-Vis absorption spectra of the Fe(III) – PicHA system at ligand-to-metal molar ratio 4:1, within the pH range 0.90–3.92;  $c_{\text{Fe(III)}} = 5.0 \times 10^{-4} \text{ mol L}^{-1}$ . (b) Molar absorption coefficients for the complexes in the Fe(III) – PicHA system.

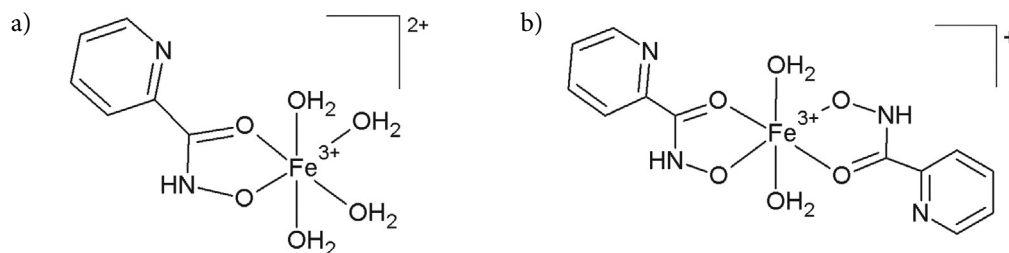


Fig. 3. Suggested coordination modes in the Fe(III) – PicHA system: (a)  $[\text{FeL}]^{2+}$ , (b)  $[\text{FeL}_2]^+$ .

**Table 1.** Decimal logarithms of overall formation constants  $\beta_{mLh} = [\text{M}_m\text{L}_l\text{H}_h]/[\text{M}]^m[\text{L}]^l[\text{H}]^h$  at  $25.0 \pm 0.1^\circ\text{C}$ ,  $I = 1.0$  (NaCl) and UV-Vis spectral data; standard deviations in parentheses after overall stability constants refer to random errors only

Species	$\log_{10} \beta_{mLh}$	$\lambda_{\text{max}} (\epsilon_{\text{max}})$
$[\text{FeL}]^{2+}$	10.25(1)	509 (897)
$[\text{FeL}_2]^+$	20.18(1)	420 <sup>sh</sup> (107)
$\sigma^a$	0.003	
$[\text{VOL}]^+$	7.64(1)	500 <sup>sh</sup> (704)
$\sigma^a$	0.076	

<sup>a</sup> $\sigma$  – the value of the normalized sum of squared residuals

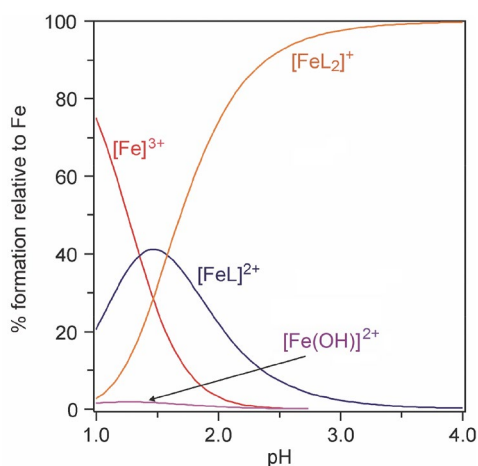


Fig. 4. Species distribution curves as a function of pH for the complexes formed in the Fe(III) – PicHA system at 4:1 ligand-to-metal molar ratio,  $c_{\text{Fe(III)}} = 5.0 \times 10^{-4} \text{ mol L}^{-1}$ .

As it follows from Fig. 2a, the Fe(III) complexes are formed already in a very acidic medium (below pH 1.0) just at the beginning of titrations. This is demonstrated by the presence of the absorption band at ca. 510 nm, characteristic of octahedral coordination of Fe(III) with one hydroxamic acid molecule,<sup>16,21,22</sup> and confirmed by the species distribution graph (Fig. 4). The presence of ligand-to-metal charge transfer absorption bands, often obscuring the low intensity *d-d* absorption, is characteristic of the iron(III) interaction.<sup>44</sup> During the titration, the intensity of this absorption band increased, reaching the maximum absorbance at pH 1.5. However, as the pH in-

creased further, the band decreased with a blue shift to 470 nm at pH about 2.9. This was connected with the simultaneous existence of the two forms: a decrease of the  $[\text{FeL}]^{2+}$  concentration and formation of  $[\text{FeL}_2]^+$  species (Fig. 4). A blue shift of the molar absorption coefficients of  $[\text{FeL}_2]^+$  in relation to  $[\text{FeL}]^{2+}$  was also observed for other hydroxamic acid complexes with metal ions.<sup>9,15,26</sup> A slight decrease of the complex stability (Table 1) most likely occurred due to an increase of the ligand field.

As shown in Fig. 4, a small share (about 2% of the total iron) of the  $[\text{Fe(OH)}]^{2+}$  complex is observed in solution at the initial pH range. Moreover, 509 nm corresponds to the maximum molar absorption coefficient of the  $[\text{FeL}]^{2+}$  species (Table 1, Fig. 2). At this wavelength, the aqua-hydroxido complex shows a molar absorption coefficient value of almost ten times lower (Fig. S1) than the iron(III) complex with one PicHA molecule.

Further alkalization caused the formation of a shoulder at 370–450 nm at the pH above 3.19 (Fig. 2a), and the change of color from pale pink to orange, reasonably correlated with increasing share of the  $[\text{FeL}_2]^+$  complex. According to the species distribution curves, this pH range corresponded to reaching almost 100% share of  $[\text{FeL}_2]^+$  in the solution (Fig. 4). An increase of pH above 4 caused a disturbance in the UV-Vis absorption spectra by light scattering arising from poorly soluble hydrolytic products.

After the precipitation (at pH approximately 4.0), the mixture was again acidified to pH below 1.50. Then the absorption band at ca. 510 nm, characteristic of  $[\text{FeL}]^{2+}$  was observed again. This indicated the possible partial reversibility of the complexes in Fe(III) – PicHA system and allowed the authors to assume that some of the iron(III) aqua-ions were released into the solution (Fig. 4), by that indicating the siderophoric character of PicHA.

### 3. 1. 2. VO(IV) Complexes

UV-Vis absorption spectra obtained for the VO(IV) – PicHA system indicate the complex formation starting from pH below 1.0 (Fig. 5a). Beside the *d-d* bands relative to the VO(IV) aqua-ion, 763 nm ( $\epsilon = 13.4$ ) and the shoulder 625 nm ( $\epsilon = 6.0$ ), an additional rising *d-d* transition at about 500 nm was observed (Fig. 5b,c). Three intra *d* shell electronic transitions are typical of  $C_{4v}$  square pyramidal structure at the vanadyl ion.<sup>44</sup> Further alkalization led to in-

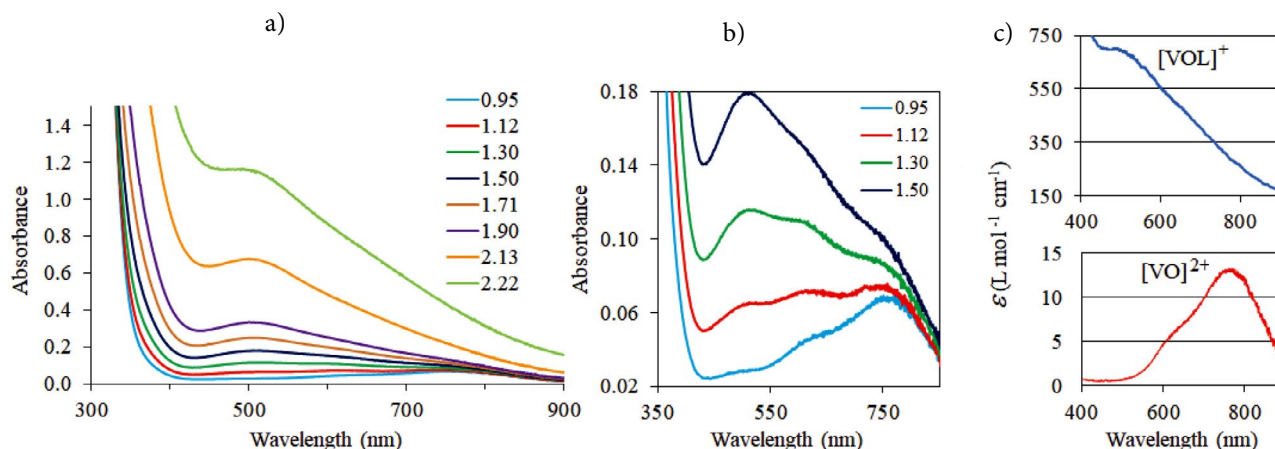


Fig. 5. UV-Vis absorption spectra of the VO(IV) – PicHA system at ligand-to-metal molar ratio 2:1,  $c_{\text{VO(IV)}} = 5.0 \times 10^{-3} \text{ mol L}^{-1}$  within the pH range (a) 0.95–2.22, (b) 0.95–1.50 – narrowed part of spectra. (c) Molar absorption coefficients for the complexes in the VO(IV) – PicHA system.

creased intensity of the transition bands, up to precipitation (at pH 2.2). Due to the low pH values, precipitation is most likely not connected with the aqua-hydroxido complexes of VO(IV),<sup>31,32</sup> but rather with low water solubility of subsequent species formed in the VO(IV) – PicHA system.

During the first titration step within the pH range of 0.95–1.90 (Fig. 5a), the increase of absorbance was concomitant with a small wavelength change (the differences were within the slit width value). This most likely indicates the formation of only one VO(IV) complex with the PicHA molecule in the equilibrium solution.

The stability constant and the maximum molar absorption coefficient of the  $[\text{VOL}]^+$  complex has been determined based on the spectrophotometric titrations of the VO(IV) – PicHA system (Table 1, Fig. 5c). The calculations also indicated the possible formation of  $[\text{VOL}_2]$ . Unfortunately, the values of the molar absorption coefficients were affected by high errors due to low participation of this complex in the equilibrium solution. This induced the rejection of  $[\text{VOL}_2]$  from the equilibrium model. As previously observed for the Fe(III) – PicHA system,<sup>22</sup> the stabil-

Presumably, this complex forms pentacoordinated species, as suggested by DFT calculations carried out for acetohydroxamic acid.<sup>9</sup> Moreover, as shown in,<sup>44</sup> a very strong V=O axial bond is exceptionally short as compared to the equatorial bonds.

The  $[\text{VOL}]^+$  complex confirmed is represented in the species distribution curves (Fig. 7). The VO(IV) aqua-ion was the dominant form in the system whereas  $[\text{VOL}]^+$  was formed at a pH above 1, reaching only 18% of the total vanadium at a pH of 2.2.

Similarly to the Fe(III) – PicHA system, in order to check the reversibility of the interaction between oxido-vanadium(IV) and the ligand, the samples were acidified from pH 2.5 to pH below 1. The absorbance decreased at about 500 nm and the color changed from brown to transparent, which confirmed the reversible dissociation of the complexes, such as previously observed in the VO(IV) – deferoxamine B system.<sup>26</sup>

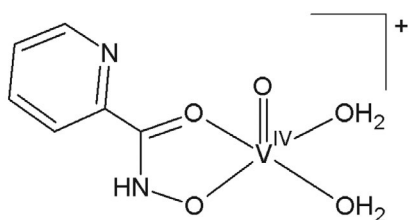


Fig. 6. Suggested coordination mode of  $[\text{VOL}]^+$  in the VO(IV) – PicHA system.

ity constant value of the  $[\text{VOL}]^+$  is of the same order of magnitude as the reference data for other hydroxamic acid species.<sup>17</sup> The literature EPR study<sup>17</sup> as well as high value of the present stability constant indicate the chelated nature of the  $[\text{VOL}]^+$  complex in  $\{\text{O,O}^-\}$  mode (see Fig. 6).

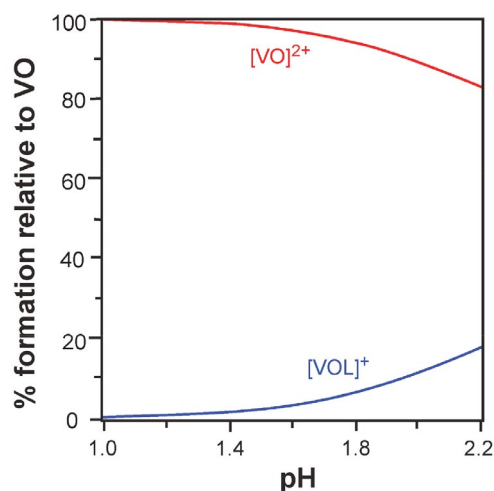


Fig. 7. Species distribution curves as a function of pH for the complexes formed in VO(IV) – PicHA system at 2:1 ligand-to-metal molar ratio,  $c_{\text{VO(IV)}} = 5.0 \times 10^{-3} \text{ mol L}^{-1}$ .

### 3. 2. ESI-MS Results

ESI-MS spectra were taken of PicHA as well as of its systems with Fe(III) and VO(IV). Structural investigation by the tandem mass spectrum (Fig. S2) of the protonated ligand molecule  $[\text{LH}_2]^+$  ( $m/z = 139.0$ ) (Fig. 1) indicated the possibility of its degradation. The first step ( $m/z = 138.0$ ) was related to the loss of hydrogen atom, most likely from pyridine group  $-\text{NH}^+$ , as indicated by potentiometric studies.<sup>27</sup> Detachment of  $-\text{NH}_{\text{hydroxamic}}$  from  $[\text{LH}_2]^+$ , probably due to rearrangement of the molecule, gave the ion with  $m/z = 124.0$ . Then the ion with  $m/z = 122.0$  was formed by the loss of hydrogen atoms. The competitive fragmentation of  $[\text{LH}_2]^+$  involved the loss of  $\text{H}_2\text{O}$  ( $m/z = 121.0$ ), probably by the intramolecular migration of a pyridine hydrogen to  $-\text{OH}$  group. As a result of further fragmentation, peaks  $m/z = 106.0$  and  $m/z = 78.0$  were obtained. The first was formed after the detachment of  $\text{NH}_{\text{hydroxamic}}$ , the second  $\text{C}=\text{O}$ , respectively.

The structural analysis of both PicHA systems used negative- and positive-ion mass spectra. The ESI-MS spectra of Fe(III) – PicHA complexes were taken at three pH values (1.6, 3.2, 6.5). The use of the 50/50% (v/v) methanol/water mixture resulted in precipitation at pH about 7.0, higher than in spectrophotometric measurements, probably due to the stabilizing properties of methanol.<sup>45</sup> At pH 1.6, the negative-ion spectrum of the  $[\text{Fe(III)L} + 2\text{Cl} + \text{OH}]^-$  ( $m/z = 280.0$ ) and the adduct of Fe(III) ( $m/z = 256.0$ ) containing the fragment ion  $m/z = 78.0$  were registered (Fig. S3). The  $m/z$  values for all ions in the paper were related to the stable isotopes  $^{56}\text{Fe}$  and  $^{35}\text{Cl}$ . Moreover,  $[\text{Fe(III)} + 4\text{Cl}]^-$  ( $m/z = 196.0$ ) was also detected, which confirms a share of iron(III) aqua-ions in very acidic medium (cf. Fig. 4). Alkalization to pH 3.2 led to an appearance of further complexes with one PicHA molecule. This concerned both the negative adduct of Fe(II) ( $m/z = 269.0$ ) with the fragment ion  $m/z = 122.0$  (Fig. S4a) and the positive adducts/associate of Fe(II) ( $m/z = 197.0$ ; 255.0) with the fragment ion  $m/z = 106.0$  (Fig. S4b). The reduction process of Fe(III) to the Fe(II) state is most probable in ESI-MS measurements.<sup>46,47</sup> The formation of the  $[\text{Fe(III)L}_2]^+$  complex ( $m/z = 330.0$ ), confirmed by the species distribution curves (Fig. 4), was also shown in Fig. S4b. A further pH increase (to 6.5) affected a number of signals of bi-ligand complexes (Fig. S5);  $[\text{Fe(II)L}]^+$  ( $m/z = 271.0$ ) with the fragment ion  $m/z = 78.0$ , the  $\text{Cl}^-$  adduct of Fe(II) ( $m/z = 303.0$ ) with two fragment ions  $m/z = 106.0$  and its associate ( $m/z = 606.0$ ) were detected. Interestingly, the ESI-MS studies showed the presence of iron complexes with three PicHA molecules:  $[\text{Fe(III)L}_3 + \text{Na} + 2\text{Cl}]^-$  ( $m/z = 560.0$ ) in Fig. S5a,  $[\text{Fe(III)L}_3 + \text{H}]^+$  ( $m/z = 468.0$ ) and  $[\text{Fe(III)L}_3 + 2\text{Na} + \text{Cl}]^+$  ( $m/z = 548.0$ ) in Fig. S5b. This was possible due to the achievement of a higher pH values than in spectrophotometric studies (Fig. 2a).

The ESI-MS spectra for the VO(IV) – PicHA system were performed in the positive and negative ion mode at pH 1.4 and 2.6. Nevertheless, no significant signal was ob-

served in the negative ion mode. According to the spectrophotometric data (Fig. 7), mainly  $\text{VO}^{2+}$  aqua-ions were observed at pH 1.4. This has been confirmed by a high relative intensity signal for  $[\text{VO} + \text{SO}_4 + \text{H}]^+$  ( $m/z = 164.0$ ) (Fig. S6) as well as the high abundance of the ligand alone and its fragment ions, which were observed in the tandem mass spectrum of the  $[\text{LH}_2]^+$  (Fig. S2). However, a number of signals for the VO(IV) – PicHA complexes with one ligand molecule has been identified, as adducts:  $[\text{VOL} + \text{H}_2\text{O} + \text{CH}_3\text{OH}]^+$  ( $m/z = 254.0$ ),  $[\text{VOL} + \text{NaOH} + \text{NaCl} + \text{CH}_3\text{OH}]^+$  ( $m/z = 334.0$ ),  $[\text{VO} + \text{Cl}]^+$  ( $m/z = 224.0$ ) with the fragment ion  $m/z = 122.0$  and associates:  $[(\text{VO})_2\text{L} + \text{SO}_4]^+$  ( $m/z = 445.0$ ) with the fragment ion  $m/z = 78.0$  and  $[(\text{VO})_2\text{L}_2 + \text{SO}_4 + \text{NaOH} + \text{Na}]^+$  ( $m/z = 567.0$ ). In addition, there were PicHA complexes formed in a ratio of 2:1 with oxidovanadium(IV), confirmed by signals of low relative intensity:  $[\text{VOL}_2 + \text{Na}]^+$  ( $m/z = 364.0$ ) and others ( $m/z = 282.0$ ; 326.0) with fragment ions  $m/z = 78.0$  and 122.0 (see Fig. S6). Further alkalization was carried out to pH 2.6, without precipitation in the methanol/water mixture, in contrast to the aqueous solution, where precipitation appeared at pH above 2.22. This enabled the identification of new VO(IV) complexes with one or two ligand molecules in the system:  $[\text{VOL}]^+$  ( $m/z = 204.0$ ),  $[\text{VOL} + \text{H}_2\text{O}]^+$  ( $m/z = 222.0$ ),  $[\text{VOL} + 2\text{H}_2\text{O}]^+$  ( $m/z = 240.0$ ) in Fig. S7a,  $[\text{VOL} + \text{H}_2\text{SO}_4]^+$  ( $m/z = 302.0$ ),  $[\text{VOL}_2 + \text{H}]^+$  ( $m/z = 342.0$ ),  $[\text{VOL}_2 + \text{Na} + \text{H}_2\text{O}]^+$  ( $m/z = 382.0$ ) Fig. S7b. In addition, various forms of the ligand, such as  $[\text{LH} + \text{Na} + \text{HCl}]^+$  ion ( $m/z = 197.0$ ) and others observed in the tandem mass spectrum (Fig. S2), have been demonstrated.

### 4. Conclusions

The UV-Vis electronic spectroscopy method was used to determine the stability and molecular formula of the 2-picolinehydroxamic acid complexes with Fe(III) as well as VO(IV). The ligand showed more effective binding to iron(III) than oxidovanadium(IV), indicating formation of ML and  $\text{ML}_2$  metal-ligand species and higher values of formation constants for the first metal ion. The 2-picolinehydroxamic acid was found to have a tendency to form complexes coordinated in the  $\{\text{O}, \text{O}^-\}$  mode. The formation of mononuclear iron(III) and oxidovanadium(IV) complexes with 2-picolinehydroxamic acid was also confirmed at various pH levels by means of ESI-MS studies, despite the necessity of using another solvent (methanol/water) than in spectrophotometric measurements. During the latter measurements, the presence of methanol in the mixture probably stabilized the complex structures, causing the formation of precipitation at a higher pH than in an aqueous solution. This allowed the ESI-MS spectra to suggest subsequent types of complexes in both metal systems.

The tested complexes with Fe(III) and VO(IV) offer the advantage of reversibility to the aqua-ion and ligand

alone. This may indicate the siderophoric character of PicHA and confirm a lack of oxidation of the VO(IV) ion to V(V) under the conditions of the experiment. Our research provides information for the interaction of PicHA with two biologically important metal ions in aqueous solution. The knowledge of complexation equilibria may enhance the understanding of the mechanism of siderophore action and increase protection against excess of toxic metal ions.

## Conflict of Interest

The authors declare that they have no conflicts of interest.

## Acknowledgements

This work was supported by the Medical University of Lodz [Statute Fund No. 503/3-014-02/503-31-001]. We offer our thanks to Prof. Igor O. Fritsky and Dr. Irina A. Golenya (Department of Chemistry, National Taras Shevchenko University of Kiev) for the synthesis of 2-picolinehydroxamic acid.

## Supplementary material

Supplementary electronic absorption spectra, molar absorption coefficients and species distribution curves for the Fe(III) aqua-hydroxido complexes (Fig. S1) as well as mass spectra (Figs. S2–S7) can be found here.

## 5. References

1. I. Correia, P. Adão, S. Roy, M. Wahba, C. Matos, M. R. Mau-rya, F. Marques, F. R. Pavan, C. Q. F. Leite, F. Avecilla, J. C. Pessoa, *J. Inorg. Biochem.* **2014**, *141*, 83–93. DOI:10.1016/j.jinorgbio.2014.07.019
2. C. Karami, A. Alizadeh, M. A. Taher, Z. Hamidi, B. Bahrami, *J. Appl. Spectrosc.* **2016**, *83*, 687–693. DOI:10.1007/s10812-016-0349-3
3. A. Bazmandegan-Shamili, A. M. Haji Shabani, S. Dadfarnia, M. Saeidi, M. Rohani Moghadam, *Turk. J. Chem.* **2015**, *39*, 1059–1068. DOI:10.3906/kim-1504-9
4. C. C. McLauchlan, H. A. Murakami, C. A. Wallace, D. C. Crans, *J. Inorg. Biochem.* **2018**, *186*, 267–279. DOI:10.1016/j.jinorgbio.2018.06.011
5. D. C. Crans, K. A. Woll, K. Prusinskas, M. D. Johnson, E. Norkus, *Inorg. Chem.* **2013**, *52*, 12262–12275. DOI:10.1021/ic4007873
6. B. Monzyk, A. L. Crumbliss, *J. Am. Chem. Soc.* **1982**, *104*, 4921–4929. DOI:10.1021/ja00382a031
7. E. Farkas, H. Csóka, G. Micera, A. Dessi, *J. Inorg. Biochem.* **1997**, *65*, 281–286. DOI:10.1016/S0162-0134(96)00144-4
8. D. N. Chasteen, The biochemistry of vanadium. In: Copper, Molybdenum, and Vanadium in Biological Systems. Structure and Bonding. Springer, Berlin, Heidelberg, **1983**, pp. 105–138. DOI:10.1007/BFb0111304
9. J. M. Da Silva Santos, S. Carvalho, E. B. Paniago, H. A. Duarte, *J. Inorg. Biochem.* **2003**, *95*, 14–24. DOI:10.1016/S0162-0134(03)00072-2
10. E. D. Carpio, L. Hernández, C. Ciangherotti, V. V. Coa, L. Jiménez, V. Lubes, G. Lubes, *Coord. Chem. Rev.* **2018**, *372*, 117–140. DOI:10.1016/j.ccr.2018.06.002
11. J. C. Pessoa, S. Etcheverry, D. Gambino, *Coord. Chem. Rev.* **2015**, *301–302*, 24–48. DOI:10.1016/j.ccr.2014.12.002
12. K. H. Thompson, J. Lichter, C. LeBel, M. C. Scaife, J. H. McNeill, C. Orvig, *J. Inorg. Biochem.* **2009**, *103*, 554–558. DOI:10.1016/j.jinorgbio.2008.12.003
13. H. Sakurai, Y. Kojima, Y. Yoshikawa, K. Kawabe, H. Yasui, *Coord. Chem. Rev.* **2002**, *226*, 187–198. DOI:10.1016/S0010-8545(01)00447-7
14. L. J. Hernández-Benítez, P. Jiménez-Cruz, K. E. Cureño-Hernández, A. Solano-Peralta, M. Flores-Álamo, A. Flores-Parra, I. Gracia-Mora, S. E. Castillo-Blum, *Inorg. Chim. Acta.* **2018**, *480*, 197–206. DOI:10.1016/j.ica.2018.05.013
15. P. Buglyó, E. M. Nagy, I. Sóvágó, A. Ozsváth, D. Sanna, E. Farkas, *Polyhedron* **2016**, *110*, 172–181. DOI:10.1016/j.poly.2016.02.031
16. E. Farkas, E. Kozma, M. Petho, K. M. Herlihy, G. Micera, *Polyhedron* **1998**, *17*, 3331–3342. DOI:10.1016/S0277-5387(98)00113-2
17. P. Buglyó, N. Pótári, *Polyhedron* **2005**, *24*, 837–845. 7
18. B. Monzyk, A. L. Crumbliss, *J. Am. Chem. Soc.* **1979**, *101*, 6203–6213. DOI:10.1021/ja00515a009
19. C. D. Hardy, A. Butler, *J. Biol. Inorg. Chem.* **2018**, *23*, 957–967. DOI:10.1007/s00775-018-1584-2
20. T. Lifa, W. Tieu, R. K. Hocking, R. Codd, *Inorg. Chem.* **2015**, *54*, 3573–3583. DOI:10.1021/acs.inorgchem.5b00141
21. D. A. Brown, D. McKeith (nee Byrne), W. K. Glass, *Inorg. Chim. Acta.* **1979**, *35*, 5–10. DOI:10.1016/S0020-1693(00)93409-1
22. N. Gálvez, B. Ruiz, R. Cuesta, E. Colacio, J. M. Domínguez-Vera, *Inorg. Chem.* **2005**, *44*, 2706–2709. DOI:10.1021/ic048840s
23. D. Cheshmedzhieva, N. Toshev, M. Gerova, O. Petrov, T. Dudev, *J. Mol. Model.* **2018**, *24*:114. DOI:10.1007/s00894-018-3651-6
24. H. Wen, Y. Qin, W. Zhong, C. Li, X. Liu, Y. Shen, *Enzyme Microb. Technol.* **2016**, *92*, 9–17. DOI:10.1016/j.enzmictec.2016.06.006
25. M. T. Caudle, A. L. Crumbliss, *Inorg. Chem.* **1994**, *33*, 4077–4085. DOI:10.1021/ic00096a037
26. P. Buglyó, N. Culeddu, T. Kiss, G. Micera, D. Sanna, *J. Inorg. Biochem.* **1995**, *60*, 45–59. DOI:10.1016/0162-0134(95)00001-5
27. M. Woźniczka, M. Świątek, M. Pająk, J. Gądek-Sobczyńska, M. Chmiela, W. Gonciarz, P. Lisiecki, B. Pasternak, A. Kufelnicki, *J. Inorg. Biochem.* **2018**, *187*, 62–72. DOI:10.1016/j.jinorgbio.2018.07.010
28. J. B. Hynes, *J. Med. Chem.* **1970**, *13*, 1235–1237. DOI:10.1021/jm00300a056



29. P. Gans, B. O'Sullivan, *Talanta* **2000**, *51*, 33–37. DOI:10.1016/S0039-9140(99)00245-3
30. J. Torres, S. Domínguez, M. F. Cerdá, G. Obal, A. Mederos, R. F. Irvine, A. Díaz, C. Kremer, *J. Inorg. Biochem.* **2005**, *99*, 828–840. DOI:10.1016/j.jinorgbio.2004.12.011
31. D. C. Crans, J. J. Smee, E. Gaidamauskas, L. Yang, *Chem. Rev.* **2004**, *104*, 849–902. DOI:10.1021/cr020607t
32. M. Jansson-Charrier, E. Guibal, J. Roussy, B. Delanghe, P. Le Cloirec, *Wat. Res.* **1996**, *30*, 465–475. DOI:10.1016/0043-1354(95)00154-9
33. P. Gans, A. Sabatini, A. Vacca, *Talanta* **1996**, *43*, 1739–1753. DOI:10.1016/0039-9140(96)01958-3
34. L. Alderighi, P. Gans, A. Ienco, D. Peters, A. Sabatini, A. Vacca, *Coord. Chem. Rev.* **1999**, *184*, 311–318. DOI:10.1016/S0010-8545(98)00260-4
35. R. Kostianen, T. J. Kauppila, *J. Chromatogr. A* **2009**, *1216*, 685–699. DOI:10.1016/j.chroma.2008.08.095
36. L. Marchiò, N. Marchetti, C. Atzeri, V. Borghesani, M. Remel-lib, M. Tegoni, *Dalton Trans.* **2015**, *44*, 3237–3250. DOI:10.1039/C4DT03264K
37. E. Gumienna-Kontecka, I. A. Golenya, A. Szebesczyk, M. Haukka, R. Krämer, I. O. Fritsky, *Inorg. Chem.* **2013**, *52*, 7633–7644. DOI:10.1021/ic4007229
38. G. H. Khoe, P. L. Brown, R. N. Sylva, R. G. Robins, *J. Chem. Soc., Dalton Trans.* **1986**, 1901–1906. DOI:10.1039/DT9860001901
39. M. Iuliano, G. De Tommaso, *J. Chem. Eng. Data* **2010**, *55*, 400–404. DOI:10.1021/jc900394c
40. W. N. Perera, G. Hefter, *Inorg. Chem.* **2003**, *42*, 5917–5923. DOI:10.1021/ic034087b
41. R. N. Collins, K. M. Rosso, A. L. Rose, C. J. Glover, T. D. Waite, *Geochim. Cosmochim. Acta* **2016**, *177*, 150–169. DOI:10.1016/j.gca.2016.01.021
42. A. E. Martell, R. D. Hancock, *Metal complexes in aqueous solutions*, Springer Science+ Business Media, New York **1996**. DOI:10.1007/978-1-4899-1486-6
43. A. E. Martell, R. J. Motekaitis, *Determination and use of stability constants*, second ed., VCH Publishers, Inc., New York **1992**.
44. A. B. P. Lever, *Inorganic electronic spectroscopy*, second ed. Elsevier, Amsterdam **1984**.
45. M. Tegoni, M. Remelli, *Coord. Chem. Rev.* **2012**, *256*, 289–315. DOI:10.1016/j.ccr.2011.06.007
46. G. Weber, N. von Wirén, H. Hayen, *Rapid Commun. Mass Spectrom.* **2006**, *20*, 973–980. DOI:10.1002/rcm.2402
47. H. Neubert, R. C. Hider, D. A. Cowan, *Rapid Commun. Mass Spectrom.* **2002**, *16*, 1556–1561. DOI:10.1002/rcm.756

## Povzetek

Z UV-Vis spektrofotometričnimi metodami smo določili kompleksacijske lastnosti 2-pikolinhidroksamske kisline za vezavo na železove(III) in oksidovanadijeve(IV) ione v vodnih raztopinah. Speciacijske modele smo potrdili in razširili z masno spektrometrijo z ionizacijo z elektrorazprševanjem (ESI-MS). Pri obeh sistemih nastanejo enojedrni kompleksi pri vrednostih pH pod 1 s kelatno koordinacijo {O,O<sup>-</sup>}, ki vodi do nastanka petčlenskega obroča. Določili smo vrednosti stabilizacijskih konstant in jih primerjali s sorodnimi sistemi, ki kažejo na bolj učinkovito vezavo liganda s Fe(III) v primerjavi z VO(IV). Kisel medij v sistemu VO(IV) – 2-pikolinhidroksamska kislina preprečuje oksidacijo VO(IV) v V(V). 2-Pikolinhidroksamska kislina je bila izbrana zaradi predhodno potrjenih bioloških lastnosti. Kot posledica nakisanja smo opazili reverzibilno disociacijo kompleksa v obeh sistemih, kar kaže, da bi lahko bila 2-pikolinhidroksamska kislina potencialni siderofor.



Except when otherwise noted, articles in this journal are published under the terms and conditions of the Creative Commons Attribution 4.0 International License



# Vanadium(V) Complexes with Bromo-Substituted Hydrazones: Synthesis, Characterization, X-ray Crystal Structures and Antimicrobial Activity

Cui-Lin Zhang,<sup>1</sup> Xiao-Yang Qiu<sup>1,2,\*</sup> and Shu-Juan Liu<sup>1</sup>

<sup>1</sup> College of Science & Technology, Ningbo University, Ningbo 315212, P.R. China

<sup>2</sup> State Key Laboratory of Structural Chemistry, Fujian Institute of Research on the Structure of Matter, Chinese Academy of Sciences, Fuzhou, Fujian 350002, P.R. China

\* Corresponding author: E-mail: xiaoyang\_qiu@126.com

Received: 05-05-2019

## Abstract

Two new V<sup>V</sup> complexes with the bromo-substituted hydrazones *N*'-(3-bromo-2-hydroxybenzylidene)-3-hydroxy-4-methoxybenzohydrazide (H<sub>2</sub>L<sup>1</sup>), *N*'-(3-bromo-2-hydroxybenzylidene)-3,5-dimethoxybenzohydrazide (H<sub>2</sub>L<sup>2</sup>), [VOL<sup>1</sup>(OCH<sub>3</sub>)(CH<sub>3</sub>OH)] (1) and [VOL<sup>2</sup>(OCH<sub>3</sub>)(CH<sub>3</sub>OH)] (2), were synthesized and structurally characterized by IR, UV-Vis and <sup>1</sup>H NMR spectroscopy, as well as single-crystal X-ray determination. The V atom in the mononuclear complexes are six-coordinated in octahedral geometry. The free hydrazones and the complexes were studied on their antibacterial activity on *S. aureus*, *B. subtilis*, *E. coli* and *P. fluorescence*, and antifungal activity on *C. albicans* and *A. niger*. The bromo groups of the hydrazone ligands may increase their antibacterial activity.

**Keywords:** Vanadium complex; hydrazone; crystal structure; mononuclear complex; antimicrobial activity

## 1. Introduction

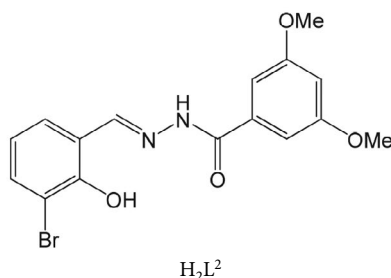
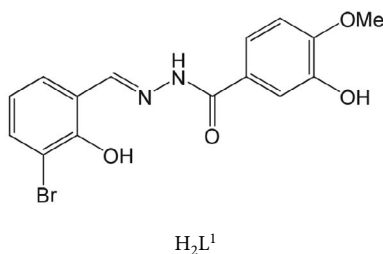
Hydrazones and their complexes have received much interest because of their excellent biological applications in antibacterial,<sup>1</sup> antifungal,<sup>2</sup> as well as antitumor.<sup>3</sup> The compounds with electron-withdrawing groups have been proved to possess increased antimicrobial activity.<sup>4</sup> Recently, a series of chloro, fluoro, iodo- and bromo-substituted compounds have been assayed for their remarkable antimicrobial activity.<sup>5</sup> Schiff base vanadium complexes have distinguish antibacterial activity.<sup>6</sup> In pursuit of new antimicrobial material, we report herein two new bromo-substituted hydrazone compounds *N*'-(3-bromo-2-hydroxybenzylidene)-3-hydroxy-4-methoxyben-

zohydrazide (H<sub>2</sub>L<sup>1</sup>), *N*'-(3-bromo-2-hydroxybenzylidene)-3,5-dimethoxybenzohydrazide (H<sub>2</sub>L<sup>2</sup>), and their vanadium(V) complexes, [VOL<sup>1</sup>(OCH<sub>3</sub>)(CH<sub>3</sub>OH)] (1) and [VOL<sup>2</sup>(OCH<sub>3</sub>)(CH<sub>3</sub>OH)] (2), and studied their antimicrobial activities.

## 2. Experimental

### 2. 1. Materials and Methods

3-Bromosalicylaldehyde, 3-hydroxy-4-methoxybenzohydrazide, 3,5-dimethoxybenzohydrazide and VO(acac)<sub>2</sub> were obtained from Sigma-Aldrich. The remaining reagents with AR grade were obtained from Xiya Chemi-



cal Reagent Co. Ltd. The hydrazones were prepared by the literature method.<sup>7</sup> Elemental analyses (C, H, N) were determined with a Perkin-Elmer automated model 2400 Series II CHNS/O analyzer. The molar conductivity was determined using a DDS-11A conductor device. FT-IR spectra were carried out on a Perkin-Elmer 377 FT-IR spectrometer with KBr disks. The electronic spectra were performed on a Lambda 35 spectrometer. <sup>1</sup>H NMR were carried out on a Bruker 300 MHz instrument. Single crystal X-ray determination was collected on a Bruker APEX II CCD diffractometer.

## 2. 2. Synthesis of the Hydrazones

To the MeOH solution (30 mL) of 3-bromosalicylaldehyde (0.01 mol, 2.01 g) a MeOH solution (20 mL) of 3-hydroxy-4-methoxybenzohydrazide (0.01 mol, 1.82 g) or 3,5-dimethoxybenzohydrazide (0.01 mol, 1.96 g) was added drop wise. The solution was stirred at room temperature for 30 min, and filtered. The filtrate was evaporated to give colorless crystalline product, which were re-crystallized from MeOH and dried at reduced pressure above anhydrous CaCl<sub>2</sub>.

For H<sub>2</sub>L<sup>1</sup>: Yield 94%. *Anal.* Calc. for C<sub>15</sub>H<sub>13</sub>BrN<sub>2</sub>O<sub>4</sub>: C, 49.3; H, 3.6; N, 7.7. Found: C, 49.5; H, 3.7; N, 7.6%. IR data (cm<sup>-1</sup>): 3429, 3195, 1642, 1612. UV-Vis data (MeOH, λ<sub>max</sub>, nm): 225, 293, 307, 325, 400. <sup>1</sup>H NMR (300 MHz, d<sup>6</sup>-DMSO): δ 12.76 (s, 1H, OH), 12.30 (s, 1H, OH), 11.27

(s, 1H, NH), 8.63 (s, 1H, CH=N), 7.63 (d, 1H, ArH), 7.50–7.40 (m, 3H, ArH), 7.13 (d, 1H, ArH), 6.92 (t, 1H, ArH), 3.85 (s, 3H, OCH<sub>3</sub>). For H<sub>2</sub>L<sup>2</sup>: Yield 97%. *Anal.* Calc. for C<sub>16</sub>H<sub>15</sub>BrN<sub>2</sub>O<sub>4</sub>: C, 50.68; H, 3.99; N, 7.39. Found: C, 50.53; H, 4.08; N, 7.46%. IR data (cm<sup>-1</sup>): 3433, 3197, 1644, 1612. UV-Vis data (MeOH, λ<sub>max</sub>, nm): 225, 295, 307, 328, 400. <sup>1</sup>H NMR (300 MHz, d<sup>6</sup>-DMSO): δ 12.65 (s, 1H, OH), 11.33 (s, 1H, NH), 8.63 (s, 1H, CH=N), 7.63 (d, 1H, ArH), 7.45 (d, 1H, ArH), 6.92 (t, 1H, ArH), 6.71 (s, 1H, ArH), 6.45 (d, 2H, ArH), 3.84 (s, 6H, OCH<sub>3</sub>).

## 2. 3. Synthesis of the Complexes

The MeOH solution (10 mL) of hydrazones (0.10 mmol each) was reacted with the MeOH solution (10 mL) of VO(acac)<sub>2</sub> (0.10 mmol, 26.5 mg). The solution was stirred and refluxed for 1 h, and cooled to room temperature. Brown single crystals were generated upon slowly evaporation within 6 days. The crystals were washed with MeOH and dried at reduced pressure above anhydrous CaCl<sub>2</sub>.

For **1**: Yield 36%. *Anal.* calc. for C<sub>17</sub>H<sub>18</sub>BrN<sub>2</sub>O<sub>7</sub>V: C, 41.4; H, 3.7; N, 5.7; found: C, 41.3; H, 3.7; N, 5.6%. IR data (cm<sup>-1</sup>): 3454 (w), 1603 (s), 958 (m). UV-Vis data (MeOH, λ<sub>max</sub>, nm): 272, 335. <sup>1</sup>H NMR (300 MHz, d<sup>6</sup>-DMSO): δ 12.71 (s, 1H, OH), 12.20 (s, 1H, OH), 9.39 (s, 1H, ArH), 8.56 (s, 1H, CH=N), 7.61 (q, 1H, ArH), 7.51–7.41 (m, 2H, ArH), 7.08 (d, 1H, ArH), 6.91 (t, 1H, ArH), 3.86 (s, 3H, OCH<sub>3</sub>), 3.33 (s, 6H, CH<sub>3</sub>OH and OCH<sub>3</sub>). Λ<sub>M</sub> (10<sup>-3</sup> M in

Table 1. Crystallographic and refinement data for complexes **1** and **2**

Complex	H <sub>2</sub> L <sup>1</sup>	<b>1</b>	<b>2</b>
Formula	C <sub>15</sub> H <sub>13</sub> BrN <sub>2</sub> O <sub>4</sub>	C <sub>17</sub> H <sub>18</sub> BrN <sub>2</sub> O <sub>7</sub> V	C <sub>18</sub> H <sub>20</sub> BrN <sub>2</sub> O <sub>7</sub> V
Formula weight	365.18	493.18	507.21
<i>T</i> (K)	298(2)	298(2)	298(2)
Crystal system	Monoclinic	Triclinic	Monoclinic
Space group	<i>P</i> 2 <sub>1</sub> / <i>c</i>	<i>P</i> -1	<i>P</i> 2 <sub>1</sub> / <i>n</i>
<i>a</i> (Å)	17.2603(13)	7.6101(9)	13.5326(10)
<i>b</i> (Å)	7.2902(12)	10.3404(13)	9.3050(7)
<i>c</i> (Å)	12.1706(19)	13.1269(16)	16.1808(13)
α (°)	90	81.517(1)	90
β (°)	104.431(1)	75.965(1)	94.621(1)
γ (°)	90	68.939(1)	90
<i>V</i> (Å <sup>3</sup> )	1483.1(4)	933.1(2)	2030.9(3)
<i>Z</i>	4	2	4
<i>D</i> <sub>calc</sub> (g cm <sup>-3</sup> )	1.635	1.755	1.659
μ (Mo Kα) (mm <sup>-1</sup> )	2.791	2.716	2.499
<i>F</i> (000)	736	496	1024
Measured reflections	8532	8761	18003
Unique reflections	2764	3455	3606
Observed reflections ( <i>I</i> ≥ 2σ( <i>I</i> ))	1896	2906	2900
Parameters	205	260	269
Restraints	1	1	1
Goodness of fit on <i>F</i> <sup>2</sup>	1.025	1.030	1.039
<i>R</i> <sub>1</sub> , <i>wR</i> <sub>2</sub> [ <i>I</i> ≥ 2σ( <i>I</i> )] <sup>a</sup>	0.0437, 0.1036	0.0285, 0.0679	0.0345, 0.0776
<i>R</i> <sub>1</sub> , <i>wR</i> <sub>2</sub> (all data) <sup>a</sup>	0.0717, 0.1159	0.0378, 0.0721	0.0498, 0.0857

<sup>a</sup> *R*<sub>1</sub> = *F*<sub>o</sub> - *F*<sub>c</sub>/*F*<sub>o</sub>, *wR*<sub>2</sub> = [Σ *w*(*F*<sub>o</sub><sup>2</sup> - *F*<sub>c</sub><sup>2</sup>)/Σ *w*(*F*<sub>o</sub><sup>2</sup>)<sup>1/2</sup>]

acetonitrile): 41  $\Omega^{-1} \text{ cm}^2 \text{ mol}^{-1}$ . For **2**: Yield 41%. Anal. calc. for  $\text{C}_{18}\text{H}_{20}\text{BrN}_2\text{O}_7\text{V}$ : C, 42.62; H, 3.97; N, 5.52; found: C, 42.73; H, 3.89; N, 5.61%. IR data ( $\text{cm}^{-1}$ ): 3450 (w), 1602 (s), 953 (m). UV-Vis data (MeOH,  $\lambda_{\text{max}}$ , nm): 275, 323.  $^1\text{H}$  NMR (300 MHz,  $d_6$ -DMSO):  $\delta$  12.56 (s, 1H, OH), 9.30 (s, 1H, ArH), 8.59 (s, 1H, CH=N), 7.66 (d, 1H, ArH), 7.53 (d, 1H, ArH), 7.17–6.91 (m, 2H, ArH), 6.70 (s, 1H, ArH), 3.84 (s, 3H,  $\text{OCH}_3$ ), 3.78 (s, 3H,  $\text{OCH}_3$ ), 3.38 (s, 6H,  $\text{CH}_3\text{OH}$  and  $\text{OCH}_3$ ).  $\Lambda_{\text{M}}$  ( $10^{-3} \text{ M}$  in acetonitrile): 32  $\Omega^{-1} \text{ cm}^2 \text{ mol}^{-1}$ .

## 2. 4. X-ray Crystallography

Single crystal X-ray determination was performed on a Bruker APEX II CCD area diffractometer with Mo K $\alpha$  radiation at 0.71073 Å. The data were reduced with the program SAINT<sup>8</sup> and corrected by multi-scan using the program SADABS.<sup>9</sup> The vanadium complexes were solved readily by direct method. The complexes were refined by the full-matrix least-squares method against  $F^2$  using the program SHELXTL.<sup>10</sup> The non-H atoms were anisotropically refined. The H atoms of the methanol molecules were assigned from the difference Fourier maps, and isotropically refined with  $d_{\text{O-H}}$  restrained to 0.85(1) Å. The other H atoms were in calculated geometrical positions. The crystallographic data and refinement parameters are summarized in Table 1.

## 2. 5. Antimicrobial Study

The activities against *B. subtilis*, *S. aureus*, *E. coli*, and *P. fluorescence* of the compounds were assayed with MH (Mueller–Hinton) medium. The activities against *C. albicans* and *A. niger* of the compounds were assayed with RPMI-1640 medium. The dye MTT was used in the determination of the MIC values by a colorimetric method.<sup>11</sup> A specified quantity of the medium with the tested compound was poured into micro-titration plates. Suspension of the microorganism containing  $1.0 \times 10^5 \text{ cfu mL}^{-1}$  was applied to micro-titration plates with the compounds in DMSO to be tested and incubated at 37 °C for 24 h and 48 h for bacteria and fungi, respectively. The MIC values were visually determined on each of the microtitration plates, Phosphate buffered saline (50  $\mu\text{L}$ , 0.01  $\text{mol L}^{-1}$ , pH = 7.4) containing 2 mg of MTT  $\cdot \text{mL}^{-1}$  was poured into the well. Incubation was continued for 4–5 h at room temperature. The content of the well was removed and isopropanol (100  $\mu\text{L}$ ) containing 5% 1  $\text{mol L}^{-1}$  HCl was added to extract the dye. The optical density was determined with a micro-plate reader at 550 nm after 12 h of incubation at room temperature.

## 3. Results and Discussion

### 3. 1. Chemistry

The hydrazones  $\text{H}_2\text{L}^1$  and  $\text{H}_2\text{L}^2$  were synthesized by the reaction of 3-bromosalicylaldehyde and 3-hydroxy-

4-methoxybenzohydrazide and 3,5-dimethoxybenzohydrazide, respectively in ethanol. The vanadium complexes were synthesized by the reaction of the hydrazones  $\text{H}_2\text{L}^1$  and  $\text{H}_2\text{L}^2$  with  $\text{VO}(\text{acac})_2$  in MeOH followed by re-crystallization. Elemental analyses (C, H, N) of the complexes are in accordance with the results of single-crystal X-ray analysis.

### 3. 2. Spectroscopic Studies

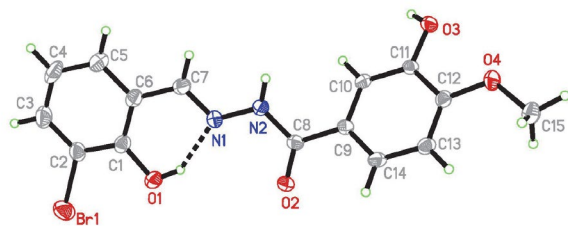
In the spectra of the compounds, the broad and weak absorptions at 3400–3500  $\text{cm}^{-1}$  can be attributed to the  $\nu(\text{O-H})$ . The sharp and weak bands of  $\text{H}_2\text{L}$  located at ca. 3195  $\text{cm}^{-1}$  can be attributed to the  $\nu(\text{N-H})$ . The strong absorption at 1643  $\text{cm}^{-1}$  of  $\text{H}_2\text{L}$  are generated by  $\nu(\text{C=O})$ , whereas the typical bands at 1612  $\text{cm}^{-1}$  are the  $\nu(\text{C=N})$ . The absence of the  $\nu(\text{C=O})$  and  $\nu(\text{N-H})$  in the spectra of the complexes, suggests that the hydrazone ligands are enolized during the coordination. The intense bands at 1602  $\text{cm}^{-1}$  of the complexes are due to the  $\nu(\text{C=N})$ . The characteristic  $\nu(\text{V=O})$  at 955  $\text{cm}^{-1}$  for the complexes can be obviously identified.<sup>12</sup>

The bands in the UV-Vis spectra of the compounds at 320–340 nm are attributed to the intra-ligand  $\pi \rightarrow \pi^*$  absorption. The lowest energy transition bands of the complexes are located at 400 nm, which can be attributed to LMCT transition. The LMCT and to some extent  $\pi \rightarrow \pi^*$  bands observed at 275 nm for complexes **1** and **2** are attributed to the O donor atoms bound to V atoms.<sup>12</sup>

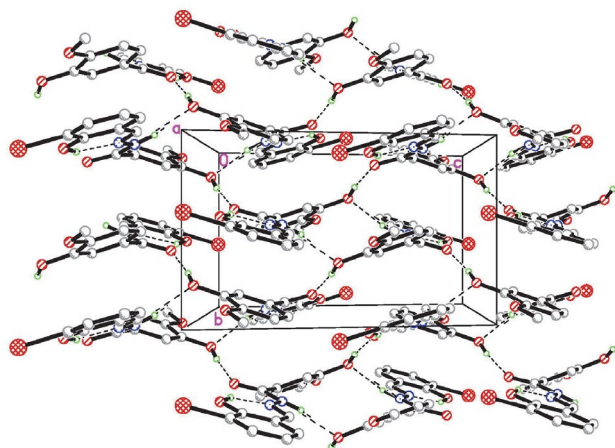
The  $^1\text{H}$  NMR spectra of the free hydrazones  $\text{H}_2\text{L}^1$  and  $\text{H}_2\text{L}^2$  exhibit OH (phenolic) resonances at 12.76 and 12.30 ppm, and 12.65 ppm, respectively. Signals for one CH proton at 8.63 ppm, and one NH proton at 11.27 ppm for  $\text{H}_2\text{L}^1$ , and signals for one CH=N proton at 8.63 ppm, and one NH proton at 11.33 ppm for  $\text{H}_2\text{L}^2$ . Signals for aromatic protons are found in the 7.63–6.45 ppm range. Signals for methoxy protons are found at about 3.84–3.85 ppm. The  $^1\text{H}$  NMR spectrum of complex **1** exhibits two sets of proton signals at 12.71 and 12.20 ppm, and that of complex **2** exhibits one proton signal at 12.56 ppm. There are no NH signals observed, indicating the coordination of the hydrazones through enolate form. The aromatic protons appear in the range 9.39–6.70 ppm. In addition, there exhibits bands at 3.33–3.38 ppm due to the coordinated methoxide and methanol ligands. The CH=N proton signals are observed at 8.56 ppm for **1** and 8.59 ppm for **2**.

### 3. 3. Structure Description of $\text{H}_2\text{L}^1$

The molecular structure of  $\text{H}_2\text{L}^1$  is depicted in Figure 1. The compound adopts *E* configuration about the CH=N unit. The methylenide bond C7–N1 (1.281(5) Å) is within typical double bond. The distance of C8–N2 bond (1.356(4) Å) is shorter, and the distance of C8–O2 bond (1.230(4) Å) is longer than usual, suggests the conjugation effects in the hydrazone molecule. The bond values are within normal ranges.<sup>4a</sup> The two aromatic rings form a dihedral angle of



**Figure 1.** A perspective view of  $H_2L^1$  with the atom labeling scheme. Thermal ellipsoids are drawn at the 30% probability level. Hydrogen bond is indicated by a dotted line.

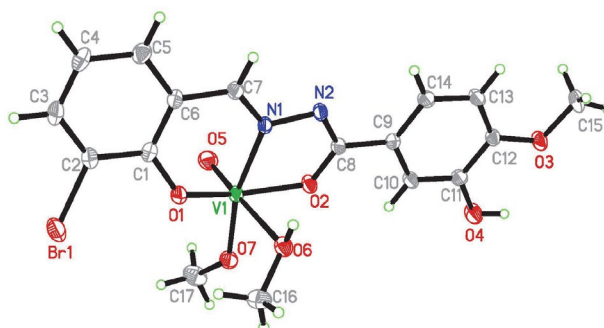


**Figure 2.** Molecular packing structure of  $H_2L^1$ , with hydrogen bonds indicated by dotted lines.

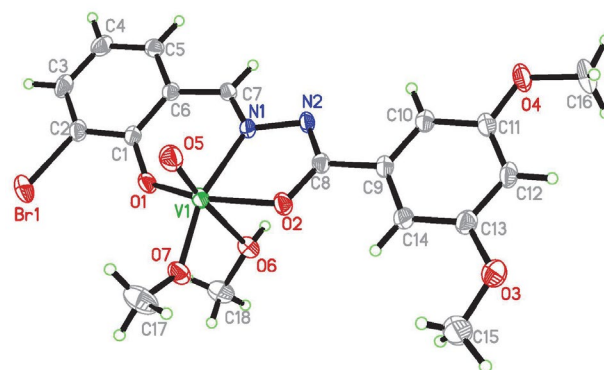
39.0(3)°. Crystal structure of the compound is stabilized by intermolecular hydrogen bonds (Table 3, Figure 2).

### 3. 4. Structure Description of the Vanadium Complexes

The molecular structures of the vanadium complexes are depicted in Figures 3 and 4, respectively. Selected bond lengths and angles are listed in Table 2. The V atoms are in distorted octahedral geometry with the hydrazone ligand coordinated in a meridional fashion. The hydrazones form five- and six-membered chelate rings with the V atoms. The chelate angles are 74.0–74.2° and 82.8–83.5°, respectively, which are not uncommon for this type of ligand systems.<sup>13</sup> The hydrazone ligand lies in a plane with one hydroxylato ligand which lies *trans* to the hydrazone imino N atom. One O atom of the MeOH ligand *trans* to the oxido group completes the octahedral geometry at rather elongated distances of 2.40–2.44 Å. The displacements of the V atoms from the planes defined by the four equatorial donors toward the apical oxido atoms are 0.32–0.33 Å. The hydrazones coordinate in their doubly deprotonated enolate form which is consistent with the observed O2–C8 and N2–C8 bond lengths of about 1.29–1.32 Å. This agrees with reported metal complexes containing the enolate form of this ligand type.<sup>14</sup>

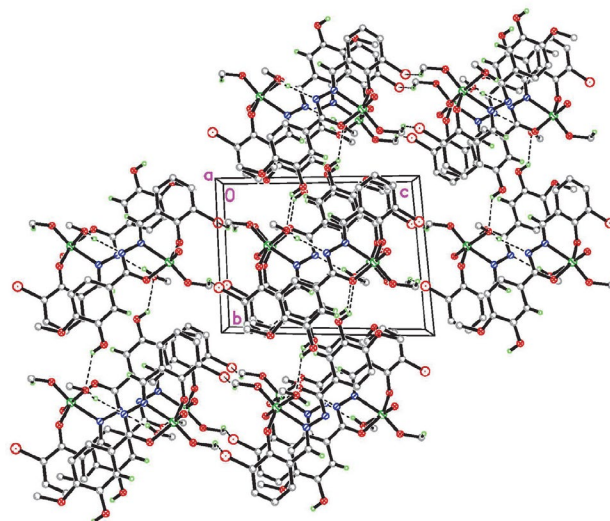


**Figure 3.** A perspective view of complex **1** with the atom labeling scheme. Thermal ellipsoids are drawn at the 30% probability level.



**Figure 4.** A perspective view of complex **2** with the atom labeling scheme. Thermal ellipsoids are drawn at the 30% probability level.

In the crystal structure of complex **1**, the molecules are linked by intermolecular hydrogen bonds (Table 3), leading to the formation of 3D network (Figure 5). In the crystal structure of complex **2**, the molecules are linked by hydrogen bonds (Table 3), leading to the formation of dimers (Figure 6).



**Figure 5.** Crystal structure of complex **1**, with hydrogen bonds indicated by dotted lines.

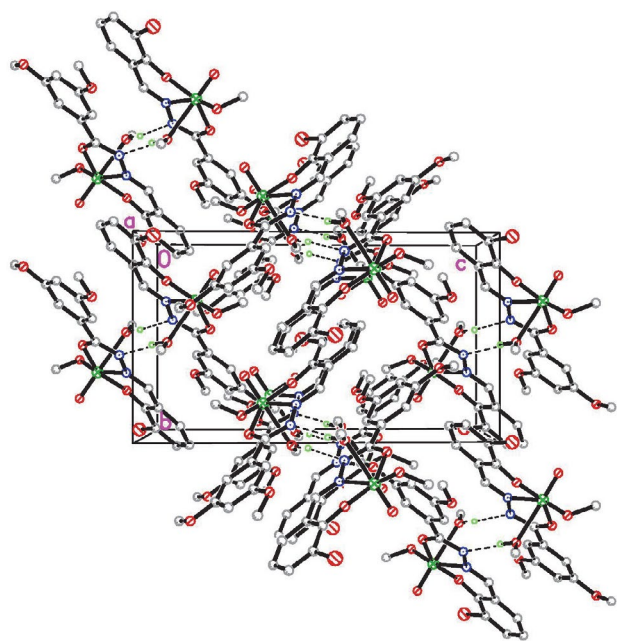


Figure 6. Crystal structure of complex 2, with hydrogen bonds indicated by dotted lines.

Table 2. Selected bond distances (Å) and angles (°) for the complexes

	1	2
V1–O1	1.8676(16)	1.8594(18)
V1–O2	1.9309(15)	1.9445(18)
V1–O5	1.5831(17)	1.581(2)
V1–O6	2.4343(17)	2.407(2)
V1–O7	1.7698(16)	1.7559(19)
V1–N1	2.1330(18)	2.129(2)
O5–V1–O7	102.51(8)	103.79(11)
O5–V1–O1	99.01(9)	99.96(10)
O7–V1–O1	98.66(7)	99.68(9)
O5–V1–O2	100.53(8)	97.85(10)
O7–V1–O2	97.74(7)	96.05(9)
O1–V1–O2	151.03(7)	152.61(9)
O5–V1–N1	96.04(8)	96.01(10)
O7–V1–N1	160.86(7)	159.01(9)
O1–V1–N1	82.88(7)	83.45(8)
O2–V1–N1	74.00(6)	74.12(8)
O5–V1–O6	177.35(8)	174.54(9)
O7–V1–O6	80.15(7)	80.79(8)
O1–V1–O6	80.48(7)	82.00(8)
O2–V1–O6	79.01(6)	78.55(8)
N1–V1–O6	81.32(6)	79.10(7)

Table 3. Hydrogen bond values for the compounds

D–H...A	d(D–H)	d(H...A)	d(D...A)	Angle (D–H...A)
H <sub>2</sub> L <sup>1</sup>				
N3–H2...O3 <sup>i</sup>	0.90(1)	2.00(1)	2.885(3)	169(4)
O3–H3...O2 <sup>ii</sup>	0.82	1.84	2.654(3)	172(4)
O1–H1...N1	0.82	1.87	2.577(4)	144(4)
1				
O4–H4...O6 <sup>iii</sup>	0.82	2.39	3.009(2)	133(5)
O6–H6...N2	0.84(1)	2.06(1)	2.893(2)	171(3)
C7–H7...O4 <sup>iv</sup>	0.93	2.58	3.381(2)	144(5)
2				
O6–H6...N2 <sup>v</sup>	0.85(1)	2.07(1)	2.911(3)	172(4)

Symmetry codes: (i) 1 – x, 1 – y, 1 – z; (ii) x, ½ – y, ½ + z; (iii) x, 1 + y, z; (iv) x, –1 + y, z; (v) 1 – x, 1 – y, –z.

### 3. 5. Antimicrobial Activity

The free hydrazones and the complexes were assayed for antibacterial activities against two Gram (+) bacterial strains (*B. subtilis* and *S. aureus*) and two Gram (–) bacterial strains (*E. coli* and *P. fluorescence*) by MTT method. The MIC (minimum inhibitory concentration,  $\mu\text{g mL}^{-1}$ ) values are given in Table 4. Penicillin G was assayed as the reference drug. Both the free hydrazones show medium activity against *B. subtilis* and *S. aureus*, weak activity against *P. fluorescence*, and no activity against *E. coli*. The two vanadium(V) complexes in this work have superior activity against the bacteria than the free hydrazones. The complexes have excellent activity against *B. subtilis*, *S. aureus* and *E. coli* which are comparable to Penicillin G. Complex 1 has no activity against *P. fluorescence*, while complex 2 has weak activity. Both complexes have no activity on the fungal strains *Aspergillus niger* and *Candida albicans*.

Table 4. Antimicrobial results with MIC ( $\mu\text{g mL}^{-1}$ )

	<i>B. subtilis</i>	<i>S. aureus</i>	<i>E. coli</i>	<i>P. fluorescence</i>
H <sub>2</sub> L <sup>1</sup>	37.5	18.8	75	> 150
H <sub>2</sub> L <sup>2</sup>	18.8	18.8	75	> 150
1	4.6	9.4	9.4	> 150
2	2.3	9.4	9.4	75
Penicillin G	2.3	4.7	>150	> 150

## 4. Supplementary Data

CCDC 1913947 (H<sub>2</sub>L<sup>1</sup>), 1913948 (1) and 1913949 (2) contain the supplementary crystallographic data for the compounds. The data can be obtained free of charge via <http://www.ccdc.cam.ac.uk/conts/retrieving.html>, or from the Cambridge Crystallographic Data Centre, 12

Union Road, Cambridge CB2 1EZ, UK; fax: (+44) 1223-336-033; or e-mail: deposit@ccdc.cam.ac.uk.

## 5. Acknowledgments

This work was financially supported by K.C. Wong Magna Fund in Ningbo University, Ningbo Natural Science Fund (Project No. 201701HJ-B01019), State Key Laboratory Development Fund of Structural Chemistry and Ningbo Education Research Project (Project No. 2017YZD001).

## 6. References

- (a) K. Pyta, A. Janas, M. Szukowska, P. Pecyna, M. Jaworska, M. Gajecka, F. Bartl, P. Przybylski, *Eur. J. Med. Chem.* **2019**, *167*, 96–104; DOI:10.1016/j.ejmech.2019.02.009  
(b) R. Fekri, M. Salehi, A. Asadi, M. Kubicki, *Inorg. Chim. Acta* **2019**, *484*, 245–254; DOI:10.1016/j.ica.2018.09.022  
(c) H. Y. Qian, *Inorg. Nano-Met. Chem.* **2018**, *48*, 461–466; DOI:10.1080/24701556.2019.1569689  
(d) H. Y. Qian, *Russ. J. Coord. Chem.* **2017**, *43*, 780–786. DOI:10.1134/S1070328417110070
- (a) D. A. Megger, K. Rosowski, C. Radunsky, J. Kusters, B. Sitek, J. Muller, *Dalton Trans.* **2017**, *46*, 4759–4767; DOI:10.1039/C6DT04613D  
(b) N. R. Palepu, J. R. Premkumar, A. K. Verma, K. Bhat-tacharjee, S. R. Joshi, S. Forbes, Y. Mozharivskyj, K. M. Rao, *Arabian J. Chem.* **2018**, *11*, 714–728. DOI:10.1016/j.arabjc.2015.10.011
- (a) Y.-C. Liu, H.-L. Wang, S.-F. Tang, Z.-F. Chen, H. Liang, *Anticancer Res.* **2014**, *34*, 6034–6035;  
(b) A. Erguc, M. D. Altintop, O. Atli, B. Sever, G. Iscan, G. Gormus, A. Ozdemir, *Lett. Drug Des. Discov.* **2018**, *15*, 193–202.
- (a) M. Zhang, D.-M. Xian, H.-H. Li, J.-C. Zhang, Z.-L. You, *Aust. J. Chem.* **2012**, *65*, 343–350; DOI:10.1071/CH11424  
(b) L. Shi, H.-M. Ge, S.-H. Tan, H.-Q. Li, Y.-C. Song, H.-L. Zhu, R.-X. Tan, *Eur. J. Med. Chem.* **2007**, *42*, 558–564. DOI:10.1016/j.ejmech.2006.11.010
- N. P. Rai, V. K. Narayanaswamy, T. Govender, B. K. Manuprasad, S. Shashikanth, P. N. Arunachalam, *Eur. J. Med. Chem.* **2010**, *45*, 2677–2682. DOI:10.1016/j.ejmech.2010.02.021
- (a) L.-H. Wang, X.-Y. Qiu, S.-J. Liu, *J. Coord. Chem.* **2019**, DOI:10.1080/00958972.2019.1590561  
(b) X. W. Zhu, *Russ. J. Coord. Chem.* **2018**, *44*, 335–339; DOI:10.3103/S1068367418040213  
(c) Z. H. Chohan, S. H. Sumrra, M. H. Youssoufi, T. B. Hadda, *Eur. J. Med. Chem.* **2010**, *45*, 2739–2747; DOI:10.1016/j.ejmech.2010.02.053  
(d) O. Taheri, M. Behzad, A. Ghaffari, M. Kubicki, G. Dutkiewicz, A. Bezaatpour, H. Nazari, A. Khaleghian, A. Moham-madi, M. Salehi, *Transition Met. Chem.* **2014**, *39*, 253–259. DOI:10.1007/s11243-014-9798-9
- D. Qu, F. Niu, X. Zhao, K.-X. Yan, Y.-T. Ye, J. Wang, M. Zhang, Z. You, *Bioorg. Med. Chem.* **2015**, *23*, 1944–1949. DOI:10.1016/j.bmc.2015.03.036
- Bruker, SMART (Version 5.625) and SAINT (Version 6.01). Bruker AXS Inc., Madison, Wisconsin, USA, 2007.
- G. M. Sheldrick, SADABS. Program for Empirical Absorption Correction of Area Detector, University of Göttingen, Germany, 1996.
- G. M. Sheldrick, SHELXTL V5.1 Software Reference Manual, Bruker AXS, Inc., Madison, Wisconsin, USA, 1997.
- J. Meletiadis, J. F. G. M. Meis, J. W. Mouton, J. P. Donnelly, P. E. Verweij, *J. Clin. Microbiol.* **2000**, *38*, 2949–2954.
- A. Sarkar, S. Pal, *Polyhedron* **2007**, *26*, 1205–1210. DOI:10.1016/j.poly.2006.10.012
- (a) D.-L. Peng, *Transit. Met. Chem.* **2016**, *41*, 843–848; DOI:10.1007/s11243-016-0086-8  
(b) X. W. Zhu, *Russ. J. Coord. Chem.* **2018**, *44*, 421–424. DOI:10.1134/S1070328418070084
- (a) D. L. Peng, *Russ. J. Coord. Chem.* **2017**, *43*, 404–410; DOI:10.1134/S1070328417060045  
(b) Y. Li, L. Xu, M. Duan, J. Wu, Y. Wang, K. Dong, M. Han, Z. You, *Inorg. Chem. Commun.* **2019**, *105*, 212–216; DOI:10.1016/j.inoche.2019.05.011  
(c) S. Guo, N. Sun, Y. Ding, A. Li, Y. Jiang, W. Zhai, Z. Li, D. Qu, Z. You, *Z. Anorg. Allg. Chem.* **2018**, *644*, 1172–1176; DOI:10.1002/zaac.201800060  
(d) L.-Y. He, X.-Y. Qiu, J.-Y. Cheng, S.-H. Liu, S.-M. Wu, *Polyhedron* **2018**, *156*, 105–110; DOI:10.1016/j.poly.2018.09.017  
(e) S.-J. Li, K. Li, X.-J. Yao, X.-Y. Qiu, *J. Coord. Chem.* **2015**, *68*, 2846–2857; DOI:10.1080/00958972.2015.1056171  
(f) X.-Y. Qiu, *Chin. J. Inorg. Chem.* **2014**, *30*, 1667–1672;  
(g) M. Liang, N. Sun, D.-H. Zou, *Acta Chim. Slov.* **2018**, *65*, 964–969; DOI:10.17344/acsi.2018.4625  
(f) Z.-Q. Han, S. Han, Y. Wang, *Acta Chim. Slov.* **2016**, *63*, 200–203; (g) S.-S. Qian, X. Zhao, J. Wang, Z. You, *Acta Chim. Slov.* **2015**, *62*, 828–833.



## Povzetek

Sintetizirali smo dva nova  $V^V$  kompleksa z bromo-substituiranimi hidrazonoma,  $N'$ -(3-bromo-2-hidroksibenziliden)-3-hidroksi-4-metoksibenzohidrazidom ( $H_2L^1$ ) in  $N'$ -(3-bromo-2-hidroksibenziliden)-3,5-dimetoksibenzohidrazidom ( $H_2L^2$ ),  $[VOL^1(OCH_3)(CH_3OH)]$  (**1**) in  $[VOL^2(OCH_3)(CH_3OH)]$  (**2**) ter ju okarakterizirali z IR, UV-Vis in  $^1H$  NMR spektroskopijo ter z monokristalno rentgensko analizo. V enojedrnih kompleksih je vanadijev atom oktaedrično koordiniran. Prostima hidrazonoma in kompleksoma smo določili antibakterijsko aktivnost na *S. aureus*, *B. subtilis*, *E. coli* in *P. fluorescence* ter antimikotično aktivnost na *C. albicans* in *A. niger*. Bromov atom na hidrazonskem ligandu lahko poveča antibakterijsko aktivnost.



Except when otherwise noted, articles in this journal are published under the terms and conditions of the Creative Commons Attribution 4.0 International License

# Usefulness of Combinations of Vertex-Degree Weighted Path Indices and Elements of a Universal Matrix

Anton Perdih

Faculty of Chemistry and Chemical Technology, University of Ljubljana (retired)  
Večna pot 113, 1000 Ljubljana, Slovenia

\* Corresponding author: E-mail: a.perdih@gmail.com

Received: 06-19-2019

## Abstract

The mutually optimized combinations of vertex-degree weighted path indices and the vertex-degree vertex-distance weighted elements of the Universal matrix were applied in the way of  $TI_{new} = \sum k_N \times PN(a_N, b_N, \dots) + k_{ij} \times u_{ij}(a_{ij}, b_{ij}, c_{ij})$ . They were correlated to the boiling points of octanes. Using the mutually optimized combination of vertex-degree weighted path indices **P2**( $a_2, b_2, c_2$ ), **P3**( $a_3, b_3, c_3, d_3$ ), and **P4**( $a_4, b_4, c_4, d_4, e_4$ ) there was observed  $R = 0.99950$ . When in addition to **P2**( $a_2, b_2, c_2$ ), **P3**( $a_3, b_3, c_3, d_3$ ), and **P4**( $a_4, b_4, c_4, d_4, e_4$ ) also **P1**( $a_1, b_1$ ) or  $u_{72}(a_{72}, b_{72}, c_{72})$  or  $u_{76}(a_{76}, b_{76}, c_{76})$  or  $u_{62}(a_{62}, b_{62}, c_{62})$  or  $u_{74}(a_{74}, b_{74}, c_{74})$  or  $u_{52}(a_{52}, b_{52}, c_{52})$  have been applied, then the goodnesses of up to  $R = 0.99988$ ,  $S = 0.098$ ,  $IC = 98.5\%$  have been observed.

The mutually optimized combinations of vertex-degree weighted path indices and the vertex-degree vertex-distance weighted elements of the Universal matrix are promising indices also for other physicochemical properties of octanes.

**Keywords:** Boiling point; Octanes; Matrix elements; Path indices; Structural interpretation

## 1. Introduction

Path indices<sup>1,2</sup> were first used by Wiener<sup>3,4</sup> and together with the connectivity indices<sup>5-8</sup> they are being used by numerous other authors. The path indices<sup>1,2</sup> and the connectivity indices<sup>5-8</sup> were previously considered to be two different groups of indices. It has been, however, shown<sup>9</sup> that both groups of them are parts of the vertex-degree weighted path indices **PN**( $a, b, \dots$ ). The mutually optimized combinations of vertex-degree weighted path indices gave rise in the case of 29 physicochemical properties of octanes to  $R(\mathbf{P1..P4}) > 0.9$ .<sup>9</sup> In the mutually optimized combinations with some of the elements of the Universal matrix the values were  $R = 0.994$  or higher.

Ivanciuc<sup>10,11</sup> described the **Dval** matrix and presented its characteristics. His approach was developed into the Universal matrix by using the vertex-degree vertex-distance weighted elements. The indices derived from it were tested for their usefulness as descriptors of a number of physicochemical properties of alkanes in general and of octanes in particular.<sup>12,13</sup> For the definition of the Universal matrix and its elements see Appendix 3 in ref.<sup>13</sup> The mutually optimized combinations of the vertex-degree

vertex-distance weighted elements of the Universal matrix were tested for their usefulness as descriptors of a number of physicochemical properties of octanes.<sup>14</sup>

Here is presented the approach using the mutually optimized combinations of vertex-degree weighted path indices and the vertex-degree vertex-distance weighted elements of the Universal matrix. The correlations to the boiling points (BP) of octanes are used to illustrate the usefulness of the approach, which is generally applicable. These combinations allow to be made also some structural interpretations of indices involved in them.

## 2. Definitions, Data and Methods

Vertex-degree weighted path indices are defined as  $PN(a_N, b_N, \dots) = \sum v_i^a \times v_j^b \times \dots$ , where  $v_i$ ,  $v_j$ , etc. are the vertex degrees.<sup>9</sup> The vertex-degree vertex-distance weighted elements of the Universal matrix are defined as  $u_{ij}(a_{ij}, b_{ij}, c_{ij}) = v_i^a \times v_j^b \times d_{ij}^c$ , where  $v_i$  and  $v_j$  are the vertex degrees and  $d_{ij}^c$  is the distance between the vertices  $i$  and  $j$ .<sup>14</sup> In the text, they are often presented in a shorthand form as **PN** and  $u_{ij}$ , respectively.

The mutual optimization of these indices and matrix elements is performed in the way of  $TI_{new} = \sum k_N \times PN(a_N, b_N, \dots) + k_{ij} \times u_{ij}(a_{ij}, b_{ij}, c_{ij})$  using one or more of the vertex-degree weighted path indices  $PN(a_N, b_N, \dots)$  and/or the vertex-degree vertex-distance weighted elements of the Universal matrix  $u_{ij}(a_{ij}, b_{ij}, c_{ij})$ , where  $\sum |k_N| + |k_{ij}| = 1$ . The indication of mutual optimization is presented in the text or tables mainly in a shorthand form. For example, the form **P2 & P3 & P4 &  $u_{72}$**  is indicating the optimization of  $TI_{new} = k_2 \times P2(a_2, b_2, c_2) + k_3 \times P3(a_3, b_3, c_3, d_3) + k_4 \times P4(a_4, b_4, c_4, d_4, e_4) + k_{72} \times u_{72}(a_{72}, b_{72}, c_{72})$ .

The values of exponents  $a, b, \dots$  and the value of the smallest of the factors  $k$  are taken here generally to have two significant digits. When a different number of significant digits is employed, this is explicitly mentioned. When necessary, one decimal more is used than the number of significant digits, for example 0.092 in the case of two significant digits or 0.0921 in the case of three significant digits.

As measures for the goodness of the linear correlation the following are used: the correlation coefficient  $R$ , the standard error  $S$  and the information content regarding the influence of branching<sup>14</sup>  $IC$ . In most cases only the correlation coefficient  $R$  is given. The software for statistics calculations included in the program package MS Excel was used.

The values of boiling points of octanes were taken from Li<sup>15</sup> converting °C to K, ref.<sup>14</sup> Appendix 1.

### 3. Results and Discussion

The aim of this paper is to demonstrate in the case of the boiling points of octanes the way of how to proceed to develop the best possible descriptors using the vertex-degree weighted path indices in combination with the vertex-degree vertex-distance weighted elements of the Universal matrix.

In the first step, the values of exponents in individual vertex-degree weighted path indices as well as vertex-degree vertex-distance weighted elements of the Universal matrix are optimized. For the individual vertex-degree weighted path indices this is demonstrated in Table 1. The same should be done for the individual vertex-degree vertex-distance weighted elements of the Universal matrix. The best-observed values of the correlation coefficient  $R$  between optimized individual vertex-degree vertex-distance weighted elements of the Universal matrix and the boiling point of octanes using two significant digits in their exponents are  $-0.82 < R < -0.88$ , thus between those of **P2** and **P4** in Table 1.

In the second step, the mutually optimized combinations of two of them should be made. The best results for vertex-degree weighted path indices are presented in Table 2.

The best individual result gives the vertex-degree weighted path three index **P3**( $-0.9739, -1.3213, -1.667, -0.1944$ ) with  $R < 0.95$  as presented in Table 1. In the mu-

**Table 1.** The values of the correlation coefficient  $R$  between optimized individual vertex-degree weighted path indices and the boiling point of octanes as a function of the number of significant digits in their exponents. In bold: the best of them.

Significant digits	$R(PN, BP)$			
	P1	P2	P3	P4
grid <sup>14</sup>	-0.8961	-0.9083	0.9127	0.7967
one	-0.8961	-0.9095	0.9424	0.7970
two	-0.9125	-0.9107	0.9433	0.7973
three	-0.9161	-0.9107	0.9433	0.7974
four	-0.9175	-0.9107	<b>0.9433</b>	0.7974

**Table 2.** The goodness of correlation between mutually optimized combinations of the vertex-degree weighted path indices and the boiling point of octanes.

$TI_{new}$	$R$	$S$	$IC (\%)$	Sign. dig.
<b>P2 &amp; P3</b>	0.9797	1.266	79.9	2
	0.9804	1.241	80.3	3
<b>P2 &amp; P4</b>	0.9926	0.767	87.8	2
	<b>0.9928</b>	0.755	88.0	3
<b>P3 &amp; P4</b>	0.9803	1.246	80.3	2
	0.9870	1.013	83.9	3
<b>P2 &amp; P3 &amp; P4</b>	0.9956	0.588	90.7	2
	<b>0.99950</b>	0.202	96.8	3
<b>P1 &amp; P2 &amp; P3 &amp; P4</b>	0.999579	0.183	97.1	2
	<b>0.999763</b>	0.137	97.8	3

Sign. dig. - No. of significant digits in exponents  $a, b, \dots$  and the smallest factor  $k$  In **bold** - The best of that group

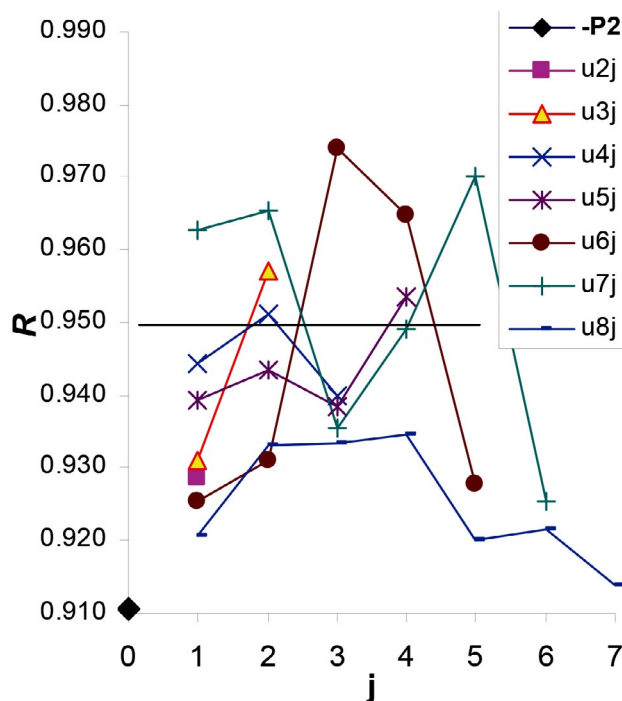
tually optimized combination of two of vertex-degree weighted path indices (Table 2) the best result is observed using the vertex-degree weighted path indices **P2 & P4** in the form  $TI_{new} = -0.519 \times P2(-0.421, -0.408, -0.304) - 0.481 \times P4(0.364, -0.075, -0.728, -0.705, -\infty)$  giving rise to  $R > 0.99$ .

The procedure is continued including additional vertex-degree weighted path indices or vertex-degree vertex-distance weighted elements of the Universal matrix.

The mutually optimized combination of four vertex-degree weighted path indices using two significant digit values in exponents and the smallest factor  $k$  in the form of  $TI_{new} = P1 \& P2 \& P3 \& P4 \equiv k_1 \times P1(a_1, b_1) + k_2 \times P2(a_2, b_2, c_2) + k_3 \times P3(a_3, b_3, c_3, d_3) + k_4 \times P4(a_4, b_4, c_4, d_4, e_4)$  is  $TI_{new} = -0.0033 \times P1(-0.40, 1.88) - 0.6537 \times P2(-0.087, -0.68, -0.007) - 0.2947 \times P3(0.004, -0.56, -1.89, -7.3) - 0.0483 \times P4(0.45, -0.005, -0.52, 0.28, 0.91)$ , giving rise to  $R = 0.999579, S = 0.183, IC = 97.1\%$ .

Using three significant digits, it is  $TI_{new} = -0.0257 \times P1(-0.1799, 1.595) - 0.6522 \times P2(-0.0266, -0.680, -0.0233) - 0.2759 \times P3(0.0266, -0.618, -1.876, -\infty) - 0.0462 \times P4(0.457, -0.0966, -0.535, 0.278, 1.076)$  giving rise to  $R = 0.999763, S = 0.137, IC = 97.8\%$ . This demonstrates that it is advisable to use at least two or, even better, three significant digits.

The mutually optimized combinations of a vertex-degree weighted path index with particular vertex-degree vertex-distance weighted elements of the Universal matrix are presented in Figure 1 for **P2**( $a_2, b_2, c_2$ ). For the vertex-degree weighted path indices **P1**( $a_1, b_1$ ), **P3**( $a_3, b_3, c_3, d_3$ ), and **P4**( $a_4, b_4, c_4, d_4, e_4$ ) they are presented in Appendix 2.



**Figure 1.** Correlation coefficients of the mutually optimized combinations of the vertex-degree weighted path two index with vertex-degree vertex-distance weighted elements of the Universal matrix  $u_{ij}(a_{ij}, b_{ij}, c_{ij})$ .

As can be seen in Figure 1 and in additional Figures in Appendix 2, some of the vertex-degree vertex-distance weighted elements of the Universal matrix improve substantially the goodness of correlation obtained by the individual vertex-degree weighted path indices.

In combinations of one vertex-degree weighted path index with one vertex-degree vertex-distance weighted element of the Universal matrix the most promising are on average the matrix elements  $u_{63}(a_{63}, b_{63}, c_{63})$ ,  $u_{75}(a_{75}, b_{75}, c_{75})$ ,  $u_{32}(a_{32}, b_{32}, c_{32})$ ,  $u_{71}(a_{71}, b_{71}, c_{71})$ ,  $u_{72}(a_{72}, b_{72}, c_{72})$ , and  $u_{53}(a_{53}, b_{53}, c_{53})$ .

Table 3 demonstrates that some of the vertex-degree vertex-distance weighted elements of the Universal matrix improve the optimized combination of the vertex-degree weighted path indices **P2** & **P3** & **P4** better than the vertex-degree weighted path one index.

The best of them is  $TI_{new} = \mathbf{P2} \& \mathbf{P3} \& \mathbf{P4} \& u_{72} \equiv k_2 * \mathbf{P2}(a_2, b_2, c_2) + k_3 * \mathbf{P3}(a_3, b_3, c_3, d_3) + k_4 * \mathbf{P4}(a_4, b_4, c_4, d_4, e_4) + k_{72} * u_{72}(a_{72}, b_{72}, c_{72}) = -0.69059 * \mathbf{P2}(-0.0132, -0.675, 0.0435) - 0.04476 * \mathbf{P4}(0.404, 0.0793, -0.498, 0.288, 1.106)$

**Table 3.** The best observed results in the mutually optimized combinations of vertex-degree weighted path indices with the vertex-degree vertex-distance weighted elements of the Universal matrix in relation to the boiling points of octanes using three significant digits.

	<i>R</i>	<i>S</i>	<i>IC</i> (%)
<b>P2</b> & <b>P3</b> & <b>P4</b> & $u_{72}$	0.99988	0.098	98.5
<b>P2</b> & <b>P3</b> & <b>P4</b> & $u_{76}$	0.99983	0.115	98.2
<b>P2</b> & <b>P3</b> & <b>P4</b> & $u_{62}$	0.99983	0.117	98.1
<b>P2</b> & <b>P3</b> & <b>P4</b> & $u_{74}$	0.99981	0.123	98.0
<b>P2</b> & <b>P3</b> & <b>P4</b> & $u_{52}$	0.99978	0.133	97.9
<b>P2</b> & <b>P3</b> & <b>P4</b> & <b>P1</b>	0.99976	0.137	97.8
<b>P2</b> & <b>P3</b> & <b>P4</b>	0.99950	0.199	96.8

$-0.25706 * \mathbf{P3}(-0.1118, -0.601, -1.905, -2.53) - 0.00759 * u_{72}(-2.08, 1.137, 0.0315)$  giving rise to  $R = 0.99988$ ,  $S = 0.098$ ,  $IC = 98.5\%$ . Its values are presented in Table 4. In the case of octane isomers its values are not degenerated.

**Table 4.** Values of the descriptor  $TI_{new} = \mathbf{P2} \& \mathbf{P3} \& \mathbf{P4} \& u_{72}$  rounded to five decimals.

Octane	$TI_{new}$
Oct	-3.09185
2M7	-3.19772
3M7	-3.18390
4M7	-3.20116
3Et6	-3.18612
25M6	-3.31415
24M6	-3.31140
23M6	-3.22836
34M6	-3.19898
3Et2M5	-3.22757
22M6	-3.34633
33M6	-3.27560
3Et3M5	-3.19138
234M5	-3.25649
224M5	-3.44826
223M5	-3.30526
233M5	-3.23618
2233M4	-3.35245

But one should not forget that the values of the descriptor  $TI_{new} = \mathbf{P2} \& \mathbf{P3} \& \mathbf{P4} \& u_{72}$  are good in relation to the boiling points of octanes. For other properties of octanes, some different mutually optimized combinations of vertex-degree weighted path indices with the vertex-degree vertex-distance weighted elements of the Universal matrix are to be developed in the way demonstrated above.

One of the earliest descriptor combinations used was the combination of the Wiener index (*W*) with the path three index ( $p_3$ ).<sup>3,4</sup> Correlations in combinations of descriptors  $p_3$  and *W* are presented in Table 5.

**Table 5.** Correlations of the combinations of descriptors  $p_3$  &  $W$  with the boiling points of octanes ( $TI_{new} = k_3 \cdot p_3 + k_w \cdot W$ ;  $k_3 + k_w = 1$ ).

	<i>R</i>	<i>S</i>	<i>IC</i> (%)
$k_3 = k_w = 0.5$	0.6740	4.660	26.1
optimized $k_3$ *	0.9888	0.943	85.1
optimized $k_3$ **	0.9892	0.926	85.3

\* two significant digits \*\* three significant digits

They are not as good as in the mutually optimized combination of **P2 & P4 & P3** &  $u_{72}$ . In comparison of optimized combinations  $p_3$  &  $W$  vs. **P2 & P4 & P3** &  $u_{72}$  it is  $R = 0.9892$  vs.  $0.99988$ ,  $S = 0.926$  vs.  $0.098$ , and  $IC$  (%) =  $85.3$  vs.  $98.5$ .

The results of the optimized combinations of vertex-degree weighted path indices with the indices  $W$ ,<sup>7,8</sup>  $RW$ ,<sup>16</sup> and  $\chi$ ,<sup>5</sup> are presented in Table 6. For comparison, the goodness of the correlation of the optimized combination of indices  $W$ ,<sup>7,8</sup>  $RW$ ,<sup>16</sup> and  $\chi$ ,<sup>5</sup> is  $R = 0.9565$ ,  $S = 1.840$ .

**Table 6.** Best correlations with boiling points of octanes of the combinations of indices  $W$ ,  $RW$ , and  $\chi$  with the optimized vertex-degree weighted path indices,  $R(BP, PN)$ , using two significant digits in factors  $k$  and exponents. In bold:  $R > 0.95$ .

PN &:	<i>W</i>	<i>RW</i>	$\chi$
<b>P1</b>	0.9421	0.9175	0.9142
<b>P2</b>	0.9124	0.9174	0.9295
<b>P3</b>	<b>0.9892</b>	<b>0.9696</b>	0.9447
<b>P4</b>	0.7990	0.7976	0.8609

Best correlation with BP of the optimized combination of index  $W$  with the vertex-degree weighted path three index **P3**( $a_3, b_3, c_3, d_3$ ) taking three significant digits in factors  $k$  and exponents, is:  $R = 0.9931$ ,  $S = 0.738$ ,  $IC = 88.3$  (%).

The goodness of correlations presented here in Table 3 is, regarding  $S$ , between one and two orders of magnitude better than those presented in Tables 4–7.

**Table 7.** Goodness of correlation of descriptor combinations with the boiling point data of octanes

Author(s) Ref.	No. of indices	<i>R</i>	<i>S</i>
Ivanciuc et al. <sup>17</sup>	3	0.994	2.79
Ivanciuc et al. <sup>18</sup>	2	0.984	4.94
Randić <sup>19</sup>	2	0.914	2.56
This work	4	0.99988	0.098

The goodness of correlation of individual path/walk indices<sup>19</sup> with boiling point data of octanes is low,  $|R| < 0.71$ ,  $S > 4.5$ . The goodness of  $R > 0.9$  and  $S < 2.6$  gives the

optimized combination of  $p_2/w_2$  &  $p_3/w_3$ ,<sup>19</sup> Table 7. Comparing it to  $p_2$  &  $p_3$  ( $R = 0.919$ ,  $S = 2.49$ ) it is a slightly less good descriptor for the boiling point of octanes, and comparing it to **P2 & P3**, Table 3, ( $R = 0.9797$ ,  $S = 1.266$ ) it is much less good.

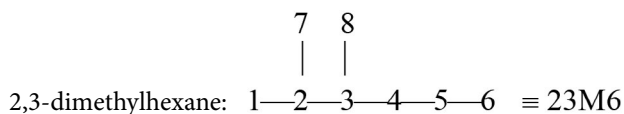
Better than  $p_2/w_2$  &  $p_3/w_3$ ,<sup>19</sup> are the optimized combinations  $p_2/w_2$  &  $p_3/w_3$  &  $p_5/w_5$  ( $R = 0.9206$ ,  $S = 2.463$ ) and  $p_2/w_2$  &  $p_3/w_3$  &  $p_4/w_4$  ( $R = 0.9780$ ,  $S = 1.315$ ). Comparing the latter to  $p_2$  &  $p_3$  &  $p_4$  ( $R = 0.9674$ ,  $S = 1.598$ ) indicates that the combinations of the path/walk indices are more promising than the combinations of the path indices. Comparing to **P2 & P3 & P4**, Table 3, ( $R = 0.99950$ ,  $S = 0.202$ ), the optimized combination of  $p_2/w_2$  &  $p_3/w_3$  &  $p_4/w_4$  is much less good than the corresponding optimized combination of the vertex-degree weighted path indices.

The optimized combination of four path/walk indices of octanes,  $TI_{new} = \sum k_i \cdot p_i/w_i = k_2 \cdot p_2/w_2 + k_3 \cdot p_3/w_3 + k_4 \cdot p_4/w_4 + k_5 \cdot p_5/w_5 = -0.403 \cdot p_2/w_2 + 0.115 \cdot p_3/w_3 - 0.305 \cdot p_4/w_4 - 0.177 \cdot p_5/w_5$  gives rise to  $R = 0.9883$ ,  $S = 0.962$ , which is better than the optimized combination of  $p_2$  &  $p_3$  &  $p_4$  &  $p_5$  ( $R = 0.9780$ ,  $S = 1.317$ ) and slightly better than the combination **P3 & P4**, Table 2.

Among the vertex-degree vertex-distance weighted elements of the Universal matrix, which improve the correlation of **P2 & P3 & P4** more than **P1**, Table 3, there are  $u_{72} > u_{76} > u_{74}$  and  $u_{72} > u_{62} > u_{52}$ . In the five vertex-degree vertex-distance weighted elements of the Universal matrix, which improve the correlation of **P2 & P3 & P4** better than **P1**, there appear the vertices No. 2 and No. 7 three times each, vertex No. 6 two times, and vertices No. 4 and 5 once. Thus, the vertices No. 2 and 7 contribute the larger part of the improvement, whereas the vertices No. 4, 5, and 6 contribute less.

The structural interpretation of the contribution of vertices No. 2, 4, 5, 6, and 7 can be based on two criteria, i.e. whether they are interior or peripheral vertices. The interior vertices are either bearing the branches and they are thus contributing the information about the branching of octanes or they are exposed to intermolecular contacts, which are modified by the sterical hindrance of neighbouring branches. The peripheral vertices are exposed to and modifying the intermolecular contacts.

For illustration is presented the structure of 2,3-dimethylhexane:



In 2,3-dimethylhexane, the vertices No. 1, 6, 7, and 8 are of degree one, the vertices No. 4, and 5 are of degree two, the vertices No. 2 and 3 are of degree three, whereas there is no vertex of degree four.

Among octane isomers, the vertices No. 1 and 8 are in all cases peripheral. The vertex No. 2 is in all cases an interior vertex. By the IUPAC Chemical Nomenclature

used here for the enumeration of vertices, the vertex No. 2 is of degree two in 7 out of 18 cases, of degree three in 7 out of 18 cases as well, and of degree four in 4 out of 18 cases. The same holds true for the vertex No. 3. They are bearing the majority of the information about branching of octanes. However, the vertex-degree vertex-distance weighted elements of the Universal matrix containing the vertex No. 3 give rise to  $R$  between 0.9995 and 0.9996 and  $S$  between 0.199 and 0.177, whereas the vertex-degree vertex-distance weighted elements of the Universal matrix containing the vertex No. 2 mentioned in Table 3 give rise to  $R$  between 0.99978 and 0.99988 and  $S$  between 0.133 and 0.098.

The vertex No. 4 is peripheral in one case only, when it is of degree one. In other cases, it is an interior vertex. It is of degree two in 12 out of 18 cases, of degree three in 5 out of 18 cases, and in no case it is of degree four.

The vertex No. 5 is interior in 11 out of 18 cases, whereas it is peripheral in 7 out of 18 cases. It is of degree three in one case only.

The vertex No. 6 is peripheral in 14 out of 18 cases and when interior, it is of degree two only.

The vertex No. 7 is of degree one among all octanes with the exception of *n*-octane, thus in 17 out of 18 cases. It is thus mainly a peripheral vertex exposed to intermolecular contacts and modifying them.

The boiling point is dependent on intermolecular attraction. Among octanes, it is dependent on attraction and repulsion between the structural groups C, CH, CH<sub>2</sub>, and CH<sub>3</sub>, i.e. speaking in terms of mathematical chemistry, between vertices of degree four, three, two and one. Whereas at the equilibrium distance the contribution to attraction between equal functional groups is  $C \gg CH > CH_2 > CH_3$ , its dependence on intermolecular distance  $d$  is  $d^{-6}$ .<sup>20</sup> The interplay of different contribution to attraction by structural groups, which are represented in topological indices by vertices of different degrees, and of different distances between them in different liquid octane isomers, contributes to differences in boiling points of octane isomers. The structural interpretation of the contribution of different vertices reflects this interplay.

The differences between the experimental data of the boiling points of octanes and the calculated ones using combinations presented in Table 3 are shown in Figure 2.

In Figure 2 we see that in the optimized combination of vertex-degree weighted path indices **P2 & P3 & P4** the difference between the experimental data and the calculated ones is larger than 0.1 K at octane isomers *n*-octane, 2-methylheptane, 3-methylheptane, 2,4-dimethylhexane, 2,3-dimethylhexane, 3-ethyl-2-methylpentane, as well as among all octanes having three resp. four branches. In the best observed case, the optimized combination of **P2 & P3 & P4 &  $u_{72}$** , the difference between the experimental data and the calculated ones is larger than 0.1 K at octane isomers 2-methylheptane, 4-methylheptane, 3-ethylhexane, 2,3,3-trimethylpentane, and 2,2,3,3-tetramethylbutane.

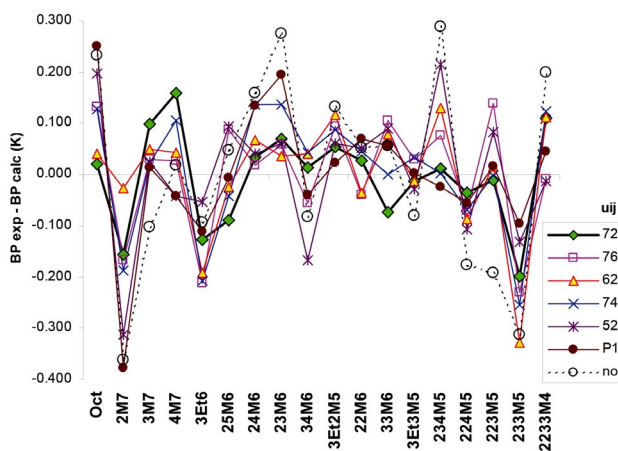


Figure 2. Differences between the experimental data of the boiling points of octanes and the calculated ones using correlations with **P2 & P3 & P4 &  $u_{ij}$** .

If we compare the results observed here in the mutually optimized combination of **P2 & P3 & P4 &  $u_{72}$**  with those reported by some other authors using more than one variable in their equations,<sup>17–19</sup> we can see that the results obtained here are better than those by using other models with several (2 to 3) other indices at once.

As a conclusion it can be said that the mutually optimized combinations of the vertex-degree weighted path indices and the vertex-degree vertex-distance weighted elements of the Universal matrix in the form of  $TI_{new} = \sum k_N \times PN(a_N, b_N, \dots) + k_{ij} \times u_{ij}(a_{ij}, b_{ij}, c_{ij})$  give rise in the case of the boiling points of octanes up to  $R = 0.99988$ ,  $S = 0.098$ ,  $IC = 98.5\%$  and similar combinations are thus promising indices also of other properties. That the approach demonstrated here in detail is generally applicable has been shown previously for the mutually optimized combinations of the vertex-degree vertex-distance weighted elements of the Universal matrix<sup>14</sup> as well as for the mutually optimized combinations of vertex-degree weighted path indices.<sup>9</sup> There can be seen that at different physico-chemical properties of octanes different mutually optimized combinations of the vertex-degree weighted path indices,<sup>9</sup> respectively the vertex-degree vertex-distance weighted elements of the Universal matrix<sup>14</sup> give rise to the best correlation.

## 4. References

1. J. R. Platt, *J. Chem. Phys.* **1947**, 15, 419–420.  
DOI:10.1063/1.1746554
2. M. Randić, *J. Chem. Educ.* **1992**, 69, 713–718.  
DOI:10.1021/ed069p713
3. H. Wiener, *J. Am. Chem. Soc.* **1947**, 69, 17–20.  
DOI:10.1021/ja01193a005
4. H. Wiener, *J. Am. Chem. Soc.* **1947**, 69, 2636–2638.



- DOI:10.1021/ja01203a022
5. M. Randić, *J. Am. Chem. Soc.* **1975**, 97, 6609–6615.  
DOI:10.1021/ja00856a001
6. M. Randić, C.L. Wilkins, *J. Phys. Chem.* **1979**, 83, 1525–1540.  
DOI:10.1021/j100474a032
7. L. B. Kier, L. H. Hall, *J. Pharm. Sci.* **1976**, 65, 1806–1809.  
DOI:10.1002/jps.2600651228
8. L. B. Kier, L. H. Hall, *Molecular Connectivity in Structure–Activity Analysis*, Wiley, New York, 1986.
9. A. Perdih, *Acta Chim. Slov.* **2016**, 63, 88–96.  
DOI:10.17344/acsi.2015.1975
10. O. Ivanciuc, *Rev. Roum. Chim.* **1999**, 44, 519–528.  
DOI:10.1097/00006123-199903000-00054
11. O. Ivanciuc, *Rev. Roum. Chim.* **2000**, 45, 587–596.
12. A. Perdih, B. Perdih, *Acta Chim. Slov.* **2004**, 51, 598–609.
13. A. Perdih, F. Perdih, *Acta Chim. Slov.* **2006**, 53, 180–190.
14. A. Perdih, *Acta Chim. Slov.* **2015**, 62, 879–888.  
DOI:10.17344/acsi.2015.1607
15. X. H. Li, *Chem. Phys. Lett.* **2002**, 365, 135–139.  
DOI:10.1007/978-3-322-99997-9\_9
16. M.V. Diudea, *J. Chem. Inf. Comput. Sci.* **1997**, 37, 292–299.  
DOI:10.1021/ci960037w
17. O. Ivanciuc, T. Ivanciuc, A.T. Balaban, *Internet Electron. J. Mol. Des.* **2002**, 1, 467–487.
18. O. Ivanciuc, T. Ivanciuc, D. Cabrol-Bass, A.T. Balaban, *Internet Electron. J. Mol. Des.* **2002**, 1, 319–331.
19. M. Randić, *J. Chem. Inf. Comput. Sci.* **2001**, 41, 607–613  
DOI:10.1021/ci0001031
20. F. M. Fowkes, in R. L. Patrick, Ed., *Treatise on Adhesion and Adhesives. Vol. 1: Theory*, M. Dekker, New York, 1967, pp. 325–449.

## Povzetek

Uporabljene so bile kombinacije uteženih indeksov poti in uteženih elementov Univerzalne matrike, optimirane na način  $TI_{novi} = \sum k_N \times PN(a_N, b_N, \dots) + k_{ij} \times u_{ij}(a_{ij}, b_{ij}, c_{ij})$ . Korelirane so bile z vrelišči oktanov. Kombinacije uteženih indeksov poti  $P2(a_2, b_2, c_2)$ ,  $P3(a_3, b_3, c_3, d_3)$  in  $P4(a_4, b_4, c_4, d_4, e_4)$  so dale korelacijo  $R = 0.99950$ . Ko so bili poleg uteženih indeksov poti  $P2(a_2, b_2, c_2)$ ,  $P3(a_3, b_3, c_3, d_3)$  in  $P4(a_4, b_4, c_4, d_4, e_4)$  uporabljeni tudi  $P1(a_1, b_1)$  ali  $u_{72}(a_{72}, b_{72}, c_{72})$  ali  $u_{76}(a_{76}, b_{76}, c_{76})$  ali  $u_{62}(a_{62}, b_{62}, c_{62})$  ali  $u_{74}(a_{74}, b_{74}, c_{74})$  ali  $u_{52}(a_{52}, b_{52}, c_{52})$ , so dali  $R$  do 0.99988,  $S$  do 0.098,  $IC$  do 98.5%. Optimirane kombinacije uteženih indeksov poti in uteženih elementov Univerzalne matrike so obetajoči indeksi tudi za druge fizikokemijske lastnosti oktanov.



Except when otherwise noted, articles in this journal are published under the terms and conditions of the Creative Commons Attribution 4.0 International License

# Enzyme Immobilization Onto Biochar Produced by the Hydrothermal Carbonization of Biomass

Mateja Primožič,<sup>1</sup> Gordana Hojnik Podrepšek,<sup>1</sup> Irena Pavlovič,<sup>1</sup>  
Mojca Škerget,<sup>1</sup> Željko Knez<sup>1,2</sup> and Maja Leitgeb<sup>1,2,\*</sup>

<sup>1</sup> University of Maribor, Faculty of Chemistry and Chemical Engineering, Laboratory for Separation Processes and Product Design, Smetanova 17, 2000 Maribor, Slovenia

<sup>2</sup> University of Maribor, Faculty of Medicine, Taborska ulica 8, 2000 Maribor, Slovenia

\* Corresponding author: E-mail: maja.leitgeb@um.si

Received: 02-01-2019

## Abstract

For improving enzyme utilization in biotechnological processes, process costs have to be reduced, enzyme stability during industrial processes should be enhanced, and the recycle and reuse step should be favorable. The immobilization of enzymes is an important step for enhancing enzyme catalytic properties and operational stability. In order to reduce the costs of immobilization and consequently the cost of processes, a cheaper carrier (e.g. materials reclaimed as by-products) should be used. To achieve this, cellulase from *Trichoderma sp.* was immobilized on biochar obtained by low temperature hydrothermal carbonization (LTHTC) in two ways: by adsorption and by covalent binding via a crosslinking agent. The effect of immobilization time, enzyme concentration, type and concentration of the crosslinking agent and the types of carrier - biochar (LTHTC of waste from olive oil production (LTHTC of OL waste) or LTHTC of cellulose) on the immobilization efficiency and the residual activity of biocatalyst was studied. Higher immobilization efficiency and residual enzyme activity was achieved when the enzyme was covalently bound to biochar obtained by LTHTC of cellulose.

**Keywords:** Hydrothermal carbonization; biochar; enzyme; immobilization; enzyme activity.

## 1. Introduction

Energy shortages, the environmental crisis and rising consumer demands for better materials have led to new research into lightweight, inexpensive, environmentally friendly and non-toxic new functional materials. Biomass is a source of raw carbon for the synthesis of valuable carbon materials, since it is available in high quality (for example, as a pure sucrose) and in large quantities as environmentally friendly renewable sources. Among various techniques, the hydrothermal carbonization (HTC) of biomass is a promising method for the synthesis of new materials based on carbon (commonly named as biochar or hydrochar) and other carbonaceous materials (e.g. carriers for enzyme immobilization<sup>9</sup>) with a wide range of possible applications in the field of precursor preparation of activated carbon<sup>1,2,3</sup> in wastewater pollution remediation,<sup>4,5</sup> soil remediation applications,<sup>5</sup> solid fuels,<sup>6,7</sup> gas sensors<sup>8</sup> and other carbonaceous materials (e.g. carrier for enzyme immobilization<sup>9</sup>). The concept of HTC was initially intro-

duced by Friedrich Bergius in 1913.<sup>10</sup> Low temperature hydrothermal carbonization (LTHTC) of biomass is a process based on the reaction of biomass with sub-critical water at temperatures up to 250 °C to form nano- and micro-porous carbon structures with reactive surfaces consisting of hydroxyl and carboxyl groups that have potential for binding different compounds. For converting biomass into biochar, LTHTC is preferable, because the process itself is closer to the natural process of biomass transformation into charcoal. Advantages of the HTC process are very low toxicological impact of material and processes, use of renewable materials without prior dewatering (water acts as a reaction media), simple apparatus and techniques for the synthesis, and high energy and highly efficient atom economy.<sup>11–13</sup> Methods of saccharide treatment (glucose, sucrose, and starch) under hydrothermal conditions (in an aqueous medium at temperatures > 170 °C) leads to the formation of solid carbonaceous residue (biochar) with a structure of micrometer sized spheres (0.4 to 6.0 μm). The diameter of these spheres can be altered

by changing the synthesis conditions.<sup>11,14,15</sup> Thus, synthesized biochar has two important properties that make it suitable for use in the field of catalysis, as a carrier for drugs with controlled release,<sup>16</sup> or for immobilization of enzymes (purified<sup>17,18,19</sup> or within microbial cells<sup>20,21</sup>). First, it contains a high concentration of oxygen groups on the surface, which means that it can be easily connected to other substances with complementary features and it is suitable for the manufacture of functional nanocomposites. Secondly, the diameter can be smaller than 500 nm, which is compatible with *in vivo* applications. All these properties are also suitable for biochar usage as a carrier for biocatalysts. A good carrier should be insoluble, non-toxic, easily accessible, inexpensive, stable and suitable for regeneration. For example, carriers used for adsorption or binding on the surface should have a high porosity to ensure that the contact area is as large as possible.<sup>22</sup>

The production of biochar from waste biomass is sustainable and zero waste production with the goal of eliminating greenhouse gas emissions and reducing carbon footprint. Biochar is therefore, from both an environmental and an economical perspective, a very suitable carrier for enzyme immobilization, since it is biodegradable, biocompatible, and inexpensive to produce from food industry waste. Biochar thus has primarily an economic and environmental advantages over other carriers for the immobilization of enzymes.

The application of biochar as a carrier for enzyme immobilization has not been widely studied. Noritomi et al.<sup>23</sup> found that bamboo charcoal powder (BCP), which was prepared from bamboo wastes by pyrolysis at low temperatures, is very useful as a carrier for the thermal stabilization of hen egg white lysozyme (HEWL) and  $\alpha$ -chymotrypsin (CT), which were effectively adsorbed onto BCP. The thermal stability of BCP-adsorbed HEWL was strongly dependent upon adsorption conditions, such as solution pH, ionic strength, and temperature. Unmodified charcoal support was used for the immobilization of amyloglucosidase for starch hydrolysis. Without any additional treatment, immobilized amyloglucosidase retained over 90% of its free enzyme catalytic activity.<sup>24</sup> Additionally, activated carbon was used as a carrier for pancreatin using adsorption immobilization techniques with a total immobilization yield that resulted in the creation of biocatalytic systems with good catalytic properties.<sup>25</sup>

In recent years, enzyme immobilization has been presented as a powerful tool for the improvement of enzyme properties such as stability and reusability. However, the type of support material used plays a crucial role in the immobilization process due to the strong effect of these materials on the properties of the produced catalytic system.

Better stability, longer enzyme life time, easier separation of the enzyme from the reaction mixture, reusability of the enzyme and reduced contamination of the product during the process are decisive factors which encourage

the use of immobilized against non-immobilized enzymes in biocatalysis.<sup>26</sup>

Enzyme immobilization by adsorption on an active material is a simple process, wherein the enzyme is reversibly adsorbed on the insoluble carrier, easily achieved by contact of the carrier with an aqueous solution of the enzyme. It is well known that any carrier can be applied for enzyme adsorption, but not every enzyme can be immobilized on all carriers. For successful adsorption of the enzyme onto the carrier, certain conditions must be fulfilled, among which an enzyme-carrier affinity is most important. The presence of specific active groups on the carrier which enable the generation of the enzyme-carrier interactions assures this affinity.<sup>27</sup> This method includes particular weak interactions such as electrostatic, van der Waals forces, ionic and hydrogen bonds. For this reason, covalent immobilization of the enzyme on an insoluble substrate is more prevalent.

An immobilized enzyme can be reused several times, which results in a simple process and lower production costs. Immobilization may also be a tool to improve enzyme properties, including stability, activity, selectivity or specificity.<sup>28,29</sup>

Microbial cellulases have shown their potential application in various industries, including pulp and paper, textile, laundry, biomass treatment, biofuel production, the food and feed industries, brewing, and agriculture. Cellulase from *Trichoderma* sp. has been successfully immobilized on different magnetic nanoparticles,<sup>30</sup> chitosan micro-particles,<sup>31</sup> surface modified coffee,<sup>32</sup> silica particles grafted with polyacrylic acid polymer brushes,<sup>33</sup> and as a cross-linked cellulase aggregates,<sup>34</sup> but until now, no immobilization on biochar has been reported. Therefore, cellulase from *Trichoderma* sp. (Cellusoft conc. L) was immobilized on biochar in two ways: by adsorption and by covalent binding via crosslinking agent. The effect of immobilization time, enzyme concentration, type and concentration of the cross-linking agent and the types of carrier – biochar (LTHTC of waste from olive oil production (LTHTC of OL waste) or LTHTC of cellulose) on immobilization efficiency and the residual activity of biocatalyst was studied.

## 2. Experimental

### 2. 1. LTHTC of Waste from the Olive Oil Production and Cellulose

Carbonized material used in the experiments was prepared by the LTHTC of semi-solid olive mill waste (about 75% (w/w) water) and cellulose. Hydrothermal carbonization was carried out in a 75 mL Parr Instruments autoclave (Moline, IL, USA), designed for a maximal operating temperature and pressure of 550 °C and 586 bar, respectively. The autoclave was filled with a suspension of wet waste from the production of olives or cellulose and

deionised water. The reaction was carried out for 4 hours at 220 °C and 3 MPa. After reaction, the carbonized residue was separated from the aqueous phase by filtration through filter paper (pore size 10 mm), washed with deionized water and methanol and dried overnight in an oven at 105 °C.

## 2. 2. Characterization of the Biochar

The pore size and BET surface areas of biochar were determined by nitrogen physisorption using a TriStar 3000 surface area and porosimetry analyser from Micromeritics.

Average particle size was measured with a granulometer (Fritsch analysette 22, Germany) operating on the principle of laser diffraction spectroscopy.

## 2. 3. Adsorption of Biocatalysts on Biochar

Various cellulase concentrations (liquid form – Cellusoft conc. L, NovoNordisk A/S) were adsorbed on 5 mg of selected biochar. Adsorption took place for 24 hours with continuous stirring (300 rpm) on an orbital shaker (Innova® 2000, New Brunswick) in the presence of phosphate buffer (PBS) pH 5 or 7 at ambient temperature and atm. pressure. After adsorption, the biochar was separated from the rest of the solution by centrifugation (Centrifuge 5804 R, Eppendorf), washed with deionized water and dried in an exicator. The experiments were repeated three times.

## 2. 4. Covalent Immobilization of Enzyme Onto Biochar

Cellulase in liquid form (Cellusoft conc. L, NovoNordisk A/S) was covalently immobilized on 5 mg of selected biochar. First, the crosslinking agent (homobifunctional agent – glutaraldehyde (GA) or pentaethylenehexamine (PEHA)) was bound on the biochar. Activation lasted 1 hour at ambient temperature and atm. pressure during continuous shaking on an orbital shaker (300 rpm). The activated carrier was washed with PBS (3 × 20 mL). The immobilization of cellulase on activated carrier was carried out at ambient temperature and atm. pressure by shaking on an orbital shaker for different time (2, 7 or 24 hours) and in the presence of the PBS with selected pH. After immobilization, the immobilized carrier was washed with PBS until no proteins in the supernatant were detected. The experiments were repeated three times.

## 2. 5. Determination of the Protein Concentration

The total protein concentration was assayed using the Bradford method at a wavelength of 595 nm.<sup>35</sup> The method for determination of protein concentration is based on the binding of Coomassie Brilliant Blue dye via

electrostatic interactions in the protein molecule. Measurements were carried out using UV-Vis spectrophotometer (Varian Cary Probe 50, Agilent technologies) at a wavelength of 595 nm. The protein concentration in the supernatant was determined on the basis of the calibration curve. The resulting protein concentrations represent the concentration of the proteins, which are not adsorbed or bound to the carrier. Thus, the efficiency of adsorption or immobilization could be recalculated.

## 2. 6. Determination of Cellulase Activity

Cellulase activity was determined by a specific activity assay.<sup>36</sup> 4 mL of a Sigmacell (crystalline cellulose – Type 20, 20 µm, from Sigma Aldrich S 3504) solution (5% w/v) was added to the immobilized or adsorbed enzyme with different concentrations (1.06 mg/ml, 2.31 mg/ml or 4.21 mg/ml) 4 mL of a Sigmacell (crystalline cellulose – Type 20, 20 µm, from Sigma Aldrich S 3504) solution (5% w/v) was added and the mixture was shaken on an orbital shaker for 2 hours at a temperature of 37 °C. Next, the initial rate of the reaction with a UV-Vis spectrophotometer at 340 nm was defined. The residual activity of an immobilized enzyme according to the initial value of the free cellulase was determined based on these measurements.

## 3. Results and Discussion

### 3. 1. Characteristics of Obtained Biochars

Biochars, produced from different materials by LTH-TC (OL waste or cellulose), were used as carriers for immobilization of cellulase. Characteristics of biochars are presented in Table 1.

**Table 1.** Surface area, pore size and average particle size of biochar produced by LTHTC of OL waste and biochar produced by LTHTC of cellulose.

	Biochar produced by LTHTC of OL waste	Biochar produced by LTHTC of cellulose
Surface Area (m <sup>2</sup> /g)	6.40 ± 0.11	41.70 ± 0.54
Pore Size (nm)	35.90 ± 0.63	23.71 ± 0.37
Average Particle Size (nm)	938.02 ± 0.97	143.88 ± 0.72

Although both biochars were produced under the same conditions, significant differences in their surface characteristics appeared. Biochar produced by LTHTC of cellulose had a larger surface area (41.70 ± 0.54 m<sup>2</sup>/g), but bigger pore size was defined at biochar produced by LTHTC of OL waste (35.90 ± 0.63 nm). The average particle size of biochars produced by LTHTC of OL waste was 938.02 ± 0.97 nm, and of cellulose, 143.88 ± 0.72 nm. The high surface area and small particle size of biochars pro-

duced by LTHTC present suitable properties as potential carriers for enzyme immobilization.

### 3. 2. Adsorption of Cellulase onto Biochar

The liquid form of cellulase (Cellusoft conc. L) was adsorbed onto the biochar produced by LTHTC of OL waste and LTHTC of cellulose. Adsorption of enzymes onto insoluble supports is a simple and widely used method capable of providing high enzyme loading (about one gram per gram of matrix). The driving force causing this binding is usually a combination of hydrophobic effects and the formation of several salt links per enzyme molecule. Therefore, the binding of an enzyme to the carrier is enabled mainly by hydrogen bonds, multiple salt linkages, and van der Waal's forces. Different concentrations of enzyme in PBS with pH 7 were added to 5 mg of selected biochar and the immobilization procedure described under section 2.3 Adsorption of biocatalysts on biochar was achieved. The concentration of added enzyme was optimized and its influence on the immobilization efficiency and residual enzyme activity was studied. Immobilization efficiency increased proportionally with the increase in the concentration of added enzyme, regardless of the type of biochar (Fig. 1). Both types of biochar contain many specific active groups on the carrier, which enable the generation of enzyme-carrier interactions, and consequently higher concentration of enzyme was adsorbed on both carriers. The highest immobilization efficiency was achieved when the concentration of added enzyme was 2.31 mg/ml. Immobilization efficiency remains unchanged with further increase in the enzyme concentration. Comparison between the types of biochar (LTHTC of OL waste or LTHTC of cellulose) shows that the biochar produced from OL waste is better adsorbent since the higher effi-

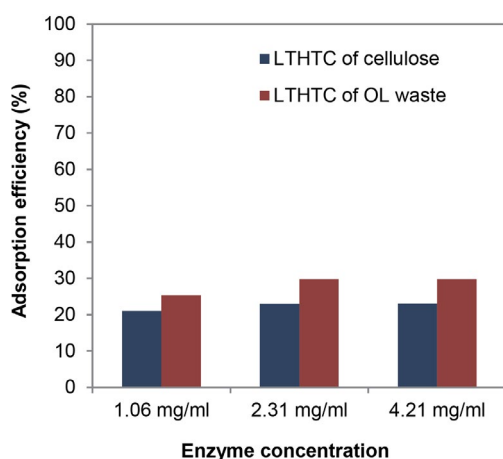
ciency of enzyme adsorption was achieved. The reason for higher obtained efficiency using biochar produced from OL waste as a carrier could be in bigger pore size of carrier in comparison to the biochar produced from cellulose. Due to bigger pores size of OL waste, better accessibility for the enzyme and also higher active surface area for the immobilization of the enzyme onto OL waste carrier was provided. Therefore, the enzyme adsorption was more successful because of better matching of the enzyme into the pores of the biochar. Consequently, the active side of the enzyme could be better oriented toward the substrate.

### 3. 2. Covalent Immobilization of Cellulase onto Biochar

Enzyme immobilization on carriers via a spacer arm presents a good way to avoid steric hindrance and to increase enzyme activity. Using this type of immobilization, a spacer arm is formed between enzyme and carriers by means of a bifunctional reagent such as GA, PEHA, or isocyanate. With the introduction of a flexible spacer arm onto the supports, the enzyme can be allowed to stretch flexibly and catch the substrate more easily.<sup>37</sup>

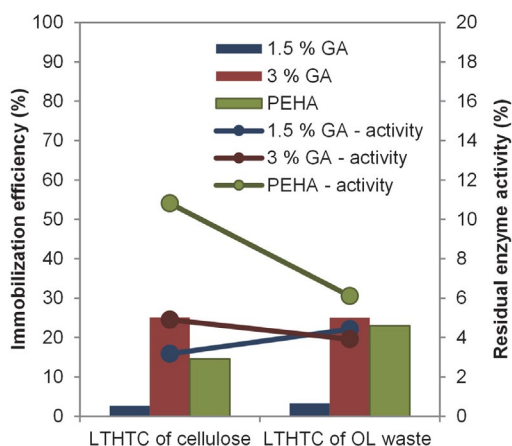
#### 3. 3. 1. The Impact of Crosslinking Agents on the Immobilization Efficiency and Activity of a Biocatalyst

In the process of covalent immobilization of the enzyme on a solid support, active sites on the carrier are required to form a covalent bond between the carrier and the enzyme. Therefore, the carrier has to be activated by a crosslinker. As a crosslinker, various concentrations of GA (1.5 (v/v)% and 3 (v/v)% and PEHA (0.02 M) were used. After one-hour activation of the carrier, 24-h immobilization of the enzyme on the carrier was followed at ambient temperature and atm. pressure. Higher immobilization efficiency was achieved when 3 (v/v)% GA was used (Fig. 2), but higher residual activity of the enzyme was detected using PEHA as a crosslinker. Too high concentration of GA could lower enzyme activity. The reaction mechanism of GA with proteins is not limited to just one mechanism, because the main reactive species of GA are found in equilibrium between their monomeric and polymeric conformations. Moreover, every structure can react in a different way with the protein. Under acidic and neutral conditions, aldehyde groups from GA can react with proteins by formation of Schiff bases, while under basic conditions it has been proposed that GA quickly suffers intramolecular aldolic condensations, producing a polymeric form of an  $\alpha,\beta$ -unsaturated aldehyde, which may react with amino groups from proteins through two mechanisms, firstly, by formation of Schiff bases between internal aldehyde groups from the polymeric form of GA and primary amino groups from the protein. The second mechanism involves a Michael addition to the double C-C linkage, re-



**Figure 1.** Influence of enzyme concentration on adsorption efficiency of biochar from two different sources (LTHTC of OL waste or LTHTC of cellulose). Reaction conditions: 5 mg of chosen biochar, PBS with pH 7, 24-h adsorption with continuous stirring at 300 rpm, at ambient temperature and at atm. pressure. Standard deviation for all measurements was less than  $\pm 3\%$ .

sulting in a less stable product.<sup>38</sup> Too much cross-linker can result in a loss of the minimum flexibility needed for enzyme activity,<sup>39</sup> and low concentrations of GA are not able to form sufficient crosslinkages to effect precipitation of the enzyme. Partial enzyme inactivation due to chemical modification is often unavoidable.<sup>40</sup> Chui and Wan<sup>41</sup> indicated that enzymatic activity was inversely proportional to the concentration of added GA, because extensive crosslinking may result in a distortion of the enzyme structure (i.e., the active site conformation). As can be seen from Fig. 2, biochar produced from cellulose shows higher residual activity of immobilized biocatalyst than biochar produced by LTHTC of OL waste. Moreover, cellulose has good potential for varied derivatization due to the presence of three hydroxyl groups in every monomeric unit.<sup>42</sup> The addition of PEHA increases the number of free amino groups ( $-NH_2$ ) on the outer surface of the enzyme, thus facilitating the crosslinking. Additionally, activation of biochar via PEHA provides active primary amino groups via a long spacer arm. A 19-atom spacer arm of PEHA contains hydroxyl and amino groups onto which immobilization of the cellulase can be performed. The presence of PEHA ensures that steric limitations during the protein immobilization are kept to a minimum. A second benefit arising from the use of a PEHA is that interactions between the protein and the surface of the carrier can be minimized because the protein is kept away from the particle surface by the long space arm.<sup>43</sup>



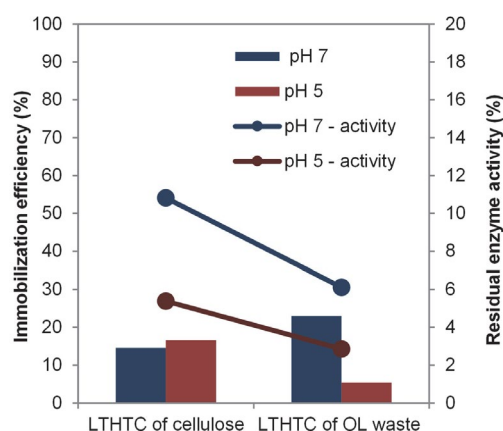
**Figure 2.** Influence of crosslinker on immobilization efficiency and residual enzyme activity. Reaction conditions: 5 mg of chosen biochar, enzyme concentration of 2.3 mg/mL, PBS with pH 7, 7-h immobilization of enzyme with continuous stirring at 300 rpm, at ambient temperature and at atm. pressure. Standard deviation for all measurements was less than  $\pm 3\%$ .

As can be seen from Fig. 2, despite the lower immobilization efficiency for biochar produced by LTHTC of cellulose, higher residual enzyme activity when using PEHA as a crosslinker was detected. This could be due to the orientation of the active sides of the immobilized enzyme. If a higher amount of enzyme is attached to the carrier, the orienta-

tion of enzyme active sides could be unsuitable for successful contact between the active site of the enzyme and the substrate. Besides, the immobilization efficiency and enzyme activity are also dependent on the carrier properties (surface area, pore size, and particle size) and subsequent internal and external mass transfer phenomena.<sup>44,45</sup>

### 3. 3. 2. The Influence of pH on the Immobilization Efficiency and Activity of the Biocatalyst

Most enzymes have an optimal pH at which their activity is maximal. It is well known that the pH of the immobilization medium has a significant effect on immobilization efficiency and enzyme activity. If the pH value of the medium in which the reaction is carried out is changed, a change in the three-dimensional structure of the protein and a subsequent loss of protein activity may occur. pH may affect the activity of the enzyme, and therefore the effect of pH on immobilization efficiency and immobilized cellulase activity was studied. For the study, PBS pH 7 and acetate buffer pH 5 were used. From Fig. 3, it is evident that higher residual activity of the immobilized enzyme was obtained when buffer PBS with pH 7 was used, regardless of the selected biochar. Noritomi et al.<sup>46</sup> also reported that maximum adsorptions of  $\alpha$ -chymotrypsin on adzuki bean charcoal and bagasse charcoal were observed at near neutral pH. The loss in enzymatic activity at too high and too low pH values may be attributed to alterations in enzyme conformation resulting in decrease in immobilization efficiency.



**Figure 3.** Influence of pH on immobilization efficiency and residual enzyme activity. Reaction conditions: 5 mg of chosen biochar, enzyme concentration of 2.3 mg/mL, crosslinker PEHA, 7-h immobilization of enzyme with continuous stirring at 300 rpm, at ambient temperature and at atm. pressure. Standard deviation for all measurements was less than  $\pm 3\%$ .

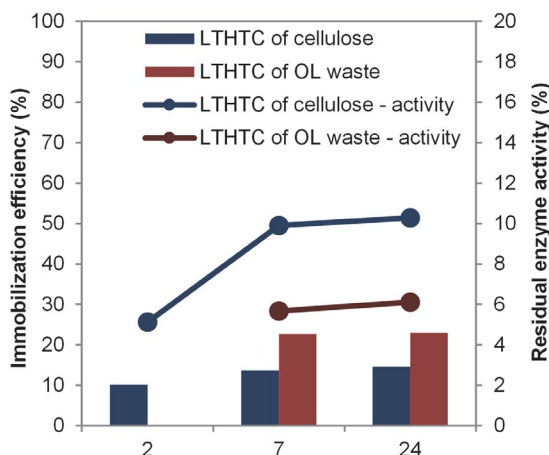
### 3. 3. 3. Influence of Immobilization Time on the Immobilization Efficiency and Activity of the Biocatalysts

The effect of coupling time on immobilization was investigated in terms of residual activity of cellulase and im-



mobilization efficiency. The liquid form of cellulase (Cellu-soft conc. L) was immobilized on two different carriers (LTHTC of OL waste or LTHTC of cellulose), and the time of immobilization (2, 7 or 24 h) was optimized (Fig. 4).

With an increase in the immobilization time, immobilization efficiency and residual enzyme activity increased. The optimal immobilization time was found to be 7 hours, since with further increases in the immobilization time no significant differences in immobilization efficiency and residual enzyme activity were detected in spite of the origin of the biochar.



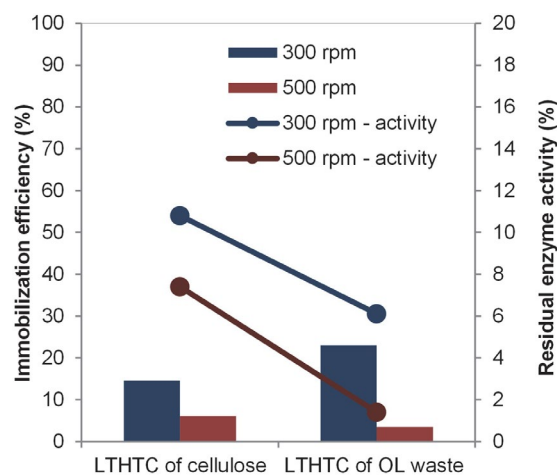
**Figure 4.** Influence of immobilization time on immobilization efficiency and residual enzyme activity. Reaction conditions: 5 mg of chosen biochar, enzyme concentration of 2.3 mg/mL, crosslinker PEHA, PBS with pH 7, ambient temperature and atm. pressure. Standard deviation for all measurements was less than  $\pm 3\%$ .

### 3. 3. 4 The Influence of Agitation Speed on Immobilization Efficiency and Activity of Biocatalysts

During the immobilization process, the enzyme is in contact with the carrier. Shaking allows more intensive contact between the enzyme and the carrier and consequently the immobilization efficiency can be improved. The effect of agitation speed on immobilization efficiency and residual activity of immobilized cellulase was studied. The enzyme and carrier were intensively shaken on a shaker at 300 rpm and 500 rpm for 7 hours. Higher immobilization efficiency and residual enzyme activity were achieved when the carrier and the enzyme were shaken at lower agitation speed. Higher agitation speeds obviously shortened the time of contact between the enzyme and the carrier; therefore, immobilization efficiency and residual enzyme activity decreased (Fig. 5).

## 4. Conclusions

LTHTC of semi-solid waste from olive oil and cellulose production was performed to produce biochar. A



**Figure 5.** Influence of agitation speed on immobilization efficiency and residual enzyme activity. Reaction conditions: 5 mg of chosen biochar, enzyme concentration of 2.3 mg/mL, crosslinker PEHA, PBS with pH 7, 7-h immobilization of enzyme with continuous stirring at ambient temperature and at atm. pressure. Standard deviation for all measurements was less than  $\pm 3\%$ .

higher surface area was detected when the biochar was produced by LTHTC of cellulose, but bigger pore size was detected in biochar produced by LTHTC of OL waste. Biochars produced by LTHTC were successfully used as carriers for enzyme immobilization.

Studies have shown that biochars produced by LTHTC are suitable carriers for enzyme immobilization. Various parameters that affect the immobilization efficiency and residual activity of immobilized cellulase were tested. Biochar from cellulose proved to be a more suitable carrier for cellulase immobilization, because immobilized cellulase on those biochar retains higher residual activity as in the case when the cellulase was immobilized on the biochar produced by LTHTC of OL waste. Higher immobilization efficiency and enzyme activity was achieved when the enzyme was covalently bound onto biochar obtained by LTHTC of cellulose. Moreover, immobilization of an enzyme on these carriers results in a closed-loop productive system, which is the basis for a circular economy. Joining immobilization of enzymes on one hand with production of biochar on the other leads not only to a reduction of costs for biocatalysts, but also to more sustainable production.

## Acknowledgments

The authors acknowledge the financial support of the Slovenian Research Agency (research core funding No. P2-0046 - "Separation Processes and Product Design").

## 5. References

1. T. Wanga, Y. Zhaia, Y. Zhu, C. Lia, G. Zenga, *Renew. Sust. Energ. Rev.* **2018**, 90, 223–247.

2. H. S. Kambo, A. R. Dutta, *Renew. Sust. Energ. Rev.* **2015**, *45*, 359–378. DOI:10.1016/j.rser.2015.01.050
3. A. Jain, R. Balasubramanian, M. P. Srinivasan, *Chem. Eng. J.* **2016**, *283*, 789–805. DOI:10.1016/j.cej.2015.08.014
4. K. Vikrant, K. H. Kim, Y. S. Ok, D. C. W. Tsang, Y. F. Tsang, B. S. Giri, R. S. Singh, *Sci. Total. Environ.* **2018**, *616*, 1242–1260. DOI:10.1016/j.scitotenv.2017.10.193
5. M. Ahmad, A. U. Rajapaksha, J. E. Lim, M. Zhang, N. Bolan, D. Mohan, M. Vithanage, S. S. Lee, Y. S. Ok, *Chemosphere.* **2014**, *99*, 19–33. DOI:10.1016/j.chemosphere.2013.10.071
6. A. Sharma, V. Pareek, D. K. Zhang, *Renew. Sust. Energ. Rev.* **2015**, *50*, 1081–1096. DOI:10.1016/j.rser.2015.04.193
7. Z. G. Liu, G. H. Han, *Fuel.* **2015**, *158*, 159–165. DOI:10.1016/j.fuel.2015.05.032
8. D. Ziegler, P. Palmero, M. Giorcelli, A. Tagliaferro, J.-M. Tulliani, *Chemosensors.* **2017**, *5*, 35. DOI:10.3390/chemosensors5040035
9. H. Noritomi (December 31, 2018). Application of Biochar to Enzyme Carrier for Stress Tolerance of Enzymes, IntechOpen, <https://www.intechopen.com/online-first/application-of-biochar-to-enzyme-carrier-for-stress-tolerance-of-enzymes>. DOI:10.5772/intechopen.82094
10. F. Bergius, *J. Soc. Chem. Ind.* **1913**, *32*, 462–467. DOI:10.1002/jctb.5000320904
11. B. Bo Hu, K. Wang, L. Wu, S. H. Yu, M. Antonietti, M. M. Titirici, *Advan. Mater.* **2010**, *22*, 813–828. DOI:10.1002/adma.200902812
12. B. M. Ghanim, D. S. Pandey, W. Kwapinski, J. J. Leahy, *Biore-sour. Technol.* **2016**, *216*, 373–380. DOI:10.1016/j.biortech.2016.05.087
13. M. Volpe, L. Fiori, *J. Anal. Appl. Pyrolysis.* **2017**, *124*, 63–72. DOI:10.1016/j.jaap.2017.02.022
14. M. Sevilla, A. B. Fuertes, *Chem. Eur. J.* **2009**, *5*, 4195–4203. DOI:10.1002/chem.200802097
15. S. Malghani, G. Gleixner, S. E. Trumbore, *Soil Biol. Biochem.* **2013**, *62*, 137–146. DOI:10.1016/j.soilbio.2013.03.013
16. N. A. Salem, S. M. Yakoot, *Int. J. Pharmacol.* **2016**, *12*, 729–736. DOI:10.3923/ijp.2016.729.736
17. N. Li, Q. Xia, M. Niu, Q. Ping, H. Xiao, *Sci. Rep.* **2018**, *8*, Article number: 13947.
18. J. A. Ghafil, *World J. Exp. Biosci.* **2013**, *1*, 33–36. DOI:10.1016/S0262-1762(13)70213-X
19. M. A. Abu-Tahon, H. H. Arafat, G. S. Isaac, *Int. J. Adv. Bio-technol. Res.* **2018**, *9*, 341–356.
20. L. Lu, A. A. Li, X. Q. Ji, C. P. Yang, S. Y. He, *RSC Adv.* **2018**, *8*, 23426–23432. DOI:10.1039/C8RA03529F
21. N. J. Pino, L. M. Munera, G. A. Penuela, *Soil Sediment Con-tam.* **2016**, *25*, 419–430. DOI:10.1080/15320383.2016.1148010
22. S. C. S. Martins, C. M. Martins, L. M. C. Fiuza, *Afr. J. Biotech-nol.* **2013**, *2*, 4412–4418.
23. H. Noritomi, S. Kurihara, N. Endo, S. Kato, K. Uchiyama, *Int. J. GEOMATE* **2016**, *11*, 2123–2128.
24. A. S. Rani, M. L. M. Das, S. Satyanarayana, *J. Mol. Catal. B Enzym.* **2000**, *10*, 471–476. DOI:10.1016/S1381-1177(99)00116-2
25. V. D. M. Silva, L. M. De Marco, F. M. Delvivo, J. V. Coelho, M. P. C. Silvestre, *Acta Sci. Health Sci.* **2005**, *27*, 163–169.
26. S. Datta, L. R. Christena, Y. R. Sriramulu Rajaram, *3 Biotech* **2013**, *3*, 1–9. DOI:10.1007/s13205-012-0071-7
27. T. Jesionowski, J. Zdzarta B. Krajewska, *Adsorption* **2014**, *20*, 801–821. DOI:10.1007/s10450-014-9623-y
28. C. Mateo, J. M. Palomo, G. Fernandez-Lorente, J. M. Guisan, R. Fernandez-Lafuente, *Enzyme Microb. Technol.* **2007**, *40*, 1451–1463. DOI:10.1016/j.enzmictec.2007.01.018
29. S. A. Ansari, Q. Husain, *Biotechnol. Adv.* **2012**, *30*, 512–523. DOI:10.1016/j.biotechadv.2011.09.005
30. K. Khoshnevisan, F. Vakhshiteh, M. Barkhi, H. Baharifar, E. Poor-Akbar, N. Zari, H. Stamatis, A. K. Bordbar, *Mol. Catal.* **2017**, *442*, 66–73. DOI:10.1016/j.mcat.2017.09.006
31. A. Hamzah, L. L. Sitompul, I. N. F. Putri, Soeprijanto, A. Wid-jaja, *Indones. J. Chem.* **2019**, *19*, 495–502. DOI:10.22146/ijc.39714
32. A. Buntic, M. Pavlovic, D. Antonovic, V. Pavlovic, D. Vrucin-ic, S. Siler-Marinkovic, S. Dimitrijevic-Brankovic, *Int. J. Biol. Macromol.* **2018**, *107*, 1856–1863. DOI:10.1016/j.ijbiomac.2017.10.060
33. A. Samaratunga, O. Kudina, N. Nahar, A. Zakharchenko, S. Minko, A. Voronov, S. W. Pryor, *Appl. Biochem. Biotechnol.* **2015**, *175*, 2872–2882. DOI:10.1007/s12010-014-1463-4
34. L. Sutarlie, K. L. Yang, *J. Colloid. Interface. Sci.* **2013**, *1*, 76–81. DOI:10.1016/j.jcis.2013.09.005
35. M. M. Bradford, *Anal. Biochem.* **1976**, *72*, 248–254. DOI:10.1006/abio.1976.9999
36. M. Leitgeb, M. Čolnik, M. Primožič, P. Zalar, N. Gunde Ci-merman, Ž. Knez, *J. Supercrit. Fluid.* **2013**, *78*, 143–148. DOI:10.1016/j.supflu.2013.03.029
37. D.-H. Zhang, L.-X. Yuwen, L.-J. Peng, *J. Chem.* **2013**, *2013* (Article ID 946248), 1–7. DOI:10.1155/2013/946248
38. O. Barbosa, C. Ortiz, A. Berenguer-Murcia, R. Torres, R. C. Rodrigues, R. Fernandez-Lafuente, *RSC Adv.* **2014**, *4*, 1583–1600. DOI:10.1039/C3RA45991H
39. J. D. Cui, L. L. Li, H. J. Bian, *PLoS ONE* **2013**, *8*, e80581. DOI:10.1371/journal.pone.0080581
40. I. Migneault, C. Dartiguenave, M. J. Bertrand, K. C. Waldron, *BioTechniques* **2004**, *37*, 790–802. DOI:10.2144/04375RV01
41. K. W. Chui, S. L. Wan, *J. Microencapsul.* **1997**, *14*, 51–61. DOI:10.3109/02652049709056467
42. M. D. Trevan, (ed.): An Introduction and Applications in Bi-otechnology, J. Wiley & Sons, Chichester, 1980.
43. J. Anilyte, J. Bryjak, J. Liesiene, *Proc. Estonian Acad. Sci. Chem.* **2006**, *55*, 61–69.
44. K. Buchholz, V. Kasche, U. T. Bornscheuer, in: Biocatalysts and Enzyme Technology, 2<sup>nd</sup> Edition, Wiley-VCH, Wein-heim, Germany, 2012.
45. P. M. Doran, in: Bioprocess Engineering Principles, 2<sup>nd</sup> Edi-tion, Academic Press, Elsevier, Waltham, USA, 2013.
46. H. Noritomi, K. Hishinuma, S. Kurihara, J. Nishigami, T. Takemoto, N. Endo, S. Kato, *J. Surf. Eng. Mater. Adv. Technol.* **2013**, *3*, 269–274. DOI:10.4236/jsamat.2013.34036www

## Povzetek

Nizkotemperaturna hidrotermalna karbonizacija (LHTC) biomase je proces, ki temelji na reakciji biomase s subkritično vodo pri temperaturah do 250 °C. Pri tem pride do tvorbe nano- in mikro-poroznih ogljikovih struktur z reaktivno površino, ki je sestavljena iz hidroksilnih in karboksilnih skupin, ki imajo potencial za vezavo različnih spojin. Imobilizacijo encima na bioogljje smo izvedli na dva načina: z adsorpcijo in s kovalentno vezavo z dodatkom mrežnega povezovalca. Proučevali smo vpliv časa imobilizacije, koncentracije encimov, vrste in koncentracije mrežnega povezovalca in vrste nosilca - bioogljja (LHTC odpadkov iz proizvodnje oljčnega olja (LHTC OL odpadkov) ali LHTC celuloze) na učinkovitost imobilizacije in preostale aktivnosti biokatalizatorja. Večja učinkovitost imobilizacije in preostala encimska aktivnost je bila dosežena v primeru kovalentne vezave encima na bioogljje, pridobljeno z LHTC celuloze.



Except when otherwise noted, articles in this journal are published under the terms and conditions of the Creative Commons Attribution 4.0 International License

# Chemoselective Reduction of Nitroarenes with Hydrazine over a Highly Active Alumina-Supported Cobalt Nanocatalyst

Jalal Albadi,<sup>1,\*</sup> Heshmat Allah Samimi<sup>1</sup> and Mehdi Jalali<sup>2</sup>

<sup>1</sup> Department of Chemistry, Faculty of Science, Shahrekord University, Shahrekord, Iran

<sup>2</sup> National Petrochemical Company, Petrochemical Research and Technology Company, Tehran, Iran

\* Corresponding author: E-mail: chemalbadi@gmail.com; albadi@sci.sku.ac.ir;  
Tel./Fax.: +9838132324419

Received: 06-09-2018

## Abstract

A green and efficient procedure is reported for the chemoselective reduction of nitroarenes catalyzed by a highly active alumina-supported cobalt nanocatalyst in the presence of hydrazine hydrate. The nanocatalyst can be applied under mild reflux conditions for the synthesis of arylamines in high yields. Moreover, the catalyst can be easily recovered by simple filtration and reused several times without obvious loss in its catalytic activity.

**Keywords:** Cobalt catalysis; nanocatalyst; chemoselective reduction; nitroarenes; arylamines

## 1. Introduction

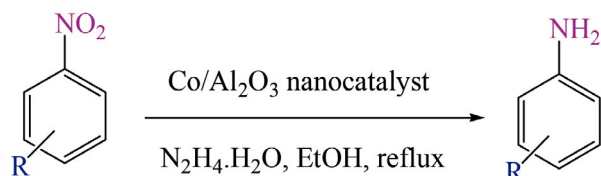
Arylamines are industrially important organic intermediates and attractive compounds for the chemical synthesis due to their wide utility in fine chemicals dyes and polymers.<sup>1</sup> These compounds are important components in many biologically active natural products, medicinally compounds, materials with useful electrical and mechanical properties.<sup>2–3</sup> Arylamines were synthesized by various processes such as reduction of corresponding nitroarenes in the presence of metallic catalysts. Thus exploring new procedures or catalysts for the chemoselective reduction of nitroarenes have been attracted considerable attention.

In the previous studies, a variety of metallic catalysts and methods were reported for the synthesis of arylamines.<sup>4–16</sup> However, some of these catalysts possess the lack of chemoselectivity, adaptability to nitro-containing substrates and recyclability. Moreover, some of these methods include the use of toxic solvents, hard work-up, low selectivity and harsh reaction conditions. Therefore, the catalytic activity need to be further improved, and introduction of alternative methods for the chemoselective reduction of nitroarenes to their corresponding arylamines in terms of potential simplicity, high activity and environmental process is still in demand.

In recent years, supported cobalt catalysts have been attracted significant attention on the organic synthesis reactions and proved to be useful for the reduction of nitroarenes. Various supported cobalt catalysts were prepared and their catalytic activity studied on the reduction of nitroarenes.<sup>17–23</sup> It is confirmed that supported cobalt catalysts had good activity and selectivity for the chemoselective reduction of nitro compounds. However, to the best of our knowledge, there is no report on the reduction of nitroarenes in the presence of alumina supported cobalt nanoparticles. Moreover, recently, the use of supported metallic nanoparticles as catalysts have gained a great attention. These compounds show an important role in nanoscience and nanotechnology. It is proved that the supported nanoparticles have higher stability. Separation and recycling properties also increase. Therefore, due to these properties, the practical applications of supported metallic nanoparticles as catalysts on the organic synthesis reactions have increased.<sup>24–28</sup>

Recently, we have reported the preparation and characterization of cobalt nanoparticles supported on Al<sub>2</sub>O<sub>3</sub> as support (Co/Al<sub>2</sub>O<sub>3</sub> nanocatalyst), as well as its catalytic activity on the various organic reactions.<sup>29–30</sup> Co/Al<sub>2</sub>O<sub>3</sub> nanocatalyst is safe, stable, easy to handle, environmentally benign and its preparation is simple. It was observed that Co/Al<sub>2</sub>O<sub>3</sub> nanocatalyst had high activity, selectivity

and recyclability in the aerobic oxidation of alcohols. In continuation of our studies on the catalytic activity of different nanocatalysts on organic reactions,<sup>31–36</sup> herein, we report an efficient and green procedure for the chemoselective reduction of nitroarene compounds catalyzed by cobalt nanoparticles supported on  $\text{Al}_2\text{O}_3$  support (Co/ $\text{Al}_2\text{O}_3$  nanocatalyst) in ethanol under reflux conditions (Scheme 1).



R: Ph, Me, OMe, OH, N(Me)<sub>2</sub>, Cl, Br, CHO, H

**Scheme 1.** Chemoselective reduction of nitroarenes catalyzed by Co/ $\text{Al}_2\text{O}_3$  nanocatalyst.

## 2. Results and Discussion

Results confirmed that cobalt nanoparticles supported on  $\text{Al}_2\text{O}_3$  support (Co/ $\text{Al}_2\text{O}_3$  nanocatalyst) can be considered as a simple, efficient, green and recyclable nanocatalyst for the synthesis of various functionalized arylamines. In this process, conversion of different substrates with high selectivity of corresponding arylamines have been achieved and  $\text{N}_2$  was only obtained as the by-product. Therefore, this process can present a highly efficient and clean procedure for the reduction of nitroarenes and synthesis of functionalized arylamines.

Co/ $\text{Al}_2\text{O}_3$  nanocatalyst was prepared by a co-precipitation method. Scanning electron microscopy (SEM), energy dispersive spectroscopy (EDS), BET surface area, X-ray diffraction (XRD) and TEM analysis were used to characterize the catalyst.<sup>25</sup>

To optimize the reaction conditions, reduction of 4-chloronitrobenzene in the presence of hydrazine hydrate, was chosen as a model reaction and its performance was studied under a variety of conditions. The effect of various factors such as solvent, catalyst amount and temperature were investigated. The reaction was studied in the presence of different amounts of the nanocatalyst, and found that the catalyst amount confirmed different activities in this reaction. Amongst various amount of the catalyst studied, it was found that in the presence of the Co/ $\text{Al}_2\text{O}_3$  nanocatalyst (0.1 g), 4-chloro-aniline was obtained in highest yield and lower reaction times. While the nanocatalyst amount was decreased, the corresponding product obtained in the lower yields. Moreover, overloading had no significant effect on the yield and time of the reaction (Table 1).

**Table 1.** Effect of the catalyst amount on the reduction of 4-chloronitrobenzene.<sup>a</sup>

Entry	Catalyst amounts (g)	Time (h)	Yield (%) <sup>b</sup>
1	0.03	10	35
2	0.05	8.5	55
3	0.07	5.2	70
4	0.1	3	94

<sup>a</sup> Reaction conditions: 4-chloro-nitrobenzene (1 mmol),  $\text{N}_2\text{H}_4\cdot\text{H}_2\text{O}$  (3 mmol), in ethanol at reflux conditions. <sup>b</sup> Isolated pure products.

The effect of various solvents in this reaction was also investigated (Table 2). It was confirmed that the reaction in organic solvents such as  $\text{CH}_3\text{CN}$  and toluene is significantly low, whereas the reduction proceeded efficiently in ethanol under reflux condition. The rate of the reaction was slower in water and yield of corresponding product was decreased. Other solvents such as methanol and ethyl acetate were less effective for this reaction. Therefore, ethanol was selected as the solvent for the reduction reaction (Table 2). Moreover, the effect of various amounts of hydrazine hydrate were investigated. The best results were obtained in the presence of 3 mmol of hydrazine hydrate (Table 2).

**Table 2.** Optimization study of the hydrazine hydrate and different solvents on the reduction of 4-chloronitrobenzene.<sup>a</sup>

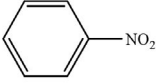
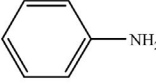
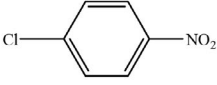

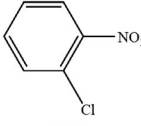
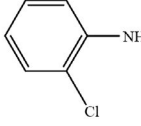
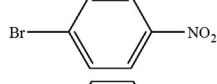
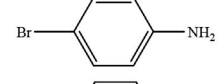
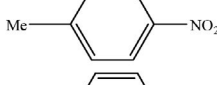
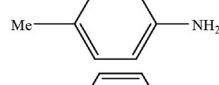
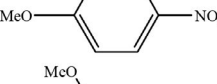
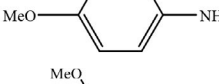
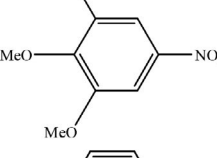
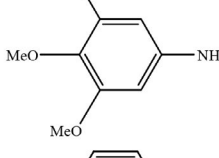
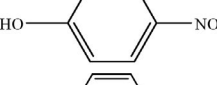
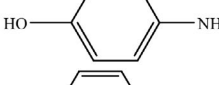
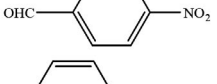
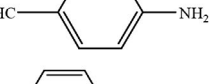
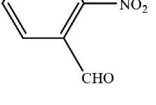
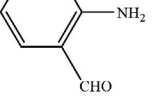
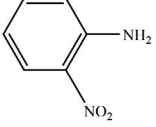
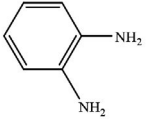
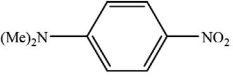
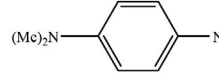
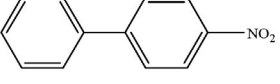
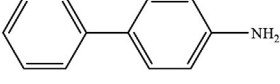
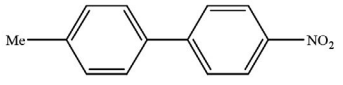
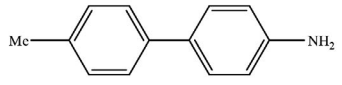
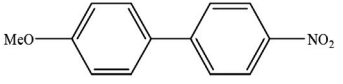
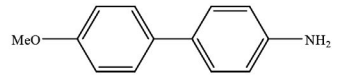
Entry	Conditions	$\text{N}_2\text{H}_4\cdot\text{H}_2\text{O}$ (mmol)	Time (h)	Yield (%) <sup>b</sup>
1	$\text{H}_2\text{O}/\text{r.t.}$	3	18	–
2	$\text{H}_2\text{O}/\text{reflux}$	3	8	70
3	$\text{EtOH}/\text{r.t.}$	3	18	Trace
4	$\text{EtOH}/\text{reflux}$	1.5	7	45
5	$\text{EtOH}/\text{reflux}$	2	5	76
6	$\text{EtOH}/\text{reflux}$	3	3	94
7	$\text{MeOH}/\text{reflux}$	3	7	50
8	$\text{CH}_3\text{CN}/\text{reflux}$	3	8	40
9	Ethyl acetate/ reflux	3	12	40
10	Toluene /reflux	3	12	20

<sup>a</sup> Reaction conditions: 4-chloronitrobenzene (1 mmol), 0.1 g catalyst. <sup>b</sup> Isolated pure products.

To study the scope of this procedure, the reduction reactions of various nitroarene compounds were investigated. A wide range of substituted aromatic nitro compounds were reduced to the corresponding aryl amine derivatives in the presence of Co/ $\text{Al}_2\text{O}_3$  nanocatalyst (Table 3).

The obtained results represented that various substituted nitroaromatics including electron-withdrawing groups and electron-donating groups were reduced under the optimized reaction conditions and corresponding arylamines were obtained in high yields. Halogeno-substi-

Table 3. Chemoselective reduction of nitroarenes catalyzed by Co/Al<sub>2</sub>O<sub>3</sub> nanocatalyst.<sup>a</sup>

Entry	Substrate	Product <sup>b</sup>	Time (h)	Yield (%) <sup>c</sup>
1			3	91
2			3	94
3			4	91
4			3	93
5			3	94
6			3	93
7			2	92
8			3	91
9			4.5	89
10			5	88
11			4.5	90
12			3	90
13			3	91
14			3	92
15			3	89

<sup>a</sup> Reaction conditions: nitro compound (1 mmol), N<sub>2</sub>H<sub>4</sub> · H<sub>2</sub>O (3 mmol) and Co/Al<sub>2</sub>O<sub>3</sub> nanocatalyst (0.1 g) in ethanol at reflux conditions. <sup>b</sup> Products were characterized by comparison of their spectroscopic data and melting points with those reported in the literature.<sup>5,9,11,13,35</sup> <sup>c</sup> Isolated pure products.



tuted nitroarenes were reduced to the corresponding products without any dehalogenation in high yields (Table 3, entries 2–4). Moreover, the reducible functional groups on aromatic rings like OH and aldehyde group remained completely unchanged under the reaction conditions (Table 3, entries 8–10). Especially, the reduction reaction of nitroaniline also occurred efficiently to give the corresponding phenyl diamine in high yield (Table 3, entry 11). The reduction of biphenyl nitrocompounds also gave the excellent yields of the corresponding products with good selectivity under the reaction conditions (Table 3, entry 13–15).

Various methoxy-substituted nitro compounds such as 3,4,5-trimethoxynitrobenzene gave the corresponding methoxy anilines in high yields (Table 3, entry 6,7). The chemoselective reduction of the nitroarene compounds in the presence of an aldehyde group was also studied by reduction of nitrobenzaldehydes (Table 3 entry 9, 10). It was found that only NO<sub>2</sub> group on aromatic ring was reduced and CHO group remained intact. Analysis of reaction products confirmed that corresponding aminobenzaldehydes were obtained in excellent yields with no by-product detected.

Generally, our procedure introduces the clean and efficient method for the chemoselective reduction of nitroarenes into aryl amines in the presence of Co/Al<sub>2</sub>O<sub>3</sub> nanocatalyst. In these processes, no intermediate products were found in the reaction mixtures, and the corresponding products were obtained in good to high yields. Work-up procedure is simple and all products were isolated with simple filtration and evaporation of the solvent. Therefore, this method introduced Co/Al<sub>2</sub>O<sub>3</sub> nanocatalyst as a simple and promising catalyst for the chemoselective reduction of nitroarene compounds.

Moreover, the recyclability of the catalyst was also studied using 4-chloronitrobenzene as starting material, and reacted under optimized reaction conditions (Table 4). After the completion of the reaction, the catalyst was washed with hot ethanol, dried, and stored for another run. This process was repeated for five times, and no considerable decrease in the catalytic activity was observed.

**Table 4.** Recyclability study of Co/Al<sub>2</sub>O<sub>3</sub> nanocatalyst in reduction of 4-chloronitrobenzene.<sup>a</sup>

Run	1	2	3	4	5
Time (h)	3	3	3.3	4	4.2
Yield (%) <sup>a</sup>	94	94	93	91	90

<sup>a</sup> Isolated pure products.

### 3. Experimental

Chemicals were purchased from Aldrich and Merck chemical companies. Products were characterized by comparison of their spectroscopic data (NMR and IR) and physical properties with those reported in the literature.

The NMR spectra were recorded on a Bruker Avance 400 MHz. IR spectra were recorded on a Perkin Elmer 781 Spectrophotometer. Obtained yields refer to the isolated pure products. Co/Al<sub>2</sub>O<sub>3</sub> nanocatalyst was prepared according to the our previously reported method.<sup>29</sup>

### 3. 1. General Procedure

Nitro compounds (1 mmol), hydrazine hydrate (3 mmol) and Co/Al<sub>2</sub>O<sub>3</sub> nanocatalyst (0.1 g) were added to round-bottom flask containing 10 mL of ethanol. The mixture was stirred under reflux condition for the appropriate reaction time (Table 3). The progress of the reaction was monitored by TLC (*n*-hexane: EtOAc, 4:1). After reaction completion, the catalyst was filtered, and washed with hot ethanol. Evaporation of the solvent was followed by column chromatography on the silica gel which afforded the pure products in high yields.

## 4. Conclusions

We have reported an efficient and clean procedure for the chemoselective reduction of various nitroarenes catalyzed by Co-based nanoparticles (Co/Al<sub>2</sub>O<sub>3</sub> nanocatalyst) in the presence of hydrazine in ethanol, as solvent. The catalyst could be easily separated, and reused at least 5 times without notable drop in its catalytic activity. Moreover, high yields, easy work-up and clean reaction procedure make the present method a useful and important reaction for the reduction of nitroamines. Studies on other functions of this catalyst are underway in our laboratory.

## 5. Acknowledgement

We are thankful to research council of Shahrekord University for the support of this research.

## 6. References

1. C. Desmarets, R. Schneider, Y. J. Fort, *J. Org. Chem.* **2002**, 67, 3029–3036. DOI:10.1021/jo016352l
2. A. M. Tafesh, J. Weijuny, *Chem. Rev.* **1996**, 96, 2035–2052. DOI:10.1021/cr950083f
3. T. Ohno, K. Moriwaki, T. Miyata, *J. Org. Chem.* **2001**, 66, 3397–3401. DOI:10.1021/jo001100q
4. Y. J. Jang, S. Kim, S. W. Jun, B. H. Kim, S. Hwang, I. K. Song, B. M. Kim, T. Hyeon, *Chem. Commun.* **2011**, 47, 3601–3603. DOI:10.1039/c0cc04816j
5. V. Pandarus, R. Ciriminna, F. B eland, M. Pagliaro, *Adv. Synth. Catal.* **2011**, 353, 1306–1316. DOI:10.1002/adsc.201000945
6. S. Zhao, H. Liang, Y. Zhou, *Catal. Commun.* **2007**, 8, 1305–1309. DOI:10.1016/j.catcom.2006.11.033

7. S. S. Kotha, N. Sharma, G. Sekar, *Tetrahedron Lett.* **2016**, 57, 1410–1413. DOI:10.1016/j.tetlet.2016.01.111
8. A. K. Shil, D. Sharma, N. R. Guha, P. Das, *Tetrahedron Lett.* **2012**, 53, 4858–4861. DOI:10.1016/j.tetlet.2012.06.132
9. P. F. Luo, K. L. Xu, R. Zhang, L. Huang, J. Wang, W. H. Xing, J. Huang, *Catal. Sci. Technol.* **2012**, 2, 301–304. DOI:10.1039/C1CY00358E
10. N. R. Guha, D. Bhattacharjee, P. Das, *Tetrahedron Lett.* **2014**, 55, 2912–2916. DOI:10.1016/j.tetlet.2014.03.047
11. S. Park, I. S. Lee, J. Park, *Org. Biomol. Chem.* **2013**, 11, 395–399. DOI:10.1039/C2OB27025K
12. X.-U. Chen, B.-R. Ai, Y. Dong, X.-M. Zhang, J.-Y. Wang, *Tetrahedron Lett.* **2017**, 58, 3646–3649. DOI:10.1016/j.tetlet.2017.08.009
13. U. Sharma, N. Kumar, P. K. Verma, V. Kumar, B. Singh, *Green. Chem.* **2012**, 14, 2289–2293. DOI:10.1039/c2gc35452g
14. M. O. Sydnese, M. Isobe, *Tetrahedron Lett.* **2008**, 49, 1199–1202. DOI:10.1016/j.tetlet.2007.12.030
15. S. Wei, Z. Dong, Z. Ma, J. Sun, J. Ma, *Catal. Commun.* **2013**, 30, 40–44. DOI:10.1016/j.catcom.2012.10.024
16. Y. Yamane, X. Liu, A. Hamasaki, T. Ishida, M. Haruta, T. Yokoyama, M. Tokunaga, *Org. Lett.* **2009**, 11, 5162–5165. DOI:10.1021/ol902061j
17. K. N. Rao, B. M. Reddy, S.-E. Park, *Catal. Commun.* **2009**, 11, 142–145. DOI:10.1016/j.catcom.2009.09.013
18. X. Cui, K. Liang, M. Tian, Y. Zhu, J. Ma, Z. J. Dong, *Colloid Interface Sci.* **2017**, 501, 231–240. DOI:10.1016/j.jcis.2017.04.053
19. P. Zhou, Z. Zhang, L. Jiang, C. Yu, K. Lv, J. Sun, S. Wang, *Appl. Catal. B. Environ.* **2017**, 210, 522–532. DOI:10.1016/j.apcatb.2017.04.026
20. C. Nethravathi, J. Prabhu, S. Lakshmi Priya, M. Rajamathi, *ACS. Omega.* **2017**, 2, 5891–5897. DOI:10.1021/acsomega.7b00848
21. S. K. Mohapatra, S. U. Sonavane, R. V. Jayaram, P. Selvam, *Tetrahedron Letters.* **2002**, 43, 8527–8529. DOI:10.1016/S0040-4039(02)02080-4
22. U. Sharma, P. Kumar, N. Kumar, V. Kumar, B. Singh, *Adv. Synth. Catal.* **2010**, 352, 1834–1840. DOI:10.1002/adsc.201000191
23. F. A. Westerhaus, R. V. Jagadeesh, G. Wienhöfer, M.-M.; Pohl, J. Radnik, A.-E. Surkus, J. Rabeah, K. Junge, H. Junge, M. Nielsen, A. Brückner, M. Beller, *Nat. Chem.* **2013**, 5, 537–543. DOI:10.1038/nchem.1645
24. C. Jiang, Z. Shang, X. Liang, *ACS Catal.* **2015**, 5, 4814–4818. DOI:10.1021/acscatal.5b00969
25. H. J. Freund, *Surf. Sci.* **2002**, 500, 271–299. DOI:10.1016/S0039-6028(01)01543-6
26. S. M. H. Nasrollahi, M.A. Ghasemzadeh, M. R. Zolfaghari, *Acta. Chim. Slov.* **2018**, 65, 199–207. DOI:10.17344/acsi.2017.3820
27. K. P. Boroujeni, S. Hadizadeh, S. Hassani, A. Fadavi, M. Shahrokh, *Acta. Chim. Slov.* **2017**, 64, 692–700. DOI:10.17344/acsi.2017.3437
28. G. M. Ziarani, E. Tavaf, V. F. Vavsari, A. Badiei, *Acta. Chim. Slov.* **2017**, 64, 701–706. DOI:10.17344/acsi.2016.3111
29. J. Albadi, A. Alihosseinzadeh, M. Jalali, M. Shahrezaei, A. Mansourneshad, *Mol. Catal.* **2017**, 440, 133–139. DOI:10.1016/j.mcat.2017.07.020
30. J. Albadi, M. Jalali, A. R. Momeni, *Res. Chem. Intermed.* **2016**, 42, 5739–5752. DOI:10.1007/s11164-015-2400-z
31. J. Albadi, A. Alihoseinzadeh, A. Mansourneshad, *Acta. Chim. Slov.* **2015**, 62, 617–624. DOI:10.17344/acsi.2014.1211
32. J. Albadi, J. Abbasi Shiran, A. Mansourneshad, *Acta. Chim. Slov.* **2014**, 61, 900–903.
33. J. Albadi, A. Mansourneshad, T. Sadeghi, *Res. Chem. Intermed.* **2015**, 41, 8317–8326. DOI:10.1007/s11164-014-1894-0
34. J. Albadi, A. Alihoseinzadeh, A. Razeghi, *Catal. Commun.* **2014**, 49, 1–5. DOI:10.1016/j.catcom.2014.01.030
35. J. Albadi, J. Abbasi Shiran, A. Mansourneshad, *J. Chem. Sci.* **2014**, 126, 147–150. DOI:10.1007/s12039-013-0537-0
36. J. Albadi, A. Mansourneshad, *Chin. J. Chem.* **2014**, 32, 396–398. DOI:10.1002/cjoc.201400138

## Povzetek

Avtorji v prispevku poročajo o učinkovitem in zelenem postopku kemoselektivne redukcije nitroarenov, ki jo katalizira visoko aktivni kobaltov nanokatalizator, nanešen na aluminijev oksid, v prisotnosti hidrazin hidrata. Nanokatalizator so uporabili priilih pogojih refluksa in pri tem sintetizirali vrsto arilaminov z visokimi izkoristki. Ob tem je možno katalizator enostavno regenerirati s filtracijo in ponovno večkrat uporabiti, brez znatne izgube katalitske aktivnosti.



Except when otherwise noted, articles in this journal are published under the terms and conditions of the Creative Commons Attribution 4.0 International License

Short communication

# Microwave-Assisted Synthesis of Benzofuran-3(2H)-ones

Xiaojing Hu,<sup>1</sup> Huimin Lai,<sup>2</sup> Fangfei Zhao,<sup>2</sup> Shuyu Hu,<sup>2</sup> Qianqian Sun<sup>2</sup>  
and Lizhen Fang<sup>2,\*</sup>

<sup>1</sup> The Third Affiliated Hospital of Xinxiang Medical University, Xinxiang, Henan 453003, People's Republic of China

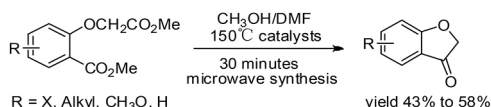
<sup>2</sup> School of Pharmacy, Xinxiang Medical University, Xinxiang, Henan 453003, People's Republic of China.

\* Corresponding author: E-mail: 2002flz@163.com or fanglizhen@xxmu.edu.cn

Received: 03-02-2019

## Abstract

A new method for the synthesis of benzofuran-3(2H)-ones under microwave conditions was developed. The reaction conditions were screened, and the scope of benzoate substrates was investigated. The results showed that our method could provide rapid access to these important dihydrobenzofuranones in 43% to 58% yields.



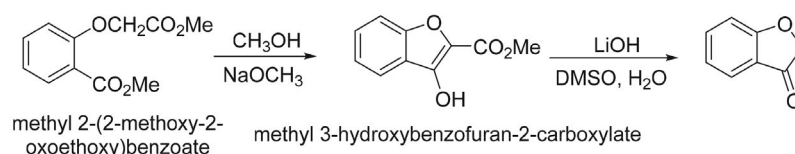
**Keywords:** Benzofuranones; microwave-Assisted Synthesis; cyclization, dihydrobenzofuranones

## 1. Introduction

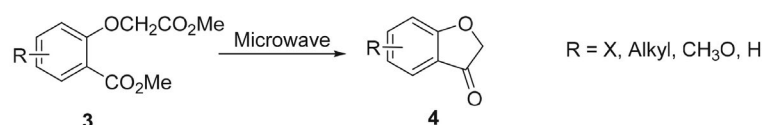
Benzofuranone is an important pharmacophore in medicinal and natural products,<sup>1</sup> in addition to being a very common motif in organic synthesis.<sup>2</sup> The previously reported classical synthesis of benzofuranones involved two steps, as shown in **Scheme 1**: cyclization of methyl 2-(2-methoxy-2-oxoethoxy)benzoate to give methyl 3-hydroxybenzofuran-2-carboxylate, and subsequent Krapcho reaction of it to provide benzofuran-3(2H)-one.

While this method seems to be simple and reliable theoretically, the yield in the Krapcho reaction is typically not very high (40% to 60%, as revealed in our experiments); furthermore, prolonged reaction with heating is required in both the steps. Recently, microwave-assisted synthesis has seen widespread use in many kinds of organic reactions,<sup>3</sup> especially in the synthesis of heterocyclic compounds.<sup>4</sup> This is a quick and facile method for organic synthesis, often giving higher product yields and allowing for easier isolation.<sup>5</sup> However, microwave synthesis of

Previous work:<sup>8</sup>



Our work:



**Scheme 1:** The proposal of the research work.

benzofuranones has seldom been reported.<sup>6</sup> We have adopted the microwave-assisted synthesis to obtain the desired benzofuranones for our study on chiral dihydrobenzofuranones.<sup>7</sup>

## 2. Experimental

All commercial reagents were purchased from Sigma-Aldrich, Alfa-Aesar, and Acros and used without further purification, unless otherwise specified. The progress of the reaction was monitored by Thin-layer Chromatography. Microwave reactions were carried out in a Biotage Initiator system (Biotage Initiator +, Sweden), and the temperature of the reaction mixture was measured using the external IR sensor present in the instrument. <sup>1</sup>H and <sup>13</sup>C NMR spectra were recorded on Bruker AV-400 spectrometers operating at 400 MHz and 100 MHz, respectively. The peaks were internally referenced to TMS (0.00 ppm) or to the residual undeuterated solvent signal. Peak multiplicities are reported as follows: s = singlet, br s = broad singlet, d = doublet, t = triplet, m = multiplet. All melting points were measured using an SGWX-4 micro melting point apparatus and are reported uncorrected. IR spectra were recorded as KBr disks on a Perkin-Elmer FT-IR spectrometer.

**General procedure for the preparation of compounds 2 (2a as a model).** To a solution of **1a** (5 mmol) in CH<sub>3</sub>OH (25 mL) concentrated sulfuric acid was added dropwise (10 drops). After stirring under reflux for 12 h, the reaction mixture was concentrated under reduced pressure, diluted with water, and extracted with ethyl acetate. The organic layer was washed with saturated aqueous NaHCO<sub>3</sub> solution and brine, dried over Na<sub>2</sub>SO<sub>4</sub>, and concentrated under reduced pressure. The crude mixture was purified by flash chromatography (petroleum ether/ethyl acetate = 5:1) to afford **2a**.

**General procedure for the preparation of compounds 3 (3a as a model).** To a solution of **2a** (304 mg, 2 mmol) in acetone (10 mL) K<sub>2</sub>CO<sub>3</sub> (966 mg, 7 mmol) and BrCH<sub>2</sub>CO<sub>2</sub>Me (367 mg, 2.4 mmol) were added. After stirring under reflux for 3 h, the reaction mixture was concentrated under reduced pressure, diluted with water, and extracted with ethyl acetate. The organic layer was washed with brine, dried with Na<sub>2</sub>SO<sub>4</sub>, and concentrated under reduced pressure. The residue was purified by silica gel chromatography using petroleum ether/ethyl acetate = 3:1 as the eluent to give **3a** (417 mg, 93%) as a white solid.

**Methyl 2-(2-methoxy-2-oxoethoxy)benzoate (3a):**<sup>9</sup> White solid; yield: 93%; m.p. 49–50 °C; FT-IR (KBr,  $\nu_{\max}/\text{cm}^{-1}$ ): 2950, 1771, 1725, 1598, 1582, 1494, 1439, 1258. <sup>1</sup>H NMR (400 MHz, CDCl<sub>3</sub>):  $\delta$  7.84 (dd,  $J_1 = 1.6$  Hz,  $J_2 = 7.7$

Hz, 1H), 7.48–7.42 (m, 1H), 7.06 (t,  $J = 7.6$  Hz, 1H), 6.89 (d,  $J = 8.4$  Hz, 1H), 4.74 (s, 2H), 3.91 (s, 3H), 3.80 (s, 3H); <sup>13</sup>C NMR (100 MHz, CDCl<sub>3</sub>):  $\delta$  169.3, 166.5, 157.6, 133.6, 132.2, 121.9, 121.4, 114.4, 66.8, 52.5, 52.3; HRMS (ESI): calcd. for C<sub>11</sub>H<sub>12</sub>NaO<sub>5</sub> [M+Na]<sup>+</sup>: 247.0577; found: 247.0578.

**Methyl 2-(2-methoxy-2-oxoethoxy)-3-methylbenzoate (3b):** Yellow oil; yield: 81%; FT-IR (KBr,  $\nu_{\max}/\text{cm}^{-1}$ ): 2953, 1765, 1728, 1593, 1466, 1434, 1275. <sup>1</sup>H NMR (400 MHz, CDCl<sub>3</sub>):  $\delta$  7.67 (d,  $J = 7.5$  Hz, 1H), 7.36 (d,  $J = 7.3$  Hz, 1H), 7.10 (t,  $J = 7.6$  Hz, 1H), 4.60 (s, 2H), 3.88 (s, 3H), 3.84 (s, 3H), 2.35 (s, 3H); <sup>13</sup>C NMR (100 MHz, CDCl<sub>3</sub>):  $\delta$  169.6, 166.6, 156.4, 135.6, 133.0, 129.6, 124.6, 124.5, 70.6, 52.4, 52.3, 16.3; HRMS (ESI): calcd. for C<sub>12</sub>H<sub>14</sub>NaO<sub>5</sub> [M+Na]<sup>+</sup>: 261.0733; found: 261.0734.

**Methyl 2-(2-methoxy-2-oxoethoxy)-4-methylbenzoate (3c):** White solid; yield: 92%; m.p. 47–49 °C; FT-IR (KBr,  $\nu_{\max}/\text{cm}^{-1}$ ): 2947, 1733, 1609, 1573, 1505, 1428, 1255. <sup>1</sup>H NMR (400 MHz, CDCl<sub>3</sub>):  $\delta$  7.76 (d,  $J = 7.9$  Hz, 1H), 6.87 (d,  $J = 7.9$  Hz, 1H), 6.69 (s, 1H), 4.72 (s, 2H), 3.89 (s, 3H), 3.81 (s, 3H), 2.36 (s, 3H); <sup>13</sup>C NMR (100 MHz, CDCl<sub>3</sub>):  $\delta$  169.4, 166.4, 157.9, 144.8, 132.3, 122.8, 118.4, 115.4, 66.9, 52.5, 52.2, 22.0; HRMS (ESI): calcd. for C<sub>12</sub>H<sub>14</sub>NaO<sub>5</sub> [M+Na]<sup>+</sup>: 261.0733; found: 261.0737.

**Methyl 4-chloro-2-(2-methoxy-2-oxoethoxy)benzoate (3d):** White solid; yield: 87%; m.p. 88–89 °C; FT-IR (KBr,  $\nu_{\max}/\text{cm}^{-1}$ ): 2964, 1755, 1723, 1595, 1573, 1488, 1253, 773. <sup>1</sup>H NMR (400 MHz, CDCl<sub>3</sub>):  $\delta$  7.80 (d,  $J = 8.4$  Hz, 1H), 7.04 (dd,  $J_1 = 8.4$ ,  $J_2 = 1.8$ , 1H), 6.88 (d,  $J = 1.8$  Hz, 1H), 4.73 (s, 2H), 3.90 (s, 3H), 3.82 (s, 3H); <sup>13</sup>C NMR (100 MHz, CDCl<sub>3</sub>):  $\delta$  168.6, 165.6, 158.3, 139.4, 133.3, 122.2, 119.7, 114.9, 66.7, 52.6, 52.4; HRMS (ESI): calcd. for C<sub>11</sub>H<sub>11</sub>ClNaO<sub>5</sub> [M+Na]<sup>+</sup>: 281.0187; found: 281.0189.

**Methyl 5-methoxy-2-(2-methoxy-2-oxoethoxy)benzoate (3e):**<sup>10</sup> White solid; yield: 81%; m.p. 81–83 °C; FT-IR (KBr,  $\nu_{\max}/\text{cm}^{-1}$ ): 2960, 1759, 1725, 1588, 1565, 1503, 1436, 1220, 1206. <sup>1</sup>H NMR (400 MHz, CDCl<sub>3</sub>):  $\delta$  7.35 (d,  $J = 3.2$  Hz, 1H), 7.00 (dd,  $J_1 = 3.2$  Hz,  $J_2 = 9.0$  Hz, 1H), 6.92 (d,  $J = 9.0$  Hz, 1H), 4.66 (s, 2H), 3.91 (s, 3H), 3.80 (s, 6H); <sup>13</sup>C NMR (100 MHz, CDCl<sub>3</sub>):  $\delta$  169.6, 166.3, 154.6, 152.0, 122.5, 119.8, 118.0, 116.1, 68.5, 56.0, 52.5, 52.4; HRMS (ESI): calcd. for C<sub>12</sub>H<sub>14</sub>NaO<sub>6</sub> [M+Na]<sup>+</sup>: 277.0683; found: 277.0683.

**Methyl 5-ethyl-2-(2-methoxy-2-oxoethoxy)benzoate (3f):** Colorless oil; yield: 85%; FT-IR (KBr,  $\nu_{\max}/\text{cm}^{-1}$ ): 2960, 2875, 1760, 1731, 1612, 1589, 1498, 1437, 1255. <sup>1</sup>H NMR (400 MHz, CDCl<sub>3</sub>):  $\delta$  7.66 (d,  $J = 2.3$  Hz, 1H), 7.28–7.25 (m, 1H), 6.83 (d,  $J = 8.5$  Hz, 1H), 4.70 (s, 2H), 3.90 (s, 3H), 3.80 (s, 3H), 2.61 (q,  $J = 7.6$  Hz, 2H), 1.22 (t,  $J = 7.6$  Hz, 3H); <sup>13</sup>C NMR (100 MHz, CDCl<sub>3</sub>):  $\delta$  169.5, 166.7, 155.7, 137.9, 133.0, 131.3, 121.2, 114.9, 67.2, 52.4, 52.3,

28.0, 15.7; HRMS (ESI): calcd. for  $C_{13}H_{16}NaO_5$   $[M+Na]^+$ : 275.0890; found: 275.0892.

**Methyl 2-ethyl-6-(2-methoxy-2-oxoethoxy)benzoate (3g):** Colorless oil; yield: 82%; FT-IR (KBr,  $\nu_{\max}/\text{cm}^{-1}$ ): 2970, 2955, 1761, 1732, 1601, 1585, 1470, 1435, 1254.  $^1\text{H}$  NMR (400 MHz,  $\text{CDCl}_3$ ):  $\delta$  7.26 (t,  $J = 8.0$  Hz, 1H), 6.90 (d,  $J = 7.7$  Hz, 1H), 6.65 (d,  $J = 8.3$  Hz, 1H), 4.64 (s, 2H), 3.92 (s, 3H), 3.78 (s, 3H), 2.60 (q,  $J = 7.6$  Hz, 2H), 1.21 (t,  $J = 7.6$  Hz, 3H);  $^{13}\text{C}$  NMR (100 MHz,  $\text{CDCl}_3$ ):  $\delta$  169.2, 168.6, 154.8, 143.2, 130.6, 124.2, 122.2, 110.0, 66.4, 52.4, 52.4, 26.7, 15.5; HRMS (ESI): calcd. for  $C_{13}H_{16}NaO_5$   $[M+Na]^+$ : 275.0890; found: 275.0887.

**General procedure for the preparation of compounds 4 (4a as a model).**  $\text{K}_3\text{PO}_4$  (159 mg, 0.75 mmol) was added to a solution of **3a** (224 mg, 1 mmol) in DMF (1.0 mL) and MeOH (0.5 mL). The mixture was heated at 150 °C for 30 min under stirring and 300 W microwave irradiation power. After cooling to ambient temperature, the mixture was diluted with ethyl acetate (5 mL). The resulting organic layer was washed with 1 N HCl (5 mL) and dried ( $\text{Na}_2\text{SO}_4$ ). The organic layer was then concentrated and purified by column chromatography using petroleum ether/ethyl acetate = 10:1 as the eluent and further purified on a gel column to give **4a** (58 mg, 43%) as a yellow solid.

**Benzofuran-3(2H)-one (4a):**<sup>11</sup> Yellow solid; yield: 43%; m.p. 95–98 °C; FT-IR (KBr,  $\nu_{\max}/\text{cm}^{-1}$ ): 2933, 1723, 1614, 1591, 1473, 1466, 1317.  $^1\text{H}$  NMR (400 MHz,  $\text{CDCl}_3$ ):  $\delta$  7.69 (d,  $J = 7.6$  Hz, 1H), 7.62 (t,  $J = 8.4$  Hz, 1H), 7.15 (d,  $J = 8.4$  Hz, 1H), 7.10 (t,  $J = 7.6$  Hz, 1H), 4.64 (s, 2H);  $^{13}\text{C}$  NMR (100 MHz,  $\text{CDCl}_3$ ):  $\delta$  200.1, 174.2, 138.1, 124.3, 122.2, 121.4, 113.9, 74.9; HRMS (ESI): calcd. for  $\text{C}_8\text{H}_7\text{O}_2$   $[M+H]^+$ : 135.0441; found: 135.0444.

**7-Methylbenzofuran-3(2H)-one (4b):**<sup>12</sup> Yellow solid; yield: 52%; m.p. 86.5–87.5 °C; FT-IR (KBr,  $\nu_{\max}/\text{cm}^{-1}$ ): 2925, 1704, 1603, 1497, 1451, 1434, 1323.  $^1\text{H}$  NMR (400 MHz,  $\text{CDCl}_3$ ): 7.51 (d,  $J = 7.7$  Hz, 1H), 7.42 (d,  $J = 7.2$  Hz, 1H), 7.00 (t,  $J = 7.5$  Hz, 1H), 4.64 (s, 2H), 2.33 (s, 3H);  $^{13}\text{C}$  NMR (100 MHz,  $\text{CDCl}_3$ ):  $\delta$  200.6, 173.0, 138.5, 124.1, 122.1, 121.5, 120.8, 74.9, 14.4; HRMS (ESI): calcd. for  $\text{C}_9\text{H}_8\text{NaO}_2$   $[M+Na]^+$ : 171.0417; found: 171.0414.

**6-Methylbenzofuran-3(2H)-one (4c):**<sup>13</sup> Yellow solid; yield: 47%; m.p. 85–86 °C; FT-IR (KBr,  $\nu_{\max}/\text{cm}^{-1}$ ): 2927, 1705, 1619, 1594, 1495, 1449, 1325.  $^1\text{H}$  NMR (400 MHz,  $\text{CDCl}_3$ ): 7.55 (d,  $J = 7.9$  Hz, 1H), 6.93 (s, 1H), 6.91 (d,  $J = 7.9$  Hz, 1H), 4.61 (s, 2H), 2.44 (s, 3H);  $^{13}\text{C}$  NMR (100 MHz,  $\text{CDCl}_3$ ):  $\delta$  199.5, 174.8, 150.2, 123.8, 123.8, 119.0, 113.8, 75.1, 22.7; HRMS (ESI): calcd. for  $\text{C}_9\text{H}_8\text{NaO}_2$   $[M+Na]^+$ : 171.0417; found: 171.0422.

**6-Chlorobenzofuran-3(2H)-one (4d):**<sup>14</sup> Yellow solid; yield: 58%; m.p. 126–127 °C; FT-IR (KBr,  $\nu_{\max}/\text{cm}^{-1}$ ):

3065, 1703, 1612, 1589, 1438, 1320, 794.  $^1\text{H}$  NMR (400 MHz,  $\text{CDCl}_3$ ): 7.60 (d,  $J = 8.2$  Hz, 1H), 7.17 (d,  $J = 1.6$  Hz, 1H), 7.08 (dd,  $J_1 = 8.2$ ,  $J_2 = 1.6$  Hz, 1H), 4.67 (s, 2H);  $^{13}\text{C}$  NMR (100 MHz,  $\text{CDCl}_3$ ):  $\delta$  198.4, 174.3, 144.3, 125.1, 123.3, 120.0, 114.3, 75.5; HRMS (ESI): calcd. for  $\text{C}_8\text{H}_6\text{ClO}_2$   $[M+H]^+$ : 169.0051; found: 169.0053.

**5-Methoxybenzofuran-3(2H)-one (4e):**<sup>15</sup> Yellow solid; yield: 55%; m.p. 90–92 °C; FT-IR (KBr,  $\nu_{\max}/\text{cm}^{-1}$ ): 2941, 2837, 1713, 1601, 1490, 1433, 1343, 1248.  $^1\text{H}$  NMR (400 MHz,  $\text{CDCl}_3$ ): 7.26–7.23 (m, 1H), 7.09–7.05 (m, 2H), 4.65 (s, 2H), 3.81 (s, 3H);  $^{13}\text{C}$  NMR (100 MHz,  $\text{CDCl}_3$ ):  $\delta$  200.4, 169.6, 155.2, 128.2, 121.3, 114.7, 104.0, 75.7, 56.1; HRMS (ESI): calcd.  $\text{C}_9\text{H}_9\text{O}_3$   $[M+H]^+$ : 165.0546; found: 165.0549.

**5-Ethylbenzofuran-3(2H)-one (4f):** Yellow solid; yield: 45%; m.p. 117–119 °C; FT-IR (KBr,  $\nu_{\max}/\text{cm}^{-1}$ ): 2966, 1717, 1621, 1598, 1491, 1458, 1317.  $^1\text{H}$  NMR (400 MHz,  $\text{CDCl}_3$ ): 7.50–7.44 (m, 2H), 7.06 (d,  $J = 8.4$  Hz, 1H), 4.62 (s, 2H), 2.66 (q,  $J = 7.6$  Hz, 2H), 1.24 (t,  $J = 7.6$  Hz, 3H);  $^{13}\text{C}$  NMR (100 MHz,  $\text{CDCl}_3$ ):  $\delta$  200.3, 172.9, 138.5, 138.4, 122.4, 121.3, 113.5, 75.2, 28.2, 15.8; HRMS (ESI): calcd. for  $\text{C}_{10}\text{H}_{11}\text{O}_2$   $[M+H]^+$ : 163.0754; found: 163.0753.

**4-Ethylbenzofuran-3(2H)-one (4g):** Yellow solid; yield: 49%; m.p. 100–101 °C; FT-IR (KBr,  $\nu_{\max}/\text{cm}^{-1}$ ): 2972, 1725, 1617, 1586, 1479, 1447, 1322.  $^1\text{H}$  NMR (400 MHz,  $\text{CDCl}_3$ ): 7.51–7.46 (m, 1H), 6.94 (d,  $J = 8.3$  Hz, 1H), 6.87 (d,  $J = 7.4$  Hz, 1H), 4.58 (s, 2H), 3.01 (q,  $J = 7.5$  Hz, 2H), 1.25 (t,  $J = 7.5$  Hz, 3H);  $^{13}\text{C}$  NMR (100 MHz,  $\text{CDCl}_3$ ):  $\delta$  200.5, 174.8, 146.4, 137.8, 121.6, 118.7, 111.0, 74.7, 24.9, 14.7; HRMS (ESI): calcd. for  $\text{C}_{10}\text{H}_{11}\text{O}_2$   $[M+H]^+$ : 163.0754; found: 163.0757.

### 3. Results and Discussion

First, various conditions, including temperature, reaction time, catalyst, and solvent, for the microwave-assisted cyclization reaction using methyl 2-(2-methoxy-2-oxoethoxy)benzoate were extensively screened (Table 1). The results showed that the temperature was the key factor influencing the reaction, and that the optimal temperature for cyclization was 150 °C (Table 1, entries 1–6). The reaction was fast and proceeded to completion in 30 min (entries 1–42). The solutions were subsequently examined. Cosolvent systems seemed to be better than single solvents (Table 1, entries 1–8). Among the catalysts investigated,  $\text{K}_3\text{PO}_4$ ,  $\text{CH}_3\text{CO}_2\text{K}$ , and  $\text{Cs}_2\text{CO}_3$  were more efficient during these common alkaline salts (Table 1, entries 19–31). Combined with the temperature, the reaction time, the catalyst, and the solution, the optimum condition was achieved with the best yield 43% (Table 1, entry 25).

**Table 1:** Optimization of Reaction Conditions for Microwave-assisted Synthesis of Benzofuranones

COC(=O)c1ccccc1COC(=O)C (3a)  $\xrightarrow[\text{Microwave}]{\text{catalysts, temperature, solvents, time}}$  COC(=O)c1cc2c(c1)oc(=O)c2 (4a)

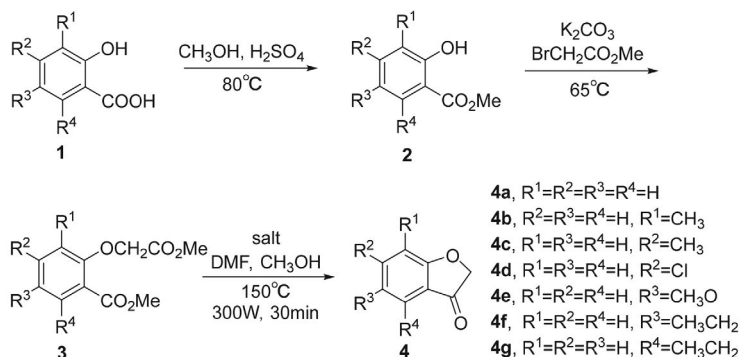
Entry	T (°C)	Time (min)	Catalyst (eq)	Solvent	Yield <sup>f</sup> (%)
1	60	20	K <sub>2</sub> CO <sub>3</sub> (1.0)	CH <sub>3</sub> OH/DMF <sup>b</sup>	0
2	100	20	K <sub>2</sub> CO <sub>3</sub> (1.0)	CH <sub>3</sub> OH/DMF	0
3	120	20	K <sub>2</sub> CO <sub>3</sub> (1.0)	CH <sub>3</sub> OH/DMF	0
4	140	20	K <sub>2</sub> CO <sub>3</sub> (1.0)	CH <sub>3</sub> OH/DMF	17
5	150	20	K <sub>2</sub> CO <sub>3</sub> (1.0)	CH <sub>3</sub> OH/DMF	23
6	170	20	K <sub>2</sub> CO <sub>3</sub> (1.0)	CH <sub>3</sub> OH/DMF	19
7	150	20	K <sub>2</sub> CO <sub>3</sub> (1.0)	DMF	8
8	170	20	K <sub>2</sub> CO <sub>3</sub> (1.0)	DMF	7
9	170	20	K <sub>2</sub> CO <sub>3</sub> (1.0)	DMSO <sup>c</sup>	7
10	140	20	K <sub>2</sub> CO <sub>3</sub> (1.0)	DMF	8
11	140	30	K <sub>2</sub> CO <sub>3</sub> (1.0)	DMF	10
12	150	15	K <sub>2</sub> CO <sub>3</sub> (1.0)	DMF	6
13	150	20	K <sub>2</sub> CO <sub>3</sub> (1.0)	DMSO	9
14	190	20	K <sub>2</sub> CO <sub>3</sub> (1.0)	DMSO	5
15	150	20	K <sub>2</sub> CO <sub>3</sub> (0.5)	DMF	7
16	150	30	K <sub>2</sub> CO <sub>3</sub> (0.75)	MEG <sup>d</sup>	15
17	170	20	K <sub>2</sub> CO <sub>3</sub> (0.5)	MEG	8
18	170	20	K <sub>2</sub> CO <sub>3</sub> (0.75)	MEG	13
19	150	30	K <sub>2</sub> CO <sub>3</sub> (0.75)	CH <sub>3</sub> OH/DMF	27
20	150	20	Cs <sub>2</sub> CO <sub>3</sub> (0.5)	CH <sub>3</sub> OH/DMF	31
21	150	30	Cs <sub>2</sub> CO <sub>3</sub> (0.75)	CH <sub>3</sub> OH/DMF	37
22	150	30	Cs <sub>2</sub> CO <sub>3</sub> (0.5)	MEG	12
23	150	30	Cs <sub>2</sub> CO <sub>3</sub> (0.5)	CH <sub>3</sub> OH/DMF	34
24	150	30	K <sub>3</sub> PO <sub>4</sub> (0.5)	CH <sub>3</sub> OH/DMF	39
25	150	30	K <sub>3</sub> PO <sub>4</sub> (0.75)	CH <sub>3</sub> OH/DMF	43
26	150	30	K <sub>3</sub> PO <sub>4</sub> (1.0)	CH <sub>3</sub> OH/DMF	37
27	150	30	K <sub>3</sub> PO <sub>4</sub> (0.75)	MEG	23
29	150	30	NaHCO <sub>3</sub> (0.75)	CH <sub>3</sub> OH/DMF	17
30	150	30	NaHCO <sub>3</sub> (1.0)	CH <sub>3</sub> OH/DMF	15
31	150	30	NaHCO <sub>3</sub> (0.75)	MEG	11
32	150	30	NaHCO <sub>3</sub> (0.75)	DMSO	9
33	150	30	Na <sub>2</sub> CO <sub>3</sub> (1.0)	CH <sub>3</sub> OH/DMF	28
34	150	30	Na <sub>2</sub> CO <sub>3</sub> (0.75)	CH <sub>3</sub> OH/DMF	33
35	150	30	C <sub>2</sub> H <sub>10</sub> N <sub>6</sub> · H <sub>2</sub> CO <sub>3</sub> <sup>a</sup> (0.5)	CH <sub>3</sub> OH/DMF	13
36	150	30	C <sub>2</sub> H <sub>10</sub> N <sub>6</sub> · H <sub>2</sub> CO <sub>3</sub> (0.75)	CH <sub>3</sub> OH/DMF	17
37	150	30	C <sub>2</sub> H <sub>10</sub> N <sub>6</sub> · H <sub>2</sub> CO <sub>3</sub> (0.75)	CH <sub>3</sub> OH	0
38	150	30	C <sub>2</sub> H <sub>10</sub> N <sub>6</sub> · H <sub>2</sub> CO <sub>3</sub> (0.75)	DMF	11
39	150	30	Ag <sub>2</sub> CO <sub>3</sub> (0.75)	CH <sub>3</sub> OH/DMF	0
40	150	30	K <sub>2</sub> CO <sub>3</sub> (0.75)	DMF/CH <sub>3</sub> CH <sub>2</sub> OH	13
41	150	30	K <sub>2</sub> CO <sub>3</sub> (0.75)	CH <sub>3</sub> OH/DMAc <sup>e</sup>	15
42	150	30	CH <sub>3</sub> CO <sub>2</sub> K (0.75)	CH <sub>3</sub> OH/DMF	38

<sup>a</sup> Guanidine Carbonate. <sup>b</sup> *N,N*-Dimethylformamide. <sup>c</sup> Dimethyl Sulfoxide. <sup>d</sup> Ethylene Glycol.<sup>e</sup> *N,N*-Dimethylacetamide. <sup>f</sup> Isolated yield.

Next, scope of the substrates was investigated, as shown in Scheme 2. In order to observe the effect of the functional group at different positions on the benzene ring, phenyl compounds **3** were prepared from easily available 2-hydroxybenzoic acids **1** with alkyl, alkoxy, or halogen substituents. Esterification of **1** provided compounds **2**, which

upon etherification with methyl 2-bromoacetate furnished the target products **3**. Cyclization of **3** under the optimal microwave conditions was performed as depicted in Scheme 2. All the substrates **3** could give the corresponding benzofuran-3(2*H*)-ones and the product yields were only slightly different from those in our experiments (43% to 58%).





Entry	T (°C)	Time (min)	Catalyst (eq)	Solvent	Yield <sup>f</sup> (%)
<b>4a</b>	150	30	K <sub>3</sub> PO <sub>4</sub> 0.75	CH <sub>3</sub> OH/DMF <sup>b</sup>	43
<b>4b</b>	150	30	CH <sub>3</sub> CO <sub>2</sub> K 0.75	CH <sub>3</sub> OH/DMF	52
<b>4c</b>	150	30	K <sub>3</sub> PO <sub>4</sub> 0.75	CH <sub>3</sub> OH/DMF	47
<b>4d</b>	150	30	CH <sub>3</sub> CO <sub>2</sub> K 0.75	CH <sub>3</sub> OH/DMF	58
<b>4e</b>	150	30	K <sub>3</sub> PO <sub>4</sub> 0.75	CH <sub>3</sub> OH/DMF	55
<b>4f</b>	150	30	Cs <sub>2</sub> CO <sub>3</sub> 0.75	CH <sub>3</sub> OH/DMF	45
<b>4g</b>	150	30	K <sub>3</sub> PO <sub>4</sub> 0.75	CH <sub>3</sub> OH/DMF	49

<sup>b</sup> N,N-Dimethylformamide. <sup>f</sup> Isolated yield.

**Scheme 2:** Preparation of different benzoates and their cyclization under microwave condition.

## 4. Conclusions

In conclusion, a new synthetic route to benzofuran-3(2H)-ones was established. The proposed method provides rapid and facile access to these important motifs, although the yields are still low and need to be improved in a future study.

## 5. Acknowledgements

This project was sponsored by the program for Science and Technology Innovation Talents in Universities of Henan Province (Grant 17HASTIT043), and the support project for the Disciplinary group of Psychology and Neuroscience, Xinxiang Medical University (Grant 2016PNK-FKT-15).

## 6. References

- (a) R. S. Ward, *Nat. Prod. Rep.*, **1999**, 16, 75–96; DOI:10.1039/a705992b  
(b) S. Apers, D. Paper, J. Bürgermeister, S. Baranikova, S. V. Dick, G. Lemiere, A. Vlietinck, L. Pieters, *J. Nat. Prod.*, **2002**, 65, 718–720; DOI:10.1021/np0103968  
(c) K. C. Nicolaou, Q. Kang, T. R. Wu, C. S. Lim, D. Y. K. Chen, *J. Am. Chem. Soc.*, **2010**, 132, 7540–7548; DOI:10.1021/ja102623j  
(d) F. Li, Q. Tu, S. Chen, L. Zhu, Y. Lan, J. Gong, Z. Yang, *Angew. Chem., Int. Ed.*, **2017**, 56, 5844–5848.
- (a) S. J. O'Malley, K. L. Tan, A. Watzke, R. G. Bergman, J. A. Ellman, *J. Am. Chem. Soc.*, **2005**, 127, 13496–13497; DOI:10.1021/ja052680h  
(b) M. A. Calter, N. Li, *Org. Lett.*, **2011**, 13, 3686–3689; DOI:10.1021/ol201332u  
(c) N. Kesava Reddy, B. V. D. Vijaykumar, S. Chandrasekhar, *Org. Lett.*, **2012**, 14, 299–301; DOI:10.1021/ol203060v  
(d) Y. H. Liu, C. Zhou, M. Xiong, J. J. Jiang, J. Wang, *Org. Lett.*, **2018**, 20, 5889–5893. DOI:10.1021/acs.orglett.8b02555
- (a) G. La Regina, V. Gatti, V. Famigliani, F. Piscitelli, R. Silvestri, *ACS Comb. Sci.*, **2012**, 14, 258–262; DOI:10.1021/co200165j  
(b) C. Cesari, L. Sambri, S. Zacchini, V. Zanotti, R. Mazzoni, *Organometallics*, **2014**, 33, 2814–2819; DOI:10.1021/om500335m  
(c) J. W. Puckett, J. T. Green, P. B. Dervan, *Org. Lett.*, **2012**, 14, 2774–2777; DOI:10.1021/ol3010003  
(d) N. E. Leadbeater, *J. Am. Chem. Soc.*, **2011**, 133, 2011–2011. DOI:10.1021/ja111493p
- (a) R. B. Sparks, A. P. Combs, *Org. Lett.*, **2004**, 6, 2473–2475; DOI:10.1021/ol049124x  
(b) Y. Oeda, Y. Iijima, H. Taguchi, A. Ohkubo, K. Seio, M. Sekine, *Org. Lett.*, **2009**, 11, 5582–5585; DOI:10.1021/ol902142w  
(c) K. Tambara, N. Ponnuswamy, G. Hennrich, G. D. Pantoş, *J. Org. Chem.*, **2011**, 76, 3338–3347; DOI:10.1021/jo200177s  
(d) T. M. Monos, A. C. Sun, R. C. McAtee, J. J. Devery, C. R. Stephenson, *J. Org. Chem.*, **2016**, 81, 6988–6994. DOI:10.1021/acs.joc.6b00983

5. (a) V. Sharma, P. K. Jaiswal, D. K. Yadav, M. Saran, J. Prikhodko, M. Mathur, A. K. Swami, I. V. Mashevskaya, S. Chaudhary, *Acta Chim. Slov.* **2017**, *64*, 988–1004. DOI:10.17344/acsi.2017.3709  
(b) L. Moradi, M. Aghamohammad Sadegh, *Acta Chim. Slov.* **2017**, *64*, 506–512. DOI:10.17344/acsi.2017.3417  
(c) A. Srinivas, M. Sunitha, B. Ravinder, S. Anusha, T. Rajasri, P. Swapna, D. Sushmitha, D. Swaroopa, G. Nikitha, C. Govind Rao, *Acta Chim. Slov.* **2017**, *64*, 319–331. DOI:10.17344/acsi.2016.3153
6. D. Farran, P. Bertrand, *Synth. Commun.*, **2012**, *42*, 989–1001. DOI:10.1080/00397911.2010.533806
7. L. Z. Fang, F. F. Zhao, S. Y. Hu, L. L. Han, X. J. Hu, M. Y. Wang, Q. Q. Sun, H. P. Wu, *J. Org. Chem.*, **2018**, *83*, 12213–12220. DOI:10.1021/acs.joc.8b01613
8. L. Z. Fang, S. S. Liu, L. L. Han, H. H. Li, F. F. Zhao, *Organometallics*, **2017**, *36*, 1217–1219. DOI:10.1021/acs.organomet.7b00022
9. C. F. Carvalho, M. V. Sargebt, *J. Chem. Soc. Perkin Trans.*, **1984**, 1605–1612. DOI:10.1039/p19840001605
10. Y. Yamaguchi, I. Akimoto, K. Motegi, T. Yoshimura, K. Wada, N. Nishizono, K. Oda, *Heterocycles*, **2013**, *87*, 1727–1739. DOI:10.3987/COM-13-12744
11. C. R. Ogle, L. Main, *J. Chem. Research (S)*, **2001**, *2001*, 472–473. DOI:10.3184/030823401103168721
12. Y. Nakada, S. Muramatsu, M. Asai, H. Tsuji, Y. Yura, *Agric. Biol. Chem.*, **1978**, *42*, 1767–1772. DOI:10.1080/00021369.1978.10863243
13. J. A. Elvidge, R. G. Foster, *J. Chem. Soc.*, **1964**, 981–991. DOI:10.1039/JR9640000981
14. T. P. C. Mulholland, R. I. W. Honeywood, H. D. Preston, D. T. Rosevear, *J. Chem. Soc.*, **1965**, 4939–4953. DOI:10.1039/jr9650004939
15. M. L. Hammond, R. A. Zambias, M. N. Chang, N. P. Jensen, J. McDonald, K. Thompson, D. A. Boulton, I. E. Kopka, K. M. Hand, E. E. Opas, S. Luell, T. Bach, P. Davies, D. E. MacIntyre, R. J. Bonney, *J. Med. Chem.*, **1990**, *33*, 908–918. DOI:10.1021/jm00165a005

## Povzetek

V prispevku je opisan razvoj nove metode za sintezo benzofuran-3(2H)-onov z uporabo mikrovalov. Podan je pregled reakcijskih pogojev in širši nabor benzoatnih substratov. Predstavljeni rezultati kažejo, da opisana metoda omogoča hitro pripravo dihidrobenzofuranonov s 43 % do 58 %-nim izkoristkom.



Except when otherwise noted, articles in this journal are published under the terms and conditions of the Creative Commons Attribution 4.0 International License

## **DRUŠTVENE VESTI IN DRUGE AKTIVNOSTI**

## **SOCIETY NEWS, ANNOUNCEMENTS, ACTIVITIES**

### **Vsebina**

Koledar važnejših znanstvenih srečanj s področja kemije, kemijske tehnologije in kemijskega inženirstva .....	S53
Navodila za avtorje .....	S56

### **Contents**

Scientific meetings – chemistry, chemical technology and chemical engineering .....	S53
Instructions for authors .....	S56



# KOLEDAR VAŽNEJŠIH ZNANSTVENIH SREČANJ S PODROČJA KEMIJE IN KEMIJSKE TEHNOLOGIJE

## SCIENTIFIC MEETINGS – CHEMISTRY AND CHEMICAL ENGINEERING

### 2019

#### September 2019

---

- 8 – 13                    33<sup>ND</sup> CONFERENCE OF EUROPEAN COLLOID AND INTERFACE SOCIETY (ECIS)  
Leuven, Belgium  
Information: <https://kuleuvencongres.be/ecis2019/>
- 9 – 13                    EUROPEAN CORROSION CONGRESS  
Seville, Spain  
Information: <https://eurocorr.org/EUROCRR+2019.html>
- 11 – 14                   7<sup>TH</sup> INTERNATIONAL CONFERENCE ON SEMICONDUCTOR  
PHOTOCHEMISTRY – SP7  
Milano, Italy  
Information: <https://www.sp7.unimi.it/>
- 15 – 19                   11<sup>TH</sup> EUROPEAN CONGRESS OF CHEMICAL ENGINEERING – ECCE11 & 4<sup>TH</sup>  
EUROPEAN CONGRESS OF APPLIED BIOTECHNOLOGY – ECAB5  
Florence, Italy  
Information: [http://efce.info/ECCE12\\_ECAB5-p-112545.html](http://efce.info/ECCE12_ECAB5-p-112545.html)
- 25 – 27                   SLOVENIAN CHEMICAL SOCIETY ANNUAL MEETING 2019  
Portorož, Slovenia  
Information: <http://chem-soc.si/slovenian-chemical-society-annual-meeting-2019>

#### October 2019

---

- 01 – 06                   14<sup>TH</sup> CONFERENCE ON SUSTAINABLE DEVELOPMENT OF ENERGY, WATER AND  
ENVIRONMENT SYSTEMS (SDEWES)  
Dubrovnik, Croatia  
Information: <http://www.dubrovnik2019.sdewes.org/>
- 14 – 16                   WMFmeetsIUPAC2019  
Belfast, Northern Ireland United Kingdom  
Information: <https://www.worldmycotoxinforum.org/>
- 17 – 18                   2019 WATER DAYS, INTERNATIONAL SYMPOSIUM – CONNECTED TO WATER FOR 25  
YEARS  
Bernardin Congress Centre, Portorož, Slovenia  
Information: <https://sdzv-drustvo.si/en/water-days-2019/>
- 21 – 24                   24<sup>RD</sup> INTERNATIONAL CONGRESS OF CHEMICAL AND PROCESS ENGINEERING  
CHISA 2019  
Seč, Czech Republic  
Information: <http://2019.chisa.cz/>

**November 2019**

- 04 – 08 A GLOBAL APPROACH TO THE GENDER GAP IN MATHEMATICAL, COMPUTING, AND NATURAL SCIENCES: HOW TO MEASURE IT, HOW TO REDUCE IT?  
Trieste, Italy  
Information: <https://gender-gap-in-science.org>
- 13 BIOCIDES: WHAT DOES THE FUTURE HOLD?  
Frankfurt/Main, Germany  
Information: <https://www.lexxion.eu/en/events/3636/>
- 28 COUNTDOWN TO THE MEDICAL DEVICE REGULATION – CURRENT TRENDS AND LEGAL CHALLENGES  
Basel, Switzerland  
Information: <https://www.lexxion.eu/en/events/3632/>
- 27 – 29 EAPRIL  
Tartu, Estonia  
Information: <https://eapril.org/eapril-2019>

**December 2019**

- 05 IYPT2019 CLOSING CEREMONY  
Tokyo, Japan  
Information: <https://iypt.jp/en.html>
- 15 – 18 12<sup>TH</sup> INTERNATIONAL SYMPOSIUM ON BIOORGANIC CHEMISTRY (ISBOC-12)  
Shenzhen, China  
Information: <http://www.sz-isboc.com/>
- 16 – 19 CHEMCON 2019  
Delhi, India  
Information: <https://www.chemcon19.com/>

**2020****February 2020**

- 08 – 12 INTERNATIONAL NATURAL SCIENCES TOURNAMENT  
Warsaw, Poland  
Information: <http://www.scitourn.com/inst/>
- 19 – 21 CHEMISTRY CONFERENCE FOR YOUNG SCIENTISTS (CHEMCYS 2020)  
Blankenberge, Belgium  
Information: <https://www.chemcys.be>

**March 2020**

- 23 – 27 SNOW COVER, ATMOSPHERIC PRECIPITATION, AEROSOLS: CHEMISTRY AND CLIMATE  
Listvyanka, Russian Federation  
Information: <http://snow-baikal.tw1.ru/index-eng>

**May 2020**

- 05 – 10 44<sup>TH</sup> INTERNATIONAL CONFERENCE ON COORDINATION CHEMISTRY  
Rimini, Italy  
Information: <https://www.iccc2020.com>



- 18 – 22                    POLY-CHAR 2020 [VENICE] – INTERNATIONAL POLYMER CHARACTERIZATION FORUM  
Venezia Mestre, Italy  
Information:            <https://www.poly-char2020.org/>
- 24 – 27                    THE 30<sup>TH</sup> EUROPEAN SYMPOSIUM ON COMPUTER AIDED PROCESS ENGINEERING  
Milano, Italy  
Information:            <https://www.aidic.it/escape30/enter.php>

---

**June 2020**

- 02 – 05                    14<sup>TH</sup> MEDITERRANEAN CONGRESS OF CHEMICAL ENGINEERING  
Barcelona, Spain  
Information:            <https://www.mecce.org/>
- 08 – 12                    11<sup>TH</sup> EUROPEAN CONFERENCE ON SOLAR CHEMISTRY AND PHOTOCATALYSIS: ENVIRONMENTAL APPLICATIONS (SPEA)  
Turin, Italy  
Information:            <http://www.spea11.unito.it/home>
- 14 – 18                    12<sup>TH</sup> EUROPEAN SYMPOSIUM ON ELECTROCHEMICAL ENGINEERING  
Leeuwarden, The Netherlands  
Information:            <http://www.electrochemical-engineering.eu/2020/>

---

**July 2020**

- 05 – 09                    48<sup>TH</sup> WORLD POLYMER CONGRESS – MACRO2020  
Jeju Island, Republic of Korea  
Information:            <http://www.macro2020.org>

# Acta Chimica Slovenica

## Author Guidelines

### Submissions

Submission to ACSi is made with the implicit understanding that neither the manuscript nor the essence of its content has been published in whole or in part and that it is not being considered for publication elsewhere. All the listed authors should have agreed on the content and the corresponding (submitting) author is responsible for having ensured that this agreement has been reached. The acceptance of an article is based entirely on its scientific merit, as judged by peer review. There are no page charges for publishing articles in ACSi. The authors are asked to read the Author Guidelines carefully to gain an overview and assess if their manuscript is suitable for ACSi.

### Additional information

- Citing spectral and analytical data
- Depositing X-ray data

### Submission material

Typical submission consists of:

- full manuscript (PDF file, with title, authors, abstract, keywords, figures and tables embedded, and references)
- supplementary files
  - **Full manuscript** (original Word file)
  - **Statement of novelty** (Word file)
  - **List of suggested reviewers** (Word file)
  - **ZIP file containing graphics** (figures, illustrations, images, photographs)
  - **Graphical abstract** (single graphics file)
  - **Proposed cover picture** (optional, single graphics file)
  - **Appendices** (optional, Word files, graphics files)

Incomplete or not properly prepared submissions will be rejected.

### Submission process

Before submission, authors should go through the checklist at the bottom of the page and prepare for submission.

Submission process consists of 5 steps.

#### Step 1: Starting the submission

- Choose one of the journal sections.
- Confirm all the requirements of the **checklist**.
- Additional plain text comments for the editor can be provided in the relevant text field.

#### Step 2: Upload submission

- Upload full manuscript in the form of a Word file (with title, authors, abstract, keywords, figures and tables embedded, and references).

#### Step 3: Enter metadata

- First name, last name, contact email and affiliation for all authors, in relevant order, must be provided. Corresponding author has to be selected. Full postal address and phone number of the corresponding author has to be provided.

- **Title and abstract** must be provided in plain text.
- Keywords must be provided (max. 6, separated by semicolons).
- Data about contributors and supporting agencies may be entered.
- **References** in plain text must be provided in the relevant text field.

#### Step 4: Upload supplementary files

- Original Word file (original of the PDF uploaded in the step 2)
- **Statement of novelty** in a Word file must be uploaded
- All **graphics** have to be uploaded in a single ZIP file. Graphics should be named Figure 1.jpg, Figure 2.eps, etc.
- **Graphical abstract image** must be uploaded separately
- **Proposed cover picture** (optional) should be uploaded separately.
- Any additional **appendices** (optional) to the paper may be uploaded. Appendices may be published as a supplementary material to the paper, if accepted.
- For each uploaded file the author is asked for additional metadata which may be provided. Depending of the type of the file please provide the relevant title (Statement of novelty, List of suggested reviewers, Figures, Graphical abstract, Proposed cover picture, Appendix).

#### Step 5: Confirmation

- Final confirmation is required.

### Article Types

**Feature Articles** are contributions that are written on editor's invitation. They should be clear and concise summaries of the most recent activity of the author and his/her research group written with the broad scope of ACSi in mind. They are intended to be general overviews of the authors' subfield of research but should be written in a way that engages and informs scientists in other areas. They should contain the following (see also general directions for article structure in ACSi below): (1) an introduction that acquaints readers with the authors' research field and outlines the important questions to which answers are being sought; (2) interesting, new, and recent contributions of the author(s) to the field; and (3) a summary that presents possible future directions. Manuscripts normally should not exceed 40 pages of one column format (letter size 12, 33 lines per page). Generally, experts in a field who have made important contribution to a specific topic in recent years will be invited by an editor to contribute such an **Invited Feature Article**. Individuals may, however, send a proposal (one-page maximum) for an Invited Feature Article to the Editor-in-Chief for consideration.

**Scientific articles** should report significant and innovative achievements in chemistry and related sciences and should exhibit a high level of originality. They

should have the following structure:

1. Title (max. 150 characters),
2. Authors and affiliations,
3. Abstract (max. 1000 characters),
4. Keywords (max. 6),
5. Introduction,
6. Experimental,
7. Results and Discussion,
8. Conclusions,
9. Acknowledgements,
10. References.

The sections should be arranged in the sequence generally accepted for publications in the respective fields and should be successively numbered.

**Short communications** generally follow the same order of sections as Scientific articles, but should be short (max. 2500 words) and report a significant aspect of research work meriting separate publication. Editors may decide that a Scientific paper is categorized as a Short Communication if its length is short.

**Technical articles** report applications of an already described innovation. Typically, technical articles are not based on new experiments.

## Preparation of Submissions

**Text** of the submitted articles must be prepared with Microsoft Word. Normal style set to single column, 1.5 line spacing, and 12 pt Times New Roman font is recommended. Line numbering (continuous, for the whole document) must be enabled to simplify the reviewing process. For any other format, please consult the editor. Articles should be written in English. Correct spelling and grammar are the sole responsibility of the author(s). Papers should be written in a concise and succinct manner. The authors shall respect the ISO 80000 standard [1], and IUPAC Green Book [2] rules on the names and symbols of quantities and units. The Système International d'Unités (SI) must be used for all dimensional quantities.

**Graphics** (figures, graphs, illustrations, digital images, photographs) should be inserted in the text where appropriate. The captions should be self-explanatory. Lettering should be readable (suggested 8 point Arial font) with equal size in all figures. Use common programs such as MS Excel or similar to prepare figures (graphs) and ChemDraw to prepare structures in their final size. Width of graphs in the manuscript should be 8 cm. Only in special cases (in case of numerous data, visibility issues) graphs can be 17 cm wide. All graphs in the manuscript should be inserted in relevant places and **aligned left**. The same graphs should be provided separately as images of appropriate resolution (see below) and submitted together in a ZIP file (Graphics ZIP). Please do not submit figures as a Word file. In **graphs**, only the graph area determined by both axes should be in the frame, while a frame around the whole graph should be omitted. The graph area should be white. The legend should be inside the graph area. The style of all graphs should be the same. **Figures and illustrations** should be of sufficient quality for the printed version, i.e. 300 dpi minimum. **Digital images and photographs** should be of high quality (minimum 250 dpi resolution). On submission, figures should be of good enough resolution to be assessed by the referees, ideally as JPEGs. High-resolution figures (in JPEG,

TIFF, or EPS format) might be required if the paper is accepted for publication.

**Tables** should be prepared in the Word file of the paper as usual Word tables. The captions should appear above the table and should be self-explanatory.

**References** should be numbered and ordered sequentially as they appear in the text, likewise methods, tables, figure captions. When cited in the text, reference numbers should be superscripted, following punctuation marks. It is the sole responsibility of authors to cite articles that have been submitted to a journal or were in print at the time of submission to ACSi. Formatting of references to published work should follow the journal style; please also consult a recent issue:

1. J. W. Smith, A. G. White, *Acta Chim. Slov.* **2008**, *55*, 1055–1059.
2. M. F. Kemmere, T. F. Keurentjes, in: S. P. Nunes, K. V. Peinemann (Ed.): *Membrane Technology in the Chemical Industry*, Wiley-VCH, Weinheim, Germany, **2008**, pp. 229–255.
3. J. Levec, Arrangement and process for oxidizing an aqueous medium, US Patent Number 5,928,521, date of patent July 27, **1999**.
4. L. A. Bursill, J. M. Thomas, in: R. Sersale, C. Collela, R. Aiello (Eds.), *Recent Progress Report and Discussions: 5th International Zeolite Conference*, Naples, Italy, 1980, Gianini, Naples, **1981**, pp. 25–30.
5. J. Szegezdi, F. Csizmadia, Prediction of dissociation constant using microconstants, [http://www.chemaxon.com/conf/Prediction\\_of\\_dissociation\\_constant\\_using\\_microconstants.pdf](http://www.chemaxon.com/conf/Prediction_of_dissociation_constant_using_microconstants.pdf), (assessed: March 31, 2008)

Titles of journals should be abbreviated according to Chemical Abstracts Service Source Index (CASSI).

## Special Notes

- Complete characterization, **including crystal structure**, should be given when the synthesis of new compounds in crystal form is reported.
- Numerical **data should be reported with the number of significant digits corresponding to the magnitude** of experimental uncertainty.
- **The SI system of units and IUPAC recommendations** for nomenclature, symbols and abbreviations should be followed closely. Additionally, the authors should follow the general guidelines when citing spectral and analytical data, and depositing crystallographic data.
- **Characters** should be correctly represented throughout the manuscript: for example, 1 (one) and l (ell), 0 (zero) and O (oh), x (ex), D7 (times sign), B0 (degree sign). Use Symbol font for all Greek letters and mathematical symbols.
- The rules and recommendations of the **IUBMB** and the **International Union of Pure and Applied Chemistry (IUPAC)** should be used for abbreviation of chemical names, nomenclature of chemical compounds, enzyme nomenclature, isotopic compounds, optically active isomers, and spectroscopic data.
- **A conflict of interest** occurs when an individual (author, reviewer, editor) or its organization is involved in multiple interests, one of which could possibly corrupt the motivation for an act in the

other. Financial relationships are the most easily identifiable conflicts of interest, while conflicts can occur also as personal relationships, academic competition, etc. **The Editors** will make effort to ensure that conflicts of interest will not compromise the evaluation process; potential editors and reviewers will be asked to exempt themselves from review process when such conflict of interest exists. When the manuscript is submitted for publication, **the authors** are expected to disclose any relationships that might pose potential conflict of interest with respect to results reported in that manuscript. In the Acknowledgement section the source of funding support should be mentioned. The statement of disclosure must be provided as Comments to Editor during the submission process.

- **Published statement of Informed Consent.** Research described in papers submitted to ACSI must adhere to the principles of the Declaration of Helsinki (<http://www.wma.net/e/policy/b3.htm>). These studies must be approved by an appropriate institutional review board or committee, and informed consent must be obtained from subjects. The Methods section of the paper must include: 1) a statement of protocol approval from an institutional review board or committee and 2), a statement that informed consent was obtained from the human subjects or their representatives.
- **Published Statement of Human and Animal Rights.** When reporting experiments on human subjects, authors should indicate whether the procedures followed were in accordance with the ethical standards of the responsible committee on human experimentation (institutional and national) and with the Helsinki Declaration of 1975, as revised in 2008. If doubt exists whether the research was conducted in accordance with the Helsinki Declaration, the authors must explain the rationale for their approach and demonstrate that the institutional review body explicitly approved the doubtful aspects of the study. When reporting experiments on animals, authors should indicate whether the institutional and national guide for the care and use of laboratory animals was followed.
- To avoid conflict of interest between authors and referees we expect that not more than one referee is from the same country as the corresponding author(s), however, not from the same institution.
- Contributions authored by **Slovenian scientists** are evaluated by non-Slovenian referees.
- Papers describing **microwave-assisted reactions** performed in domestic microwave ovens are not considered for publication in *Acta Chimica Slovenica*.
- *Manuscripts that are **not prepared and submitted** in accord with the instructions for authors are not considered for publication.*

## Appendices

Authors are encouraged to make use of supporting information for publication, which is supplementary material (appendices) that is submitted at the same time as the manuscript. It is made available on the Journal's web site and is linked to the article in the

Journal's Web edition. The use of supporting information is particularly appropriate for presenting additional graphs, spectra, tables and discussion and is more likely to be of interest to specialists than to general readers. When preparing supporting information, authors should keep in mind that the supporting information files will not be edited by the editorial staff. In addition, the files should be not too large (upper limit 10 MB) and should be provided in common widely known file formats to be accessible to readers without difficulty. All files of supplementary materials are loaded separately during the submission process as supplementary files.

## Proposed Cover Picture and Graphical Abstract Image

**Graphical content:** an ideally full-colour illustration of resolution 300 dpi from the manuscript must be proposed with the submission. Graphical abstract pictures are printed in size 6.5 x 4 cm (hence minimal resolution of 770 x 470 pixels). Cover picture is printed in size 11 x 9.5 cm (hence minimal resolution of 1300 x 1130 pixels)

Authors are encouraged to submit illustrations as candidates for the journal Cover Picture\*. The illustration must be related to the subject matter of the paper. Usually both proposed cover picture and graphical abstract are the same, but authors may provide different pictures as well.

\* The authors will be asked to contribute to the costs of the cover picture production.

## Statement of novelty

Statement of novelty is provided in a Word file and submitted as a supplementary file in step 4 of submission process. Authors should in no more than 100 words emphasize the scientific novelty of the presented research. Do not repeat for this purpose the content of your abstract.

## List of suggested reviewers

List of suggested reviewers is a Word file submitted as a supplementary file in step 4 of submission process. Authors should propose the names, full affiliation (department, institution, city and country) and e-mail addresses of three potential referees. Field of expertise and at least two references relevant to the scientific field of the submitted manuscript must be provided for each of the suggested reviewers. The referees should be knowledgeable about the subject but have no close connection with any of the authors. In addition, referees should be from institutions other than (and preferably countries other than) those of any of the authors.

## How to Submit

Users registered in the role of author can start submission by choosing USER HOME link on the top of the page, then choosing the role of the Author and follow the relevant link for starting the submission process. Prior to submission we strongly recommend that you familiarize yourself with the ACSi style by browsing the journal, particularly if you have not submitted to the ACSi before or recently.

## Correspondence

All correspondence with the ACSi editor regarding the paper goes through this web site and emails. Emails are sent and recorded in the web site database. In the correspondence with the editorial office please provide ID number of your manuscript. All emails you receive from the system contain relevant links. **Please do not answer the emails directly but use the embedded links in the emails for carrying out relevant actions.** Alternatively, you can carry out all the actions and correspondence through the online system by logging in and selecting relevant options.

## Proofs

Proofs will be dispatched via e-mail and corrections should be returned to the editor by e-mail as quickly as possible, normally within 48 hours of receipt. Typing errors should be corrected; other changes of contents will be treated as new submissions.

## Submission Preparation Checklist

As part of the submission process, authors are required to check off their submission's compliance with all of the following items, and submissions may be returned to authors that do not adhere to these guidelines.

1. The submission has not been previously published, nor is it under consideration for publication in any other journal (or an explanation has been provided in Comments to the Editor).
2. All the listed authors have agreed on the content and the corresponding (submitting) author is responsible for having ensured that this agreement has been reached.
3. The submission files are in the correct format: manuscript is created in MS Word but will be **submitted in PDF** (for reviewers) as well as in original MS Word format (as a supplementary file for technical editing); diagrams and graphs are created in Excel and saved in one of the file formats: TIFF, EPS or JPG; illustrations are also saved in one of these formats. The preferred position of graphic files in a document is to embed them close to the place where they are mentioned in the text (See **Author guidelines** for details).
4. The manuscript has been examined for spelling and grammar (spell checked).
5. The **title** (maximum 150 characters) briefly explains the contents of the manuscript.
6. Full names (first and last) of all authors together with the affiliation address are provided. Name of author(s) denoted as the corresponding author(s), together with their e-mail address, full postal address and telephone/fax numbers are given.
7. The **abstract** states the objective and conclusions of the research concisely in no more than 150 words.
8. Keywords (minimum three, maximum six) are provided.
9. **Statement of novelty** (maximum 100 words) clearly explaining new findings reported in the manuscript should be prepared as a separate Word file.
10. The text adheres to the stylistic and bibliographic requirements outlined in the **Author guidelines**.
11. Text in normal style is set to single column, 1.5 line spacing, and 12 pt. Times New Roman font is

recommended. All tables, figures and illustrations have appropriate captions and are placed within the text at the appropriate points.

12. Mathematical and chemical equations are provided in separate lines and numbered (Arabic numbers) consecutively in parenthesis at the end of the line. All equation numbers are (if necessary) appropriately included in the text. Corresponding numbers are checked.
13. Tables, Figures, illustrations, are prepared in correct format and resolution (see **Author guidelines**).
14. The lettering used in the figures and graphs do not vary greatly in size. The recommended lettering size is 8 point Arial.
15. Separate files for each figure and illustration are prepared. The names (numbers) of the separate files are the same as they appear in the text. All the figure files are packed for uploading in a single ZIP file.
16. Authors have read **special notes** and have accordingly prepared their manuscript (if necessary).
17. References in the text and in the References are correctly cited. (see **Author guidelines**). All references mentioned in the Reference list are cited in the text, and vice versa.
18. Permission has been obtained for use of copyrighted material from other sources (including the Web).
19. The names, full affiliation (department, institution, city and country), e-mail addresses and references of three potential referees from institutions other than (and preferably countries other than) those of any of the authors are prepared in the word file. At least two relevant references (important papers with high impact factor, head positions of departments, labs, research groups, etc.) for each suggested reviewer must be provided.
20. Full-colour illustration or graph from the manuscript is proposed for graphical abstract.
21. **Appendices** (if appropriate) as supplementary material are prepared and will be submitted at the same time as the manuscript.

## Privacy Statement

The names and email addresses entered in this journal site will be used exclusively for the stated purposes of this journal and will not be made available for any other purpose or to any other party.

ISSN: 1580-3155

---

## Koristni naslovi

---

Slovensko kemijsko društvo  
Slovenian Chemical Society



**Slovensko kemijsko društvo**

[www.chem-soc.si](http://www.chem-soc.si)

e-mail: [chem.soc@ki.si](mailto:chem.soc@ki.si)

---



**Wessex Institute of Technology**

[www.wessex.ac.uk](http://www.wessex.ac.uk)

---



**SETAC**

[www.setac.org](http://www.setac.org)

---



**European Water Association**

<http://www.ewa-online.eu/>

---



**European Science Foundation**

[www.esf.org](http://www.esf.org)

---



**European Federation of Chemical Engineering**

<https://efce.info/>

---



**IUPAC**

INTERNATIONAL UNION OF  
PURE AND APPLIED CHEMISTRY

**International Union of Pure and Applied Chemistry**

<https://iupac.org/>

---

---

## Novice evropske zveze kemijskih društev (EuCheMS) najdete na:

---

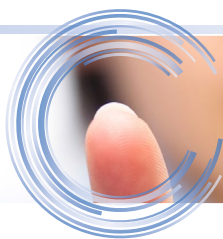


**EuCheMS: Brussels News Updates**

<http://www.euchems.eu/newsletters/>

---





**DONAU LAB** Ljubljana  
Member of LPPgroup

Donau Lab d.o.o., Ljubljana  
Tbilisjska 85  
SI-1000 Ljubljana  
[www.donaulab.si](http://www.donaulab.si)  
[office-si@donaulab.com](mailto:office-si@donaulab.com)

# Planetarni centrifugalni mikser

## ARM-310CE

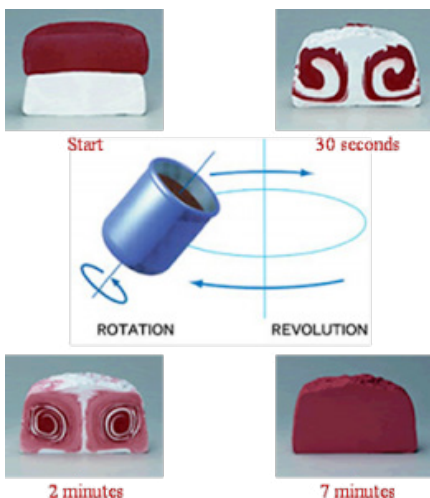
Brezkontaktno mešanje in disperzija

Tudi za zelo viskozne materiale

Širok spekter uporabe

Atraktivna cena

# THINKY





# Napredek, obarvan v zeleno

V Heliosu načela trajnostnega razvoja in skrbi za okolje vpeljujemo na vsa področja našega delovanja. Nove rešitve in proizvode razvijamo tudi z namenom, da bi zmanjšali porabo vseh vrst virov in ogljični odtis produktov.



[www.helios-group.eu](http://www.helios-group.eu)



Designing Excellence





# Izjemen dan se začne z izjemnim spancem.

Odpravite nespečnost in začnite dan spočiti.

## Noctiben Mea®

doksilaminijev hidrogensukcinat



Učinkuje hitro –  
vzame se  
15 do 30 minut  
pred spanjem.



Deluje  
celo noč.



Izboljša kakovost  
spanca in  
naslednjega dne.



NOVO

[www.noctibenmea.si](http://www.noctibenmea.si)

Noctiben Mea®, doksilaminijev hidrogensukcinat, filmsko obložene tablete, 15 mg

**Kaj je zdravilo Noctiben Mea in za kaj ga uporabljamo** Jemanje tega zdravila se priporoča pri občasni nespečnosti pri odraslih. Če se znaki vaše bolezni poslabšajo ali ne izboljšajo v 5 dneh, se posvetujte z zdravnikom. **Kaj morate vedeti, preden boste vzeli zdravilo Noctiben Mea** Ne jemljite tega zdravila, če ste alergični na doksilamin, antihistaminike ali katerikoli sestavino tega zdravila, če ste imeli v preteklosti akutni glavkom (zvišan očesni tlak), če ste moški in imate težave z odvajanjem vode (zaradi težav s prostato ali drugih težav), če ste mlajši od 18 let. Pred začetkom jemanja zdravila se posvetujte z zdravnikom ali s farmacevtom. Pri starejših je treba zdravilo uporabljati previdno zaradi tveganja za poslabšanje kognitivnih sposobnosti, zaspanost, počasne odzive in/ali omotico, ki lahko poveča tveganje za padce. Tako kot pri drugih uspavalih in pomirjevalih bo tudi pri jemanju tega zdravila verjetno prišlo do poslabšanja sindroma spalne apneje. Med zdravljenjem ni priporočljivo pitje alkohola. Če imate dolgotrajno jetrno ali ledvično bolezen, se posvetujte z zdravnikom, da bo lahko prilagodil odmerek. Zdravilo vsebuje laktozo. Če ne prenašate nekaterih sladkorjev, se pred jemanjem tega zdravila posvetujte z zdravnikom. Otroci in mladostniki, mlajši od 18 let, zdravila ne smejo jemati. Da bi se izognili morebitnim interakcijam med različnimi zdravili, morate o kakršnemkoli drugem zdravljenju obvestiti svojega zdravnika ali farmacevta. Če ste noseči ali dojite, če menite, da bi lahko bili noseči, ali če načrtujete zanositev, se posvetujte z zdravnikom ali s farmacevtom, preden vzamete to zdravilo. Med nosečnostjo lahko to zdravilo jemljete samo, če vam je tako svetoval zdravnik. Jemanje med dojenjem ni priporočljivo. Zavedati se morate, da sta z jemanjem tega zdravila povezani zaspanost podnevi in zmanjšana pozornost. Med upravljanjem vozil in strojev ni priporočljivo sočasno jemanje drugih sedativnih zdravil, natrijevega oksibata ter seveda pitje alkohola ali jemanje zdravil, ki vsebujejo alkohol. Pri nezadostnem trajanju spanja je tveganje za pojav zmanjšane pozornosti še povečano. **Kako jemati zdravilo Noctiben Mea** Priporočeni odmerek je ½ tablete do 1 tableta na dan, po potrebi se lahko poveča na 2 tableti na dan. Pri starejših in bolnikih z ledvično ali jetrno okvaro se priporoča najmanjši odmerek. Tableta se lahko deli na enaka odmerka. Pogoltnite jo z nekaj vode. Dnevni odmerek vzemite zvečer, 15 do 30 minut pred spanjem. Zdravljenje traja od 2 do 5 dni. Brez posveta z zdravnikom lahko zdravilo jemljete največ 5 dni. Če ste vzeli večji odmerek zdravila, kot bi smeli, se takoj posvetujte z zdravnikom ali s farmacevtom. Če ste pozabili vzeti prejšnji odmerek, ne vzemite dvojnega. Naslednji odmerek vzemite ob običajnem času. **Možni neželeni učinki** Zaspanost podnevi, zaprtje, zastoj urina, suha usta, zmedenost, rabdomioliza, povečane vrednosti kreatin fosfokinaze v krvi, motnje vida, palpitacije srca, sedacija, kognitivne in psihomotorične motnje. **Izgled zdravila Noctiben Mea in vsebina pakiranja** Filmsko obložene tablete so blede vijoličasto sive do vijoličasto sive, ovalne, izbočene, z razdelilno zarezo na eni strani. Zdravilo je na voljo v 3 pakiranjih z 10 tabletami v pretisnem omotu. **Način izdajanja zdravila** Zdravilo se brez recepta izdaja v lekarnah. **Imetnik dovoljenja za promet z zdravili** Krka, d. d., Novo mesto, Šmarješka cesta 6, 8501 Novo mesto, Slovenija. **Datum zadnje revizije navodila** 17. 5. 2019.

Pred začetkom jemanja zdravila natančno preberite navodilo, ker vsebuje za vas pomembne podatke. Pri jemanju tega zdravila natančno upoštevajte napotke v tem navodilu ali navodila zdravnika ali farmacevta. Če opazite katerikoli neželeni učinek, se posvetujte z zdravnikom, farmacevtom ali drugim zdravstvenim delavcem. O domnevnem neželenem učinku lahko poročate tudi neposredno nacionalnemu centru za farmakovigilanco, na način, kot je objavljeno na spletni strani [www.jazmp.si](http://www.jazmp.si).

Pred uporabo natančno preberite navodilo!

O tveganju in neželenih učinkih se posvetujte z zdravnikom ali s farmacevtom.

KRKA



Corrosion is a degradation of a material (usually a metal) due to its reaction with environment. Majority of corrosion processes on metals are electrochemical in nature. The occurrence of corrosion is dependent on number of factors including inherent material properties like composition and microstructure and environmental conditions such as corrosiveness of medium, temperature, stress and load (page 511).



Year 2019, Vol. 66, No. 3

